Papers presented to the

THIRD INTERNATIONAL COLLOQUIUM ON MARS

Pasadena, California
August 31 - September 2, 1981

Co-sponsored by

National Aeronautics and Space Administration

Lunar and Planetary Institute

Division of Planetary Sciences of the American Astronomical Society

Hosted by

Jet Propulsion Laboratory
California Institute of Technology

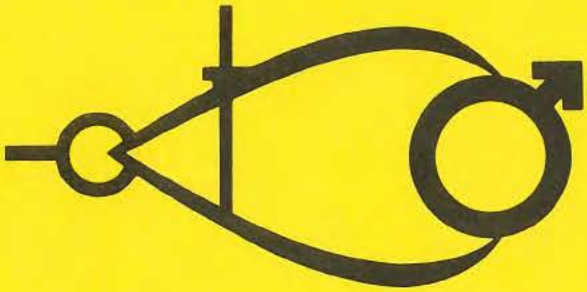

Papers Presented to the

THIRD INTERNATIONAL COLLOQUIUM ON MARS

CO-SPONSORED BY

NATIONAL AERONAUTICS AND SPACE ADMINISTRATION
LUNAR AND PLANETARY INSTITUTE
DIVISION OF PLANETARY SCIENCES OF THE AMERICAN ASTRONOMICAL SOCIETY

AUGUST 31 - SEPTEMBER 2, 1981

Compiled by the
Lunar and Planetary Institute
3303 NASA Road One
Houston, Texas 77058

LPI CONTRIBUTION 441

Compiled in 1981

by

LUNAR AND PLANETARY INSTITUTE

PREFACE

This volume contains papers which have been accepted for publication by the Organizing Committee for the Third International Colloquium on Mars. Papers were solicited which address one of the following major topics:

1. The Geophysics of Mars
2. Volcanism on Mars
3. The Geology of Mars
4. The Atmosphere of Mars
5. Long-term History of the Atmosphere-cap-regolith Volatile Regime

The Organizing Committee consisted of A. L. Albee (Chairman), Jet Propulsion Laboratory and California Institute of Technology; R. E. Arvidson, Washington University; J. M. Boyce, NASA Headquarters; D. L. DeVincenzi, NASA Headquarters; F. P. Fanale, Institute for Planetary Geoscience; R. Greeley, Arizona State University; G. E. Hunt, U. S. Geological Survey, Denver; T. B. McCord, Hawaii Institute of Geophysics; R. E. Murphy, Goddard Spaceflight Center; R. J. Phillips, Lunar and Planetary Institute; J. B. Pollack, NASA Ames Research Center; C. W. Snyder, Jet Propulsion Laboratory; J. Veverka, Cornell University.

Logistic and administrative support for this conference has been provided by C. W. Snyder, Executive Secretary (Jet Propulsion Laboratory); C. L. Snyder (Jet Propulsion Laboratory) and P. H. Jones (Lunar and Planetary Institute).

This abstract volume has been prepared under the supervision of K. Hrametz (Technical Editor, Lunar and Planetary Institute, Houston).

Papers are arranged alphabetically by the name of the first author. Indexes are provided by heavenly body, subject, & author.

The Lunar and Planetary Institute is operated by the Universities Space Research Association under Contract No. NASW-3389 with the National Aeronautics and Space Administration.

TABLE OF CONTENTS

INDICES

THE SURFACE SOIL OF MARS Carlton C. Allen[1], James L. Gooding[2], Michael J. Jercinovic[1], and Klaus Keil[1], [1]Department of Geology and Institute of Meteoritics, University of New Mexico, Albuquerque, NM 87131, [2]Jet Propulsion Laboratory, Pasadena, CA 91109.

The surface soil of Mars is commonly referred to as an aeolian blanket dominated by smectite clays. After nearly five years of Viking data analysis it is worthwhile to reexamine the data that led to this conclusion and to attempt to define reasonable sources for the Martian soil. Two proposed sources are the alteration products of volcanic glass (palagonite) and the alteration products of impact melt rocks.

Data The Martian surface has been characterized by ground-based visible and near-infrared reflectance spectroscopy and radar roughness measurements, flyby and orbital photography at resolutions as high as 8 m, orbital thermal inertia mapping and by experiments aboard the two Viking landers. The landers provided high resolution multi-band photography, bulk soil chemical analyses, estimates of soil moisture and semi-quantitative information on soil particle size, cohesion, density and magnetic properties. Few solid data exist concerning soil mineralogy, thickness, age or the geologic histories of the two landing sites.

Mineralogy Toulmin, et al. (1) summarized the initial efforts to translate the Viking lander bulk chemical analyses into likely mineral assemblages. The elemental data were converted to likely oxides and attempts were made to match this composition with mixtures of minerals. The best matches to the Martian soil are mixtures of the alteration products of basaltic rocks, with the smectite clays nontronite, montmorillonite and saponite dominating. Despite the obvious pitfalls of inferring mineralogy from bulk chemistry, and explicit warnings from the original authors concerning the non-uniqueness of their solution, a smectite clay composition for the Martian soil has become entrenched in much of the current thought which prevails among planetary geologists.

The assumption that particular clay minerals dominate the Martian surface can have serious implications if the properties of these clays are used to calculate planetary properties such as the volatile storage capacity of the regolith. Therefore, this assumption requires critical examination. The thermodynamic stability of smectites and their formation in the absence of liquid water have been questioned by Gooding (2). The contradiction between red (ie. oxidized) surface rocks and clays which are indicative of a reducing environment was noted by Baird, et al. (3). Singer (4) reported that both pure crystalline smectites and mixtures of these clays yield poor visible and near-infrared reflectance spectral matches to the areas of Mars thought to be similar to the Viking landing sites. Thus, a simple smectite-dominated composition seems an inadequate analog to the soil of Mars.

Palagonite The dominant alteration product of mafic volcanic glass is a yellow-orange, semi-amorphous mineraloid commonly referred to as palagonite. Toulmin, et al. (1) specifically proposed palagonite as a possible analog to Martian soil, and the suggestion still appears valid. Allen, et al. (5) have shown that the range of chemical compositions of

palagonite matches the Viking soil analyses for all major elements except aluminum. In addition, the characteristic particle size, bulk magnetic susceptibility and spectral reflectance signature are reasonably close to the rather uncertain Martian values. Singer (4) stated that the "alteration products of mafic volcanic glass currently provide the spectrally most reasonable terrestrial analogs to bright soils on Mars." Evans and Adams (6) concluded that similar "amorphous gels" have spectral signatures compatible with the colors of certain surface units at the Viking 1 landing site.

Terrestrial palagonite is a product of low temperature alteration of mafic volcanic glass in the presence of ground water or hydrothermal fluids. A generally similar mafic surface composition on Mars is often assumed (1), but liquid water cannot currently exist as a thermodynamically stable phase on the Martian surface. Gooding and Keil (7) have proposed gas-solid reactions between the atmosphere and volcanic and impact glass on the surface as a possible source of clay-like minerals on Mars. Allen, et al. (5) favor the interaction of volcanic lava with near-surface ice, analogous to subglacial volcanism on Earth which produces massive palagonite deposits by hydrothermal alteration of glass.

Altered impact melt rocks Newsom (8) and Kieffer and Simonds (9) also appealed to hydrothermal alteration to produce the Martian soil, but prefer impact energy as a heat source. They cited the alteration which is common in the melt sheets and suevite of terrestrial craters and postulated similar processes on Mars.

Direct comparison of alteration products in terrestrial and Martian craters is hampered by expected large differences in target materials. Most Martian craters, at least in the plains areas such as those sampled by Viking, probably formed in mafic volcanic rocks. However, nearly all terrestrial craters formed in rocks with bulk compositions approaching that of granite. Thus the alteration products themselves are probably not directly comparable to those on the Martian surface. However, the terrestrial material can indicate the conditions of alteration after an impact and thus point to the types of material that should form in more mafic target materials on Mars.

We have studied melt rock from seven craters to date, and found two distinct alteration product compositions. The rocks at Ries, Lake St. Martin and Lake Mien predominantly alter to a high-silicon montmorillonite composition (10). Samples from Brent, Clearwater East, Sääksjärvi and Rochechouart alter to a low-silicon, high-iron and high-magnesium material which approximates the composition of chlorite (11, 12). These clays and their associated zeolites and other authigenic minerals are the products of low pressure hydrothermal alteration at temperatures of only a few hundred degrees Celsius (13). These conditions are similar to those which produce palagonite when rocks of basaltic composition are altered. Thus, palagonitic material may be expected to be formed as the impact melt rocks of a basalt target cool in the presence of ground water.

The volume of the melt rock component in the Martian regolith is an open question. Significant quantities of ground water in terrestrial target rocks decrease the volume of impact melt relative to that in craters formed in dry rocks by approximately two orders of magnitude (9). Experimental impacts into dry and wet granitic powders support these observations. A shock pressure of 320 kb lithified and partially melted

the dry powder. However, after a similar shock a sample containing approximately 15 wt % water retained its particulate form and showed little evidence of melting. Similar experiments using basalt targets are in progress. If the Martian regolith contains substantial quantities of water or ice the production of impact melt may be extremely low.

Conclusions Viking lander data are generally interpreted to indicate a smectite clay mixture as the dominant component of the surface soil of Mars. This interpretation is questionable, based on thermodynamic calculations and reflectance spectroscopy. Palagonite, the low temperature hydrothermal alteration product of basaltic glass, provides a good match to available data. Glass may be produced on Mars by volcanic or impact processes, and both could provide the starting material for palagonitic alteration. Melting by impact may be severely inhibited, however, by the presence of significant quantities of near-surface water or ice.

Acknowledgments We thank F. Hörz, R.A.F. Grieve and D. Stöffler for providing samples for analysis, and F. Hörz for assistance with the impact experiments. This research was supported by NASA Grant NSG-7579 to Klaus Keil. JPL contributions were funded by NASA Contract NAS 7-100.

References

(1) Toulmin, P. III, et al. (1977) J. Geophys. Res. 82, p. 4625-4634.
(2) Gooding, J.L. (1978) Icarus 33, p. 483-513.
(3) Baird, A.K., et al. (1977) J. Geophys. Res. 82, p. 4595-4624.
(4) Singer, R.B. (1981) Lunar and Planetary Science XII (abs), p. 996-998.
(5) Allen, C.C., et al. (1981) Icarus (in press).
(6) Evans, D.L., and Adams, J.B. (1980) Proc. Lunar Planet. Sci. Conf. 11th, p. 757-763.
(7) Gooding, J.L., and Keil, K. (1978) Geophys. Res. Lett. 5, p. 727-730.
(8) Newsom, H.E. (1980) Icarus 44, p. 207-216.
(9) Kieffer, S.W., and Simonds, C.H. (1980) Rev. Geophys. and Space Phys. 18, p. 143-181.
(10) Stöffler, D., et al. (1977) Geol. Bavarica 75, p. 163-189.
(11) Papunen, H. (1973) Bull. Geol. Soc. Finland 45, p. 29-34.
(12) Lambert, P. (1977) in Impact and Explosion Cratering, Pergamon, p. 449-460.
(13) Deer, W.A., et al. (1962) Rock Forming Minerals, Vol. 3, Longarms, Green and Co., London.

A LAPIES STRUCTURE IN CYDONIA

Gerard Andlauer, C P R 67000, Strasburg, France

The Cydonia site is streaked by a range of parallel grooves that are to refer to the terrestrial analogue of the lapies. The lapies is an erosive structure that occurs in a carbonate bed rock under the influence of acid rain water.

The volcanic oxide material of Mars has been altered in carbonates under the effect of the air carbon dioxide (1). The early planet implied a notable water cycle that infers the occurrence of frequent rains of diluted carbonic acid - $H_2O + CO_2 - H_2CO_3$. The carbonate bed rock dissolves in the rain flood in the feature of regular groove scrape.

(1) G. Eglington and J. R. Maxwell, Nature 1977, vol. 265, p. 493-494.

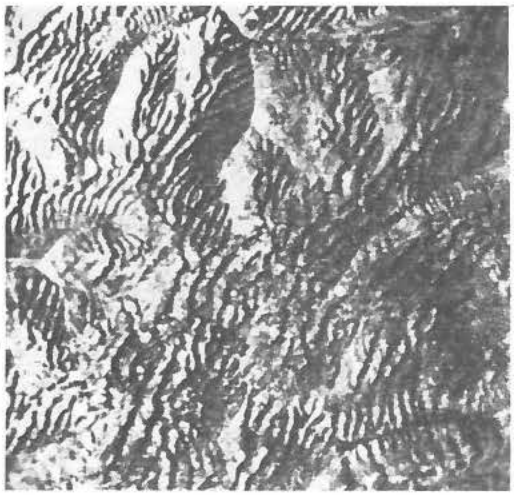

The Air Abdi - Dogger - plateau
on the scale of 1/50000th

A LAPIES STRUCTURE IN CYDONIA

Andlauer G.

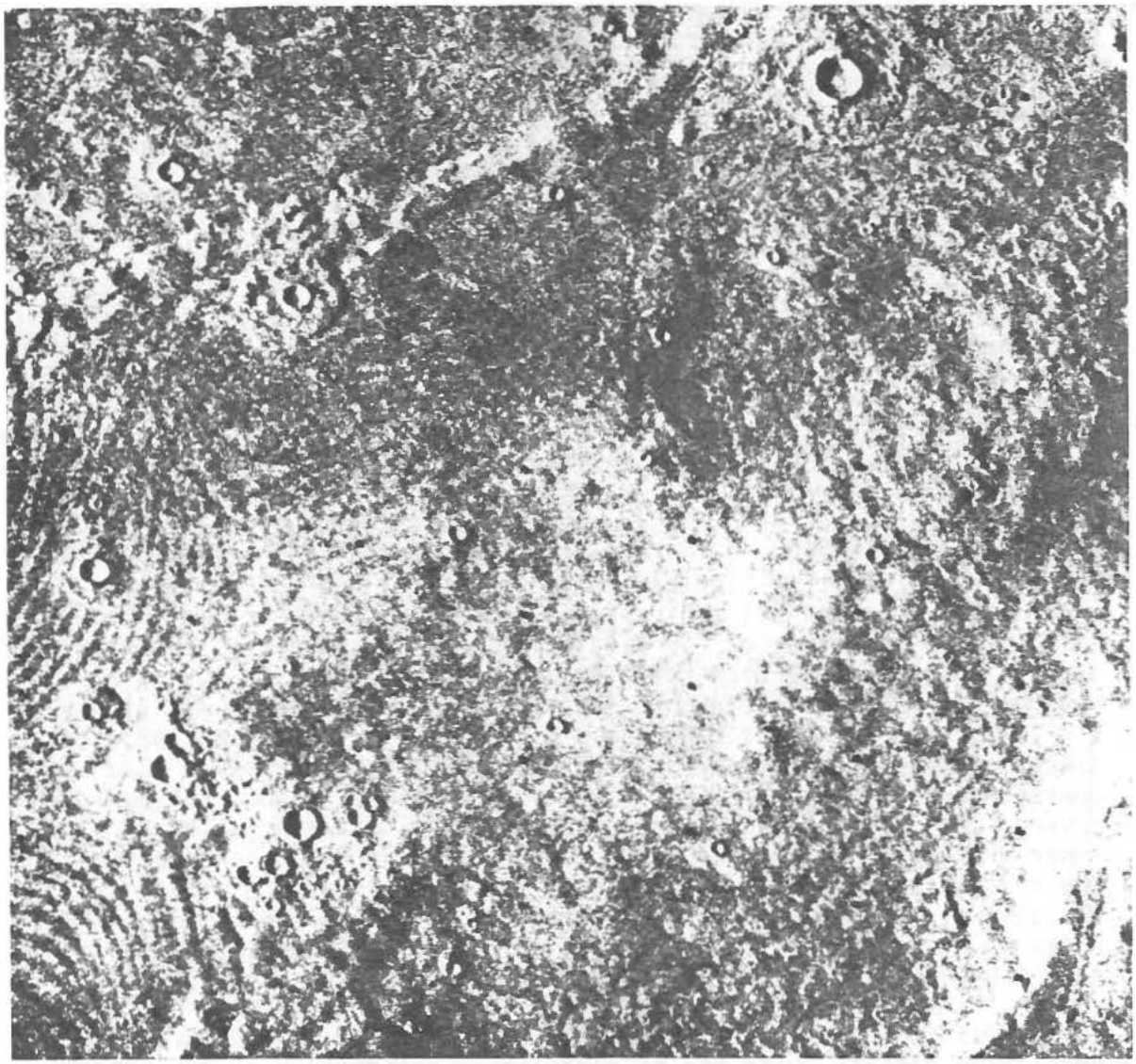

The Cydonia site 44° N
at an altitude of 2000 km

EFFICACY OF AEOLIAN PROCESSES ON MARS - PRESENT AND PAST;
Raymond E. Arvidson, Edward A. Guinness and Aaron P. Zent, McDonnell Center for the Space Sciences, Dept. of Earth and Planetary Sciences, Washington University, St. Louis, Missouri 63130

The role played by aeolian processes in modifying the Martian surface has been greatly clarified through use of both Viking Orbiter and Lander data. In this abstract we describe: (a) the variety of materials seen from the Lander, (b) the characteristics (color, thickness, etc.) of the aeolian deposits that have accumulated since the Landers touched-down in 1976, (c) how the materials at the sites compare to the global variety seen on Mars, and (d) the evidence for long-term erosion rates for rock and soil deposits. Our goal is to summarize our understanding of the efficacy of aeolian processes on Mars at present and during the past. In a companion paper, Strickland (1) describes in detail a model stratigraphy for soils at the landing sites and how the soil types and stratigraphy may be extended on a regional scale, based on Viking Lander and Orbiter data.

Landing Sites: Brightness values derived from the 6 channel (.4 to 1.0 micrometers) Lander data for materials exposed at the landing sites are highly correlated. Typical values for the linear correlation coefficients between pairs of channel brightness values range from 0.95 to 0.98. The high degree of correlation between the channels implies a surface where the red/blue ratio dramatically increases with increasing brightness. These correlations suggest that particle size variations play a role in the color variations seen for the soils exposed at the sites, since finer-grained materials are usually brighter and redder than coarser-grained materials (2). In particular, the bright, red soil that covered only part of the sites before the 1977 dust storms may be finer-grained than the underlying darker, bluer soils. However, not all the color variations can be explained on the basis of grain-size variations. For instance, the duricrust is relatively orange and the rocks at the sites display a variety of colors that may exceed the range seen from Earth (3,4). Neither of these two examples can be easily related directly to grain size variations. The scattering properties of the red soils at the sites are strongly backscattering and have prominent opposition effects, with the bi-directional reflectance at a 5° phase angle being .11 and .17 averaged over the Lander blue and green channel passbands (2). The bi-directional reflectance at 5° phase angle ranges from .30 to .39 averaged over the red band (2). The red soils are most like classic Martian bright areas as seen from Earth (2,4).

Landing Site Changes: In 1977, two global-scale dust storms could be seen from both Orbiters and Landers. Both landing sites were blanketed with a new layer of bright, red dust that is probably no more than a few micrometers in thickness (5). In addition, the VL2 site accumulated a layer of condensates during the winter season that took approximately 200 sols to evaporate back into the atmosphere. The new soil deposit is probably somewhat thicker at the VL2 site, based on the degree of obscuration of the color of underlying materials, suggesting a coupling of the condensates and dust. It is conceivable that the new dust at VL2 accumulated as the nuclei of snow, although direct evidence for such a process does not exist. The photometric properties of the new soil are statistically indistinguishable from the properties of the bright, red soil seen at the VL1 site after touchdown. The landing sites were probably blanketed by classic Mars bright area materials. Orbiter VIS color enhancements show that the blanketing deposit of red dust extended

over the Chryse basin, but not over the Lunae Planum complex to the west (1). Thus far, the new dust deposit has not been disturbed by wind erosion. It is likely, however, that no more than a few seconds would be needed to remove the new dust deposits, once the rare but significant gust of high velocity wind occurs.

Global Variations: The R/G, R/V, G/V color data, albedo, and thermal inertia Mars Consortia data for the ± 15° lat. band were examined to statistically define the variety of materials seen globally on Mars. The set can be thought of as a 5 dimensional representation of the surface properties of Mars. We performed a 5 dimensional principal components rotation on the data set. The first principal component vector trends in a direction that explains the maximum possible fractional variance of the data. In effect, it is the direction of the dominant data trend. We find that 58% of the variance is explained by the first component. Displayed as an image, it is clear that this trend corresponds to "typical" Mars, with high albedo areas having low thermal inertia and high values of R/V, G/V, R/G. Dark areas have high thermal inertia, and low values of the color ratios. The other principal component directions show other trends and clusters, i.e., deviations from "typical" Mars, that correspond, at least in part, to local and regional geological units. We find for example, that in some cases the degree of stripping (10's of meters) seen in high resolution Viking Orbiter frames is correlated with these data. However, in other cases there is no correlation. The distribution of surface materials of Mars thus appears to be controlled by aeolian deposits that overlay and intermingle with local and regional intrinsic variations. The new soil deposits at the landing sites are probably the same materials as the bright, low thermal inertia, high R/V, G/V, and R/G materials, seen in the Mars Consortia data.

Long Term Variations: The wind-blown deposits at the VL1 site exhibit cross bedding and sculpting that indicate an accumulation during a time period when the winds were blowing in a N-S direction. This direction is consistent with the direction of peak winds during current dust storms (2). However, the direction of peak winds at the VL1 site undoubtedly varies over a timescale of tens of thousands of years due to obliquity oscillations (8). It is fairly safe to assume that these deposits are therefore younger than about ten thousand years. Since the deposits are, on the average, a few centimeters thick, this implies an average soil redistribution rate of about a micrometer/year. The extent of stripping of soil materials at the VL2 site as seen from the Viking Orbiters also implies a soil redistribution rate of about a micrometer/year, but averaged over several billion years (8). Thus, averaged over timescales of one, tens of thousands, and several billion years, not more than about a micrometer/year of soil redistribution is needed to explain the characteristics of the landing sites. On the other hand, the relatively pristine state of many of the craters surrounding the VL1 site (and much of the equatorial zone) implies a rate of rock breakdown and removal by wind and other processes that is several orders of magnitude less than the soil redistribution rate, averaged over several billion years (8). These results imply that soil is relatively rapidly redistributed on Mars, forming regional blankets (deposition) or stripped zones (erosion) over relatively short timescales. On the other hand, the rate of breakdown and removal of rock by wind has been relatively low over much of geological time. Rock breakdown by UV or other methods must, therefore, have been minimal in extent. Wind-blown soils on Mars were either produced early in geologic time or they orginated from friable

(early eroded) ash deposits. Finally, dramatic climatic excursions over the past several billion years would seem to be ruled out, since an increase in atmospheric density should lead to a dramatic increase in aeolian abrasion rates. The degree of preservation of rocky materials and similarities in soil redistribution rates argues against such an increase.

REFERENCES

1. Strickland, E.L. III, 1981, these abstracts.

2. Guinness, E.A., 1981, J. Geophys. Res., in press.

3. Strickland, E.L. III, 1979, Proc. Lunar Planet. Sci. Conf. 10th, 3055-3077.

4. Singer, R.B. and E.L. Strickland III, 1981, Abs., Lunar Planet. Sci. Conf. 12th, 999-1001.

5. Guinness, E.A., R.E. Arvidson, D.G. Gehret, L.K. Bolef, 1979, J. Geophys. Res., 84, 8355-8364.

6. Jones, K.L., R.E. Arvidson, E.A. Guinness, S.L. Bragg, S.D. Wall, C.E. Carlson, D.G. Pidek, 1979 , Science, 204, 799-806.

7. Sagan, C., D. Pieri, P. Fox, R. Arvidson, E. Guinness, 1977, J. Geophys. Res., 82, 4430-4438.

8. Arvidson, R.E., E.A. Guinness, S. Lee, 1979, Nature, 278, 533-535.

HYDRAULIC FRACTURING ON MARS?

Babaei,A. and Whitford-Stark,J.L. Geology Department,University of Missouri, Columbia, Missouri 65211.

The structures of the Syria-Thaumasia block have been variously ascribed to tensional failure due to membrane stresses arising from polar wander(1), lateral motions of a tectonic plate(e.g.,2), and gravity flow and slide of a surficial lithosphere off the Tharsis bulge(3). Detailed mapping shows that there were several episodes of volcanism and faulting within the Syria Planum area(4). The present authors propose that at least some of the fractures may be the product of hydraulic fracturing(e.g.,5) resulting from the intrusion of magmatic material.

Figure 1 shows one of the longest and most discrete fractures in Solis Planum. For the purpose of this discussion it will be named the Solis fault. The measured length of the Solis fault is approximately 350 km. It is, however, buried by lava at latitude 27°S and may have originally continued another 150 km further north. It does not appear that extrusive material was emitted from the fault. The Solis fault is composed of at least 13 discrete sections with both right- and left-stepping displacements; although left-stepping displacements predominate. In each case the separation of the tips of the segments either overlaps or is zero; they are never apart. It would appear that the ends of right-stepping sections have become connected. This supports the arguments of Segall and Pollard(6) who show that propogation of left-stepping extension cracks is away from each other whereas for right-stepping, propogation is toward each other.Additionally there is no evidence for lateral repitition of the fault planes.

The authors made a literature survey for terrestrial faults that might be comparable to the Solis fault. Although some terrestrial faults are of considerable length(e.g.,Anatolian fault; $\sim$ 100 km) there are few that exhibit non-curved,en echelon fracture segments. Structures such as the mid-Atlantic ridge rift are complicated by offsets produced by transform faults. Close analogies are the fractures on volcanoes and small volcanic rifts (7,8). The Solis fault differs, however, from terrestrial volcanic rifts in that the latter structures tend to have several parallel fault segments. The lengths of segemnts of both terrestrial and the Solis faults were measured. Additionally, the separation distances(the along strike distance between the end points of adjacent segments) and the displacement distances(the horizontal distance between adjacent fault segments) were measured.These were normalized to the length of the longest feature within each area and are plotted in figures 2a and 2b. Although there are gross differences in scale between the terrestrial and martian structures, the normalized values do not fall into distinct domains. This would indicate that the process which led to the production of both the terrestrial and martian structures may have been similar.

The closest terrestrial analogies to the Solis fault in term of morphology are some dike systems. Figure 3 shows the Tertiary dike swarm of northern England. In spite of poor exposure and erosion, the Cleveland dike displays a regular en echelon

HYDRAULIC FRACTURING

Babaei,A. and Whitford-Stark,J.L.

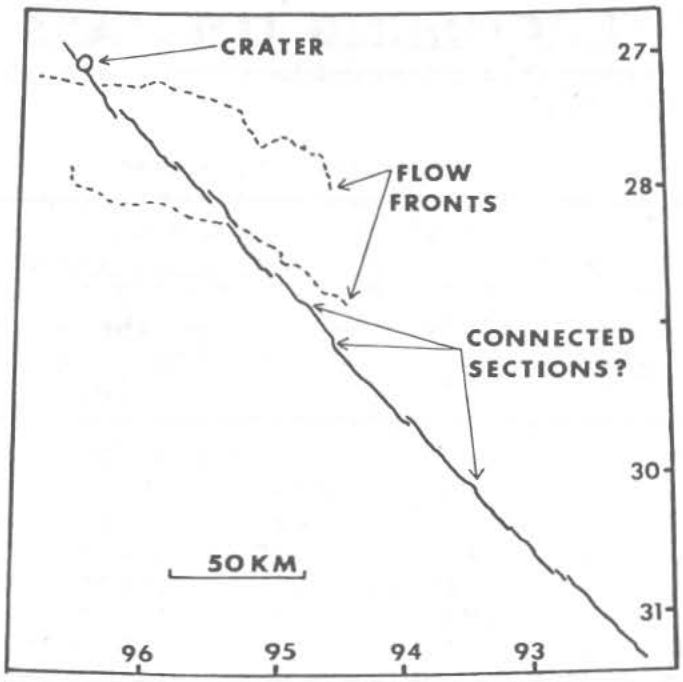

Figure 1: Map of the Solis fault in sothwest Solis Planum on Mars. Note the offsets and overlapping of fault segments. Also that the fault cuts through two older flow fronts yet to the north it would appear to be buried by lava. The fault was thus produced while volcanism was still active in the area.

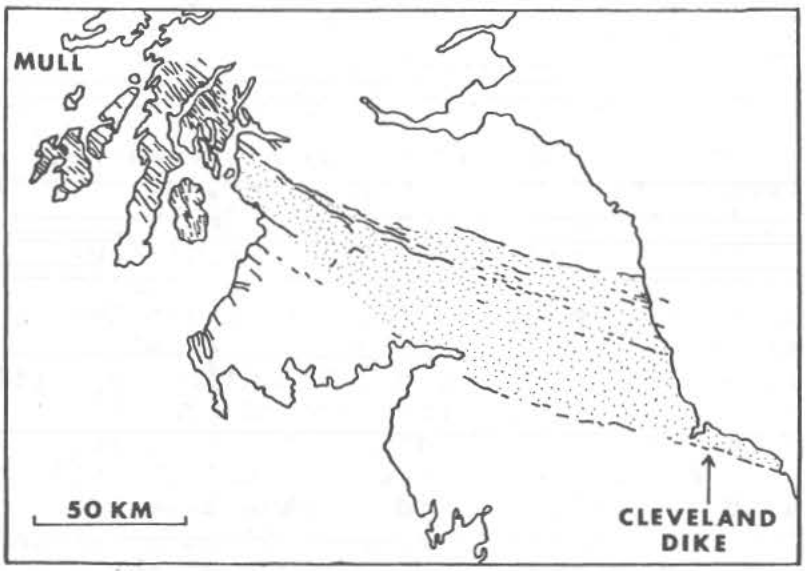

Figure 3: Map showing the Tertiary dike swarm of northern England;modified after Holmes and Harwood(9). The dot pattern illustrates the fan-like pattern of the dike system which (9) believed to be centered on Mull. Other dikes are related to other intrusive centers.

pattern. It does differ, however, from the Solis fault in that the segment tips are apart rather than overlapping. The Tertiary dike-Solis fault analogy is appealing since the former is also related to a major volcanic center and has been interpreted(9) to display the fan-like appearance characteristic of the martian Thaumasia area.

In summary, it is concluded that some of the graben structures on the Tharsis dome could be the product of hydraulic fracturing. Although the Solis fault does not appear to have been a source for lava, it is possible that it is underlain by a dike. The lack of apparent lateral repetition of fault planes along the Solis fault may result from the burial of such structures by later lava or wind-blown materials. Alternatively, such structures may have been prevented from being formed if the surface

HYDRAULIC FRACTURING

Babaei,A. and Whitford-Stark,J.L.

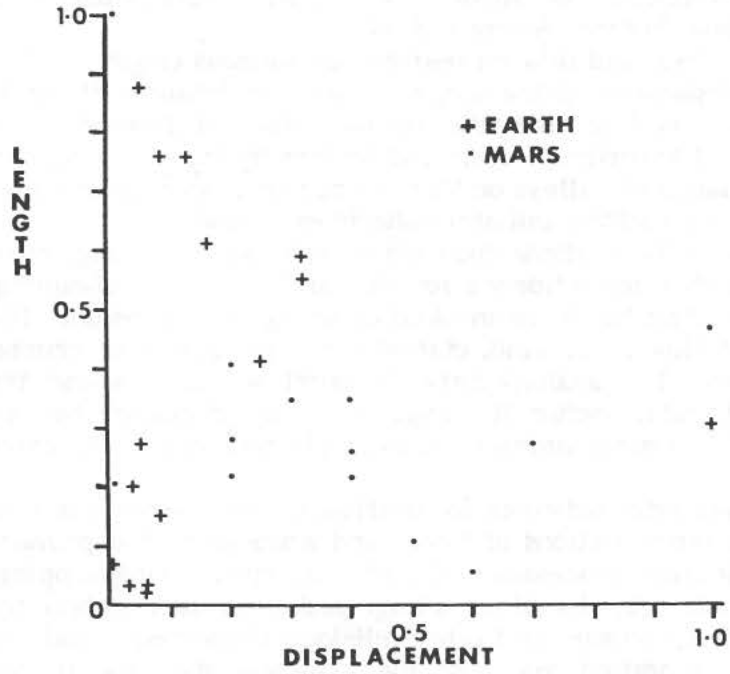

Figure 2a: Plot of the displacement versus segment length for the Solis fault and some terrestrial graben structures. The data have been normalized to the length of the longest feature within each area. The terrestrial data were derived from maps in 7,8,and 10. Note that the data from the two planets do not fall into distinct domains.

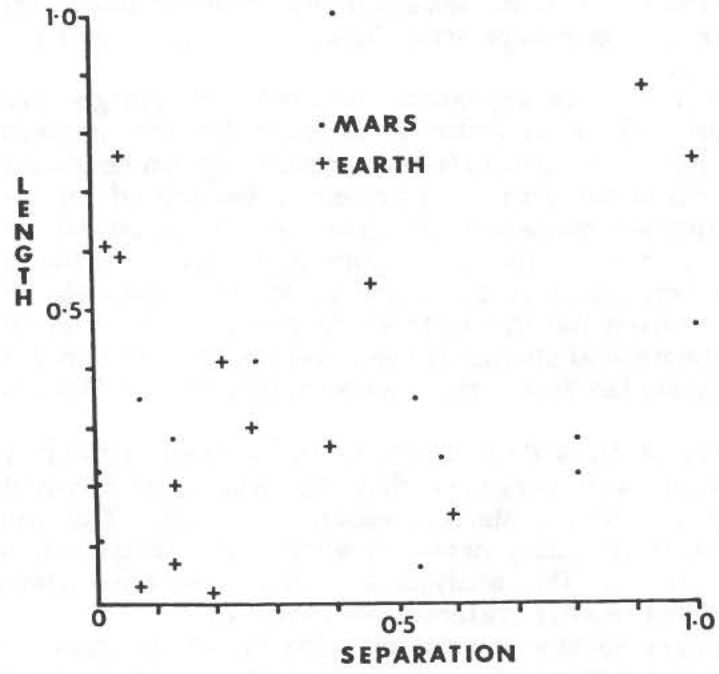

Figure 2b: Plot of the separation versus segment length for the Solis fault and some terrestrial graben structures. The data have been normalized to the length of the longest features within each area. The terrestrial data were derived from maps in 7,8, and 10. Note that the data from the two planets do not fall into distinct domains.

materials were sufficiently cohesive. Such a situation might arise as a result of the presence of massive surface basalts and ground ice.

References:1) McAdoo,D.C. and Burns,J.A.(1975) Earth Planet.Sci. Lett.25,347-354. 2)Courtillot,V.E. et al(1975) Earth Planet.Sci. Lett.25,279-285. 3)Wise,D.U. et al(1979)Icarus 38,456-472. 4) Scott,D.H. & Tanaka,K.L.(1980) Proc.Lunar Planet.Sci.Conf.11th, p.2403-2421. 5)Pollard,D.D. & Holzhausen,G(1979)Tectonophys.53, 27-57. 6)Segall,P.& Pollard,D.D.(1980)J.Geophys.Res.85,4337-4350. 7)Sylvester,A.G.(1974)Norsk.Geol.Tidds.54,385-393. 8)Sigurdsson, H.& Sparks,R.S.J.(1978)Bull.Volc.41,1-19. 9)Holmes,A. & Harwood, H.F.(1929)Min.Mag.22,1-52. 10) McGill,G.E. & Stromquist,A.W. (1979) J.Geophys.Res. 84, 4547-4563.

THE CHANNELS AND VALLEYS OF MARS. Victor R. Baker, Department of Geosciences, University of Arizona, Tucson, Arizona 85721

The discovery of channels, valleys, and related features of aqueous origin on Mars is of profound importance in comparative planetology. The significance of these landforms can be appreciated by recalling that the fundamentals of geology were established by studies of the origin of terrestrial rivers and valleys by Hutton, Playfair, and Lyell. The diversity and abundance of valleys on Mars comprise a major problem to be resolved by our models of planetary surface and atmospheric evolution.

Although Schumm (1) attributed the outflow channels to tension fracturing, most other investigators have concluded that the evidence for fluidal flow is overwhelming. However, nearly every conceivable fluid has been invoked as an agent of erosion. The list includes low-viscosity turbulent-flow lava, wind, glacial ice, liquefaction of crustal materials, debris flows, and water. The analogy between outflow channels and the Channeled Scabland, a product of catastrophic flooding, has been demonstrated by detailed morphological mapping (2), by morphometric analysis (3), and by consideration of flow physics (4).

A difficulty with any of the proposed schemes for outflow channel genesis is that the channels experienced extensive modifications of floors and walls after the primary fluid-flow events (5). The modification processes included cratering, spring sapping, thermokarst phenomena, eolian processes, slumping, rilling, pedimentation, debris fan development, talus production, debris flowage, and other hillslope phenomena. Indeed, such a variety of processes have modified many of the channels that the unique signature of any one has proven difficult to isolate. Moreover, the channels and valleys may have served as conduits for more than one large-scale flow, leading to a composite of erosional and depositional landforms.

The fluid flows on Mars appear to have repeatedly invaded and enlarged pre-existing depressions on the Martian surface in order to account for the immense volumes of the channels (Figure 1). Also many channels have probably grown headwards as chaotic terrain was created at points of subsurface fluid release. Because of this and because of various secondary modification processes, the cross-section of an outflow channel is not necessarily the cross-section of the responsible fluid flows. Although various terrestrial analogs have proven useful in the study of Martian channels and valleys, no one analog has fully accounted for the suite of features observed in the Martian examples. This has led to theoretical studies of the basic flow physics and how various flow systems might induce unique landforms that can be recognized on Mars (4, 6, 7).

The small channels and valleys of Mars ("runoff channels") proved difficult to interpret from Mariner 9 imagery. Early work suggested that they originated by runoff processes, requiring rainfall during an ancient Martian epoch (8, 9, 10). The first systematic sudy (11) revealed that the small valley networks were nearly ubiquitous on the older cratered surfaces of the planet. This analysis was confirmed when Viking imagery provided high resolution views of heavily cratered zones (12, 13).

The term "valley network" applies to Martian trough systems, which appear to form by fluid flow, but which, unlike the outflow channels, lack a suite of bedforms on their floors. The Martian valleys of greatest interest consist of interconnected, digitate networks that dissect extensive areas of heavily cratered uplands on the planet. These valley networks can be distinguished from trunk valleys, which display one or a few dominant troughs and relatively short tributaries. Examples of the latter valley type include Nirgal Vallis (14), Nanedi Vallis, and Bahram Vallis.

Junction angle statistics (13) and other morphological attributes of Martian networks indicate that rainfall, acting through overland processes, was probably not the direct cause of the patterns. Rather, a headward sapping process appears best able to account for the observed morphology (15, 16). Ground water, derived from an ice-rich permafrost, probably played a key role in valley network genesis.

CHANNELS AND VALLEYS

Baker, V. R.

On Mars the appearance of flowing surface water seems to be either perserverance-limited or release-limited. The former case includes the valley networks for which relatively slow release from the Martian permafrost poses few problems. Temperature changes, volcanic heating, and other phenomena can easily release the water; the problem is in maintaining prolonged flows on the planets surface. Prolonged surface flow requires such assumptions as a warmer, denser, ancient atmosphere (17), ice-covered rivers (18), or freezing point depressants. For the outflow channels the formative mechanism is release-limited. Short-duration floods are less severely constrained even by the present Martian atmosphere (19). The major problem is in yielding the immense quantities of water implied by the flow hydraulics of the outflow channels. The proposed release mechanisms include jokullhlaups of melted ground ice from an ice-rich permafrost heated by volcanism (12), liquefaction of sensitive subsurface materials on Mars (20), and sudden release of immense aquifers of very high permeability confined by the ice-rich permafrost (21). Although an extensive planet-wide permafrost system appears to have been involved(22), the precise release mechanism for fluids to form outflow channels remains highly speculative.

The channels and valleys of Mars indicate an ancient epoch of Martian atmospheric environment with higher temperatures and pressures that at present. If a ground-water flow system was involved in channel and network formation, the cessation of that system indicates that major changes occurred in the hydrologic cycle on Mars. However, the range of possible states in the responsible fluid flows does not allow a precise estimate of atmospheric conditions to be derived from geomorphological considerations alone. Channels, valleys, and related geomorphic features indicate that Mars possessed or retains a thick, ice-rich permafrost. The data suggest that either Mars was volatile-rich during its early history, especially the period of valley network formation, or that the planet was extremely effective at recycling its limited inventory of water.

REFERENCES: (1) Schumm S. A. (1974) Icarus 22, 371-384. (2) Baker V. R. and Kochel R. C. (1978) Proc. Lunar Planet. Sci. Conf. 9th, 3181-3192. (3) Baker V. R. and Kochel R. C. (1978) Proc. Lunar Planet. Sci. Conf. 9th, 3193-3203. (4) Baker V. R. (1979) Jour. Geophys. Res. 84, 7985-7993. (5) Baker V. R. and Kochel R. C. (1979) Jour. Geophys. Res 84, 7961-7983. (6) Komar Ph. D. (1979) Icarus 37, 156-181. (7) Komar P. D. (1980) Icarus 43, 317-329. (8) Masursky H. (1973) Jour. Geophys. Res. 78, 4009-4030. (9) Milton D. J. (1973) Jour. Geophys. Res. 78, 4037-4047. (10) Sagan C. et al. (1973) Science 181, 1045-1049. (11) Pieri D. C. (1976) Icarus 27, 25-50. (12) Masursky H. et al. (1977), Jour. Geophys. Res. 82, 4016-4038. (13) Pieri D. C. (1980) Science 210, 895-897. (14) Baker V. R. (1980) NASA Tech. Memo. 82385, 345-347. (15) Pieri D. C. et al. (1980) NASA Tech. Memo. 87116, 292-294. (16) Baker V. R. (1980) NASA Tech. Memo. 81776, 54-56, 286-288. (17) Pollack J. B. (1979) Icarus 37, 479-553. (18) Wallace D. and Sagan C. (1979) Icarus 39, 385-400. (19) Sharp R. P. and Malin M. C. (1975) Geol. Soc. America Bull. 86, 593-609. (20) Nummedal D. (1978) NASA Tech. Memo. 79729, 257-259. (21) Carr M. H. (1979) Jour. Geophys. Res. 84, 2995-3007. (22) Soderblom L. A. and Wenner D. B. (1978) Icarus 34, 622-637.

Figure 1. Sketch map (on next page) of channels, valleys, and related landforms around the southern margins of Chryse Planitia, Mars.

CHANNELS AND VALLEYS

Baker, V. R.

A NEW GLOBAL MODEL OF MARS GRAVITY FIELD

G. Balmino, B. Moynot, N. Valès (GRGS, Toulouse, France)

A spherical harmonic model of Mars gravitational potential up to degree and order 18 has been derived from a combination of two way Doppler tracking data of Mariner 9, Viking 1 and Viking 2 orbiters. The contribution of the low periapsis (300 km altitude) observations of the Viking orbiters shows up in the details of the martian geoidal surface, correlated with topographic features and results also in a very significant improvement or orbit computation.

All available Mariner and Viking data were processed in the form of long (up to 11 days) and short arcs (a few hours) so as to bring information about all the gravity field spectrum. This spectrum is discussed together with the spectrum of the topography and some conclusions are drawn about the level of compensation of features at various wavelengths.

COMPOSITION AND PROPERTIES OF THE MARTIAN SOIL AS INFERRED FROM VIKING BIOLOGY DATA AND SIMULATION EXPERIMENTS WITH SMECTITE CLAYS.

A. Banin, J. Rishpon and L. Margulies, The Seagram Centre for Soil and Water Sciences, The Hebrew University, Rehovot, Israel.

On the basis of the chemical-elemental composition of the Martian soil Toulmin et.al. (1), proposed that clays, mainly smectites such as montmorillonite and nontronite, are present in the Mars soil as major components. This was corroborated by spectral observations (2) and geomorphological evidence (3).

We have proposed (4,5) an hypothesis which seeks to explain the Viking biology experimental results (6) by chemical mechanisms and on the basis of the known surface properties of smectite clay minerals. These minerals have extensive, negatively charged surface area capable of adsorption of liquids, gases and ions and are active in catalytic reactions (see, e.g.,7). They are active ingredients of many soils on Earth and are abundant and chemically-stable minerals. Many features of the Viking Labeled Release (LR) experiment (8) were recently reproduced by us using smectite clays particularly in the iron and the hydrogen forms. Labeled carbon was released from the medium solution used in the Viking LR experiment when reacted with the clays, at rates and quantities similar to those measured by Viking on Mars, (Fig.1). The component in the solution that decomposes most readily was found to be formate, followed by lactate; glycine did not decompose at a measurable rate. The decomposition curve of the complete medium was essentially a summation of the decomposition of the formate and lactate, accounting for the slow-rate decomposition reactions that were measured by Viking on Mars (Fig.2). The reaction rate and its extent were affected by the pH, by the type of exchangeable ion, by salt additives and by preheating. Heating of the active clay (mixed with soluble salts) to 160°C in CO_2 atmosphere showed, in some cases, a decrease in the decomposition rate and activity, similar to the Viking results on Mars. However, heating in air or N_2 atmosphere usually enhanced the decomposition rate.

The main features of the Viking Pyrolytic Release (PR) experiment were also simulated recently using the PR TSM with iron and hydrogen clays supplied by us (Fig.3). The Ca-clay did not behave similar to the Martian soils. Thus the clay hypothesis seems to be supported by experimental simulation work using two independent methods.

According to our hypothesis, clay surface activity is responsible for decarboxylation and/or oxidation of organic acids in the LR experiment that results in the release of $^{14}CO_2$. The acalytic activity is modulated and affected by the surface properties of the soil, its rate being dependent on an optimal combination of pH, adsorbed ions, water content and substrate availability. Gas adsorption on the soil material, which presumably has a large specific surface area characteristic of the clays of the smectite group, is basically the cause for the N_2, CO_2 and Ar/CO release observed in the GEX experiment (13). The excessive O_2 release in the GEX experiment, observed only in the first "humid" run in VL-1 and not clearly observed in the later humid runs nor in the wet runs, remains to be explained. The small $^{14}CO_2$ fixation into organic matter observed in the Pyrolytic Release (PR) experiment may be explained by surface-catalyzed synthesis reactions from CO_2 and water or adsorbed hydrogen.

COMPOSITION AND PROPERTIES OF MARS SOIL

Banin, A. et al.

Though not intended for that originally, the results of the three Viking biology experiments are a valuable and unique source of information on the chemical nature of the Martian soil. These experiments, in essence, studied the interaction of the soil with gases, water, salts and organic compounds. By comparing the results of simulation experiments, (using various mixtures of active smectite clays with other minerals and soluble salts) to the Viking biology results, we may deduce, in a speculative way some additional constraints to the probable composition and properties of the Martian soil. On this basis we suggest that the soil pH is slightly acidic. Calcite ($CaCO_3$) content can not be high and should probably be almost zero. Gypsum ($CaSO_4 \cdot 2H_2O$) and possibly dolomite ($CaMg(CO_3)_2$) may be present as calcium bearing minerals. Saponite, a Mg-rich smectite and kieserite ($MgSO_4 \cdot H_2O$) may be present as the Mg bearing minerals. Gypsum and kieserite, both sulfur bearing minerals, are soluble enough to dissolve and redistribute in the soil profile forming the salt-rich surface crusts. The soil may contain some oxo-iron minerals and the adsorbed ions on the smectites contain a significant amount of iron and hydrogen.

In conclusion, the chemistry of the Mars surface soil, its equilibrium with the atmosphere and its morphology may be profoundly controlled by the complex properties of smectite clays, in the presence of various soluble salts.

References:

(1) Toulmin, P. III, A.K. Baird, B.C. Clark, K. Keil, H.J. Rose, P.H. Evans and W.C. Keliher (1977). J. Geophys. Res.82,4625-4658.
(2) Huck, F.O., D.J. Jobson, S.K. Park, S.D. Wall, R.E. Arvidson, W.R. Patterson and W.D. Benton (1977). J. Geophys. Res.82, 4401-4411.
(3) Nummedal, D. (1980). Reports of Planetary Geology Program. NASA TM 82385, 400.
(4) Banin, A. and J. Rishpon (1978). Life Sci. and Space Res.XVII, 55-64.
(5) Banin, A. and J. Rishpon (1979). J. Mol. Evol. 14, 133-152.
(6) Klein, H.P. (1979). Rev. Geophys. Space Phys. 17, 1655-1662.
(7) Anderson, D.M. and A. Banin (1975). Origins of Life 6, 23-33.
(8) Levin, G.V. and P.A. Straat (1977). J. Geophys. Res. 82, 4663-4667.
(9) Banin, A. and J. Rishpon (1980). Unpublished data.
(10) Hubbard, J.S. (1979). J. Mol. Evol. 14, 211-221.
(11) Hubbard, J.S. (1980). Personal Communication.
(12) Horowitz, N.G., G.L. Hobby and J.S. Hubbard. (1977). J. Geophys. Res. 82, 4659-4662.
(13) Oyama, V.I. and B.J. Berdahl (1979). J. Mol. Evol. 14, 199-210.

COMPOSITION AND PROPERTIES OF MARS SOIL

Banin, A. et al.

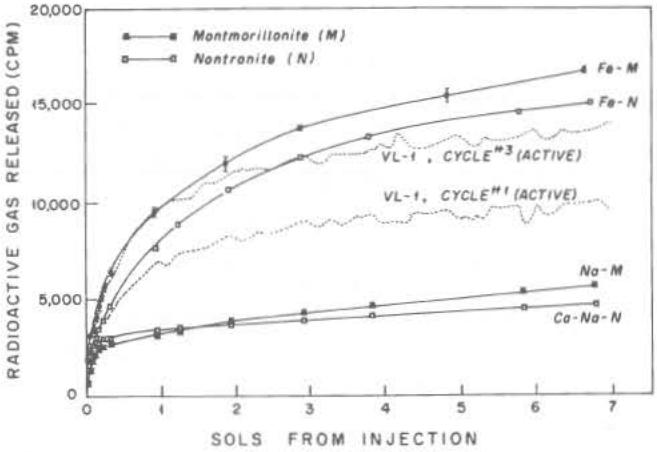

Fig.1

Comparison of radioactive gas release from the Viking LR medium (a dilute solution of seven simple organic substances) when reacted with the Mars soil in Viking Landers (VL; dotted lines) with that obtained upon reaction with various smectite clays in the laboratory (continuous lines). Viking data are redrawn from Levin and Straat (8). Simulation data by Banin and Rishpon (5).

(Figure published courtesy of Springer-Verlag, N.Y.)

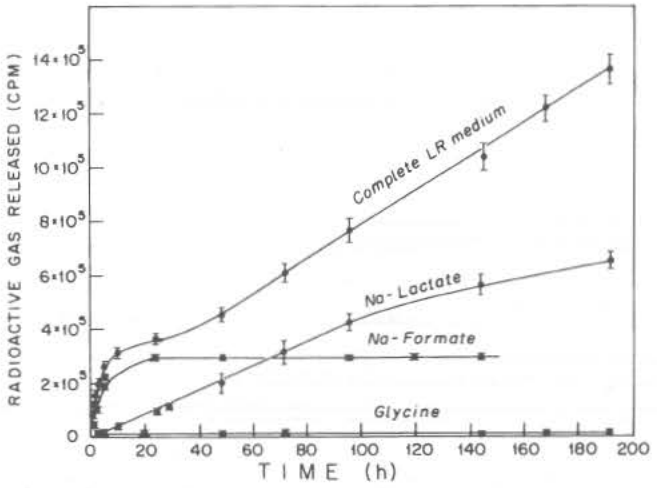

Fig.2

Decomposition curves of labeled format, lactate, glycine and the complete LR medium reacting with H-montmorillonite in simulation of the LR reaction on Mars. (CO_2 adsorption technique; Banin and Rishpon, 9).

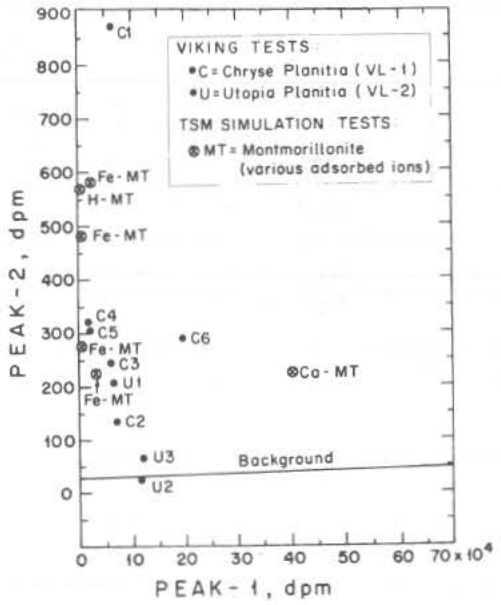

Fig.3

Comparison of Viking PR results with TSM simulation using H-, Fe- and Ca-montmorillonite. TSM simulation was conducted in the "Light, dry, active" mode. The modified montmorillonite clays were supplied by us and experiments were conducted by Hubbard (10,11). Data for the Mars soil were taken from Horowitz et al. (12). Note the similarity of the behavior of the iron- and hydrogen- montmorillonite samples to that of the Martian soils.

LINEAR MODELING OF MARTIAN BAROCLINIC WAVES; Jeffrey R. Barnes, Department of Atmospheric Sciences AK-40, University of Washington, Seattle, Wash. 98195

Analysis of the pressure, wind, and temperature data returned by the two Viking Landers has revealed the existence of transient weather disturbances during the fall, winter, and spring seasons of two annual cycles (1,2,3). Time spectral analysis shows that the data from both years are characterized by dominant spectral peaks at periods of 6-8 sols and at several periods between 2-4 sols. Cross-spectral analysis of the highly coherent pressure, wind, and temperature oscillations at Lander 2 yields phase lags consistent with those expected for eastward travelling, baroclinic waves centered to the north of Lander 2 (2,3). Planetary zonal wavenumbers and phase speeds of the disturbances have been determined using geostrophic wind values calculated on the basis of analysis of the observed semi-diurnal atmospheric tides. The zonal wavenumbers fall into two ranges: 1.5-2.0 corresponding to the 6-8 sol periodicity, and 3-5 for the 2-4 sol periods. The phase speeds are $\sim$ 10-20 m/sec, with some indication of an inverse dependence on wavelength. These wavenumbers and phase speeds are roughly consistent with those expected on the basis of the results of simple linear baroclinic instability theory (2,4).

Two numerical models have been used to further investigate the properties of linear barolinic waves in the Martian atmosphere: (1) a quasi-geostrophic, β-plane model, and (2) a quasi-geostrophic, spherical model. Both models allow the specification of arbitrary vertical profiles of basic state temperature (static stability) and zonal wind with high resolution, and the spherical model permits an arbitrary meridional profile of zonal wind as well. The characteristics of the most unstable linear mode at a given wavenumber are determined by time integration. Three physical effects relevant to baroclinic waves in the Martian atmosphere have been incorporated in both models: (1) radiative damping of the waves (in the form of Newtonian cooling), (2) surface friction (Ekman pumping), and (3) zonally symmetric topography (a sloping lower boundary). Mariner 9 IRIS and radio occultation data, and Viking IRTM and radio occultation data have been used to construct plausible basic states for the models.

The typical model growth rate spectrum, for no friction and no topography, displays a peak at wavenumber m = 3, with growth rates falling off relatively sharply towards lower m and more slowly at higher m. Growth rate peaks at m = 2-5 have been found for the basic states examined, the shorter wave instability being very sensitive to the lower level static stability and wind shear. Maximum growth rates are $\sim$ 0.5-1.0 $(\text{sols})^{-1}$, with radiative damping reducing growth relatively slightly ($\sim$ 10-20%). The phase speeds of the model waves lie primarily in the range 10-20 m/sec, with a somewhat variable wavelength dependence.

Ekman friction is found to have a very strong effect on the growth rate spectra, for values of the eddy viscosity of $\sim$ 5-10 m^2/sec. The short wave growth (m > 4) is sharply reduced relative to that at longer wavelengths. The model results indicate that zonally symmetric topography also has strong effects on the waves. A reduced and smoothed Martian topography is strongly stabilizing at all wavelengths and increases the phase speeds of the waves in the spherical model (zonal topography as large as the Martian topography cannot be validly treated by such a pressure coordinate model).

LINEAR MODELING OF BAROCLINIC WAVES

Barnes, J. R.

The structure of the model Martian waves is quite similar to that found for model terrestrial baroclinic waves in the linear regime (5). The wave geopotential has a surface maximum, with wavenumber 2 displaying a secondary upper-level maximum for some of the cases. The shorter waves ($m > 4$) are extremely shallow in all cases. The eddy fluxes, especially of heat, tend to be shallow, and the momentum fluxes are almost entirely poleward. At the surface the waves are situated poleward of the jet axis (by 5-15° of latitude), and essentially do not penetrate south of 30°. The existence of significant wave amplitudes at the Lander 1 site is thus not readily explained by these linear results. However, nonlinear simulations of terrestrial baroclinic waves have shown greater vertical and meridional extents relative to the linear case (6). Non-geostrophic effects may be very important as well, particularly the meridional variation of static stability.

References

(1) Ryan, J. A., Hess, S. L., Henry, R. M., Leovy, C. B., and Tillman, J. E. (1978) Geophys. Res. Lett., 5, p. 715-718.

(2) Barnes, J. R. (1980) J. Atmos. Sci., 37, p. 2002-2015.

(3) Barnes, J. R. (1981) J. Atmos. Sci., 38, p. 225-234.

(4) Leovy, C. B. (1979) Martian Meteorology. In Annual Rev. of Astronomy and Astrophysics, Vol. 17, Annual Reviews, Inc.

(5) Simmons, A. J. and Hoskins, B. J. (1976) J. Atmos. Sci., 33, p. 1454-1477.

(6) Simmons, A. J., and Hoskins, B. J. (1978) J. Atmos. Sci., 35, p. 414-432.

OZONE AND WATER VAPOR ON MARS, Charles A. Barth, Department of Astro-Geophysics and Laboratory for Atmospheric and Space Physics, University of Colorado, Boulder, CO 80309

In 1972, ozone was measured in the atmosphere of Mars by the Mariner 9 UVS experiment. These observations extended over the winter and spring seasons in the north and the summer and fall seasons in the south. The ozone observations were correlated with atmospheric temperature measurements made by the Mariner 9 IRIS experiment. These results showed that ozone is present only when the atmosphere is very cold. The hypothesis is that the atmospheric temperature controls the amount of water vapor present in the atmosphere and that water vapor and ozone do not co-exist. During 1976-1978, the Viking MAWD and IRTM experiments measured water vapor and atmospheric temperature throughout an entire Mars year. The Viking observations showed that there was a release of water vapor from the north polar cap at the time of summer solstice, but there was not a release of water from the south polar cap throughout the summer season in that hemisphere. Viking observations in 1977 showed that the temperature of the south polar cap apparently did not rise above the frost point of carbon dioxide. The comparison of Mariner 9 ozone measurements and Viking water vapor measurements as a function of solar longitude and Mars latitude shows quantitatively the anti-correlation between ozone and water vapor. The theory of the photochemistry of ozone and water vapor on Mars has been developed since the Mariner observations. The photodissociation of carbon dioxide produces atomic oxygen which in the presence of the small amount of molecular oxygen in the Mars atmosphere is converted into ozone. When water vapor is present, the photodissociation products, atomic hydrogen and hydroxyl, start a catalytic chain of reactions which consumes the odd oxygen. The presence of ozone is an indicator of the oxidizing state of the atmosphere. Ozone itself to a small degree affects the temperature structure of the atmosphere. In a clean, dry atmosphere the presence of ozone is also an indicator of the presence of molecular oxygen.

POSSIBLE "ROCK CITIES" ON MARS: A PRELIMINARY OBSERVATION; C.A. Baskerville, U.S. Geological Survey, Reston, VA 22092

Several areas located in Protonilus Mensae (1) (38-45N and 303-315W), Nilosyrtis Mensae (2) (30-36N and 285-300W) and southeast of Chryse Planitia (.2N and 38W), have been noted to contain large and small block fields. The large block fields tend to be located at sites along the boundary scarp of the northern plains in plateau material. The small block fields are mostly concentrated in impact craters (~3N-290W, for example). Schultz (3) refers to block fields in craters as floor-fractured craters. He has stated that some authors have interpreted such craters as being due to volcanic modification, rapid isostatic rebound, and/or resurgent cauldrons. Anderson and others (4) and Baker and Kochel (5) include block fields as geomorphic indicators of ground ice and permafrost.

The individual blocks range in size from ~ 2x2 km to 25x40 km and larger, and are rectangular to irregular in outline. These blocks are separated by open fractures ~ 1-2 km in width.

The fractures in areas of block fields along the scarp follow a nearly rectangular pattern, typical of terrestrial tectonically formed joint sets, whereas the blocks on the fractured crater floors tend to be radial from the center and annular to the crater circumference. The set of fractures developed in the craters may have been due to the force of the impacting object against a sub-crater floor of brittle rock material.

Open-jointed massive blocks, similar to those seen on Martian imagery, have been observed on the Allegheny Plateau, although on a smaller scale. These blocks, found in Rock City, Cattaraugus County, New York, consist of a 15-27 m-thick massively bedded, lower Pennsylvanian conglomerate. The spacing between blocks is several meters. Smith (6) considered these blocks at the Rock Cities in both Cattaraugus and neighboring Chautauqua County in southwestern New York State to be produced by periglacial frost wedging. The Allegheny Plateau in this area has dips of less than 30.5 m per 1.6 km and an overall plateau surface slope of 3.5 m per 1.6 km (7).

The frost wedging that occurred during the waning of Pleistocene glaciation in southwestern New York, caused these blocks of conglomerate to move down the plateau gradient on the unconformably underlying, incompetent Oswayo shale formation.

Large conjugate canyons can also be seen in the Zion National Park, Kolob Terrace, portion of the Colorado Plateau. The canyons are incised into Navajo sandstone capped with Carmel Formation limestone. Kolob Terrace is traversed by many narrow, deep (~ 5 + km), angular canyons that are tributary to the Virgin River. The terrace is bounded westward by the Hurricane fault and eastward by the Sevier fault, both striking

northeast. The two faults apparently formed stresses which resulted in a conjugate joint set trending northwest and northeast, along which the canyons have formed. These canyons appear on the Cedar City, Utah (east) Landsat scene (8). The joints have probably been widened by frost action as well as by free-flowing water. There is no indication in the Landsat scene that the inter-joint blocks have moved.

The analogous fracture systems on Mars were more than likely processed initially by frost wedging from either or both water ice and CO_2 ice. Gravitational sliding and erosion of blocks have caused additional widening of these fractures. In the case of the fractures in the large block fields along the scarp, the fracture spacing widens, as one looks farther from the scarp face. This is the picture one would see standing on the crest of the escarpment looking across Nilosyrtis Mensae and Protonilus Mensae toward the lower Utopia Planitia. It appears that with each freeze-thaw cycle, the set of blocks that started moving first have moved the farthest with time, creating a greater spacing between the outermost set of blocks and those next inward toward the scarp. The block fields within the craters, being confined similar to the Kolob Terrace inter-joint blocks, have been widened in place.

Sparks (9) shows a good example of progressive opening of joints, which may be due to freeze-thaw, in his plates 9, 10, and 11. This block phenomenon is in the Cambrian Barmouth Grits on Foel Penolau, near Trawsfynydd.

The slopes in the areas of the probable block-field movements on Mars are $\sim$1 km per 80 km, which help facilitate movement of the blocks. The sub-block strata may be fine-grained, incompetant material containing interstitial water ice.

REFERENCES

(1) Lucchita, B.K., (1978), U.S.G.S. Misc. Invest. Series, MAP I-1065.

(2) Greeley, Ronald and Guest, J.E., (1978), U.S.G.S. Misc. Invest. Series, MAP I-1038.

(3) Schultz, P.H., (1976), Reports of Accomplishments of Planetology Programs, NASA TM X-3364, p. 159-160.

(4) Anderson, D.M., Gatto, L.W., and Ugolini, F.C., (1973), Permafrost, Nat. Academy Sci., Wash., D.C. p. 499-508.

(5) Baker, V.R. and Kochel, C.R., (1979), Jour. Geophys. Res., vol. 84, no. B14, p. 7961-7983.

(6) Smith, H.T.U., (1953), Geol. Soc. America Bull. 64, p. 1474.

(7) Fenneman, N.M., (1938), Physiography of Eastern United States Mc Graw-Hill Book Co., Inc., p. 290-319.

(8) Gregory, H.C., (1950), U.S.G.S. Professional Paper 220, p. 1-12, 141-188.

(9) Sparks, B.W., (1971), Rocks and Relief, St. Martins Press, N.Y., p 54-60.

OXIDATIVE WEATHERING OF PRIMARY IRON SULFIDES UNDER MARS SURFACE CONDITIONS. T.R. Blackburn, Program in Chemistry, St. Andrews Presbyterian College, Laurinburg, NC; E.K. Gibson, Jr., SN7, Geochemistry Branch, NASA Johnson Space Center, Houston, TX; and V. Young, Dept. of Chemistry, Texas A & M University, College Station, TX.

Introduction

The work reported here is part of a continuing effort to model the weathering of primary minerals under conditions of temperature, atmospheric pressure, and composition characteristics of the surface of Mars in the absence of liquid water but in the presence of ultraviolet light at wavelengths longer than 200 nm.

The Martian regolith is rich in sulfur at the two Viking lander sites, and Clark and Baird (1979) have reviewed the likelihood of a sulfur-rich lithosphere in view of these results and of McGetchen and Smyth's (1978) model of a high-density mantle, possibly including FeS. Reduced sulfur, including Fe(II) sulfides, is thermodynamically unstable under the oxidizing conditions prevalent on the surface of Mars (Gooding, 1977). Further, the Viking GEX result (Oyama and Berdahl, 1977) indicates that species more oxidizing than the equilibrium oxygen fugacity are present there. Thus, we might reasonably expect that iron sulfides should undergo some oxidation on a geologic time scale because of weathering, and so the thermodynamic end products of sulfide weathering are of less interest than alteration rates and mechanisms and kinetically determined product set--for example, whether production of $FeSO_4$ will prevail over production of Fe_2O_3 + S (Gooding, 1977).

The present work was undertaken to model the photochemical weathering of three iron sulfides, troilite (FeS), pyrrhotite ($Fe_{(1-x)}S$), and pyrite (FeS_2), under Martian surface ambient conditions. Evidence of surface alteration and the chemical nature of the alteration products were obtained by X-ray photoelectron spectroscopy (XPS).

Experimental Conditions

Samples were located on a liquid nitrogen-cooled sample tray in 3.3 liter stainless steel irradiation vessel (Fig. 1). Chips 0.80 mm thich with surface areas of at least 1 cm^2 were prepared with a diamond saw, ultrasonically cleaned in ultra-high purity freon, dried by a 110°C bakeout, and polished with fine SiC paper under argon. All samples remained under CO_2, Ar, or N_2 atmospheres from the time of preparation until post-irradiation analysis. Irradiations were conducted without the intentional introduction of water vapor ("dry irradiations") and in the presence of water vapor in equilibrium with ice at 200-260°K ("humid irradiations"). Runs conducted without UV light ("dark runs") were also made. The water content of the CO_2 gas was less than 0.01%. During the humid irradiation, samples became coated with a frost that, from its vapor pressure, we conclude to have been either a mixed H_2O-CO_2 frost or CO_2-H_2O clathrate; the temperature and CO_2 pressure in the chamber during humid irradiation were well within the stability field of the clathrate (Miller, 1974). Duplicate chips were located in the UV beam ("in-beam" samples) and out of the direct beam ("out-of-beam") but on the heat sink. Thermocouples in direct contact with the samples and in contact with the heat sink but out of the UV beam did not differ in temperature by more than 10°K. Ultraviolet irradiation was produced by a deuterium discharge lamp operating at 30 W. The atmosphere during irradiation was high-purity dry CO_2 at a pressure maintained at 6 torr by continuously pumping with the vacuum system.

Results

XPS spectra (Fig. 2) indicate significant oxidation of sulfides to sulfates for both in-beam and out-of-beam samples in the humid irradiation. In the dry runs, modest amounts of sulfates were produced only on in-beam samples. During the dark runs carried out in the dry mode, the amounts of sulfates observed by XPS were equal to those observed in the reference samples which had been stored under either CO_2, N_2, or Ar. The results obtained to date suggest that gas-phase photochemical products may result from experiments carried out in the dry mode but the experiment carried out in the humid mode, under modest abundances of water vapor, indicates that gas-solid interactions involving photochemical oxidation products of water vapor also play a very important role in the production of alteration products. There is also some XPS evidence for oxidation of Fe(II) to Fe(III) under humid conditions but not under dry irradiation (Fig. 3). Evidence that some sulfur-oxide (e.g., SO_2, SO_3, or SO) is involved in the weathering studies comes from the fact that $CaCO_3$ powders placed in the irradiation chamber (out-of-beam) show increased SO_2 release during pyrolysis gas chromatography, indicating that at least some sulfur-oxide gas phase was formed during irradiation (cf., Clark et al., 1979).

These experimental results have important implications for Martian surface processes and the behavior of volatiles which may be stored or trapped within the regolith. It has previously been shown that carbonate production is possible within the Martian regolith materials (Booth and Kieffer, 1978). In light of the sulfate production from our experiments, the opportunity exists for volatile-containing phases (e.g., $CaCO_3$) produced during cold-environment weathering to act as a very effective scrubber for the removal of volatiles (e.g., SO_2) produced during UV irradiation and movement of water vapor on the planetary surface.

References

Bates, D.R. and Nicolet, M. (1950) J. Geophys. Res. 55, 301.

Booth, M.C. and Kieffer, H.H. (1978) J. Geophys. Res. 83, 1809-1815.

Clark, B.C. and Baird, A.K. (1979) J. Geophys. Res. 84, 8495-8503.

Clark, B.C. et al. (1979) J. Mol. Evol. 14, 91-102.

Gooding, J.L. (1977) Icarus 32, 483-513.

McGetchin, T.R. and Smyth, J.R. (1978) Icarus 34, 512-536.

Miller, S.L. (1974) In Natural Gases in Marine Sediments, ed. I.R. Kaplan, Plenum, NY, pp. 151-177.

Oyama, V.I. and Berdahl, B.S. (1977) J. Geophys. Res. 82, 4669-4676.

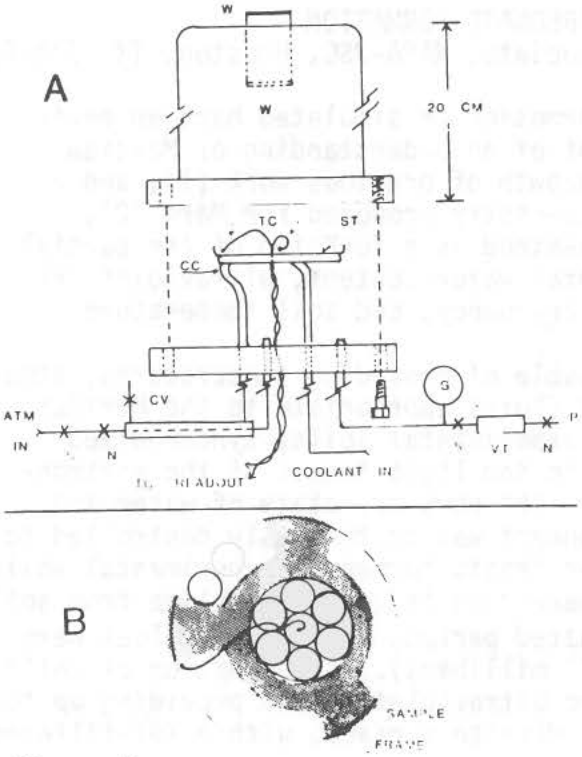

Figure 1.

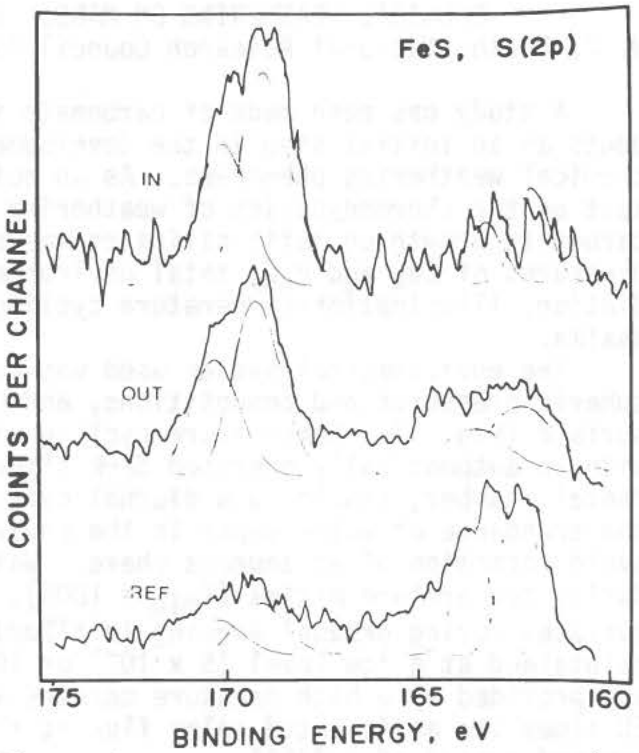

Figure 2.

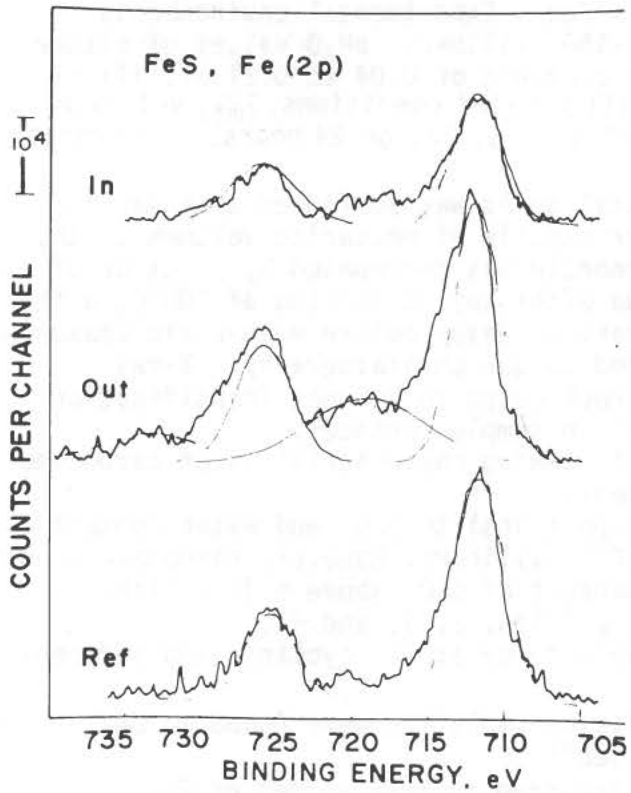

Figure 3.

Fig. 1. (A) Schematic of irradiation chamber. UV from deuterium source enters through windows W. (B) Sample tray. Seven samples in interior ring are "in-beam." Other samples are "out-of-beam."

Fig. 2. Sulfur ($2p_{3/2,1/2}$) XPS of troilite. Sulfate region, 169-170 eV; sulfide, 163 eV. Growth of sulfate and decrease of sulfide is evident after humid irradiation.

Fig. 3. Iron ($2p_{3/2,1/2}$) XPS of troilite. Fe(II) peaks at 712 and 726 eV; Fe(III) peaks at 719 and 733 eV. Increase in the latter is detectable after humid irradiation, especially in the out-of-beam sample.

CHEMICAL WEATHERING ON MARS: CARBONATE FORMATION

M. C. Booth, National Research Council Associate, NASA-JSC, Houston, TX 77058.

A study has been made of carbonate formation in simulated Martian environments as an initial step in the development of an understanding of Martian chemical weathering phenomena. As an outgrowth of previous work (1), and a test of the thermodynamics of weathering chemistry proposed for Mars (2), carbonate growth on mafic silicates was examined as a function of the partial pressures of CO_2 and H_2O, total environmental water content, ultraviolet irradiation, illumination/temperature cycling frequency, and soil temperature maxima.

The environmental system used was capable of providing temperatures, atmospheric pressures and compositions, and UV fluxes appropriate to the Martian surface (Fig. 1). Temperature cycling of experimental soils, synchronized with an automatically operated dark slide in the light tunnel of the environmental chamber, simulated a diurnal cycle. The physical state of water and the abundance of water vapor in the environment was continuously controlled to avoid formation of an aqueous phase. Water frosts formed on experimental soils during temperature minima (T_{min} = 180K), were then induced to sublime from soil surfaces during gradual warming in illuminated periods while pH_2O values were maintained at a low level (5×10^{-5} or 10^{-3} millibars). Illumination of soils was provided by a high pressure mercury arc ultraviolet source providing up to 50 times the anticipated solar flux at the Martian surface, with a KBr-filtered low end cutoff of $\sim$ 2300Å.

Materials of five types were used in experiments: olivine, two compositions of augite, enstatite, and an olivine tholeiite, all of which were crushed to powders having surface areas of 1-5 m^2/cc. Experimental environments included pCO_2 values in the range of 20-150 millibars, pH_2O values of either 10^{-3} or 5×10^{-5} millibars, total water contents of 0.04 to 0.21 ml, illuminated, non-illuminated, or indirectly illuminated conditions, T_{max} values of 240, 260, 270, or 297K, and diurnal cycles of 6, 12, or 24 hours. Experiments ranged in length from 18 to 114 hours.

Analysis of carbonate in experimental soils was performed on a vacuum system having a high precision manometer capable of measuring volumes in the range of 0.160 to 0.700 $\pm$ .005 ml. Carbonate was decomposed by reaction of soils with 100% phosphoric acid in vacuo after soil degassing at 300°C, with the carbonate CO_2 separated from accompanying gases before volumetric measurement. Purity of the CO_2 gas was verified by gas chromatography. X-ray photoelectron spectroscopy was used on rock chips to attempt identification of submonolayer coatings of $CO_3^=$ species on sample surfaces.

Experimental studies revealed the following characteristics of carbonate formation in simulated Martian environments:

1. Carbonate growth is directly proportional to pCO_2 and water content for $pH_2O = 10^{-3}$ millibars. At $pH_2O = 5 \times 10^{-5}$ millibars, however, carbonate growth is proportional to water content, independent of pCO_2 above $\sim$ 30 millibars, and approaches a limiting value with time (Figs. 2, 3, and 4).

2. Carbonate growth is dependent upon temperature cycling, and independent of exposure time at T_{max}.

3. Rates of carbonate growth on olivine tholeiite were found to be 1.0×10^{11} to 1.5×10^{12} molecules m^{-2} sec^{-1}.

4. Measurable carbonate formation occurred to T_{max} values of 240K.

5. Olivine, augite, and the olivine tholeiite all exhibited measurable carbonate growth while enstatite did not.

CHEMICAL WEATHERING ON MARS: CARBONATE FORMATION

Booth, M.C.

6. The carbonate species formed was thermally stable to 400°C at pCO_2 values of 10^{-4} millibar.

7. Ultraviolet irradiation, either of the soils or of the chamber interior only, was not required for carbonate to form.

From experimental results, gaseous CO_2 is indicated to react at silicate surfaces with hydroxyl ions derived from the dissociation of adsorbed "unfrozen" water (3) to form either HCO_3^- or $CO_3^=$ ions by either

$$CO_2(g) + OH^-_{(ads)} = HCO_3^- \quad (1)$$

$$CO_2(g) + 2OH^-_{(ads)} = CO_3^= + H_2O \quad (2)$$

Rates of reaction are mineral selective, probably related to the ability of cations at silicate surfaces to dissociate adsorbed water molecules, and are surface limited. Unless impeded by competing chemical reactions, carbonate formation by this process should be an important form of chemical weathering on Mars and is a viable mechanism for the progressive decline of Martian atmospheric CO_2 over geologic time under conditions forbidding aqueous carbonate chemistry.

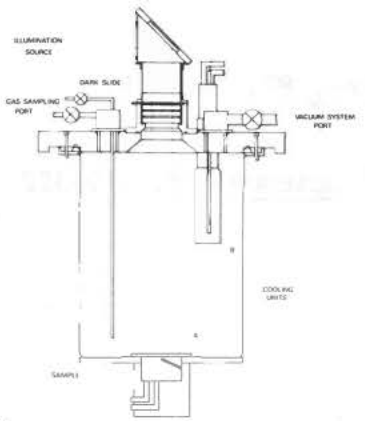

1

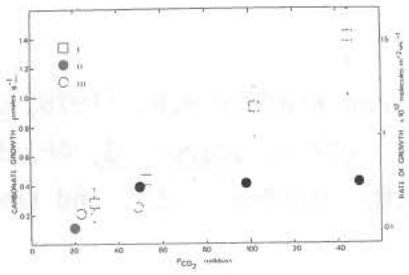

2

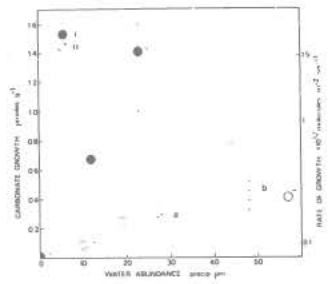

3

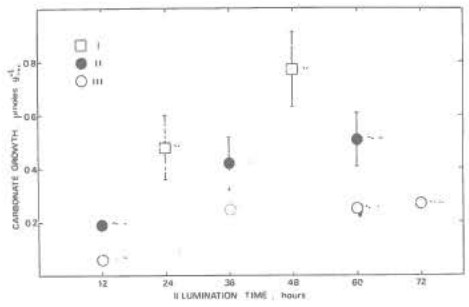

4

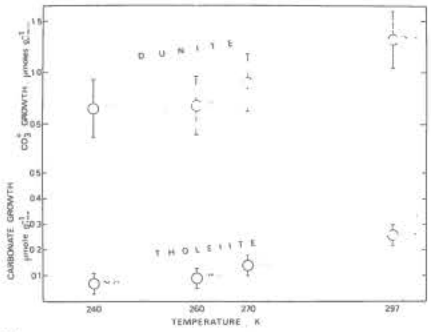

5

CHEMICAL WEATHERING ON MARS: CARBONATE FORMATION

Booth, M. C.

Fig. 1. The environmental chamber.

Fig. 2. $CO_3^=$ growth versus pCO_2 in olivine tholeiite for 66-hour experiments:

I: $pH_2O = 10^{-3}$ mb, total water = 20 precip. μm cm^{-2}
II: $pH_2O = 5 \times 10^{-5}$ mb, total water = 50 precip. μm cm^{-2}
III: $pH_2O = 5 \times 10^{-5}$ mb, total water = 30 precip. μm cm^{-2}

Fig. 3. $CO_3^=$ growth versus H_2O in olivine tholeiite in 66-hour experiments:

I: $pH_2O = 10^{-3}$ mb, $pCO_2 = 150$ mb
II: $pH_2O = 5 \times 10^{-5}$ mb, $pCO_2 = 100$ mb

Fig. 4. $CO_3^=$ growth with time:

I: $pCO_2 = 100$ mb, $pH_2O = 100$ mb, total water = 55 precip. μm cm^{-2}
II: $pCO_2 = 150$ mb, $pH_2O = 5 \times 10^{-5}$ mb, total water = 50 precip. μm cm^{-2}
III: $pCO_2 = 50$ mb, $pH_2O = 5 \times 10^{-5}$ mb, total water = 20 precip. μm cm^{-2}

Fig. 5. $CO_3^=$ growth versus T_{max} for dunite and olivine tholeiite in 66-hour experiments for $pCO_2 = 150$ mb, $pH_2O = 5 \times 10^{-5}$ mb, total water = 20 precip. μm cm^{-2}

References:

Booth M.C. and Kieffer H.H. (1978) J. Geophys. Res. 88, 1809-1815.

Gooding J.L. (1978) Icarus 33, 483-513.

Anderson D.M., Gaffney E.S., and Low P.F. (1967) Science 155, 319-322.

THE ORIGINS OF MARTIAN FRETTED AND TROUGHED TERRAIN. George A. Brook, Department of Geography, University of Georgia, Athens, Georgia 30602

Fretted and troughed terrains on Mars (1, 2) evolve by the gradual coalescence of closed depressions in the manner depicted in Fig. 1 and discussed previously by Brook (3). Fretted terrains have developed at the erosional scarp which separates upland ancient cratered terrain from the low-lying plains to the north. Fretted topography appears to evolve in a manner similar to inselbergs in terrestrial arid areas (4) except for an early stage of closed depression development behind the retreating scarp. Sharp (2) has attributed scarp recession to undermining by evaporation of exposed ground ice or by the emergence of ground water. Carr and Schaber (5) and Squyres (6) have both drawn attention to valley floor lineations which parallel valley walls. These they have explained as being due to flow of ice-ladened debris.

A small-scale terrestrial analog of fretted terrains may be ice-wedge thermokarst (7). French (8) has described scarp retreat of such terrain on eastern Banks Island in the Canadian Arctic. Here thermal melting acting preferentially along ice wedges in lake silts has isolated conical baydjarakhs more than 8 m high. Once isolated in front of the retreating scarp the baydjarakhs, subject to thawing from all sides, quickly degrade. Fretted terrain is thought to be developed in a thick-blanket of volatile-rich regolith (2). Linear depressions probably parallel major structural trends in the underlying bedrock. Bedrock fractures may define zones of increased geothermal heat flow. Vaporization of frozen volatiles in the regolith above these zones would lead to the formation of linear chains of shallow subsidence depressions behind the retreating scarp.

Troughed terrains have developed in the equatorial regions of Mars east of the Tharsis-Syria Rise and include Noctis Labyrinthus and Valles Marineris. These terrains, unlike fretted terrains, are dominated by numerous parallel and intersecting grabens. Strings of pits have developed along grabens. These pits are circular to elliptical in plan and in shape resemble subsidence and suffosion sinkholes in terrestrial karst regions. Evidence at -5.23° latitude and 104.68° longitude confirms that subsidence into subsurface cavities has occurred in Noctis Labyrinthus. At this location large-size debris mantling the floor of a closed depression, and presumably originating from collapse of its walls, has been funnelled underground near the intersection of two narrow grabens. A narrow depression approximately 4 km long has developed (Fig. 2). Subsidence depressions have also been observed in the sand-covered floors of grabens in the Grabens district of Canyonlands National Park, Utah. These features are generally up to 20 m deep and 100 m long. They occur near graben walls or where faults cross graben floors.

Subsidence of regolith into subsurface cavities appears, therefore, to have played a part in the formation of troughed terrains. The origin of the subsurface cavities is conjectural. Gaps along fault planes produced at the time of faulting probably account for some subsidences. Blasius et al. (9) have suggested that if the normal faults of the grabens splay out at depth to form reverse faults this would allow substantial collapse away from the fault trace at the surface.

In the Grabens district of Utah graben development fragmented several stream canyons and modified the regional drainage. Much of the surface flow was diverted into the newly formed grabens where it was channelled underground along faults. There is no evidence of surface stream flow either before or after graben development on horst surfaces in Martian troughed terrains.

However, stream channels (-4.91°, 93.6°) and mudflows (-11.31°, 96.52° and -9.06°, 94.69°) in depression floors at the eastern end of Noctis Labyrinthus, as well as apparent headward extension of valleys by sapping (-3.50°, 94.76°) suggest that water originated from within the regolith in these areas--perhaps by degradation of ground ice (Fig. 3). Sharp (1) has proposed that evaporation or melting of frozen volatiles could create subsurface cavities in troughed terrains but admits that these would probably not be of sufficient size to account for the larger depressions in these areas.

Subsurface cavities could also have developed by solution. In the Grabens district, Utah, cavities along faults have been enlarged by solution of the calcite cement in the sandstone bedrock. Samples of well and spring waters collected in the area in May 1981 contained from 34-61 p.p.m. Ca^{2+}. Experiments by Booth and Kiefer (10) have demonstrated that carbonate may be produced on Mars by the chemical weathering of basalt with or without an aqueous phase of H_2O. Soderblom and Wenner (11) and Clifford and Huguenin (12) have postulated the existence of subpermafrost ground water. Rich in CO_2, such a ground water body may have removed carbonates and other salts produced during chemical weathering. Subsurface cavities may have resulted. Cavity development by solution would help to explain the remarkable morphologic similarities between Martian troughed terrains and terrestrial labyrinth karst (3).

Subsurface cavities produced by faulting, solution, and ground ice degradation could explain many subsidence features in troughed terrain but they can not in themselves be responsible for the development of the larger troughs. It is almost certain that for these to have developed there must have been a steady removal of accumulated, weathered regolith from depression floors. Wind is the most likely medium for accomplishing such transport. The Martian dust storms are proof of its efficiency. Low-albedo patches on the floors of many depressions in Noctis Labyrinthus (e.g. at -6.48°, 100.01° and -6.78°, 98.31°) suggest that fine material has been removed from these depressions leaving a coarse lag. Production of dust-sized particles may be accomplished by salt weathering (13). Not only can this process reduce rock to sand- and gravel-sized particles but recent experiments by Cooke (14) have demonstrated that it can reduce desert sand to silt-sized particles resembling loess, which can be removed easily by wind. Salts in Martian depressions may originate as products of chemical weathering or by the volatilization of saline ground water or ground ice.

References

(1) Sharp R. P. (1973) J. Geophys. Res., 78: 4063-4072.
(2) Sharp R. P. (1973) J. Geophys. Res., 78: 4073-4083.
(3) Brook G. A. (1980) NASA Tech. Mem., 81776: 57-59.
(4) Breed C. S., McCauley J. F. and Grolier M. J. (1980) NASA Tech. Mem., 82385: 307-311.
(5) Carr M. M. and Schaber G. G. (1977) J. Geophys. Res., 82: 4039-4054.
(6) Squyres S. W. (1978) Icarus, 34: 600-613.
(7) Brook G. A. (1980) NASA Tech. Mem., 82385: 369-372.
(8) French H. M. (1974) Can. J. of Earth Sci., 11: 785-794.
(9) Blasius K. R., Cutts J. A., Guest J. E. and Masursky M. (1977) J. Geophys. Res., 82: 4067-4091.
(10) Booth M. C. and Kiefer H. M. (1978) J. Geophys. Res., 83: 1809-1815.
(11) Soderblom L. A. and Wenner D. B. (1978) Icarus, 34: 622-637.
(12) Clifford S. M. and Huguenin R. L. (1980) NASA Tech. Mem., 81776: 144-146.
(13) Malin M. C. (1974) J. Geophys. Res., 79: 3888-3894.
(14) Cooke R. U. (1981) personal communication.

FRETTED AND TROUGHED TERRAINS

Brook, G. A.

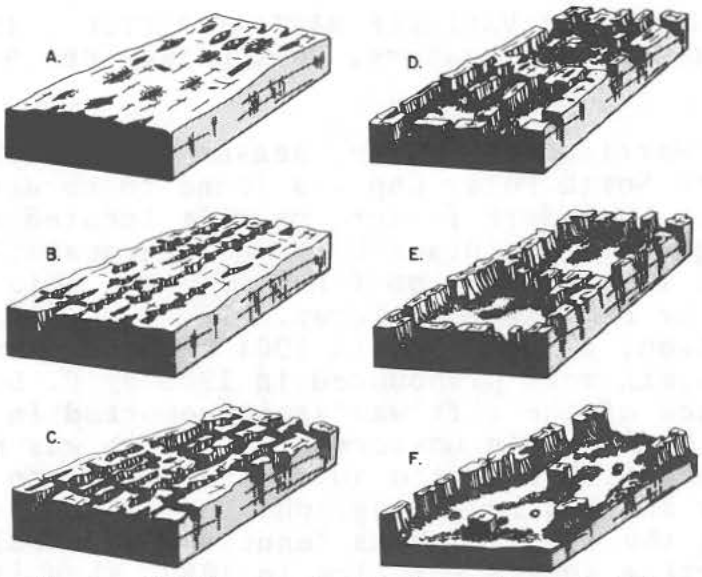

Fig. 1 Stages in the evolution of fretted and troughed terrain. During early stages strings of pits develop in fractures or in regolith above fractures (A). By enlargement and coalescence these strings of pits are converted to intersecting networks of narrow linear depressions which dissect the plateau surface (B and C). As these depressions deepen and widen the intervening rock ridges are dissected and ultimately destroyed. Replacing them are large closed depressions (D and E). As these depressions continue to grow in size a lower-elevation plain surmounted by residual towers replaces the upland plateau (F).

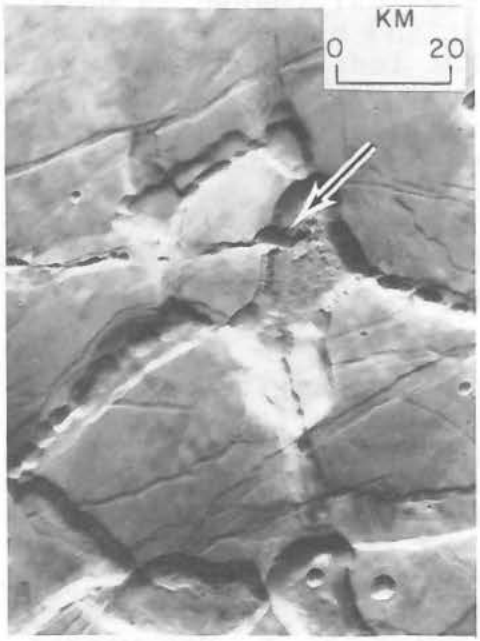

Fig. 2 Subsidence into a subsurface cavity, Noctis Labyrinthus, Mars.

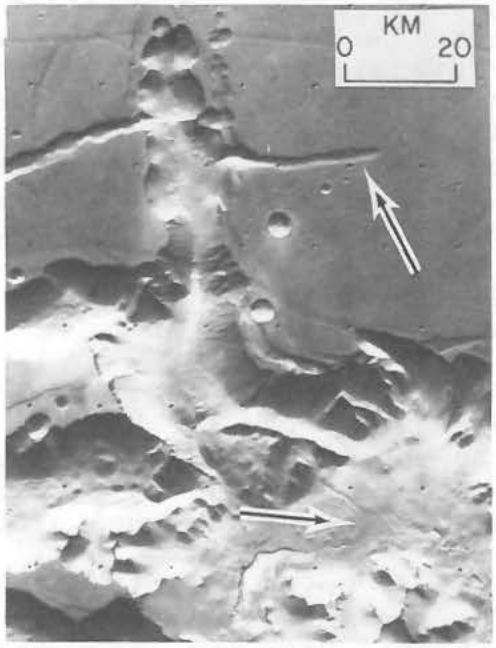

Fig. 3 Stream channels in a depression floor, and headward extension of valleys in the upland plateau by sapping, Noctis Labyrinthus.

EVIDENCE FOR A VARIABLE MARTIAN ARCTIC CLIMATE.

C. F. Capen, Braeside Observatory, Post Office Box 906, Flagstaff, Arizona 86002

During the Martian late-spring season of the aphelic apparition of 1888, the North Polar Cap was found to be divided into two unequal parts by a dark fissure or rift located along the 150°-330°W areographic meridians by G. V. Schiaparelli of Brera. He named it Rima Tenuis, thin or fine fissure. This furrow was later confirmed by Perrotin and Terby. It was again seen at the same Martian season, 61°-65° L_S, in 1901 by A. E. Douglass at Flagstaff, and again more pronounced in 1903 by P. Lowell. A similar appearance of the rift was again reported in 1918 by M. Moggini at Florence. An unsuccessful search was made for Rima Tenuis in the 1960's by the author using 61- to 208-cm telescopes. Mariner and Viking photography showed no trace of the dark rift during the 1970's. Rima Tenuis unexpectedly appeared again before Martian summer solstice in 1980, when it was easily seen and photographed with small telescopes of 20- to 30-cm apertures. The bright, peripheral feature Olympia, which is located on the North Cap at 210°W longitude and which is seasonally separated from the cap by Chasma Boreale, appears regularly each Martian year. Then why doesn't Rima Tenuis form regularly each Martian year?

One possible explanation is that the Martian arctic climate is variable. Phil James, in his studies of the Mariner and Viking photography, suspected a year-to-year change in polar deposits. An extensive search of past and present telescopic observational literature indicates that independent measurements of the North Cap diameters by Antoniadi, Dollfus, Myimoto, Capen, and Parker showed a variable cap regression rate over short periods within decades. A correlation between rift appearance and cap diameter was found. When the summer cap remnant was smaller in diameter by 5° to 7°, as it was in 1888, 1901, 1903, 1918, and 1980, the Rima Tenuis was observed. When the cap diameter was large, as in 1898 and during the 1960's and the 1970's, the dark rift was not seen.

In 1903, P. Lowell first noted an association between dark albedo features and the Martian polar cap's rifts. Topographic maps show no relationship to the Rima Tenuis, whereas albedo charts do. A possible association can be made with the dark defrosted bands or trenches studied by J. Cutts *et al.*

A study using relative temperatures for the years 1881 to 1979 for the northern hemisphere of Earth supplied by the Environmental Data and Information Service, U. S. Department of Commerce, and with solar activity reports is currently in progress. Can the presence of the Rima Tenuis be a measure of the Martian arctic climate and, therefore, be an indicator of weather on both planets Mars and Earth?

SURVEY OF MARTIAN GLOBAL DUST STORMS. C. F. Capen, Braeside Observatory, Post Office Box 906, Flagstaff, AZ 86002.

Ocher-colored veils were suggested as the cause for certain obscurations of Mars by H. Flaugergues as a result of his observations made between 1796 and 1809. This is the earliest record of observations of what is now commonly called yellow dust clouds or storms on Mars. Fifty years later, Father Secchi noted that a fading of the reddish color of Mars coincided with a weakening of its dark albedo features. In 1879 C. Burton reported that orange colored clouds were present and responsible for a yellow tinge upon the South Polar Cap. A. E. Douglass stated that in 1899 he had observed a general haze which lowered the contrast of surface features and appeared to be yellow dust rather than white mist. Planetwide obscurations on Mars have been observed during each of the most favorable perihelic apparitions since 1877, when G. V. Schiaparelli first described the phenomenon. Yellow dust clouds have been reported in most all Martian seasons and in both hemispheres; however, most known global storms have begun in the southern hemisphere during Martian summer when the subsolar point is far south of the geometric equator and when the insolation is greatest on the planet. Former studies by C. Capen of the historical literature and observations from 1956 through 1969 indicated that most perihelic global dust storms share similar characteristics, e.g., seasonal recurrence, initial locations, and evolutionary behavior. These similarities were used as criteria for the search and identification of yellow dust storms contained in the Lowell Observatory historic photographic collection pertientnt to all of the perihelic apparitions from 1907 to 1971. A total of 2,700 photographic plates in red, orange, and yellow light were examined, covering thirteen perihelic apparitions. The results of this "Photographic Survey of Martian Yellow Storms" was never formally published, but instead, was used to make future predictions of global storms.

Today, we know much more about the occurrence, origin, and behavior of the dust storms because of international planetary patrol programs and the close-up view afforded us by Viking Orbiters. The purpose of this paper is to expand in time and to consolidate for future reference all known material, e.g., the classical visual observations, the old and new telescopic photographic record covering the aphelic and perihelic apparitions, and the Mariner and Viking data.

FLUVIAL HISTORY OF MARS. Michael H. Carr, U. S. Geological Survey, Menlo Park, Ca.

The broad outlines of the fluvial history of Mars have been constructed on the basis of a global survey of the location and characteristics of martian channels. The channels were mapped at a scale of 1:5M from Viking frames with resolutions between 125 and 300 m/pixel. The maps were then digitized and transposed into a format in which the $\pm 65^{\circ}$ latitude belt was divided into $1/4^{\circ}$ cells and the presence or absence of a fluvial feature indicated for each cell (figure 1). The format allows channel presence to be correlated with other surface features. Following Sharp and Malin (1975) three types of channels are distinquished: runoff channels which have tributaries, start small, and increase in size downstream, outflow channels which have few tributaries, start full size, and maintain their width downstream, and fretted channels which are broad, flat-floored, steep walled valleys that narrow upstream.

Runoff channels are probably not true channels but valleys formed by slow erosion of water with modest discharges. While the most common type is a simple gully, elaborate branching networks are common. The pattern of dissection is distinctively different from most regions of the Earth. Individual networks are open with wide, undissected interfluves between tributaries, and the networks are generally widely spaced with little competition between adjacent drainage basins. Most networks are short and only rarely exceed 300 km in length from the farthest tributary to termination of the trunk valley. Most valleys terminate abruptly with little indication of deposition at their mouths. Even in the most intensely dissected parts of the cratered terrain large areas remain unaffected by fluvial processes. Most channels wind between craters; fluvial erosion appears to have had a negligible effect on the relief of the craters themselves. Most drainage shows no regional trend, although along the plains/upland boundary drainage is toward the plains and in Margaritifer Sinus it is toward the chaos. All these characteristics suggest an immature drainage system in which erosion has not been sufficiently sustained for single drainage basins to dominate large areas or for erosion to have significantly reduced local relief.

Over 99% of runoff channels are in the old cratered terrain. Both cratered plateau and intercrater plains are dissected, the former more than the latter. Channel frequency tends to decline at high latitudes ($> 50^{\circ}$) and runoff channels are relatively sparse east of Chryse and Argyre. Runoff channels are almost entirely absent in the sparsely cratered plains. Exceptions are some channels on the flanks of Alba and tributaries to Valles Marineris. Within the old cratered terrain, runoff channels are preferentially in regions of high elevations, low albedo, low violet/red ratio, and intermediate thermal inertia. The simplest explanation of the distribution is that runoff channels are restricted to old terrain because they themselves are old, and that within the old cratered terrain they are preferentially located where there are fewer intercrater plains. Less likely alternatives are that the runoff channels have a wide range of ages but are concentrated in the old terrain because it is easily eroded, or because groundwater or ground ice are present.

FLUVIAL HISTORY

Carr, M. H.

Outflow channels are of two types: (1) unconfined which scour broad swaths of terrain and have low depth/width ratios, and (2) confined types where erosion is restricted to discrete channels with high depth/width ratios. Unconfined channels are restricted to mostly around Chryse, and in the Memnonia-Amazonis region. Confined channels occur mainly to the northwest of Elysium and in the Hellas region. Outflow channels have a wide range of ages. Most around Chryse have 1500 to 2100 craters >1 km/10^6 km^2. The Memnonia-Amazonis channels have less than 1000 craters>1 km/10^6 km^2. Reliable counts are not available for the confined outflow channels because of their small surface areas.

Fretted channels are mostly in two latitude belts centered on 40^oN and 45^oS. At these latitudes sparsely cratered debris flows commonly occur at the base of escarpments (Squyres, 1979) and within the fretted channels to form smooth sparsely cratered floors. Fretted channels appear to form by enlargement of other channels by the same mass wasting processes that caused the debris flows. Crater counts on their floors is thus a measure of the rate of resurfacing by mass wasting rather than a measure of the timing of any fluvial activity.

The following sequence of events is a possible explanation of the observations just outlined. Previous to 3.9 billion years ago both the rate of impact and fluvial erosion were high. Continual reshaping of the landscape by impact prevented development of a mature drainage system and resulted in channels with a wide range of preservation. Around 3.9 billion years ago the impact rate declined and the landscape stabilized. Fluvial action continued as evidenced by well preserved runoff channels, particularly in the intercrater plains. The absence of channels on almost all other plains suggests however that conditions conducive to formation of runoff channels were not sustained long after the decline in impact rates. Climatic conditions appear to have changed. Much of the water that cut the channels and that which outgassed subsequently may have accumulated underground as ground ice or ground water beneath a thick permafrost. The trapped water broke out catastrophically at various times (Carr, 1979) to form the large outflow channels or seeped out to feed glaciers (Lucchitta,1980). Runoff channels appear to indicate a thicker atmosphere, at least early in the history of the planet. Outflow channels could form under present climatic conditions.

Carr, M.H., 1979, Formation of martian flood features by release of water from confined aquifers: J. Geophys. Res. v. 84, p. 2995-3007

Lucchitta, B.K., 1980, Martian outflow channels sculpted by glaciers: Lunar and Planetary Science Inst., Houston, Tex.

Squyres, S.W., 1979, Distribution of lobate debris aprons on Mars: NASA TM-80339, P. 50-52.

Sharp, R.P., and Malin, M.C., 1975, channels on Mars: Geol. Soc. America Bull., v. 86, p. 593-609.

FLUVIAL HISTORY

Carr, M. H.

Figure 1

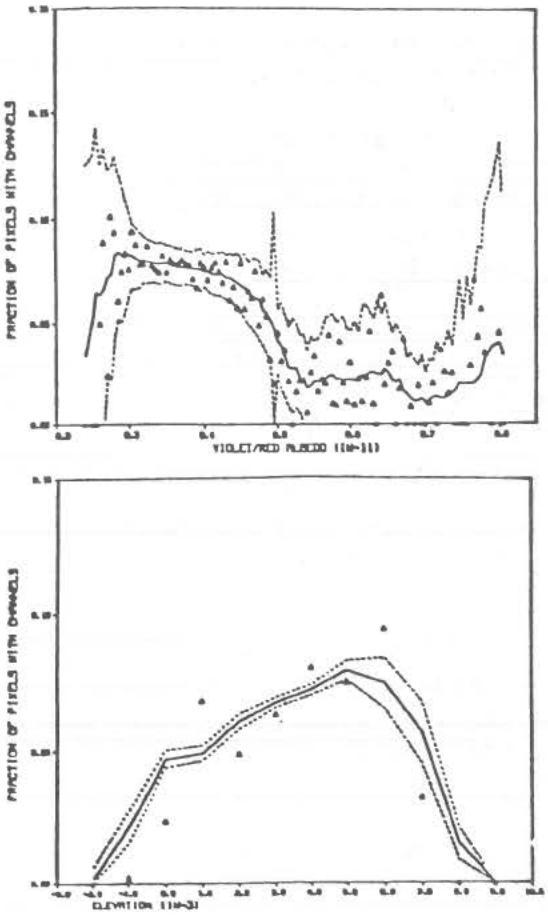

Figure 1. Mercator projection of the martian surface within 65° of the equator showing channel locations.

Upper left. Correlation of channel presence with violet/red albedo within the old cratered terrain.

Lower left. Correlation of channel presence with elevation in the old cratered terrain.

DUST DEPOSITION AND REMOVAL AS INFERRED FROM MARTIAN THERMOPHYSICAL PROPERTIES. P.R. Christensen, Dept. of Earth & Space Sciences, Univ. of Calif., Los Angeles, CA 90024.

The Viking Infrared Thermal Mapper (IRTM) made observations in four surface sensing thermal bands centered at 7, 9, 11 and 20 μm and in a 0.3 to 3.0 μm solar reflectance band. The wavelength-dependent flux emitted by the surface and atmosphere is used to determine the brightness temperature in each thermal band (e.g. T_7). A model has been developed which relates surface block populations, thermal emissivities and atmospheric dust content to the differences in the brightness temperature between bands (1). Global determinations of these parameters can be used to estimate the degree of mantling of the surface by studying the occurrence and density of blocks exposed on the surface. Because the model is sensitive to atmospheric opacity, it is also possible to determine the spatial variability of atmospheric dust content. This variability may be due to local removal of storm deposited dust from the surface.

The surface contribution to the spectral differences was modeled by combining various fractions of a high-inertia component, corresponding to approximately 10 cm blocks, and a low-inertia component, corresponding to the fine particulates, whose inertia was variable. Thermal emissivity was assumed to be constant within each band. The resultant flux from the composite surface was converted to a brightness temperature in each IRTM band.

The effect of atmospheric dust on the spectral differences has not been explicitly included in the model, but can be estimated using a Delta-Eddington approximation to solve for radiative transfer in the atmosphere (2). The dust optical properties used were those of montmorillonite sample 219B. For the low opacities observed during the time period studied, this model predicts a $T_7 - T_{20}$ difference of 1 - 2 K and a $T_9 - T_{20}$ difference of approximately 0 K at noon. All of the spectral differences are near-zero at night.

Using the composite surface model, the abundance of patches or blocks of high-inertia material exposed at the surface was found to vary by less than a factor of 4 between 0 and 30°N. Within this region, the minimum surface fraction covered by high-inertia material is 5%, with even the low-inertia regions having high-inertia material exposed on the surface. The Viking 1 landing site was found to have 15% block cover, compared to a value of 8% measured by the lander. The discrepancy is probably due to the presence of larger blocks than those used in the model, and to patches of exposed bedrock.

The ubiquity of high-inertia (non-aeolian) materials exposed on the surface between -30°S and 30°N implies that there has not been substantial dust deposition within this region. In the low-inertia regions, where subsurface duricrusts are hypothesized to occur (3), the high-inertia features may be exposed patches of this material, rather than blocks. This distinction may not be important for determining the sedimentation rate, however, because rapid deposition would bury both types of high-inertia features. North of 60°N, the surface appears to have few exposed blocks. The poleward decrease in block population is consistent with a model of preferential dust deposition in the polar regions due to ice condensation-sedimentation (4).

The surface thermal emissivity was found to be strongly correlated with

MARTIAN DUST DEPOSITION

Christensen, P. R.

albedo, varying from near-unity at all wavelengths for materials with an albedo greater than 0.28, to emissivities of 0.98, 0.94, 0.92 and 0.92 at 7, 9, 11 and 20 μm, respectively, for materials with an albedo of 0.10. The correlation between emissivity and albedo can be reproduced by a linear combination of these two end-members. This suggests that, at the resolution of the IRTM spectral data, Mars consists of two principal components. The petrologic determination of these end-members is hindered by the lack of appropriate laboratory data.

The atmospheric dust content can be estimated by comparing the observed diurnal behavior of the $T_7 - T_{20}$ difference to models which only incorporated surface parameters. In the high-albedo, low-inertia regions, such as Arabia and Tharsis, the data can be well modeled by surface properties alone. However, in other equatorial regions, the daytime $T_7 - T_{20}$ differences are approximately 1 - 2 K larger than the models predicted. This difference is very close to the predicted signature of montmorillonite dust. Further evidence for dust comes from the observed lack of any discrepancy between the $T_9 - T_{20}$ data and the surface property model. This is expected if atmospheric dust were the case of the $T_7 - T_{20}$ discrepancy, because dust affects 9 and 20 μm nearly equally, and will not be apparent when these bands are differenced.

Dust variability can be estimated globally using the noontime $T_7 - T_{20}$ data, by first removing the surface contribution to this difference. During the relatively clear period studied (L_s 126 - 163), the region from 30 - 60°N was uniformly "clear" ($\tau_9 < 0.02$) and the region from 0 to -30°S was uniformly "dusty" ($\tau_9 \approx 0.05$). Between 0 and 30°N, the atmospheric dust content varied laterally, with the atmosphere over low-inertia, high-albedo regions having approximately a factor of two lower opacity than elsewhere in this region.

The observed spatial variability of atmospheric dust content is probably due to local differences in the rates of dust generation and removal, with source regions having higher opacities. A model is proposed whereby the small amounts of storm-deposited dust are removed from the surface in most areas and placed into the atmosphere locally. In low-inertia areas, the dust is not removed from the surface, resulting in lower opacities over these regions. Removal of dust from dark regions would account for the permanence of albedo features, while the gradual accumulation of dust in low-inertia, bright regions could explain the existence of these regions (5).

Differences in dust removal rates can come about in the following ways. First, the abundance of surface blocks, which enhance dust removal through increased near-surface turbulence, can vary between regions. Second, the distribution of particle sizes can vary, with 160 μm particles being the easiest to set into motion. Very low inertia materials require higher wind velocities to be moved. Third, the wind velocity and circulation pattern vary spatially, which will affect the rate at which dust is raised and distributed. Finally, the rate of dust removal from the atmosphere by ice condensation-sedimentation can vary between regions because the atmospheric temperature is influenced by the surface temperature and is therefore inertia dependent. Ice condensation is more likely to occur in low-inertia regions which are extremely cold at night. All of these mechanisms will lead to lower opacity over the low-inertia regions of Arabia and Tharsis.

MARTIAN DUST DEPOSITION

Christensen, P. R.

Conclusions

The region between -30°S and 30°N does not appear to be a region of dust deposition, while the region north of 60°N may be. The small amounts of dust which are deposited within the equatorial region are reworked locally, and appear to be removed from the surface in most areas, leading to increased atmospheric opacity over those areas. Dust does not appear to be removed from low-inertia, high-albedo regions, and the accumulation of this material may lead to the values of inertia and albedo observed. However, the total amount of deposition must be small, because high-inertia (non-aeolian) materials are still exposed at the surface in the low-inertia regions. The strong correlation observed between albedo and thermal emissivity can be explained by a two end-member model, which implies that Mars is not petrologically diverse. This conclusion is also supported by near-infrared reflectance data (6).

References

(1) Christensen, P.R. (1981). Lunar and Planet. Sci. XII, p. 135-137.

(2) Zurek, R.W. (1981). In preparation.

(3) Ditteon, R. (1981). Icarus, in preparation.

(4) Pollack, J. et al. (1979). J. Geophys. Res., 84, p. 2929-2945.

(5) Zimbelman, J. and H.H. Kieffer (1979). J. Geophys. Res., 84, p. 8239-8251.

(6) Singer, R.B. (1979). J. Geophys. Res., 84, p. 8415-8426.

CHEMICAL COMPOSITION OF MARTIAN FINES, PART 1: FINAL ANALYTICAL RESULTS; B. C. Clark, Martin Marietta Aerospace, Denver, CO 80201 and A. K. Baird, Geology Department, Pomona College, Claremont, CA 91711

A total of 21 samples of loose fines and duricrust clods have been analyzed at the two Viking Lander sites by the on-board X-ray fluorescence spectrometers. In some cases, complete analyses were not possible because of collection of inadequate amounts of material. Duricrust fragments were successfully isolated and analyzed in three different samples at Lander I. All similar attempts to obtain crust material failed at Lander II, apparently because of a more fragile nature of such material at the second site. Although elements such as S and Cl varied significantly, all 21 samples are nonetheless of the same general chemical class. The deeper samples taken at each Lander site are virtually indistinguishable on a chemical basis, implying homogeneity on a scale far broader than the known variety of soil units on both earth and the moon. Laboratory experiments to reconstruct appropriate analog materials exhibit particle-size effects such that our estimates of Fe, S, and Cl are probably lower limits to the actual absolute concentrations if the Martian fines are extremely fine-grained. Final tabulated results of elemental analyses for all samples will be presented.

CHEMICAL COMPOSITION OF MARTIAN FINES, PART 2: IMPLICATIONS FOR WIDESPREAD MAFIC VOLCANISM; A. K. Baird, Geology Department, Pomona College, Claremont CA 91711 and B. C. Clark, Martin Marietta Aerospace, Denver, CO 80201

The derived chemical compositions for Martian fines, including all reasonable compositional ranges which encompass analytical uncertainties (e.g., particle size and matrix effects), are silica, alumina and alkali poor, and iron and magnesia rich. They do include significant S and Cl and unknown proportions of other volatiles that could have been supplied volcanogenically or as precipitates. In the absence of specific mineralogic information, the petrologic interpretations of the nature of the probable silicate fraction of the fines seem limited to:

1) Material derived directly and mostly isochemically from mafic or very mafic igneous rocks;

2) Material formed from mixtures of ultramafic and less mafic rocks;

3) Material isochemically weathered from 1) or 2), as mechanically derived fines or converted directly via weathering reactions into nontronitic clays or broken down to simple oxides and carbonates;

4) Material formed by nonisochemical weathering which concentrated a mafic residuum and removed felsic constituents.

A number of observations and inferences might serve to further limit these interpretations:

a) Nonisochemical weathering producing a mafic residuum seems geochemically unlikely and argues against 4) above.

COMPOSITION OF MARTIAN FINES

Clark, B. C. and Baird, A. K.

b) The apparent global homogeneity of fines might suggest a restricted range of source compositions, thus arguing against 2) above.

c) The rocks at the Lander sites are apparently not weathered and do not have rinds of soft alteration products, perhaps arguing against the latter part of 3) above.

d) The proposals for widespread aeolian action and glaciation (including equatorial regions) on Mars could provide the mechanisms to produce abundant fine-grained materials representative of the prevalent planetary rock types, thus arguing for 1), 2) or the first part of 3) above.

e) Results of laboratory experiments, intended to simulate proposed UV-induced Martian weathering reactions have been largely negative, arguing against the production of abundant clays, oxides and carbonates.

f) Fluids other than water have been proposed as the erosive agents of many Martian channels and chasma, and no evidence of persistent standing water bodies (seas, lakes) has been found, thus perhaps arguing for a limited role for water and therefore the extent of chemical weathering. Further, even if liquid H_2O produced valleys, the ancient crater-density ages for most of the Martian surface suggests water may not have been an important surface agent for billions of years.

g) Analyses of both Lander and earth-based spectra in the visible and near infrared have been interpreted as being produced from mafic rock on Mars, or its weathering products, thus arguing for 1) or 3) above.

Taken together, these arguments suggest to us that the silicate chemistry of fines at two widely spaced localities on Mars could be representative of a prevalent, primary crustal rock type. This rock type could be a mafic flood basalt, rich in pyroxene (as suggested by normative calculations). Compatible analog rock types include komatiitic basalts, shergottite and howardite meteorites, and certain ultrabasic lunar glasses. The relatively high Fe/Mg in the postulated Martian lavas could reflect a mantle similarly enriched in Fe relative to Mg, compared to earth's mantle.

Work supported by NASA contract NASW-3284 (Clark) and NASA grant NSG-7566 (Baird), Mars Data Analysis Program.

A MODEL FOR THE CLIMATIC BEHAVIOR OF WATER ON MARS. S.M. Clifford, Dept. of Physics and Astronomy, University of Massachusetts, Amherst, MA 01003

In an attempt to address several important questions concerning the climatic behavior of water on Mars, a model hydrologic cycle has been proposed (1). Briefly, the model is based on the continuous, or climatically cyclic, existence of an interconnected global subpermafrost groundwater system. The proposed cycle is initiated when near surface brines and ice, formed by the diffusion of water vapor and migration of thin films of liquid from the groundwater below, are depleted by evaporation at the latitudes of maximum annual insolation. The subsequent transport and deposition of dust and H_2O condensate in the polar regions produces a layer of insulation which results in a readjustment of the local geothermal gradient and the eventual rise of the melting isotherm beneath the cap. As the process continues a polar thickness is finally reached where basal melting will occur. Assuming a permeable base, the basal meltwater will eventually drain into the proposed groundwater system. From the recharged system the near surface brines and ice are ultimately replenished.

Essentially the model discussed above attempts to provide a mechanism for the global replenishment of regolith H_2O without the need to resort to frequent and significant periods of climatic change. Without such a mechanism, the inventory of water on Mars might rapidly be cold-trapped at the poles. This conclusion is supported by present estimates of the rate of H_2O deposition at the poles (4,5) and by a study of the stability of permafrost in the equatorial regions of Mars (6). The basic outline of the model was first presented in (1), and was expanded upon in (2) and (3). In (2), it was shown that basal melting can occur based on a reasonable range of estimates for the present thickness of the martian polar caps, their dust content and the local geothermal heat flux. (Recently this process was discussed in a slightly different context as a possible mechanism for the removal and subsurface storage of a primitive martian ice sheet (7)). In (3), a number of processes for the vertical transport of water and solutes in the martian regolith were suggested. It was noted that shock-waves resulting from impacts, earthquakes and explosive volcanic eruptions, could produce a transient compression of water bearing sediments - forcing water to the surface through fractures and pores. In addition, local geothermal sources, could drive the hydrothermal convection of water up narrow openings in the crust in a fashion similar to that of terrestrial hot springs and geysers. Such a process was suggested for the origin of the stream-line channels frequently observed to eminate from the outside rim of craters in the heavily cratered terrain of Mars. Finally, the theory of thermal moisture movement proposed by Phillip and deVries (8) was discussed as a means by which water vapor, liquid, and solutes could be vertically transported on a global scale in response to local geothermal gradients. The mechanism of thermally induced moisture transport was suggested as the primary means by which permafrost in the equatorial regions could be replenished from below by the proposed groundwater system. Concurrent ionic migration from the groundwater could result in large quantities of salts being transported to the martian surface. Such a model is consistent with the discovery of a duricrust at Viking lander sites and with the composition of the soils determined by the inorganic chemical analysis experiments on board each spacecraft (9). More recently Huguenin (10)

has made the suggestion that significant solute transport may occur preferentially at certain localized equatorial sites where dust storm activity might then transport salts as aerosol particles over much of the martian surface. Either process could have significant geochemical implications for the state of the martian regolith.

In summary, a model hydrologic cycle has been proposed to explain the climatic behavior of water on Mars. The model has potential applications to a variety of current problems in martian hydrology. Several such applications, and various aspects of the model, are currently being reviewed. A more extensive discussion of this model is in preparation.

Acknowledgment: This research has been supported under NASA grants NSG 7397, NSG 7405 and NAGW 40.

References

(1) Clifford, S.M. and Huguenin, R.L. (1980) The H_2O Mass Balance on Mars: Implications for a Global Subpermafrost Groundwater Flow System. NASA TM 81776, 144-146.

(2) Clifford, S.M. (1980) Mars: Polar Cap Basal Melting as a Recharge Mechanism for a Global Groundwater System. Lunar Plan. Sci. Conf. XI, 165-167.

(3) Clifford, S.M. (1980) Mars: Ground Ice Replenishment from a Subpermafrost Groundwater System. Proc. 3rd. Colloq. Plan. Water, (in press).

(4) Farmer, C.B. and Doms, P.E. (1970) Global Seasonal Variations of Water Vapor on Mars and Implications for Permafrost. JGR 84: 2881-2888.

(5) Pollack, J.R., Colburn, D.S., Flasar, F.M., Kahn, R., Carlston, C.E. and Pidek, D. (1979) Properties and Effects of Dust Particles Suspended in the Martian Atmosphere. JGR 84:2929-2945,

(6) Clifford, S.M. (1981) The Stability of Permafrost in the Equatorial Region of Mars. In preparation.

(7) Clifford, S.M. (1980) A Model for the Removal and Subsurface Storage of a Primitive Martian Ice Sheet. NASA TM 82385, 405-407.

(8) Phillip, J.R. and deVries, D.A. (1957) Moisture Movement in Porous Materials Under Temperature Gradients. Trans. A.G.U. 38:222-232.

(9) Clark, B.C. (1978) Implications of Abundant Hygroscopic Minerals in the Martian Regolith. Icarus 34: 645-665.

(10) Huguenin, R.L. (1980) Possible Source of the Martian Salts. NASA TM 82385, 502-503.

A PORE VOLUME ESTIMATE OF THE MARTIAN MEGAREGOLITH BASED ON A LUNAR ANALOG. S.M. Clifford, Dept. of Physics and Astronomy, University of Massachusetts, Amherst, MA 01003

Knowledge of the porosity of the martian crust and its variation with depth can place important constraints on both the distribution and total inventory of water on Mars. At the present time, the only means of making such a determination is by analogy with either the Earth or Moon. While comparisons of the Earth and Mars are often justified, it is doubtful that many of the processes which have contributed to the widespread occurrence of young, thick, and highly porous geologic units on the Earth (e.g. extensive fluvial erosion and marine sedimentation) can also be invoked for Mars. In this context, the differences between the Moon and Mars appear somewhat less severe. Both planets have comparable crustal ages as determined by crater counts (1) and their surfaces clearly reveal the similar and considerable extent to which impact and volcanic processes have played a role in the structural modification of their respective crusts. In light of the above, it would seem more appropriate to develop a structural model of the martian crust based on a lunar analog (with due consideration given to the potential effects of an atmosphere and subsurface water) than to attempt such a model based on the far more complex constructional and erosional history of the Earth.

Field studies of terrestrial impact craters (2,3) and theoretical models of the cratering process (4,5) have established that impacts alter the structure of a planetary crust in two ways: *i*) by the production and dispersal of large quantities of ejecta, and *ii*) through the intense fracturing of the surrounding and underlying basement. By these processes, repeated impacts have led to the production of a lunar megaregolith (6). This view is supported by an analysis of the seismic propagation characteristics of the outer layer of the lunar crust which suggests that it is brecciated to considerable depth (7).

For the near-surface of the Moon, P wave velocities are observed to increase with depth until they reach a local maximum at about 20 km. (7,8,9). This bevavior has been attributed to a reduction of pore volume within the crust as lithostatic pressure increases with depth (7,8,9). The transition between fractured and coherent lunar basement is believed to coincide with the beginning of the constant velocity zone observed at a depth of 20 km. -- where lithostatic pressure is thought to be sufficient (> 1 kbar) to completely close all fracture and intergranular pore spaces (7,8,9). To account for these lunar seismic observations Binder (8) and Binder and Lange (9) have presented a model of the lunar crust in which the porosity declines exponentially with depth -- falling to essentially zero at a depth of 20 km. Based on such a model, the porosity at any depth 'z' (measured in kilometers), is given by:

$$\phi(z) = \phi(0)\ \exp(-z/6.5\ \text{km}) \qquad \{1\}$$

where $\phi(0)$ is the porosity at z=0 (assumed by Binder and Lange (9) to have a value of .2) and where the decay constant is assumed to be 6.5 km.

If the density and initial porosity of the martian breccia zone is comparable to its lunar counterpart, then by a simple gravitational scaling of the decay constant in {1} we can obtain a similar expression to calculate the porosity and depth to self-compaction of the martian megaregolith. Following this procedure, we find that for Mars:

THE MARTIAN MEGAREGOLITH

Clifford, S.M.

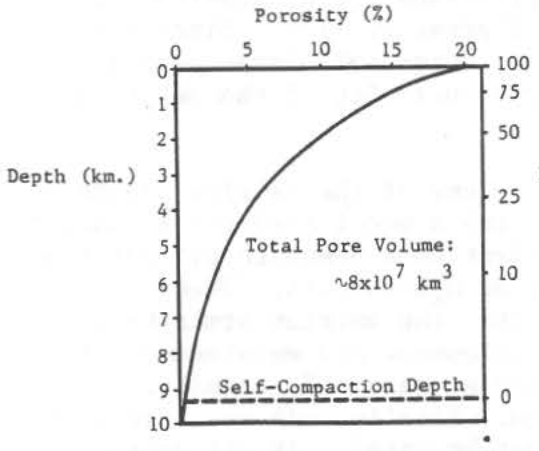

Figure 1. A porosity profile of the martian crust based on the lunar model of Binder and Lange (9,10) as gravitationally scaled to Mars.

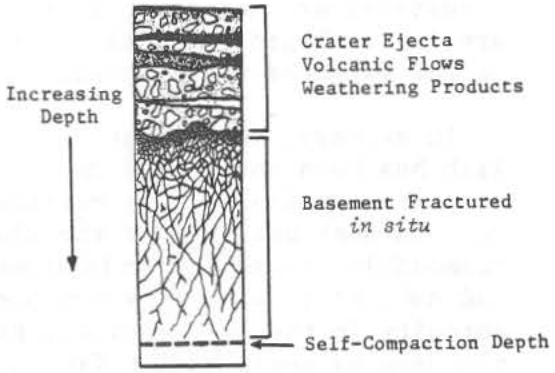

Figure 2. An idealized statigraphic column of the martian crust based on the discussions of Fanale (15) and Carr (21).

$$\phi(z) = .2 \exp(-z/3 \text{ km.}). \qquad \{2\}$$

This equation was used to generate the graph in Figure 1, which illustrates the relationship between porosity and depth for Mars. Based on this model, the depth to self-compaction is ~ 9.3 km.; by integrating the porosity down to this depth, the total pore volume of the martian crust is found to be ~ 10^8 km^3. Thus, the martian megaregolith has the ability to store a volume of H_2O equivalent to a layer of liquid water ~ 600 meters deep over the entire planet. This is enough storage capacity to readily accomodate all but one of the post-Viking estimates for the amount of H_2O on Mars. Lewis (personal communication, 1980) maintains that the primitive solar nebula was sufficiently enriched with H_2O at the distance of Mars that the planet may easily possess an inventory of water which exceeds a layer 1000 meters deep over the surface of the planet. Although such an inventory is in excess of the storage capacity calculated here, there is reason to believe that this calculation of porosity may, for various reasons, underestimate the total pore volume of the martian crust.

The effect that an atmosphere and subsurface water can have on the development and maintenance of high porosity in the martian megaregolith is substantial. Consider, for example, the implications of the wide variety of weathering processes which have been proposed for Mars (10,11,12,13,14). The net effect of these various processes is the production of large quantities of fines at the expense of larger and more coherent units. This mechanism alone can lead to a significant increase in the overall porosity of the martian surface layer; indeed, Fanale (15) has suggested that porosities as high as 50 to 60% could be expected in the upper 2 km of the crust.

The presence of substantial quantities of groundwater in the martian crust might affect the porosity of this unit in a more direct way. As discussed by Hubert and Rubey (16) and others (17,18), the hydrostatic pressure of water within a pore can reduce the net lithostatic pressure acting to close it. Thus, for a "wet" Mars, significant porosity can occur at depths well beyond those calculated for the "dry" model in Figure 1. It should be noted, however, that the presence of groundwater can also act to reduce overall porosity by solution,

compaction, and cementation (19, 20). Such processes are of greatest significance under conditions of high temperature and pressure (19). Since these conditions are met only at great depth on Mars, where calculated porosities are low to begin with, the impact on the overall porosity of the megaregolith is not expected to be large.

In summary, an estimate of the total pore volume of the martian megaregolith has been made based on a lunar analog. Such a model predicts a potential storage capacity for the martian crust sufficient to accomodate all but the very largest estimate of the global inventory of H_2O on Mars. When reasonable consideration is given to the role that the martian atmosphere and subsurface water may have played in the development and maintenance of porosity in the megaregolith, even an inventory of water of the magnitude proposed by Lewis should find adequate storage. Finally, one qualification to the applicability of this model to Mars must be noted. As discussed by Neukum and Wise (1), the lunar highlands are generally believed to have reached saturation for crater diameters < 50 km while the heavily cratered terrain on Mars is evidently undersaturated at all crater diameters. Because of the number of variables involved, the effect that this difference in crater densities may have on the depth of the martian megaregloith is not readily apparent. A more detailed analysis of this entire question is in preparation.

Acknowledgment: This research has been supported under NASA grants NSG 7397, NSG 7405, and NAGW 40.

References: (1) Neukum, G. and Wise, D.U. (1976) Science 194, 1381; (2) Dence et al., (1977) in Impact and Explosion Cratering, Pergamon, New York; (3) Pohl et al., ibid; (4) Werner, S.W. and Simonds, C.H. (1980) Rev. Geophys. Space Phys. 18, 143; (5) O'Keefe, J.D. and Ahrens, T. (1981) Rev. Geophys. Space Phys. 19, 1; (6) Hartmann, W.K. (1973) Icarus 18, 634; (7) Toksoz, M.N. (1979) Rev. Geophys. Space Phys. 17, 1641; (8) Binder, A.B. (1980) JGR 85, 4872; (9) Binder, A.B. and Lange, M.A. (1980) JGR 85, 3194; (10) Malin, M.C. (1974) JGR 79, 3888; (11) Huguenin, R.L. (1976) Icarus 28, 203; (12) Gooding, J.L. (1978) Icarus 33, 483; (13) Booth, M.C. and Kieffer, H.H. (1978) JGR 83, 1809; (14) Newsom, H.E. (1980) Icarus 44, 217; (15) Fanale, F.P. (1976) Icarus 28, 179; (16) Hubert, M.K. and Rubey, W.W. (1959) Bull. Geol. Soc. Am. 79, 115; (17) Byerlee, J.D. and Brace, W.F. (1972) Bull. Seismol. Soc. Am. 62, 657; (18) Serafim, J.L. (1969) in Rock Mechanics in Engineering Practice, Wiley, London; (19) Maxwell, J.C. (1964) Am. Assoc. Petrol. Geol. Bull. 48, 697; (20) Rittenhouse, G. (1971) Am. Assoc, Petrol. Geol. Bull. 55, 80; (21) Carr, M.G. (1979) JGR 84, 2995.

ULTRAVIOLET SPECTROSCOPY OF THE MARS AIRGLOW. R. R. Conway, E. O. Hulburt Center for Space Research, Naval Research Laboratory, Washington, D.C. 20375.

Observations by the ultraviolet spectrometer experiment on Mariner 9 show that the brightest emission in the wavelength region between 1800 and 3400 Å is the Cameron System of carbon monoxide. Comparison of the observed intensities with model calculations show that the most important mechanism for the excitation of the Cameron bands is electron-impact dissociation of carbon dioxide.

Molecular nitrogen and nitric oxide were detected in the Mars atmosphere by the mass spectrometer experiments on Viking landers 1 and 2. The observed concentrations can be used to predict ultraviolet emission in the N_2 Vegard-Kaplan bands and the NO gamma bands with intensities near the detection limit of the Mariner 9 ultraviolet spectrometer.

Spectra of the airglow at altitudes between 88 and 180 km were analyzed using a high resolution synthesis of the molecular emissions. The NO gamma bands due to resonant fluorescent scattering of sunlight would be blended with the much brighter Cameron System at the spectral resolution of the Mariner instrument. Separation of the gamma bands depends on understanding how the Cameron bands are broadened by the dissociative excitation mechanism. The Vegard-Kaplan bands occur at wavelengths which cause them to be blended with the Cameron System, the bright atomic oxygen emission at 2972 Å and the bands of CO_2^+. The data are compared to theoretical spectra for several rotational temperatures of N_2.

Synthetic spectra of the Mars airglow at higher resolution are presented as a guide to future observations.

POLAR LAYERED DEPOSITS AND CLIMATE CHANGE ON MARS: PARALLELISM WITH THE EARTH, James A. Cutts and Karl R. Blasius, Science Applications, Inc., Planetary Science Institute, 283 S. Lake Ave., Suite 218, Pasadena, CA 91101

Polar layered deposits on Mars (Murray et al., 1972) are now widely thought of as a geological expression of long term quasi-periodic variations in the martian climate (Cutts et al., 1981). One possibility is that variations in the orbital/axial elements of Mars (Ward 1973, 1974) which are large enough to affect the martian climate (Ward 1973; Briggs 1974; Fanale and Cannon 1974, 1978; Pollack 1979; Toon et al., 1981) are recorded in the deposits. Other possibilities such as variations in the output of the sun and episodic variations in the supply of volatiles at the martian surface still cannot be excluded. The terrestrial geologic record reveals significant control of climate by orbit/axial variations during the Pleistocene (Hayes et al., 1976), dramatic climate changes of unexplained origin during the Miocene (Woodruff et al., 1981) and episodic changes in global sea level of unknown cause throughout the Tertiary (Vail et al., 1978). The fascinating parallelisms between the Earth and Mars in the mechanisms of developing sedimentary deposits and the role of climate in forming stratification in these deposits are just beginning to be explored.

Investigation of the topography and stratigraphy of martian polar deposits have primarily involved qualitative observations (Cutts 1973; Howard 1978; Cutts et al., 1976; Cutts et al., 1979). However, the Viking Orbiter imaging data now permit accurate quantitative analysis of the shapes of landforms and the thickness of strata. Our preliminary work has provided estimates of average heights of the terraces that are believed to represent the thicknesses of polar strata (Table 1).

DATA SET	SECTION/PROFILE	ELEVATION CHANGE	SLOPE	BAND PAIR COUNT	STRATA INFERRED	THICKNESS PER BAND PAIR	THICKNESS PER STRAT
A. 77B21, 77B51	A(FIG. 7A)	600M±30M	7.8°	13	16	46±2	37
STEREO PAIR,	B	200M	5.6°	8	9	25±4	22
~50M/PX	C	200M	5.9°	5	7	40±6	29
SUMMER SEASON	D	400M	5.6°	14	16	25±2	25
B. 77B22, 77B54	A(FIG. 7B)	200M±30M	4.3°	7	7	29±4	29
STEREO PAIR,	B	200M	4.1°	7	17	29±4	12
~50M/PX	C	200M	4.3°	10	11	20±3	18
SUMMER SEASON	D	200M	4.9°	7	7	29±4	29
	E	200M	1.4°	14	14	14±2	14
	F	200M	1.8°	13	13	15±2	15
C. 566B75, 566B53	4(FIG. 5)	270M± <60M	1.9°	12	12	23±5	23
STEREO PAIR,	3B	290M	3.2°	12	12	24±5	24
~50M/PX	9	270M	3.7°	13	13	21±5	21
SPRING SEASON	1,5B	460M	3.0°	19	19	24±3	24
566B75 PHOTOCLINOMETRY	6	335M	4.0°	10	10	34±6	34

Table 1: Terrace height and layer thicknesses inferred from photoclinometric and stereophotogrammetric measurements. Note that the thinnest strata are observed on the shallowest slopes indicating that resolution is affecting the definition of polar layers.

These results show that it is critical to use images of shallow slopes in order to make terrace height determinations of useful resolution. Our preliminary data indicate that typical layer thickness may be as low as 15 meters or less (Blasius et al., 1981). Using improved photogrammetric and photoclinometric techniques we

POLAR LAYERED DEPOSITS

Cutts, J.A.

are now attempting to measure individual layer thicknesses across an exposure. This measurement program is critical to making progress in studies of polar deposits.

Theoretical understanding of the processes of formation of polar deposits is also moving from the qualitative to the quantitative domain. In recent work (Cutts et al., 1981) two broad classes of models have been considered. Uniform deposition rate models assume that the major constituent of the layered deposits is laid down at a constant rate. Climate is assumed to change the concentration of some minor constituent which modifies locally the resistance to erosion of the deposited materials. Climate-modulated deposition rate models assume that the deposition rate of the major constituent is controlled by climate. Discrete layers are defined by intervals during which deposition slowed down or temporarily ceased. Conceptually they resemble models for the formation of terrestrial or ocean margin sedimentary records where there are hiatuses in deposition in association with glaciation or change of sedimentary base level. The two types of models are illustrated and described in Fig. 1.

We have also developed models which have a physical basis in meteorology and surface processes on Mars and which include the controlling effects of eccentricity and longitude of perihelion as well as obliquity. Two specific climate-modulated deposition rate models have been formulated in physical detail: in one case, the major constituent is dust, in the other case, it is water ice. The effects of varying the threshold obliquity condition for sedimentation (Fig. 1) have also been examined. For certain ranges of threshold values the stratigraphic models are characterized by a single anomalously thick layer followed by a series of thinner ones; in the remaining range the layer thickness has only a slight quasi-periodic modulation. Pattern recognition techniques are being developed for distinguishing characteristics of particular models.

The characteristics of sediment accumulation at the margins of the perennial ice caps are also being explored. Some of the approaches taken to study sedimentation variations at the ocean margins during globally synchronous changes of sea level (Pitman) 1979) are being applied here. Models for the mode of formation of polar troughs, which are the most controversial of all the martian polar landforms, are also being examined.

The geologic investigation of the martian polar regions is continuing to yield rich results. Mars is unique among Earth's neighbors in recording a history of its climatic experience. In investigating that history we are learning about mechanisms of climate change that Mars may share with Earth.

POLAR LAYERED DEPOSITS

Cutts, J.A.

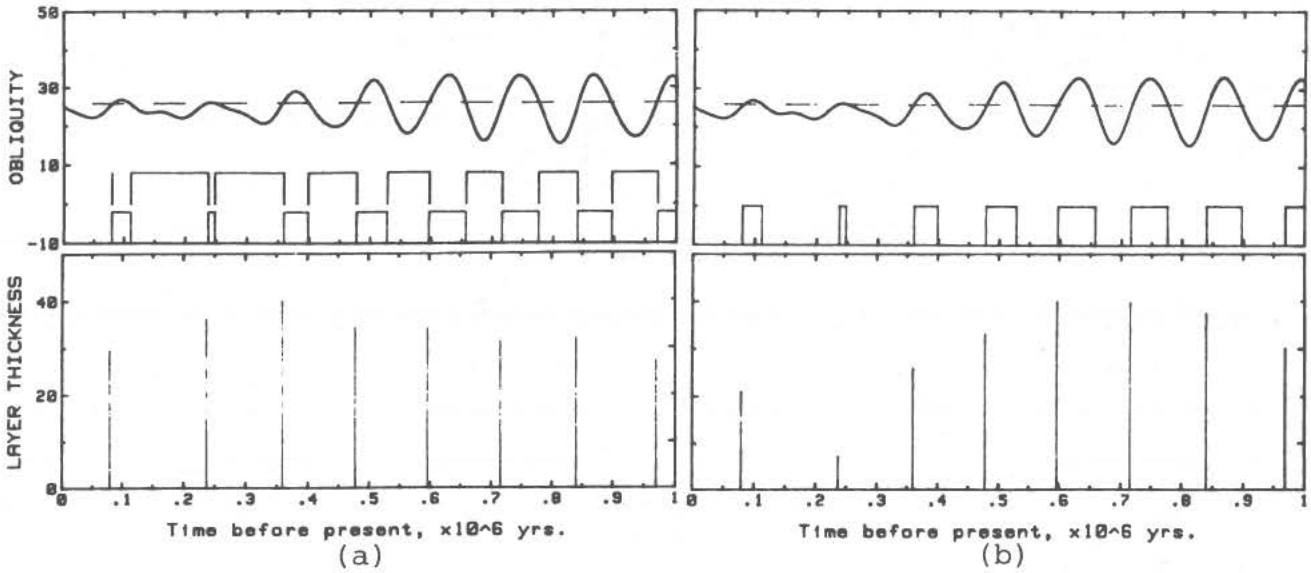

(a) (b)

Fig. 1(a):Continuous Deposition Rate Model for formation of polar layered deposits. Deposition of material A or B which differ only in a minor constituent is determined by the value of a function of obliquity, eccentricity and longitude of perihelion. In this example, the function is proportional to obliquity, and the material type changes when obliquity crosses 26° terminating a period of accumulation of material B; a photogeologically recognizable layer is formed. The thickness of each completed layer as a function of completion time appears in the lower plot.
Fig. 1(b): Climate-Modulated Deposition Rate Model for formation of polar layered deposits is similar to the Continuous Deposition Rate Model (Fig. 1(a)) in that a function of the orbit/axial elements controls deposition. It differs from the latter in that no deposition occurs when the function (here merely the obliquity) falls below threshold. A different pattern of layer thickness as a function of completion time results.

References

Blasius, K.R. et al., submitted to Icarus (1981).
Briggs, G.A., Icarus, v. 23, 167-191 (1974).
Cutts, J.A., JGR, v. 78, 4231-4249 (1973).
Cutts, J.A. et al., Science, v. 194, 1329-1337 (1976).
Cutts, J.A. et al., JGR, v. 84, 2975-2994 (1979).
Cutts, J.A. et al., submitted to Icarus (1981).
Fanale, F.P. et al., JGR, v. 79, 3397-3402 (1974).
Fanale, F.P. et al., JGR, v. 83, 2321-2325 (1978).
Howard, A.D., Icarus, v. 34, 581-599 (1978).
Murray, B.C. et al., Icarus, v. 17, 328-245 (1972).
Pitman, W.C. (abstract), Ancient Sea Level Changes Symposium, Lamont-Doherty Geological Observatory (1979).
Pollack, J.B., Icarus, v. 37, 479-553 (1979).
Toon, O.B. et al., submitted to Icarus (1981).
Vail, P.R. et al., Oceanus, v. 22, 71-77 (1978).
Ward, W.R., Science, v. 181, 260-262 (1973).
Ward, W.R. et al., JGR, v. 79, 3387-3395 (1974).
Woodruff, F. et al., Science, v. 212, 665-668 (1981).

MARS ARCTIC WATER VAPOR OBSERVATIONS,

D. W. Davies, Aerospace Corp., El Segundo, CA 90245

Viking orbiter water vapor observations of the northern arctic area of Mars are now complete for over a full Mars' year.

A series of maps of the arctic have been prepared that show the evolution of water vapor during the spring and summer; an example of the type of coverage and resolution is shown in fig. 1.

In addition, higher spatial resolution one-dimensional scans were obtained at the time of peak water vapor abundance (fig. 2); finer time resolution histories of selected areas have also been generated (fig. 3).

The water vapor abundances observed on two successive Mars' years are identical within experimental error where the observation periods overlap ($140^\circ < L_s < 170^\circ$). Maximum water vapor abundances of $\sim$ 120 prμm are observed at latitudes of 70-80° N during the time from L_s = 100 to 120°. These peak amounts occur over the dark circumpolar collar, and extend to the edge of the permanent ice cap. Over the permanent ice cap, the water amounts are substantially lower, reaching a seasonal peak of 40 prμm. This latitude behavior suggests that the vapor amounts are being controlled by surface temperature, probably through control of atmosphere temperature (and therefore the saturation vapor pressure).

The occurrance of the peak amounts in the circumpolar region, and the phase relations of the seasonal peaks at other latitudes suggests that these arctic vapor amounts are the major seasonal source of water vapor in the northern hemisphere. There is a very rapid drop in average surface temperature from $\sim$210°K to $\sim$190°K, with an associated drop in maximum saturated vapor amounts from O(100 prμm) to O(10 prμm). This reduction in atmospheric temperature may cause much of the vapor to freeze out locally, thus providing the source of most of the vapor appearing the following spring.

Part of this work was carried out while the author was at the Jet Propulsion Laboratory, California Institute of Technology, under contract NAS 7-100, sponsored by the National Aeronautics and Space Administration.

ARCTIC WATER

Davies, D. W.

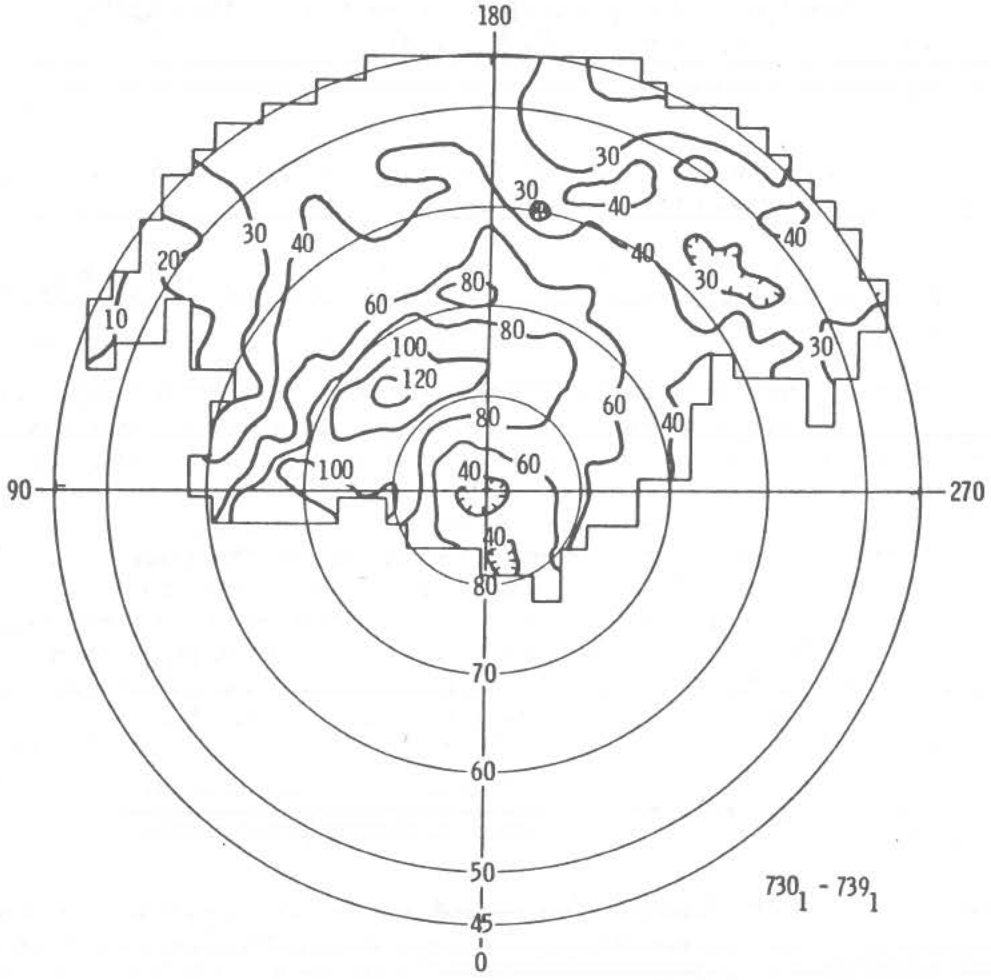

Fig. 1. Map of water vapor obtained by Orbiter 1 on revs 730-739 ($101^{\circ} \leq L_s \leq 105^{\circ}$)

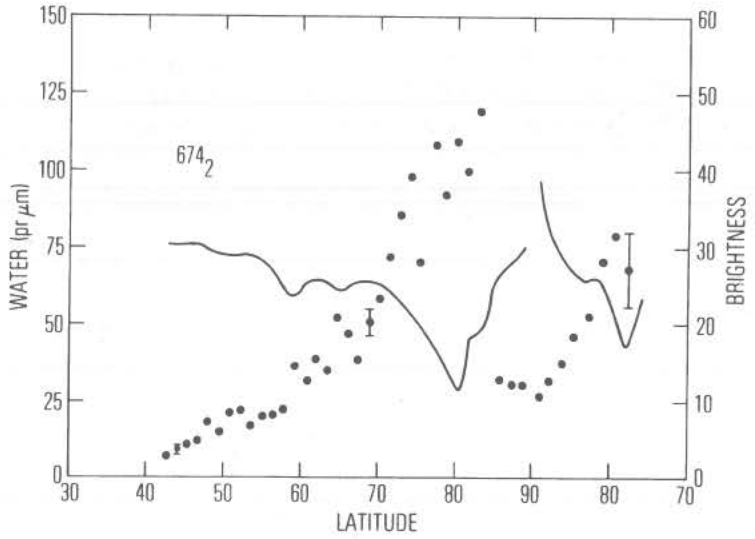

Fig. 2.

One-dimensional scan obtained by VO2 on rev 674, $L_s = 103^{\circ}$, constant longitude (130° W on left side of plot). Solid line is measured brightness (right scale), points are water vapor measurements.

ARCTIC WATER

Davies, D. W.

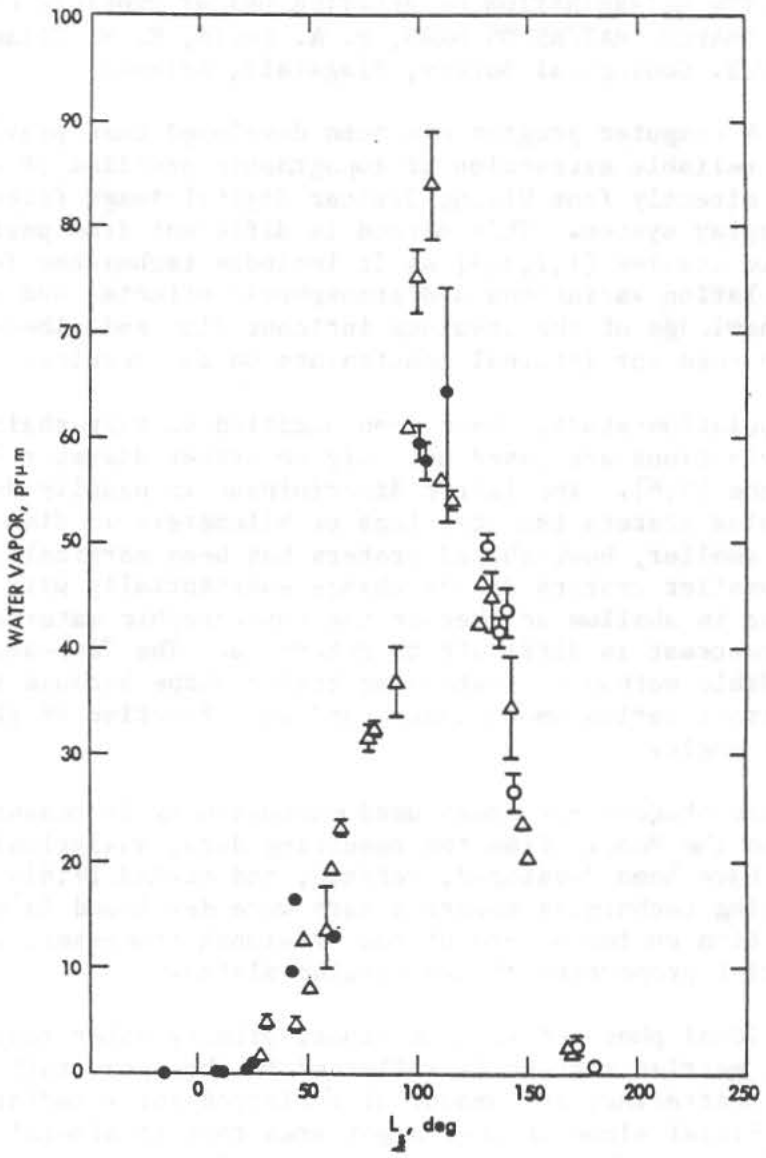

Fig. 3. Time history water vapor measurements for the area 70-75° N, 270-360° W. Open circles: Orbiter 2, first year. Filled circles: Orbiter 2, second year. Triangles: Orbiter 1, second year.

RAPID COMPUTER DETERMINATION OF RELATIVE HEIGHT PROFILES OF PARTLY-SHADOWED, BOWL-SHAPED CRATERS ON MARS, P. A. Davis, E. M. Eliason, and L. A. Soderblom, U.S. Geological Survey, Flagstaff, Arizona

Introduction: A computer program has been developed that provides rapid, efficient, and reliable extraction of topographic profiles of martian impact craters directly from Viking Orbiter digital-image files on an interactive display system. This method is different from past photoclinometric studies [1,2,3,4] as it includes techniques for separating albedo and insolation variations and atmospheric effects, and eliminates the need for knowledge of the absolute incident flux and albedo of the surface and the need for internal constraints on the results.

Crater-population studies have been modified so that their size-frequency distributions are based not only on crater diameter but also on crater appearance [5,6]. The latter discriminant is usually determined from large complex craters (several tens of kilometers in diameter); its application to smaller, bowl-shaped craters has been marginally useful because these smaller craters do not change substantially with erosion. Whether a crater is shallow or whether the photographic materials are simply low in contrast is difficult to determine. The "appearance" method is not a dependable method for obtaining crater shape because the brightness contrast varies among images and as a function of photographic process and sun angle.

Identifiable shadows have been used successfully to measure shapes of small craters on the Moon. From the resulting data, analytical models for crater erosion have been developed, refined, and tested [7,8]. The computer-profiling techniques reported here were developed in order to extract information on the nature of the erosional processes, relative ages, and material properties of the martian plains.

Method: Under ideal photometric conditions, primary solar radiation incident on the martian surface is reflected to the spacecraft unaffected by atmospheric scattering; the amount of reflected solar radiation depends only on the surficial slope of the target area that is mineralogically homogeneous. However, the martian atmosphere reduces the amount of reflected radiation by (1) scattering the incident flux and reflected flux away from the surface and/or the spacecraft, and (2) scattering the incident flux to the surface and reflecting it back to the spacecraft. The incident flux can also be scattered by the atmosphere directly to the detector without reaching the martian surface. Topographic scattering of the reflected radiation from the bright wall of a crater into its dark wall and then to the spacecraft accounts for less than 1 percent of the image brightness in most cases. We assume that the important contributions to the radiation detected consist of the scattered, incident solar flux directly to the spacecraft, the reflected radiation from the surface whose incident radiation had been scattered to the surface by the atmosphere, and the unscattered, primary radiation reflected directly to the spacecraft from the surface.

The radiation scattered to the spacecraft by the atmosphere without surface interaction can be considered a constant throughout the image because of the narrow field of view of the camera. The illumination of the

surface by scattered light from the atmosphere is considered to depart from isotropic uniformity by a negligible amount compared to the other two major sources of reflected radiation. This atmospheric effect is referred to as haze and can be removed by simply subtracting the brightness of shadows from the brightness profile. The techniques that follow do not require knowledge of the surface albedo, the absolute flux incident on the surface, or the flux reflected from the surface directly to the spacecraft. The need to know these values are precluded by the following two assumptions for bowl-shaped craters: the topography of the crater is symmetrical, and the albedos of the crater floor, walls, and exterior are also radially symmetrical. The latter assumption is insured by testing the crater-brightness values for bilateral symmetry across the axis in the down-sun direction. Under these assumptions the following procedure is used to obtain topographic profiles from Viking digital images.

The digital image, radiometrically decalibrated, is stored in an interactive display system. The pixel coordinates and their respective brightness numbers (DN) are fed into the computer program by means of user-controlled cursors displayed on the screen. The center of the crater is obtained by a weighted, center-of-mass triangulation process using crater-rim positions designated by one of the cursors. The presence and direction of bilateral symmetry of DN within the crater is determined by rotating a line about the center and ratioing DN values on both sides of orthogonal lines to the rotating axis. Using the following two profile methods, we assume a Lambertian law for the surface, where the brightness at a pixel (x) from the center of the crater is represented as:

$$B_{(x)} = H + S\, A_{(x)} \cos (I - \Theta_{(x)}) \qquad (1)$$

H is the haze obtained from shadows, S is the combined solar flux, attenuation by atmospheric scattering, and camera sensitivity, $A_{(x)}$ is the albedo at the pixel x, I is the solar incidence angle, and $\Theta_{(x)}$ is the slope of the surface at pixel x.

In method I we assume the presence of a flat field in the image, in which case equation (1) reduces to:

$$B_{(x)} = H + \left(\frac{B_F - H}{\cos I}\right) \cos (I - \Theta_{(x)}) \qquad (2)$$

where B_F is the brightness of the flat field. The slope at pixel x can be obtained from the solution:

$$\Theta_{(x)} = I - \tan^{-1} \left[\left(\frac{B_F - H}{B_{(x)} - H} \sec I\right)^2 - 1 \right]^{1/2} \qquad (3)$$

The relative change in height (Δh) from pixel to pixel is equal to tan $\Theta_{(x)}$. This increment Δh is summed from the center to some point outside the crater to produce the profile.

Method II ratios the brightness equations for pixels in the down-sun direction (numerator) and in the up-sun direction (denominator) at equal distances from the crater center:

CRATER PROFILES

Davis, P. A., et al.

$$R_{(x)} = \frac{B_{(x)}-H}{B_{(-x)}-H} = \frac{S\,A_{(x)}\cos(I-\Theta_{(x)})}{S\,A_{(-x)}\cos(I+\Theta_{(-x)})} = \frac{\cos(I-\Theta_{(x)})}{\cos(I+\Theta_{(-x)})} \qquad (4)$$

The slope is obtained by transformation of this equation to the following:

$$\Theta_{(x)} = \cot^{-1}\left[\tan I \frac{(R_{(x)}+1)}{(R_{(x)}-1)}\right] \qquad (5)$$

The advantage of Method II over Method I is that the former precludes the need to define a flat-field (B_F) in the digital image; the user need only enter the haze factor.

Results: These two profile methods have been applied to bowl-shaped craters of known profiles between Tithonium and Ius Chasmata (9) (Viking 1 high-resolution frame 64A18, I = 29°) and to bowl-shaped craters in Solis Planum that are included in several moderate-resolution frames covering a range of I and H values (606A06, I = 62°, H = 52; 643A92, I = 68°, H = 42; and 608A63, I = 79°, H = 60).

Method II reproduces the topographic profile of two bowl-shaped craters between Tithonium and Ius Chasmata to within 10%; Method I is reliable to within 10% for the larger crater (60-km diameter) and 20% for the smaller crater (30-km diameter). The greater disparity in Method I is attributed to uncertain estimation of albedo ($A_{(x)}$) and the combined solar flux (S) by assuming a flat field in the image. Method II is more reliable because the ratio eliminates the need to know the values for $A_{(x)}$ and S. The agreement between the topographic profiles for craters photographed with various sun angles and haze conditions is within 10% by both methods.

Alternative photogrammetric equations will be programmed into the system to deal with photogrammetric situations less simplified than the Lambertian case. A profile method is now being developed that derives photogrammetric variables from the simultaneous equations given by two or more craters within the same image.

References:

[1] Mouginis-Mark, P. J. and Wilson, L. (1981) Computers and Geosciences, v. 7, p.35-45.
[2] Bonner, W. J. and Schmall, R. A. (1973) U.S. Geol. Survey Prof. Paper 812-A, 16 p.
[3] Watson, K. (1968) U.S. Geol. Survey Prof. Paper 599-B, 10 p.
[4] Rindfleisch, T. (1965) NASA Tech. Report No. 32-786, 16 p.
[5] Chapman, C. R. (1974) Icarus, v. 22, p. 272-291.
[6] Jones, K. L. (1974) Jour. Geophys. Res., v. 79, p. 3917-3931.
[7] Soderblom, L. A. and Lebofsky, L. A. (1972) Jour. Geophys. Res., v. 77, p. 279-296.
[8] Boyce, J. M. and Johnson, D. A. (1977) Proc. Lunar Sci. Conf. 8th, p. 3495-3502.
[9] Wu, S. S. C. (1970) Jour. Geophys. Res. v. 84, p. 7955-7959.

THICKNESS OF VOLCANIC MATERIALS ON THE EAST FLANK OF THE THARSIS PLATEAU. R. A. De Hon, Department of Geosciences, Northeast Louisiana University, Monroe, LA 71209.

The Tharsis Plateau is characterized by a long eruptive history and the accumulation of a large volcanic pile. The plateau rises 10 km above the martian datum and is capped by three large volcanic shields, each of which rises an additional 17 km. Three major volcanic units (Hprg, Apc and Apt; 1) comprise the eastern flank of the Tharsis Plateau (Fig. 1).

The oldest identifiable volcanic unit (Hprg) is characterized by long sinuous ridges which resemble lunar mare ridges. The original extent of the ridged plains material is obscured by superposed younger materials to the west and by erosion to the north and northeast. The ridged plains material is overlain by a rather featureless plains materials (unit Apc) which is wide spread in the northern hemisphere of Mars. Despite the probability of a mixed origin and multiple sources, these materials in the Tharsis region are generally accepted as volcanic flow materials derived from early Tharsis vents or fissures (1, 2, 3). The youngest material (unit Apt) that forms the crest of the plateau is characterized in Viking photographs by fresh-appearing, discrete flow lobes.

The thicknesses of the volcanic units in the Tharsis region were estimated by employing techniques similar to those used to measure lunar mare basalts (4, 5). Plescia and Saunders (6) used partially buried craters to establish thickness limits for the young martian volcanic materials (units Apc and Apt). The thickness was estimated at individual partly buried craters by using measured crater diameter to estimate original rim height. Mercurian crater parameters (7) were used in the estimates because corresponding martian data does not exist, and martian gravity and substrate conditions more nearly resemble those of Mercury than those of the moon. Use of the lunar trend would reduce the values slightly but would not significantly alter the conclusions. Finally, because measurements of the exposed rim height are difficult on Viking imagery, only those craters that are almost completely buried are used in the thickness estimates.

Only the ridged plains material (unit Hprg) contains a sufficient number of data points to construct an isopach map. Although the overall precision of the map is low, the isopachus lines provide a generalized trend of the thickness distribution. Buried craters within the younger plains units are too widely spaced and too few in number for such analysis. Spot elevations on these units do provide some insights into the nature and distribution of the young volcanic materials.

THICKNESS OF VOLCANIC MATERIALS

De Hon, R. A.

The results generally agree with those of Plescia and Saunders (6). The younger volcanic materials (units Apc and Apt) of the Tharsis region exhibit uniform and similar thicknesses (approximately 0.7 km each) over a wide areal extent (Fig. 1). The ridged plains material ranges from a thickness of zero at the distal margin of the flow in the south and east to 1.3 km near the western contact with younger materials. Isolated lensing in excess of 1 km thick occurs along the eastern margin, but the general trend is thickening of the ridged plains material westward toward the axis of the plateau.

The oldest flows probably originate from fissure vents on the Tharsis Plateau as precursors to later flows that cap the plateau. The ridged nature of the surface of this unit suggests that it was erupted at very high effusion rates and emplaced in a manner similar to the lunar mare basalts (8). One major difference between martian ridged plains and similar appearing lunar basalts is the depositional setting. Lunar basalts are confined to basin interiors and other lowlands. In contrast, ridged plains materials of the Tharsis region are emplaced on the flanks of a prominent arch. The thickness of the ridged plains material ($\geq$1 km) is thicker than that of the overlying materials. Each of the younger units appears to be thinner (approximately 0.7 km each). The surface characteristics of the younger volcanics indicate high extrusion rates but not as high as that of the ridged plains materials. The rate of thickening of materials westward toward the crest of the plateau is less than the surface slope of the eastern flank of the Tharsis Plateau. The maximum thickness of volcanics in the Tharsis region is probably 3 to 5 km. Hence, a major part of the Tharsis Plateau elevation is probably structural in origin.

References

1. Scott D. H. and Carr M. H. (1978) U. S. Geol. Survey, Misc. Investigations Map I-1083.
2. Carr M. H. (1975) U. S. Geol. Survey, Misc. Investigations Map I-893.
3. McCauley J. F. (1978) U. S. Geol. Survey, Misc. Investigations Map I-897.
4. De Hon R. A. and Waskon J. D. (1976) Proc. Lunar Sci. Conf. 7th, p. 2729-2746.
5. De Hon R. A. (1979) Proc. Lunar Planet. Sci. Conf. 10th, p. 2935-2955.
6. Plescia J. B. and Saunders R. S. (1980) Proc. Lunar Planet. Sci. Conf. 11th, p. 2423-2436.

THICKNESS OF VOLCANIC MATERIALS

De Hon, R. A.

7. Cintala M. J. (1979) Proc. Lunar Planet. Sci. Conf. 10th, p. 2635-2650.
8. Greely R. and Spudis P. D. (1981) Rev. Geophys. Space Phys. 19 13-41.

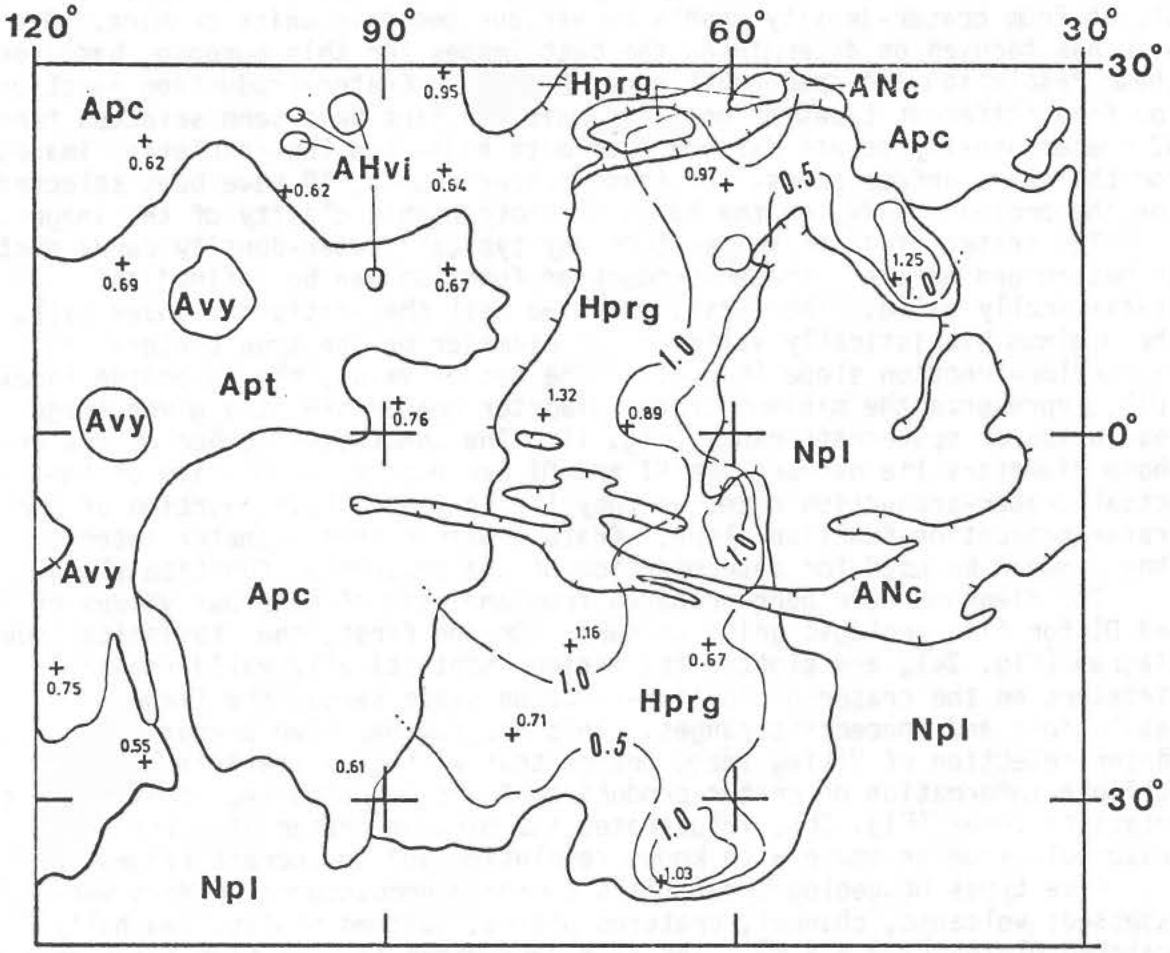

Figure 1. Geologic sketch map of the eastern flank of the Tharsis Plateau. Symbols modified from Scott and Carr (1). Isopach lines at 0.5 km interval show thickness of ridged plains materials (unit Hrpg). Selected spot thicknesses indicated for the three major volcanic units. Hachured contact line denotes erosion of ridged plains material prior to deposition of younger materials.

VIKING ORBITER IMAGES: THEIR PROPER SELECTION FOR THE DETERMINATION OF CRATER-PRODUCTION RATES ON GEOLOGIC UNITS OF DIVERSE ORIGINS--Arthur L. Dial, Jr., and Gerald G. Schaber, U.S. Geological Survey, Flagstaff, Arizona 86001

Medium- to high-resolution Viking Orbiter images have enabled planetary geologists to determine statistically valid crater-production-function slopes from crater-density counts on various geologic units on Mars. Our work has focused on determining the best images for this purpose, based on their resolution and spacecraft range [1,2,3]. Crater-production functions for five different types of geologic units on Mars have been selected from 92 crater-density counts derived from both high- and low-resolution images for the same surface areas. Of these crater counts, 40 have been selected for the present study, on the basis of photographic clarity of the images.

Two crater-diameter values from any typical crater-density curve must be determined before a crater-production function can be defined as statistically valid. The first, which we call the Statistics Index (SI), is the minimum statistically valid crater diameter on the true crater-production-function slope (Fig. 1). The second value, the Detection Index (DI), represents the minimum crater diameter measurable at a given image resolution or spacecraft range (Fig. 1). The cumulative number of craters whose diameters lie between the SI and DI are not representative of the actual crater-production rate, as they lie in the rollover portion of the crater-production-function slope. Craters within this diameter interval should never be used for determination of the production function slope.

Two diagrams have been prepared from analysis of numerous values of SI and DI for five geologic units on Mars. On the first, the Statistics Index diagram (Fig. 2a), are plotted the minimum statistically valid crater diameters on the crater-production-function slope versus the image resolutions and spacecraft ranges. This diagram has been prepared for use in the selection of Viking image frames that will give statistically reliable information on crater-production function. The second diagram, the Detection Index (Fig. 2b), illustrates the minimum crater diameter measurable from an image with known resolution and spacecraft range.

Five types of geologic materials commonly encountered on Mars were assessed: volcanic, channel, cratered plains, mantled plains, and hilly cratered plains [1,2,3,4,5]. The SI's determined for the five types appear to fall into two distinct major envelopes (Fig. 2a). One envelope includes SI's for channel and volcanic deposits. The second envelope includes SI's for materials of the cratered plains, mantled plains, and hilly cratered plains.

To determine a statistically valid crater-production function for the channel and younger volcanic materials, one must use images with resolutions of less than 80 m/pixel (range <3000 km) and crater diameter values of between 80 and 600 m. For older volcanic plains, image resolutions of about 220 ± 40 m/pixel (range as great as 10,000 km) and crater diameters of 1 km or less should be used.

The second major envelope shown in Figure 2a overlaps the crater-diameter range of the first envelope and extends to crater diameters of 60 ± 10 km. Because the cratered plains and hilly cratered plains were originally defined on the basis of the number of superposed craters $\leq$ 1 km in diameter [2], these geologic units form lower and higher secondary SI envelopes, respectively, within the major SI envelopes. SI values for the mantled plains material [1,2] span the secondary SI envelopes of the younger cratered plains and the older hilly cratered plains materials.

VIKING ORBITER IMAGES

Dial, A. L., Jr. and Schaber, G. G.

Figure 2a shows that a valid crater-production function will be obtained for the cratered plains unit (lower secondary SI envelope) on the 60 m to 8 km segment of the crater-density curve if image resolution is less than 130 m/pixel (range <5000 km). The secondary SI envelope of the mantled plains unit indicates that a true crater-production function for this type of surface can be obtained only from images with resolutions that range between 20 and 200 m/pixel (range 1000 to 8000 km) and equivalentcrater diameters between 300 m and 15 km. The crater-production function for the hilly cratered plains unit (upper secondary SI envelope) can be determined from images whose resolution is 180 m/pixel (range >5000 km) or more and for crater diameters greater than 4 km.

Before the SI crater diameter is determined, the crater-production slope must be defined on the crater-density curve generated for any geologic unit studied [6,7]. This procedure is critical in the case of the mantled plains and hilly cratered plains materials, because on these units the true slope of the crater-production function is found at large crater diameters: 3 to 6 km for the mantled plains unit and 8 to 65 km for the hilly-cratered plains unit.

These diagrams should be used as guides by persons performing crater-count analyses of different geologic units on Mars in order to prevent unnecessary counting of images whose resolutions do not give valid crater-production-function information for the measured crater diameters. For a thorough guide to actual crater-count procedures and crater-analysis techniques, the reader is referred to [7]. U.S. Geological Survey research on this project was funded under NASA Contract W14,575.

References:

[1] Soderblom, L. A., Condit, C. D., West, R. A., Herman, B. M., and Kreidler, T. J. (1974) Icarus, v. 22, p. 239-263.

[2] Scott, D. H., and Carr, M. H. (1978) U.S. Geol. Survey Misc. Inv. Ser. Map I-1083.

[3] Dial, A. L., Jr. (1978) NASA Tech. Memo. 7979, p. 171-174.

[4] Schaber, G. G., Horstman, K. C., and Dial, A. L., Jr. (1978) Proc. Lunar Planet. Sci. Conf. 9th, p. 3433-3458.

[5] Masursky, Harold, Strobell, M. E., and Dial, A. L., Jr. (1979) Jour. of Molecular Evolution, v. 14, p. 39-55.

[6] Neukum, G., and Hiller, K. (1980) Jour. Geophys. Res., in press.

[7] Crater Analysis Techniques Working Group (1979) Icarus, v. 37, p. 467-474.

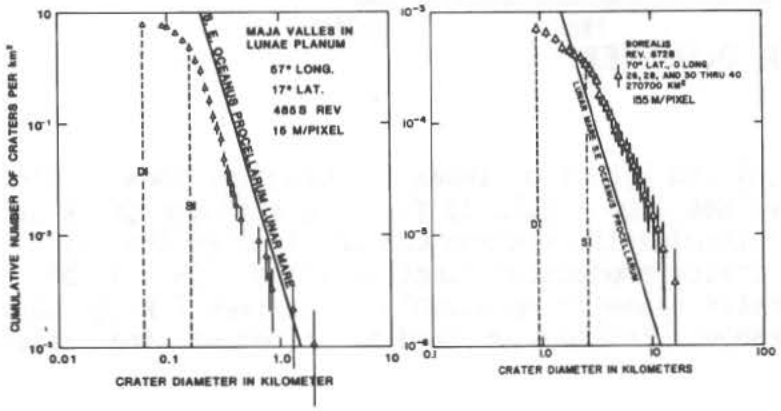

Figure 1. Plots of the Statistical Index (SI) and Detection Index (DI) in relation to the crater density curves of two geologic units--channel deposits (left) and mantled plains materials (right).

VIKING ORBITER IMAGES

Dial, A. L., Jr. and Schaber, G. G.

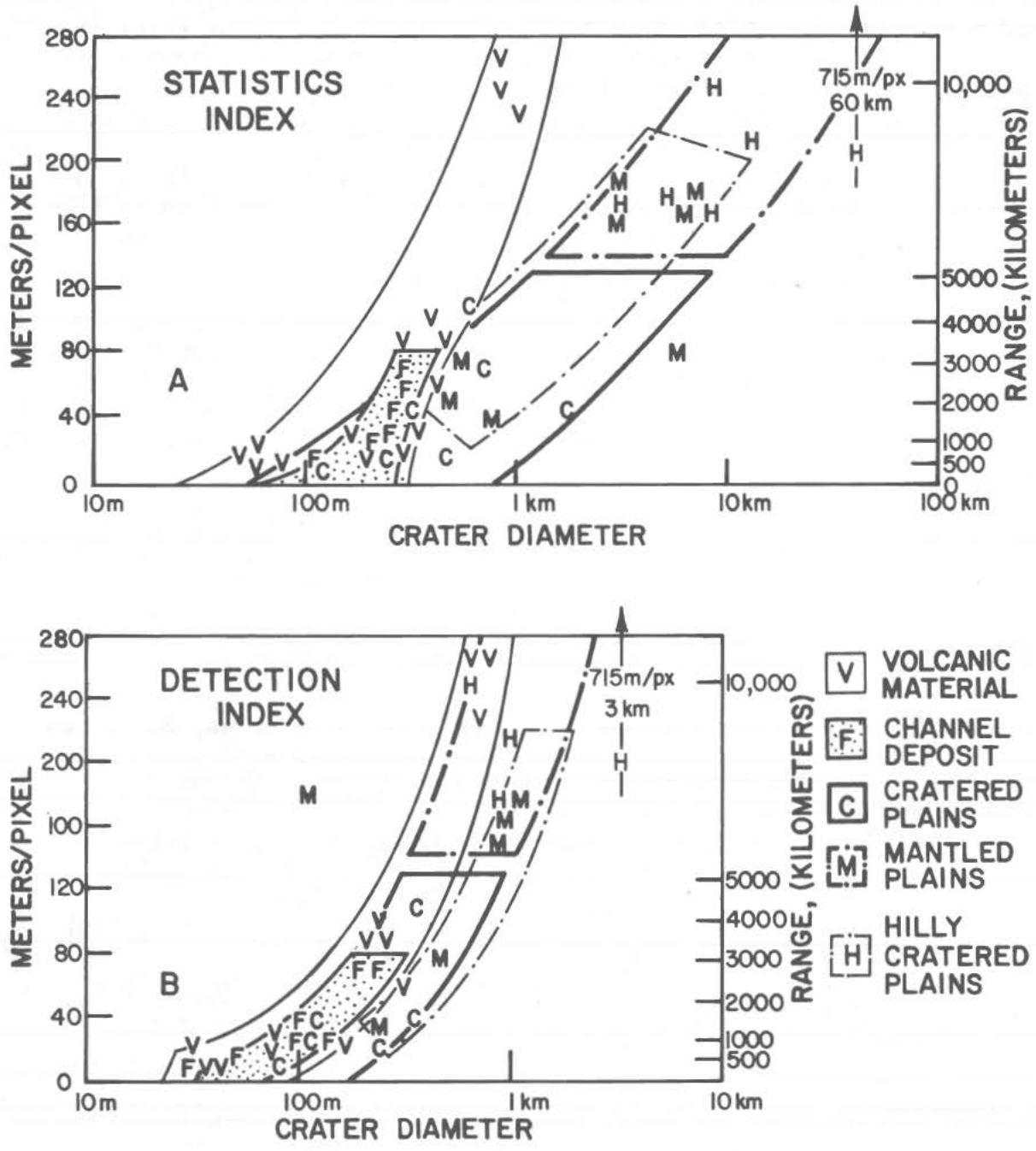

Figure 2. Statistics Index (A) and Detection Index (B) diagrams showing the distribution of SI and DI values (see Figure 1) for five geologic units on Mars. (A) can be used to determine the minimum crater diameter that is statistically valid on the crater production function slope. (B) can be used to determine the minimum crater diameter resolvable at a given Viking image resolution and spacecraft range. Envelops defined by different line patterns discussed in text.

DAILY TEMPERATURE VARIATIONS ON MARS: A LAYERED SOIL. R. Ditteon, Dept. of Earth & Space Sciences, Univ. of Calif., Los Angeles, CA 90024.

The Viking infrared thermal mapper (IRTM) has measured the infrared brightness temperature of Mars for more than a full Martian year. The daily variation of the 20 μm brightness temperature can be predicted to within ±5K for most of the Martian surface during any season. The thermal model used for these predictions determines the temperature of a spherical, homogeneous, conductive solid which is heated by absorbed insolation and cooled by radiating to space (1). The free parameters of this model are the bolometric bond albedo, A, and the thermal inertia, I. However, for approximately 32% of the Martian surface area, the standard model does not adequately fit the observations. Instead, a model with layered soil is needed.

Because of the orbital characteristics of the Viking spacecraft it is necessary to average data to get reasonable diurnal coverage. Spatial averaging was accomplished by dividing the planet into 90 2° latitude bins. Each latitude bin was subdivided into 4 bins of approximately 90° longitude. The longitude boundaries were chosen to separate areas of low thermal inertia from areas of high thermal inertia (2). The Martian day was divided into 24 equal time bins with local midnight at 0H and noon at 12H (1H = 1/24 Martian day). All of the Viking data were averaged in this way for 23 "seasons". Each "season" lasted about 20° in areocentric solar longitude, which is approximately equivalent to three weeks on Earth (3).

These data were fit in a least squares sense with standard model temperatures. In this way the "best" albedo and inertia for each latitude-longitude bin were determined for each of the 23 seasons. The quality of the fit was measured by the maximum deviation of the observations from the model temperature. A somewhat arbitrary limit of ±5K was chosen as a limit for defining a "good" fit. Except near the retreating southern polar cap, all areas south of -20° are well fit by the standard model. All areas north of 45° are well fit. Areas between -20° and 45° are generally poorly fit by the standard model. The observations are warmer than the model in the morning and cooler than the model in the afternoon. The largest deviations (-30K) occur during the late afternoon (17H to 19H) in the longitude bins with the lowest thermal inertia. The longitude bin which includes Syrtis Major and Isidis Planitia has the best fits between -20° and 45° (maximum deviation -10K). Fits made on the data taken during the global dust storms have significantly higher values for the fit inertia and albedo, but do not show larger deviations than fits made on data during clear periods. The areas which show the greatest deviations during clear periods show the greatest deviations during dusty periods. Areas which are well fit during clear periods are well fit during dusty periods.

The results mentioned above indicate that certain areas of Mars are not well fit by the standard thermal model. To learn more about these areas it is necessary to study data which has not been spatially averaged. Again, it is necessary to average data to get good diurnal coverage, but now the averaging has been done temporally. Data from all periods when the Martian atmosphere was relatively clear were used by Palluconi and Kieffer to find the best thermal inertia and radiometric albedo as a function of location (4). These inertia and albedo values allow the "best" model temperature to be calculated at any time of day for any area of the planet. These model temp-

eratures were subtracted from the observed 20 μm brightness temperatures and the resulting deviations averaged over 24 local time bins and 2° by 2° area bins.

These localized data can be compared with local properties of the surface to determine any dependencies. The time of maximum deviation of the observations from the model generally occurs between 18H and 19H. There is no correlation between the maximum deviation and elevation. There is a very strong correlation between the maximum deviation and the thermal inertia. Areas with low inertia have large deviations. Except for Sinai Planum, all areas with Lambert albedo, A_L, (1) less than 0.18 are well fit by the standard thermal model. All bright areas (A_L > 0.28) have deviations larger than -5K. There are no other correlations between the maximum deviation and geology or topography. The maximum deviations have been mapped between -35° and 60° latitude. This map shows that for most of the Martian surface the standard thermal model is sufficient for predicting the observed 20 μm brightness temperatures. However, 32% of the surface area shows large deviations of the observations from the model. This area is contiguous and connects the three low inertia regions (2). The VL1 site is just within this anomalous region and the VL2 site is outside it.

There are a large number of physical processes known to occur on Mars which are not included in the standard thermal model (5). All of these processes were considered as the cause of the deviations. Except for vertical inhomogeneity, all of these processes were rejected because their characteristics did not match the characteristics of the deviations. These processes can be separated into atmospheric and surface effects. Examples of atmospheric processes are: sensible heat exchange between the atmosphere and surface, H_2O clouds and ground fogs, CO_2 clouds and suspended dust. In general, atmospheric effects cannot account for the large deviations discussed above because the deviations are localized on the surface and do not decrease with elevation. Examples of surface effects are: temperature-dependent thermal properties, surface roughness, horizontal and vertical inhomogeneities. In general, the effects of these surface processes can be modelled by merely combining different members of the family of standard models. Only vertical inhomogeneity of the thermal properties can cause large deviations of the surface temperature from the standard model temperature.

For the vertical inhomogeneous thermal model, a layer of low thermal inertia material blankets a high thermal inertia material. At sunrise the top layer heats up quickly, and at sunset it cools quickly. During the night and at noon the surface temperature is moderated by the heat stored in the lower layer. This model accounts for all of the characteristics of anomalous afternoon cooling described above. By varying the inertia of the top layer and the radiometric albedo, good agreement between this model and the observations was acheived. The inertia of the lower layer is not important in determining the surface temperature as long as it is at least several times larger than the top inertia. The thickness of the top layer was found to be about one thermal skin depth.

A tentative explanation for the cause of the layering follows. After the global dust storms, a thin layer of dust is deposited on most of the Martian surface. If this layer is not removed during the subsequent year, a thermally thick layer will eventually develop. This is one explanation

for the three low inertia regions. The low inertia at the surface will cause large temperature variations and increased cycling of H_2O between the surface and the atmosphere. This enhanced H_2O cycling could cause the formation of a duricrust below the surface. The duricrust would form at a depth of approximately one thermal skin depth. Above this depth the high noon temperatures would drive off the H_2O in the low inertia soil. Since deposition is currently taking place (6), duricrust formation must also be taking place.

References

(1) Kieffer, H.H., Martin, T.Z., Peterfreund, A.R., Jakosky, B.M., Miner, E.D., and Palluconi, F.D. (1977). J. Geophys. Res., 82, 4249-4291.

(2) Zimbelman, J.R., and Kieffer, H.H. (1979). J. Geophys. Res., 84, 8239-8251.

(3) Martin, T.Z. (1981). Icarus, 45, in press.

(4) Palluconi, F.D., and Kieffer, H.H. (1981). Icarus, 45, in press,

(5) Jakosky, B.M. (1979). J. Geophys. Res., 84, 8252-8262.

(6) Guinness, E.A., Arvidson, R.E., Gehret, D.C., and Bolef, L.K. (1979). J. Geophys. Res., 84, 8355-8364.

FORMATION AND EVOLUTION OF SURFACE FEATURES IN EGYPT'S WESTERN DESERT: A SUMMARY OF MARTIAN ANALOGIES. Farouk El-Baz, National Air and Space Museum, Smithsonian Institution, Washington, DC 20560

The Western Desert of Egypt is part of the eastern Sahara, the driest large expanse of desert on Earth. This desert has evolved through a series of alternating wet and dry climates during the Quaternary. Specifically, the vast depressions in the Western Desert appear to have reached their present configuration in Acheulean time, 200,000 B.P. About 100,000 years later, a dry climate prevailed that was followed by a wet Mousterian period, 60,000 B.P. Several oscillations continued until about 25,000 years ago, where a long period of dryness persisted for 15,000 years. This was followed by a wet climate during the Neolithic 10,000 B.P., before the last drought set in over 5,000 years ago (1). The present aeolian episode has greatly modified, but not obliterated, products of previous climates. Because a similar evolutionary history may have occurred on the surface of Mars, even on a larger scale, it is important to consider the Martian features in light of their Saharan counterparts, which include:

A. Dry Channels

In this hyperarid Western Desert there are remnants of pluvial-interpluvial cycles including lacustrine deposits, inverted wadis, and terrace deposits along escarpments. Most prominent among the pluvial features are the dry channels in the Gilf Kebir plateau, which is capped by wind-resistant silicified sandstone. Incised into the 300m-high cliffs of the Gilf are 10 to 30 km-long channels that end abruptly as box canyons. The lack of significant catchments on the plateau surface suggests that the channels were formed by ground water sapping at the base of cliffs (2). Another possibility is that former catchment areas were present in softer beds that have been deflated by aeolian action (3). In both cases, analogies could be drawn to cliff-related channels on Mars.

B. Crescent Dunes

It is significant that in the open parts of the Western Desert, linear dunes predominate singly, as dune bundles, or in the vast Great Sand Sea. However, crescent dunes occur basically in depressions, particularly along escarpments. Crescentic dune accumulations are analogous to the larger dune mass in the north polar region of Mars, which may be similarly confined in a low area bounded by a plateau. The rate of motion of dunes in one of the Western Desert depressions, varies between 20m and 100m per year; the smaller the dune, the faster it moves (4). This may give us a basis for estimating the rate of motion of Martian crescentic dunes, with consideration of the differences in the two wind regimes.

C. Crater Splotches

A circular crater, 4 km in diameter, among the dunes of the Great Sand Sea displays dark colored material in the southern part of the crater interior. More importantly there is a distinct dark patch in the lee of the crater. This El-Baz Crater

(5) appears to have modified the patterns of material transport by the wind in exactly the same way as do craters in the Cerberus region of Mars.

D. Shadow Streaks

Dark streaks in the wind shadow of mountains and hills in the Western Desert form streamlined patterns that are similar to those in the lee of craters on Mars (6). The spindle-shaped streaks in the Egyptian desert change boundaries in response to changes in the depositional pattern of sand on either side; alterations of the deposition of sand occur due to changes in wind direction.

E. Knob Streaks

Unlike shadow streaks which form due to the lack of deposition in the lee of large topographic prominences, knob streaks develop from the deposition of aeolian material downwind of gaps between knobs. In the Sahara as on Mars these streaks are usually lighter in color than the surrounding surfaces (6). Study of the shape parameter in both cases shows a higher degree of streamlining of the terrestrial streaks, indicating a more efficient aeolian regime.

F. Knobs and Yardangs

Much like the equatorial region of Mars, the Western Desert of Egypt displays large fields of parallel corrasion features and numerous yardangs (7). In addition, remnants of scarps in the Western Desert are usually in the shape of inselbergs or knobs. Similarly, knobby terrain on Mars occurs near boundaries between plains and plateau units. The length to width ratios for measured knobs in Farafra (Egypt) and in Cerberus (Mars) are 0.63 and 0.65 respectively, even though the Martian knobs are 100-times larger than those in the Western Desert.

G. Surface Rocks

Blocks of varying sizes occasionally litter the surface of the Western Desert. Such areas resemble the block-strewn surfaces in the Viking lander sites. Two block fields in the southwestern part of the Egyptian desert were studied and compared to Martian block fields (8). One of the block fields surrounded a basaltic hill of Quaternary age with angular blocks 20-40 cm in diameter. In this field blocks are equidimensional, angular, with planar fractures, and slightly embedded in the sandy substrate, with few fillets, moats or wind tails. The other field consists of blocks, 20-50 cm across, which appear to have been placed there by floods during infrequent fluvial episodes. In this field the rocks are elongate, subangular, and usually with bimodal surface texture. The two block fields correlate well with the Viking lander sites in overall rock elongation form, rock roundness, and the presence of facets. From this correlation, it is plausible that the blocks in the Martian sites are made of massive basalt like those in the Western Desert. Also the blocks in both cases appear to have been emplaced by cataclysmic events such as occasional floods (Egypt) or meteorite impacts (Mars).

H. Pits and Flutes

The blocks in the Egyptian desert discussed above, although internally homogeneous and non-vesicular, exhibit pitted and

EGYPT'S WESTERN DESERT: MARTIAN ANALOGIES

El-Baz F.

fluted surfaces. The pits occur singly or in rows. Often a row of elongated pits forms a flute, and some of the flutes have pits in them (8). Wind tunnel studies of air flow over and around non-streamlined hand specimens show that windward abrasion coupled with negative air flow, secondary flow, and vorticity in a unidirectional wind explain the complex array of pits and flutes (9). These pits and flutes bear a striking resemblance to the pits and flutes in Martian rocks photographed at the Viking landers. This suggests that the blocks in the lander sites may have also been pitted and fluted by the wind.

I. Reddened Sands

Aeolian sands in the Western Desert of Egypt, like those in many other terrestrial deserts display a thin coating on the surface, which imparts a reddish color. Whether in sand sheets or sand dunes, it was established that clays and iron oxides are the major constituents of this coating on quartz sands of the Western Desert. In this case quartz grains are coated by kaolinite platelets, which in turn are coated by submicroscopic, powdery hematite (10). It was further established that the coatings vary in thickness from 0.5 micrometers to about 5 micrometers; the farther the sand from the source, the thicker the coating (11). These coatings clearly influence the spectral reflectance of the Western Desert sands as measured from space. Considering the reddish color of the surface of Mars, it is also likely that mineral grains are covered with similarly complex coatings that affect the spectral reflectance of the Martian surface.

The above summary of correlations indicates that the Western Desert of Egypt probably exhibits the largest number of terrestrial analogies to the surface of Mars. This is perhaps due to the fact that although fluvial action played a major role in terrain sculpture during Tertiary times, water-induced erosion did not overshadow the effects of the wind during much of the Quaternary. Furthermore, the features of the eastern Sahara have evolved through alternation of wet and dry climates during the past 200,000 years. Alternations of wet and dry cycles may have been responsible for the similar features on Mars.

References

1. Haynes C.V. (1981) in press.
2. Peel R.F. (1939) *Geogr. Jour.*, 113/4, 295-307.
3. McCauley J.F. et al. (1981) in press.
4. Embabi N.S. (1971) Soc. Geogr. Egypte Bull., 43-44, 7-71.
5. El-Baz F. (1981) In *Lunar and Planetary Science XII.*
6. El-Baz F. and Maxwell T.A. (1979) *Proc. LPSC 10th*, 3017-3030.
7. El-Baz F. et al. (1979) *JGR*, 84/B14, 8205-8221.
8. Garvin J.B. et al. (1981) In *Lunar and Planetary Science XII.*
9. McCauley J.F. et al. (1979) *JGR*, 84/B14, 8222-8232.
10. El-Baz F. and Prestel D.J. (1980) In *Lunar and Planet. Sci.XI.*
11. McKay D. et al. (1980) In *Rept. Planet. Geol. Prog.*, 304-306.

TERRESTRIAL AND SYNTHETIC ANALOGS TO MARTIAN WEATHERING PRODUCTS, D.L. Evans, J.B. Adams, T.G. Farr, T.L. Roush, Department of Geological Sciences, Univ. of Washington, Seattle, WA 98195; R.B. Singer, Hawaii Institute of Geophysics, Univ. of Hawaii, Honolulu, HI 96822.

Laboratory reflectance spectra of Hawaiian samples have been compared to earth-based telescopic spectra, and to Viking Lander and Orbiter images of Mars (1,2,3,4). Based on these studies, we have identified materials in the suite of Hawaiian samples that have similar spectral characteristics to the telescopic data and to units in the Viking Lander and Orbiter images, and examined the weathering sequence of the samples in detail in order to develop a possible model for Martian surface unit formation.

We found in (3) that weathered basalts in Hawaii are coated with layers of an amorphous material consisting of silica gel and locally derived soil containing weathering products of adjacent basalts and aeolian materials such as ferric iron-rich weathered tephra. Using the technique described in (2), we have found that certain weathered basaltic tephras and a powdered coating that was scraped off a basalt have similar spectral reflectance properties to surface units seen at VL1 (Figures 1 and 2). The weathered tephra and powdered coating also have similar spectral characteristics to global units seen in Viking Orbiter images (Figures 3 and 4). Furthermore, some coated basalts were also found to have spectral characteristics similar to Martian surface units seen in the Orbiter images (Figure 5).

Weathered tephra and coated basalts from Hawaii are also the materials most consistent with earth-based spectrophotometry of Martian regions (5). Bright region spectral characteristics are very similar to those of x-ray amorphous, weathered tephra (1). Telescopic data for dark regions is consistent with relatively fresh basalt thinly coated with weathered tephra (4). Basalts synthetically coated with ferric iron-rich gels and with fine grained weathered tephra have also provided good spectral analogs to Martian dark regions.

Comparisons of laboratory spectra of these synthetic samples and weathered basalts and basaltic tephras with earth-based telescopic spectra and spectral reflectance data derived from Viking Lander and Orbiter images support the conclusion that terrestrial weathering processes of basalts and basaltic glasses in arid to semi-arid regions (such as the high altitudes in Hawaii) provide excellent analogs for surface materials on Mars.

REFERENCES

(1) Singer, R.B. (1981) Lunar and Planet. Sci. XII, 996-998, (2) Evans, D.L. and J.B. Adams (1979) Proc. Lun. Planet. Sci. Conf. 10th, 1829-1834, (3) Evans, D.L., T.G. Farr, and J.B. Adams (1981) Submitted to Proc. Lun. Planet. Sci. Conf. 12th, (4) Singer, R.B. (1981) Jour. Geophys. Res., in press, (5) Singer, R.B., T.B. McCord, and R.N. Clark (1979) Jour. Geophys. Res., 84: 8415-8426, (6) Soderblom, L.A., K. Edwards, E.M. Eliason, E.M. Sanchez, and M.P. Charette (1978) Icarus 34: 446-464.

ANALOGS TO MARTIAN WEATHERING

Evans D.L. et.al.

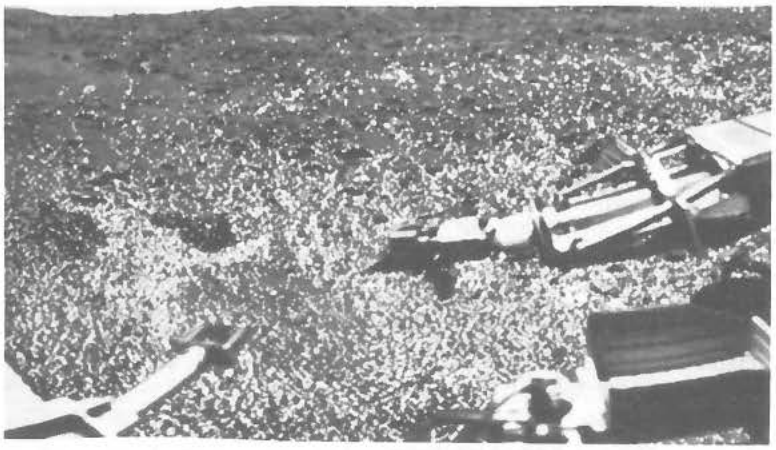

Figure 1. Viking Lander frame 11A147/026. Materials with same DN values as those calculated for a weathered basaltic tephra are shown in white.

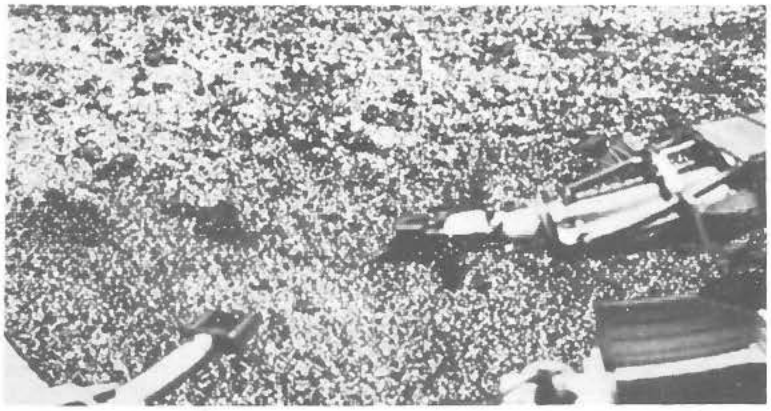

Figure 2. Viking Lander frame 11A147/026. Material with same DN values as those calculated for a powdered coating from a basalt are shown in white.

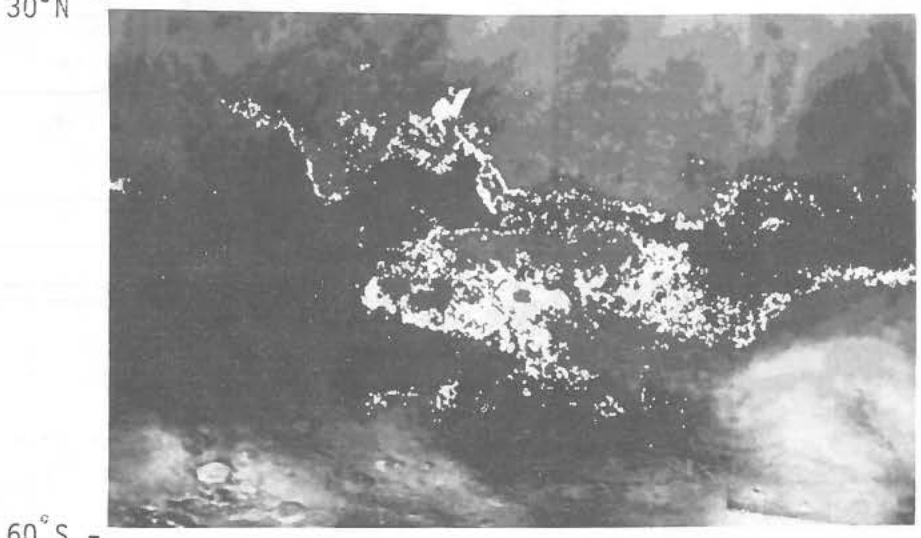

Figure 3. Viking Orbiter mosaic from (6). Material with same DN values as those calculated for a weathered basaltic tephra are shown in white.

Figure 4. Viking Orbiter mosaic from (6). Material with same DN values as those calculated for a powdered coating from a basalt are shown in white.

Figure 5. Viking Orbiter mosaic from (6). Material with same DN values as those calculated for a coated basalt are shown in white.

THE MARS ATMOSPHERE-CAP-REGOLITH SYSTEM AND CLIMATE CHANGE, F.P. Fanale, Planetary Geosciences, Hawaii Institute of Geophysics, U. of Hawaii; W.B. Banerdt, and R.S. Saunders, Jet Propulsion Laboratory, Calif. Institute of Technology.

Amount of Reversibly Stored "Regolith" CO_2: A near polar regolith of clay (ρ = 1.5) in equilibrium with a 6 mb CO_2 atmosphere at ~160°K would contain ~3 scc gm^{-1} of adsorbed CO_2* and the corresponding value for basaltic soil is 0.4 gm^{-1}. At ~200°K (mid latitude subsurface T) values are ~0.7 and 0.2 gm^{-1} respectively. Nominal estimates of regolith mass leads to estimated CO_2 contents 10X-100X that of the atmosphere (Fanale and Cannon, 1974, 1979; Toon et al., 1981). Also, it appears that the North cap is dirty H_2O ice (Kieffer et al., 1979) and the quasi permanent South cap is (though probably CO_2) only 10^{-4} of the Mars surface and very thin,containing at most a couple of equivalent millibars of CO_2. Thus the regolith reservoir of adsorbed CO_2 is much larger than the atmosphere + cap system. However it is still less than estimates of total degassed Mars CO_2, which leaves a possible role for irreversible storage in carbonates.

Long Term Exchange. The main period of thermally driven exchange is ~10^5 years, driven by obliquity/orbital variations (Ward et al., 1974, 1979). Given reasonable assumptions concerning regolith thermal properties, the surface thermal wave should penetrate the entire regolith that is subject to vapor exchange (Fanale and Cannon, 1974). The most important effect is desorption from near polar terrain because 1) polar regions suffer the greatest ΔT during the obliquity cycle (the equatorial ΔT is much smaller and opposite in sign), 2) the deepest unconsolidated regolith is in the layered terrain and collaring debris mantle, and 3) the greatest concentration of highly absorbing weathering products may be there. These considerations, plus our experimental determination of isoteres for weathering products and pulverized rock under Mars regolith conditions suggest a climatic response qualitatively mimicking that from a huge polar CO_2 surface deposit once thought to be present. Models with wide ranging assumptions concerning regolith properties, etc. yield maximum PCO_2's of up to 30 mb at maximum obliquity and minimum PCO_2's of <1 mb at minimum obliquity (Fanale and Cannon, 1979; Toon et al., 1981). Conversely, a deep highly adsorbing regolith acts as a capacitor preventing excursions of PCO_2 > 100 mb given current available CO_2. Conceivably the regolith may once have been ineffective as a buffer for the atmosphere-cap system. This, coupled with a greater available CO_2 inventory (now partly stored in carbonates?), may have contributed to ancient high PCO_2's. The atmosphere is buffered on a geological time scale by the regolith reservoir, not the very small and possibly non permanent south cap. (Fanale and Cannon, 1974, 1978, 1979; Toon et al., 1981). The existence of near-polar condensed CO_2 essentially reflects the operation of wide excursions of polar surface temperature on an atmospheric pressure subject to long term control by the regolith buffer isotere. Some hysteresis may be involved so that cap mass may partly reflect limitations on the rate of continuing CO_2 reequilibrium with the regolith.

Seasonal Exchange. The problem of seasonal exchange of CO_2 in the atmospheric-cap-regolith system is complex because the regolith is vastly deeper than the seasonal thermal skin depth (~1m). The regolith can behave as an isothermal buffer (Dzurisian and Ingersoll, 1975) or a thermal exchanger depending on the relation between thermal conductivity and vapor diffusivity. To model seasonal migration of CO_2 through the topmost regolith, we performed measurements of the isothermal migration of CO_2 in a cold fine-grained soil

*i.e. Each 5 m of regolith column contains as much CO_2 as the overlying atmosphere.

under Mars-like conditions of T, PCO_2, ΔPCO_2, and have compared these results to those derived from theory of diffusion in a porous, highly absorbing medium. Our results, still preliminary, suggest 1) the theory provides good approximations for diffusion rates under martian regolith conditions, 2) that typical penetration (1/e) depths of any externally imposed "pressure wave" in soils at a nominal -70°C for a 300 day season* are: 2.3m season^{-1} for basalt with 1 μm pore radius, 16 m season^{-1} for basalt with 50 μm pore radius and 1.1 m season^{-1} for a clay with 1 μm pore radius. Thus the contrary isothermal buffering response of these soils (adsorbing CO_2 in response to a P increase and desorbing it in respond to a P decrease) can be estimated. Based on these skin depths and our adsorption isotherms, we estimate that for an initial cap-imposed ΔP of ∿2 mb, the contrary isothermal responses would be: 0.03 mb for the 1 μm pore space basalt, 0.05 mb for the 1 μm clay and 0.2 mb for basaltic soil with 50 μm pores. Thus we conclude that although isothermal buffering of the seasonal wave might prove detectable; it would be dominant only if the pore spaces were very large (no silt).

On the other hand, the thermal responses of these soils could be considerable. For clay with a 1 m thermal skin depth, spring warming, from 160°K to 220°K, could desorb up to 1 gcm^{-2} or ∿0.5 mb - equivalent to ¼ the full seasonal effect - from the warming part of the disc. Thus it is hard to predict from first principles whether cap-atmosphere interaction is modified by the thermal or isothermal responses of a regolith on a seasonal time scale and there is nothing in the Viking seasonal pressure data that requires either (Hess et al., 1979). Post-Viking "cap only" models should be used to "predict" the seasonal pressure variation using observed values for cap albedo, extent of the cap etc. If a residual exists, regolith effects are a likely candidate, and the nature of such residuals, if any, might be suggestive of soil properties. Analogously, seasonal H_2O regolith-cap exchange models have been suggested (Pollack et al., 1970; Fanale and Cannon, 1974) and quantitative versions show promise for explaining Viking H_2O data (Jakosky and Farmer, 1981).

Consequences, Tests and Problems. Obviously, a periodic PCO_2 variation of >x20 would have profound effects. While maximum pressures envisioned are not high enough to induce a significant greenhouse effect or even profoundly to affect polar heat transport, still it could greatly affect dust transport rates (e.g. Greeley et al., 1981) and other aspects of Mars' atmosphere-surface environment (e.g. Will H_2O boil? What is crater ejecta distribution?) The deposition of the layered terrain is tied to variations in the quantity and size distribution of dust transported to the poles as the result of obliquity/orbital variations. Variations in cap mass and extent are also thought to have played a role (Cutts et al., 1979; Toon et al., 1981) and these could also result from periodic regolith-atmosphere-cap CO_2 exchange with a change in cap mass of up to 10^{20} g suggested in some models (Fanale and Cannon, 1979). Although regolith-atmosphere-cap exchange probably causes variations in cap extent, quantitative modeling requires some knowledge of adsorption laws for possible regolith materials. (e.g. Heat adsorption vs. heat of sublimation?) Although data on CO_2 adsorption on ground basalt and nontronite was published, CO_2 adsorption data on more recently suggested candidate surface materials such as amorphous gels are needed. A search for seasonal regolith effects is important not only for meteorology but because it is our only chance to observe directly the processes we invoke to produce long-term harmonic climate change. (It should be noted, however that the regolith may have properties of thermal and vapor diffusivity that allow it to control long term exchange while playing only a second order seasonal role,

*Assuming porosity = 0.6, tortuosity = 0.5 and adsorbed gas ÷ pore gas = 62 (basalt)

which may be undetectable in the face of cap-induced pressure change.) Also, our models must satisfy the need for flushing atmospheric O_2 at a geologically constant and high rate to prevent enrichment in ^{18}O comparable to the ^{15}N enrichment observed by Viking (McElroy et al., 1976). This rate is satisfied by our model and is $\sim 1 \times 10^3$ gcm^{-2} my^{-1}. Another test, (C. Leovy, 1981) is that the atmospheric CO_2 pressure cannot be so high for so long, on the average, that it shields the ^{14}N from preferential escape. The surface properties, specifically the BET area, of Mars soil were inferred indirectly from Viking measurements (Ballou et al., 1976) and found similar to that assumed in our model calculations and laboratory simulations. Direct observation of the adsorbed CO_2 by Viking is not claimed since CO_2 released at low temperatures might also have come from very thermal labile carbonates (Biemann et al., 1977) although recent laboratory simulations argue for the adsorbed phase (Gibson, 1981). Otherwise "tests" of the atmosphere-cap-regolith model are sparse. Orbiter images provide indications of distribution of debris, but no direct measurement of deep regolith properties. Orbiter imagery has provided a perplexing result for our model: the layered terrain appears to be less than 600 my old whereas processes in our model should have been continuing for billions of years. If anything, obliquity variation - driven exchange should have been more effective before Tharsis development (cf. Ward et al., 1979). No satisfying explanation has been found. Many uncertainties remain, but it is clear that Mars volatile history and climate change can only be understood in terms of a three part atmosphere-cap-regolith model.

References: Ballou, E.V. et al., Nature 271, 644-645, 1978. Biemann, K. et al., J.G.R., 82, 1979. Cutts, J.A., et al., J.G.R., 84, 2975-2994, 1979. Dzurisian, D. and Ingersoll, A.P., Icarus 26, 437-440, 1975. Fanale, F.P. and Cannon, W.A., J.G.R., 24, 3397-3402, 1974. Fanale, F.P. and Cannon, W.A. J.G.R., 83, 2321-2325, 1978. Fanale, F.P. and Cannon, W.A., J.G.R., 84, 8404-8414, 1979. Greeley, R. et al., Icarus, in press, 1981. Gibson, E.K., pers. comm., 1981. Hess, S. et al., J.G.R., 82, 4559-4573, 1979. Jakosky, B. and Farmer, C.B., Icarus, in press, 1981. Kieffer, H.H. et al., Science 194, 1341-1344, 1978. Leovy, C., Icarus, in press, 1981. McElroy, M. et al., Science 194, 70-72, 1976. Toon, O.B. et al., Icarus, in press, 1981. Ward, W.R. et al., J.G.R., 243-259, 1979. Ward, W.R. et al., J.G.R., 79, 3387-3395, 1974.

Acknowledgments: We thank J. Stevens, E. Laue, P. Diffendaffer, R.Sanger, L. Johansen and L. Muradian for technical assistance and C. Leovy, J.B. Pollack, W.R. Ward and O.B. Toon and B. Jakosky for useful discussions. This work was performed in part at the Univ. of Hawaii and in part at the Jet Propulsion Laboratory under NASA contract NAS7-100.

A PETROLOGIC MODEL FOR AN ISOSTATICALLY-COMPENSATED THARSIS REGION OF MARS, A.A. Finnerty, Jet Propulsion Laboratory, California Institute of Technology, Pasadena, CA 91109, R.J. Phillips, Lunar and Planetary, Institute, Houston, TX 77058

The Tharsis region of Mars is characterized by abundance of extrusive volcanic material of probable basaltic affinity, radial fracture pattern, high topographic relief and correlated free-air gravity anomaly. Sleep and Phillips (1979) found that it is possible to fit the gravity and topography data to an isostatic model if the crust in the Tharsis region is thinner than average crust, and if the upper mantle is thick (200-500km) and has abnormally low density.

Other solutions to the gravity and topography data are possible, but we have developed a petrologic model that appears to be qualitatively consistent with isostatic compensation, abundance of volcanics, and tensile failure contemporaneous with volcanism. Even if only 20-30% of the topography of Tharsis (Plescia and Saunders, 1980) is due to volcanic extrusions, this material must be derived from beneath the lithosphere, with unavoidable changes in composition, density and volume of the source region.

During partial melting of a peridotite source region, magmas are evolved that are successively more Fe-rich than the initial rock, and the residuum is correspondingly Fe-poor and therefore of lower than original density. The magma ascends to the surface because despite Fe-enrichment, the liquid is of lower density than surrounding rock. Upon extrusion, the magma freezes to a lower pressure mineral assemblage and/or glass, having a lower density than the rock that would form from the same composition at depth. The area above the source region must subside as magma is removed, but the net height of the rock column including source region, upper mantle, crust and extrusive rock must increase because mass is conserved while density is becoming lower. Isostatic conditions can be maintained continuously throughout the process, but the redistribution of mass and increase of volume causes a gravity anomaly correlated with, and subsidence contemporaneous with creation of a volcanic construct, and causes tensional fractures to form within and surrounding the volcanic field, with fractures both covered by and cutting extrusive units.

There are few experimental data relating partial melting to density changes in Fe-rich systems. However, a suite of garnet peridotite xenoliths from Northern Lesotho, South Africa may be interpretted to provide bounds for the Tharsis problem. These xenoliths range in composition from near that of pyrolite (model Earth mantle, Ringwood, 1975), to a composition equivalent to that of pyrolite but depleted in basaltic components. The trend of densities of these xenoliths (Jordan, 1979) with $Fe^{+2}/(Fe^{+2} + Mg)$ is displayed in Fig. 1, along with several model Mars mantle compositions (Wood et al., 1981). The point marked "1611" represents the xenolith least depleted in basaltic components, while 1569 is the most depleted.

If this trend represents the change in composition and density of the residuum of partial melting of a mantle with initial composition of 1611, then the process of partial melting has resulted in a decrease of density by $0.1 gm/cm^3$ in one terrestrial example. From the experiments of Harrison (1979) on 1611 it may be inferred that less than 10% melting of 1611 will yield this density change. For partial melting of the model Mars compositions, all but one of which would have garnet lherzolite mineralogy in the source region, a decrease in density of 0.2gm/cm in the source region by

PETROLOGIC MODEL FOR THARSIS

Finnerty, A. A.

partial melting seems plausible and would provide the low density region in the upper mantle required by the Sleep and Phillips (1979) model.

To calculate the mass-conserved volume change due to magma evolution a simple model has been set up (Fig. 2). In the initial pre-Tharsis state, a crust of density ρ_c, volume V_c and mass M_c overlies a mantle unit that will become the source region for magmas (ρ_m, V_s, M_s). In the final state are three units: a residuum (ρ_R, V_R, M_R) whose volume, mass and density are less than the original source region because of withdrawal of magma, a crustal unit unchanged from the initial crustal unit except for having subsided, and an extrusive unit (ρ_c, V_E, M_E) composed of the solidified liquid that has been tapped off from source region. This is considered to be a crust-forming process, so the density of the extrusive unit is assumed to be the same as that of the crust.

Assuming crustal density is 0.5gm/cm^3 less than initial mantle density, and that density of the ultimate residium (ρ_R*) is that of forsterite (3.22gm/cm^3), the relative volume change with mass fraction of melt is shown in Fig. 3. The two curves represent the limits for all Mars mantle model compositions (3.454 to 3.607gm/cm^3). The influence of different crustal density assumptions is represented by open circles at the right axis, which would be connected to the origin by similar curves.

Tholeiitic basalts of the ocean floors may be formed by 20-30% partial melting of garnet peridotite. For the much more Fe-rich mantle of Mars, where the lack of plate tectonics may signify that the source region is not replenished by mantle convection, 50% partial melting is not implausible. At 30% partial melting, volume increases by 7% and is manifested solely by a height increase. To get 10km of relief, as for Tharsis, a source region of about 140km initial thickness is required. Plescia and Saunders (1980) have estimated that only 20-30% of the Tharsis topography can be attributed to readily identifiable lava units, but given the tensile stress environment due to subsidence over the diminishing source region we think it plausible that sills and laccoliths could intrude the crust laterally and contribute to the topographic high. We note that, from the detailed stratigraphic studies of Scott and Tanaka (1980), it is clear that tensile failure and magmatism were simultaneous throughout the evolution of Tharsis, as predicted by this model.

In any real process for formation of Tharsis, it is likely that finite strength of the rocks contributes to the support of the topography (Phillips, Banerdt, Sleep and Saunders, abstract, this volume). The simultaneous withdrawal of melt from beneath the lithosphere and deposition on top of the lithosphere would result in a stress field as calculated in the Phillips et al. model. We intend to test this model further with stress field and gravity-topography calculations.

This work was performed at the Jet Propulsion Laboratory, California Institute of Technology, under contract to NASA.

REFERENCES: Harrison, W.J. (1979) Carnegie Inst. Wash. Yearbook 78, 562-568. Jordan, T.H. (1979) In: F.R. Boyd and H.O.A. Meyer (eds.) Proc. of Second Int. Kimberlite Conf., Amer. Geophys. Union, Washington, D.C. pp. 1-14. Plescia, J.B., and Saunders, R.S. (1980) Proc. Lunar Planet. Sci. Conf. 11th, 2423-2435. Ringwood, A.E. (1975) Composition and Petrology of the Earth's Mantle, McGraw-Hill, New York. Scott, D.H., and Tanaka, K.L. (1980) Proc. Lunar Planet. Sci. Conf. 11th, 2403-2421. Sleep, N.H., and Phillips, R.J. (1979) Geophys. Res. Lett. 6, 803-806. Wood, J.A., et al. (1981) In: Basaltic Volcanism on the Terrestrial Planets, Pergamon Press, New York, in press.

PETROLOGIC MODEL FOR THARSIS

Finnerty, A. A.

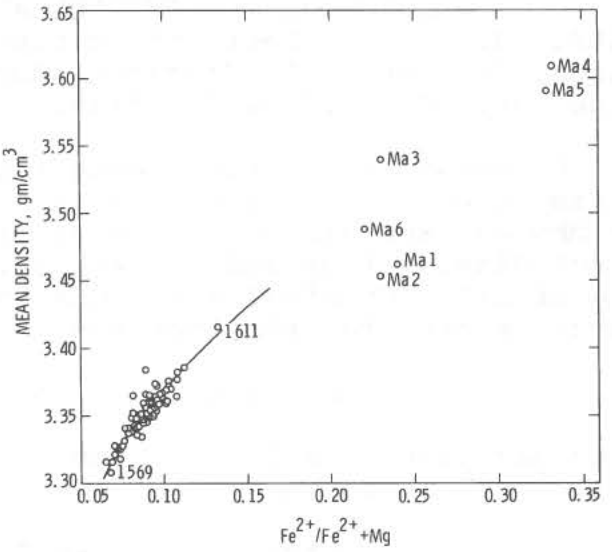

Fig. 1 - Trend of density vs. composition for ultramafic xenoliths (Jordan, 1979), with model Mars mantles from Wood et al. (1981).

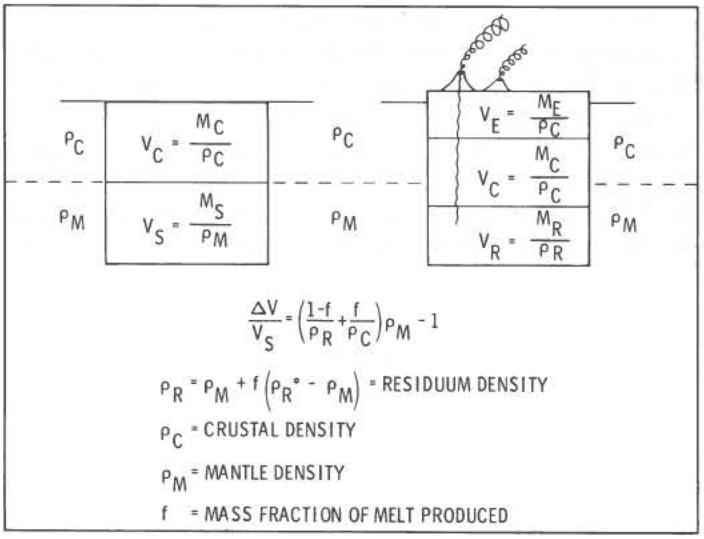

Fig. 2 - Model for formation of Tharsis plateau of Mars.

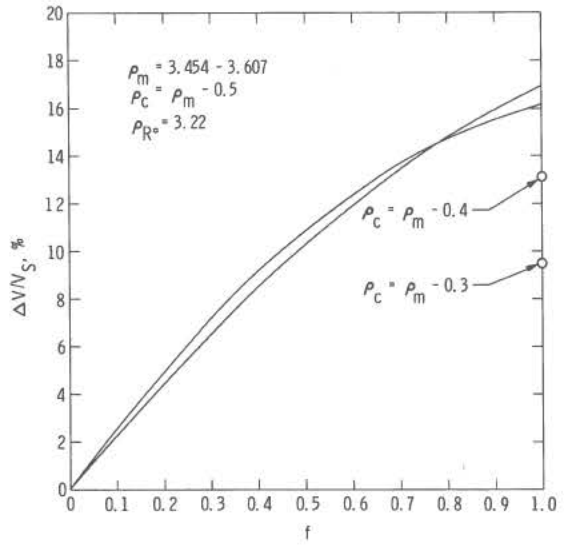

Fig. 3 - Relative volume change with fraction of partial melting for Tharsis model.

THE ESCAPE OF NITROGEN ATOMS FROM THE MARTIAN ATMOSPHERE. J. L. Fox, Dept. of Chemistry, University of Illinois, Urbana, IL 61801. A. Dalgarno, Center for Astrophysics, 60 Garden St., Cambridge, MA 02138.

Calculations of the escape rate of nitrogen atoms from the Martian atmosphere are presented. The major escape mechanisms are photodissociation and photoionization of N_2, photoelectron impact dissociation and ionization, and dissociative recombination of N_2^+. Chemical reactions constitute a somewhat smaller source, except for the reaction

$$O^{++} + N_2 \rightarrow O^+ + N^+ + N$$

which may produce a large escape flux at the exobase of about 4×10^5 $cm^{-2}s^{-1}$. The reaction

$$O^+(^2D) + N_2 \rightarrow N_2^+ + O$$

has been found to be much faster than previously assumed. The enhanced N_2^+ densities will result in an increased rate of escape by dissociative recombination, although the magnitude of the effect depends on the unmeasured rate of reaction of $O^+(^2D)$ with CO_2. The large total escape rate implies an initial reservoir of N_2 in excess of 10^{22} cm^{-2} and an enhancement in the $^{15}N/^{14}N$ isotope ratio, consistent with the ratio measured by Viking of 1.62 ± 0.16 relative to the terrestial value.

SILICIC PYROCLASTIC VOLCANISM ON MARS: ABSENCE OF EVIDENCE

[1]Peter W. Francis and [2]Charles A. Wood, [1]Lunar and Planetary Inst., 3303 NASA Road 1, Houston, TX 77058, [2]Geology Branch/Code SN6, NASA Johnson Space Center, Houston, TX 77058

Many workers have postulated the existence of large volumes of "pyroclastic" rocks on Mars. For example, one of several interpretations of the aureole surrounding Olympus Mons is that it is an apron of ash flow tuffs (ignimbrites)[1] while highland paterae such as Tyrrhenum Patera have been considered to be constructed largely of ash flow materials[2,3]. Apart from features actually associated with volcanic edifices, pyroclastic deposits have been either mapped or postulated in areas distant from known volcanoes. Scott and Tanaka have mapped deposits provisionally classified as "ignimbrites" covering more than one million km^2 in the Amazonis, Memnonia and Aeolis quadrangles. Other units have been identified as being possibly of pyroclastic origin due to their erosional characteristics[5].

Evidence supporting the existence of large volumes of pyroclastic rocks on Mars is at best circumstantial, and often entirely lacking. Scott and Tanaka, for example, concluded the the best criterion (for the recognition of ignimbrites) "...on a planet such as Mars, where volcanic flows prevail over sedimentary deposits (sic) is the very absence of features characteristic of lava flows."[4] Furthermore, few of those who have described Martian pyroclastic rocks have discussed the composition of their "ignimbrites" and "ash flows." Since terrestrial ignimbrites and ash flows are almost without exception silicic, the implication is that the Martian examples also are.

Here we review briefly the characteristics of the large volume terrestrial pyroclastic flows and their source structures; the physical constraints on production of pyroclastic rocks on Mars; and the geochemical evidence for differentiated rocks on the planet.

Characteristics of terrestrial pyroclastic flows and source structures.

Pyroclastic flows form broad, featureless flat-lying deposits that are not easy to identify on air or space-craft imagery. The most characteristic features are predominant pale tones, and patterns of wind or water eroded gully patterns. In arid areas of known volcanic activity these can be diagnostic[6,7]. In the absence of ground control, however, they can easily be confused with sedimentary deposits. Identification of terrestrial ignimbrites is most secure near their sources. These are often inconspicuous, even for large flows less than 1 m.y. old, since many are structures with low or even negative relief[8,9], such as the Taupo volcano, New Zealand.

Pyroclastic flows may be erupted from linear or arcuate fissures[8], but the largest flows are associated with resurgent calderas[10], such as Valles, New Mexico, and Cerro Galan, Argentina[7]. Studies of LANDSAT imagery reveals that the most easily recognizable features of ignimbrite source regions are the presence of eroded deposits; the presence of caldera ring fractures, linear or arcuate fissures; post eruption resurgence, and most important, presence of post eruption dacitic or rhyolitic extrusions[8]. The latter often have volumes less than 0.1% of the volume of the flows with which they are associated, but their morphology and location on fractures or fissures are conspicuous.

SILICIC PYROCLASTIC VOLCANISM ON MARS

Francis, P. W. and Wood, C. A.

Physical constraints on pyroclastic eruptions on Mars.

Wilson and Head[11] have reviewed the mechanisms of explosive volcanic eruptions on Mars. They argue that because relatively smaller mass eruption rates are combined with wider vent radii on Mars, pyroclastic flow formation should be rather easier on Mars than on the Earth, assuming that the chemical environments are similar.

Terrestrial pyroclastic flows owe their great mobility to the fact that they are emplaced as partially fluidized bodies, in which large clasts are dispersed in a fine grained, fluidized matrix[12]. The lower surfact atmospherеic pressure on Mars means that pyroclastic flows resulting from collapse of convecting eruption columns will loose their fluidizing gas much more quickly than terrestrial ones, and thus will come to a halt more quickly. This effect will be partially offset by the lower surface gravity, but overall it seems likely that Martian pyroclastic flows will be shorter and thicker than their terrestrial equivalents.

Pyroclastic fall deposits on Mars, by contrast, are likely to be thinner and more widespread than comparable deposits on Earth, since convecting eruption columns on Mars are likely to rise higher and become more widely dispersed.

Composition of volcanic rocks on Mars.

Evidence of the composition of Martian volcanic rocks comes from three sources:

1. Soil sample analyses at the Viking 1 and 2 lander sites, coupled with observations on the nature of the boulders imaged at the landing site[13].

2. Earth based and spacecraft based remote sensing observations of both light and dark areas of the planet[14].

3. Measurement of lava flow morphologies on Olympus Mons and other volcanoes, which provides constraints on the yield strength of the flows and thus their compositions[15].

These three techniques all provide strong positive evidence for the presence of volcanic rocks of basaltic composition on Mars, but no evidence for the existence of material of more evolved, silicic composition.

Discussion.

The physical parameters outlined by Wilson and Head[11] and the clear evidence of basaltic volcanism on Mars suggest that pyroclastic fall and flow deposits of basaltic composition may be widespread, though individual examples are not easy to document.

Although the physical models suggest that pyroclastic flow formation should take place more easily on Mars than the Earth, there is no evidence that the chemical environments are similar, and no direct evidence for silicic rocks at all, pyroclastic or otherwise. While accepting the possibility that large volcanoes such as Olympus Mons may have been the source of

differentiated rocks during their history, and that there are many topographic features on Mars with peculiar or enigmatic morphologies, we know of none that positively suggests the presence of silicic pyroclastic rocks or their source structures. In the case of Olympus Mons itself, the suggestion advanced by King and Riehl[1] and Morris[16] that the aureole deposits are ignimbrites at least has in its favour the fact that they are seen in association with a major volcano. In the absence of other compelling evidence, however, we feel that evidence that they are debris flow deposits associated with the circumferential scarp around the volcano is convincing[17].

Thus in the absence of any strong direct evidence for their identification as ignimbrites, we conclude that the deposits mapped as such on Mars would be better mapped in terms of processes known to operate on Mars, rather than purely speculative ones. The ubiquitous evidence for aeolian processes and the climate, for example, suggest that the accumulation of loess like deposits is inevitable. In this context, it is interesting to note that material such as that mapped by Scott and Tanaka[4] has been interpreted as paleo polar deposits by Schultz and Lutz-Garihan[18].

REFERENCES

1. King J. S. and Riehle J. R. (1974) *Icarus* 23, 300-317. 2. Reimers C. E. and Komar P. D. (1979) *Icarus* 39, 88-110. 3. Greeley R. and Spudis P. D. (1981) *Rev. Geophys. Space Phys.* 19, 13-41. 4. Scott D. H. and Tanaka K. L. (1980) NASA Tech. Memo 82385, 255. 5. Ward A. W. (1979) *J. Geophys. Res.* 84, 8147-8166. 6. Guest J. E. (1969) *Geol. Soc. Amer. Bull.* 80, 337-362. 7. Francis P. W. and Baker M. C. W. (1978) *J. Volcanol. Geotherm. Res.* 4, 81-87. 8. Baker M. C. W. (1981) *J. Volcanol. Geotherm. Res.* (in press.) 9. Sparks R. S. J. (1975) *Geol. Rundsch.* 64, 497-523. 10. Smith R. L. and Bailey R. A. (1968) *Mem. Geol. Soc. Amer.* 116, 613,662. 11. Wilson L. and Head J. W. (1981) *Lunar and Planetary Science XII*, 1194-1196, (abstract) Lunar and Planetary Institute, Houston. 12. Sparks, R. S. J. (1976) *Sedimentology* 23, 147-188. 13. Toulmin P. *et al.* (1977) *J. Geophys. Res.* 82, 4625-4634. 14. Singer R. B. *et al.* (1979) *J. Geophys. Res.* 84, 8415-8426. 15. Moore H. J., Arthur D. W. S. and Schaber S. S. (1978) *Proc. Lunar Planet. Sci. Conf. 9th*, p. 3351-3378. 16. Morris E. C. (1980) NASA Tech. Memo 82385, 252-253. 17. Lopes R. M. C., Guest J. E. and Wilson, C. J. W. (1980) *Moon and Planets* 22, 221-234. 18. Schultz P. H. and Lutz-Garihan A. B. (1981) *Lunar and Planetary Science XII*, 946-949, Lunar and Planetary Institute, Houston.

SMALL CONES ON MARS: DISTRIBUTION AND PROPERTIES

Herbert Frey and Martha Jarosewich, Geophysics Branch, Goddard Space Flight Center, Greenbelt, MD 20771

The most abundant (apparently) volcanic structures on Mars are small pitted mounds generally $\lesssim$ 1 km across. A systematic search of the available high resolution Viking I and II imagery has shown these features exist on a variety of plains units (1), most of which are mapped as volcanic (2). Most of the observed fields are in the northern hemisphere, especially in the Acidalia Planitia region (3), although one abundant group of similar structures has been found near Hellas (4). We have mapped the locations of these fields, correlated them with local geology, and measured diameters of the cones and central pits for more than 2000 well imaged structures. This report covers part of the results for features in Acidalia, Elysium and Utopia-Isidis.

In Acidalia small cones are observed on smooth, fractured and subdued fractured plains, and are especially abundant near Cydonia Mensae (38 to 41°N, 8 to 15°W). This area displays a variety of geological features, some of which have been ascribed to volcano-ice interactions (5,6). Within Cydonia differences in both base diameter and crater/cone ratio occur: the northern group of 140 measured cones is strongly bimodal in base diameters, with peaks at 600 and 850 m. The more southerly cones (152 cones) cluster at the 600 m diameter. Crater/cone ratios are also different: the northern group is more strongly peaked at 0.45-0.54 than the southern group. The differences in base diameter may be associated with the kinds of plains on which the cones are found, as described below.

Elsewhere in Acidalia other groups of small pitted cones are found, some of which tend to be larger than the Cydonia mounds. Throughout Acidalia, however, crater/cone ratios are characteristically 0.45-0.54, a value found for these structures in Elysium and Utopia-Isidis as well (see Figure 1A). We note that this value is also characteristic of Icelandic pseudocraters near Lake Myvatn, measured from an airphoto of that region, and shown in Figure 1A. The similarity of crater/cone diameters does not prove these martian cones are pseudocraters, although we and others have suggested this is a possible explanation (1,3,5,6). While pseudocraters in Iceland are produced by steam explosions which result when lava flows over trapped water (7), on Mars a lava-ice contact may be the comparable process (3,5).

Differences in the distribution of cone diameters occurs between regions on Mars, and also between different terrain types with which the cones are associated. Figure 1B compares the sizes of cones in Utopia-Isidis (242 cones) with those in Acidalia (552 cones). In Utopia, the generally more scattered features are found only on smooth plains; in Acidalia small cones 300-1250 m across are found in both smooth and fractured plains, and are displayed separately in Figure 1B. The Acidalia structures show a bimodal distribution in diameters, as described above. In the smooth plains the peak occurs at ~600 mm diameter with a weaker secondary peak at 750-850 m. In fractured plains the large diameters dominate and the peaks are more nearly comparable. This bimodal distribution does not occur in Utopia-Isidis, where a broad range of diameters 500-650 m is seen. The crater/cone ratio (shown on an expanded scale in Figure 1B) is quite similar in distribution for the Acidalia cones, with very little difference seen between fractured and smooth plains. This may suggest the structures are all formed by a similar process. Note the absence of a strong peak at crater/cone = 0.50-0.54 in the Utopia-Isidis data, but otherwise the distributions are similar to those in Acidalia.

Small Cones on Mars

Frey, H. et al.

Maps showing the density distribution of these and similar features in the northern plains and near Hellas are being prepared, and we are plotting histograms of the cones in order to relate their properties to geologic setting, age of plains formations and association with other structures. Based on our results to date, it is not possible so far to unambiguously identify the origin of these structures. We have previously suggested, based on general morphology, size and distribution, that these small cones are ice-volcano analogs of pseudocraters (1,2,3). This possibility is supported, especially in Acidalia, by the association of the cones with volcanic plains on which other possible volcano-ice structures have been identified (5). However, it is not possible to rule out cinder cones (8) or pingoes (9), both of which have been suggested. The crater/cone ratios shown in Figure 1A are consistent with Icelandic pseudocraters, but also fall into the range described by Wood (10) for pingoes. The martian ratio is, however, larger than that quoted by Wood for cinder cones. Furthermore, the limited literature available on terrestrial pingoes suggest they are often irregular in form, and their nature may not permit their survival over long periods of geologic time (11). Our data suggest variations in the properties of the martian cones from region to region and within regions, and some of this variation may be associated with geologic setting. If the cones are pseudocraters, then a natural explanation for the bimodal distribution of diameters in Cydonia might be two different thicknesses of lava flows in which they had formed. Theoretical work (Rocha, unpublished) suggests that thicker flows will produce larger cones, which is consistent with the observations of Thorarinsson (7) in Iceland.

(1) Frey, H. and Jarosewich, M., 1981, Lunar Planet. Sci. Conf. XII, 297. (2) Scott, D.H. and Carr, M.H., 1978, Geologic Map of Mars M25M, I-1083. (3) Frey, H., Lowry, B.L. and Chase, S.A., 1979, J. Geophys. Res., 84, 8075. (4) Frey, H., Jarosewich, M. and Partridge, K., 1981, Lunar Planet. Sci. Conf. XII, 300. (5) Allen, C.C., 1980, NASA TM 81979, 161. (6) Hodges, C.A., 1979, NASA TM 80339, 247. (7) Thorarinsson, S., 1953, Bull. Volcanol. Ser. 2, 14, 3. (8) Wood, C.A., 1979, Proc. Lunar Planet. Sci. Conf. 10th, p. 2815. (9) Judson, S. and Rossbacher, L., 1979, NASA TM 80339, 229. (10) Wood, C.A., 1980, Third Coll. Planet. Water. (11) Muller, F., 1959, Meddelelserom Grønland, 153, p. 127.

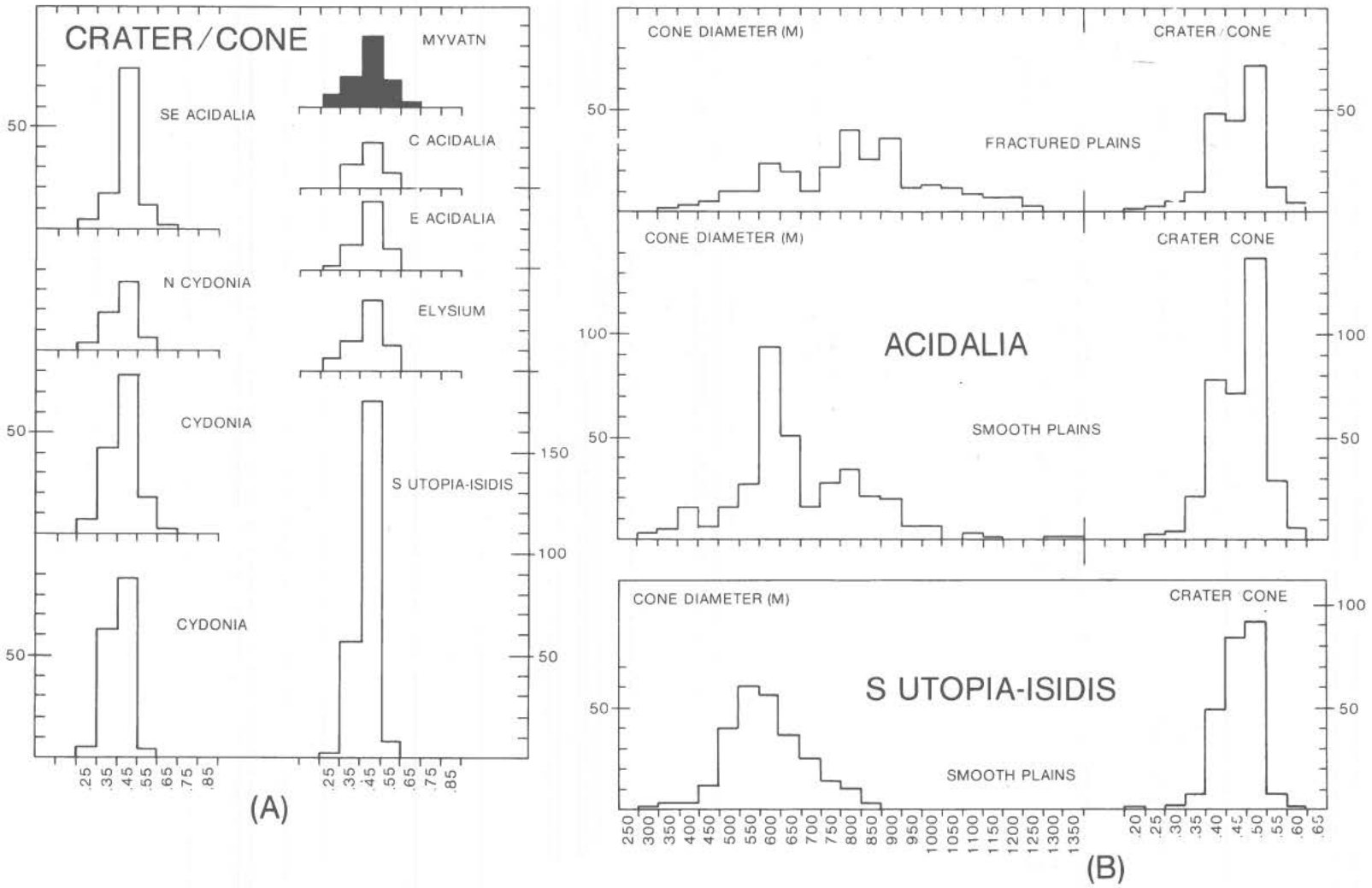

Figure 1. (A) Measured ratio of crater diameter to cone diameter for small martian cones in the northern hemisphere of Mars, and for pseudocraters in Iceland (shaded).

(B) Cone diameter and crater/cone ratio for Acidalia cones (separated by fractured and smooth plains) and Utopia-Isidis cones (smooth plains only). See text for details.

CHARACTERIZATION OF ROCK POPULATIONS ON THE SURFACES OF MARS, VENUS, AND EARTH: A SUMMARY. J. B. Garvin, P. J. Mouginis-Mark, and J. W. Head, Dept. of Geol. Sci., Brown University, Providence, RI 02912.

Introduction. Rock populations on planetary surfaces reflect both local-scale and global-scale geologic processes [1]. Modes of formation, emplacement, and modification for individual blocks can be inferred from their morphology and morphometry (i.e. dimensions). This information can be related to planet-wide geologic phenomena such as volcanism, eolian erosion, chemical weathering, and meteorite impact. Over the past two years we have been establishing a data base for interplanetary rock population comparisons. Qualitative morphologic data concerning rock modification features (pits, flutes, facets, wind tails etc.), features diagnostic of a particular mode of origin (columnar joints, vesicles, flow bands etc.), and local environment have been collected from Viking lander images of Mars (VL-1, VL-2), Venera 9 and 10 panoramas of Venus, and from photographs of test sites in Egypt (WMB, GKR), Hawaii (MKS, HLM), and Iceland (ICB) [1,2]. Morphometric information (length and width axes) was also collected when viewing geometry was well-known. Table I summarizes some of the presently available data. Clustering analysis of the morphologic and morphometric data for Mars, Egypt, Iceland and Venus has been completed [1,6,7]. Power law fits to the rock size distributions available for martian, Hawaiian, and Egyptian sites, along with the determination of two-dimensional sphericity were also carried out [1,2,8]. Objectives in the martian analyses have been to infer 1) the types of rocks present at the Viking lander sites, 2) the emplacement mechanisms (i.e. debris flows vs. in situ lavas), and 3) modification histories (wind weathering vs. chemical and water-related erosion). Parallel studies of distinctive Earth environments provides an understanding of the basic processes operating at these scales.

Mars. [Table I; 1,3,4] VL-1 and VL-2 are quite similar in terms of general rock shape (form ratios of -0.25 to -0.30 indicate moderate elongation) and sphericity. However, rocks at VL-2 are generally larger than those at VL-1, where pebble size fragments dominate. The "b" parameter in a power law fit to the rock sizes (see Table I) at VL-1 is similar to disintegrated igneous boulders on Earth [5], or Tycho impact debris near Surveyor VII [5]. At VL-2, the "b" value is consistent with multiply fractured basalts as observed at Halemaumau (HLM) or near the summit of Mauna Kea (MKS). Both Viking rock populations have form ratios indicative of isotropic, homogeneous igneous rocks (see ICB basalts in Table I) [1]. In terms of morphology, the VL-1 and VL-2 sites display highly pitted surfaces with abundant flutes. Most rocks are somewhat elongate and sub-angular. Small, shallow cavities abound at VL-1, whereas larger, deeper and more spherical cavities dominate VL-2 rocks. Wind features such as sediment moats, tails, and fillets (aprons) are more common at VL-1 than at VL-2, most likely due to the higher surface area block cover at VL-2 relative to VL-1 (20% vs 8%) [3,4]. Pit distributions on VL-1 blocks are typically uniform, whereas those at VL-2 are bimodal. Faceted rocks are common at VL-1, but much less so at VL-2. Large (cm size), multi-level cavities are observed at VL-2, but none can be seen at VL-1. These cavities resemble the small-scale tafoni (honeycomb weathering) that have been observed in a variety of salt weathering environments on Earth [9] as well as certain vesiculation patterns. While most rocks at the Viking lander 1 locality are at least slightly buried, many blocks at VL-2 appear to be perched, and no VL-2 rocks give the impression of a high degree of burial.

CHARACTERIZATIONS OF ROCK POPULATIONS

Garvin, et al.

Clustering analysis of the morphologic data for VL-1 and VL-2 suggests that rock groups at VL-1 can be separated on the basis of surface texture, pit distribution, angularity, and linear features (fissures, bands, cracks). At VL-2, surface texture, angularity, and degree of elongation are the best rock class separation criteria. If modification features only are considered in clustering the data, cavity (i.e. pit) distribution, flute presence, and cavity size are the critical parameters in separating rock morphologic groups at VL-1, whereas degree of burial, cavity distribtuion, and presence of linear features (cracks, bands) are most diagnostic at VL-2 [1,7].

These preliminary analyses indicate fundamental differences in the rock populations at the two VL sites on Mars. These differences are best reflected in the styles of pitting in the rocks at the two localities. At present, we are conducting a detailed study of pits in near-field rocks at VL-1 and VL-2 in order to correlate them with volcanic (i.e. vesicular) or weathered (i.e. wind pitted or chemical) terrestrial rocks. At this stage in our analysis, it appears likely that the pits and flutes on VL-1 blocks are wind-related, while most of those visible on VL-2 rocks are related to the rock formation process and could be vesicles. Some VL-2 rocks display a pitting style that resembles tafoni in vesicular tholeiitic basalts observed on Hawaii, and could represent salt-weathering pits resulting from frosts [9].

The actual composition of the rocks at the Viking sites cannot be inferred from the analysis of VL images at this time. However, studies of a variety of lithologies under conditions similar to those on Mars in several ways can constrain the realm of possibilities. We have analyzed high resolution photographs of block fields in the Western Desert of Egypt [6,7], at two localities on the island of Hawaii [8,9], and at one site on Iceland in a fashion identical to that used for the Viking lander images. All of these terrestrial analog sites have extrusive igneous rock populations ranging from tholeiitic basalts to more alkalic basalts (Iceland and Mauna Kea).

Terrestrial analogs. (Western Desert of Egypt) Two basaltic localities in the hyperarid Gilf Kebir of Egypt were studied. The WMB site is a basalt plug that intruded the sandstones at Wadi Mashi during the Quaternary. The columnar jointed, wind pitted basalts at WMB are non-vesicular, aphanitic, and homogeneous. The GKR locality displays wind-fluted basalt fragments resting upon a desert pavement (reg) surface. Analysis of the morphologic data for these sites [6,7] reveals the importance of emplacement and modification processes in shaping a basaltic rock population under arid conditions. Wind pits and flutes are the only surface markings on the Egyptian basalts, and resemble VL-1 fragments quite closely. None display the high degree of pitting, or the deep cavities observed in many VL-2 rocks. We are using the Egyptian localities as end-members in which wind erosion is the dominant rock modification process on blocks not originally pitted from their formation process (i.e. vesicular). In addition, the WMB boulders have abundant columnar joints and linear features (cracks), both of which could be present in martian rocks. The GKR rocks were likely transported by floods caused by torrential rains in the desert pedeplain. The VL-1 site lies near the mouth regions of several large channels in Chryse Planitia [3], and fluvial or flood transported fragments could be present there. Based on comparisons with the GKR fragments, however, VL-1 does not resemble a water-affected arid locality.

Hawaii: (Mauna Kea and Halemaumau) Two field sites in Hawaii have been studied in terms of their rock size distributions. Glaciated alkali basalt flows near the summit of Mauna Kea (MKS) are comparable to VL-2 in terms of their power law distribution (see Table I). Phreatic basalt ejecta from

Halemaumau pit crater in Kilaueau caldera (HLM) resembles VL-2 as well, but is more analogous to the Surveyor III site on the moon in terms of its power law distribution [5]. The basalts at MKS are vesicular and elongated. They have been affected by wind, rain and snow, and are less angular than the recently emplaced (1924) massive tholeiite fragments at HLM. Both Hawaiian sites display rocks that are more spherical and elongate than martian or Egyptian ones (see Table I). Morphologic studies of these rocks are in progress.

Other localities: The Venera 9 and 10 localities on Venus have also been compared to the VL sites on Mars in terms of rock morphology [1,2]. The blocky Venera 9 site has a "b" parameter that indicates that the platy rocks there are very simply broken [5], unlike those at the Viking sites. The Venera 13 and 14 missions to Venus in 1982 may provide better imagery of Venus, and permit more detailed Mars-Venus rock population comparisions.

Table I. Summary of morphometric parameters for planetary surface block fields. N is size of rock population. See text for details. N/A means "not available".

Site	Location	N	Form Ratio*	Mean Diam. (cm)	Mean W/L#	Size Range (cm)	b@	K@
VL-1	Chryse Planitia, Mars	240	-0.25	5.8	0.634	1.8-21.3	0.78	2438
VL-2	Utopia Planitia, Mars	210	-0.30	7.3	0.631	1.3-25.1	0.69	1955
WMB	Wadi Mashi Basalt Hill, Egypt	101	-0.42	2.9	0.660	0.2-17.0	0.50	91
MKS	Mauna Kea Summit Basalts, Hawaii	114	-0.49	6.9	0.720	2.2-24.9	0.69	1040
HLM	Halemaumau Phreatic Ejecta, Hawaii	109	-0.56	6.6	0.740	1.3-24.5	0.71	991
GKR	Gilf Kebir Reg Basalts Egypt	51	-0.56	N/A	N/A	N/A	N/A	N/A
ICB	Iceland Basalts	31	-0.29	N/A	N/A	N/A	N/A	N/A
Venera 9+	Beta Regio (NE), Venus	63	-0.17	~7.5	N/A	3.0-40.0	0.27	427
Venera 10	Beta Regio (SE), Venus	30	+0.45	N/A	N/A	N/A	N/A	N/A

*Based on morphologic data
Values < 0 are elongate; Values > 0 are platy

#W is width, L is length in cm; W/L is 2-dim. sphericity
Values near 1.0 are spherical

@From power law fit to rock size data (r=rock radius): $N_r = Kr^{(-3b)}$, b is exponent and K is constant. Correlation > 0.90 in all cases

+Based on data from Keldysh [10]

References: 1] J. B. Garvin et al. (1981) The Moon & Planets 24, 355-387. 2] J. B. Garvin et al. (1980) LPS XI, 317-319. 3] A. B. Binder et al. (1977) J. Geophys. Res. 82, 4439-4451. 4] T. A. Mutch et al. (1977) J. Geophys. Res. 82, 4452-4467. 5] W. K. Hartmann (1969) Icarus 10, 201-213. 6] J. B. Garvin et al. (1981) LPS XII, 327-329. 7] J. B. Garvin (1981) NASA SP in press. 8] J. B. Garvin et al. (1981) NASA TM 82385, 238-240. 9] J. B. Garvin and P. J. Mouginis-Mark (1981) LPS XII, 330-332. 10] M.V. Keldysh (ed.) (1979) NASA TM 75706, 193 pp.

WEATHERING PROCESSES IN MARTIAN-LIKE ENVIRONMENTS: COLD DESERT ANALOGS. E.K. Gibson, Jr., SN7, NASA Johnson Space Center, Houston, TX 77058.

Weathering of planetary surface materials result from both chemical and physical interactions of the planet's surface with the atmosphere and, if present, the hydrosphere and biosphere. The net result of weathering is to modify the original surface materials and produce secondary materials that are the products of equilibrium between the atmosphere and solid body. In order to properly study the weathering processes operating on planetary bodies, analog studies must be carried out either in the field or in the laboratory under controlled conditions. We have been studying the weathering processes operating in the Earth's coldest and driest desert. The Dry Valleys of Antarctica are considered by many workers (1,2) to be the best terrestrial analog of the surface of Mars. The weathering processes operating in the Dry Valleys are related to the Martian surface in the following manner: Low temperatures (mean temperature of -17°C in Wright Valley), low absolute humidities, diurnal freeze-thaw cycles (even during daylight hours), low annual precipitations, desiccating winds, low magnetic fields, and oxidizing environment. In the Dry Valleys physical or mechanical weathering predominates over chemical weathering processes (3). Even though chemical alteration is a secondary weathering process in the Dry Valleys, it is still present and plays an important role in regolith processes. In order to better understand the formation and modification processes operating on the Martian surface, a suite of systematically sampled soils, rocks, and cores from the valleys and brine ponds of Taylor and Wright Dry Valleys in Antarctica were collected during the 1979-80 austral summer. The samples have been stored at temperatures below -10°C since their time of collection. X-ray fluorescence analyses have been made on the soils along with total carbon, sulfur, and water measurements. In addition, the water soluble cation and anion (Ca^{2+}, Na^{+}, K^{+}, NO_3^{--}, SO_4^{--}, and Cl^{-}) abundances were determined and their relationships studied for the regolith processes operating on the soils obtained from the Prospect Mesa Formation in Wright Valley.

Soils of the Prospect Mesa Formation are one of the oldest, if not the oldest, soils present in Antarctica (4). Soil samples were collected from a one-meter deep soil pit and these soils sampled the aeolian zone, salt formation zone, active zone, seasonally frozen zone, and permanently frozen zones. Soils were analyzed and the results are given in Figures 1 and 2. The aeolian zone (top 2 cm) represents an area of deflation and showed slight depletions in total water, sulfur, chloride, sodium, potassium, and sulfate concentrations as compared to the salt layer immediately below this surface. Concentrations of sodium, chloride, nitrate, sulfate, potassium, and total sulfur were the highest in the salt or evaporite-rich zone. Sulfur concentrations as high as 2.21% were found. Concentrations of water soluble ions (K^{+}, Ca^{2+}, SO_4^{2-}, NO_3^{-}, Na^{+}, and Cl^{-}) systematically decreased (Fig. 2) in the zones above the permanently frozen ground (depth of 35 to 40 cm) and remained essentially constant below the permanently frozen ground (Fig. 2). This suggests that essentially no exchange or transport of these cations or anions is occurring and the major geochemical changes are occurring above the permafrost level. It is interesting to note that the molar concentration ratio of Na^{+} to Cl^{-} was almost identical. The presence of halite is suggested by these results. Secondary minerals previously identified in the Dry Valley soils include the following: halite, mirabilite, bloedite, gypsum, calcite, aragonite, monohydro-calcite, soda niter, therardite, antarcticite, bishovite, sylvite, trona, and limonite (5,6). The sulfur enrichments in water soluble cations and anions near the

WEATHERING PROCESSES IN MARTIAN-LIKE ENVIRONMENTS

Gibson, E. K., Jr.

surface represent addition of these components from lateral transport and not from upward movement through the soils.

A comparison of the total sulfur and water soluble chloride concentrations present in the Dry Valley soils with those measured at the Viking 1 and 2 sites on Mars is given in Figures 1 and 2. The S and Cl data are from Clark (7). The chloride concentrations (Fig. 2) in the Dry Valley soils from below the permafrost level are almost identical to the 15 soils analyzed on Mars. The sulfur concentrations (Fig. 1) from the salt-rich regions are similar to those reported for the Martian regolith. From the normal weathering processes operating in the cold environment of Antarctica on the source rocks (Beacon sandstone and Ferrar dolerite), the enriched sulfur and chlorine concentrations are similar to the soils analyzed on Mars. Thus, such enrichments can be produced by normal weathering processes, and no "exotic" sulfur- or chloride-rich source rocks are necessary.

Detailed studies of the soils present within the Dry Valleys of Antarctica have produced an idealized soil profile for the regolith (8) which is very applicable to the Martian regolith (Fig. 3). The soil profile is composed of five basic zones: an aeolian, a salt formation, active, seasonally frozen, and a permanently frozen. The four zones above the permanently frozen zone are the regions where the majority of the chemical and physical weathering occur. The aeolian zone (upper 1-2 cm) represents the region where daily activity is occurring. Effects of the surface winds, temperature fluctuation, moisture deposition, and radiation environment are obviously recorded within this regolith zone. The salt formation zone represents the area where salts are forming and deposited. Salts are associated with the duricrust and their presence has recently been reviewed (9). The salt zone is located within 1 to 5 cm of the surface. The active zone represents the region of transition between the salt zone and the frozen zones where the abundances of surface deposited salts decrease as a function of depth and daily temperature fluctuations and are damped as compared to the upper zones. The seasonally frozen zone represents the region of the regolith which undergoes melting-thawing and freezing depending upon the season. The permanently frozen zone remains at a temperature below the frost point throughout the Martian year. In such a region, ice is stable on a yearly basis. From the study of the Dry Valley soils, a model of processes operating within the Martian regolith has been developed which should assist in the understanding of processes operating within the Martian regolith.

References:

1. Horowitz, N.H. et al. (1972) Science 176, 242-245.
2. Morris, E.C. et al. (1972) U.S.G.S. Interagency Report: Astrogeology 52, 156 pages.
3. Harris, H. (1980) Ph.D. Dissertation, Univ. of Illinois, and Ugolini, F.C. (1963) Ph.D. Dissertation, Rutgers Univ.
4. Bockheim, J. (1979) Personal communication.
5. McKay, D.S. and Prestell, D. (1980) NASA Tech. Memorandum 82385, 496-498.
6. Watanuki, K. et al. (1979) Memoirs of Natl. Inst. of Polar Res., Special Issue No. 14, 52-56.
7. Clark, B. (1980) Personal communication.
8. Gibson, E.K. and Ransom, B. (1981) In Lunar and Planetary Science XII, 342-344.
9. Clark, B. and Van Hart, D.C. (1981) Icarus (submitted).

WEATHERING PROCESSES IN MARTIAN-LIKE ENVIRONMENTS

Gibson, E. K., Jr.

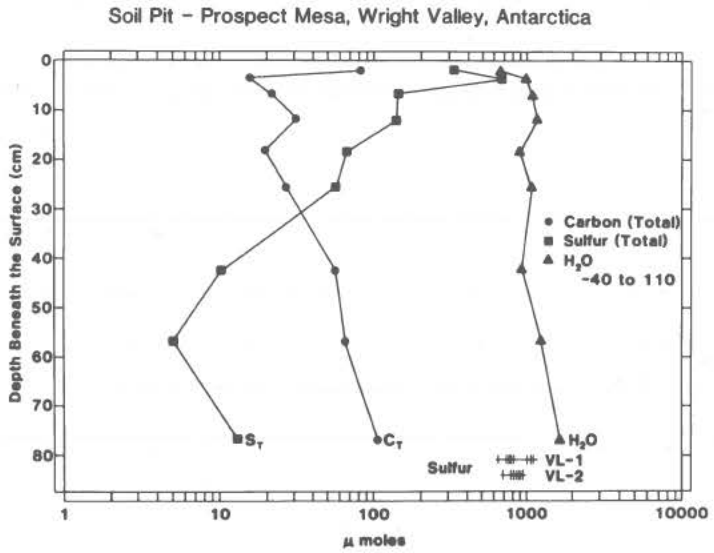

Fig. 1. Total carbon, sulfur, and water (-40° to 110°C) fraction of soils from soil pit, Prospect Mesa, Wright Valley, Antarctica. Sulfur and chlorine abundances for Mars from (7).

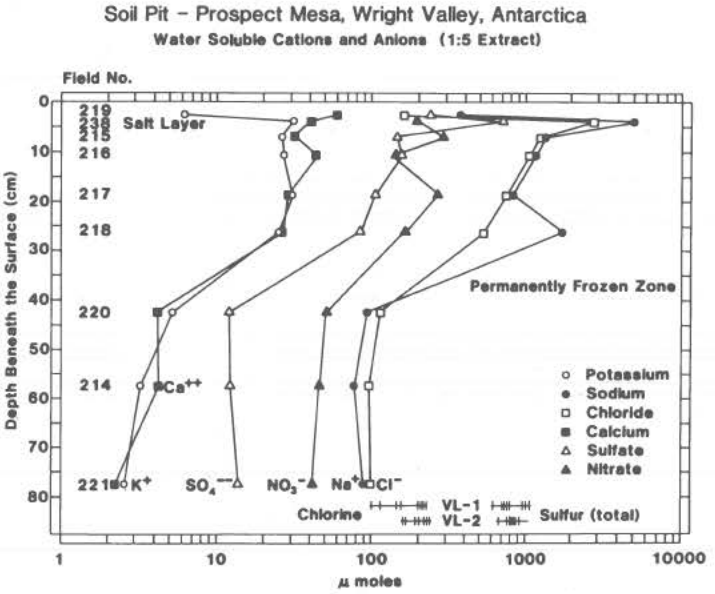

Fig. 2. Water soluble cation and anion abundances of soils from soil pit. Note enrichments in salt layer (2-4 cm depth) with progressive decreases to the permanently frozen zone. Concentrations below permanently frozen zone are essentially constant.

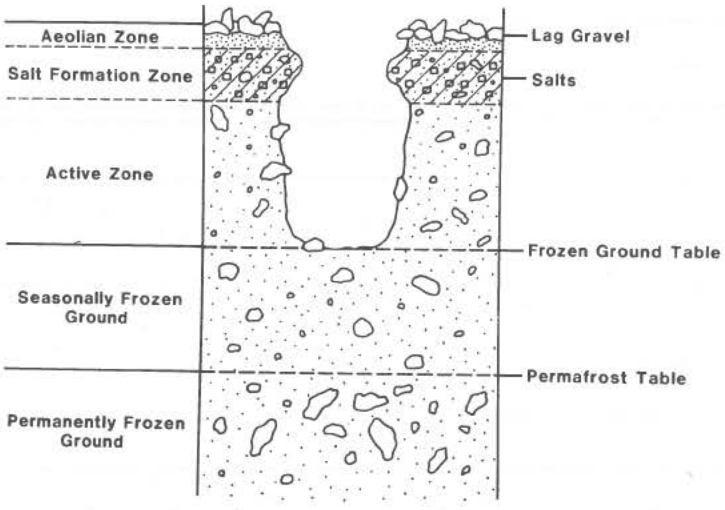

Fig. 3. Idealized soil profile for the Martian regolith. Most of the chemical alterations and secondary mineral formation occur within or above the active zone.

RIDGE SYSTEMS OF MARS. Ann W. Gifford, National Air and Space Museum, Smithsonian Institution, Washington, D.C. 20560.

Mare ridges, which were first observed on the Moon, have been the subject of much discussion with proposed models of their origin ranging from volcanic to structural (Lucchitta and Klockenbrink, 1981). A global study of mare-type ridges on Mars based on Viking images has recently been completed at the Center for Earth and Planetary Studies. This abstract is a summary of a Master's thesis which will appear in the Advances in Planetary Geology series (Gifford, 1981). Ridge maps for the whole planet are included; ridges were systematically mapped and described on a quadrangle basis. Five kilometers was used as the lower limit of ridges resolvable at the global scale of the study. In addition, ridge trends were measured to compare with global and regional trends and stress orientations.

The ridges mapped in this study range from 5 to 400 km long and 1 to 10 km wide. Most of the ridges on Mars are on plains and plateau units; 4321 ridges with a total length of 153,835 km were mapped on these unit types.

There are three main areas of ridged plains on Mars (Hesperia Planum, Sinai and Solis Plana, and Lunae Planum). Hesperia Planum, an irregularly shaped plains region surrounding the ancient volcanic construct, Tyrrhena Patera, is characterized by a polygonal arrangement of ridges with a major northwest trend. Western Sinai Planum contains parallel curvilinear ridges, and farther east, a more reticulate arrangement. The curvilinear trends are concentric to the Tharsis uplift, an elevated volcanic plateau that may dominate much of the tectonic pattern of Mars (Phillips and Lambeck, 1980). Lunae Planum is an area of extremely long, parallel, north and northwest trending ridges. Numerous smaller, intercrater plains areas also contain ridges; these generally display polygonal patterns.

Ridges are preferentially developed in older, thinner plains and plateau units. In areas of younger, thicker fill, especially in volcanic flows, older ridges may have been buried, or they were not developed.

This study supports the conclusions of Saunders et al. (1981) that sub-parallel ridge arrangements are formed in areas of thicker plains fill while irregular, reticulate ridge patterns are formed in places where the plains are thinner. In these areas if the fill is thin enough the effects of irregular underlying topography are apparent in the surface pattern of ridges.

Ridges which resemble lunar mare ridges are also mapped in craters, basins, and several volcanic calderas on Mars. Ridges in the large (> 100 km diameter) craters and basins tend to mirror the north and northwest trends of regional structures, rather than displaying radial and concentric basin-related trends as in lunar mare basins (Maxwell and Gifford, 1981). Ridges are present in the summit calderas of several of the large volcanic constructs on Mars, including Olympus Mons. Ridges also locally take the form of rings. These are either complete circular ridges, which range in diameter from 10 to 40 km, or they are partial arcs that follow the trend of buried crater rims (Gifford, 1980).

The presence of a planetwide predominance of north to northwest trends suggests that ridges are compressional tectonic features which reflect global and regional stresses. Global ridge trends are related to changes in the planet's rotational equilibrium figure. The ridges are concurrent with a planetwide fracture system which may have formed in response to the same stresses. Regional ridge patterns are modified by local tectonic regimes (e.g. in the area near Tharsis), fill thickness, underlying topography, and

local confining topography (e.g. within a crater, basin, or small lowland area).

References

Gifford, A.W. (1980) Reports Planet. Geol. Prog.-1980, NASA TM 82385, 90-92.
Gifford, A.W. (1981) Ridge Systems of Mars. Master's Thesis, The George Washington University, Washington, D.C., 136 p.
Lucchitta, B.K. and Klockenbrink, J.L. (1981) The Moon and the Planets 24, 415-429.
Maxwell, T.A. and Gifford, A.W. (1981) Sub. to Proc. Lunar Planet. Sci. Conf. XII.
Phillips, R.J. and Lambeck, K. (1980) Rev. Geophys. Space Phys. 18, 27-76.
Saunders, R.S., Bills, T.G., and Johansen, L. (1981) Lunar Planet. Sci. XII, 924-925.

LITHOLOGICAL EVOLUTION OF THE MARTIAN REGOLITH J.L. Gooding, Earth and Space Sciences Division, Jet Propulsion Laboratory, California Institute of Technology, Pasadena, CA 91109

INTRODUCTION. The current state of the Martian regolith should reveal important clues to the geologic history of the planet. Although much information about the Martian surface has been gleaned from Mariner and Viking spacecraft data and from Earth-based telescopic observations, little real knowledge exists concerning the regolith: the collection of rock fragments, soils, and sediments which overlie bedrock. The Martian surface and regolith have apparently been affected by processes which include impact cratering, volcanism, tectonism, fluvial and eolian erosion and deposition, and weathering and soil formation. It is important to review the possible influences of these various processes on the mineralogical/petrological/geochemical evolution of the regolith as an aid to directing future problem-oriented studies.

PARTICLE-SIZE DISTRIBUTION. Particle-size distributions at the two Viking lander (VL) sites have been estimated, for surface fines, by applying principles of soil mechanics to the interpretation of VL surface sampler data (1,2) and, for rocks, by quantitative analysis of VL imagery (3). These results, converted here into estimated cumulative volume- or weight-frequency curves, are summarized in Fig. 1 along with similar data for various analog materials. Mason (4) pointed out that ablational filtering and stagnation of small (<10-g) meteorites by the Martian atmosphere should preclude agglutination as a significant process in the Martian regolith and predicted a modified lunar-analogous particle-size distribution as shown in Fig. 1. Volumetrically, though, the VL blocks appear too well sorted to be part of a single-population, lunar-analogous continuum of particle sizes. The field estimated for fine-grained surface soils at the VL sites overlaps that of <10-mm lunar fines but also overlaps those of terrestrial pyroclastic ejecta, Sedan Crater (nuclear explosion in terrestrial alluvium) ejecta, and Hawaiian volcanic soils. However, geomorphic features of VL surface fines (5,6) indicate that they are eolian deposits which have become indurated to various degrees, possibly by chemical cementation. In fact, the estimated lower boundary curve for VL soils (Fig. 1) is comparable to that for terrestrial loess (7) whereas the estimated upper boundary curve resembles that obtained by artificial sorting of case-hardened volcanic silt (8). Thus, although VL-1 is located in a region populated by several craters of ~ 500-m size (9), the interpretation of the VL-1 surface particle-size distribution (and probably that at VL-2, also) solely in terms of an impact-ejecta model seems clearly inadequate. Furthermore, interpretation of bulk regolith properties in terms of fine-grained VL surface soils alone is geologically unreasonable. Estimation of median diameter (Md) and other statistics for the bulk regolith must accomodate the probable existence of both vertical and lateral particle-size variations at any one site as well as regional variations which should depend on the types of regolith-forming processes which have dominated each area. Heavily cratered areas should be characterized by mature regolith with Md $\simeq$ 0.5-10 mm whereas plains dominated by flood deposits should have Md $\simeq$ 8-50 mm, decreasing with distance from the source. Pyroclastic ejecta should display Md $\simeq$ 0.08-4 mm whereas soils developed by weathering of mafic bedrock should possess Md $\simeq$ 0.1-5 mm. Eolian drift deposits (as opposed to "sand" dunes) should have Md $\simeq$ 0.01-0.03 mm. Thus, Md for "average" global

LITHOLOGICAL EVOLUTION OF THE MARTIAN REGOLITH

Gooding, J. L.

regolith, a parameter of convenience in certain physical models, can be meaningfully estimated only with great difficulty. In the absence of precise information about Md values and relative volumetric proportions of various regolith-forming materials, Md for the bulk regolith can be only crudely estimated to lie between ~ 0.1 and 10 mm. The thickness of the regolith is likewise unknown although, by strict lunar analogy (24), its global median value may be ~ 10 m.

MINERALOGY AND PETROLOGY. Despite the enormous success of Viking, information about the mineralogical composition of the Martian regolith remains meager. No mineralogical analyses have been made although possible mineralogical interpretations have been inferred from bulk elemental compositions of VL surface fines (10,11) and from Earth-based spectral reflectance studies of selected areas on the Martian surface (12). Bulk elemental compositions of VL surface soils are distinctively different from those of most terrestrial, lunar, and meteoritic rocks (Fig. 2) but are similar, in some respects, to those of various other materials such as shergottite meteorites (13), komatiites (14), or mixtures of iron-rich smectites (10,11). Thus, no unique petrological interpretation exists for the elemental composition of VL surface fines. Given the geological context of the VL sites and sample fields, though, the fines are most reasonably interpreted to be eolian deposits derived from reworked soils. Reflectance spectra of Martian "bright" areas, which may be surficially rich in such fine material, are interpretable in terms of weathering products of mafic (or basic) igneous rocks (12). Neglecting the abundant sulfur and chlorine which is present, possibly as salt minerals (10,11), the VL fines can be interpreted either as isochemical equivalents of primary igneous rocks (14) or as nonisochemical, fractionated representations of igneous source rocks (15). The first interpretation would imply ultrabasic magmatism characterized by partial or bulk melting of various iron-rich peridotites (16) with little or no subsequent chemical change introduced by weathering and reworking. In contrast, the second interpretation would permit ordinary "basaltic" volcanism to prevail, as on Earth and Moon, but with geochemical fractionations introduced by weathering and reworking to form the surface fines. Therefore, major implications for the geologic evolution of Mars rest on determination of the mineralogical/petrological composition of the Martian regolith. Unfortunately, current data on elemental abundances are restricted to surface fines. Given the compositional fractionations which occur with decreasing particle size in both lunar (17) and terrestrial (18,19) soils, the compositions of surface fines at the VL sites cannot be assumed to be representative of the bulk Martian regolith. Instead, they probably represent only one component with its volumetric significance yet to be determined. The research described in this abstract was carried out by the Jet Propulsion Laboratory, California Institute of Technology, under contract with the National Aeronautics and Space Administration.

REFERENCES. (1) Shorthill R.W. et al. (1976) Science, 194, 91. (2) Moore H.J. et al. (1977) J. Geophys. Res., 82, 4497. (3) Garvin J.B. et al. (1980) Lunar Planet. Sci. XI, 317. (4) Mason C.C. (1971) Geol. Soc. Amer. Bull., 82, 2625. (5) Binder A.B. et al. (1977) J. Geophys. Res., 82, 4439. (6) Mutch T.A. et al. (1977) J. Geophys. Res., 82, 4452. (7) Pewe T.L. (1951) J. Geol., 59, 400. (8) Gooding J.L. (1980) NASA Tech. Memo. 82385, 209. (9) Morris E.C. and Jones K.L. (1980) Icarus, 44, 217. (10) Baird A.K. et al. (1976) Science, 194, 1288. (11) Toulmin P. III et al. (1977) J. Geophys. Res., 82, 4625. (12) Singer R.B. et al. (1979) J.

Geophys. Res., 84, 8415. (13) McSween H.Y. Jr. et al. (1979) Earth Planet. Sci. Lett., 45, 275. (14) Baird A.K. and Clark B.C. (1981) Icarus, in press. (15) Gooding J.L. (1980) Lunar Planet. Sci XI, 342. (16) McGetchin T.R. and Smyth J.R. (1978) Icarus, 34, 512. (17) Laul J.C. and Papike J.J. (1980) Proc. Lunar Planet. Sci. Conf. 11th, 1307. (18) Chepil W.S. (1957) Am. J. Sci., 255, 206. (19) Japp J.M. and Gooding J.L. (1980) NASA Tech. Memo. 82385, 212. (20) Baker V.R. (1978) In The Channeled Scabland, NASA, p. 81. (21) Roberts W.A. (1968) In French and Short (eds.), Shock Metamorphism of Natural Materials, p. 101. (22) King E.A. Jr. et al. (1971) Proc. Second Lunar Sci. Conf., 737. (23) McKay D.S. et al. (1974) Proc. Fifth Lunar Conf., 887. (24) Oberbeck V.R. et al. (1973) Icarus, 19, 87. (25) Sheridan M.F. (1971) J. Geophys. Res., 76, 5627.

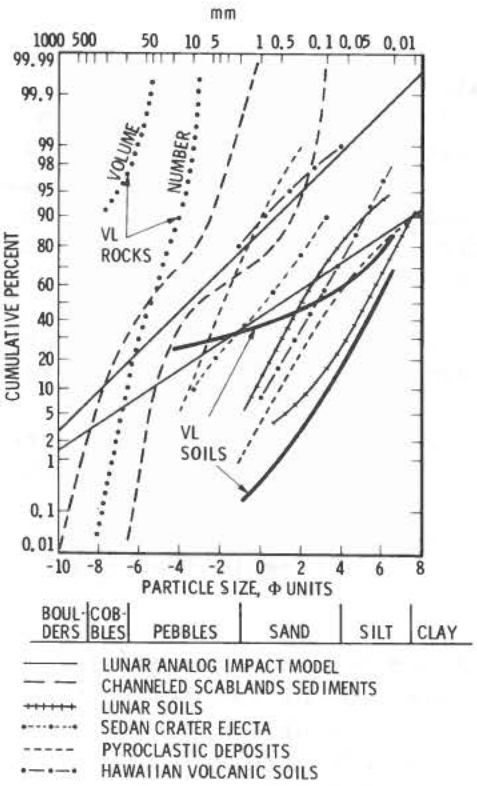

Figure 1 (Left). Particle-size distributions of surface fines (1,2) and rocks (3) at the Viking lander (VL) sites compared with generalized particle-size fields of various terrestrial (8,19,20,21,25) and lunar (22, 23) materials and with that predicted (4) by a lunar-analogous impact model. All data are in weight or volume units except as noted for VL rock number percent curve.

Figure 2 (Below). Bulk elemental composition of surface fines at VL-1 site (10,11) compared with average compositions of terrestrial, lunar, and meteoritic rocks. Compiled from numerous literature sources. Terrestrial komatiites, shergottite achondrites, and iron-rich smectites (not shown) all plot near the VL-1 point.

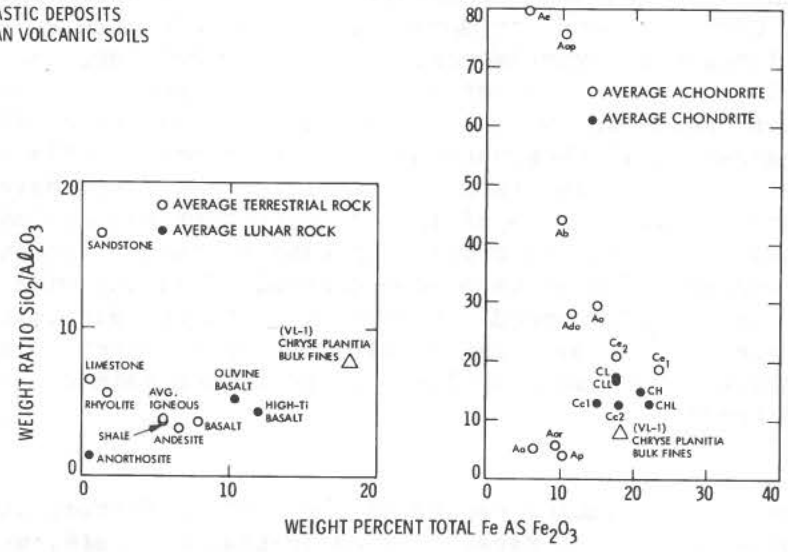

WIND ABRASION ON MARS: CONSIDERATIONS, SIMULATIONS, AND IMPLICATIONS

R. Greeley, R.N. Leach, S.H. Williams, B.R. White, J.C. Pollack, D.H. Krinsley, and J.R. Marshall, *Department of Geology, Arizona State University, Tempe, Arizona 85287*

After a decade of intensive study, there is general agreement that wind is the dominant agent modifying the surface of Mars. Prior to the Viking mission most investigators considered aeolian abrasion to be extremely effective (1). This conclusion was based on: 1) observations of frequent dust storms; 2) the high wind velocities needed to set grains into motion on Mars; and 3) the variety and large numbers of features attributed to aeolian activity. It was reasoned that sand grains, once set into motion by the wind, would be accelerated to high speed and would be very effective in "sand blasting" the surface.

Viking results have caused a reassessment of rates of abrasion on Mars. High resolution images show surfaces having small ($\sim$10 m) fresh-appearing impact craters; the frequency of these craters signals surfaces at least hundreds of millions of years old that have been little modified (2). In addition, wind speeds and observations at the two lander sites show little aeolian activity, at least during the last 4 years. Resolving the conflict between predictions of high wind abrasion and constraints posed by Viking results is important for addressing several questions, including:

1) What is the lifetime of landforms on Mars, especially impact craters? This has direct bearing on the use of crater frequencies for relative dating of surfaces.
2) Do martian sand dunes and other aeolian features represent the current wind regime or are they relict features? This has bearing on derivation of the climatic history of Mars.
3) What is the role of aeolian abrasion in exposing fresh "bedrock" surfaces? This has bearing on the interpretation of geological results.

Approach

Knowledge of three factors is required to determine the rate of wind abrasion on Mars: 1) S_a, the susceptibility to abrasion of various rocks (e.g., 'coefficient' of abrasion for basalt); 2) q, flux of windblown particles; and 3) f, wind frequency on Mars. These factors were assessed through a combination of laboratory experiments, numerical modelling, and analyses of Viking meteorological data. Whenever possible, the laboratory experiments were conducted under both Earth and Mars conditions, with the Earth laboratory results tested against field observations. Eight common materials (including basalt and volcanic tuff, rocks likely to be present on Mars) have been tested to determine S_a under a wide range of impact velocities and angles for sand-size particles, using both quartz grains and basalt grains. Individual particle velocities and mass fluxes have been determined in the wind tunnel as functions of free stream wind speed, atmospheric density, particle size, and height above the surface. From these results and from theory, a computational model has been derived that enables flux data to be determined for a wide range of planetary conditons.

Rate of Abrasion

There are many uncertainties regarding the various factors in the calculation of a wind abrasion rate on Mars. For an initial estimate, we assume a basalt surface (S_a basalt = 8×10^{-6}, impacted with sand-size particles at 90°

WIND ABRASION ON MARS

Greeley, R. et al.

in a free stream wind of 60 to 75 m/s)(3), with an infinite supply of particles having a flux, $q = 5.3 \times 10^{-2}$ gm/cm^{2}x sec; derived from (4) q at a height of 10 cm above the surface = $2.61(u_*)^3 \rho_A (1 - v_{*_t}/v_*)(1 + v_{*_t}^2/v_*^2)/g$; in cgs units surface stress $v_* = 281$, atmospheric density $\rho_A = 1.05 \times 10^{-5}$, threshold speed $v_{*_t} = 225$, and gravity $g = 375$. Winds above threshold speed at the Viking landers (3) have a frequency, $f = 10^{-4}$. The rate of abrasion based on these factors = $S_a \cdot q \cdot f$ or 5×10^{-4} cm per year for a smooth surface, or 5×10^{-5} cm per year for a surface comparable to the landing sites (the saltation cloud would be dispersed to a greater height due to grains bouncing from rocks and boulders, reducing q at a height of 10 cm by a factor of about 10).

The estimated rate ($\sim$5 m/10^6 yr) is much higher than 'allowable' by impact crater frequencies observed in the vicinity of the landers, even taking various uncertainties of the parameters into account. This result implies one or more of the following possibilities: 1) windblown sand particles on Mars do not consist of holocrystalline materials, but may be of some other composition such as aggregates (5) which would be ineffective agents of abrasion; 2) the climate in the past was less conducive to aeolian processes (e.g., lower atmospheric density); or 3) the cratered surfaces that provide a 'constraint' on the age were mantled for much of geological history (thus 'removed' from the aeolian abrasion environment), and have been recently exhumed. Refinement of the calculation and photogeological analyses of wind eroded/abraded features on Mars may enable narrowing the possible conflicts between the observed estimated rates and the apparent antiquity of the martian surface.

References

(1) Sagan C. (1973) *J. Geophys. Res. 78*, 4155.
(2) Arvidson R. et al. (1979) *Nature 278*, 533.
(3) Williams S.A. (1981) *Unpub. Masters Thesis*, Arizona State Univ.
(4) White B.R. (1979) *J. Geophys. Res. 84*, 4643.
(5) Greeley R. (1979) *J. Geophys. Res. 84*, 6248.

THE GEOLOGIC HISTORY OF MARS DURING THE LATE HEAVY BOMBARDMENT.

Michael Gurnis, Lunar and Planetary Laboratory, University of Arizona, Tucson, Arizona 85721

We are quite fortunate that during a very active stage of self-generated geologic processes, Mars experienced a torrential rain of impacting bodies. The signatures left in the crater populations allow us to deduce a history. These events are recorded in the cratered terrain covering most of the southern hemisphere of Mars. We recognize two major stages in the development of this modified physiographic province. The first stage was dominated by small valley formation, while the latter by volcanic plains emplacement. This history follows from our understanding of the martian cratering record.

The martian cratering history has been likened in its major aspects to lunar cratering history. Strom (1) recognized two principal populations of lunar craters: a highlands population with a differential slope of -2.15 and a post-maria (slope:-2.80) for diameters 8. to 90.5 km. The highlands population is characterized by a series of well defined bends, where the slope of the population changes. In the process of gathering a catalog of martian craters, we recognize both these populations on Mars with a high level of confidence. The average martian cratered terrain population is compared in Fig. 1 with the lunar highlands--there is a remarkable similarity. The crater population superposed on the martian northern plains is indistinguishable from the lunar post-maria population. We hypothesize that the production functions of of the martian cratered terrain and the lunar highlands were the same and that the terra craters formed during a very short and early epoch. (Most workers would consider the latter point established.)

The dissected terrain is one of two units which we have divided the cratered terrain into (Fig 2, D). This is stratigraphically the lowest unit in the cratered terrain and is characterized by: a rough texture, a dissection by valleys, and a large occurrence of flat-floored, rimless craters. Also the craters are areally clumped.

The intercrater plains superpose and embay the dissected terrain (Fig. 2,Ip). This unit is characterized by: smooth surface texture, a general circularness in plane, and the presence of numerous rinkle ridges. In addition, some possible flow fronts have been identified. This morphology suggests the intercrater plains are volcanic in origin.

The density difference between the martian and lunar terrae crater populations is enigmatic since endogenetic processes usually alter the size-frequency distribution (1).We experimented with Monte Carlo models of crater obliteration to constrain the types of obliteration mechanisms which could have occured on Mars. Our models included crater-crater interactions because exogenetic processes also actively obliterate craters. The endogenetic mechanism in these models was areally limited plains. We find that randomly occuring intercrater plains significantly altered the

"shape" of the distribution in an antithetical way to that observed. But when a certain fraction of plains form in larger craters and obliterate them, the size-frequency distribution retains its "shape" as the density decreases. An example of a simulation in which intra- and intercrater plains form in concert during the last quarter of the period of heavy bombardment is shown in Figure 3. This is not a unique solution. These results are consistent with the morphology of martian intercrater plains (i.e. the plains are partially circular in plane).

We also measured the craters which clearly superpose the cratered terrain (Fig.2, arrow). The differential slope of this population is -2.51, but when the post-northern plains population is subtracted, a slope of -2.27 is obtained (Fig. 4). In addition we can reject the hypothesis that this population and the post-northern plains population are the same with a confidence of 95 %. But, this population is statistically indistinguishable from the terra population. This suggests a formation during the tail end of the Late Heavy Bombardment.

1. Strom, R. G. (1977). Phys. Earth Planet. Int. 15, 156-172.

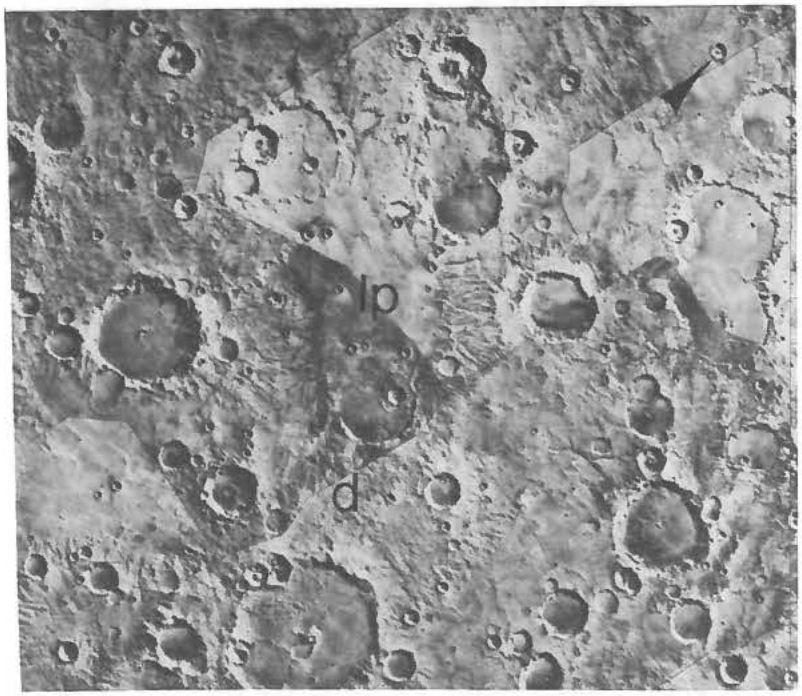

Figure 2

EARLY MARTIAN HISTORY

Gurnis, Michael

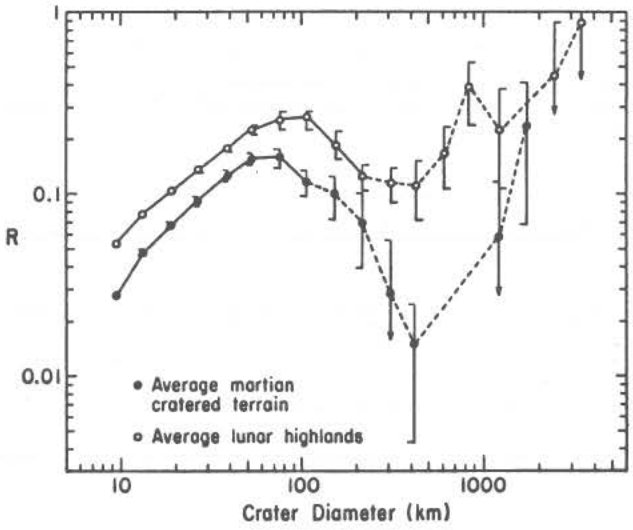

Figure 1

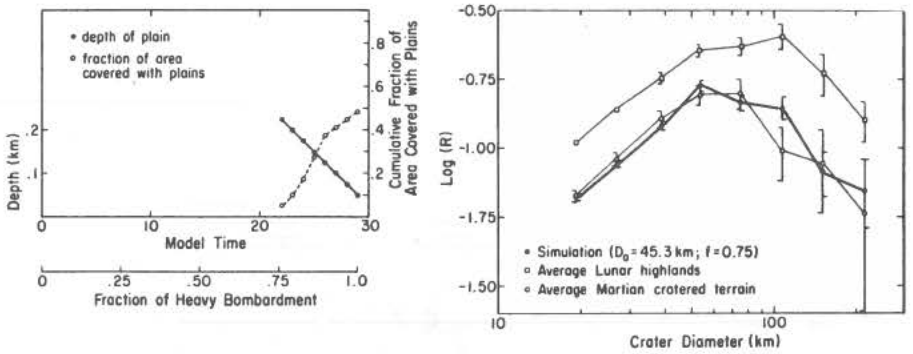

Figure 3

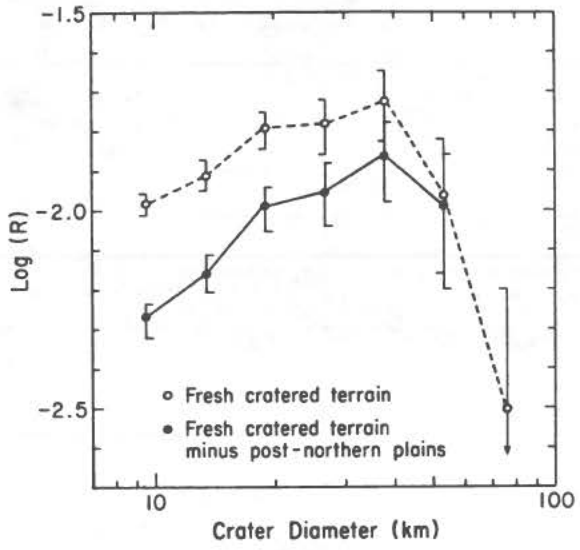

Figure 4

EFFECTS AND SIMULATION OF GLOBAL DUST STORMS ON MARS

Robert M. Haberle, NASA/Ames Research Center, Space Sciences Division, MS 245-3, Moffett Field, CA 94035

The response of the Martian atmosphere to various dust loads and the ability of its meridional circulation to transport dust globally are simulated with a numerical model based on a two-dimensional (2D) version of the primitive equations in spherical-sigma coordinates. The circulation is driven by the daily averaged heating rate which is computed from algorithms that account for the solar and infrared opacity of gaseous CO_2 and suspended dust particles, as well as convective exchange with the ground. Frictional dissipation takes place only through vertical momentum exchange by subgrid scale motions and is parameterized using linear diffusion theory. No attempt is made to parameterize the effects of large scale eddy motions.

In the first set of experiments, quasi steady solutions for a uniformly mixed and time independent dust distribution are computed. The results show that for optical depths up to 5 or so, the introduction of dust into the atmosphere causes a significant strengthening and expansion of the tropical circulation cell. For optical depths greater than 5, however, very little change in the circulation is evident, suggesting that the mean meridional circulation is not the principle dust raising component of the general circulation. In the second set of experiments, the evolution of a global dust storm is simulated by specifying a southern hemisphere subtropical source and allowing the circulation to determine the subsequent distribution of dust. The results of these experiments show that the meridional circulation, which intensifies as the dust spreads, is a very effective transport agent, mixing dust to heights in excess of 30 km throughout the tropics and subtropics of both hemispheres.

However, in none of the experiments could the observed warmth of the north polar atmosphere during the second storm of 1977 be reproduced, a likely consequence of the limitations of 2D modelling. Nor in none of the dust storm simulation experiments was the circulation able to transport dust into the high latitudes of either hemisphere. In view of the role of dust in the formation of the polar laminated terrain, this result may also be attributed to the inadequacies of 2D modelling, and emphasizes the importance of understanding the cause of the north polar warming.

CENTRAL STRUCTURES IN MARTIAN CRATERS: PRELIMINARY IMPLICATIONS FOR SUBSTRATE VOLATILE EFFECTS, Wendy S. Hale and James W. Head, Dept. of Geological Sciences, Brown University, Providence, R. I. 02912.

Martian impact craters display two types of morphologic features which have been attributed to the interaction of crater-forming processes with a volatile component in the substrate: prominent circular cavities or pits atop central peaks or in place of central peaks in some craters (1,2,3,4), and lobate ejecta deposits with distal ramparts which show some evidence of fluidization (5,6,7). Lobate ejecta deposits have been studied in detail (7,8), and may reflect entrainment of vaporized or liquid volatiles and/or atmosphere into the crater ejecta plume (7,8,9,10). Central peak summit pits or crater floor pits (those which replace peaks) are less well characterized. Pits have been suggested to result from explosive decompression of a volatile component in the substrate following nearly adiabatic compression by the impact shock wave (2,3). Thus pit distributions may serve as a tool in delineating volatile contents of different substrate units (2). Since central uplifts in craters represent the deepest material sampled by the event (11) pit distributions may reflect sampling of substrate layers at depths otherwise inaccessible for study. However, recent attempts to determine pit distributions have produced conflicting results (2,3).

Morphometric analysis of central peaks in lunar and mercurian craters indicate that relationships exist between central peak diameter and crater rim diameter, and between peak height and rim diameter. These are the same on both planets, despite differences in gravity and modal impact velocity (12, 13). Mercury has a surface gravity approximately the same as Mars, but mercurian craters lack summit or floor pits. These observations suggest that morphometric analysis of central structures in martian craters may provide insight on the relative contributions of gravity and substrate to the processes of central structure formation. The purposes of this study are to: 1) characterize the morphology and morphometry of central structures in martian craters; 2) Compare any morphometric relationships to those found in lunar and mercurian craters; 3) Determing the relative distributions of central pits as a function of terrain and ejecta type. In this preliminary report we present results for 462 fresh craters (as defined in ref. 1) from 1.6×10^7 km^2 of the martian southern hemisphere: this region (0-30° lat., 45-180° long.) spans seven terrain types and the percent of total craters on each type is as follows: ancient terrains (57.2%), ridged plains (25.7%), young Tharsis lavas (4.5%), rolling plains (4.5%) cratered plains (2.4%), smooth plains (2.4%), and channel deposits (2.4%), (14). All data are derived from Viking Orbiter images and U.S.G.S. Geologic and Topographic map series.

Central Peak and Pit Morphometry - Rim diameter, floor diameter, central peak and/or central pit diameter were recorded for each crater. Of the 462 craters examined, 387 have central peaks and 76 of these (19.6%) possess summit pits. Central peak diameters (Dcp) display a relationship to crater rim diameter (Drc) which may be expressed by the power-law relation $Dcp = 0.234\ Drc^{1.037}$, $r = 0.86$ (Figure 1). Statistical tests indicate no significant variation in this relation for pitted versus unpitted peaks. However, the slope of the fit is steeper than that for Dcp/Drc defined for lunar and mercurian central peak craters (Figure 2), and statistical tests indicate that the two populations are different. Pits, either summit or floor, occur in 151 craters, and a power-law relation exists between pit diameter (Dp) and rim crest diameter (Drc) expressed as $Dp - 0.144\ Drc^{1.0}$, $r - 0.85$ (Figure 3). This relation is

Central Structures in Martian Craters

Hale, W. S. and Head, J. W.

the same for floor pits and summit pits (combined Figure 3).
Morphology of Peaks and Pits: Terrain and ejecta distributions - Central structures in martian craters may be classed as central peaks, pitted central peaks, or floor pits. Central peaks may be further divided by complexity (simple, complex) and geometry (symmetric, linear or arcuate) as was done in lunar and mercurian craters (12). Simple, symmetric peaks dominate the data set. Further, central peaks (unpitted) are found to dominate on all terrain types so far investigated, with the possible exception of the cratered plains unit (Figure 4). Ejecta deposits were classified according to degree of fluidization (after 7,9). Pits do not correlate directly with any one ejecta type, but an increase in pit frequency occurs as ejecta becomes more fluidized (single-multi-lobed) (Figure 5).
Discussion - A power-law relation exists between central peak diameter and crater diameter which remains constant in the presence of a summit pit, indicating that pit formation does not strongly effect peak morphometry. However, the relatively steeper slope of the Dcp/Drc relation on Mars compared to the Moon and Mercury suggests an important substrate effect on Mars. Summit or floor pits also display a common relation to crater rim diameter, suggesting that the pit formation process is continuous from summit to floor pits. Pits occur in >20% of all craters regardless of terrain type (Fig. 4). If pit formation is due to a volatile component in the substrate, then this data supports the presence of a regionally extensive volatile component (4) rather than a terrain-restricted one (3). However, the dominance of unpitted peaks on all terrain units indicates that some vertical variations in volatile component may be present. Pits occur with greater frequency as ejecta deposits become more fluidized, suggesting a link between the volatile reservoirs for these two processes. Studies of unit-to-unit variations in depth to a volatile component and extension of the data set to include other regions, is continuing.

References: 1) Smith, E. I. (1976) Icarus 28, p. 543. 2) Wood, C. A. et al. (1978) PLPSC 9, p. 3691. 3) Hodges, C. A. (1978) LPS XI, p. 521. 4) Hodges, C. A. et al. (1979) LPS XI, p. 450. 5) Head, J. W. and Roth, R. (1976) Symp. on Crater Mech., p. 50. 6) Carr, M. H. et al. (1977) JGR 82, p. 4055. 7) Mouginis-Mark, P. (1979) JGR 84, p. 8011. 8) Mouginis-Mark, P. (1981) Icarus 41, in press. 9) Schultz, P. H. and Gault, D. E. (1979) JGR 84, p. 7669. 10) Pike, R. J. (1980) PLPSC 11, p. 2159. 11) Dence M. R., et al. (1977) Imp. and Exp. Cratering (Roddy et al., eds) p. 247. 12) Hale, W. and Head, J. W. (1980) PLPSC 11th, p. 2191. 13) Malin M. and Dzurisin, JGR 83, p. 233, 14) Scott. D. H. and Carr, M. H. (1978) U.S.G.S Map I-1083.

Central structures in Martian craters

Hale, W. S. and Head, J. W.

Figure 1.

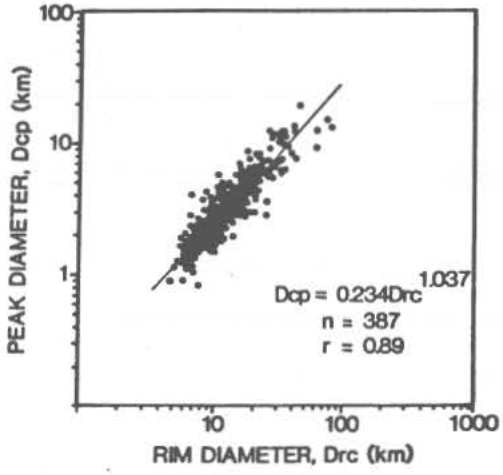

Figure 2. Dotted line is Moon-Mercury relation.

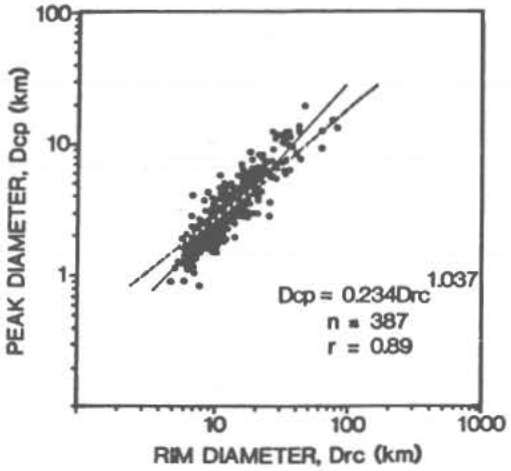

Figure 3.

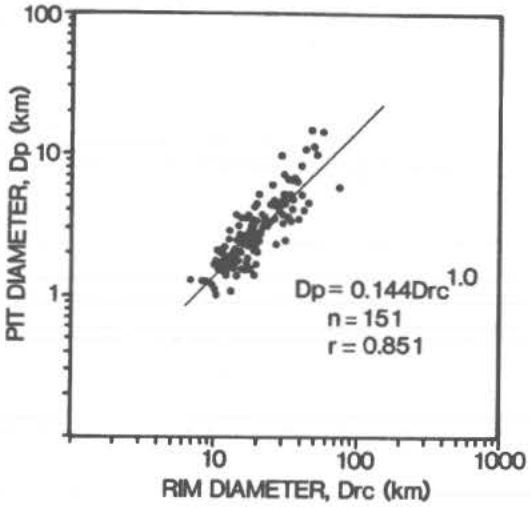

Figure 4.

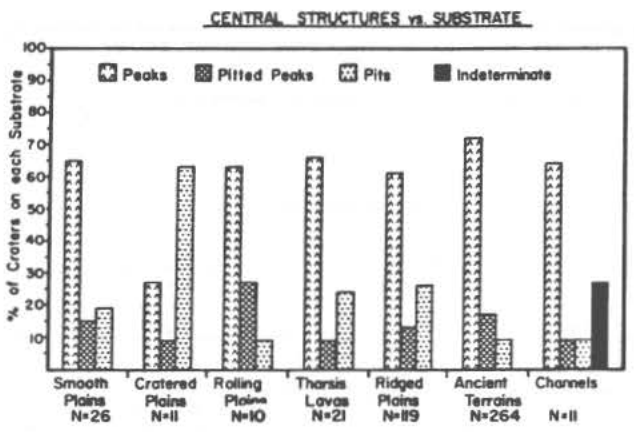

Figure 5.

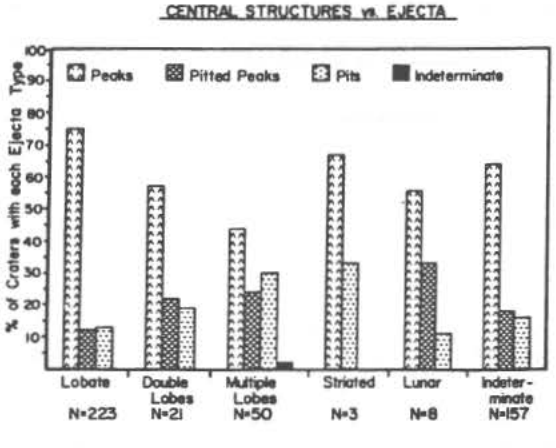

IDENTIFICATION OF THE MARTIAN PANG BANDS AS CO_2 FROST FEATURES.
B. Hapke, E. Wells, J. Wagner, Dept. of Geology & Planetary Science, Univ. of Pittsburgh, Pittsburgh, PA 15260, and W. Partlow, Westinghouse Research Center, Pittsburgh, PA 15235.

Pang et al (1) analyzed observations of Martian dust clouds by the UV spectrometer on Mariner 9 and estimated that the complex refractive index of the dust particles in the UV was about $n = 1.8 - .02i$. Pang and Ajello (2) discovered two absorption bands in the Martian data at approximately 210 and 250 nm. They interpreted these bands as features caused by a TiO_2 component of the dust. We believe that this identification is unsatisfactory because the 210 nm band in TiO_2 is actually due to the Ti(+3) ion, but this valence state of Ti is not stable under the strongly oxidizing conditions of the Martian surface (3), as evidenced by the abundant Fe(+3).

We have discovered weak absorption bands in the reflectance spectrum of CO_2 frost at 210 and 245 nm (4) and suggest that the Martian UV features are due to this material. Although the refractive index of CO_2 is about 1.2, considerably less than the value deduced by Pang et al (1) for the Martian dust, the CO_2 could be present as a coating on silicate dust acting as condensation nuclei or as atmospheric haze between the spacecraft and the dust. We also point out that the above values for the refractive index were derived on the basis of details of Mie scattering diagrams, which are of only marginal applicability to irregular particles, so that the actual values of the refractive index of the Martian scatterers may be quite different.

Finally, the detailed reflectance spectra of H_2O and CO_2 frosts are different in the far UV. This fact may be useful in interpreting the UV spectrum of the Martian polar regions.

REFERENCES:

1.Pang,K.,Ajello, J., Hord, C. and Egan, W. (1976). Icarus, 27, 55-67.
2.Pang,K. and Ajello, J. (1977). Icarus, 30, 63-74.
3.Wells, E. and Hapke, B. (1977). Science, 195, 977-979.
4.Hapke, B., Wells, E., Wagner, J. and Partlow, W. (1981). Submitted to Icarus.

THE BEARING OF PLANET SIZE ON INTERNAL STRUCTURE: TECTONIC IMPLICATIONS FOR MARS. Claude T. Herzberg, Department of Geological Sciences, Rutgers University, New Brunswick, N.J. 08903

A simple mechanism was recently proposed (1) to account for the geochemical observation that the continental crust of the Earth was extracted from only the uppermost part of the mantle (2,3,4,5). Mantle material below 600-700 kilometers depth did not contribute to the formation of the crust in any significant way during or subsequent to the initial differentiation and stratification of the Earth into crust-mantle-core (3,5). It was argued that heat transfer may be permitted across this 650 kilometer boundary, but significant mass transfer may not because all material of the upper mantle may be greatly buoyant in relation to that of the lower mantle below 650 kilometers.

Along the mantle solidus olivine peridotite in the lower part of the upper mantle ($\rho = \sim 3.4$ gm/cm^3) transforms to spinel polymorph peridotite ($\rho = \sim 3.7$ gm/cm^3) and eventually into either (Mg, Fe)O (Rocksalt) + stishovite + garnet or rocksalt + (Mg, Fe) SiO_3 (Perovskite) + garnet with densities of 3.95-4.00 gm/cm^3 at pressures in the 170-200 kilobar range. These discontinuous density increases over a small pressure interval reflect compaction by polymorphism and increased coordination of Mg, Fe, and Si. The densities of magmas in the upper and lower mantle are poorly constrained; however, preliminary work (1,6) indicates that they may adopt properties which are not intuatively obvious. Available bulk modulus and thermal expansion parameters indicate that magmas in the highest pressures of the olivine stability field may be marginally more or less dense than olivine itself, because silicate liquids are 3 to 10 times more compressible than silicate solids. Pressure-induced coordination changes of cations in silicate liquids exposed to pressures in excess of 200 kilobars may result in magmas of the lower mantle having densities below those of rocksalt + stishovite or rocksalt + perovskite, but greater than those of olivine + pyroxene in the upper mantle. These pressure-induced transformations operating over a relatively small pressure interval can result in an overall density contrast of up to 15% between material of the upper and lower mantle, regardless of this material's phase identity in the liquid or solid state.

The first order effect to be anticipated is a convecting dense lower mantle coupled to a convecting buoyant upper mantle with heat transfer by conduction and minimal mass transfer across the density boundary layer located at about 200 kilobars [ie., 650 kilometers on Earth; this will also be a thermal boundary layer (7)]. 'Leakage' of matter from the lower to the upper mantle may be a second order phenomenon, arising from chemical diffusion across the boundary layer as well as material transfer promoted by 'turbulent' convection during the early history of the Earth which presumably had a higher heat flow. In other words, differentiation of the Earth to form the continental crust is adequately explained by a phase equilibrium-density-gravity controlled process in the traditional sense of Bowen's fractional crystallization. This is the most simple hypothesis which unifies the most fundamental petrologic, geochemical, and geophysical observations. Any revision of this hypothesis can only be entertained if a 650 kilometer thick residual mantle modelled geochemically (3,5) is underestimated due to uncertainties in the assumed bulk Earth isotopic composition For example, a 1000 kilometer mantle complementary to the crust would imply considerable 'leakage' across the 200 kilobar density barrier.

INTERNAL STRUCTURE AND TECTONICS OF MARS

Herzberg, C.T.

If history should treat the hypothesis of a 200 kilobar density barrier with favor, it will have to be considered a physical-chemical property of peridotite chemical systems regardless of the terrestrial planet it is found in. However, the depth of its location will vary according to the planet's mass which in turn determines the value of its acceleration due to gravity. Whereas 200 kilobars on the Earth is the pressure imposed by a column of rock 650 kilometers deep, the same pressure on Mars is equivalent to a lithostatic load at about 1600 kilometers depth. Depending on the size of the core of Mars, most or all of the mantle should have been processed to yield a very thick crust. For example, if the volume proportions of the Earth's crust to upper mantle can be scaled directly to Mars, the average crustal thickness should be about 31 kilometers compared to the Earth's 18 kilometers. If the bulk Mars composition is enriched in CaO and Al_2O_3 relative to the Earth (8), Mars may have a crust which is around 4 times thicker than that of the Earth. This scaling excersize is admittedly rather simple-minded in that it ignores real differences in the physical-chemical processes (eg., efficiency of phase separation) which operated during the differentiation of the two planets. These differences, however, are considered to be second order effects which must operate within the bounds imposed by a 200 kilobar density barrier. All other variables being equal, the reality of this barrier would require that there be a constant and predictable relationship between terrestrial planet size and its internal structure; smaller planets should have thicker crusts and upper mantles.

A number of estimates have been made of the thickness of an elastic lithosphere which is required to support the superisostatic load of Olympus Mons (9, 10). Compared to the Earth's 65-140 kilometer thick lithosphere, that below Olympus Mons is likely to extend to depths greater than about 200 kilometers. In the absence of well understood creep contributions to the rheological properties of rocks, the most simple way of explaining the change from elastic properties of a lithosphere to plastic properties of an asthenosphere for the Earth has been shear strength reduction through partial melting of a peridotite containing traces of H_2O and CO_2 (11). For geothermal gradients below continental shields and ocean plates on Earth, melting begins at pressures greater than 25-35 kilombars but can vary depending on the composition of the vapor phase. This would correspond to depths greater than 210-290 kilometers on Mars and would lend credibility to the notion of incipient melting as determining Martian lithospheric thickness. For lower Martian geothermal gradients, the lithospheric thickness may be correspondingly greater. Because Olympus Mons appears totally uncompensated whereas the Tharsis volcanoes are compensated to a large extent, large variations in the thickness of the lithosphere has been suggested (10). This could be explained by local variations in the H_2O and CO_2 content and composition of mantle volatiles and hence depth of melting. If extensive melting of the mantle beneath Olympus Mons exhaled all volatile components, the solidus temperature of the residual mantle may be 500°C higher than that below the Tharsis volcanoes. Whatever the present-day geothermal gradient may be below Olympus Mons, the amount of partial melt in the mantle (if any) is expected to be small or negligible compared to neighbouring areas. Indeed, if the geothermal gradient is confined to temperatures below those of the solidus at all depths, the concept of a Martian asthenosphere is rendered meaningless unless creep mechanisms are invoked.

INTERNAL STRUCTURE AND TECTONICS OF MARS

Herzberg, C.T.

Whereas convection cell sizes in the Earth's upper mantle may be constrained by the interval between the low velocity zone and the 650 kilometer discontinuity, thus permitting about 75 cells with an average diameter of about 500 kilometers as viewed in a cross section of the Earth, Mars may have had about 10 convection cells as seen in cross section each measuring about 1350 kilometers in diameter. For convection velocities comparable to those of the Earth, a larger proportion of the total convective momentum in the asthenosphere may be imparted to the lithosphere than that for the Earth if cooling was asymmetric. Considerable absolute displacements between the lithosphere and asthenosphere at some time in the Martian past might be anticipated. Indeed, the equatorial paleopole deposits near 155°W and on the opposite side of Mars (12) is strong evidence favouring large global displacements of the spin-axis intercept with the crust. Fragmentation of the lithosphere into 'plates' would have been inhibited due to the thick outer shell of crust and lithosphere. Mars appears to have been an extreme case of 'thick shelled' tectonics.

REFERENCES

(1) Herzberg C.T. (1981) Lunar and Planetary Sciences 12, 439-441.
(2) Wasserburg G.R. and DePaolo D.J. (1979) Proc. Natl. Acad. Sci. 76, 3594-3598.
(3) Jacobson S.B. and Wasserburg G.R. (1979) J.G.R. 84, 7411-7427.
(4) O'Nions R.K. et al. (1979) J.G.R. 84, 6091-6101.
(5) DePaolo D.J. (1981) EOS 62, 137-140.
(6) Stolper et al. (1981) J.G.R., in press.
(7) Jeanloz R. and Richter F.M. (1979) J.G.R. 84, 5497-5504.
(8) Morgan J.W. and Anders E. (1979) Geochim. Cosmochim. Acta 43, 1601-1610.
(9) Thurber C.H. and Toksöz M.N. (1978) Geophys. Res. Lett. 4, 977.
(10) Comer R.P. and Solomon S.C. (1981) Lunar and Planetary Science 12, 166-168.
(11) Wyllie P.J. (1978) J. Geology 86, 687-713.
(12) Schultz P.H. and Lutz-Garihan A.B. (1981) Lunar and Planetary Science 12, 946-948.

OLYMPUS MONS AUREOLE: STRATIGRAPHY K. Hiller and G. Neukum, Geology Department, Ludwig-Maximilians Universitat, 8000 München 2, F.R.G., R. Lopes and J. E. Guest, University of London Observatory, Mill Hill Park, London NW 7

The photogeological units of the Olympus Mons sheild and aureole material have been mapped and on this basis dated by impact crater counts.

The age data and photogeological evidence (*) suggest an emplacement history as follows:

During the early history and simultaneous to the emplacement of the old northern lowland plains the original volcanoe was formed (Cumulative Crater Frequency N (km^{-2}) at D = 1 km $> 4 \cdot 10^{-3}$). Due to tectonic processes and permafrost melting parts of the shield collapsed and the aureole materials of slightly different ages (N $4 \cdot 10^{-3}$ to 10^{-3}) formed.

After a long period of non activity the area became active again. This is documented by the interaureole plains, the lava flows of the shield and the caldera floors (N 2 to $5 \cdot 10^{-4}$).

Very high resolution imagery of a small area allows the dating of extremely young erosional processes (N ~ $8 \cdot 10^{-5}$).

(*) Lopes, R. et al. (1979), 'The Moon and the Planets', 22, 231-234.

MARTIAN MAGNETISM: A BASIS FOR FUTURE MEASUREMENTS, L. L. Hood and C. P. Sonett*, Lunar and Planetary Laboratory, The University of Arizona, Tucson, Az. 85721 (*also Dept. of Planetary Sciences).

Ambiguities in the interpretation of spacecraft observations of the Martian interaction with the solar wind have made it difficult to establish the existence or absence of an intrinsic planetary magnetic field for Mars. Mariner 4 detected a standing bow shock wave implying an intrinsic dipole moment $\leq 3 \times 10^{-4}$ of the earth's moment (1). The Mars 3 orbiter, with a periapsis altitude of $\sim$1300 km, detected one possible pair of magnetopause crossings containing field measurements consistent with a moment near the upper limit allowed by the Mariner 4 data (2). However, the latter interpretation has been challenged on the basis of plasma data by Wallis (3) and in reanalyses of published magnetic field measurements from both Mars 3 and Mars 5 by Russell (4). Vaisberg (5) has used Mars 2, 3, and 5 bow shock crossings identified from plasma measurements to infer a subsolar magnetopause altitude of $\sim$400 km implying a moment less by at least a factor of 3 than that advocated in ref. 2. Calculations of ionospheric gas pressures at altitudes $\geq$ 300 km by Intriligator and Smith (6) indicate that an atmospheric interaction alone would not be sufficient to stand off the solar wind at such altitudes unless the electron temperature is 4 times the ion temperature. Assuming that the additional internal pressure required for a standoff is due to the existence of an intrinsic Martian field, they estimate a moment of $\sim 10^{-4}$ of the earth's moment, corresponding to an equatorial field strength of about 20 nT. However, the evidence for this result is sufficiently indirect that the only safe conclusion is that existing measurements are consistent with a Martian-to-terrestrial moment ratio of $\leq 3 \times 10^{-4}$, i.e. essentially the same as that reported in 1965 following the Mariner 4 flyby. A low-altitude Martian orbiter and/or landers equipped with magnetometers would resolve this issue and thereby place significant constraints on the metallic core size and internal thermal history of Mars. In this paper, we discuss minimum mission requirements for achieving this goal.

Assuming the existence of a small intrinsic planetary field, the probable small subsolar solar wind standoff distance (< 400 km) means that any surface or orbital magnetometer would detect a significant field due to magnetopause boundary currents as well as the planetary field. Except for the possible existence of additional ionospheric current systems at Mars, this situation is comparable to that at Mercury (7) so that analytic methods developed to account for such nearby magnetopause current systems (8) may also be applicable to Mars. The sunward magnetopause boundary is approximately hemispherical so, near the subsolar point, the total magnetospheric field due to a centered dipole of moment $m\hat{z}$ is given to first order by

$$\underline{B} = m[2\cos\theta(r^{-3} - R^{-3})\hat{r} + \sin\theta(r^{-3} + 2R^{-3})\hat{\theta}] \qquad (1)$$

where r, θ are spherical polar coordinates about $\hat{z}$, a is the planetary radius, and R is the planetocentric distance to the subsolar stagnation point. More exact estimates for the confined planetary field can be obtained using numerical techniques that have been applied in studies of the terrestrial magnetosphere (9). If $R \simeq a$, corresponding to a low-altitude

ionospheric interaction, then

$$\underline{B}(a,\underline{\theta}) \simeq m \sin\theta (3a^{-3})\hat{\theta}. \qquad (2)$$

In the latter case, a single surface magnetometer on the sunward hemisphere would be sufficient to determine the product $m \sin\theta$ while two surface instruments could determine both m and θ, i.e. the moment and tilt of an assumed centered dipole. Two simultaneously operating surface instruments also represent a minimum for inductive sounding of the mantle as shown, for example, in the analysis of Herbert (10). Higher-order moments (yielding an effective offset distance for a single dipole) would require additional surface magnetometers. Emplacement of nearby pairs of magnetometers would allow the identification and separation of the possibly large local crustal fields at Mars. A determination of higher-order moments would place quantitative bounds on the radial extent of the source region, presumably the core radius (11). In the former case, for $R > (a + 100$ km), a low-altitude orbiter would be capable of determining both $R(t)$ and a number of low-order harmonics of the planetary field provided that ionospheric current fields can be identified and removed. The addition of one or more simultaneously operating surface instruments would be of assistance in this regard and would also allow application of the measurements to infer the upper mantle electrical conductivity profile. A large diurnal variation in the magnetic field detected by a given surface magnetometer would provide part of the required forcing field, the remainder being supplied by externally driven time variations in the magnetopause boundary position.

In the absence of a small intrinsic planetary field, the form of the solar wind interaction becomes "Venusian" so that external field penetration of the conducting ionosphere would be small and surface inference of the mantle conductivity profile would be more difficult. In this case, establishment of the existence and origin of crustal magnetization would become of particular interest. The identification of a 1 - 7% strongly magnetic phase in the surface material sampled by Viking Landers 1 and 2 (possibly γ Fe_2O_3; ref. 12) increases the likelihood of widespread crustal magnetization on Mars. Although experience at the moon requires caution in immediately interpreting such a finding as indicating the former existence of a planetary field (13), the probable existence of at least a formerly molten Martian core (e.g. ref. 14) and the special nature of lunar magnetization carriers (primarily metallic iron grains in impact-generated glasses and soils) makes such an hypothesis more plausible for Mars. Thus, if a present global field is absent, an investigation of Martian crustal magnetism may yield useful observational constraints on the internal thermal history that are otherwise obtainable at present only by interpretation of surface geology. Unfortunately, orbital detection of crustal anomalies would be inhibited by ionospheric current systems that are probably most intense near the F2 peak identified by the Viking retarding potential analyzer at 130 km altitude. Measurements at low latitudes and at altitudes of $\sim$ 100 km may yield useful results.

MARTIAN MAGNETISM

Hood, L. L. and Sonett, C. P.

REFERENCES

(1) Smith, E.J., , L. Davis, Jr., P.J. Coleman, Jr., and D.E. Jones (1965) Science, 149, 1241.
(2) Dolginov, Sh. Sh., Ye. G. Yeroshenko, and L.N. Zhuzgov (1973) J. Geophys. Res., 78, 4779.
(3) Wallis, M.K. (1975) Geophys. J. Roy. Astron. Soc., 41, 349.
(4) Russell, C.T. (1978) Geophys. Res. Lett., 5, 81. Russell, C.T. (1978) Geophys. Res. Lett., 5, 85.
(5) Vaisberg, O.L. (1976) in Physics of Solar Planetary Environments, Vol. 2, D.J. Williams, ed., p. 845, AGU, Washington, D.C.
(6) Intriligator, D.S. and E.J. Smith (1979) J. Geophys. Res., 84, 8427.
(7) Ness, N.F., K.W. Behannon, R.P. Lepping, and Y.C. Whang (1975) J. Geophys. Res., 80, 2708.
(8) Hood, L.L. and G. Schubert (1979) J. Geophys. Res., 84, 2641.
(9) Mead, G.P. (1964) J. Geophys. Res., 69, 1181. Choe, J.Y., D.B. Beard, and E.C. Sullivan (1973) Planet. Space Sci., 21, 285.
(10) Herbert, F. (1980) The Moon and the Planets, 23, 127.
(11) Hide, R.H. (1978) Nature, 271, 640.
(12) Hargraves, R.B., D.W. Collinson, R.E. Arvidson, and C.R. Spitzer (1977) J. Geophys. Res., 82, 4547.
(13) Hood, L.L. (1981) EOS Trans. Am. Geophys. Un., 62, 161. Hood, L.L. (1981) Proc. Lunar Planet. Sci. Conf. 12th, in press.
(14) Young, R.E. and G. Schubert (1974) Geophys. Res. Lett., 1, 157.

MARTIAN EJECTA FLOW CRATERS

V. M. Horner and R. Greeley, *Department of Geology, Arizona State University, Tempe, Arizona 85287*

Even prior to Viking Mission results, flow-like forms on the ejecta blankets of some martian craters were suspected from study of high resolution Mariner 9 images (1). Interpretation of these features as representative of a flow instead of erosion was substantiated and greatly amplified by analyses of Viking images (2). Several different morphologic expressions of the flow-like ejecta (2, 3, 4 and others) are observed. Ejecta flow craters exist globally and in all terrains (5). Three lines of research provide data on martian ejecta flow craters: photogeologic studies, impact experiments and theoretical modelling. The objective of this review is to synthesize the research carried out on the martian ejecta flow craters.

Most photogeologic studies have approached the ejecta flow phenomenon by first classifying the different ejecta blanket morphologies. It was generally believed that morphologic types represented different degrees of fluidization of the ejecta. Most researchers agree that there is a continuum of ejecta flow morphologies from the most fluid–usually taken to be thin, multilobate ejecta flows–to the dry, lunar-mercurian ejecta blankets (2, 3). It is also generally accepted that ejecta flow is the result of impacts into a volatile-rich target, although there is still disagreement on the details of the emplacement. An alternate viable explanation for the emplacement of the outer lobes of multilobate ejecta flow craters involves the interaction of ejecta particles below a given size with the martian atmosphere (6, 7). These particles would be aerodynamically decelerated and emplaced as a flow *after* the ballistic emplacement of larger ejecta closer to the crater rim.

Assuming that different ejecta morphologies reflect differences in near-surface volatilization, the volatile content of different geologic units and/or latitudes may be characterized by the predominant crater ejecta morphology. Some investigators found differences in proportions of crater ejecta types among geologic units (3, 9). However, perhaps because of differing data bases, there is no general agreement on the relative proportions which characterize a given terrain. Although early studies suggested that "fluidity" of ejecta blankets increased poleward (4), other studies did not find this correlation, or found it only for the pedestal craters (3 and others). A later study of latitude dependencies of ejecta flow craters, taking into account the terrain type, is in progress (8), and early results confirm the latitude dependency of ejecta fluidization. Although very little has also been done concerning the effect of altitude on ejecta morphology, there are indications that the fluidity of martian crater ejecta decreases with increasing altitude (3). From our studies of martian ejecta flow craters, the interior morphology of these craters seems more indicative of terrain type than crater ejecta morphology; however, a rigorous analysis has not yet been reported.

Recent attention has focused on the morphometry of ejecta flow craters and include analyses of the ratio of ejecta area to crater area (10), the ejecta mobility ratio r_e/r_c (3, 9). However, the various measures of ejecta flow distances adopted by researchers are so dissimilar in their reported usage that comparisons between authors is difficult.

A recent development has been the extrapolation of martian ejecta flow studies to large craters and basins (11 and others). Early results suggest that larger impacts "punch through" the volatile-rich layer, as the crater is surrounded by a complex combination of lunar-mercurian and martian-style ejecta. Depth/diameter relations change for martian craters larger than about 50 km (12), supporting indications that the volatile-rich layer ends at depth.

The second approach to the study of martian ejecta flow craters involves experimental impacts into viscous media. The first of these experiments was a qualitative effort (13) that established its applicability to the observed martian ejecta flow morphologies. By varying the

MARTIAN EJECTA FLOW CRATERS

Horner, V. M. and R. Greeley

viscosity of the target material, some of the observed ejecta morphologies could be modelled. Later experiments (14, 15) controlled viscosity more quantitatively and illustrated the non-negligible effects of multilayered targets on the final ejecta morphology. Experimental impact studies (15) are the basis for one hypothesis of martian crater ejecta emplacement. The impact causes oscillations of the crater material, which rebounds from the impact in a cycle from a central mound to a central pit, back to a central mound. The number of oscillations would depend on the energy of the impact. The collapse of each central mound would send increasingly smaller pulses of material over the crater rim so that the farthest lobate deposits represent the ballistic deposit, and the inner lobes correspond to the pulses of material emplaced in response to the impact site oscillations. Impact experiments have also validated the theoretical calculations which involve aerodynamic drag acting on ejecta particles smaller than some critical size (6) to produce outer ejecta lobe deposits.

Theoretical models and computer simulations constitute the third approach to the study of martian ejecta flow craters and is critical to the understanding of the process of ejecta emplacement. As yet, no one hypothesis has gained general acceptance. One theoretically derived model for the outer lobe deposit of multilobate ejecta involves a multilayered target with the second layer being volatile-rich relative to the one above (9). Penetration of the shock wave into the second layer would generate a volatile-rich ejecta cloud which collapses and, being highly mobile, scours the earlier, inner ejecta deposit representing the volatile-poor top layer, and settles somewhere beyond the first ejecta deposit. Recently a method for estimating the water content of a region by a modelling of preflow stresses in the ejecta flow blanket just before mechanical failure has been derived and simulated by computer (16). It was assumed that each episode of failure as the ejecta flowed from the impact would produce a lobate ring.

Current research involving martian ejecta flow craters is heading in two major directions. The first involves an extrapolation of the data base of ejecta flow craters to larger craters ($>$ 100 km) and basins on Mars. The second is an ongoing attempt to better define the major variables (terrain type, impact energy, latitude, etc.) that contribute to ejecta blanket morphologies and to determine to what degree they influence the final morphology.

References

(1) Head J. W. and Roth R. (1976) Papers presented to the *Symposium on Planetary Cratering Mechanics*, Flagstaff, AZ, 50–52.
(2) Carr M. H. et al. (1977) *J. Geophys. Res. 82*, 4055.
(3) Mouginis-Mark P. J. (1979) *J. Geophys. Res. 84*, 8011.
(4) Johansen L. A. (1979) *NASA TM 80339*, 123 (abstract).
(5) Allen C. C. (1979) *Icarus 39*, 111.
(6) Schultz P. H. and Gault D. E. (1979) *J. Geophys. Res. 84*, 7669.
(7) Schultz P. H. and Singer J. (1980) *Proc. Lunar Planet. Sci. Conf. 11th*, 2243.
(8) Saunders R. S. and Johansen L. A. (1980) *NASA TM 82385*, 150 (abstract).
(9) Mouginis-Mark P. J. (1980) submitted to *Icarus*.
(10) Mutch P. and Woronow A. (1980) *Icarus 41*, 259.
(11) Mouginis-Mark P. J. and Hawke B. R. (1981) *Lunar Planet. Science Conf. XII*, 732 (abstract).
(12) Cintala M. J. and Mouginis-Mark P. J. (1980) *Geophys. Res. Lett 7*, 329.
(13) Gault D. E. and Greeley R. (1978) *Icarus 34*, 486.
(14) Croft et al. (1979) *J. Geophys. Res. 84*, 8023.
(15) Greeley R. et al. (1980) *Proc. Lunar Planet. Sci. Conf. 11th*, 2075.
(16) Woronow A. (1980) *Icarus*, in press.

This work is supported by the NASA Planetary Geology Office, Mars Data Analysis Program, through Grant NSG–7548 to Arizona State University.

A GLOBAL MARTIAN DUST STORM MODEL; Howard Houben, Mycol, Inc., Sunnyvale, CA 94087.

The rapid growth and wide extent of global Martian dust storms is thought to be due to the feedback between the radiative (usually heating) effect of atmospheric dust and the winds which raise and distribute that dust. A 2-dimensional, horizontal, vertically-averaged model is used to test this hypothesis. The effects of topography, seasonal variation of solar declination, and a latitudinally varying mean zonal wind are included. The diurnal solar tides are also modelled. Atmospheric dust load is modified by horizontal convergence and advection, as well as by an increased probability of dust-raising in the presence of strong winds. The linearized model can be used to study the origin of global dust storms or the rapid decay of a fully developed storm.

The model is based on the pressure-coordinate linearized tidal equations (1). When the equations are averaged in the vertical direction, a 3-equation eigenvalue system is obtained with the horizontal velocity components and temperature perturbation as principal dependent variables. The system is, in a formal mathematical sense, a perturbation of Laplace's tidal equation - resembling systems which have been used to study modes in the earth's atmosphere (2). The vertical averaging is constrained to yield the proper equivalent depths (3) of the Martian atmosphere in the limit of no topography and no zonal wind. The averaging is thus equivalent to an expansion in normal atmospheric modes. To these 3 equations, a dust equation is added, coupled to the others by the heating properties of the dust.

Linearly unstable global atmospheric modes are found to exist. The growth times of these modes (on the order of 1 day) are short enough to explain the rapid spread of observed storms. Because of the complicated coupling in the model, the modes need not exhibit any simple symmetries and waveforms can be quite complex.

Support by NAS2-10786 is acknowledged.

1) Zurek R.W. (1976) J. Atm. Sci. 33, 321-327.

2) Kasahara A. (1980) J. Atm. Sci. 37, 917-929.

3) Lindzen R. and Blake D. (1972) J. Geophys. Res. 77, 2166-2176.

FROST-WEATHERING AND THE VIKING BIOLOGY EXPERIMENTS: A WORKING MODEL. R.L. Huguenin, Department of Physics & Astronomy, University of Massachusetts, Amherst, MA 01003

The unusual chemical activity of soil samples discovered during the Viking lander biology experiments has driven an intensive effort by a broad spectrum of investigators to determine the origin(s) of that activity. The major goal was to find a working explanation other than a biological one that could account for the 'positive' responses that were obtained. A large number of models were proposed when the first results were received, and most of them were eliminated shortly after results from the second phase of experimentation (multiple samples, sterilization, long-term storage, etc.) were released. Now at the conclusion of the Viking mission only a couple of models remain, and they have been published in a special Viking issue of the Journal of Molecular Evolution (Volume 14, 1979). One of these, the 'Frost Weathering' model, uniquely provides a unified working explanation for the principal findings of all three Viking experiments.

The frost weathering model stemmed initially from laboratory studies of the interaction of H_2O with minerals during photochemical weathering and its implications for atmospheric chemistry were discussed in two later papers (4,5). Its potential impact on the Viking biology experiments was first pointed out in reference 5, and results of laboratory experiments that were directed at specifically testing this proposal were reported in the J. Molecular Evolution special issue. Since then our laboratoy has undergone a substantial facilities upgrade and additional experiments have been performed, and refinements to the model have been made.

We have discovered that exposure of silicate minerals (olivine and pyroxene, both identified in earth-based reflectance spectra of Mars) to H_2O vapor at low temperature (-11°C to -22°C) resulted in the formation of adsorbed H_2O/frost layers that reacted with the mineral substrates to produce an acidic oxidant. Subsequent exposure of the frost-treated samples to liquid H_2O (as occurred during the lander GEx and LR experiments) produced a sudden drop in pH of the media and it resulted in the production of O_2 gas (variable, up to $\sim 10^{20}$ molecules g^{-1}). Exposure of the frost-treated samples to solutions of .01M HCOONa resulted in the rapid oxidation of the formate to $CO_{2(g)}$. The kinetics of both reactions were qualitatively similar to the results of the GEx and LR experiments (active phases). Attempts to identify the oxidant by chemical indicators tentatively suggest that chemisorbed hydrogen peroxide may have formed. The reader is referred to reference 6 for details of the procedures and results.

It was proposed (6) that exposure of H_2O vapor to the cooling mineral surfaces resulted first in its dissociation as $H^+_{(ads)}$ and $OH^-_{(ads)}$. Following dissociation it was proposed that a fraction of the H^+ was drawn into the crystal to negatively charged lattice defects (cation vacancies, Al^{3+} substituted for Si^{4+}, etc.), where they combined with oxide ions to form lattice hydroxyl ions. Incorporation of the protons at negative defects should give the crystal a net positive charge, while the surface layer of adsorbed H_2O should become negatively charged (excess OH^- relative to H^+). It was proposed that restoration of charge balance by transfer of electrons from $OH^-_{(ads)}$ to positive defects within the crystal (e.g., anion vacancies, lattice O^-, Fe^{3+}, etc.) resulted in the formation of surface OH radicals, which then combined to form more stable chemisorbed H_2O_2. The net reaction would represent a chemical reduction of the mineral and a production of strongly adsorbed (chemisorbed) hydrogen peroxide with an enthalpy of ΔH_o = -32 kcal mol^{-1}.

FROST-WEATHERING AND THE VIKING BIOLOGY EXPERIMENTS

Huguenin, R. L.

The chemisorbed H_2O_2 that forms should only be metastable and eventually decay to $O_{(ads)} + H_2O_{(g)}$. As discussed in reference 6, the H_2O_2 should be adsorbed in the dissociated state ($HO^-_{2(ads)}$ at surface metal ion sites and $H^+_{(ads)}$ at oxide ion sites). The $HO^-_{2(ads)}$ should tend to further dissociate to the more stable $O_{(ads)}$ and OH^-, with the OH^- combining with $H^+_{(ads)}$ and desorbing as $H_2O_{(g)}$: $H_2O_{2(ads)} \rightarrow H_2O_{(g)} + O_{(ads)}$, $\Delta H_o = -32.54$ kcal mol^{-1}. It was argued that the rate determining step for the decay should be dissociation of the $O\text{-}OH^-$ bond in $HO^-_{2(ads)}$, which would have an activation energy of $\geq$ 34 kcal mol^{-1}.

The production of O_2 we proposed resulted from the iron-catalyzed decomposition of H_2O_2 when the frost-weathered minerals were exposed to liquid H_2O. Exposure to the $H_2O_{(l)}$ should have caused the sudden injection of $\sim 10^{20}$ FeO_2H^{2+}, $FeOH^{2+}$, $HO\cdot$, H^+, and OH^- (relative proportions uncertain) into the water film, which would have rapidly reacted to give $O_{2(g)}$ and the observed pH behavior. The release of those same reactants, particularly the $FeOH^{2+}$ and $OH\cdot$ components, could also explain the observed rapid production of $CO_{2(g)}$ in our experiments when the frost-treated samples were exposed to the sodium formate solution. It is significant that the model calls on the production of $CO_{2(g)}$ and $O_{2(g)}$ from independent sources of chemisorbed peroxide. The amount of CO_2 produced should have depended primarily on the amount of chemisorbed peroxide at Fe^{2+} sites, while the amount of O_2 produced should have depended on the amount of chemisorbed peroxide at Fe^{3+}: The CO_2/O_2 ratio should therefore <u>not</u> have been dependent on pH. We observed an unusually high CO_2/O_2 production ratio of $\sim 10^2$ from our frost-weathered olivine samples at pH = 5-7, which can be explained by preferential peroxide adsorption at Fe^{2+} sites. By contrast, the production of such large $CO_{2(g)}/O_{2(g)}$ ratios from conventional oxidation of formate by $H_2O_{2(aq)}$ would have required pH $\lesssim$ 3 to sufficiently inhibit O_2 production. Relatively high $CO_{2(g)}/O_{2(g)}$ ratios were observed during the Viking Gas Exchange (GEx) experiment as well, and this led Oyama and associates (Viking issue of J. Molecular Evolution) to propose models of martian mineralogy that were significantly at odds with observation.

Our experimental results were very similar to the kinetics of $CO_{2(g)}$ release during the Labeled Release (LR) and GEx active cycles, and the release of $O_{2(g)}$ during the GEx active cycles. The principal difference was in absolute magnitude (over responses were 10^3 times stronger), and it was proposed that as little as 0.1% of the soil may have been active. The model also effectively explains the unusual sterilization and prolonged storage behaviors of the GEx and LR experiments. As discussed above the chemisorbed perioxide should only be metastable and decay to $O_{(ads)} + H_2O_{(g)}$ with an activation energy of $\geq$ 34 kcal mol^{-1}, and as long as the samples were not exposed to liquid H_2O the $O_{(ads)}$ should be stable at temperatures up to $\sim 580^oC$ at Fe^{2+} sites (5). This was below the sterilization temperatures in both the GEx and LR experiments, and it should have survived until humidification or exposure to aqueous solutions. Upon exposure to $H_2O_{(l)}$ the $O_{(ads)}$ would be driven off as $O_{2(g)}$, appearing (as observed during the GEx sterilzation experiments) relatively unaffected by the sterilization. The production of $CO_{2(g)}$ would have been affected, however, since $O_{(ads)}$ and $O_{2(g)}$ would produce negligible oxidation of substrates in the LR nutrient media. The loss of activity would be roughly proportional to the extent of conversion of chemisorbed peroxide to $O_{(ads)}$

FROST-WEATHERING AND THE VIKING BIOLOGY EXPERIMENTS

Huguenin, R. L.

+ H_2O if our model was correct, and the extent of conversion would be proportional to exp $(-\Delta H_a/RT)$. Levin and Straat (Viking issue of J. Mol. Evol.) constructed an Arrhenius plot of the LR thermal and storage data and derived an activation energy for destruction of the martian oxidant to be 37-42 kcal mol^{-1}. This is in good agreement with our proposal that the activation energy for destruction of chemisorbed peroxide to $O_{(ads)}$ should be $\gtrsim$ 34 kcal mol^{-1}, and it supports the proposal that chemisorbed hydrogen peroxide and its decay product $O_{(ads)}$, were primary active species in the LR and GEx soil samples.

We propose that the decay product $O_{(ads)}$ was also responsible for the activity during the Pyrolytic Release (PR) experiment, with $O_{(ads)}$ combining with radioactive $CO_{(g)}$ during incubation of the samples to form radioactive chemisorbed CO_2. The $*CO_{2(ads)}$ would, like the $O_{(ads)}$, be stable to $\sim$ 580°C (4,5) and it is proposed that dust in the sample containing $*CO_{2(ads)}$ was swept into the pyrolysis column by the effluent. $*CO_{2(g)}$ released by desorption when T exceeded 580°C can adequately explain the PR results. The magnitudes of the responses during the PR experiment were, as one would predict from this model, much less uniform and reproducible than during the LR or GEx samples.

The frost weathering model has several advantages over other models that have been proposed. Firstly, this model calls on one active specie, chemisorbed hydrogen peroxide, and its decay product as the source of all of the observed activity in the three experiments. Secondly, all of the surface materials and environmental conditions necessary to produce the active species have been identified to exist at the surface. Thirdly, it is based almost entirely on broadly accepted theories of chemical interaction between minerals and H_2O. The differences come only from the low temperatures and lack of liquid H_2O during the reactions. Furthermore frost-weathering is an exothermic process: it does not rely on external energy sources such as mechanical abrasion, UV radiation, electrical discharge, or high energy solar wind and solar flare radiation as do other models. It also does not require the exclusive presence of special acidic minerals such as maghemite and the absence of minerals such as clays or other silicates that are known to be present.

Frost-weathering and photochemical weathering were initially proposed as principal chemical weathering models on Mars, having possible major effects on surface geology, mineralogy, and soil composition (3). They also were proposed as major sinks for H_2O and CO_2 on Mars (4), and more recently as principal mechanisms controlling the oxidation state and stability of the martian atmosphere (5). The Viking biology experiments provided important tests of these predictions, and they generally support the original conclusions.

Acknowledgement: This research was supported by NASA grants NSG-7397 (Planetary Biology), NSG-7405 (Planetary Geology), and NAGW-40 (Planetary Geophysics and Geochemistry).

References: (1) Huguenin, R.L. (1973a) J. Geophys. Res. 78:8481-8493; (2) Huguenin, R.L. (1973b) J. Geophys. Res. 78:8995-8506; Huguenin, R.L. (1974) J. Geophys. Res. 79:3895-3905; (4) Huguenin, R.L. (1976) Icarus 28:203-212; (5) Huguenin, R.L. Prinn, R.G., and Maderazzo, M. (1977) Icarus 32:270-298; (6) Huguenin, R.L., Miller, K.J., and Harwood, W.S. (1979) J. Molecular Evol. pp. 104-132.

IMPLICATIONS OF MARTIAN 'OASES' - R.L. Huguenin and S.M. Clifford, Department of Physics and Astronomy-Hasbrouck, University of Massachusetts, Amherst, MA 01003

Remote sensing evidence that there may be anomalous occurrences of liquid H_2O near the surface in Solis Lacus (25°s, 90°w) and Noachis-Hellespontus (30°s, 310°w) has been presented elsewhere (1,2). The evidence was uncovered during the eight years following our discovery of an unusual H_2O condensate phenomenon associated with the 1973 dust storm using a special spectrophotometric imaging vidicon (3). The earth-based observational record and Mariner and Viking data uncovered since that event pointed to enhanced local concentrations of atmospheric water vapor, hazes, and frosts throughout much of the martian year in these two regions. The records revealed that during the fall and winter (L_s = 340° to 180°) condensates generally extend from Solis Lacus upslope into the Tharsis volcanic complex. They generally brightened toward afternoon, suggesting orographic uplift from upslope winds or active convection as discussed by a variety of authors. Fall and winter condensates (L_s = 10° to 180°) also extend from Noachis-Hellespontus into the northern portion of the Hellas basin. Viking colorimetric imagery indicated that they are apparently ground hazes and frosts (filled craters and exposed rims) in Noachis-Hellespontus, and the vapor and hazes are swept into northern Hellas by prevailing westerly winds (as revealed by lee clouds to the east of Hellas). During spring and summer the condensate activity in Solis Lacus and Noachis-Hellespontus has often been accompanied by yellow (dust) cloud activity. Indeed these two areas have been the primary core areas of past dust storm activity.

While the primary lines of evidence were based on condensate activity, the Viking MAWD data also revealed an interesting event during the Viking primary mission. The Period 5 (L_2 = 140-155°) water vapor map showed striking water vapor anomalies over Solis Lacus and Noachis-Hellespontus (10-15 pr. microns compared to 0-6 pr. micron abundances for the other regions of that latitude). This was the only period of the first 25 that showed such sharp regional abundance contrasts within non-polar latitudinal bands. The occurrence of these anomalies was unexpected. During the period of expected maximum soil evaporation (the early morning hours of spring/summer), water vapor signatures would be expected to be effectively masked by accompanying condensate and dust absorptions near 1.4 μm (as clearly revealed on a larger scale duuring the extended mission). During the rest of the year the soil evaporation rates are expected to be much lower and sporadic, and the anomalies that might develop would be at least partially masked by condensates that would tend to accompany them. Furthermore, the observed behavior of condensates indicate that the vapors that produce them are apparently low-level, and their contribution to the overall column abundance would be expected to be relatively small even though local near-surface contrasts may be quite high. A possible explanation for the Period 5 anomaly was uncovered during this past year, when we discovered a discussion by the Viking imaging team of a sudden increase in the southern hemisphere haziness during the period. Earlier in the year atmospheric clarity was very high, but at sometime between L_s - 135 to 145 the atmosphere became very hazy in violet light (condensates). They attributed the phenomenon to an evaporation of H_2O perhaps from the retreating south polar hood. The Period 5 vapor anomalies suggest alternatively that the hazes may have orginated from local sources of vapor, which could better account for the sudden appearance of such widespread hazes. The event was similar in many ways to the outbursts of condensate

IMPLICATIONS OF MARTIAN 'OASES'

Huguenin, R. L. and Clifford, S. M.

activity during past observing periods, e.g., the outbursts concentrated in Noachis during 1962-1963 at L_s = 25 - 45° (2).

Other lines of evidence include thermal inertia highs and radar anomalies in these two regions. Based on the L_s behavior of the condensates and models of the soil column we proposed that the sources of the vapor in Solis Lacus and Noachis Hellespontus are anomalous occurrences of soil moisture extending to within a few cm of the surface. Based on geologic evidence in the imagery, it is not unreasonable that at depths of a few meters and lower there may be abundant and widespread ground ice across the planet, and that surface and subsurface physical conditions (that control the diffusion rate of vapor out of the soil) could allow the ground ice to exist much closer to the surface in some near-equatorial locations. Solis Lacus and Noachis-Hellespontus may be two such sites.

In contrast to the highly-desiccated soils at the Viking sites, soils in the 'oasis' regions may be significantly more hydrated, ranging from relatively thin films to filled porespaces and crevices (free standing water/ice). It is likely, considering the heterogenous nature of natural systems, that the H_2O is not uniformly distributed throughout the oases. It could be very spotty. It is also likely that the salt concentrations could be highly variable, considering the heterogeneous nature of natural rock and soil systems (probable sources of salts through leaching) and freeze/thaw segregation processes. A variety of other conditions associated with soil moisture would be expected to make the near-surface microenvironments at the oases very different than at the Viking sites. The oxidants that affected the Viking biology experiments and apparently destroyed organic molecules were found by the LR and GEx experiments not to be stable in the presence of liquid H_2O. At the oases these oxidants may not be present everywhere, therefore, and the abundance of organics might be higher. Significant differences in pH and temperature profiles may also exist.

We have proposed that the outgassing of H_2O from soils in the 'oasis' regions may be a primary mechanism for initiating (via dust fountains) local and sometimes global dust storms (4). This could explain a variety of previously unexplained aspects of the dust storms; such as their tendency to begin at dawn; their white, fading to yellow appearance; and their unusual geographic restrictions.

It has been further proposed that evaporation of the salty H_2O from the ground could produce aerosol salt particles (5). The salts could reach relatively high concentration during periods of high evaporation, and they could remain suspended in the atmosphere for prolonged periods. It has been suggested that these salts could have significant effect on atmospheric processes (catalysis and nucleation precipitation); impurity ions (especially Fe^{2+} and Fe^{3+}) in aerosol salts could affect reflectance spectra of the surface; and deposit of the aerosols may be the primary source of the unusual abundance of salts found in martian soil. If the latter is true, estimates of source rock mineralogy from Viking XRF data may be in substantial error.

Among the several othermajor implications of the proposed 'oases' is the extent of H_2O cycling implied from current estimated annual H_2O

evaporation rates (up to a cubic kilometer of H_2O per year) (5). If these rates are representative of past activity they imply a very dynamic H_2O evaporation/deposition cycle, involving deposition at the poles and subsurface recharging of oasis regions via a global aquifer system (5).

Acknowledgements. This work was supported under NASA grants NSG-7397 (Planetary Biology), NSG-7405 (Planetary Geology), NAGW 40 (Planetary Geophysics and Geochemistry).

References. (1) Huguenin, R.L., Clifford, S.M., Sullivan, C.A., and Miller, K.J. (1979) NASA TM 80339, 208; (2) Huguenin, R.L. and Clifford, S.M. (1980) NASA Tech. Mem. 81777, 153; (3) McCord, T.B., Huguenin, R.L., and Johnson, G.L. (1977) Icarus 31:293; (4) Huguenin, R.L., Clifford, S.M., and Greeley, R. (1980) NASA Tech. Mem. 81776, 147; (5) Clifford, S.M., and Huguenin, R.L. (1980) NASA Tech. Mem. 81777, 153.

MARTIAN NORTH POLAR CAP, 1979-1980: K. Iwasaki, Y. Saito, Kwasan Observatory, University of Kyoto, Kyoto 607, JAPAN, and T. Akabane, Hida Observatory, University of Kyoto, Kamitakara, Gifu-ken 506-13, JAPAN.

The regression curve for the north polar cap of Mars is extracted from the photographic observations of Mars at the Kwasan Observatory and at the Hida Observatory during the 1979-1980 apparition. Our observations were carried out with the 45 cm refractor telescope at the Kwasan Observatory and with the 65 cm refractor telescope at the Hida Observatory. The observation extended from September 16, 1979 to June 18, 1980. During this period we secured about 11,400 red filter negatives (6200-6500A), 11,400 green filter negatives (4900-5600A), and 2,800 yellow filter negatives (4900-6500A). Dimensions of the north polar cap were measured on the selected 84 red, 86 green, and 30 yellow filter negatives taken at the best seeing conditions.

In Figure 1 the latitude of the edge of the polar cap is plotted against the areocentric longitude of the sun Ls. In our observations the polar cap was first recognized at about Ls=26°, and the latitude of the edge of the polar cap was then about 65°N. In this apparition the retreat of the cap stopped until Mars reached Ls=56° and then started to shrink. Miyamoto (1) found that the retreat of the cap in 1963 stopped for a while around Ls=20°-40°. Baum (2) suggested that the edge of the north polar cap change rather little until Mars reaches Ls=55°. In our obserbations during 1977-1978 apparition, the north polar cap started to shrink at Ls=50°. The time when the north polar cap started to shrink appears to be different from year to year.

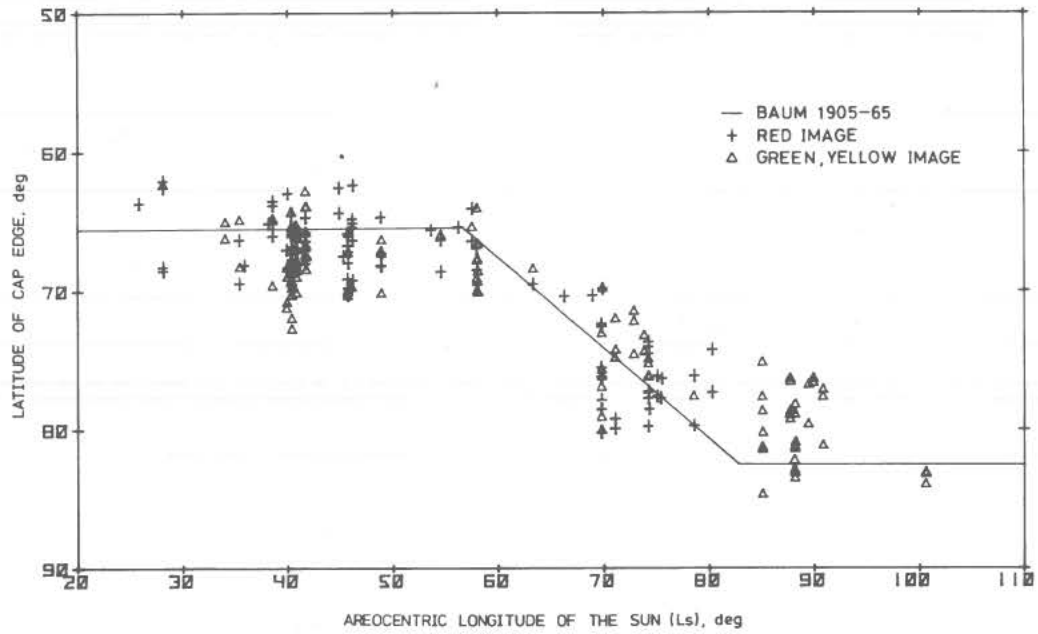

Fig. 1. Comparison of the present measurements (crosses and triangles) with measurements on the plates taken from 1905 to 1965 at the Lowell Observatory plus more recent Patrol films by Baum (1974) (solid line).

MARTIAN NORTH POLAR CAP, 1979-1980

Iwasaki,K. et al.

The shrinking edge reaches the latitude around 80°N at Ls=85° and then become almost stationary, i.e., it is the edge of the permanent polar cap. Baum et al. (2-4) reported the behavior of the north polar cap obtained from the Lowell Observatory plate collection covering more than 60 years from 1905 plus more recent data from Patrol films. Measurements by Baum (2) are compared with our data in Figure 1. The agreement of their values with ours is almost perfect. The temporally stop of north polar cap shrinking before Ls=56° is seen on the data by Miyamoto (1), Baum and Martin (4), Viking orbiter observations measured by James (5), and our data in the 1977-1978 apparition (6). This temporally stop appears to be a regular phenomenon in the north polar cap.

The planetocentric latitude of the polar cap edge for the longitude of the central meridian is plotted in a polar map of Martian coordinates centered on the North pole (Figure 2-4). Figure 2 describes the overall shape of the polar cap for Ls=35° -49°. The latitude of the edge of the polar cap located around 67°N and appears not to change with longitude. The shape of the polar cap for Ls=69°-76° and 79°-84° is shown in Figure 3. The edge of the polar cap well receded for the longitude range between 0° and 180° and between 270° and 360°. However, the edge of the polar cap receded little in the range of longitudes 180° to 270°. For the interpretation of the appearance of the large polar cap in this range of longitudes as seen in Figure 3, we may consider two types of situation, one is: some patches may break away from receding main cap, the other is: large cloud may cover this area. In Figure 4, the edge of the polar cap for Ls=84°-101° is plotted on the picture of the permanent polar cap by Mariner 9 (Ls=97°). The edge of the permanent polar cap runs

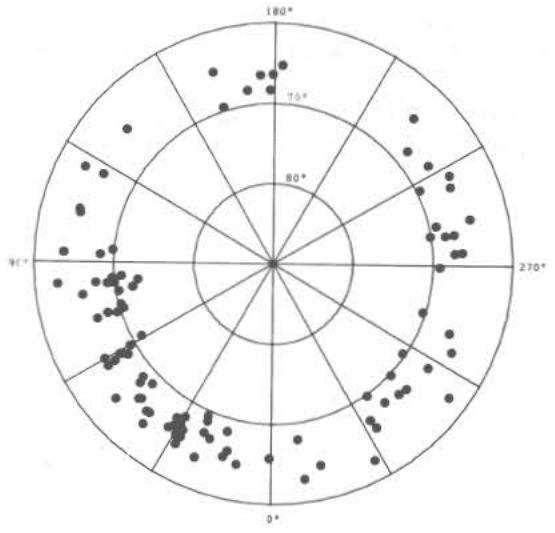

Fig. 2. Contour map of the north polar cap of Mars reduced for Ls=35°-49°.

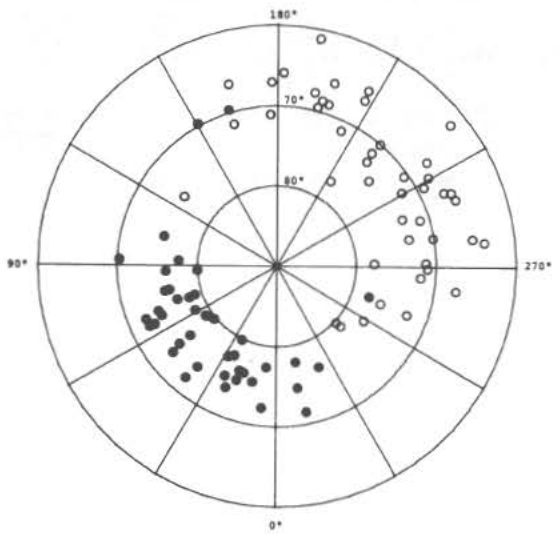

Fig. 3. Contour map of the north polar cap of Mars reduced for Ls=69-76° (filled circles) and Ls=79-84° (open circles).

from about 85°N latitude on one side to 78°N on the other. This asymmetry with respect to the North pole is also seen in our measurements. The shape of the permanent north polar cap appears to be the same each Martian year.

Fig. 4. Contour of the permanent north polar cap of Mars for Ls=85°-101° plotted on the Mariner 9 picture (Ls=97°) ("Mars as viewed by Mariner 9", p. 137, NASA, 1974).

References

1. Miyamoto S. (1963) Contr. Inst. Astrophys. Kwasan Obs., Univ. of Kyoto, No. 124.
2. Baum W. A. (1974) Exploration of the Planetary System, p. 241-251, D. Reidel, Dordrecht.
3. Fischbacher G. E., Martin L. J., and Baum W. A. (1969) Report under JPL Contract No. 951547, Lowell Obs..
4. Baum W. A. and Martin L. J. (1973) Bull. Amer. Astron. Soc., 5, p. 296.
5. James P. B. (1979) J. Geophys. Res., 84, p. 8332-8334.
6. Iwasaki K., Saito Y., and Akabane T. (1979) J. Geophys. Res. 84, p. 8311-8316.

THE GLOBAL AND SEASONAL BEHAVIOR OF MARS ATMOSPHERIC WATER VAPOR: RESULTS OF THE VIKING ATMOSPHERIC WATER DETECTOR EXPERIMENT. Bruce M. Jakosky and Crofton B. Farmer, Division of Geological and Planetary Sciences, California Institute of Technology, Pasadena, CA 91125.

Viking Orbiter Mars Atmospheric Water Detector (MAWD) observations have allowed us to map the atmospheric vapor content spatially over the planet for about one and one half martian years, from June, 1976, to April, 1979. This allows quantitative arguments to be made regarding the seasonal sources and sinks of water and the processes responsible for its behavior. The possible reservoirs include: the regolith (ground ice or permafrost, adsorbed water, or chemically-bound water); the seasonal polar caps (water ice or CO_2-H_2O clathrate); and the residual polar caps. Seasonal variations of vapor may also be due to: advection resulting from circulation of the atmosphere, with water transported in the form of atmospheric vapor, clouds, or water sorbed onto airborne dust particles; or local saturation of the atmosphere, with the temperature profile controlling the amount of vapor present.

The detailed local and global behavior of vapor is indicative of the seasonal response of the atmosphere and surface. The local vapor abundances closely follow the surface thermal behavior, being greatest during the warmer and least during the colder seasons. As northern summer approaches and abundances begin to increase, they do so first and (initially, at least) fastest in the northern mid-latitudes. This behavior is not consistent with supply of vapor from only the receding seasonal polar cap, because the maximum of vapor abundance occurs too far south of the cap edge. As summer ends and abundances drop, at about L_S=140°, they do so at all latitudes north of about +25°. This relatively early decline in vapor cannot be due to entrapment onto the forming seasonal polar cap because the cap has not yet begun to form. Atmospheric circulation at this season has been shown to be inefficient in transporting the vapor to the residual cap at the pole. The drop in abundance also cannot be due to obscuration of vapor by the polar hood, which did not form during the year observed by Viking until sometime after L_S=160°, and which does not extend southward of about 40° in any year. Both types of vapor behavior strongly imply the existence of a seasonally-accessible reservoir of water within the regolith in the northern hemisphere. Southern-hemisphere behavior is complicated by the effects of the global dust storms at the interesting seasons, both real and observational.

There is a strong latitudinal gradient of water vapor, with typically twice as much water in the north as in the south. This implies a net annual flow of vapor toward the south, with the north and south polar caps acting as a net source and sink for water, respectively. The continuity of the latitudinal gradient does not allow there to be any significant net annual sources or sinks for water at any intermediate latitude. Specifically, the local and global behavior both indicate that no significant amount of water is outgassed from the Solis Lacus region.

The atmosphere above the south polar summer residual cap contains almost 15 precipitable microns (pr μm) of vapor. Because the surface is cold enough to retain CO_2 frost year-round, there must be a thermal inversion over the cap in order to hold this much vapor. The atmospheric vapor over the cap must be advected in from elsewhere, and water will condense onto the cap at all seasons. Earth-based observations in 1969 show as much as 50 pr μm (disk-averaged) at

MARS ATMOSPHERIC WATER VAPOR

Jakosky, B. M. and Farmer, C. B.

this season, indicating that the CO_2 cap may sublime away completely in some years, revealing the water cap which must lie beneath. Retention of CO_2 throughout the year may be related to the occurrence of major global dust storms, which act to protect the cap against sublimation.

There is a strong correlation between the annual average atmospheric vapor abundance and the local elevation of the surface. Although the concept of a constant uniform vapor mixing ratio must be an oversimplification, it helps in understanding this relationship. If this effect is removed by dividing by the local airmass ($a = \exp(-z/H)$), the resulting abundance map correlates well with the albedo and the thermal inertia of the surface. This can be caused by control of the water holding capacity of either the atmosphere or sub-surface by the thermal behavior of the surface and sub-surface.

It appears that interaction with the regolith on a seasonal basis is probably a significant determinator of the atmospheric water vapor behavior. The relative importance of each of the above-mentioned mechanisms for controlling the seasonal vapor behavior will have important implications regarding the global subsurface distribution of water as well as its behavior on much longer timescales. During the martian year observed by Viking, there was a net transport of water toward the south, with a net increase of the amount of water ice in the south polar cap. Equating the water vapor behavior observed by Viking, however, to that which is typical of the current epoch should be done with care in light of the possible year-to-year variations in the water cycle.

THE SEASONAL CO_2 CYCLE ON MARS

Philip B. James
Physics Dept., U. Missouri-St. Louis, 63121

William Herschel was the first observer to identify the variations in the martian polar caps with the change of seasons. For 187 years after his inference astronomers monitored the waxing and waning of the polar caps and speculated, often erroneously, concerning their composition and significance. Although the majority held that they were composed of water ice, a minority persisted in the opinion that the seasonal caps were CO_2 ice. The latter opinion, most eruditely defended by Leighton and Murray (1), was confirmed experimentally by the Mariner 7 thermal measurements in the south polar region (2).

Because carbon dioxide makes up 95% of the atmosphere, the seasonal cycle of CO_2 between the gas and solid phases is very sensitive to the planetary energy balance. For example, it has been known for many years that, for the current orbital configuration, the south winter cap is more extensive than that in the north because of the longer duration of southern winter. The seasonal cycle has been documented in visual and photographic records for many years; more recently, spacecraft observations have augmented the terrestrial data set. In particular, Viking afforded the opportunity of simultaneously monitoring the gas phase (3) and solid phase, thus allowing both the amount and location of solid deposits to be studied. It is also possible that carbon dioxide is exchanged between the atmosphere and the regolith (4), although this process may not be important on a seasonal time scale.

Observational astromoners have known for many years that there are two distinct polar phenomena: surface caps, which are deposited in autumn and early winter and which sublime in spring; and polar hoods, atmospheric phenomena which obscure the surface in fall and winter. Viking observations show that the northern and southern hoods differ substantially, with the former being more continuously conspicuous during the seasons mentioned. Morning hazes form in the south and mists shroud Hellas basin around vernal equinox, but generally the atmosphere in the south during fall and early winter was notable for its clarity. The hood in the south does not form until late winter, when the cap size is already diminishing (5). Terrestrial observers tend to support this difference between hoods; but one must remember that the winter south pole is more difficult to observe than any other phase of the caps.

The spring recessions of the caps have been intensively studied because of the relative clarity of the atmosphere and the earthward tilt of the subliming caps at opposition. Figure 1 displays the regression curves from several sources, both telescopic and spacecraft, for the north polar cap (6). Most of the data are consistent with the following general features: an abrupt transition from a boundary at about 48°N to one at 65°N at about $L_s = 0°$; a standstill at 65°N until $L_s = 40°$; and a gradual contraction to the residual cap thereafter. Some observers have

attributed the L_S = 0° transition to hood dissipation. The lack of a corresponding jump in the pressure measured by the lander implies that any surface cap present south of 65°N is very thin; this is consistent with VL-2 imaging observations (7). Simple modeling of the CO_2 balance in conjunction with lander pressure curves suggests that the north seasonal cap at L_S = 0° is equivalent to a uniform 770 kg/m^2 of solid CO_2 north of 65°N.

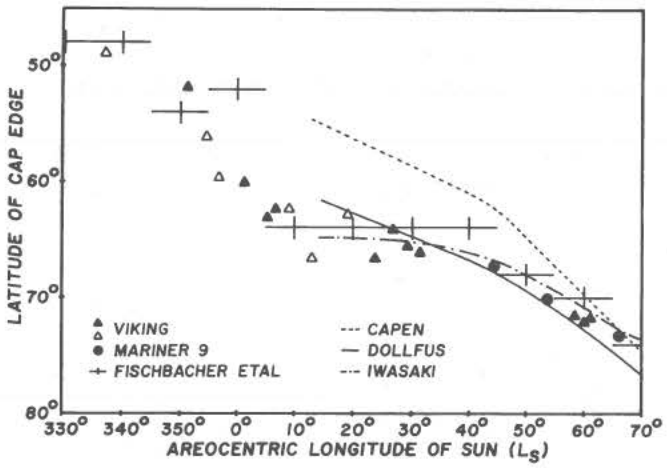

Figure 1: North polar regression curves. The data were obtained from several sources as indicated on the graph.

(Figure published courtesy of American Geophysical Union)

The south cap recession, depicted in Figure 2, is quite different in appearance. The rate of change of the cap edge with respect to latitude is relatively constant until near summer solstice when the cap approaches its residual configuration. The agreement between the 1971 telescopic and 1977 Viking data is excellent; nor is there any compelling inconsistency between the 1973 data and the Viking points. The 1956 data appear to imply a more rapid sublimation in that year however. The south polar cap contains more than twice as much solid CO_2 than the north cap at its maximum extent, although the average surface density is about 600 kg/m^2 at L_S = 180° because the condensate is spread over a much larger area.

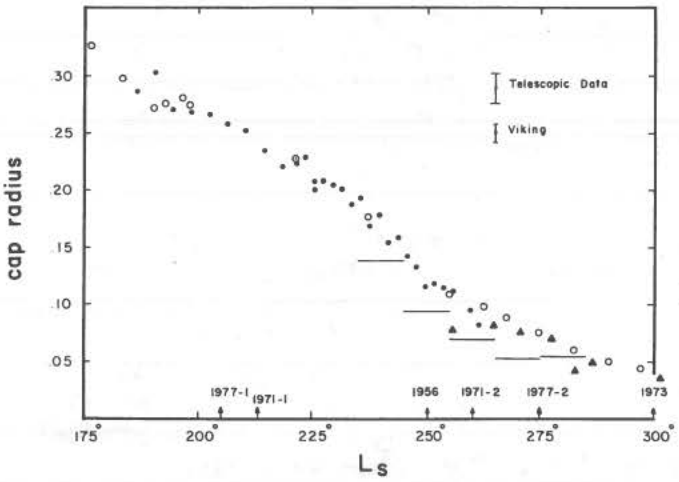

Figure 2: South polar regression curves. Data for 1977 (Viking) are denoted by open circles; for 1971 by solid dots; for 1973 by solid triangles; and for 1956 by horizontal bars. Major dust storms are also located along the abscissa.

THE SEASONAL CO_2 CYCLE ON MARS

James, P. B.

Early observers reported that ice deposits survived the summers at both poles, although there were some reports of complete disappearance of the south cap in some years, perhaps due to obscuration by dust storms. The composition of the north residual cap, observed extensively by Viking, was inferred to be water ice via an energy balance analysis (8). Mariner 9 observed a residual south cap (9); Viking observed a similar, but significantly different, residual cap in 1977 (10) and a residual cap in 1979. Temperature data strongly suggest that the remnant cap in the south is at least partly CO_2 ice (11), a conclusion which appears to be consistent with a detailed energy balance (David Paige, private communication). The circumstances which may produce this state of affairs, which contradicts much earlier discussion, are not yet entirely clear. Net cooling in the region due to dust may play a role; and the relatively high albedo of the south residual cap may be significant.

REFERENCES

1. Leighton, R. B., and B. C. Murray, Science 153, 136-144 (1966).
2. Neugebauer, G., G. Munch, H. H. Kieffer, S. C. Chase, and E. D. Miner, Astron. J. 76, 719-749 (1971).
3. Hess, S. L., R. M. Henry, and J. E. Tillman, J. Geophys. Res. 84, 2923-2927 (1979).
4. Fanale, F. P., and W. A. Cannon, J. Geophys. Res. 84, 8404-8414 (1979).
5. Briggs, G., K. Klaasen, T. Thorpe, and J. Wellman, J. Geophys. Res. 82, 4121-4149 (1977).
6. James, P. B., J. Geophys. Res. 84, 8332-8334 (1979) and references contained therein.
7. Jones, K., R. Arvidson, E. Guinness, S. Bragg, S. Wall, C. Carlston, and D. Pidek, Science 204, 799-806 (1979).
8. Kieffer, H. H., S. C. Chase, T. Z. Martin, E. D. Miner, and F. D. Palluconi, Science 194, 1341-1344 (1976).
9. Murray, B. C., L. A. Soderblom, J. A. Cutts, R. P. Sharp, D. J. Milton, and R. B. Leighton, Icarus 17, 328-345 (1972).
10. James, P. B., G. Briggs, J. Barnes, and A. Spruck, J. Geophys. Res. 84, (1979).
11. Kieffer, H. H., J. Geophys. Res. 84, 8263-8288 (1979).

LONG CLOUD OBSERVATIONS ON MARS AND IMPLICATIONS FOR BOUNDARY LAYER CHARACTERISTICS OVER SLOPES. R. A. Kahn and P. J. Gierasch, Laboratory for Planetary Studies, Cornell University, Ithaca, New York 14853.

Viking orbiter images of Mars show several instances of long continuous cloud formations on the slopes of Arsia and Pavonis Mons. We have searched all the images of the planet for occurrences of such formations. Only in the Tharsis region were long clouds unambiguously identified. We have measured the times and locations of occurrence, the wavelengths and when possible, the apparent velocity of motion of these clouds. We have also tabulated the wavelengths of patches of ripple clouds which are often associated with the long formations. The long clouds are observed only in the early morning hours, suggesting that they are associated with drainage winds due to a cold planetary boundary layer. We use simple mathematical models to examine various aspects of such boundary layer winds, which allows us to construct a complete and self-consistent explanation of all the observed features of the cloud formations. We use these results to characterize some physical properties of the Mars boundary layer. There is strong downslope flow in the boundary layer on the high slopes of both volcanos. In the saddle region between the peaks the flow slows and undergoes a hydraulic jump phenomenon, producing the long clouds. Downstream of the jump, standing internal gravity waves can exist and are excited by flow over surface irregularities. Their wavelength varies systematically behind the jump because of variation in the flow speed. Finally, we can account for the location of the jumps by the variation of relative strength of the boundary layer flows on the two volcanos.

THE MARS CONSORTIUM GLOBAL MAPS. Hugh H. Kieffer, U.S. Geological Survey, Flagstaff, AZ 86001

As the amount of quantitative information about Mars has increased, detailed studies of the relation between martian properties have been increasingly desirable. At the same time, the large quantity of data available has made such studies impractical without the aid of computer processing. The Mars Consortium is a structured organization of Mars global data and an informal organization of scientists. The intent of the Mars Consortium is to make widely available those data sets which cover all or much of Mars in a format that facilitates comparisons between them. The data preparation effort is oriented toward computer assisted analyses, but also produces graphic material which greatly aids analyses without the further use of computers.

The spatial resolution of global observations ranges from about one kilometer for the Viking apoapsis imaging to hundreds of kilometers for earth-based spectral observations. The Mars Consortium has adopted a standard data resolution of 1/4° latitude by 1/4° longitude. The data storage arrangement agrees with the Mars mapping convention. Data sets with resolution higher or lower by powers of 2 are used where appropriate; resolutions of 10° or integral fractions of 10° are less common.

The standard array contains just over one million elements and twelve of them can be stored on a standard magnetic tape (nine track, 800bpi, 2400 ft). The standard format is shown in the figure. The mathematical south pole is excluded. Data sets that are not readily put into a Mars Consortium format will be documented and distributed in appropriate special formats.

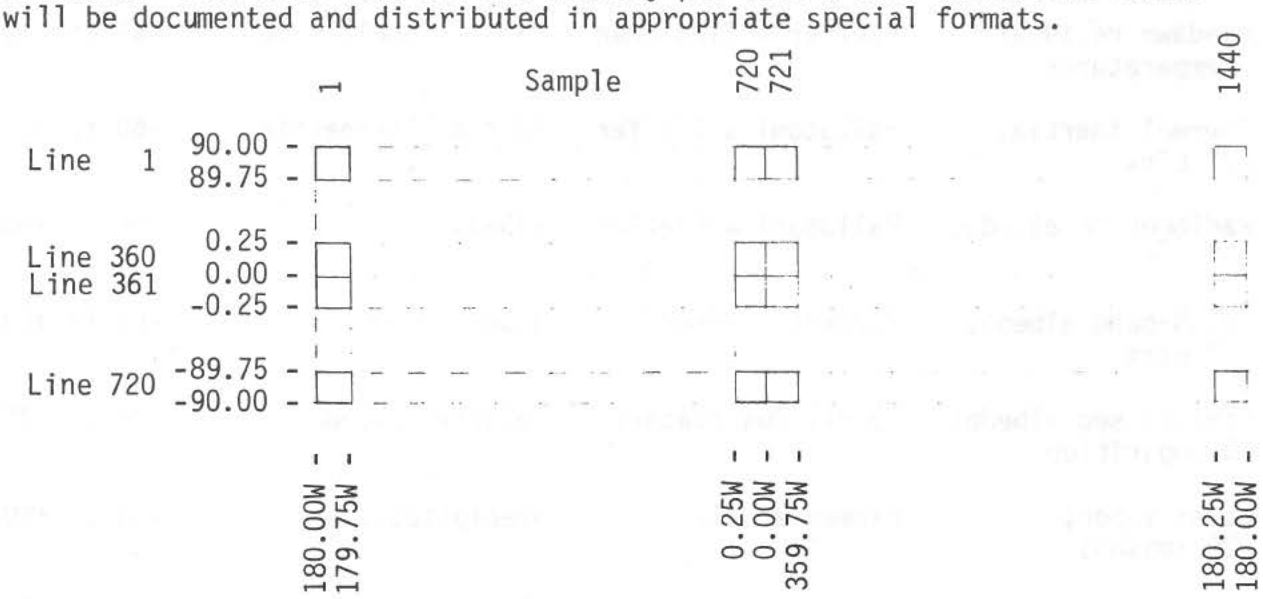

Array element (I,J) Truncate to Integer:

Line J = 4. * (90.0 - latitude) + 1.0

Sample I = 4. * (180.0 - longitude) + 1.0 ; if I >1440, I = I - 1440

Data can be submitted to the Mars Consortium as: maps in any standard projection, vector-format data representing multi-parameter observations at single points, or digital raster arrays in any standard mapping projection. The data are archived as received and, if in map form, digitized in their original projection. The data are converted into image or vector form as appropriate, retaining all the original spatial and intensity resolution. The data are converted into Mars Consortium format, using smoothing and interpola-

THE MARS CONSORTIUM GLOBAL MAPS

Kieffer, H. H.

tion techniques as appropriate to generate as complete a global image as is faithful to the original observations. All data are scaled into 8-bit integers and simple-cylindrical images are produced. Sinusoidal equal-area projections are used for statistical analyses. The maps shown represent the data sets available as of June 1981 and are listed in the table. Substantial additions of radar and crater inventory data are anticipated in the near future.

Title	Source	8-bit scaling	latitude coverage
Topography, M9	USGS 1:25M map	km * 5 +50	-90 to +90
Geology	Scott & Carr	geologic unit	-90 to +90
Volcanic units	Greeley & Spudis	volcanic unit	-90 to +90
Viking 2 approach color	Soderblom et al.	Minnaert coefficient *500	-60 to +30
4-10km crater density	Condit	craters/10^6km^2	-65 to +45
Gravity residuals	Sjogren	mgal LOS accel.	-75 to +75
Predawn residual temperatures	Kieffer & Zimbleman	(T_{20} - model) + 50	-60 to +50
Thermal inertia, 2° bins	Palluconi & Kieffer	10 * milli-inertia	-60 to +50
Radiometric albedo, 1° bins	Palluconi & Kieffer	albedo * 500	-60 to +60
Broad-band albedo, 1° bins	Pleskot & Miner	albedo * 500	-60 to +60
Earth-based albedo; 5 apparitions	Lowell Observatory	relative albedo	-70 to +70
Water vapor; 29 seasons	Farmer et al.	precipitable μm	-90 to +90
1.4μm albedo; 29 seasons	Farmer et al.	albedo *100	-90 to +90
Channels	Carr	channel type	-65 to +65
Eolian features	Ward	type, wind direction	-90 to +90
Radar, 1975-6	Simpson (Arecibo)	Hagfors C/25.56	-12 to +24
Wind streaks	Peterfreund	type	-65 to +65
Thermal/Albedo averages	Martin	Special file	-90 to +90

THE MARS CONSORTIUM GLOBAL MAPS

Kieffer, H. H.

A variety of optical stencils can be used to isolate areas which satisfy specific constraints. For example, film transparencies which are opaque where data fall below the mean value for each of the data sets; topography, broadband albedo, approach violet/red, and predawn residual temperature will in combination reveal only those areas which were higher, brighter, bluer, and warmer predawn than the martian average.

Individuals are encouraged to submit to the Mars Consortium either original observations of a global nature or derived data sets, such as maps of specific surface categories. Individuals submitting data to the Mars Consortium may impose restrictions on their distribution; such data will be processed with lower priority. All data currently in the Mars Consortium are available for distribution without restriction. Reproducible transparencies and color prints of the Mars Consortium data sets have been sent to each of the NASA Planetary Data centers. These images have a scale of 150 μm per array element, yielding a global image of 10.9 by 21.7 cm. The digital data can be obtained by sending blank magnetic tapes to the author.

The Mars Consortium is supported by the NASA Geophysics and Geochemistry program.

OLYMPUS MONS AUREOLE: MECHANISM OF EMPLACEMENT Rosaly Lopes and J. E. Guest, University of London Observatory, Mill Hill Park, London NW7, K. Hiller and G. Neukum, Geology Dept., Ludwig-Maximilians Universitat, 8000 Munchen 2, F.R.G.

The Olympus Mons aureole is interpreted as a result of rockslides removing material from the volcano's outer flanks, which at the time extended beyond the present base. The perimeter scarp was formed by this massive removal of material, and was partly covered by lava flows at a later stage (*). The aureole units and surrounding terrain have been dated by crater counts (**).

This paper discusses some features of the ridge and fracture pattern present on the aureole units, such as: (1) arcuate compressional ridges at front of slide units (convex downslope), (2) arcuate ridges at head of slide unit formed by differential movement of middle of slide (concave downslope), (3) transverse tensional cracks, (4) longitudinal grooves following direction of movement where slide is unimpeded (5) units tend to follow ground topography. These fractures are also commonly found on terrestrial mass movement deposits.

The ridge and fracture pattern on the aureole suggests that the rockslides were emplaced as a series of block units which moved differentially; some well preserved areas show that the middle block units moved further downslope and some fracturing and lateral spreading occurred at a later stage.

We consider that the emplacement of these rockslides was probably aided by melting of permafrost on the volcano's pedestal material causing general slope instability, and leading to slumping of large quantities of material from the outer flanks. Melting of permafrost may have been associated with a general increase in martian surface temperatures.

(*) Lopes, R. et al. (1979), 'The Moon and the Planets', 22, 231-234.
(**) Hiller et al. (1980), 'Reports of the Planetary Geology Program', NASA TM 83385.

ORIGIN OF MARTIAN OUTFLOW CHANNELS: WIND, WATER, MUD, OR ICE?

B. K. Lucchitta, U.S. Geological Survey, 2255 North Gemini Drive, Flagstaff, Arizona 86001

Outflow channels on Mars are long, sinuous, linear depressions that occur mostly in the equatorial area (lat ±30°). They differ from small valley networks (1) in that they are larger and arise full grown from their apparent source regions in chaotic terrains. The origin of these large channel features is controversial and has been ascribed to several different mechanisms. An eolian origin has been advocated (2), proposing that atmospheric currents moving fine debris in saltation and suspension could have carved the channels. Many of the streamlined forms in the channels seem similar in shape to wind-carved yardangs, but the wind alone seems an unlikely erosional agent, because the channels have integrated drainages and generally uniform gradients toward topographic lows. The most generally accepted origin of the channels is that of fluvial erosion by catastrophic flooding (3).

The catastrophic flood hypothesis is derived primarily from analog studies that indicate morphologic similarities between the martian outflow channels and those created by the catastrophic Spokane flood that formed the Washington scablands. These similarities have been documented extensively (3,4,5) but differences of scale remain a major problem: martian channel features are, on the average, much larger than their proposed terrestrial analogs. An origin for the martian channels by liquefaction mudflows (6) has also found favor with some investigators because it explains the chaotically disturbed region at the source of the channels. This hypothesis envisions that excess pore pressure caused liquefaction of materials in the channel source region, allowing sediments to flow rapidly down gentle gradients as highly mobile mudflows. The problem with this hypothesis is that high speed must be maintained in the mud flows for thousands of kilometers along the length of the channels.

Recently, Lucchitta et al. (7) examined the problem of channel origin from the perspective of the erosional characteristics and resultant landforms created by former and present-day ice streams and glaciers on Earth. On the basis of morphologic comparisons, they proposed an ice-stream origin to explain the occurrences and form of the outflow channels on Mars, pointing out that, in contrast with hydraulic agents, ice streams produce terrestrial and martian features of the same scale. A problem of the ice hypothesis is that movement of glaciers on Mars is difficult because of low gravity, low atmospheric temperatures, and low channel-floor gradients.

Geomorphic processes on Earth are complex and affected by many variables. The origin of martian outflow channels may also be complex, and may be some combination of the various mechanisms mentioned above, including elements of several hypotheses. Disturbance of the source regions strongly suggests that collapse by liquefaction may have occurred, and that mudflows may have been generated. Widths of the cross-sectional areas of the channels suggest that, in many places, large volumes of material were discharged, with magnitudes characteristic of catastrophic floods. Several of the small-scale channel features are also consistent with an origin by catastrophic flooding. On the other hand, the resemblance of some of the streamlined channel features to yardangs supports the idea of eolian sculpture. Many of the grooves on the floors, terraces on the walls, and shapes of islands suggest carving by ice.

MARTIAN OUTFLOW CHANNELS: WIND....

Lucchitta, B. K.

The presence of morphologic elements typical of so many different erosional agents suggests that a combination of processes formed the channels. Liquefaction of material in the source region may have created catastrophic mudflows that traveled down the regional gradient. Because of the cold ambient temperature on Mars, the mudflows may have become charged with ice, locally acquiring the characteristics of water-laden ice sheets. Continental ice sheets on Earth have left, at their margins, abundant moraines sculpted into longitudinally grooved terrain. The longitudinal grooves and ridges seen on martian channel floors may similarily result from ice-charged mudflows dropping their debris. In places, the ice, rock, and mud mixture may have been consolidated into true glaciers, creeping slowly and carving deep, U-shaped valleys and valley-wall terraces. In other places, frictional heat caused by acceleration of the icy mass on steep gradients may have melted enough ice to reconvert the moving mass into muddy slurries, or locally into catastrophic floods. After the channels were sculpted by these various agents, erosion by valley-controlled winds may well have enhanced some of the previous shapes and superimposed on them the yardang-like forms typical of wind erosion.

References

(1) Pieri, D. C. (1980) Science 210, p. 895-897.
(2) Cutts, J. A., Blasius, K. R., and Roberts, W. J. (1978) In Reports of Planetary Geology Program, 1977-1978 NASA TM 79729, p. 277-279.
(3) Baker, V. R. and Milton, D. J. (1974) Icarus 23, p. 27-41.
(4) Baker, V. R. (1978) Science 202, p. 1249-1256.
(5) Baker, V. R. (1979) J. Geophys. Res. 84, p. 7985-7993.
(6) Nummedal, Dag (1978) In Reports of Planetary Geology Program, 1977-1978, NASA TM 79729, p. 257-259.
(7) Lucchitta, B. K., Anderson, D. M., and Shoji, H. (1981) Nature 290, p. 759-763.

INFRARED OBSERVATIONS OF PHOBOS AND DEIMOS FROM VIKING;J.I.Lunine, G.Neugebauer,B.M.Jakosky,California Institute of Technology,Pasadena,CA 91125; and E.D.Miner,Jet Propulsion Laboratory,California Institute of Technology,Pasadena, CA 91109

Observations of 11 and 20 micron radiances of Phobos and Deimos, made with the Viking Infrared Thermal Mapper (IRTM), have been analyzed to determine surface thermal properties of the Martian satellites. The data for each satellite are consistent with surface material of low thermal conductivity (comparable to that of the earth's moon) at least several millimeters thick. The only previous observations of Phobos were made by the Mariner 9 infrared radiometer in 1972(1); no observations were made of Deimos. The Viking data are of higher quality due to increased sensitivity of the IRTM instrument, better information on relative sun, spacecraft and satellite positions, and greater number of observations.

The radiometric data were compared with numerical calculations of radiance versus phase angle using a thermal model developed by Kieffer, et al. (2), in connection with infrared radiometry of Mars. The single-layer model assumes an airless spherical body, of zero albedo and unit emissivity, for which incident solar flux and surface thermal emission are in equilibrium. An albedo of zero is consistent with the very low reflectivities of the Martian satellites (3). The thermal inertia I, equal to $(k\rho c)^{\frac{1}{2}}$ (k=thermal conductivity, ρ=density, c=specific heat of surface), was varied to fit theoretical curves to the observations. Density and specific heat were given fixed values of 1.5 gm/cm^3 and 0.2cal/(gm deg-K), respectively, which are assumed uniform over the satellites surfaces. To evaluate radiance data from two eclipses of Phobos and one of Deimos by Mars, thermal models were constructed which include a discontinuous removal and reapplication of solar flux. The observed radiances during and after eclipses were somewhat dependant on sun-spacecraft-satellite geometry; with satellite positions kindly provided by T. Duxbury the geometry was accounted for in the models.

Figures 1 and 2 show 11 micron-wavelength observations of Phobos and Deimos, plotted as radiance versus phase angle for each satellite. Absolute calibration of radiance was difficult since the satellites almost always did not fill the 0.3 degree field of view of the instrument(4), Phobos' diameter typically being 0.2-0.1 degrees and Deimos' 0.1-0.05 degrees. Because of pointing uncertainties and lack of TV images for many of the observations, the points plotted are lower bounds to the actual radiances. Error bars on some data points reflect uncertainties in the orientation of the satellite's major axis relative to the IRTM's line-of-sight.

Plotted on figures 1 and 2 are calculated radiometric phase curves for two values of the thermal inertia I, I given in units of 10^{-3} cal/(cm^2 sec$^{\frac{1}{2}}$ K). The I=2 curve depends on local time and latitude of subspacecraft point, and has been plotted for two different geometries (see figure caption). The I=0 curve depends on phase angle only. The I=2 curves appear to fit the data more closely than does the I=0 curve. However, since the data are lower bounds on the actual radiances, one can infer only that Phobos and Deimos have surfaces of low thermal conductivity. Radiance curves calculated at 20 microns fall below many of the 20 micron data points, but do fit well the trend of the radiances as a function of phase angle for both satellites.

Radiance data from one eclipse each of Phobos and Deimos are shown in figures 3 and 4, plotted as radiance versus time from the start of eclipse. Theoretical curves for I=0.2,0.6, and 2. are also plotted, normalized to one post-eclipse data point. Again pointing uncertainties require that some of the

data points be regarded as lower bounds. Several pointing inaccuracies were identified in the raw data and the corresponding data points are indicated on the figures. For all eclipses analyzed, at 11 and 20 microns, the data fall within the curves corresponding to I=0.2-2. The data in fact rule out an I much less than 0.6 or much greater than 2. for both Phobos and Deimos.

We interpret the data as indicating that both Phobos and Deimos are covered with material of low thermal conductivity. The data for both satellites indicate similar surface thermal inertias in the range ½ to 2. The Phobos result is entirely consistent with that from Mariner 9 (1). I for fine particulate lunar material is about 1, while for solid rock can be as high as 60 (5). Only finely divided powders (i.e.,dust) in vacuum appear to have a thermal inertia low enough to explain the results.

For a variation in solar insolation of period P, the thermal skin depth is $(kP/\rho c\pi)^{\frac{1}{2}}$, or of order 1 mm for a 1 hour eclipse. Since the eclipse data can be fitted with a simple single-layer thermal model, the dust layer must be several skin depths thick. For variation of radiance with phase angle, P is 8 hours for Phobos and 30 for Deimos, implying thermal skin depths of 2 and 3 mm, repectively. Given that the data in figures 1 and 2 fit the single-layer model,we conclude the dust layer to be at least several millimeters thick.

Acknowledgements: We thank H.Kieffer, F. Palluconi, and J. Bennett for their advice and assistance, and the entire Viking flight team for carrying out the complex observations expertly.

References:

(1) Gatley,I., et al. (1974) Astrophys. J. 190,497-503.
(2) Kieffer, H.H., et al.(1977) J. Geophys. Res. 82,4249-4291.
(3) Klaasen,K.P.,et al.(1979) J. Geophys. Res. 84,8478-8486.
(4) Chase, S.C., Jr., et al. (1978) Appl. Opt. 17,1243-1251.
(5) Jakosky, B.M. (1979) J. Geophys. Res. 84, 8252-8262.

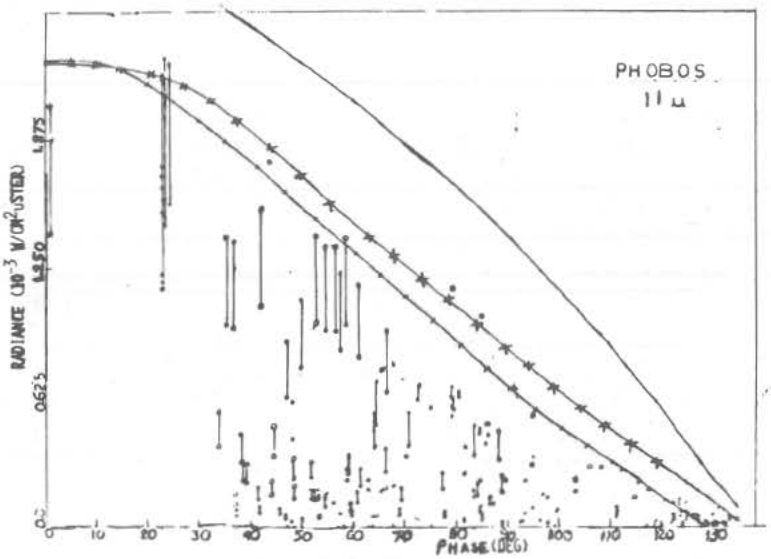

Figure 1. Radiance vs. phase angle for Phobos at 11 microns. Data plotted as circles. Three model curves are drawn: I=0, (plain line), I=2 and sub-observer point moving along satellite equator (line with bars), I=2 and subobserver point moving northward at constant longitude (line with crosses). Horizontal axis is phase angle in degrees; vertical axis is radiance in 10^{-3} W/(cm^2 micro-steradian).

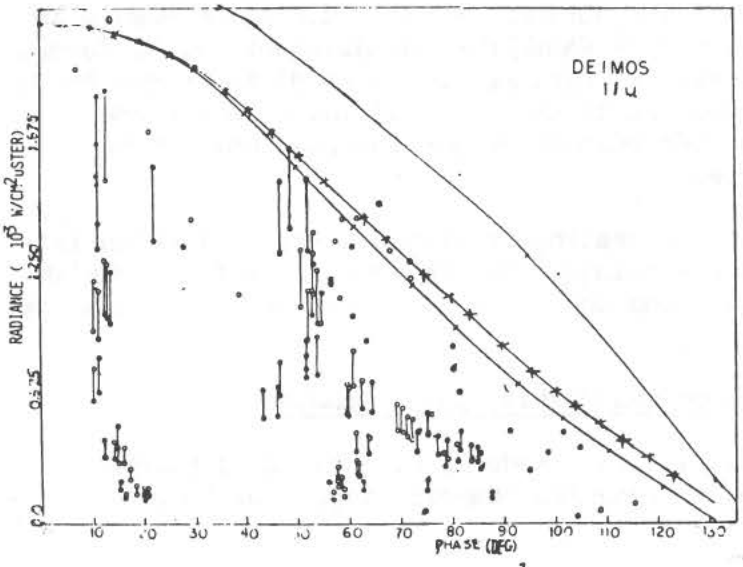

Figure 2. Same as figure 1, for Deimos.

Figure 3. Radiance vs. time for eclipse of Phobos by Mars. No data were collected at start of eclipse. Arrow indicates data point to which theoretical curves were normalized. Observations for which instrument most likely did not view entire satellite are identified by horizontal bars. Horizontal axis is time from start of eclipse in units of 10^3 seconds; vertical axis is radiance in 10^{-3} W/(cm^2 micro-ster).

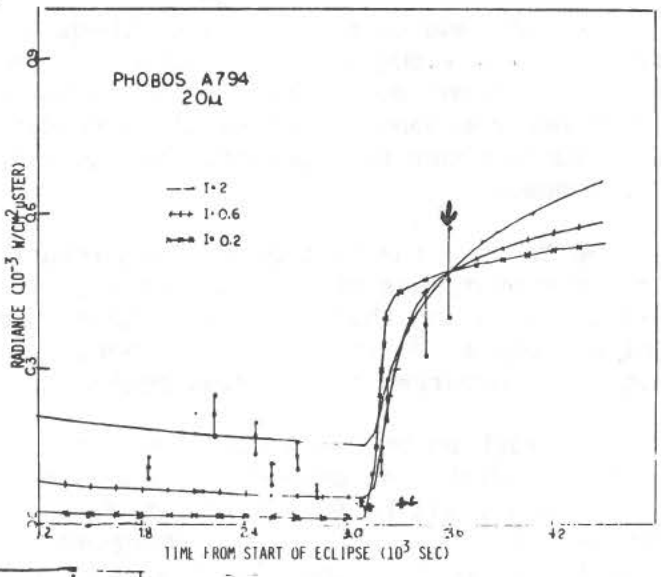

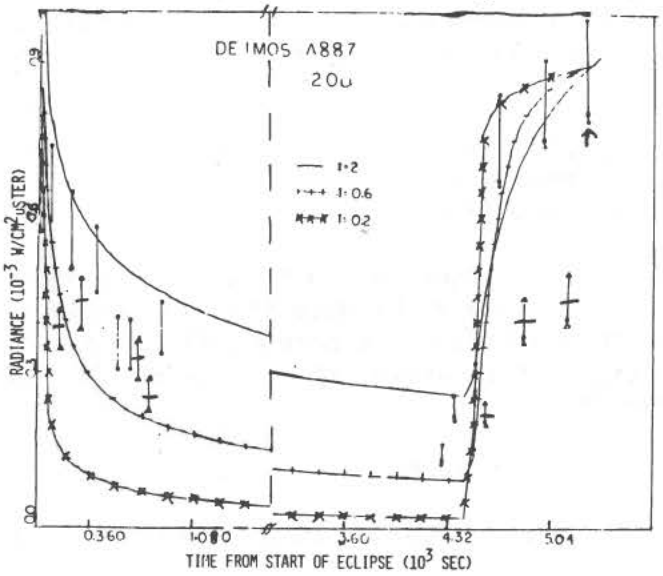

Figure 4. Same as figure 3 but for eclipse of Deimos. Note both eclipse entry and exit were observed.

COMPARATIVE STUDIES OF THE NORTHERN POLAR SANDSEAS OF MARS WITH TERRESTRIAL DUNES : EVALUATION OF OUR KNOWLEDGE, M. Mainguet, J. M. Borde, L. Cossus, Laboratoire de Géographie Physique Zonale et d'Etudes des Paysages en Roches Sédimentaires, Université de Reims, 51 100 Reims, France, and Ph. Masson, Laboratoire de Géologie Dynamique Interne, Université de Paris-Sud, 91 405 Orsay, France.

The martian polar sandsea was wealthy described by several scientists, especially American's. In the following we aim to make a brief and preliminary statement of our certitudes and doubts in the field of Mars eolian dynamics.

1. Our positive knowledge on the Martian polar sandsea

The martian polar sandsea is mainly made up by individual barchans. These barchans belong to oblique ridges/Barchanoid ridges, or to giant Barchanoidal complexes.

On Mars and on the Earth, barchans are located on the sandsea borders from where they supply the sandsea with sands. In both cases (Mars and Earth), crescent dunes are real barchans and they indicate a permanent wind direction. Barchans do not exist under dynamical regime of changing wind directions. Under such conditions, dunes have domical and/or dihedral changing shapes.

Up to now, the best processed pictures of Mars did not allow us to observe the sharpness of the dune crests. But, one can see that barchans are well outlined and that they have horns. Such landform indicates an active dynamical regime. On the Earth, barchans would blunt and lose their horns if a changement occurred in the wind regime.

The martian barchans have the same size as terrestrial dunes. On the Earth, the distances between barchan horns range from 1 m (e.g. Erdis Basin in Northern Chad) to 1 km (Pur Pur dune in Peru). On Mars and on the Earth, asymmetrical mega barchans are observed. Their formation process is known to be longer in time than for the regular barchans. None of terrestrial sandseas of comparable dimensions, shows such homogeneity. The existence of barchans has dynamical implications :

- an active source of material (particles) ;
- a topography relatively flat or smooth ;
- a wind velocity able to insure particle transportation.

Barchan concentration in barchanoidal ridges and in transverse ridges indicate that a physical or physiographic parameter hinders the displacements of isolated barchans (assuming that the particles are permanently supplied, at the geologic time scale). According to terrestrial observations, the following parameters could exist on Mars :

- aerodynamics : a diminishing deflation rate due to a decreasing wind speed (e.g. Sahel area on Earth) ;
- topography : a decreasing displacement rate due to an upwarding slope (e.g., Oubari sandsea on Earth) ;
- topography : a decreasing displacement rate due to an upwarding slope

(e.g. Oubari sandsea on Earth).

Thus, it would indicate a slow raise of the topographic surface between 110° and 240° on Mars.

2. Questionable knowledge on the martian polar sandsea

2.1. Are the martian dune ridges transversaly or longitudinally oriented ? On Earth longitudinal dune ridges are linear, and transverse dune ridges are always sinuous. These differences are due to the different formation processes. Based on these terrestrial differences, the martian dune ridges would be transverse ridges. According to the observation done during different seasons, it appears somewhat difficult to name the martian coalescent transverse dune ridges, "reverse dunes" and to conclude that wind directions are shifting from 0 to 180°. It has been observed that illumination angle may have an important effect on the dune appearance. In addition, R. A. Bagnold demonstrated that such dunes have an asymmetrical profile which is not always the case on Mars. Except the wind direction determined from the barchan symetrical axes, none of the wind directions determined from other criteria can be taken into account. For instance the lengthening principal direction of a barchan horn does not indicate a secondary wind direction because the elongated horn works like a linear dune (sif) : it is only a track dune deposited tangentially to a turbulent area. According to our terrestrial observations, it seems that elongating horn develops transversely to secondary wind axis but not along this axis, as observed for inter transverse dune corridor which never develops along the wind directions. Finally, a grid pattern observed in a sandsea surface does not indicate several wind directions, but may be the result of two different periods of formation or changements of the sandsea surface under climatic variations (e.g. the Sahel-south Sahara area on Earth).

2.2. What does the lack of linear dunes mean on Mars ? Based on two physical criteria (size and dynamics), we sorted the terrestrial linear dunes in two main groups : sifs and sand ridges. It is probably true that the second type (sand ridges) is lacking on Mars. This implies that the martian sandseas are probably younger than the terrestrial ones. On the Earth, the sand ridges are old sandseas where the amount of outgoing materials (by deflation effect) is at least equal to the amount of incoming materials. From our point of view, the lack of observed linear dunes (sif type) does not seem to be significant because these dunes are narrow and consequently difficult to observe (they develop by lengthening but never by widening), and we also know that linear dunes may be produced by lines of barchan horns. Such process does exist on Mars. But it is known on Earth that linear dunes can appear in rough morphology areas, and/or when topographic obstacles devide the wind trend into several trends. These two factors seem unlikely existing in the martian polar sandsea.

2.3. What are the grain sizes of sandsea particles ? One knows that geographic relationships exist on Mars between the boundaries of the polar ice cap and of the sanddunes. If we can assume that glacial processes may be involved in the production of individual particles from the bedrock (by mechanical processes), it seems likely that loess size particles could be produced. But it seems unlikely that these loess particles could be deposited in the sandsea. On the contrary, they could be transported southward, as observed on the Earth in China or in Tunisia (Matmata).

NORTHERN POLAR SANDSEAS OF MARS

MAINGUET, M. et al.

We noticed on Earth that the main trend of a longitudinal dune or of a dune horn, follows the same mechanisms which are available at a continental scale. In the Saharian sandseas, barchans show a general trending of their right horns, except for the sandseas located close to the large topographic obstacles (e.g. Aïr, Tibesti...). These terrestrial observations show that sands are deposited around anticyclonic areas, inside their vortex. Such observation is also probably true around the north pole of Mars. It seems that wind are circling anticlockwise around the cyclonic areas, and that they circle clockwise around the anticyclonic areas. Around the cyclonic areas, dun es will show major left trending horns, and around the anticyclonic areas the dunes will have major right trending horns. On Mars, right trending horns are mainly observed. Such observation would indicate that hight pressure may prevail in the Northern polar sandsea of Mars.

POSSIBLE VOLCANIC ACTIVITY ON MARS DURING THE VIKING MISSION; Leonard J. Martin, Planetary Research Center, Lowell Observatory, Flagstaff, Arizona 86002.

The Viking Orbiter cameras recorded several events that may be of volcanic origin. While the available evidence is not conclusive, it is sufficiently suggestive to warrant further consideration of the possibility of ongoing volcanic activity on Mars. The probability of current volcanism has been recently mentioned by Carr (1).

Arsia Mons is widely acknowledged to be a volcanic mountain. Its caldera is the largest known, and its mass rivals Olympus Mons, with lava flows forming a gentle sloping flank that extends southward for several hundred kilometers. On August 30, 1977, an unusual small, dense cloud extended upwards from the surface within the south rift zone of Arsia Mons.

This cloud was centered directly over a small crater chain just south of upper and steeper flanks of Arsia Mons. Viking I imaging over that area during that day (revolution 439) consisted of three sequences separated by half-hour intervals. The cloud appears to have formed between the first and second sequences and then moved away between the second and third sequences. Its reality was confirmed by three overlapping frames within the second sequence. All of the frames in these sequences were made using a red filter.

The Viking images were analyzed using copies of the original digital tapes and our Grinnell image data system. By applying various stretches to the density values, we found optimum definitions of the cloud and its shadow as well as other clouds and surface features within the pictures. Within the limits of resolution, the cloud and its shadow are seen to meet at the surface, where the cloud was brightest and its shadow darkest. The brightest part of the cloud had a gradation in brightness, indicating a rapid expansion and/or change in vertical distribution. It was 6 to 7 km wide and 5 to 6 km high (based upon measurements of its shadow). The cloud also appears to have had a 60-km-long plume of near-uniform brightness extending to the northwest. What may be the same cloud, seen 30 minutes later, was then spread out and shifted to the west to a height of 20 km. During the same interval, other clouds and possibly surface dust appeared to have moved out radially from the point of the suspected eruption. This same area is often one of several foci of the dark radial streaks that are in constant change around Arsia Mons.

Dark radial streaks are seen around most of the larger Martian volcanic mountains and only rarely elsewhere. Some large volcanoes such as Hecates Tholus do not seem to ever have these streaks. I have suggested a possible correlation with these ever-shifting streaks and volcanic activity (2). The small unnamed mountain at 80°W and 16°S (north of Solis Lacus) is a rare example of changing dark radial streaks on a less prominent

POSSIBLE VOLCANIC ACTIVITY ON MARS

Martin, L. J.

feature. It also may be an area of possible volcanic activity (3).

Just beyond the southeast flank of the above nameless mountain was the location of another unusual cloud that I have suggested may have been a geyser or steam vent. It was imaged on overlapping frames of a high-resolution sequence during Orbiter 1 revolution 775. Its shadow implies a conical-shaped cloud originating on or very near the surface.

The high-resolution pictures also provide evidence that this nameless mountain is heavily dust covered--more so than the lower, surrounding terrain. I have suggested the possibility that volcanic activity on this mountain could act as a triggering mechanism to initiate dust storms (4). The similarities between the 1973 planetwide storm photographed from Earth and the early-1977 storm seen by Viking were striking (5). The distinct bright protrusion displayed by both storms which falls directly over the mountain described above may be the most significant similarity.

A computer-aided analysis of the Viking pictures (Orbiter 2, revolution 178) has revealed several aspects of this 1977 storm protrusion that may be significant. Although the clouds were dense, it is possible to identify enough topographic features within the area to determine the exact position of the mountain and its immediate surroundings. A very bright clouds extends across its west-southwest flank, from within the summit crater to the base of the mountain. This cloud is believed to have been near the surface since its configuration was at least partially dictated by the topography and, even though the cloud was dense enough to obscure everything below it, its shadow cannot be identified. The cloud was bright in both the red- and violet-filter photographs, which may suggest a combination of dust and volatiles. (Large dust storms are characteristically bright in both of these colors but only in their early stages (6).) This cloud included a much brighter spot of 5 pixels that was located just within (or close to) the summit crater's rim. Unfortunately, this bright spot can be seen on the last of eight overlapping Viking frames. Therefore, its reality cannot be confirmed, although the 5 pixels do show a gradation in density.

Some of the other clouds within these same pictures also appear to correlate with the topography of the mountain. This correlation does not dictate internal origins, but suggests that the clouds in this area were probably close to the surface. Possibly they were merely dust being blown either up or down slopes and may have not yet risen to the heights seen on most dust storm pictures. If eruptions are still going on and if they can trigger storms, certain seasonal conditions may still be required for the development of large runaway dust storms.

POSSIBLE VOLCANIC ACTIVITY ON MARS

Martin, L. J.

References

(1) Carr, M. H. (1980) *American Scientist* 68, 626-635.
(2) Martin, L. J. (1980) *EOS* 61, 1021.
(3) Martin, L. J. (1980) *Bull. Amer. Astron. Soc.* 12, 724.
(4) Ibid.
(5) Martin, L. J., and Baum, W. A. (1978) *Bull. Amer. Astron. Soc.* 10, 551.
(6) Martin, L. J. (1976) *Icarus* 29, 363-380.

MARTIAN CHANNELS Harold Masursky, A. L. Dial, Jr., and M. E. Strobell, U. S. Geological Survey, Flagstaff, AZ., 86001

Recent studies of martian surface features based on late Viking photographs, a new-shaded relief map of the Chryse basin [1] and new crater-density counts (Figs. 1,2) are elucidating the relations between channel morphology and the geologic processes that have resulted in channel formation.

More than one cause for channel formation is now recognized for channels that fringe the Chryse basin. Irregular areas of chaotic terrain may be the source areas for the water that cut the large eastern channels--Ares, Tiu, and Simud Valles. These channels may have formed when a near-surface layer of permafrost was melted by a localized heat source. When melting breeched ice dams at several topographic breaks in slope [2], floods of water escaped and carved the deep channels. Original flows were cataclysmic, and deep channels were cut at their headwaters. Kasei Vallis, which debouches into northwestern Chryse, does not rise from an area of collapsed terrain; it appears to have formed by artesian discharge released by block faulting associated with the formation of the Valles Marineris grabens. In this case, a more generalized heat source may have caused melting of the permafrost layer. Features like those associated with sheetwash or broad channel flow on Earth are recognized along the wide, upstream reach of the Kasei Vallis channel. Flow within a contained channel occurred only in a relatively small area near the channel mouth; crater density curves (Fig. 2a) show the contained channel to be younger than the broad sheetwash channel. Shalbatana and Maja Valles are transitional features; the small chaotic areas at their headwater regions probably could not have supplied all the water necessary to carve these long channels. Water for channel formation may have been accumulated from more than one source of melting, and may have collected for discharge by underground flow. More detailed studies are in progress to determine the exact relations between tectonic and geothermal processes in the Chryse basin area.

Crater-density determinations presented in earlier studies [2, 3] have shown that channel-cutting episodes spanned a long period of geologic time (Fig. 2a, b), and that volcanic episodes occurred before, during, and after the channels were cut (Fig. 2c). These relations can now be verified by photogeologic analysis of the late Viking images and by crater-counting techniques [4] that determine the ages of the channels from an idealized crater-production curve [5]. Using these new methods and the latest Viking images, at least two ages have been documented for the Chryse basin channels. The increased clarity of the images also allows us to determine more accurately the relation between channeling and volcanism; for example, the older Kasei channel predates the lava flow that overlies and obliterates part of its west bank.

An even more complex geologic history is depicted in Viking Orbiter Survey 2 photographs of Mangala Vallis. Like Kasei, Mangala Vallis appears to have originated along tectonic line; it emanated from one of the Memnonia Fossae faults and then spread in typical sheetwash style along its upper reach. Farther downstream the images elucidate at least two and possibly more periods of channel cutting; channeling events and periods of intense eolian erosion were interspersed with deposition of eolian and/or volcanic clastic material within channel stretches. The age of one branch of the channel, which is nearly filled with clastic material (Fig. 2d), has been determined as equivalent to the ages of Ares Vallis and the younger channel at Kasei. Material that once filled a small sinuous channel has

been retained as a positive, cross-cutting ridge by the removal of a less channel fill.

High-resolution photographs of small channel systems cut into the ancient cratered terrain at Arabia Terra show the upstream terminations of each branch to be theatre headed. The small channels are now thought to have formed by underflow or spring sapping of a near-surface material when precipitation on a regional scale permeated the martian regolith. Precipitation may have been in the form of snow rather than rainstorms, as previously proposed [2].

Geologic maps are being completed for both the Mangala Vallis and Chryse basin areas. These studies will allow us to determine with much greater precision the times when channels were cut, and the interrelations of channeling episodes to volcanism and tectonism on Mars.

References

[1] U. S. Geological Survey, in press, Atlas of Mars.
[2] Masursky, Harold, Boyce, J. M., Jr., Dial, A. L., Jr., Schaber, G. G. and Strobell, M. E. (1977) Jour. Geophys. Res. 82, p. 4016-4038.
[3] Masursky, Harold, Dial, A. L., Jr. and Strobell, M. E. (1980) NASA Abstract in Rept. Planet. Geol. Program, p. 184-187.
[4] Dial, A. L., Jr. and Schaber, G. G. (1981) Abstract in this volume.
[5] Neukum, G. and Hiler, K. (1980) Jour. Geophys. Res., in press.

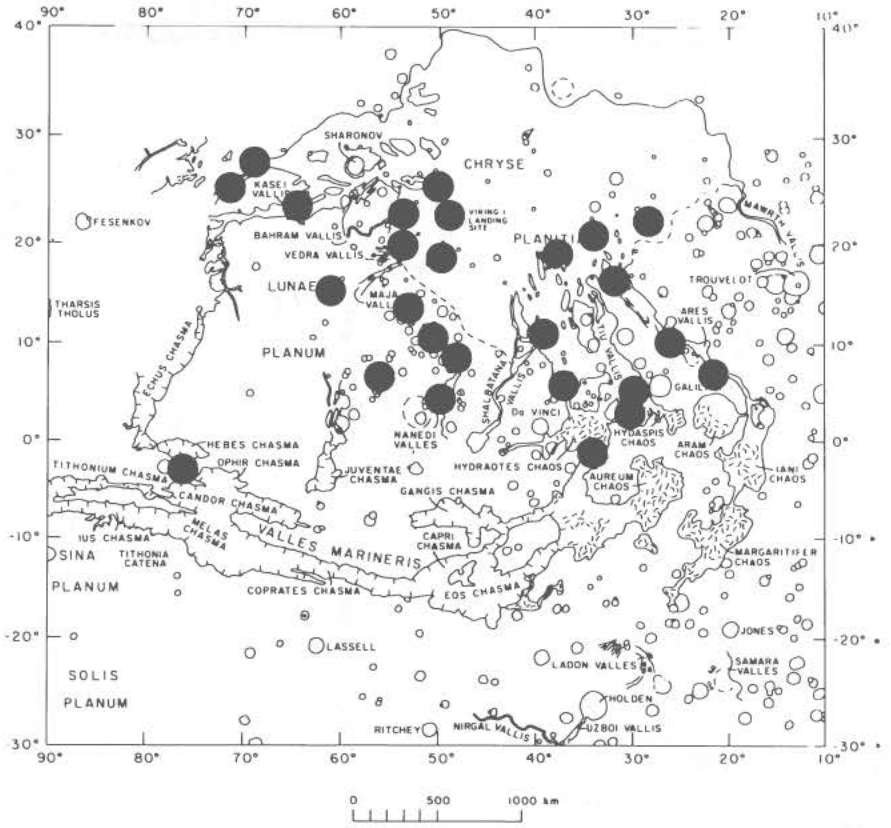

Figure 1. Sketch map of Chryse basin and surrounding areas. Circles show locations where crater density determinations have been computed.

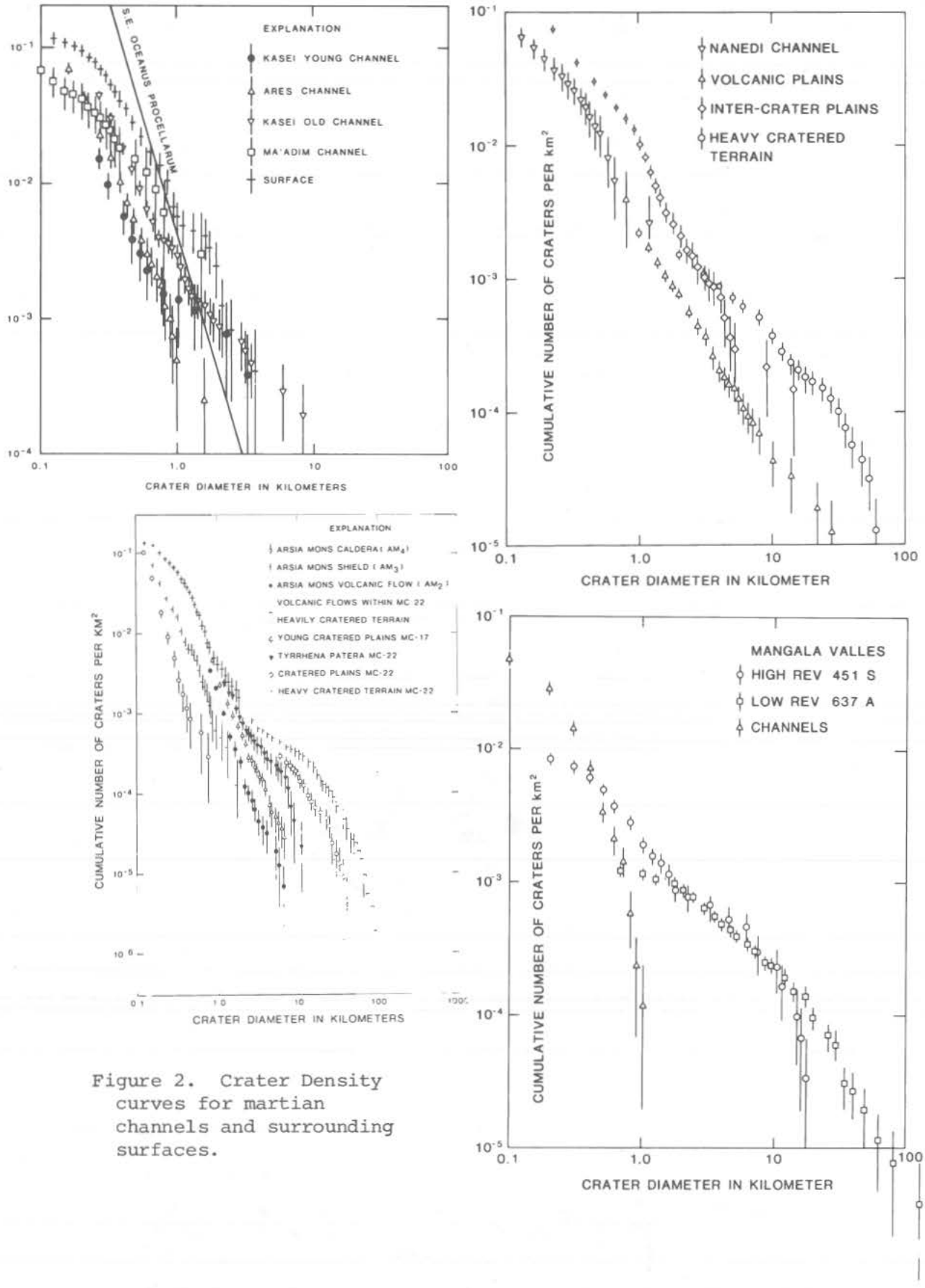

Figure 2. Crater Density curves for martian channels and surrounding surfaces.

THE INTERPLAY OF WIND WITH OTHER GEOLOGIC AGENTS ON MARS--J.F. McCauley, C.S. Breed, and M.J. Grolier, U.S. Geological Survey, Flagstaff, Arizona 86001

A new impetus was given desert studies when efforts to interpret the surface geology of Mars began with Mariner 4. In the last decade, we have studied, defined, and contrasted eolian processes and landform development in major deserts on Earth with those on Mars [1,2,3,4], while others have investigated physical constraints on the effectiveness of martian winds [5,6,7,8]. During the same period, studies of other aspects of martian surficial processes included interpretations of "fluvial" channels and valleys [9,10,11,12,13] and of possible effects of ice on Mars [14,15,16].

Viking images indicate that no single process is sufficient to explain the origin and evolution of some martian landforms. Landforms common to both Earth and Mars result from a complex interplay of geologic agents, including water, mass wasting, wind, and possibly ice. The interplay of wind with other agents on Mars, remains poorly understood; hence confusion and controversy still exist with regard to the origin of channelled, fluted, and blanketed terrain. Hypotheses for the formation and evolution of these features on Mars are based on our observations of similar landscapes resulting from the interplay of geologic agents in deserts of North Africa, Iran, Peru, and the American Southwest [1,2,4,17,18].

Observations of "fossil" drainage patterns and their relation to inselbergs and yardangs, lag gravel plains and dune fields in the hyperarid Gilf Kebir region of southwest Egypt provide a new explanation that relates the origin and evolution of the fretted terrain and northern plains on Mars to that of its north polar erg [17,18]. Inselbergs standing in groups on the plains outside the plateau in the Ismenius Lacus region appear to be remnants of divides between valleys that were continuous with the incised wadis within the plateau. Valleys between the martian inselbergs are now occupied by debris flows that may be rock glaciers [19], but this relation does not preclude initial dissection of the valleys by running water. The flow of debris is in response to, and not the cause of, initial dissection of the plateau that provided the relief required for mass wasting to begin [18]. Similar groups of hills beyond the margin of the Gilf Plateau in Egypt mark the positions of interfluves between once-vigorous, integrated streams that extended at least 100 km beyond the present plateau scarp. If the Gilf analogy is valid, then the patterns of martian inselbergs may also indicate the traces of ancient watercourses that extended beyond the present margin of the densely cratered uplands, through the fretted terrain, and onto the low northern plains.

Controversy surrounds the origin and evolution of the martian north circumpolar erg or sand sea. Dunes, which cover at least 10^6 km^2 around the ice cap, have been attributed by other workers to aggregates of dust particles carried to the polar region in suspension [20]. The north polar dunes are of the same morphologic type as most of the dunes trapped in other lowlying areas (mainly crater floors) on Mars. The barchanoid form, ubiquitous on Mars, is typical of dunes topographically trapped in many desert regions on Earth [4]. Like the dunes on Earth that they so closely resemble, the martian dunes are probably composed of resistate particles transported to depositional sites by surface creep and saltation. Lithic fragments and grains of resistant minerals on Mars can be derived from

impact, volcanism, wind erosion, and former fluvial activity. Constraints on our hypothesis of fluvial sources in the fretted terrain for the sands of the north polar erg, and the transport of these sands northward by surface winds, are 1) the lack of recognizable fluvial deposits on the plains north of the martian highlands, and 2) the general absence of north-blowing surface winds in that region under current climatic conditions, which are controlled by the presence of the north polar ice cap.

The latter constraint may be at least partially removed if past climatic conditions on Mars can be shown to differ from those of today. Climatic change could account for a cyclic presence and absence of the ice cap, a denser atmosphere, and episodic running water with erosive force sufficient to carve valleys and transport rock particles from the highlands to depositional sites on the northern plains. Given these as yet unproven climatic conditions, fluvial erosion of the highlands materials may have provided a supply of solid particles susceptible to saltation and creep by surface winds blowing toward the pole. Later, as freezing and dessication set in, running water ceased to flow, and evidence of fluvial transport and deposition on the martian plains may have been obliterated by wind action, as in southwestern Egypt, or partly buried by volcanic resurfacing. At present, the northern plains on Mars appear to be mantled with eolian dust blankets that obscure the underlying materials. In southwestern Egypt, dunes are migrating along eolian thoroughfares whose locations seem to be determined by the ancient courses of defunct master streams. If similar eolian thoroughfares for migrating sand formerly existed on Mars, they may lie buried beneath accumulations of volcanic and eolian materials on the northern plains.

On Mars, as in western Egypt, former fluvial activity has been replaced by mass-wasting and wind processes, and wind is now the dominant agent of erosion and transport. Mars apparently had at least one climatic period when conditions were very different, but the number of climatic cycles that Mars has undergone has not been determined [21]. Evidence of climate change is preserved in the landforms, such as sand seas, yardang fields, and channel networks, which record the interplay of several types of surface processes that have operated at different places under different climatic conditions. A major unanswered question is: was climate change on Mars synchronous with that on Earth?

References:

[1] Grolier, M. J., Ericksen, G. E., McCauley, J. F., and Morris, E. C. (1974) U.S. Geol. Survey Interagency Rept. Astrogeology 57, 146 p.

[2] McCauley, J. F., Grolier, M. J., and Breed, C. S. (1977) U.S. Geological Survey Interagency Rept. Astrogeology 81, 177 p.

[3] McCauley, J. F., Breed, C. S., El-Baz, F., Whitney, M. I., Grolier, M. J., and Ward, A. W. (1979) Jour. Geophys. Res., v. 84, no. B14, p. 8222-8232.

[4] Breed, C. S., Grolier, M. J., and McCauley, J. F. (1979) Jour. Geophys. Res., v. 84, no. B14, p. 8183-8204.

[5] Greeley, R., White, B., Leach, R., Iversen, J., and Pollack, J. (1976) Geophys. Res. Letters, v. 3, p. 417-420.

[6] Sagan, C., Pieri, D., Fox, P., Arvidson, R. E., and Guiness, E. A. (1977) Jour. Geophys. Res., v. 82, p. 4430-4438.

[7] Arvidson, R. E., Carlston, C., Guiness, E. A., Jones, K., Pidek, D., Sagan, C., and Wall, S. (1978) NASA Tech. Memo. 78,455, p. 3-7.
[8] Pollack, J. B. (1978) NASA Tech. Memo. 78,455, p. 40-41.
[9] Baker, V. R. and Milton, D. J. (1974) Icarus, v. 23, p. 27-41.
[10] Sharp, R. P, and Malin, M. C. (1975) Geol. Soc. America Bull., v. 86, p. 593-609.
[11] Masursky, H., Boyce, J. M., Dial, A. L., Schaber, G. G., and Strobell, M. E. (1977) Jour. Geophys. Res., v. 82, p. 4016-4038.
[12] Carr, M. H. (1979) Jour. Geophys. Res., v. 84, no. B14, p. 2995-3007.
[13] Pieri, D. (1980) Science, v. 210, p. 895-897.
[14] Sharp, R. P. (1974) Jour. Glaciology, v. 13, p. 173-185.
[15] Carr, M. H., and Schaber, G. G. (1977) Jour. Geophys. Res., v. 82, p. 4039-4054.
[16] Lucchitta, B. K., Anderson, D. M., and Shoji, H. (1981) Nature, v. 290, p. 759-763.
[17] McCauley, J. F., Breed, C. S., and Grolier, M. J. (1980) NASA Tech. Memo. 82385, p. 312-313.
[18] Breed, C. S., McCauley, J. F., Grolier, M. J. (1980) NASA Tech. Memo. 82385, p. 307-311.
[19] Squyres, S. W. (1978) Icarus, v. 34, p. 600-613.
[20] Greeley, R. (1979) Jour. Geophys. Res., v. 84, p. 6248-6254.
[21] Toon, O. B. (1979) NASA Conf. Pub. 2072, p. 84.

MARS: DEFINITION AND CHARACTERIZATION OF GLOBAL SURFACE UNITS, WITH COMPOSITIONAL EMPHASIS. T.B. McCord, R.B. Singer, B.R. Hawke, Hawaii Institute of Geophysics, University of Hawaii, Honolulu, HI 96822; J.B. Adams, D. Evans, Dept. of Geological Sciences., Univ. of Washington, Seattle, WA 96195; J.W. Head, P.J. Mouginis-Mark, C.M. Pieters, Dept. of Geological Sciences, Brown Univ., Providence, RI 02912; R.L. Huguenin, Dept. of Physics & Chemistry, Univ. of Mass., Amherst, MA 01002; S.H. Zisk, Haystack Obs., MIT, Cambridge, MA

Viking approach digital images have been used to define global surface units on Mars. A wide variety of other Viking data and groundbased telescopic spectral and albedo measurements were then used to characterize these units. This project was carried out as a consortium effort over the past several years. The Viking approach imagery data reduced to albedo were used because the albedo in the three spectral bands and the slope of the reflectance spectrum between these bands (color) are the data available most closely associated with mineralogy and which also have significant areal coverage and spatial resolution. Extremely important was the early availablility of these data in digital format. The region of Mars bounded by latitudes 30°N to 60°S and longitudes 310° to 50° was treated in which the approach data are of highest quality.

The violet and red passband data were used because these bandpasses are narrower than the green and contain more independent information. Using computer image processing techniques, the violet and red albedo values for each pixel on Mars were plotted, red-versus-violet, to form a two-dimensional histogram determining their distribution. Natural clusters of albedo values were noted and regions in the RV plot were defined as representing properties of surface units on Mars. All pixels having red and violet albedo values within each RV unit were color coded and plotted as a Mars unit map. Considerable iteration on the unit map making process was required to determine the significance of the various unit boundaries; some are clear and sharp while others are gradational. Natural distinct color units clearly exist on the surface of Mars.

All other types of data available were used to characterize these units. The telescopic reflectance spectra of regions hundreds of kilometers in diameter form the data set richest in mineralogic information. Correlations with other data, such as radar characteristics, 1.4 μm albedo, thermal inertia, topography and seasonal annual variations, were sought also. However, many of these data sets had not yet been fully calibrated and/or were unavailable in digital format.

The unit map shows two basic types of units: (1) those where rocks and soils show exclusively or at least dominate and (2) those composed of condensates. A variety of condensate units appear in the southern region and at the far north of the region mapped perhaps distinguishable by the amount of global dust entrained and by the degree to which underlying rock and soil material shows through.

A study was made to determine the effects of the Mars atmosphere, dust and condensates on the albedo and color in the Viking images. It is clear that most of the units mapped as rock and soil are largely unmodified by these effects.

Studies were made to determine which candidate Mars surface materials have optical properties which fall within the rock and soil units as defined in the unit definition diagram. Even though the Viking camera passbands were not optimized for mineralogical analysis, it was possible to make mineralogical determinations using in addition the telescopic spectra and terrestrial analogs and models. No area of fresh basalt or other rock was recognized. There is good evidence for materials like oxidized basalts and basaltic glasses with an oxidized surface or coating of two varieties: (1) amorphous ferric-oxide rich gels and/or goethitic material and (2) hemitic material indicative of primary

oxidation. Units composed of material like the global dust are present as are units which show little or no dust or condensates.

MARTIAN VOLATILE-RICH IMPACT CRATERS: A SEARCH FOR TERRESTRIAL ANALOGS

John F. McHone and Ronald Greeley, *Department of Geology, Arizona State University, Tempe, Arizona 85287*

Martian impact craters often display multilobed, flow-like ejecta deposits, a distinct morphology attributed to fluidizing by volatiles in the target or to atmospheric interaction (1–3). Analogs to these craters may exist on Earth; Earth has at least two common substances, carbonate rocks and water, which volatize under impact (4–6) and an atmosphere.

We have examined satellite images and available data for Earth impact craters (7–11) that may have involved volatile-rich targets at the time of their formation. We rejected predominately igneous and metamorphic targets, as crystalline rocks contain few volatiles and typically yield massive sheets of ponded melts, impact 'lavas' (12, 13) and tagamites (14). Forty-three craters (Table 1) were found that involve volatile-rich targets (carbonates or porous rocks).

Impact Effects in Possible Volatile-Rich Targets. Sedimentary rocks reveal at least four trends which differ from impact effects observed in crystalline rocks: 1) reduced melt production, replaced in part by suevites; 2) curtailed shock metamorphism; 3) enhanced ductile, rather than brittle, rock deformation; and 4) possible fluidized ejecta flow deposits. On Earth, impact melts formed in the presence of volatiles may be dispersed as impact 'ash' or deposited as the clay-rich, thermally altered breccia, *suevite* (5). Target porosity may retard shock metamorphic effects; in both experimental (15) and natural (16) porous-target impacts, the progressive sequence of shock effects observed in solid, homogeneous rocks (17) may not take place. Pronounced shock-wave attenuation and irregular propagation due to pore collapse and grain-edge interaction may interrupt shock-feature development. As a consequence, craters formed in porous sedimentary rocks may fail to display conventional criteria of shock history. Non-brittle rock deformation, common in impacts but best developed in sedimentary rocks, may be the result of poorly consolidated target materials. Recently buried continental shelf beds, for example, might distort into coherent folds during impact. In such an environment, ductile behavior might also be enhanced by hydrostatic confining pressures. In general, strongly contorted sediments at impact sites (e.g., Riachao, Tin Bider, Uvalde, and Wetumpka) contain only weakly developed (if any) shock indicators. Microscopic shock criteria were detected at these sites only after repeated, thorough searches. Ejecta debris, lubricated during emplacement by expanding volatiles, should show evidence of fluid flow. However, ejecta units are the impact feature most susceptible to erosion and no terrestrial crater larger than 0.5 km diameter is known with original surface morphology intact. A satellite search of known craters has revealed possible traces of multiple lobes surrounding Zhamanshin Crater in the Soviet Union (Figure 1).

Zhamanshin Crater, Kazakhstan, USSR, has recently been described in detail (18–20). A debris ring up to 11 km in diameter surrounds a 5.5 km diameter crater. Former volatiles are evidenced by suevite-like rocks and frothed 'pumices' in a 200 m sedimentary section. Topographic lobes radiate up to 5 km beyond the present debris ring. Mapped as a normal sedimentary sequence surfaced by occasional ejecta remanants, they are not true flow units. They may represent preserved "shadows" of a former resistant armor of lobate ejecta flows as has been suggested for some of the pedestal craters on Mars (21).

References

(1) Carr M. H., Crumpler L. A., Cutts J. A., Greeley R., Guest J. E., and Masursky H. (1977) *J. Geophys. Res. 82*, 4055–4065.

(2) Mouginis-Mark P. J., (1978) *Nature 272*, 691–694.

MARTIAN CRATERS: EARTH ANALOGS

McHone, John F. and Greeley, R.

TABLE 1: Confirmed and possible terrestrial impact structures with volatile-rich carbonate or porous sedimentary rocks during formation.

NAME, LOCATION	DIA Km	TARGET LITHOLOGY
VERIFIED IMPACT STRUCTURES, shock metamorphism reported.		
Araguainha, Brazil	40	Sandstones, Shales over Granitics
Barringer Crater, Arizona	1.2	Carbonates & Sandstones
Beyenchima-Salaatin, USSR	8	mostly Carbonates
B.P. Structure, Libya	2.8	Sandstones
Crooked Creek, Missouri	5.6	Carbonates & Sandstones
Decaturville, Missouri	6	Carbonates over Granitics
Flynn Creek, Tennessee	3.8	Limestones, Dolomites, Shales, Cherts
Goat Paddock, WA., Australia	5	Sandstones & Siltstones
Gosses Bluff, NT., Australia	22	Sandstones & Siltstones
Haughton Dome, NWT., Canada	20	Carbonates & Evaporites
Isle Rouleau, Quebec, Canada	4	Argillaceous Dolomite
Kaluga, USSR	15	Sandstone, Siltstones, Marl
Kamensk, USSR	25	Limestones, Sandstones, Shales, Marls
Kara, USSR	60	Carbonates & Terrigenous Sediments
Kelly West, NT., Australia	2.5	Quartzites, Cherts, Silicified Limestones
Kentland, Indiana	13	Carbonates & Sandstones
Kufra Oasis, Libya	11.5	Sandstones
Liverpool, NT., Australia	1.6	Sandstones
Manson, Iowa	32	Limestones, Sandstones over Granitics
Middlesboro, Kentucky	6	Sandstones, Conglomerates, Shales
Mishina Gora, USSR	2.5	Carbonates
Ouarkziz, Algeria	3.5	Limestones, Sandstones, Marls
Popigai, USSR	100	Sandstones, Shales, Carbonates over Gneiss
Puchezh Katunka, USSR	80	Sandstones, Shales, Carbonates over Granit
Redwing Creek, North Dakota	9	Carbonates & Evaporites
Riachao Ring, Brazil	4	Sandstones, Shales, Carbonates
Ries Basin, West Germany	24	Carbonates, Shales, Sandstones over Granit
St. Martin, Manitoba, Canada	23	Carbonates over Granite
Serpent Mound, Ohio	6.4	Carbonates & Sandstones
Serra da Cangalha, Brazil	12	Sandstones, Conglomerates, Siltstones
Sierra Madera, Texas	13	Carbonates, Shales, Sandstones
Slate Islands, Ontario, Can.	30	Basalts & Sandstones over Argillites
Spider, WA., Australia	8	Sandstones & Siltstones
Strangways, NT., Australia	24	Sandstones, Siltstones, & Shales
Steinheim, West Germany	3.4	Carbonates & Sandstones
Tin Bider, Algeria	8	Argillites, Carbonates, Sandstones
Uvalde, Texas	4	Shales & Sandstones
Wells Creek, Tennessee	14	Carbonates
Wetumpka, Alabama	6.5	Marls & Chalks over Schist
Zhamanshin, USSR	5.5	Clays, Sands, Marls over Schists & Volcs.
POSSIBLE IMPACT STRUCTURES, shock metamorphism not yet reported, highly contorted sedimentary target rocks.		
Foum Teguentour, Algeria	5	Argillites & Sandstones
Hico, Texas	10	Carbonates & Sandstones
Ramgahr, India	3	Sandstones

MARTIAN CRATERS: EARTH ANALOGS

McHone, John F. and Greeley, R.

(3) Gault D. E. and Greeley R. (1978) *Icarus 34*, 486–495.
(4) Yakovlev O. I., Parfenova O. V., and Arkhangel'skaya V. N. (1978) *Doklady Akad. NAUK SSSR 240*, 934–937. (in Russian)
(5) Kieffer S. W. and Simonds C. H. (1980) *Rev. of Geophys. and Space Sci. 18*, no. 1, 143–181.
(6) Newsom H. E. (1980) *Icarus 44*, 207–216.
(7) Monod Th. (1965) *Univ. Dakar Catalog & Doc. XVII*, 94 p.
(8) Freeburg J. H. (1969) *U. S. Geol. Surv. Bull. 1320*, 39 p.
(9) Skrynnik G. V. (1977) *Solar System Res. 11*, no. 4, 161–170.
(10) Classen J. (1977) *Meteoritics 12*, no. 1, 61–78.
(11) Grieve R. A. F. and Robertson P. B. (1979) *Icarus 38*, 212–229.
(12) Beals C. S. (1965) *Annals of N. Y. Acad. Sci. 123*, art. 2, 904–914.
(13) Dence M. R. (1971) *J. Geophys. Res. 76*, no. 23, 5552–5565.
(14) Masaytis V. L. (1976) *International Geol. Rev. 18*, no. 11, 1249–1258.
(15) Schaal R. B., Horz F., Thompson T. D., and Bauer J. F. (1978) *Proc. Lunar Sci. Conf. 10th*, 2547–2571.
(16) Robertson B. P. (1980) *Lunar and Planet. Sci. Conf. 11th*, 929–934 (abstract).
(17) Stoffler D. (1971) *J. Geophys. Res. 76*, no. 23, 5541–5551.
(18) Florensky P. V., Dabizha A. I., Aoloye A. O., Gorshkov E. S. and Miklyaev V. I. (1979) *Meteoritika 38, 86–97. (in Russian)*
(19) Bouska Vl., Florensky P. V., Randa Z., and Povondra P. (1981) *Meteoritics 15* (in press).
(20) Dabizha A. I., Florensky P. V., Vernadsky V. I., Alyuninia O. I., Alyunin A. V., and Lomonosov M. V. (1980) *Lunar and Planet. Sci. Conf. 11th*, 192–194 (abstract).
(21) McCauley J. F. (1973) *J. Geophys. Res. 78*, 4123–4137.

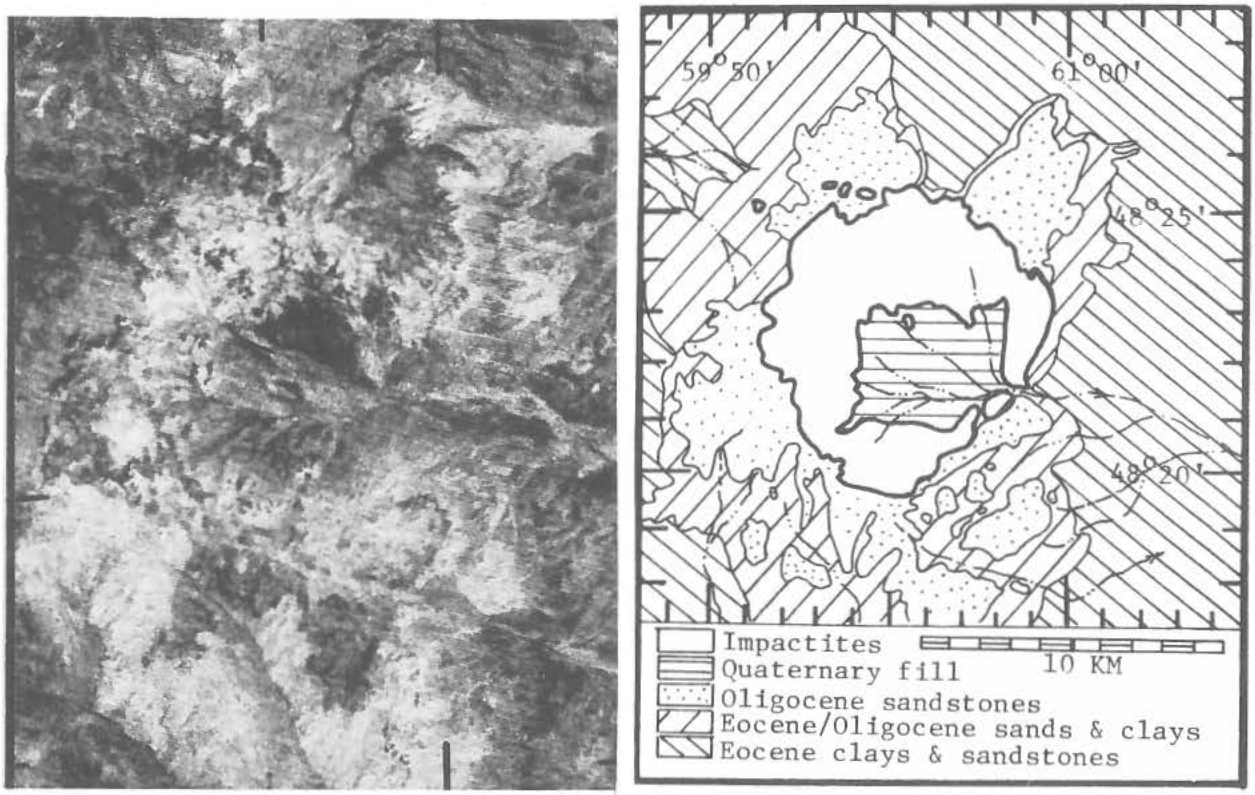

Figure 1. ZHAMANSHIN CRATER, USSR; possible analog to martian multilobed craters. (A) Lobed topographic features radiate from the 5.5 km wide central bowl on Landsat frame 2703-05585-5, 25 Dec 76. Sun elev. 12°, az. 151°. (B) Generalized geology after ref. (18). Coordinates from DMA map ONC F-5.

VARIATION IN MECHANICAL PROPERTIES OF SURFACE MATERIALS AT THE VIKING LANDING SITES, Moore, H. J., U.S. Geological Survey, Menlo Park, CA 94025, and Hutton, R. E., 1501 Palos Verde Dr., Harbor City, CA 90710.

The surface materials at the Viking Landing sites are heterogeneous. Drift material at Lander 1 is both crossbedded and crusted. Crusts with varying thickness are interlayered with weaker materials at Lander 2. The blocky materials between the rocks at Lander 1 vary in cohesion and are overlain by a veneer of drift material.

Analyses of data on the excavation of trenches in drift material using plowing theory (1) yield angles of internal friction (ϕ) between 14° and 21° (avg. 18°). When ϕ=20°, which is close to the average, two trenches yield cohesions (C) between 1,100 Pa and 2,200 Pa whereas a third trench yields C less than 800 Pa. The maximum vertical forces on footpad 2 (which penetrated drift material) inferred from landing data are compatible with forces calculated from the static bearing capacity equation for circular footings, when ϕ=20° and C=1,000-2,000 Pa assuming either general or local shear (2). However, failures of some trench walls and natural slopes suggest very low cohesions (near 5-40 Pa) when ϕ=20°. The stable slope on the left wall of the deep hole in drift material contrasts with the low cohesions because it requires that C be greater than about 100 Pa. Thus, these data require that drift material has heterogeneous mechanical properties.

The slope and relief of the tailings of disturbed drift material from the deep hole are 43° and 0.20 m and imply that C=54 Pa when ϕ=20°. The slopes and reliefs of the conical piles of drift material are 45° and 0.04 m and imply that C= 11 Pa, when ϕ=20°. If C is constrained to be a constant for all disturbed drift material, C must be very small (~1Pa) and ϕ must be large (~40°). Thus, the mechanical properties of disturbed drift material are different than undisturbed drift material.

Local planes of weakness must be present in the drift material. The natural slope failure near the leeward base of the rock, Big Joe, appears to have occurred as a planar element. Both the runout and visible parts of the exposed scarp appear to be more or less uniform in thickness; the runout appears to be 0.012-0.018 m thick, whereas the scarp is near 0.006-0.012 m high. Judging from shadows, the slope is probably near 30°. The distance from the head of the scarp to the toe of the runout is near 0.47 m. For a marginally stable slope in the absence of positive pore pressures, C = 5-16 Pa when ϕ=20° and the density (ρ) is 1,200-2,000 kg/m^3. Normal stresses across the plane of failure are in the range of 23-77 Pa and only a small fraction of the total atmospheric pressures (650-900 Pa). If atmospheric gases were trapped at the base of the failure plane, modest reductions in the pressure head at the surface caused by the wind flowing around the rock could initiate failure. If ϕ is assumed to be 45° and C=0, the positive or excess pressures at the base of the failure plane would have to reduce the normal stress to a value lower than the shear stress at the base (13-45 Pa)in order to cause failure. This requires a reduction in the pressure head at the base of the rock of only 10 to 32 Pa. A mechanism involving pore pressures in the near- surface materials might account for the initiation of martian duststorms (3,4). In the model

VARIATION IN PROPERTIES OF MATERIAL AT VIKING SITES

Moore, H. J.

above, this phenomenon would be near-surface because the overburden pressure or normal stress equals or exceeds the atmospheric pressures at depths near 0.18 m or more.

Crusty to cloddy material predominates between the rocks near Lander 2, although drift material and lumpy aggregates occur at the surface. Locally, the crusts occur as layers, 1 cm or so thick, between less cohesive materials, but in other places the crust is thicker and called "cloddy". From the plowing model, ϕ is in the range of 28°–39°. For the sample trenches in cloddy material, C varies from 800 to 5,100 Pa when $\phi=30^{\circ}$, and the successful surface- bearing test places C at 1,500-3,300 Pa for $\phi=35^{\circ}$–30°. Where the crust is thin to absent, C ranges from 200 to 1,800 Pa when ϕ is assumed to be 35° to 30°.

Angles of internal friction in the blocky material at Lander 1, despite the appearance of this material, range of 27° to 33° (average is 31°), but the cohesion varies widely. When $\phi=30^{\circ}$, C ranges from 1,800 to 5,000 Pa, from analyses of sample trenches, but for the surface bearing test C ranges from 7,900 to 9,000 Pa. For C=5,500-7,000 Pa, $\phi=30$, and ρ = 1,000-2,000 kg/m^3, the static forces on footpad 3 are compatible with the vertical forces inferred from landing data when these values are used in the static bearing capacity equation for circular footings and failure by general shear.

Other models also explain the mechanical properties of the surface materials. For example, the data on some of the trenches in drift material (ρ=1200 kg/m^3) and the forces on footpad 2 during landing could be accounted for by $\phi=10^{\circ}$ and C=3,000 Pa, or $\phi=20$ and C=1,400 Pa, or $\phi=33^{\circ}$ and C=0 Pa. Similar results are obtained for footpad 3, although the data require that higher values of C be paired with lower values of ϕ, as above, and that the drift material must come out weaker than the blocky material by the combined effects of C, ϕ, and ρ. The preferred values of C are those that are compatible with ϕ's obtained from the plowing model (1) and plausible densities. From the available data, the conclusion of markedly varying mechanical properties seems inescapable.

1. McKyes, E. and Ali, O. S., 1977, The cutting of soil by narrow blades: J. Terramechanics, v. 14, p. 43-58.
2. Terzaghi, Karl, 1948, Theoretical Soil Mechanics: John Wiley & Sons, N.Y., 509 p.
3. Fanale, F. P. and Cannon, W. A., 1979, Mars: CO_2 adsorption and capillary condensation on clays--significance for volatile storage and atmospheric history: J. Geophys. Res., v. 84, p. 8404-8414.
4. Kenny, Jeffrey, Fanale, Fraser, and Saunders, R. Stephen, 1980, Parametric study of dust fountains: Reports of Planetary Geology Program -- 1980, NASA Tech. Memo. 82385, P. 281-284.

STRUCTURE OF OLYMPUS MONS AND ITS BASAL SCARP; E. C. Morris, U.S. Geological Survey, 2255 North Gemini Drive, Flagstaff, Arizona 86001.

Olympus Mons is unique in martian vulcanism, not only with respect to its enormous size, but also because of the different kinds of vulcanism and structural features associated with it. Its complexity is exemplified by aureole deposits with a distinctive textural pattern (1), a basal scarp as much as 8 km high (2), terraced flanks (3), a flat-topped summit rising about 25 km above the surrounding plains, and a complex caldera over 80 km across offset almost 50 km north of the summit (Figs. 1 and 2.)

The flanks of Olympus Mons are covered by thin, low-viscosity lava flows (3). Flows on the lower and upper flanks differ distinctly in character. Flows on the lower flanks are typically long, narrow, and leveed; they are several hundred meters to a kilometer across and 10 to 100 km long. They streamed down the flanks, forming fine networks, and poured over the basal scarp (Fig. 3). Flows on the upper flanks and near the summit have rough, hummocky surfaces and are indistinct in places; some are stubby and a few others broad and sheetlike (Fig. 4). The lower flows are probably the youngest features on the volcano: they are fresh and pristine compared with flows on the upper flanks and summit, and they have fewer small impact craters.

Concentric terraces on the upper flanks of Olympus Mons are prominent on the east, southeast, west, and southwest flanks (Figs. 1 and 2). Terraces on the north and south flanks are not as prominent, probably due to the illumination angle. The terraces range in length from short 2- to 3-km sections to sinuous segments as long as 200 km. The segments are 20 to 50 km apart in the downslope direction. Some lava flows appear to originate at the base of the terraces.

The basal scarp of Olympus Mons, though roughly concentric, is composed of linear, concave, and convex segments. The north and northwest scarps rise more than 8 km above the basal plains (4). The southeast scarp rises about 4 km above the plains (4). The southwest, east, and northeast parts are nearly buried by young flows of Olympus Mons that stream out onto the basal plains to a distance of almost 200 km. Radial fractures break the scarp into its various segments; some fractures extend part way up the flank of the volcano. One of these fractures shows compressional features, i.e., several imbricate, steeply dipping blocks along its trace. The concentric terraces and the basal scarp are interpreted to have formed from high-angle reverse faults (terraces) and thrust faults (basal scarp) as a consequence of collapse and subsidence of Olympus Mons into its central vent or magma chamber.

References

[1] Morris, E. C. (1981) J. Geophys. Res., in press.
[2] King, J. S. and Riehle, J. R. (1974) Icarus 23, p. 300-317.
[3] Carr, M. H., Greeley, Ronald, Blasius, K. R., Guest, J. E., and Murray, J. B. (1977) J. Geophys. Res. 82, p. 3985-4015.
[4] Wu, S. S. C. (1981) Topographic map of Olympus Mons (abs.), this volume.

STRUCTURE OF OLYMPUS MONS AND ITS BASAL SCARP

Morris, E. C.

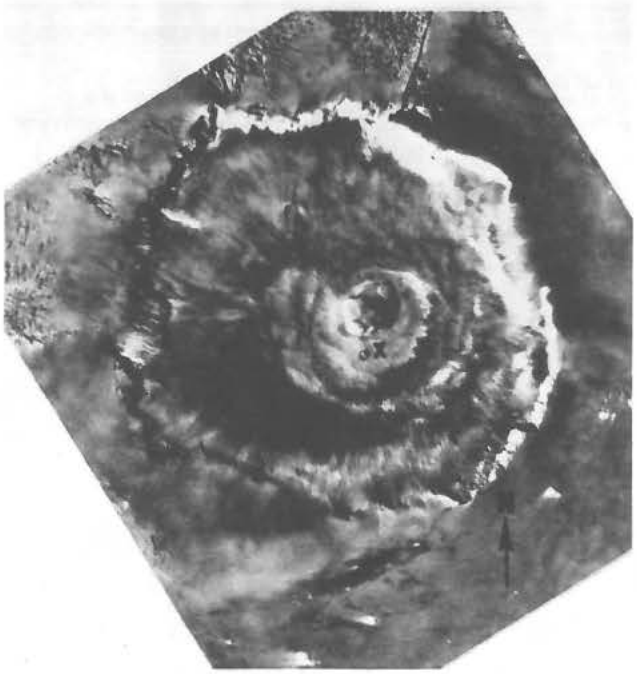

1.

Figure 1. Olympus Mons. Summit is at X, about 50 km south of the caldera. Terraces are prominent on the southeast and northwest flanks. Basal scarp is composed of several topographically dissimilar segments, some bounded by radial fractures (Viking image 646A28).

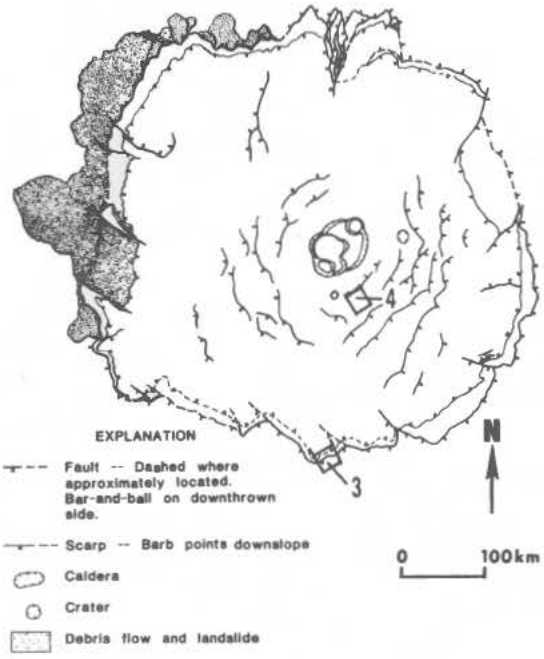

2.

Figure 2. Structure map of Olympus Mons. Terraces and basal scarp are interpreted to have formed from high-angle reverse faults and thrust faults, respectively. Location of Figures 3 and 4 are shown.

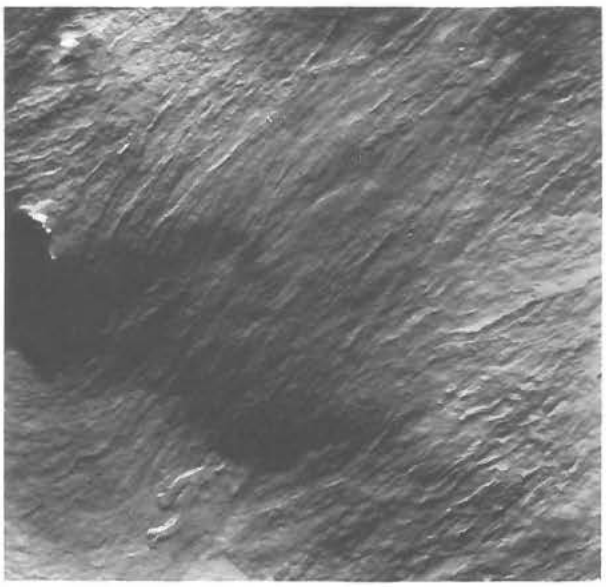

3.

Figure 3. Long, narrow, leveed flows from the lower flanks of Olympus Mons partly burying the basal scarp. Picture width approximately 46 km. (Viking image 468S35)

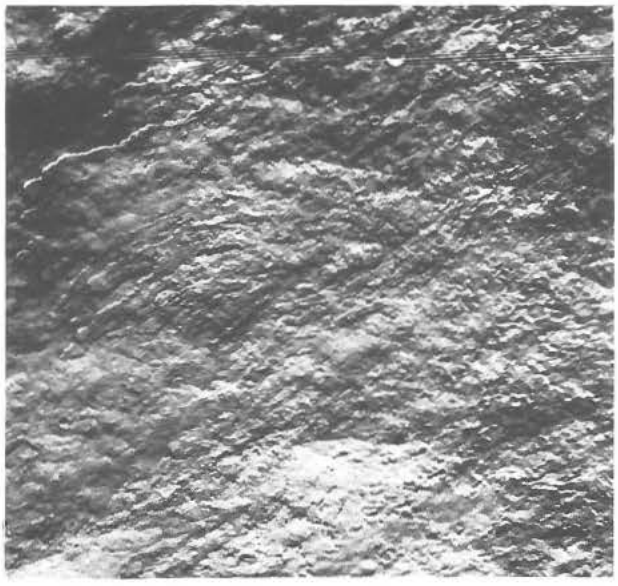

4.

Figure 4. Sheet flows, stubby, rough, and hummocky, near the summit of Olympus Mons. Picture width approximately 25 km. (Straight lines in upper part of picture are artifacts.) (Viking image 474S02)

ULTRA-VIOLET RADIATION AS A WEATHERING AGENT ON MARS: HOW IMPORTANT IS IT?

R.V. Morris, SN7, NASA Johnson Space Center, Houston, TX.

INTRODUCTION

When a planetary body has an atmosphere, the spectral distribution and intensity of radiation incident on the surface is a modification of the solar spectral distribution and intensity incident on the top of the atmosphere. The degree to which the solar radiation is modified depends primarily on the pressure and composition of the atmosphere, but other factors such as clouds and dust can also be important. On the earth with its oxygen-rich atmosphere, ozone (O_3) essentially prevents solar ultra-violet (UV) radiation having $\lambda \lesssim 0.30$ μm from reaching the surface (e.g., 1). In the case of Mars, the atmosphere is predominantly CO_2, and it virtually prevents incidence of solar UV radiation having $\lambda \lesssim 0.20$ μm (e.g., 2). Thus, on Mars as compared to the earth, UV radiation having 1.5 times as much energy is incident on the surface of the planet. This situation creates the potential for a style of weathering in which the driving force is in large part solar UV radiation.

Laboratory simulation experiments on putative Martian surface materials can be done to determine and evaluate the role of UV radiation as a weathering agent on Mars. Experiments in this area are an ongoing effort at NASA-JSC. UV photostimulated oxidation of magnetite (Fe_3O_4) and UV photodehydration of FeOOH polymorphs have been studied as potentially important processes for the surface of Mars (3,4,5). It is the purpose of this paper to review our results, compare them to previous work, and then discuss the relevance of UV radiation as a weathering agent on Mars.

EXPERIMENTAL PROCEDURES AND RESULTS

A detailed description of the experimental apparatus is given by (5). Briefly, it consisted of a high-pressure Xe arc lamp as the radiation source, a sequence of lenses and a mirror to focus the radiation on the sample, and a sample chamber in which the composition and pressure of the gas atmosphere can be controlled. A shielded thermocouple was in intimate contact with the powder samples. The spectral distribution of the incident radiation was changed by optical filters. Results discussed later are for irradiation under two optical modifications of the Xe radiation; they are denoted by Xe(A) and Xe(B), and their irradiances from 0.25 to 1.0 μm are summarized in Table 1. The gas atmosphere for the magnetite experiments was either 100 torr O_2 (relative humidity < 1%) or 250 torr air (relative humidity ∿ 45%). The FeOOH experiments were all done in 100 torr O_2 (relative humidity < 1%).

Representative results of irradiation experiments with micron to submicron powders of magnetite and of the FeOOH polymorph goethite (α-FeOOH) are shown in Figures 1 and 2, respectively, as plots of a reaction parameter versus the square root of the irradiation time. For the magnetites, $J_S(t)/J_S(0)$ is the ratio of the value of the saturation magnetization after an irradiation time t to its value at time zero; a value of 1.0 corresponds to no oxidation and a value of 0 corresponds to complete oxidation to a non-magnetic material. For the goethites, normalized $(+)H_2O(t)$ is the concentration of structural H_2O after an irradiation time t normalized to the initial value; a value of 1.0 corresponds to no dehydration and a value of 0 to complete dehydration. For irradiation under Xe(A), nearly complete oxidation and dehydration are observed for the magnetites and the goethites, respectively. It is reasonable to attribute the oxidation and dehydration entirely to thermal processes due to radiant heating of the samples, since the thermocouple measured a temperature of about 540°C, a temperature higher than both the thermal oxidation threshold of

magnetite (6) and the thermal dehydration threshold of the goethites (4,5). However, UV-induced processes could still be occurring but are masked in this case by kinetically more rapid thermal processes.

For irradiation under Xe(B), the thermocouple temperature was $\sim$ 60-80°C so that radiant heating was dramatically reduced. The data shown in Figures 1 and 2 show that the amount of oxidation or dehydration was also dramatically reduced. In fact, neither perceptible oxidation nor perceptible dehydration was observed within experimental error. Therefore, it can be concluded that under Xe(B), and also Xe(A), no perceptible UV photostimulated oxidation of magnetite and no perceptible UV photodehydration of goethite occurred during the $\sim$ 400 hour time scale of the experiments.

COMPARISON TO PREVIOUS WORK

The results given above corroborate neither the effect reported by (7,8) that magnetite undergoes UV photostimulated oxidation nor the effect reported by (9) that goethite undergoes efficient UV photodehydration. Their results are similar to those discussed above employing Xe(A) radiation. In this regard, temperature measurements made under conditions of radiant heating cannot be used unambiguously as criteria for the absence of a particular thermally-induced process (3,5). These observations suggest that the effects they reported were thermally stimulated by radiant heating rather than UV photostimulated.

UV RADIATION: A WEATHERING AGENT ON MARS?

To summarize the laboratory studies, no perceptible UV photostimulated oxidation of magnetite and no perceptible UV photodehydration of goethite were observed. However, the possibility that the processes actually occur cannot be totally eliminated because the time scale for the experiments (max. $\sim$ 400 hrs.) under Xe(B) may not have been long enough to exceed their observational thresholds. Thus, in order to address the question of the extent to which UV radiation might be a weathering agent on Mars, it is necessary to scale the laboratory results to levels of UV illumination appropriate for the Martian surface. (5) calculated that in the UV the longest irradiation time under Xe(B) corresponds to 10-100 year irradiation at the Martian spectral irradiance.

In conclusion, there is as yet no basis in laboratory experiments for inferring that UV radiation is an effective weathering agent on Mars on a time scale of at least 10-100 years for the processes of UV photostimulated oxidation of magnetite and UV photodehydration of FeOOH polymorphs. The time required for these processes to occur on Mars may be considerably longer. However, the experimental data do not preclude the possibility that the UV-induced processes are so slow that they have essentially not occurred on Mars throughout its entire geologic history.

Table 1. Irradiances from 0.25 to 1.0 μm for Xe(A) radiation, Xe(B) radiation, and 1.5 AU (the orbit of Mars) solar radiation.

Radiation	Irradiance (W/cm^2)		
	Near-UV 0.25 to 0.40 μm	Visible 0.40 to 0.70 μm	Near-IR 0.70 to 1.0 μm
Xe(A)	1.68	5.80	6.56
Xe(B)	0.77	0.080	0.30
Solar, 1.5 AU	0.0054	0.025	0.017

ULTRA-VIOLET RADIATION AS A WEATHERING AGENT ON MARS

Morris, R. V.

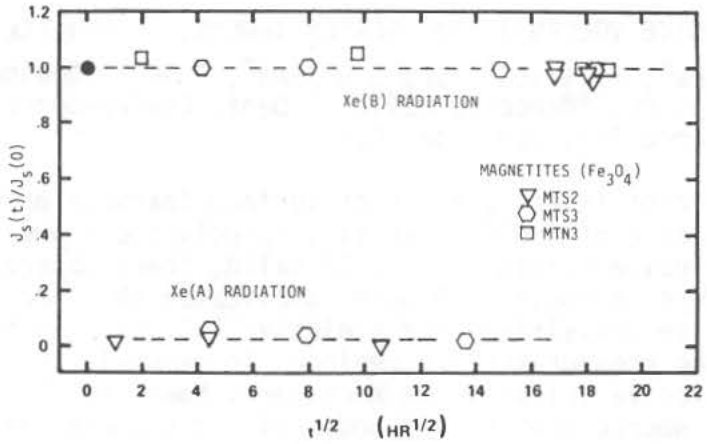

Figure 1. $J_S(t)/J_S(0)$ versus $t^{\frac{1}{2}}$ for magnetites MTS2, MTS3, and MTN3. Data from (3).

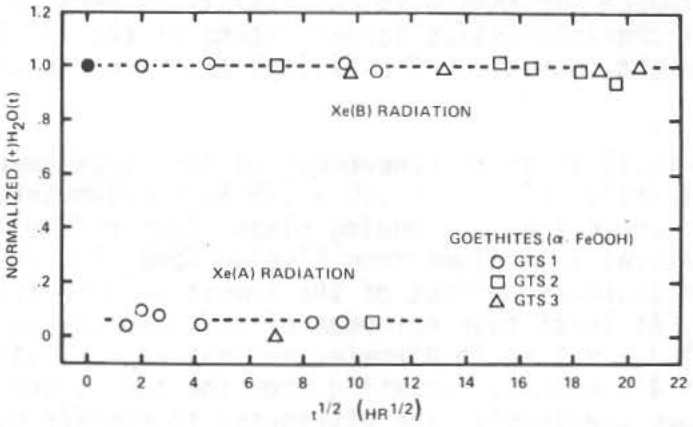

Figure 2. Normalized (+)$H_2O(t)$ versus $t^{\frac{1}{2}}$ for goethites GTS1, GTS2, and GTS3. Data from (4) and (5).

References:

1. Thekaekara M.P. (1965) NASA SP-74.
2. Kuhn W.R. and Atreya S.K. (1979) J. Mol. Evol. 14, 57-64.
3. Morris R.V. and Lauer H.V., Jr. (1980) Geophys. Res. Lett. 7, 605-608.
4. Morris R.V. and Lauer H.V., Jr. (1981) In Lunar and Planetary Science XII, 720-722.
5. Morris R.V. and Lauer H.V., Jr. (1981) Submitted.
6. Hancock K.R. (1975) In Industrial Minerals and Rocks, 4th ed., AIMMPE, 335-357.
7. Huguenin R.L. (1973) J. Geophys. Res. 78, 8481-8493.
8. Huguenin R.L. (1974) J. Geophys. Res. 79, 3895-3905.
9. Andersen K.L. and Huguenin R.L. (1977) BAAS 9, 449.

EXPLOSIVE VOLCANISM ON HECATES THOLUS, I: SURFACE MORPHOLOGY

P.J.Mouginis-Mark*, L.Wilson*+ and J.W.Head*. * Dept. Geological Sciences, Brown University, Providence RI 02912. + Dept. Environmental Sciences, University of Lancaster, Lancaster U.K.

Introduction: Recent investigations of surface features on Mars have hypothesized the existence of ignimbrites (1), pyroclastic flows (2,3) and other products of explosive volcanism (4). If valid, these observations would indicate that Mars is chemically more complicated than previously believed, with both effusive (basaltic?) and explosive (silicic?) activity responsible for producing the present surface geology. In general, the hypothesized examples of explosive volcanism on Mars were, however, old eroded features (1-3), with the source regions and modes of emplacement unidentified.

We have reexamined the Viking Orbiter images of Hecates Tholus (32°N, 209°), and believe that an excellent example of well-preserved explosive (plinian) activity exists close to the summit. As described below, our evidence differs from that given by Reimers and Komar (4), who also believed that Hecates had experienced explosive eruptions. Here we describe our morphological evidence for this plinian activity on Hecates, while the inferred eruption characteristics (areal extent of the air-fall, vent size, eruption cloud height, duration of activity) are given in our companion abstract (5).

Hecates Tholus (Fig.1) is the northernmost of the three main volcanic centers within Elysium Planitia (6). It is 160 x 175 km in diameter, and is estimated (6) to rise ~6 km above the surrounding plain. Part of the southern flanks are covered by lateral lava flows from Elysium Mons (7), which have produced an apparent 30 km southward offset of the summit caldera from the preserved center of figure. At least four episodes of collapse characterize the caldera, which measures 11.3 x 9.1 km in diameter and has an estimated (from shadow lengths) depth of 470 meters. Radiating from the summit are numerous sinuous channels which have previously been attributed to erosion by volcanic density currents (4), but which we consider below to be fluvial in origin and only indirectly related to the explosive eruptions.

Evidence for Explosive Eruptions: Two features exist which lead us to conclude that Hecates Tholus once experienced explosive activity:

1) Examination of the area immediately to the west of the summit caldera (Fig.1) indicates that there is a marked absence of all small (<2 km) craters and channels at this location. A map showing the number distribution of all the craters on Hecates (Fig.2) reveals that an area 30 x 45 km in size to the west of the caldera has less than 10 craters per 250 km^2, while typical values for the flanks range from 50-100. Such an asymmetry is also apparent in the distribution of sinuous channels (Fig.3). The lack of any recognizable flow fronts, the partial burial of the few craters within this western area, and the shape of the crater-free region, strongly suggest that this part of Hecates has not been resurfaced by recent lava flows. In contrast, the similarity of this feature to the areal distribution of terrestrial air-fall deposits (8) and its mantled appearance lead us to believe that this area does indeed represent a martian ash deposit.

2) Numerous radial striations transect the dendritic channels on the southwest flank of the volcano. These striae are very faint features, are seen at distances of 30-75 km from the caldera, and are spaced ~1-2 km apart.

EXPLOSIVE VOLCANISM

Mouginis-Mark, P. J. et al.

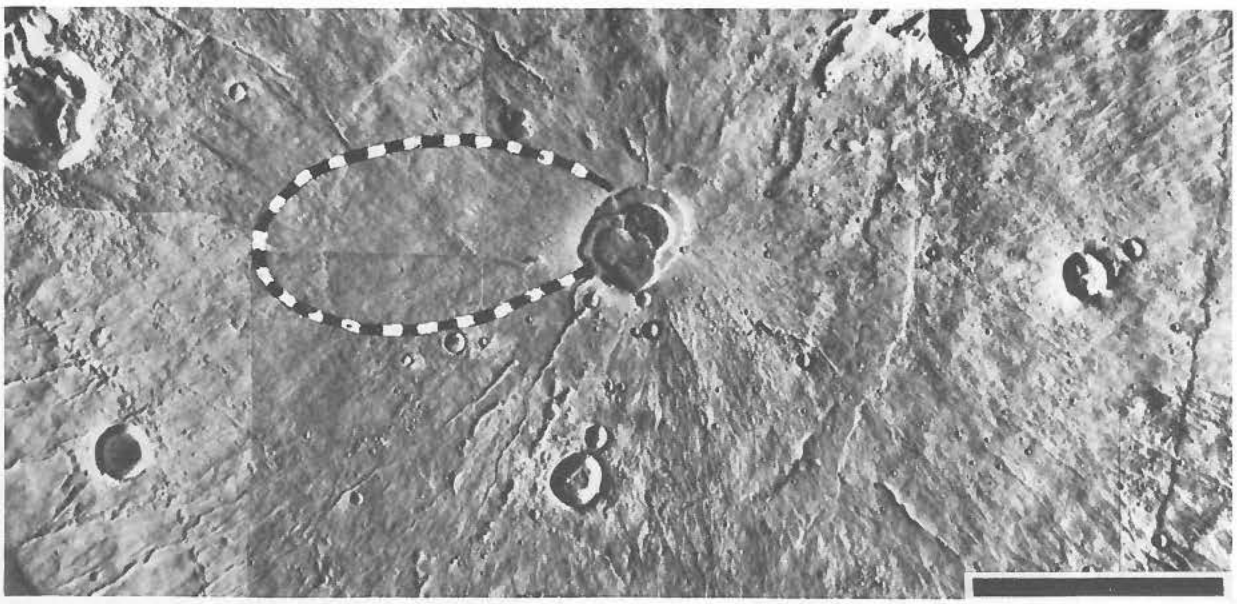

Fig.1: Photomosaic of Hecates Tholus, showing nested summit caldera, and the asymmetry in the small crater and channel distributions. Outlined area is interpreted to be the air-fall deposit, while the radial striae are found on the SW (lower left) flank. Scale bar is 25 km. Viking images 651A17-21.

We believe that a possible mode of formation for these striae is that they, rather than the channels, were created by eruption cloud collapse and subsequent scouring by pyroclastic flows during an explosive eruption.

Sinuous Channel Origin: Reimers and Komar (4) proposed that these channels (Fig.3) were created by volcanic density currents. Although we too believe that Hecates experienced explosive activity, we favor a fluvial mode of formation for these channels for the following reasons:

1) Many channels have dendritic patterns (Figs.3,4), with individual examples coalescing with increasing distance from the summit. Such an attribute is uncharacteristic of terrestrial pyroclastic channels (9,10), but resembles the immature fluvial drainage systems recognized elsewhere on Mars (11).

2) Partial burial of earlier channels would be expected during subsequent pyroclastic activity, but all the channels show the same degree of preservation.

3) Local topography has controlled the meandering channels (Fig.4). Although terrestrial pyroclastic flows may be directed by vent asymmetries (10), once mobile such flows are unaffected by local obstacles (12). This

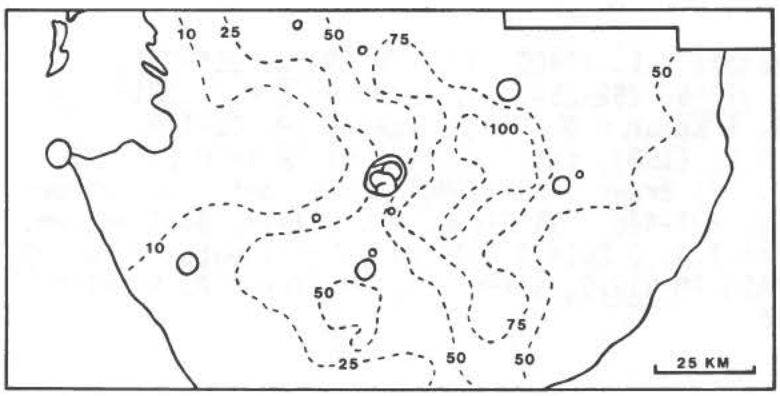

Fig.2: Isofrequency map of all craters <2 km dia. on Hecates Tholus, showing a paucity of craters to the west of the caldera. Contours are in number of craters per 250 km^2. Map prepared from Viking images 651A15-23.

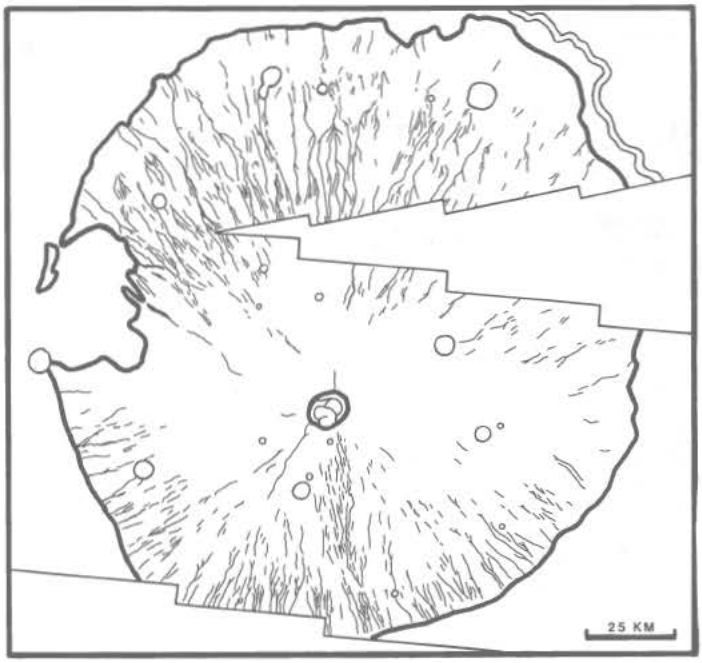

Fig.3 (left): Distribution of sinuous channels on Hecates Tholus, mapped from Viking frames 651A15-23 and 86A38-46. Fig.4 (right): The dendritic character of the sinuous channels are shown in this image. Direction of flow is from bottom to top of image. Scale bar is 10 km. Viking frame 86A42.

implies that the martian channels were created by a less energetic process than explosive volcanism, with fluvial erosion a prime candidate.

Notwithstanding the fluvial origin for the sinuous channels, they may still corroborate explosive activity on Hecates. Few martian volcanoes possess such channels (4), so that their existence on Hecates must indicate atypical conditions at this location. One possible explanation is that the channels were able to form due to an easily erodable ash deposit existing on the volcano flanks, while for example, Olympus Mons lacks fluvial channels because its flanks are made of resistant lava flows. Alternatively, more volatiles may have been released during explosive eruptions on Mars compared to effusive activity, causing greater erosion at Hecates. In either case, however, the existence of fluvial channels is consistent with the explosive history and air-fall deposits hypothesized here. We therefore feel that for the first time, a good well-preserved example of explosive volcanism on Mars has been found, and in our companion abstract (5) we consider the characteristics of this activity.

References: 1) Scott D.H. & Tanaka K.L. (1980) NASA-TM 82385, 255-257. 2) Morris E.C. (1980) NASA-TM 82385, 252-254. 3) Peterson C.M. (1981) LPS XII, 828-830. 4) Reimers C.E. & Komar P.D. (1979) Icarus 39, 88-110. 5) Wilson L. & Mouginis-Mark P.J. (1981) this volume. 6) Malin M.C. (1977) Geol.Soc.Am.Bull. 88, 908-919. 7) Brown S.H. (1980) unpub. data. 8) Walker G.P.L. (1973) Geol.Rundsch. 62, 431-446. 9) Fisher R.V. (1977) Geol.Soc.Am. Bull. 88, 1287-1297. 10) Nairn I.A. & Self S. (1978) J.Volc.Geotherm.Res. 3, 39-60. 11) Pieri D. (1980) NASA-TM 81979, 1.160. 12) Miller T.P. & Smith R.L. (1977) Geology 5, 173-176.

TERRAIN ANALYSIS OF MARS FROM EARTH-BASED RADAR

P.J.Mouginis-Mark, Dept. Geological Sciences, Brown University, Providence RI 02912; and S.H.Zisk, NEROC Haystack Observatory, Westford MA 01886

Introduction: The 1971 and 1973 Goldstone Mars radar data (1) have been employed for a wide variety of investigations of the planet's surface, including topography (2), the correlation of radar returns with Viking Orbiter images (3,4), and attempts to recognize radar-definable surface units (5). With the advent of comparable radar data for Venus (6,7), but the absence of accompanying images, understanding the radar properties of Mars as they relate to geological processes and landforms is consequently becoming increasingly important. Not only can a wider appreciation of Mars be achieved in this way, but also the developed techniques are directly applicable to the analysis of Venus. As part of our continuing attempts to characterize Mars using radar data (4,5,8), we present here some initial results obtained by applying terrain analysis techniques to radar-derived estimates of the altimetry, roughness (C-factor) and regional slope (skew) of the surface.

Terrain Analysis Techniques: A number of radar studies of Mars have utilized probability density functions of slopes (1,9), topography (2) and reflectivity (10) to describe the general surface characteristics. In each case, these probability functions gave the number (or percentage) distribution of sample elements with specific rms slope (via Hagfors' C-factor; ref.11), altimetry or reflectivity values. The Goldstone data have also been employed to generate martian hypsographic curves (8) at a much larger scale than previously attempted (12). Several other techniques also exist, however, which have not been applied simultaneously to Mars before, but which provide information on the surface characteristics at varying scales:

1) Autocorrelation (13,14) of altimetry values from individual radar profiles has the capability of detecting periodicities in elevation along the groundtrack. Together with the altimetry probability density function, autocorrelation gives an estimate of possible systematic trends in elevation on a scale of two or more radar resolution cells (i.e., > 20km).

2) Estimates of large-scale slopes (skew) within the radar data can be recognized as an asymmetry in the echo spectrum (15). Skew gives a value for the surface slope over the entire radar resolution cell (~10km).

3) Hagfors' (11) C-factor analysis of echo spectra shapes generates estimates of rms surface slopes by best-fitting theoretical models for Gaussian surfaces of known roughness to the returned radar spectra. This technique provides information on surface slopes at a scale of 0.1-10 meters, although certain limitations are inherent within this technique (9), which artificially eliminates slopes greater than 5^{o}.

Used independantly, terrain analysis techniques provide useful information on surface slope distributions, but do not uniquely describe each surface material. Cluster analysis of different radar properties (5) has, however, proven a useful method for recognizing pairings of radar reflectivity and C-factor. Here we extend this technique to investigate the possible correlations between different slope estimates for the same materials on Mars. As examples, we use four widespread surface units on Mars (cratered plateau material, ridged plains material, hilly and cratered material, and recent lava flows south of Arsia Mons; ref.16), plus Valles Marineris as an area with large-scale relief.

TERRAIN ANALYSIS OF MARS

Mouginis-Mark, P. J. and Zisk, S. H.

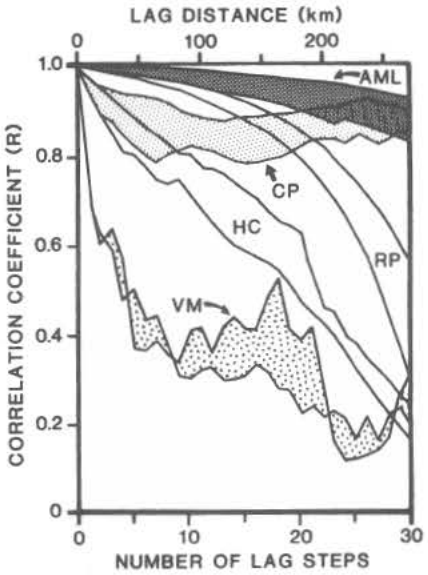

Fig.1: Autocorrelation functions for surface units considered in the text. Data are for: Arsia Mons lavas (AML) at latitudes 19.83-21.20°S, 115-130°W; Cratered plateau material (CP) at 16.20-18.25°S, 350-5°W; Ridged plains materials (RP) at 16.30-21.19°S, 65-80°W; Hilly and cratered material (HC) at 14.90-16.07°S, 165-180°W; and Valles Marineris (VM) at 15.21-16.70°S, 42.5-52.5°W. All curves are generated with 94 data points separated at 10 km intervals, except for the Valles Marineris curves, which used 62 data points. Subsequent figures use the same longitude intervals used here, with data divided into individual latitudes.

Data Analysis: Autocorrelation curves have been compiled for each of the five surface units (Fig.1). Radar profiles extending for 15° of longitude, with lag steps ranging from 1-30 sample points (∿10-290 km) were used. Because of the autocorrelation technique (13) it is not possible to distinguish between flat surfaces and slopes with a uniform gradient, or to uniquely assign a single numerical value to the randomness of the topography. Used in conjunction with the probability density functions for elevation, however, characteristic values for the systematic regional topographic randomness can be approximated by taking the value of N (number of lag steps; Fig.1) which corresponds to a correlation coefficient (R; Fig.1) of 0.75. Small-scale topographic variations can also be distinguished from regional slopes by investigating the range of height values within the probability functions. Here we have chosen a single value corresponding to the height difference between the 90% and 10% values for each sample. Each radar profile consequently allows a pairing of N vs. 90-10% height to be derived (Fig.2). In a similar manner, estimates of surface topography can be obtained from the skew and rms slope values. From our derived probability density functions of radar skew and rms slope, we have calculated individual pairings of 50% skew vs. 50% rms slope (Fig.3).

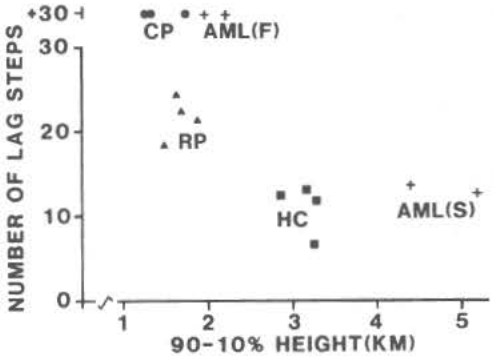

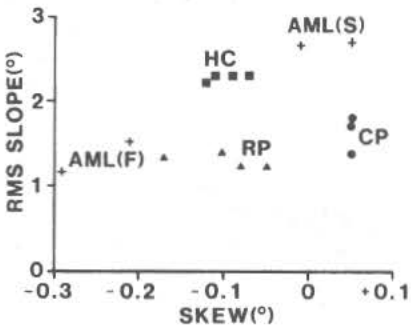

Fig.2(left): Cluster diagram of lag steps (N) at which autocorrelation = 0.75 vs. 90-10% height. AML(F) and AML(S) are Arsia Mons lavas on the flanks and summit respectively. Fig.3(right): Cluster diagram of 50% rms slope vs. 50% skew values. Data sets are same as those employed in Fig.1.

TERRAIN ANALYSIS OF MARS

Mouginis-Mark, P. J. and Zisk, S. H.

Summary of Observations: From an inspection of the two derived cluster diagrams (Figs.2 and 3), it is immediately apparent that specific pairings of slopes characterize different terrain types. Several observations relating to these properties of the surface can be made:

1) Cratered plateau material (350-5°W): This material is very flat on a regional scale, with very few random variations in elevation detected by autocorrelation (Fig.1). At both the 10km and 10 meter scale, this material is also very smooth, with a total relief of ∿1.5 km and a rms slope of ∿0.05°.

2) Ridged plains material (65-80°W): Although possessing a comparable amount of total relief as the cratered plateau material, the ridged plains have more random surface slopes at a scale larger than 10 km. Skew slopes are ∿0.05° and rms slopes are also comparable to the cratered plateau.

3) Hilly and cratered material (165-180°): Large-scale relief within this material is demonstrated by the low value of N (lag steps) and the 90-10% height (Fig.2). As recognized from our previous hypsometric analysis (8), many large craters exist within this material and are probably responsible for the random nature of the relief. Skew values for 10 km slopes indicate that there is no systematic distribution of surfaces consistent with, for example, large sand dunes (14) or fault blocks (17). The rugged nature of the topography is corroborated by the rms slopes, which are greater than 2°.

4) Arsia Mons lavas (115-130°W): As previously recognized (18) a marked difference in the radar properties exists between the summit and flank lava flows on this volcano. Summit flows appear to have very irregular slopes and (due to the relief of the volcano) a large 90-10% height value. Skew slopes are almost flat, while rms slopes are very high (∿2.5°). In contrast, flank lava flows have little random relief (N>30) and 90-10% height is ∿2 km. Skew values are the highest (0.3°) that are found in this analysis, while rms slopes are comparable to the ridged plains materials.

5) Valles Marineris (42.5-52.5°W): Although the canyon dissects ridged plains materials (16), the autocorrelation characteristics are dominated by the large-scale topography (Fig.1). In comparison to the other surface units, Valles Marineris has highly irregular relief, with a value for N of less than 2. Because topography of this magnitude effectively controls the other radar parameters, additional data for the canyon are not presented.

References: 1) Downs G.S. et al. (1975) Icarus 26, 273-312. 2) Roth L.E. et al. (1980) Icarus 42, 287-316. 3) Schaber G.G. (1980) Icarus 42, 159-184. 4) Mouginis-Mark P.J. et al. (1980) PLPSC 11th, 823-838. 5) Zisk S.H. and Mouginis-Mark P.J. (1981) LPS XII, 1236-1238. 6) Pettengill G.H. et al. (1979) Science 205, 90-93. 7) Masursky H. et al. (1980) J.Geophys.Res. 85, 8232-8260. 8) Mouginis-Mark P.J. and Zisk S.H. (1981) LPS XII, 735-737. 9) Simpson R.A. et al. (1977) Icarus 32, 147-167. 10) Zisk S.H. and Mouginis-Mark P.J. (1980) Nature 288, 735-738. 11) Hagfors T. (1964) J. Geophys.Res. 69, 3779-3784. 12) Coradini M. et al. (1980) The Moon and Planets 22, 201-210. 13) Pike R.J. and Rozema W.J. (1975) Ann.Assoc.Amer. Geog. 65, 499-516. 14) Craig R.G. et al. (1980) NASA-TM 82385, 319-321. 15) Simpson R.A. et al. (1980) J.Geophys.Res. 85, 6610-6614. 16) Scott D.H. and Carr M.H. (1978) USGS Map I-1083. 17) Plescia J.B. et al. (1980) NASA-TM 81776, 68-70. 18) Mouginis-Mark P.J. and Zisk S.H. (1980) LPS XI, 771-773.

The Seasonal Behavior of The Martian Polar Caps: A Model Calculation

Yasunori Narumi
Kyushu-Tokai University,Kumamoto,862 Japan

Very significant information about the polar cap on Mars provided by the pressure sensors in the meteorology package on the two Viking landers. By monitoring the atmospheric pressure throughout more than one Martian year, they measured the variation of the quantity of CO_2 in the caps (Hess et al.,1977,1979; Ryan et al.,1978; Snyder,1979). We developed a polar cap model which incorporated the heating effect of the polar hood cloud in order to match the seasonal variation of the atmospheric pressure, as well as the observed retreat of the north and south polar caps (Narumi,1979,1980).

Fig.1(a) shows the latitude dependence of the edge of polar caps as a function of the areocentric longitude of the Sun,Ls. The dashed lines are the observed regression curves of the north polar cap (Dollfus,1973; Iwasaki et al.,1979), and of the south polar cap (Fishbacher et al.,1969). These telescopic data are in good agreement with the Viking observations of the retreat of both caps (James,1979; James et al.,1979). The solid curves are the model results of the edge of CO_2 frost deposit (defined here as 3 gm/cm^2). Fig.1(b) shows the total amount of CO_2 deposited on the surface of each hemisphere, and the expected variation in the total atmospheric pressure. In Fig.1(b) the measurements by the Viking landers are moved in parallel with the vertical axis

THE MARTIAN POLAR CAPS

Narumi Y.

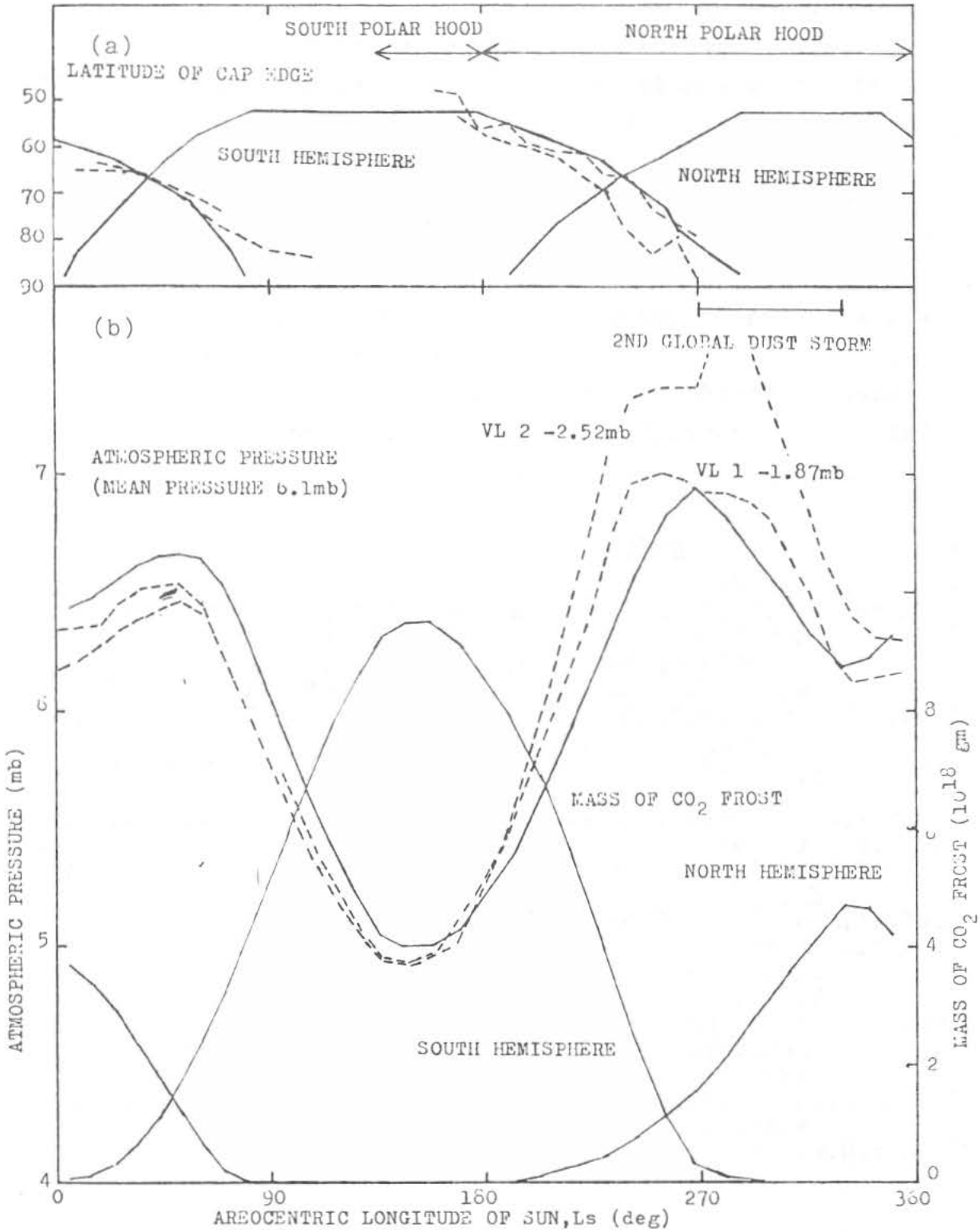

Fig.1(a) The seasonal behavior of the north and south polar caps.
(b) Total amount of CO_2 deposited on the surface of each hemisphere and the expected variation in the total atmospheric pressure.

THE MARTIAN POLAR CAPS

Narumi, Y.

for conveniance of comparison with the model results.

The effect of blocking out for insolation by dust has been examined with the model adopting the Martian atmospheric optical depth, τ =0.3 for the insolation during the 2nd global storm in 1977 (Ls=270°-330°). During this period the surface temperature should be reduced because of the depleted insolation especially in the polar regions. The model results show that in the south polar region the carbon dioxide ice survives untill the southern mid-summer. The observations of the Viking infrared thermal mapper revealed that the southern residual cap in 1977 was probably carbon dioxide ice (Kieffer,1979). It may be possible to explain this observation with the model which includes the atmospheric effects due to dust precisely.

References

Dollfus,A.(1973) Icarus,18,142

Fiscbacher,G.E.,Martin,L.J.,and Baum,W.A.(1969) Final Report, Part A under Contract No.951547 to the Jet Propulsion Laboratory, Pasadena, California, Planetary Research Center, Lowell Obs. Flagstaff, Arizona

Hess,S.L.,Henry,R.M.,Leovy,C.B.,Ryan,J.A.,and Tillman,J.E.(1977) J.Geophys.Res.,82,4559

Hess,S.L.,Henry,R.M.,and Tillman,J.E.(1979) J.Geophys.Res. 84,2923

Iwasaki,K.,Saito,Y.,and Akabane,T.(1979) J.Geophys.Res.,84,8311

James,P.B.(1979) J.Geophys.Res.,84,8332

James,P.B.,Briggs,G.,Barnes,J.,and Spruck,A.(1979) J.Geophys.Res. 84,2889

Kieffer,H.H.(1979) J.Geophys.Res.,84,8263

Narumi,Y.(1979) Proceedings of 12th Lunar and Planetary Symposium Institute of Space and Aeronautical Science, Univ.of Tokyo,234

Narumi,Y.(1980) Proceedings of 13th Lunar and Planetary Symposium Institute of Space and Aeronautical Science, Univ.of Tokyo,31

Ryan,J.A.,Henry,R.M.,Hess,S.L.,Leovy,C.B.,Tillman,J.E.,and Walec,C.(1978) Geophys.Res.Letters,5,715

Snyder,C.W.(1979) J.Geophys.Res.,84,8487

BAND-PASS FILTERING OF ONE YEAR OF DAILY MEAN PRESSURES ON MARS. D.S. Niver, Computer Sciences Corp. and S.L. Hess, Florida State University.

The daily mean pressures compiled in (1) at Viking lander 1 and 2 return almost exactly to the values observed one martian year earlier in late summer. This allows us to treat one year of such data as if they were a truly periodic set. This, in turn permits us to design a set of sharp, numerical, band-pass filters and to produce several time series showing the pressure oscillations within each frequency band. The bands isolated were:

Range of Periods (sols)	Filter Designation
Annual mean - 44.53	Seasonal Waves
44.53 - 22.27	Very Long Waves
22.27 - 11.13	Long Waves
11.13 - 6.07	Moderate Waves
6.07 - 4.00	Short Waves
4.00 - 2.00	Very Short Waves

These time series are highly non-stationary, showing variations in amplitude (and phase) with time. Several intervals can be identified in which the wave properties can be seen easily in these series but in which spectral analysis would fail because only a few cycles appear before there is a large change of amplitude and/or phase.

The most significant results are:

(A) Very short waves are a prominent feature at both landers during the cold season from $L_s \approx 180°$ to $L_s \approx 10°$, with the exception of an interval of some 50 sols during the second dust storm.

(B) A sharp decrease in amplitude of very short waves beginning near $L_s = 270°$ at both landers. This is the period of the second global dust storm. We suggest that this is the result of increased static stability in a dusty atmosphere. Theoretically, a large static stability suppresses baroclinic instability in waves of short length.

(C) An interval of large amplitude of very long waves and of long waves before and during the early part of the second global dust storm. This cannot be caused by the dust storm because it appears before the dust. These waves are not identifiable by spectral analysis.

(D) Large amplitudes of moderate waves prior to and near $L_s = 0°$ at lander 2. This phenomenon has a period close to 8 sols , is statistically significant, and has been identified in earlier studies (2,3).

(1) Tillman, J.E., Fitzgerald, K., Guest, W. R., Henry, R. M. and Strauss, C. (1981). Submitted to J. Geophys. Res.
(2) Barnes, J.R (1980) J. Atmos. Sci, 37, p. 2002-2013.
(3) Sharman, R.D. and J.A. Ryan (1980) J. Atmos. Sci., 37, p. 1994-2001.

INSTABILITY FEATURES ON THE SURFACE OF MARS. Dag Nummedal, Department of Geology, Louisiana State University, Baton Rouge, LA, 70803.

INTRODUCTION. The surface of Mars displays an extensive assemblage of instability features. Instability features are here defined as all landforms that owe their origin to gravity displacement of material in response to the removal of (subsurface or lateral) support. Their widespread occurrence and large scale suggest the existence of temporally unstable regolith coupled with extremely slow surface modification by external agents (the erosion rate over the last 3 billion years may have been as low as 10^{-3} μm/yr, [1]).

The significance of treating instability features as a class of landforms on Mars lies in the following observations:

(1) The available evidence strongly suggests that ground ice deterioration is the primary process responsible for their formation.
(2) The instabilities appear to involve the fabric-breakdown of a brecciated megaregolith with the consequent collapse of overlying rock units. These units most often are plains materials emplaced upon old cratered terrain.
(3) Instabilities and collapse (at all scales) appear to have occurred throughout most of Mars' geologic history since the emplacement of plains units on the old cratered terrain.
(4) Instability and collapse may be a primary process responsible for the destruction of the old cratered terrain.

OBSERVATIONS. Instability features on Mars are not randomly distributed, they follow a spatial pattern which indicates a communality in origin. In its broadest outlines, this pattern is as follows.

1. Large landslides are most abundant on stratigraphically downdip walls of the Valles Marineris [2, 3]. The adjacent plateau is the topographically high Syria-Sinai-Lunae Planum consisting of surface units of volcanic plains material burying old cratered terrain.
2. To the east Valles Marineris grades into the extensive areas of chaotic terrain and associated large channels of Margaritifer Sinus. It is quite significant that the adjacent surface is topographically 6 km lower than the top scarp at Ius Chasma, the region of most extensive landsliding. It is also significant that not only are the large Margaritifer Sinus channels at the base of a major topographic high, all major channels on Mars are at or near the base of major upland regions.
3. Smaller-scale instability features include pits adjacent to Valles Marineris, debris flow lobes in Hellas and Protonilus [4] and flows in the Nilosyrtis region [5]. In all these cases, the instability which triggered the flow of material appears to have occurred within the old densely cratered terrain.

THE MODEL. Following investigations by Carr [6] into the early history of Mars, this model takes as its starting point the emplacement of a planet-wide ground water system during an early Martian phase of a warmer, and presumeably denser, atmosphere. At the end of the period of heavy bombardment the climate cooled and thick ice-bonded permafrost permeated the brecciated units of the megaregolith. Emplaced upon these ground-ice charged brecciated rocks were the lava flows of the younger plains units. The development of large-scale topographic relief would create gradients in the ice-water interface and establish an interconnected ground water flow system. Assuming adequate porosity and permeability such a flow system could develop large water pockets under artesian pressure in low lying areas. Margaritifer Sinus would be a prime candidate for extensive developments of overpressured aquifers.

INSTABILITY FEATURES ON THE SURFACE OF MARS

Nummedal, D

Fluid water pockets in the brecciated zone could also form for similar reasons in Memnonia, on the flanks of Elysium, and to the east of Hesperia Planum; regions with other large channels.

Water could be released from these aquifers in different ways. Huge overpressured reservoirs might keep on growing until the geostatic pressure was exceeded, at which time doming, crustal rupture and venting would release the pressure, the water and large amounts of debris from the brecciated zone [7]. Alternatively, development of a large subsurface pocket of overpressured water in the megaregolith could make the regolith fabric unstable, inducing liquefaction, surface collapse and fluid release [8]. Either of these release mechanisms would produce large-scale channels.

A second consequence of this model is that ground-water release at regional topographic lows will always produce a restricted fluid source region. Even if water release is gradual (or in many successive floods) the channels on Mars would take on a distinctly different appearance from those of subaerial terrestrial streams which collect water from drainage basins.

This ground ice/ground water model also appears to present plausible working hypotheses for other types and scales of surface failures on Mars. The extensive landslides in Valles Marineris probably owe their origin to the effects of aquifer interruption by canyon-faulting [3]. The difference in development of the updip and downdip walls of the Valles Marineris is significant. Updip, the ground water kept seeping to the surface producing headwards extension of tributary canyons by sapping. On downdip walls, on the contrary, the water table would rise until a large volume of megaregolith had become saturated. Once the instability criterion was exceeded, slumping would occur. Such failures could have been spontaneous or triggered by quakes. The amount of liquid water released with these slides appears to have been less than that associated with the formation of many chaos. This is a most liquely consequence of the limited ground water reservoir available to slides high on the canyon walls compared to the draw-down areas feeding a chaos in Margaritifer Sinus.

This difference in liquid/solid ratio appears to have had a profound influence on the further development of the deposits of the initial failure. The differences in detailed morphology of the Valles Marineris landslides and the collapse-related channels in Margaritifer Sinus are consistent with this hypothesis.

CONCLUSIONS. Instabilities are defined as landforms that owe their origin to gravity displacement of material due to removal of underlying and lateral support. Features with this origin on Mars include many channels, chaos, landslides and debris aprons of a wide range of scales.

This paper presents a model which explains all these features as a result of the melting of ground ice with the attendant release of water from subsurface reservoirs. The different geomorphic features represent discrete stages in a continuum of surface instabilities differing only in the rate of material release (discharge) and the fluid/solid ratio of the released slurry.

The large scale of many unstability features probably reflects the presence of a thick layer of permafrost which could be fractured only after the formation of a large subsurface reservoir. The crisp appearance of a number of old instability features attests to slow modification by exogenic agents.

INSTABILITY FEATURES ON THE SURFACE OF MARS

Nummedal, D

REFERENCES

[1] Arvidson, R. E., Guinness, E. A. and Lee, S. W., 1979, Nature, 278, p. 533-535.

[2] Blasius, K. R., Cutts, J. A., Guest, J. E. and Masursky, H., 1977, J. Geophys, Res., 82, p. 4067-4092.

[3] Lucchitta, B. K., 1979, J. Geophys, Res., 84, p. 8097-8114.

[4] Carr, M. H., and Schaber, G. G., 1977, J. Geophys. Res., 82, p. 4039-4054.

[5] Eppler, D. B., and Malin, M. C., 1981, Abstr. Lunar Planet. Sci., Conf. 12th, p. 260-261.

[6] Carr, M. H., 1980, NASA Tech. Memo. 28385, p. 342-344.

[7] Carr, M. H., 1979, J. Geophys. Res., 84, p. 2995-3007.

[8] Nummedal, D., 1978, NASA Tech. Memo. 79729, p. 257-259.

ANNUAL RADIATION BALANCE OF THE MARTIAN POLAR REGIONS, David A. Paige, Division of Geological and Planetary Sciences, Caltech, Pasadena, CA 91125.

Viking Infrared Thermal Mapper (IRTM) solar reflectance and infrared emission data have been used to determine the annual radiation balance of the Martian polar regions. By using instrumentation and techniques similar to those used to study the Earth's radiation budget, it has been possible to measure the rate at which energy enters and emerges from the top of the atmosphere above the polar caps throughout a Martian year. The results of this work show that the Martian atmosphere transports energy to the polar regions from lower latitudes, and that the southern residual polar cap is indeed composed of CO_2 frost (1).

The rate of thermal emission from the polar regions was determined by using the measured fluxes in the five IRTM broadband infrared channels to synthesize an infrared spectrum, and then integrating over all wavelengths to obtain the emission rate at various emission angles. The rate of absorption was determined by using the IRTM broadband albedo channel data to constrain the hemispheric planetary albedo of the polar regions as a function of solar zenith angle and time. The albedo was constrained by constructing plots of the bi-directional reflectance of the polar regions and then contouring. In cases where the hemispheric integral of reflected energy was not well constrained by the coverage that was obtained, the minimum and maximum possible albedo that was consistent with the available observations was computed. Uncertainties in the annual radiation budget measurements are primarily due to incomplete sampling of all sun-planet-spacecraft geometries, the unsampled wavelength region beyond 30 microns, and the absolute calibration of the instruments. The magnitude of these uncertainties is estimated to be less than 10%.

Figure 1 shows the measured annual radiation budget of the north polar region of Mars (Lat=86-90N). Simple zero-dimensional radiation balance models show that the energy emerging from the top of the atmosphere during the polar fall and winter seasons is supplied by the latent heat release of condensing carbon dioxide frost. The second global dust storm of 1977 occurs just after L_s=270 (winter solstice). The rate of emission increases during the storm, even though radiative models for the dusty polar atmosphere predict that if anything, the rate of frost condensation decreases during the dust storm period (2). Therefore, some fraction of the energy that was emitted by the polar surface and atmosphere during the dust storm was transported to the region by the Martian atmosphere. Just before L_s=90 (summer solstice), the rate of absorption and emission increases. This can be interpreted to be the complete sublimation of the seasonal carbon dioxide frost cover, exposing a residual water ice cap with a lower albedo (3). The north polar region is close to being in radiative equilibrium throughout much of the summer season. This is consistent with the fact that the sublimation of water ice on Mars is a slow, diffusion-limited process, and that it doesn't represent a major source or sink for energy in the polar regions.

Figure 2 shows the measured annual radiation budget of the region defined by the minimum frost coverage of the south residual cap. The south residual cap differs from the north residual cap in that it absorbs much more energy than it emits during the summer season. The excess absorbed energy must be going into subliming frost from the residual cap during this season. MAWD observations in the south arctic show that the total column abundance of water vapor during this season was never greater than 15 precipitable microns (4). If the excess absorbed energy over emitted energy was being used to sublime water ice, the rate of production of water vapor would be greater

than 500 precipitable microns per day. The radiation balance measurements show that frost is subliming, yet the measured water vapor abundances are more than an order of magnitude lower than what would be produced if water ice was subliming even for one day. This leads to the conclusion that the frost that is subliming during the southern summer is carbon dioxide frost, and that there is a resevoir of frost at the south polar cap that remains in vapor equilibrium with the atmosphere throughout the year. The rates of emission and absorption are greatly inhanced during the height of the second global dust storm just after L_s=270. The radiation balance of the south pole is significantly affected by atmospheric opacity during the spring and summer seasons.

Table 1 shows the annual averaged rates of emission and absorption for the north and south polar regions. Both the north and the south poles emited more energy than they absorbed on an annual basis. Assuming that that there was no net annual accumulation of frost within the regions, then the excess emitted energy over absorbed energy was transported to the polar regions by the Martian atmosphere form lower, warmer latitudes. The measured transport rates of between 0.4 and 3.4 Wm^{-2} are in good agreement with the results of the Martian global circulation model calculations of Leovy and Mintz (5).

References

(1) Kieffer, H.H. (1980), J. Geophys. Res., 84, 8263.
(2) Martin, T.Z. and Kieffer, H.H. (1979), J. Geophys. Res., 84, 2843
(3) Kieffer, H.H. et al. (1976), Science, 194, 1341
(4) Davies, D.W. and Wainio, L.A., (1981), Icarus, 45, Jan.
(5) Leovy C.B. and Mintz Y., (1969), J. Atmos. Sci., 26, 1167

Figure Captions

Figure 1. The annual radiaition budget of the north polar region of Mars (Lat=86-90N). The thick line represents the rate at which energy at infrared wavelengths emerges from the top of the atmosphere as a function of time. The thin line represents the rate at which solar energy is absorbed by the surface and atmosphere.

Figure 2. The annual radiaition budget of the region defined by the minimum extent of the Martian south residual polar cap. The thick line represents the rate at which the energy at infrared wavelengths emerges from the top of the atmosphere as a function of time. The thin lines represent the rate at which solar energy is absorbed below the top of the atmosphere for two possible histories of the hemispheric planetary albedo of the south polar region.

Table 1. The annually averaged rates of emission, absorption and poleward atmospheric energy transport, and the average albedo (albedo is defined here to be the fraction of incident solar radiation that is reflected and scattered to space by the polar surface and atmosphere over the course of a year) for the north and south polar regions of Mars. Uncertainties in these measured quantities reflect uncertainties in instrument calibration and possible errors due to incomplete sampling.

POLAR RADIATION BALANCE

Paige, D.A.

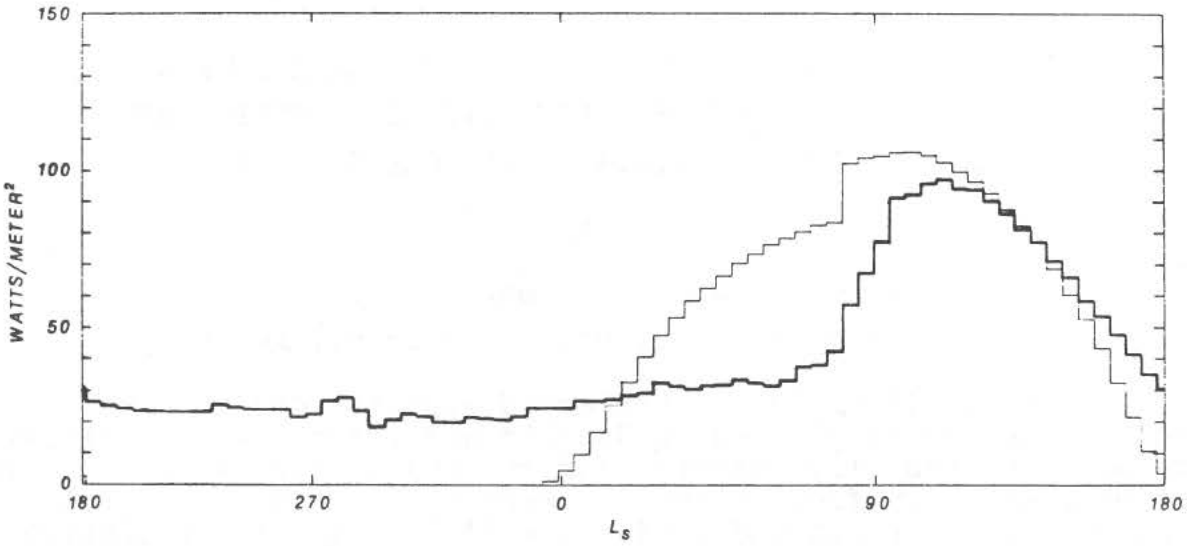

Figure 1. - North Pole

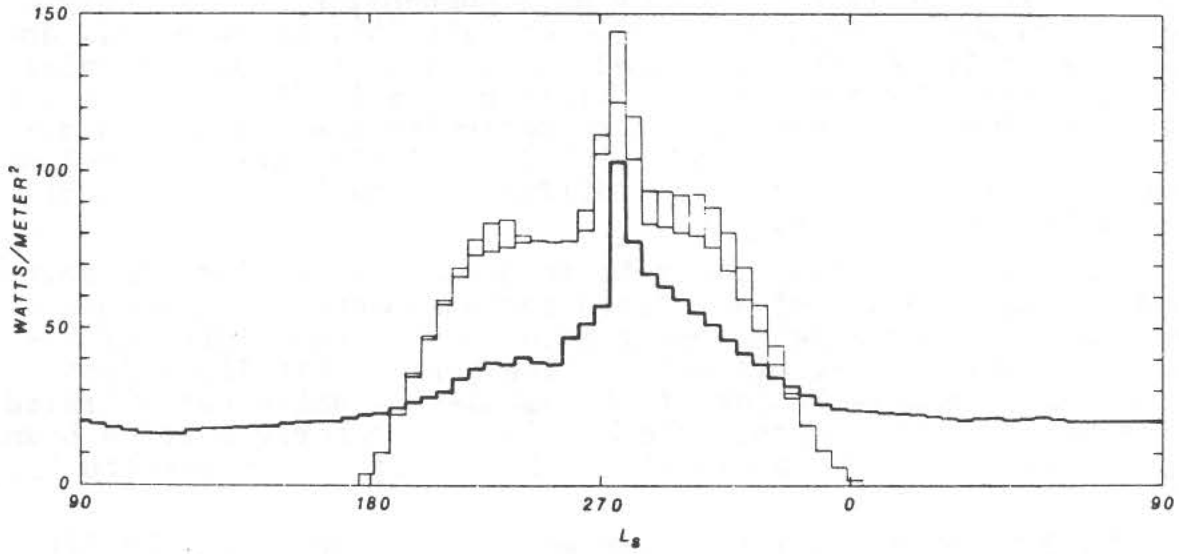

Figure 2. - South Pole

Table 1.

	Average Emission Rate W/M^2	Average Absorption Rate W/M^2	Average Transport Rate W/M^2	Average Albedo
SOUTH POLE	30.03 ± .9	27.35 29.65 ± 1.36	2.68 .38	.660 .631 ± .03
NORTH POLE	40.05 ± 1.2	36.69 ± 1.83	3.36	.545 ± .02

THE SURFACE BOUNDARY LAYER OF THE MARTIAN ATMOSPHERE AND RADIATIVE-CONDUCTIVE-CONVECTIVE HEAT TRANSFER UNDER DUST-LADEN AND CLEAR CONDITIONS.

by

A. J. Pallmann

Dept. Atmosph. Sci., St. Louis Univ., MO, 63156

Near perihelion, Mars experienced gigantic dust storms which frequently originated in Noachis and its northern vicinity. Intense solar radiative heating and subsequent lower-tropospheric destabilization by free convection were considered by several researchers. Gierasch and Goody (1,2,3) investigated radiative transfer through the lower Martian atmosphere and its dynamical structure. They established that radiative processes are of major importance to an understanding of the atmospheric dynamics on Mars. The specific impact of dust suspension on atmospheric temperature was studied by Conrath et alii (4), Conrath (5), and Pollack et alii (6) who developed the data needed for a detailed radiative transfer simulation. Kieffer et alii (7) used the Viking thermal mapping experiment to determine the surface conditions. (See also Moore et alii (8).) A simple thermal model was presented which solved the heat diffusion equation under specified surface conditions.

The purpose of this paper is to present some findings developed through the use of a refined radiative-conductive-convective heat transfer model closely attuned to variou types of Mariner and Viking data. It may suffice here to highlight just some of the characteristics of the simulation which concentrated on the heat transfer within the Martian atmospheric surface boundary layer. A more complete discussion is offered elsewhere (9, 10).

The 3 modes of heat transfer were simulated by explicitly modeling conductive flux in ground and atmosphere, convective flux for any atmospheric layer in which the preliminary radiative temperature model sounding turned out to be superadiabatic, and finally solar and planetary radiative net flux, over all 52 atmospheric levels between 0 and 50km with reduced vertical grid point spacing near the surface. The radiative upward and downward flux contribution of each layer to the respective computational level was calculated by numerically integrating the radiative transfer equation in its flux form over the total depth range. Spectral absorption line data for CO_2 were provided by the McClatchey tapes. A total of 33,000 lines was processed to obtain numerical values of the absorption function for small spectral increments (5 - 20 cm^{-1}). A quasi-random transmission function was adopted which is more sensitive to "intermediate" line intensities and more representative of the combined Lorentz-Doppler profiles (Voigt shape factor). The inhomogeneity of the

curve at ground level has the largest amplitude as expected. There is a phase difference of 1 to 2 hours between this curve and the T-oscillation at 12.5m which shows a 30 per cent reduction in its amplitude. As a matter of fact, the early afternoon maximum is shifted more than the minimum. The general pattern of this near-surface atmospheric temperature variation clearly resembles that measured at the lander sites (see Hess et alii (11); their Fig. 6).

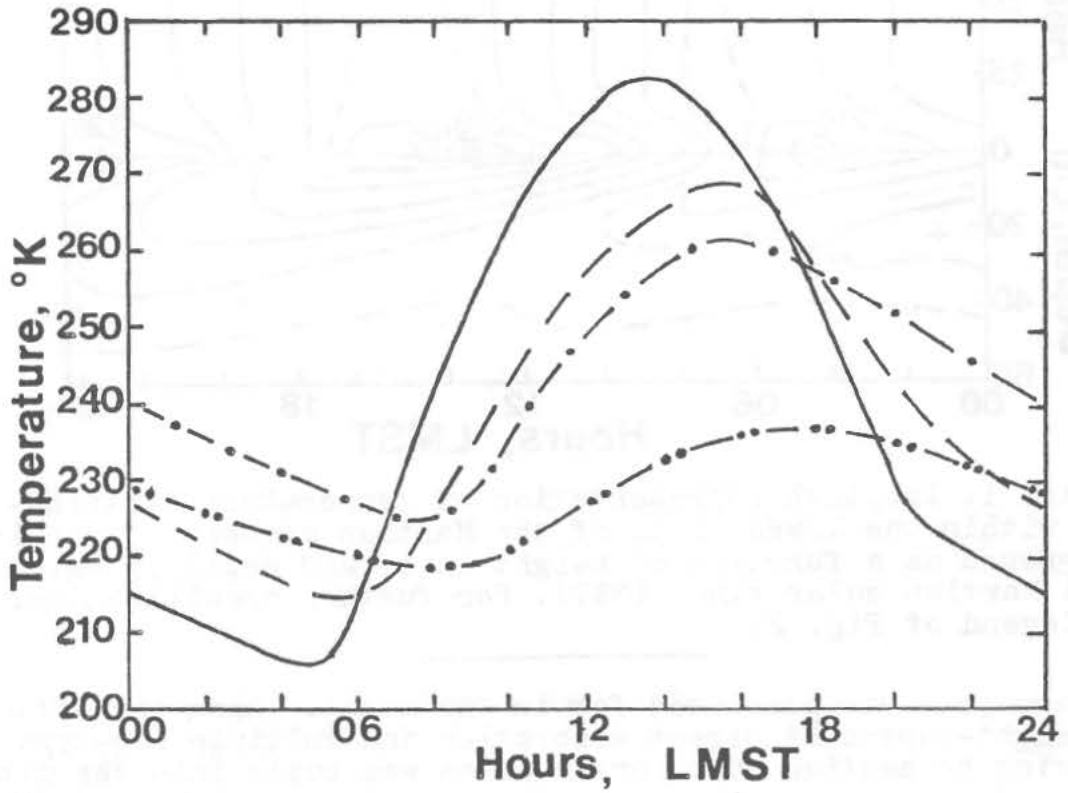

Fig. 2: Diurnal temperature oscillation in the southern-hemispheric midlatitudes between 30 and 45 degrees, shortly after summer solstice (solar declination: - 22 deg.), at 4 levels: (—) ground surface, (--) 12.5m, (-·) 1,500m, and (-··) 6,000m. LMST: local Martian solar time. The atmosphere is dust-laden (τ = 1.0).

REFERENCES

(1) Gierasch,P. & Goody,R.(1968); Plan. Sp. Sci.,16, 615-646.
(2) Gierasch,P.& Goody,R.(1972); J. Atmosph. Sci.,29, 400-402.
(3) Gierasch,P.& Goody,R.(1973); J. Atmosph. Sci.,30, 169-179.
(4) Conrath,B.J. et alii (1973); Mariner Mars 1971 Project Final Rept., Vol. IV, Jet Prop. Lab., Pasadena, California.
(5) Conrath,B.J.(1975); Icarus,24, 36-44.
(6) Pollack,J.B. et alii (1977); J. Geophys. Res,82, 4479-4496.
(7) Kieffer,H.H. et alii (1977); J. Geophys. Res.,82, 4249-4291.
(8) Moore,H.J. et alii (1977); J. Geophys. Res.,82, 4497-4523.
(9) Pallmann,A.J. et alii (1973); NASA-CR-2318; Washington,D.C.
(10) Pallmann,A.J. (1977); Riv. It. Geofisica,IV,#1/2, 47-56.
(11) Hess,S.L. et alii (1977); J. Geophys. Res.,82, 4559-4574.

SURFACE BOUNDARY LAYER ON MARS

Pallmann, A. J.

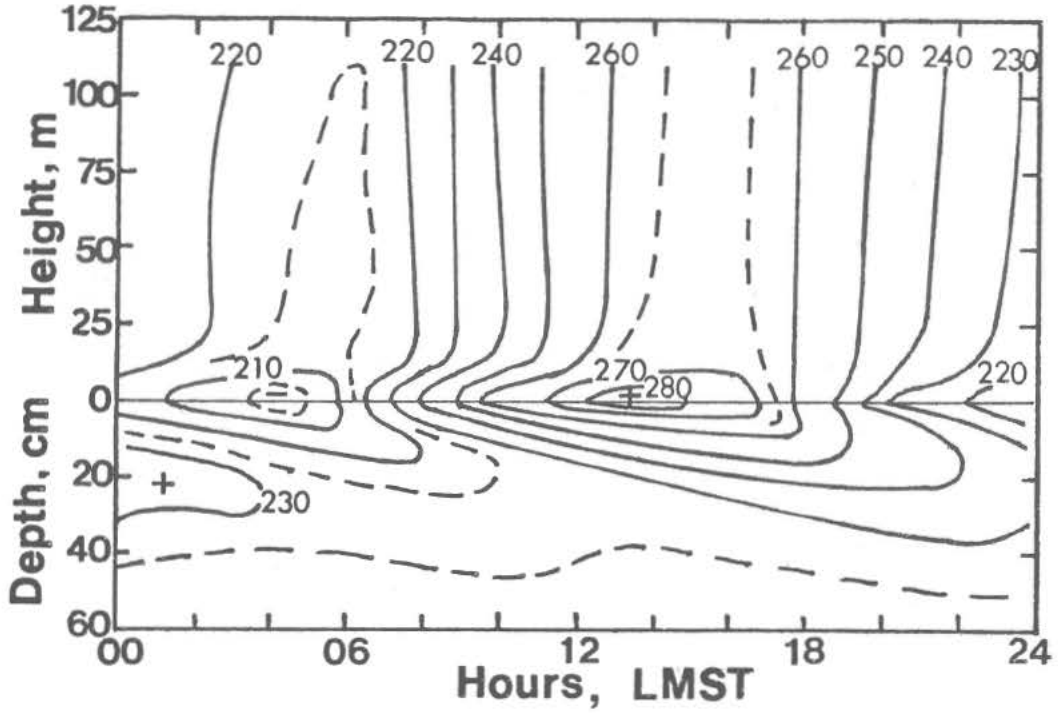

Fig. 1: Isopleth representation of temperature distribution within the lowest 125m of the Martian atmosphere and in the ground as a function of height in m, and depth in cm, and local Martian solar time (LMST). For further specification, see legend of Fig. 2.

---

radiative path was accounted for in the model. Also, the effect of a height-dependent direct absorption and multiple Mie-type scattering by aeolian dust particulates was built into the simulation.

The numerical time integration was extended over several Martian days until a cyclic diurnal balance of the outputted temperature soundings resulted. Such a balanced temperature distribution in the atmospheric near-surface boundary layer and the ground is shown in Fig. 1. This isopleth plot represents the temperature field in the southern-hemispheric midlatitudes between 30 and 45 degrees for the region near Noachis shortly after summer solstice (solar declination: - 22 deg.). Within the 125m thick atmospheric layer next to the ground, two distinct isotherm patterns are discernible. One layer from 125m down to about 20m shows very little slope with height in the isotherms, whereas the other from about 20m to 0m presents strongly bent isotherms. The latter stratum in which the steepest diurnal temperature changes occur, is considered to be the surface boundary layer. Conventionally, it is also labeled the constant flux layer. It is inferred that for the conditions previously stated the Martian atmospheric surface boundary layer has a vertical extent of about 20m. In Fig. 2, for the same seasonal and latitudinal conditions, the diurnal temperature oscillation is given as produced by the tuned simulation. The T-

ORGANIC COMPOUNDS IN THE MARTIAN ENVIRONMENT: EXTRAPOLATION OF VIKING RESULTS BY LABORATORY SIMULATIONS AND UV-IR REFLECTANCE SPECTROSCOPY.
K. D. Pang and J. M. Ajello, Jet Propulsion Laboratory, Pasadena, CA. 91109, S. F. Chun, University of California, San Francisco, CA., N. Zhao, Beijing Planetarium, M. Liang, Beijing Glass Institute, People's Republic of China.

Although some of the data from the Viking biological experiments can be interpreted as an indication of biological activity, the existence of organisms in the Martian soil samples is generally considered unlikely because of the non-detection of organic compounds in these samples (1). Viking GCMS analysis (2) detected no organic molecules above concentration of parts per 10^9. The Viking results pose new questions: Why were no organic molecules detected? Is the sterility of the two sites representative of the entire planet? Answers to these questions could affect our outlook for finding life in the Universe, as well as influence strategies for future exploration of Mars.

It is difficult to say whether results obtained at two sites are representative of the entire planet. However, once we successfully simulate the destruction of organic compounds under Mars-like laboratory conditions we can deduce their fate in other parts of the planet by comparing the environment at the landing sites with those prevailing elsewhere, e.g., the polar regions. UV and IR spectroscopy are powerful analytical techniques for extrapolating the Viking lander results. Upper limits on organic carbon content of Mars soil can be determined by remote sensing, and we may use this knowledge to assess the ability of the soil to support life forms based on carbon chemistry.

Chun et al. (3) proposed a mechanism for the destruction of organics on Mars -- UV-stimulated catalytic oxidation:

$$\left.\begin{matrix}\text{complex}\\ \text{organic}\\ \text{compounds}\\ O_2\end{matrix}\right\} \xrightarrow[TiO_2]{h\nu} \left.\begin{matrix}\text{simple}\\ \text{organic}\\ \text{compounds}\\ O_2\end{matrix}\right\} \xrightarrow[TiO_2]{h\nu} \begin{matrix}\text{inorganic}\\ \text{compounds}\end{matrix}$$

In a controlled experiment Chun et al. (4) further showed that organic compounds, present in a carbonaceous chondrite sample, are readily oxidized under Mars-like laboratory conditions. Activation energy, provided by energetic photons, is required for the reactions to take place. A catalyst, TiO_2, speeds up the reaction, but is not absolutely essential. Sancier and Wise (5) also found that the above reaction is responsible for the degradation of organic compounds in terrestrial sand dunes, where sand acts as a catalyst.

It has been suggested that organic molecules, locally synthesized and/or from infall of carbonaceous meteorites, may be preserved in Mars' polar caps. Pang et al. (6) showed that there is no basis for this speculation. First, Mariner 9 UV spectrometer observations showed that solar UV radiation easily penetrates the Martian atmosphere down to the polar cap (7). Second, sand grains exist in great abundance in Mars' polar regions -- in dunes and laminated between condensates. Third, ozone is found in Mars' polar atmosphere, although not in a concentration to significantly attenuate solar near UV (8). The presence of O_3 requires that O_2 be there also. Therefore, all conditions required for the photocatalytic oxidation of organics -- UV radiation, oxygen, and sand -- are present in the polar regions of Mars, and the destruction of any organic molecules on the polar caps seems almost assured. It is easy to do a similar analysis for other locales on Mars and show that there is no basis for optimism for finding organic molecules anywhere on the planet. It is possible that organics are buried underground, but the fact that Viking found none under a rock lends no support to this conjecture.

In addition to the above comparative analysis we can use spectral remote sensing data of Mars to extend the Viking findings. UV and IR spectroscopy are very sensitive techniques in quantitative organic analysis. UV and IR reflectance spectra of Mars, properly interpreted with the aid of laboratory measure-

ments, can yield the chemical composition of areas not examined in situ.

Almost every molecule has spectral signatures in the small range of UV wavelengths 120 to 320 nm. Pang and Ajello (9) determined the absorption index (k) of Martian dust between 190 and 340 nm by analyzing Mariner 9 UV spectra of Mars dust clouds (dotted curve in Fig. 1). Abadi and Wickramasinghe have suggested that the absorption feature at 210 nm may be a signature of highly complex organic or pre-biotic molecules in Martian dust clouds (10). Although an organic explanation is possible, an inorganic interpretation of the data is much more plausible. Pang and Ajello have suggested that the UV absorption bands in Martian dust are due to electronic transitions in TiO_2 (9). Coauthors Zhao and Liang experimentally verified this suggestion by measuring the transmission spectrum of anatase (an allotrope of TiO_2) at the Beijing Glass Institute. The continuous curve shows the relative absorptivity of the TiO_2 sample, normalized to the peak of Martian dust absorption. Molecular orbital calculations (11) predict absorption bands at 200, 250, 258, and 296 nm due to metal-ligand transitions in TiO_2 (tick marks). This conclusion is also consistent with the detection of titanium by Viking lander inorganic analysis (12). Fe^{2+} and Fe^{3+} transitions are also good candidates for explaining the spectral reflectivity of Mars (13). The UV absorptivity of magnetite (ref. 14, dash curve) does not fit the Mars UV data as well as anatase, although Fe_3O_4 can also explain the run of k with visible/near IR wavelength of Martian dust (15). The spectral variation of k of limonite (ref. 16, dot-dash curve) does not match the Mars data at all.

In addition to the UV analysis we may also reinterpret IR reflectance spectra of Mars to derive useful upper limits on the organic carbon content of its soil. Extensive IR spectroscopic studies of Mars have been carried out with extremely sophisticated groundbased, airborne, and spacecraft instruments. The wavelength interval 3.4-3.6 μm has received especially careful scrutiny because virtually all organic compounds containing C and H have absorption bands here due to excitation of the C-H stretching vibration. Stringent upper limits have been placed on undetected atmospheric constituents e. g., parts per 10^8 for CH_4 (17). Since all gases known to be present in the Martian atmosphere (18) are transparent in this spectral region, any absorption feature found superimposed on the wing of the 3-μm water of hydration band may be assigned to organic constituents in Mars surface material. The C-H bands have never been found on Mars and their absence is interpreted as follows.

Laboratory measurements are useful for making quantitative reinterpretations of IR reflectance spectra of Mars. Fig. 2 shows laboratory reflectance spectra of quartz, limonite, and representative carbonaceous meteorites (19). The methyl and methylene (symmetric and anti-symmetric) vibration bands are clearly resolved as a doublet on the long wavelength wing of the water of hydration band in the spectra of the carbonaceous chondrites. The strength of the C-H bands correlates with the organic carbon content of the meteorite, e.g., Orgueil - 2.5%, Lance and Felix - 0.4%, and Allende - 0.2%. We note that the C-H bands are detectable even in Karoonda, with an organic carbon content of only 0.08%. The 3.3-3.6 μm features are not present in quartz or limonite, representing terrestrial rocks with organic carbon contents of 0.02-0.06% (20). We conclude that the absence of the fundamental C-H stretching absorption features in Mars' reflectance spectra indicates that the organic carbon content of its average surface material is at or below parts per 10^4. Field observations in the dry valleys of Antarctica have shown that soil samples with organic carbon contents less than 0.1% are generally sterile (21, 22). This implies that Mars in general and areas examined by IR spectroscopy in particular have soil deficient in organic matter, and are unfavorable habitats for life forms based on carbon chemistry.

Acknowledgement: The research described in this paper was performed by the Jet Propulsion Laboratory, California Institute of Technology and was sponsored by the National Aeronautics and Space Administration, except where noted.

References and Notes 1. Klein H. (1979) Rev. Geophys. Space Phys.17,1655-62.
2. Biemann K. & Lavoir, Jr. J. M. (1979) J. Geophys. Res. 84, 8385-8390.
3. Chun S., Pang K., Cutts J. & Ajello J. (1978) Nature 274, 875-876.
4. Chun S. F., Pang K. D. & Ajello J. M. (1979) NASA Conf. Publ. 2072, 15.
5. Sancier K. M. & Wise H. (1981) Atmos. Environ. 15, 639-640.
6. Pang K., Chun S. & Ajello J. (1978) Proc. 2nd Colloq. Planet. Water Polar Proc. p.199-201, U.S. Army Cold Reg. Res. Eng. Lab., Hanover, NH.
7. Pang K. & Hord C. W. (1973) Icarus 18, 481-488.
8. Barth C. A. (1974) Ann. Rev. Earth Planet. Sci. 2, 333-367.
9. Pang K. D. & Ajello J. M. (1977) Icarus 30, 63-74.
10. Abadi H. & Wickramasinghe N. C. (1977) Nature 267, 687-688.
11. Loeffler B. M., Burns R. G., Tossell J. A., Vaughan D. J. & Johnson K. H. (1974) Proc. Lunar Sci. Conf. 5th, 3007-3016.
12. Toulmin III P. et al. (1977) J. Geophys. Res. 82, 4625-4634.
13. Singer R. B., McCord, T. B., Clark R. N., Adams J. B., & Huguenin R. L. (1979) J. Geophys. Res. 84, 8415-8426.
14. Huffman D. K. & Stapp J. L. (1973) In Interstellar Dust and Related Topics (ed. Greenberg M. & van de Hulst H. C.) 297-301, Reidel, Boston.
15. Pollack J. B. et al. (1979) J. Geophys. Res. 84, 2929-2946.
16. Egan W. G., Hilgeman T. & Pang K. D. (1975) Icarus 25, 344-355.
17. Maguire W. C. (1977) Icarus 32, 85-97.
18. Owen T. et al. (1977) J. Geophys. Res. 82, 4635-4639.
19. Salisbury J. W. & Hunt G. R. (1969) Nature 222, 132-136; Lebofsky L. A. (1978) Mon. Not. Roy. Astron. Soc. 182, 17p-21p.
20. Levy R. M., Grayson M. A. & Wolf C. J. (1973) Geochim. Cosmochim. Acta 37, 467-483. A detection upper limit of 5 parts per 10^4 for organic carbon can be independently established from IR absorption spectra of Holbrook, a non-carbonaceous meteorite (Urey H. Life Sci. Space Res. 4, 35-59, 1966).
21. Cameron R. E. (1971) In Research in the Antarctica (ed. Quam L. O. & Porter H. D.) 137-189. Amer. Assoc. Adv.Sci., Washington, D.C.
22. Horowitz, N., Cameron R. & Hubbard J. (1972) Science 176, 242-245.

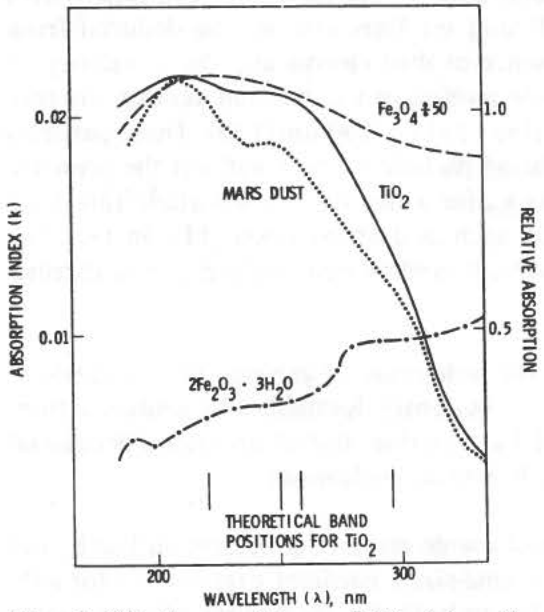

Fig.1 UV Absorption of Martian Dust, Magnetite, Anatase & Limonite

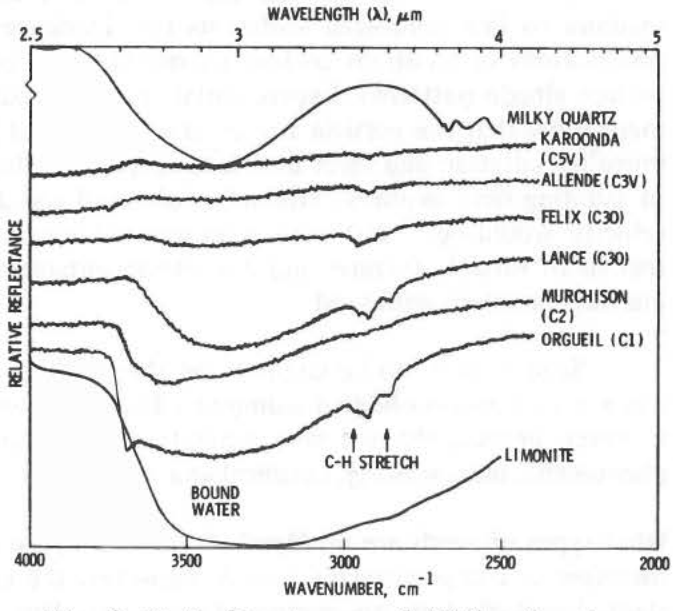

Fig.2 IR Reflectance of Milky Quartz, Limonite & Carbonaceous Chondrites

SAND ON MARS

A. R. Peterfreund, R. Greeley, and D. Krinsley, *Department of Geology, Arizona State University, Tempe, Arizona 85287*

The nature of sediments on planetary surfaces provides important information on the processes that generate, transport, deposit, and destroy those sediments. On Earth, processes involving water dominate the sedimentary cycle. On the Moon, sedimentation is mostly the result of communution due to meteoroid impacts. On Mars, sedimentation is currently dominated by aeolian processes; however, past sedimentation has also resulted from cratering, fluvial processes, periglacial phenomena, and volcanism. The types of sediments produced and the resultant landforms vary with each process. Thus, on Mars, a complex pattern of sedimentary activity is closely associated with the geologic history of the planet. What we see today is an ongoing modification by wind of the products of earlier processes. This review addresses the particular question of sand as related to the sedimentary history of Mars.

Is there sand on Mars? Although the answer to this question appears to be obvious, the presence of sand (particles 60 to 2000 μm diameter) and its physical and textural properties remain uncertain. Arguments against the widespread presence of sand include: 1) the relative absence of particles smaller than 100 μm diameter at the two Viking lander sites (1, 2); 2) an apparent lack of quartz, the primary composition of terrestrial sand, on Mars (3); 3) aeolian models that suggest the self-destruction of saltating particles, or the "kamakaze" effect (4); and 4) estimates based on laboratory simulations that abrasion by windblown sand would be exceedingly high ($10-100 m/10^6$ yr) (5). On the other hand, arguments for the widespread occurrence of sand are compelling. Dunes are observed to be ubiquitous on Mars. Terrestrially, dunes form by saltation of fine sand (125 to 250 μm); on Mars, there should be no substantial difference to this process (6). Observations of possibly active dunes (7) also strengthen the argument for sand, as saltation is required for dune migration. Viking Infrared Thermal Mapper (IRTM) observations also suggest the widespread presence of sand-sized particles based on estimates of thermal inertia which is sensitive to mean particle size. Low thermal inertia and high albedo regions are interpreted as mantled by silt-or smaller-sized particles (8) and account for less than 20% of the surface between $+60^{o}$ and -60^{o} latitude. Most of the surface is dark and contains presumably coarser sediments than the mantled regions. A comparison of the IRTM data with photogeologic results shows that most wind streaks and dunes occur in regions that have thermal inertia values consistent with medium to fine sand-sized sediments (9). Evidence of sand on Mars can also be deduced from observations of recurrent aeolian activity (i.e., the presence of dust storms and the variability of surface albedo patterns). Experimental studies of particle motion in the martian aeolian environment show that the particle size most easily moved is fine sand ($\sim$ 100 μm) (10). These particles move by saltation and eject dust into suspension. Initiating particle motion without the presence of saltating sand requires extremely high wind speeds (e.g., for a bed of 10μm particle threshold velocity would be $\sim$ 250 m/s) or an unusual mechanism such as dust injection (11). In fact, the regions of variable features and dust storm initiation contain sand-related landforms and thermal inertias consistent with sand.

Sand is likely to be common on Mars because of the wide range of geologic processes which can generate unconsolidated sediments. These processes are currently dominated by aeolian action; however, presumably past sand generation has occurred by cratering, fluvial processes, periglacial phenomena, mass-wasting, chemical and mechanical weathering and volcanism.

What types of sands are on Mars? Sand is the product of a wide range of processes on Earth, and therefore is compositionally varied. However, the only sand-sized particles that survive for substantial geologic time are composed of quartz. This is due to both the abundance of large quartz

grains derived from plutonic rocks, and the physical properties of quartz, particularly its hardness and resistance to chemical weathering. On the Moon, agglutinates, which are glass-bound comminuted rock, mineral and glass fragments, are the dominant sand-sized materials present in the soil (12, 13). Although attempts were made to collect crystalline sand-size particles at the two Viking Lander sites, all that were collected were aggregates of very fine particles (14). These aggregates are either electrostatically or chemically bound. Arguments for their occurrence have been made based on laboratory simulations (15, 16) which show that sand-sized particles abrade rapidly under martian conditions forming silt- and clay-sized particles which in turn become electrostatically-bound sand-sized aggregates. The survival of these particles in a saltating regime and their ability to form aeolian deposits remains a problem.

The evidence for crystalline sands on Mars can only be inferred from photogeologic studies and remote sensing investigations. The mechanisms for producing sand grains can be divided into two categories, primary and secondary. *Primary processes,* which introduce rock fragments, glass or minerals upon the surface, are meteoritic impact, explosive and effusive volcanism, tectonism, and weathering. The degree to which these processes have been active on Mars has declined with geologic time. *Secondary processes* are those that remobilize sediments and include: cratering, fluvial and periglacial processes, mass-wasting, weathering and aeolian abrasion. Unconsolidated sediments observed on Mars are the result of these secondary processes. Yardangs, which are erosional aeolian landforms that usually form in friable or indurated sedimentary deposits, are relatively common features in the equatorial region of Mars, particularly in regions proximal to large volcanoes. This suggests ignimbrites or lahars as possible source material (17). Many wind streaks, particularly splotch-related streaks, are also evidence of reworked deposits as they are often associated with intracrater deposits (9, 18). It appears that much of the sand on Mars consists of reworked sedimentary deposits and, as such, is compositionally as varied as in the primary processes of emplacement.

Remote sensing observations of sediments on Mars show a variety of characteristics indicative of composition. Earth-based near-infrared spectra indicate that a variety of sediment types must occur on Mars, ranging from what appear to be relatively unoxidized basalt fragments in some dark areas, such as Syrtis Major, to high desiccated mineral hydrates in bright areas such as the Arabia region (19). Correlations of IRTM data and orbiter color with photogeologic studies also suggest a wide range of sediment types on Mars (8).

In summary, sand grains on Mars are polygenetic and have a wide range of compositions and physical properties. The Viking Lander sites have been shown from IRTM studies to be atypical of Mars as a whole in terms of thermal inertia and albedo (20). Thus, studies that extrapolate lander results to the rest of Mars must be taken with a grain of "sand."

References

(1) Mutch T. A. (1976) *Science 194*, 87–91.
(2) Moore H. J. (1977) *J. Geophys. Res. 82*, 4497–4523.
(3) Smalley I. J. and Krinsley D. H. (1979) *Icarus 40*, 276–288.
(4) Sagan C. et al. (1977) *J. Geophys. Res. 82*, 4430–4438.
(5) Williams S. H. and Greeley R. (1980) *Lunar and Planet. Sci. XI*, 1254–1256.
(6) Cutts J. A. and Smith R. S. U. (1973) *J. Geophys. Res. 78*, 4138–4154.
(7) Tsoar H. et al. (1979) *J. Geophys. Res. 84*, 8167–8180.
(8) Kieffer H. H. et al. (1977) *J. Geophys. Res. 82*, 4249–4291.
(9) Peterfreund A. R. (1981) *Icarus 45*, 447–467.

(10) Greeley R. (1980) *Geophys. Res. Lett. 7*, 121–124.
(11) Greeley R. and Leach R. (1979) *NASA TM 80339*, 304–307.
(12) Duke M. B. et al. (1970) *Proc. Apollo 11 Lunar Sci. Conf.*, 347–361.
(13) Lindsay J. F. (1976) *Lunar Stratigraphy and Sedimentology*, Elsevier, N. Y., 302 pp.
(14) Moore H. J. et al. (1979) *J. Geophys. Res. 84*, 8365–8377.
(15) Greeley, R. (1979) *J. Geophys. Res. 84*, 6248–6254.
(16) Krinsley D. H. and Leach R. (1981) *Precam. Res. 14*, 167–178.
(17) Ward, A. W. (1979) *J. Geophys. Res. 84*, 8147–8166.
(18) Thomas P. and Veverka J. (1979) *J. Geophys. Res. 84*, 8131–8146.
(19) Singer R. B. et al. (1979) *J. Geophys. Res. 84*, 8415–8426.
(20) Palluconi F. D. and Kieffer H. H. (1981) *Icarus 45* (in press).

This work is supported by the NASA Planetary Geology Office, Mars Data Analysis Program, through Grants NSG–7548 and NAGW–24 to Arizona State University.

THARSIS: TEN YEARS LATER

R. J. Phillips, Lunar & Planetary Institute, Houston, TX 77058, N. H. Sleep, Dept. Geophysics & Geology, Stanford University, Stanford, CA 94305, W. B. Banerdt and R. S. Saunders, Jet Propulsion Lab, Caltech, Pasadena, CA 91109

The Tharsis region of Mars has probably changed little since our first good glimpse of this area a decade ago. Surprisingly, our perception of the origin, evolution, and present state of Tharsis has changed very little also. The same issues raised upon reception of the Mariner 9 data exist today, and some original concepts, once thought to be sacred, are slowly eroding, though probably faster than Tharsis itself.

We continue to ask the following primary questions: What is the origin and evolution of Tharsis? How is the topographic high of Tharsis maintained? The significant secondary questions include: What is the nature of the topographic high? How much is uplift and how much is volcanic-constructional? What are the origins of the fractures and ridges associated with Tharsis? What is the volcanic history? What is the nature of the gravity anomaly?

The relationship of long wavelength gravity to topography provides a convenient starting place for the discussion of Tharsis models. It is evident that simple isostatic models for the observed topography require depths of compensation both inordinately deep and disparate among wavelengths (1). More plausible models, i.e., those requiring compensation to occur within several hundred kilometers of the surface, all require substantial subsurface positive mass anomalies as part of the compensation structure. This is true over a spectrum of passive models, starting with complete local isostasy and ranging over various degrees of elastic flexural support.

The excess subsurface mass implied by the gravity analyses is obviously interpretable in a number of ways. One possible model is that described by Sleep and Phillips (2), wherein the excess mass is provided by a thin crust; i.e., a locally thickened mantle. A second possibility is that igneous intrusion into the crust has provided the excess mass.

Another approach to using the gravity data to constrain Tharsis models is to solve the boundary value problem for a self-gravitating elastic spherical shell subject to both gravity and topography boundary conditions. From these models are derived both deviatoric stress levels and stress trajectories. The former quantity can be employed as a model constraint, provided one is willing to sign up for a particular finite strength of the martian lithosphere. Stress trajectories are used to both infer the origin of tectonic features on the surface and to use the tectonic features to distinguish among geophysical models of the lithosphere (symbiotic science at its best).

The interesting result of elastic modeling (including locally isostatic models, which are the zero flexural rigidity limit) is that, in the vicinity of Tharsis, the tensile stresses are generally orthogonal to the fractures and graben and compressional stresses are generally orthogonal to wrinkle ridges. Although the theoretical-observational relationship is far from perfect, it is hard to escape the general conclusion that the tectonic features are the result of lithospheric *loading* by Tharsis, and not the result of *uplift*, which would have produced the conjugate set of tectonics. However, the level of orthogonal agreement differs for purely isostatic models and those which have a flexural component. This is because in the isostatic model, stresses at the surface are only dependent on the distribution of topography, while a flexural component dictates that surface stresses are controlled by both the topography and gravity fields. It is found for a reasonable range of flexural rigidities, that a flexural model is a better

match to the surface features than a purely isostatic model. It should be emphasized, however, that because of the long wavelengths involved, the structural makeup of the two model types is quite similar.

In sum, as a result of gravity analyses, we are willing to put forward the following constraints on any Tharsis model:

(1) There must be a significant subsurface positive mass anomaly.
(2) The model must be nearly isostatic with, however, a component of finite strength support.
(3) The majority of tectonic features must result from incumbent failure of the lithosphere by the Tharsis load, although the details and timing are, of course, not revealed by the theoretical models employed.

We propose that there is a genetic link between the extensive volcanism associated with Tharsis and the implied mass deficiency at depth that is required for the near-isostatic balance of both the surface (topographic) and subsurface positive mass anomalies. That is, the zone of mass compensation is a depleted source region resulting from the partial melting that gave rise to the extensive basaltic volcanism at the surface. The source (residuum) region, being less dense than normal mantle, would potentially provide a mechanism for buoyant uplift of Tharsis. If ρ_d and t are the density and thickness of the differentiated product, respectively, then buoyant (isostatic) uplift, h, takes place according to

$$h = \frac{\Delta\rho}{\rho_m} H - f\frac{\rho_d}{\rho_m} t \qquad (1)$$

where $\Delta\rho = \rho_m - \rho_r$, the *compositional* density difference between normal mantle and residuum mantle, and H is the thickness of the depleted region. The quantity f expresses the fraction of mass conservation in a vertical column enclosing the source region. Since mass is conserved if $\Delta\rho H = \rho_d t$, the limit f = 1 expresses a closed system. In this case, h = 0 and there is no compositional buoyant uplift (see Finnerty and Phillips, this volume). It may be possible in this case to derive a model of Tharsis that is essentially constructional (3) and satisfies the gravity constraints by insisting the differentiate be denser than the surrounding crust ($\rho_d > \rho_c$). Constraint (1), above, will be satisfied if some of the differentiated material resides within the crust either as intrusives or as a crustal displacement caused by extensive loading from that fraction of the differentiate that existed as surface volcanics.

In addition to *compositional* density difference associated with the depleted region, there would be a *thermal* density anomaly here and elsewhere, which would be independent of the value of h in equation (1), provide independent buoyant uplift, and participate in the isostatic balance. As the source region cooled, this buoyancy would decrease, leading to a departure from isostasy and an effectively increased surface load with attendant lithospheric failure, thus satisfying constraints (2) and (3).

At the other extreme f = 0, and the Tharsis topographic high would now be provided by permanent compositional buoyant uplift. In this case, constraint (1) is satisfied by a positive density contrast of uplifted depleted mantle with the crust ($\rho_r > \rho_c$). Possible mechanisms for removing mass from the system (f<1) all involve transfer of differentiate from the vertical column of the source region. This could be accomplished by lateral migration of magma within the crust or on the surface as flows. The ancient cratered terrane surrounding Tharsis could, for example, in part represent

some of this product. Alternatively, the differentiate, being iron-rich compared to normal mantle (see Finnerty and Phillips), might, at the lithostatic pressure of the source region, be *negatively* buoyant and thus lost from the system. A third possibility is that the source region was already partially differentiated before being emplaced beneath Tharsis.

We do not believe that the pure end-members (completely open or completely closed) are plausible and that, more likely, the topographic high of Tharsis is explained by a combination of volcanic construction and compositional buoyant uplift. The interaction of geophysics and petrology provides a powerful tool in attacking this hypothesis. The gravity modeling constrains $f\rho_d t$, $\Delta\rho H$, and the nature of the maximum thermal anomaly that was beneath Tharsis. For a given Mars mantle model, ρ_m, phase relationships constrain possible combinations of $\Delta\rho$ and ρ_d. Photogeologic techniques might constrain the amount of extrusive volcanism present, but, despite valiant attempts (4), to date there have been no convincing arguments presented that establish the thickness of the basalt load in the central Tharsis region.

This entire discussion, of course, begs the issue of just what thermal event led to the partial melting episode that created Tharsis (and Elysium as well). It is certainly tasteful to invoke massive convective upwellings that were concentrated at only a few places on the planet. Alternatively, isolated regional fracturing may first concentrate, and then sustain, magmatic activity on a planet that is otherwise globally ripe for volcanism. To be safe, we simply appeal to serendipity.

References

1. Phillips, R. J. and Saunders, R. S. (1975) *J. Geophys. Res.* *80*, 2893-2897.
2. Sleep, N. H. and Phillips, R. J. (1979) *Geophys. Res. Lett.* *6*, 803-806.
3. Solomon, S. C. and Head, J. R. (1980) *Reports of Planetary Geology Program 1979-1980*. NASA TM 81776, 71-73.
4. Plescia, J. B. and Saunders, R. S. (1980) *Proc. Lunar Planet. Sci. Conf. 11th* 2423-2436.

A COMPARISON OF LEE-WAVES IN THE ATMOSPHERES OF MARS AND EARTH;

A.O. Pickersgill & G.E. Hunt, Laboratory for Planetary Atmospheres, Department of Physics and Astronomy, University College London, Gower Street, London WC1E 6BT

When Mariner 9 approached the planet Mars in 1971, a global dust storm blanketed the entire planet, making it a featureless globe. After the tempest subsided, and the dust settled, delicate cloud patterns emerged in the martian atmosphere above a terrain whose variations in altitude were found to be comparable with the atmospheric scale height. Among these clouds, gravity lee-wave trains emerged whose appearance was found to resemble a ship-wake pattern centred on a topographical feature. In the winter north polar hood, systems of lee-waves formed downwind of craters which vary in size from a few kilometres to about one hundred. An account of these observations was reported in Briggs and Leovy (1).

With the advent of the Viking mission, the seasonal behaviour of lee-waves could be investigated in a depth not possible with previous explorations. Plume clouds observed near the western flank of Ascraeus Mons during early summer mornings were suggested by Briggs et al (2) to be lenticular. The daily cycle of clouds in the vicinity of two volcanoes, Ascraeus Mons and Elysium Mons, was investigated in Hunt et al (3). In addition, many ship-wake lee-wave patterns were observed in both hemispheres, similar to those seen during the Mariner 9 mission. An attempt to follow the movement of a lee-wave system near crater Kunowsky (57^{o}N 9^{o}W) was made during the survey mission over a period of approximately twelve minutes.

Besides the meteorological aspect leeward of obstacles, winds associated with these martian waves have a direct effect on the transport of surface material. Some aspects of the erosional effects in the lee of craters and hills are discussed in Thomas and Veverka (4).

By contrast, terrestrial lee-waves are often generated by mountain ranges as well as individual topographical features. Clouds which form over continental scale features such as the Rockies tend to be long, parallel and evenly spaced. However, isolated islands, such as Jan Mayen (71.0^{o}N 8.5^{o}W) in the Norwegian Sea, have been observed by satellites to generate clouds with a distinctive ship-wake pattern. An account of lee-wave observations photographed by NOAA 5 in the vicinity of Jan Mayen, Bear Island (74.4^{o}N 19.0^{o}E) and Hopen (76.6^{o}N 25.3^{o}E) appears in Gjevik and Marthinsen (5).

In this paper, a comparison is made between observations of lee-waves and isolated lenticular clouds on the two planets. An examination of the type of airflow necessary for the formation of these lee-waves is made, and a suggestion as to likely wind speeds on Mars in the presence of these clouds is introduced by comparison with a numerical model as discussed in Pickersgill and Hunt (6,7).

References

1. Briggs, G.A. and Leovy, C.B. (1974) Bull. Amer. Met. Soc. 55, p.278-296.

2. Briggs, G., Klaasen,K., Thorpe, T., Welman, J. and Baum, W (1977) J. Geophys. Res. 82, p.4121-4149.

3. Hunt, G.E., Pickersgill, A.O., James, P.B. & Johnson, G (1980) Nature 286, p.362-364.

4. Thomas, P. and Veverka, J. (1979) J. Geophys. Res. 84, p.8131-8146.

5. Gjevik, B. and Marthinsen, T. (1978) Quart. J. R. Met. Soc. 104, p.947-957.

6. Pickersgill, A.O. and Hunt, G.E. (1979) J. Geophys. Res. 84, p.8317-8331.

7. Pickersgill, A.O. and Hunt, G.E. (1981) J. Atmos. Sci. 38, p.40-51.

MARS: GLOBAL ALBEDO FEATURES VS TIME. Carle M. Pieters, Department of Geological Sciences, Brown University, Providence, RI 02912.

Although many of the same Martian albedo markings visible today can be identified in records that go back over 100 years, it is also well documented that the nature and extent of these markings vary, sometimes dramatically. Martian albedo variations as observed from earth are summarized here and on a 1:25,000,000 map. This information was derived from published data (see references); the variation map was prepared utilizing both the Lowell albedo maps (1967-1978) and the sequence of 32 maps prepared by DeMottoni (1975) based on photographs from the 1907 to 1971 oppositions.

There are three time scales to be considered: short or diurnal, seasonal, and long. It is possible, if not probable, that the cause for any observed albedo variation also has effects on different time scales. Since a Martian day is about 1 hour longer than an earth day, short term or diurnal variations can be studied visually or photographically throughout an opposition. Distinguishing seasonal from longer term variations is more difficult. The Martian surface cannot be observed continuously through the seasons of a Martian year. Each opposition (every 2 years on earth) is about half a Mars season later than for the previous opposition. Thus, over a period of about 15-16 earth years, or 8 Mars years, the full range of Martian seasons can be observed.

Map Preparation. Since the available albedo maps are qualitative, features were identified using a four level scale: bright, intermediate bright, intermediate dark, and dark. Albedo variations between the Martian latitudes 55^{o}N and 55^{o}S were then mapped in five general "units". BRIGHT (B) and DARK (D) areas are relatively stable large features for which the albedo level does not change in more than 75% of the maps available. Albedo for these areas never changes more than one level in 25% of the maps. Stable bright features include Arabia, Hellas and Elysium. Stable dark features include Meridiani Sinus, Syrtis Major and Solis Lacus. Only about 10% of the area mapped are classified as "stable" albedo features. USUALLY BRIGHT (b) and USUALLY DARK (d) areas include features that exist in most ($\sim$ 75%) albedo maps. The feature stays in the same general albedo class (bright or intermediate bright and dark or intermediate dark) but the intensity may vary. These regions include about two-thirds of the area mapped. VARIABLE areas (V) show significant variations in boundaries or nature of a feature: sometimes bright, sometimes intermediate, sometimes dark. Approximately 20% of the area mapped is highly variable in albedo. A few large regions exhibit secular variations and are mentioned below.

Short or diurnal variations. These variations include such phenomenon as cloud formation and dissipation and haze near the terminator. They are generally recognized by an experienced observer and are excluded from any of the albedo maps prepared for each opposition. Limb brightening effects are similarly excluded from the maps. Distinct dust storms can generally be identified and mapped independent of albedo features.

Seasonal variations. Most observers agree that the primary seasonal variation in albedo features is one of contrast, or relative brightness between dark and bright features. Some claim the darks get darker; others claim the brights get brighter. The strongest contrast appears during late spring or summer. This generalization is consistent with two attempts to

MARS: GLOBAL ALBEDO FEATURES VS TIME
Pieters, C. M.

measure it using photographic plates (Focas, 1959-61; Caspen, 1975). Similarly, the difference in polarization between dark and bright regions decreases during late spring-summer (Dollfus, 1961). Boundaries of the dark regions also fluctuate (sharpest in summer), but not in a rigorously predictable manner. During a favorable opposition with good seeing (e.g., 1941) dark areas can be resolved into discrete smaller regions often connected with intermediate material.

Since photographic records for Mars date back to 1907, there exist 4-5 independent maps covering the same Martian season. On the Albedo Variation Map seasonal variations are largely included in the USUALLY BRIGHT (b) and USUALLY DARK (d) units. Discrete boundaries within a dark or bright unit are lost. At least one small ($\sim$ 200 km) dark feature (Oxia, 10^{o}N, 15^{o}W) in a sea of brighter material has been present for more than 70 years. Mapped variations are thus not simply differences in effective resolution. Most other variations observed between seasons are not repeatable and are therefore included in secular variations.

Long or secular variations. Areas that have shown major albedo variations are mapped as VARIABLE (V) in the Albedo Variation Map and cover approximately 20% of the area mapped. Regional secular variations can be observed although some of the general boundary variations may be seasonal. Three regions that have shown dramatic changes are:

1) A 500 km area centered near 30^{o}S, 115^{o}W east of Sirenum (see discussion by Capen, 1975). Prior to 1971 this region had generally been bright. Just before the major (Solus Lacus) dust storm of 1973, however, this area was dark and remained dark during subsequent oppositions (e.g., 1975, 1978).

2) An extensive area (up to 1000 km) south of Sinus Sabaeus and east of Erythraeum centered near 30^{o}S, 350^{o}W. This region varies from bright to dark over long periods. In general, it has had a dark E-W band during 1909-1931, 1954-1967, and perhaps 1975.

3) The region east of Syrtis Major and along the equator to 20^{o}S and extending north 30^{o} from 10^{o}N, 260^{o}W. This area varies from bright to dark with no known regularity.

Two mysteries. 1) What is the real cause of the albedo markings and variations? There are many suggestions: dust vs no dust, frequency of streaks and splotches, slight topo control (sometimes), haze, clouds. Basically, there are many answers. Each area studied should be considered in its regional context.

2) Why are the Tharsis volcanoes distinctly dark in the Viking images, whereas on earth-based pictures the region is generally bright with frequent bright clouds observed around Nix Olimpia and Tharsis. Since small Oxia has been visible, spatial resolution is sufficient from earth. Regardless of any calibration difficulties with the Viking data, the volcanoes are darker than their surroundings. The only obvious observational difference is phase angle -- the Viking images were taken at high phase (105^{o}) compared to the earth based observations ($\lesssim 30^{o}$).

Summary. Three conclusions result from this analysis of Mars' features covering 72 years. 1) There are major bright and dark features that have remained essentially constant with time on the surface of Mars. 2) For some particular regions there are also dramatic changes of albedo, sometimes reversible. 3) There are frequent, but minor, albedo variations over most of the surface.

MARS: GLOBAL ALBEDO FEATURES VS TIME
Pieters, C. M.

The discussion presented here has been concerned primarily with large features. More detailed information exists in the data available than has been considered for this overview.

References. Capen C. F., Jr.(1976) Martian Albedo Feature Variations with Season: Data of 1971 and 1973, Icarus 28, 213-230.

Cutts J. A., Soderblom L. A., Sharp R. P., Smith B. A., and Murray B. M. (1971) The Surface of Mars 3. Light and Dark Markings, Jour. Geophys. Res., 343-356.

DeMottoni G. (1975) The Appearance of Mars from 1907 to 1971: Graphic Synthesis of Photographs from the I.A.U. Center at Meudon, Icarus 25, 296-332.

Dollfus A. (1961a) Polarization Studies of Planets, in Planets and Satellites (Kuiper and Middlehurst Eds.), Univ. of Chicago Press, Chicago, p 343-399.

Dollfus A. (1961b) Visual and Photographic Studies of Planets at the Pic du Midi, ibid. p. 534-571.

Focas J. H. (1961) Photometric study of seasonal variations, reported by Dollfus 1961b.

Frey H. (1974) Surface Features on Mars: Ground-Based Albedo and Radar Compared with Mariner 9 Topography, Jour. Geophys. Res., 79, 3907-3916.

Inge J. L. and Baum W.A. (1973) A Comparison of Martian Albedo Features with Topography, Icarus 19, 323-328.

Mutch T. A., Arvidson R. E., Head J. W., Jones K. L. and Saunders, R. S. (1976) The Geology of Mars, Princeton University Press, Princeton, N. J., pp. 400.

Sagan C., Veverka J., Fox P. and Dubisch, R. (1972) Variable Features on Mars: Preliminary Mariner 9 Television Results, Icarus 17, 346-372.

Sagan C., Veverka J., Fox P., Dubisch R., French R. and Gierasch P., (1973) Variable Features on Mars, 2, Mariner 9 Global Results, Jour. Geophys. Res., 78, 4163-4196.

Smith S. A. and Smith, B. A. (1972) Diurnal and Seasonal Behavior of Discrete White Clouds on Mars, Icarus 16, 509-521.

Soderblom L. A., Edwards K., Eliason E. M., Sanchez E. M. and Charette M. P., (1978) Global Color Variations on the Martian Surface, Icarus 34, 446-464.

MARTIAN VOLCANOES IN A CLASSIFICATION OF CENTRAL EDIFICES.

R. J. Pike and G. D. Clow, U.S. Geological Survey, Menlo Park, CA 94025.

We quantitatively compare the gross morphology (exclusive of size) of martian volcanoes with that of caldera-bearing terrestrial volcanoes -- for which processes are better understood, in order to identify volcano-forming conditions on Mars. By multivariate analysis of topographic dimensions (Fig. 1) [1,2], we examine 31 classes of volcanoes (N=740) including martian "montes" (n=6), "tholi" (n=4), and minor (e.g. Biblis) "paterae" (n=5). The updated measurements from Viking photogrammetry [3,4] were not available for the large highland "paterae" (e.g. Hadriaca) [5].

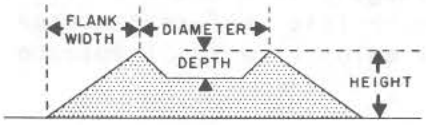

FIGURE 1. Four topographic measurements of a volcano (see Table 1). Circularity index for crater rim-crest is area of inscribed circle divided by area of circumscribed circle.

Our findings are based on a principal-components analysis of seven dimensionless variables (Fig. 1, Table 1) for each of the 740 volcanoes. Only three linear combinations (principal components P1, P2, P3) of the seven variables are needed to describe 95% of the variance in the data (Table 1). The resulting statistical scores (correlations of each volcano with each component) are averaged for each class in Figures 2 and 3.

The scores show that the initial (Mariner-9) cartographic classification of most large martian volcanoes into montes, tholi, and paterae [5,6] has genetic significance, and remains valid despite the greater detail now resolved by Viking: the three classes are mutually exclusive with respect to scores on the three principal components. The scores also indicate, however, that Hecates actually is a mons rather than a tholus and Jovis probably is a minor patera, not a tholus.

TABLE 1. PRINCIPAL-COMPONENT SCORES FOR SEVEN VARIABLES AND 31 CLASSES OF VOLCANOES*

Variable	P_1	P_2	P_3
Circularity	-0.34	0.31	**0.83**
Height/depth	**0.94**	-0.05	0.30
Width/diameter	**0.96**	-0.07	-0.14
Height/diameter	**0.89**	0.46	0.02
Depth/diameter	0.11	**0.86**	-0.42
Height/width	0.21	**0.89**	0.22
Depth/width	**-0.78**	0.61	-0.15
% variance	48.0	31.7	14.9

* Major constituents of each principal component, indicated by high scores, are circled.

We find further that the minor paterae, which have long been interpreted as buried large shields [5,7,4] are distinctive small shield volcanoes that are only slightly larger than their observable dimensions. If the visible dimensions of each patera are extrapolated to yield a buried edifice whose exhumed dimensions place it amid the martian montes (Fig. 2), then unrealistically great depths of burial (10 to 15 km $\pm$ 5 km) are required. From revision of the inverse relation between volcano age and height on Mars [8], we calculate the depth of fill embaying the minor paterae at only one to two km, which is consistent with likely geologic events in the Tharsis region [9,10,11]. Our revised age-height data show further that the unique geometry of the martian tholi

(Figs. 2, 3) requires no substantial burial by embaying plains [7,4].

Figures 2 and 3 reveal some marked topographic differences between terrestrial and martian shields, despite the abundance of fluid-lava flow features on all the martian volcanoes [6]. Montes have the same overall shape as caldera-bearing shields on Earth, but match no one class. By virtue of proportionally larger and deeper summit calderas, the montes differ substantially from large Hawaiian shields. Montes are most similar in geometry to those oceanic-tholeiitic shields that statistically overlap non-tholeiitic (or mixed-lava) shields. Martian tholi superficially resemble caldera-bearing stratovolcanoes more than they do lava shields on Earth. The tholi do share some geometric properties with lunar mare domes and with cratered terrestrial seamounts [3], both of which are believed to be largely lava constructs. The minor martian paterae are unique. Absence of ignimbritic surface textures suggests that they cannot be ash-flow plains, the sole terrestrial volcano that even approaches their unusual shape.

From analysis of gross-topographic characteristics independent of size, we conclude that not only do three classes of volcanoes on Mars differ

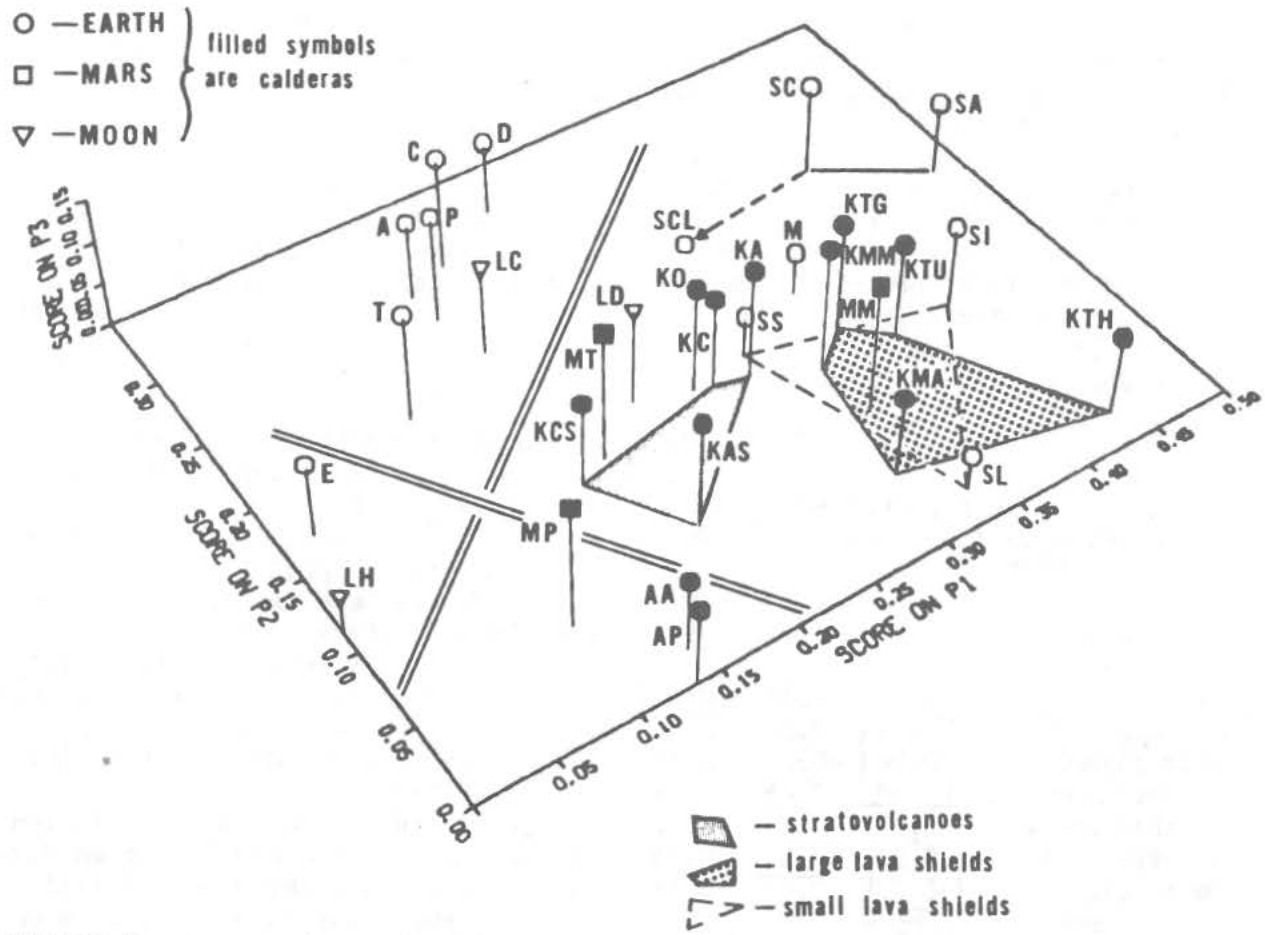

FIGURE 2. Averaged statistical scores for 31 classes of volcanoes (lettered codes explained in Fig. 3) on first three principal components P1, P2, P3. Double lines divide monogenetic eruptive styles (left) from polygenetic (right) and high-relief landforms (upper) from low-relief (lower).

CLASSIFICATION OF MARTIAN VOLCANOES

Pike, R. J. and Clow, G. D.

distinctly from one another, but also that most martian shields differ substantially from terrestrial shields. These morphologic contrasts indicate that (1) different combinations of processes and events must have formed the montes, tholi, and minor paterae, and that (2) the geologic conditions that gave rise to tholi and paterae must differ from typical shield-building conditions on Earth.

REFERENCES: (1) Pike R. J. (1978) Proc. Lunar Planet. Sci. Conf. 9th, p. 3239-3273. (2) Pike R. J. (1980) U.S. Geol. Survey Prof. Paper 1046-C. (3) Pike R. J., Jordan R., and Schafer F. J. (1980) NASA Tech. Memo. 81776, p. 192-194. (4) Blasius K. R. and Cutts J. A. (1981) Icarus, in press. (5) Plescia J. B. and Saunders R. S. (1979) Proc. Lunar Planet. Sci. Conf. 10th, p. 2841-2859. (6) Carr M. H. (1981) The Surface of Mars, Yale Univ., in press. (7) Greeley R. and Spudis P. D. (1981) Revs. Geophys. Space Physics, 19, p. 13-41. (8) Carr M. H. (1976) NASA Tech. Memo. 3364, p. 152-153. (9) Wise D. U., Golombek M. P., and McGill G. E. (1979) Icarus, 38, p. 456-472. (10) Scott D. H. and Tanaka K. L. (1980) Proc. Lunar Planet. Sci. Conf. 11th, p. 2403-2421. (11) Plescia J. B. and Saunders R. S. (1980) Proc. Lunar Planet. Sci. Conf. 11th, p. 2423-2436.

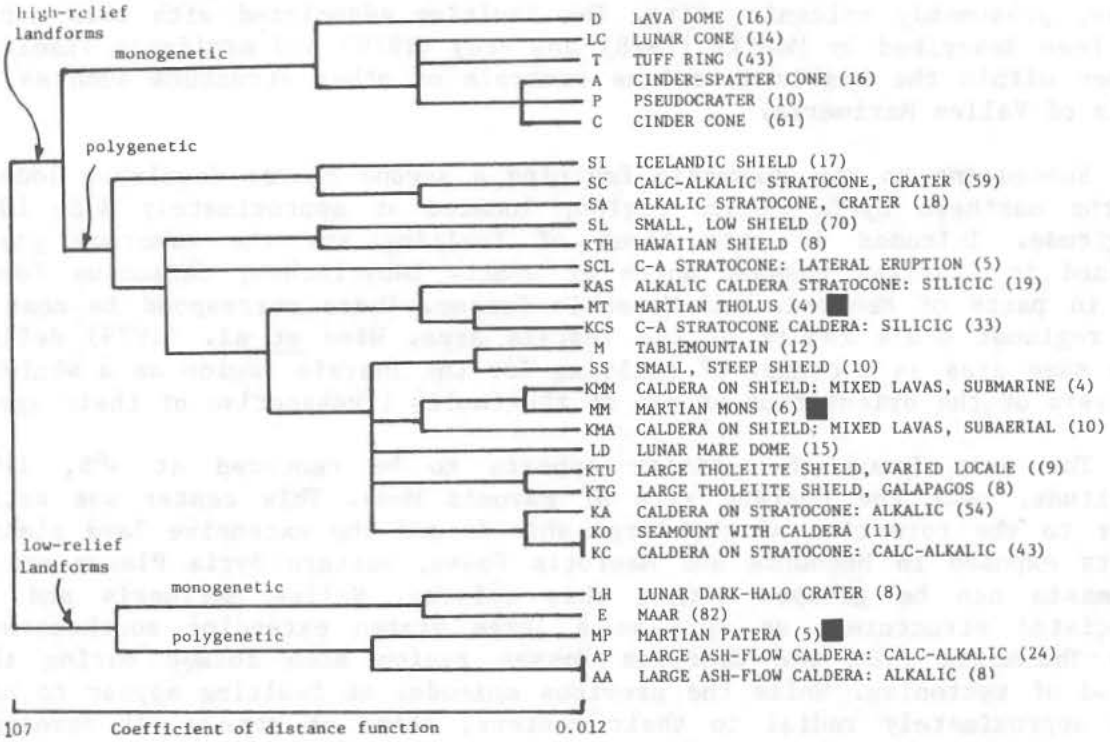

FIGURE 3. Dendrogram displaying cluster classification of 31 classes of volcanoes on four principal components (weighted) using the simple distance function [2]. Values of coefficient are low for similar classes and high for different classes. Length of horizontal line shows level of affinity at which each class or group of classes joins its cluster. Complete description of most classes given elsewhere [1,3]. Number of volcanoes in each class in parentheses.

TECTONICS OF THE THARSIS REGION, MARS.

J.B. Plescia [1,2] and R.S. Saunders [1]; [1] Jet Propulsion Laboratory, California Institute of Technology, Pasadena, CA 91106, [2] Dept. Geological Sciences, University of Southern California, Los Angeles, CA 90007.

The Tharsis region has been the topic of much study and speculation in Martian geology and geophysics. Of interest is the question of whether the myriad of tectonic and volcanic features represent the results of totally unrelated events or episodes organized on either a local or regional scale, perhaps related to some evolving process.Based on a detailed mapping of faults and fractures, combined with crater counts over a variety of surfaces, we have assembled a tectonic-volcanic history of the Tharsis region. The model includes the major regional events. Such a model, of course, would not account for event of a more localized nature. The proposed model separates the many fractures and faults into four distinct episodes of tectonic activity with well defined centers. Each of these episodes appears to be separated by a period of regional volcanism.

The oldest center of activity recognized in the region is located in the Thaumasia highlands, southeast of Tharsis. Faults of this episode are poorly exposed outside of these highlands because of subsequent burial by later, presumably volcanic units. The faulting associated with this center has been described by McGill (1978) and Frey (1979) and manifests itself as graben within the highlands and as controls on other structurs such as the walls of Valles Marineris.

Subsequent to the Thaumasia faulting a second center developed located in the northern Syria Planum region, located at approximately 8°S, 100°W longitude. Inlcuded in this locus of faulting are the numerous graben exposed in Claritas Fossae, north of Noctis Labyrinthus, Ceraunius Fossae and in parts of Memnonia and Mareotis Fossae. These correspond to most of the regional scale faults of the Tharsis area. Wise et al. (1979) defined this same area as a center of faulting for the Tharsis region as a whole by analysis of the orientation of all of the faults irrespective of their age.

The next locus of activity appears to be centered at 4°S, 110°W longitude, near the current site of Pavonis Mons. This center was active prior to the formation of the large shields and the extensive lava plains. Faults exposed in Memnonia and Maerotis Fosse, western Syria Planum and in Thaumasia can be grouped within this episode. Valles Marineris and its associated structures, as well as a large graben extending southeastward into Thaumasia from the Claritas Fossae region also formed during this period of tectonism. While the previous episodes of faulting appear to have been approximately radial to their centers, those of this event developed along a preferred northeast-southwest orientation.

The fourth and most recent episode of faulting was again centered near Pavonis Mons, but occurred after the formation of the shields and the lava plains. Faults associated with this period of activity occur on the lava plains and on the shields. This episode is the least extensive and may yet be active. Like the faults of the Pavonis center active prior to the

building of the shields, these faults also appear to have formed along a preferred northeast-southwest orientation. Generally, as opposed to the well developed graben and faults associated with the prior events, these tectonic features are lineaments or narrow graben. Another type of feature found at this time appears to be the mare like "wrinkle ridges" which occur on the plains surrounding Tharsis.

The Thaumasia, Syria, and pre-volcanic Pavonis centers all appear to be related to doming type uplifts. This type of model activity is further suggested by the elevated topography as well as the tensional nature of the faulting. By far the most common type of fault observed were radial graben, however in places concentric graben were also noted. Isolated fault scarps and lineaments are also present. In constrast to the ealier episodes the post-volcanic faulting may be related to stresses induced in the lithosphere by the load resulting from the volcanoes and volcanic plains (Phillips et al., 1981). In terms of the proposed model the faulting which characterizes Tharsis would then represent the result of organized episodes of tectonic activity. The center of doming appears to have migrated in a northwesterly direction with time, moving from Thaumasia to the central Tharsis area. Wether the progressive northwest migration of the centers of faulting, and hence doming, is merely coincidental or rather the result of movement of a zone of mantle upwelling or other deep seated process is more speculative in nature.

Along similar lines a question often debated has been the origin of the anomalously high topography of the Tharsis region. Two contrasting points of view have developed to explain the topography. The first supposes that it is constructional in nature and is the result of succesive outpourings of volcanic material (Solomon and Head, 1980). The second proposes that the topogrpahy is largely the result of tectonic uplift with only a thin veneer of volcanics on the top (Plescia and Saunders, 1981). In an attempt to examine this question we have studied the distribution of partially buried large (20 to 60 km diameter) craters, such that an estimatimation of the thickness of the Tharsis lavas could be made. The technique is similar to that employed by DeHon (1979) in his study of the thickness of the mare basalts. Using a relationship between crater diameter and rim height, estimates of the maximum lava thickness can be made where craters partially buried by lavas occur. One of the basic assumptions made here is that these large craters were formed in the pre-volcanic basement and that they do not occur at some intermediate level within the volcanic section. Based on the relatively young age of the Tharsis volcanics (Schaber et al., 1978) craters in the 20 to 60 size range occuring within the section would be unlikely. Partially buried craters occur in two principal locations; along the southern and southwestern flanks in the Memnonia and Phoenicis Lacus quadrangles, and in the northeast in the Tharsis and Lunae Palus quadrangles. Elsewhere their absence, particularly in the northwest, appears to result from the age of the pre-Tharsis volcanic basement. This basement appears to postdate the heavy bombardment and hence doesnot have large (20-60 km) craters superimposed on it.

These estimates, based on crater rim height data, indicate that the thickness of the volcanics increases toward the center of the region, near

TECTONICS OF THE THARSIS REGION

Plescia, J. B. and Saunders, R. S.

Pavonis Mons. In areas where reliable estimates can be made flow thickness range from 0 at the edge, to 600 - 700 meters well within the volcanic plains. This would account for 20 to 30% of the observed topography in these areas. If the 20-30% figure is correct and can be extrapolated over the entire region, it would indicate a 2 - 3 km maximum lava thicknesses near the center of the region. These estimates represent only the thickness of the volcanics on the plains.

REFERENCES: DeHon, R.A., 1979, Proc. Lunar Planet. Sci. Conf. 10th, 3635-3650. Frey J., 1979, J. Geophysical Res., 84, 1009-1023. McGill G.E., 1978, U.S.G.S. Misc. Inv. Series I-1077. Phillips R.J., Saunders R.S. and Banerdt W.B., 1981, in prep. Plescia J.B. and Saunders R.S., 1980, Proc. Lunar Planet. Sci. Conf. 11th, 2423-2436. Schaber G.G., Horstman K.C., and Dial A.L.,1978, Proc. Lunar Planet. Sci. Conf. 8th, 3430-3458. Solomon S.C. and Head J.W., 1980, Abs. Reports Planet. Geology Prog. 1979-1980, NASA TM 81776, 71-73. Wise D.U., Golombek M.P. and McGill G.E.,1979, Icarus, 38, 456-472.

This abstract represents one phase of research carried out at the Jet Propulsion Laboratory, California Institute of Technology, under Contract NAS 7 - 100, sponsored by the Planetary Geology Program Office, Planetary Division, Office of Space Science, National Aeronautics and Space Administration.

A CALIBRATED REFERENCE MAP OF MARTIAN BOLOMETRIC LAMBERT ALBEDOS.

L.K. Pleskot and E.D. Miner, Jet Propulsion Laboratory, 4800 Oak Grove Drive, Mail Stop 179-225, Pasadena, CA 91103.

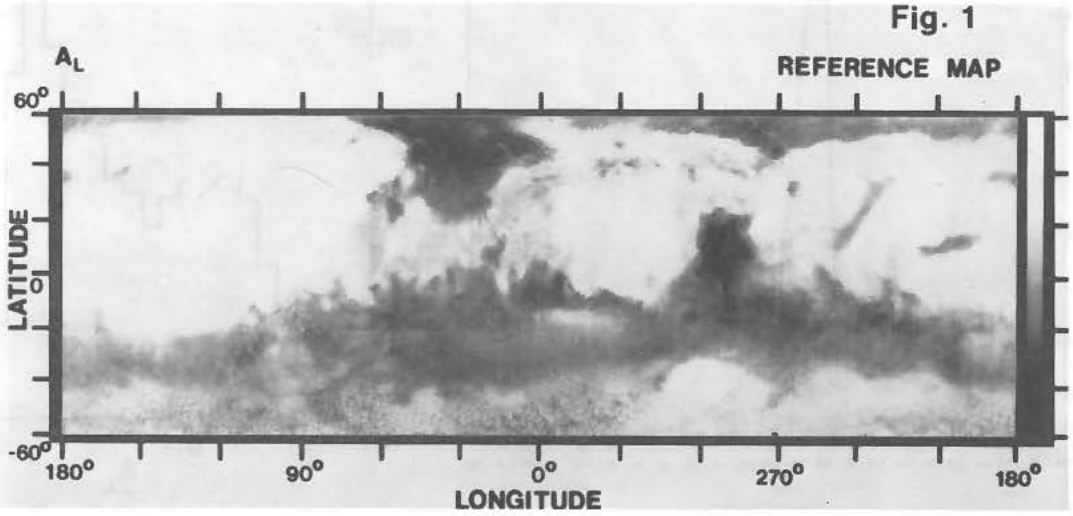

Figure 1 is a calibrated reference map of Martian bolometric Lambert albedos, as derived from solar band observations of the Viking infrared thermal mapper (IRTM). The seven IRTM solar band detectors simultaneously sample a passband of 0.3 to 3.0 μm, corresponding to the limits of significant solar illumination, and have a relatively gray spectral response (1). Lambert albedo A_L is solar band radiance divided by cos i, where i is the solar incidence angle. A_L represents a bidirectional surface albedo relative to a Lambert surface. Figure 1 is constructed as a weighted average of five maps from the set of eight time-sequential maps of Pleskot and Miner (2). The time-sequential maps and the reference map have global longitude coverage from -60^o to $+60^o$ latitude at 1^o by 1^o spatial resolution. The reference map has a linear gray scale from 0.05 at the dark end to 0.35 at the bright end, and areas in the map with no data are black. Calibration uncertainties are less than 2% of the given albedo values after correcting for inter-spacecraft, interdetector, and temporal gain variations.

Individual time-sequential maps contain data selected under strict geometric, range, quality, and time-of-day constraints for a narrow range of areocentric solar longitude L_s. These constraints are intended to minimize atmospheric or other effects at extreme conditions and albedo uncertainties caused by non-Lambertian surface photometric functions. The specific construction process used to produce the set of time-sequential maps allows the A_L maps to be indicative of true Martian bolometric albedo contrasts (2). Figure 2 shows the L_s ranges and τ_9' values associated with each time-sequential map. τ_9' is the 9-micron opacity computed from IRTM temperatures and adjusted to the surface elevation of Viking Lander 1 by assuming a 10 km dust scale height (2,3). Actual τ_9' data points are shown by crosses, and the solid curve is an estimated best fit to the data. Onsets of the first and second global dust storms of 1977 are labeled GS1 and GS2, respectively.

BOLOMETRIC ALBEDO MAP OF MARS

Pleskot, L. K. and Miner, E. D.

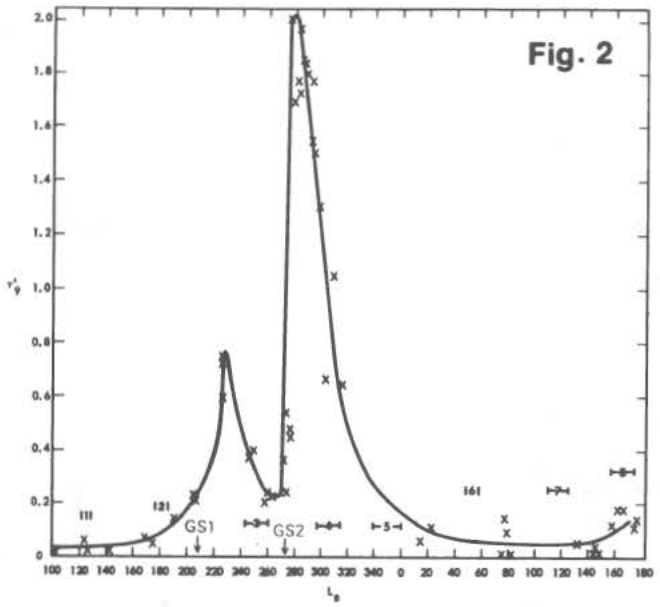

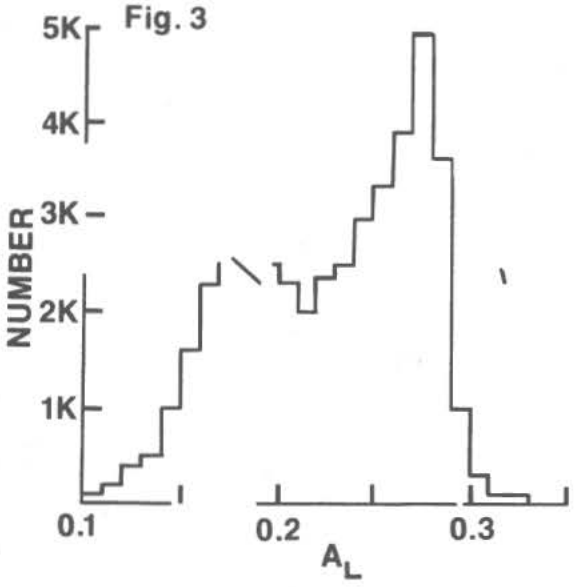

(Fig. 2 published courtesy of Academic Press, New York)

The reference map is produced by combining two maps (#1 and #2 in figure 2) before storm 1 with three maps (#5, #6, and #7) after storm 2. Maps 3 and 4 are not included in the reference map due to high dust opacity, and map 8 is excluded because it contains many transient brightenings. Latitude ranges of three of the maps ($\phi < -29^o$ for map 1, $\phi > 20^o$ for map 5, and $\phi < -32^o$ for map 6) are also not used in the reference map so that transient phenomena (local dust storms, condensate clouds, or ground frost) are minimized. Observations at phase angles from 5^o to 15^o in map 7 have been excluded from the reference map in order to remove anomalously high albedo values associated with small phase angle observations during this time period. Although map 7 has a smaller range of phase coverage than the other maps (5^o to 90^o), less than 2% of the data in any map occurs at phase angles smaller than 15^o. Hence, map 7 can be combined meaningfully with maps 1, 2, 5, and 6. Since long-term variations among the time-sequential maps are small, the reference map is probably representative of average Martian bolometric albedos.

Figure 3 is a histogram of the reference map data. The distribution of bolometric albedos is clearly bimodal with albedo population maxima corresponding to classical bright and dark Martian regions. Characteristic A_L values for bright and dark areas are 0.27 and 0.18, respectively. The reference map of bolometric Lambert albedos is generally quite similar in appearance to classical, visual albedo maps of Mars. It, therefore, seems likely that most Martian surfaces are composed of materials which are spectrally gray in the near infrared. However, this conclusion and the reference map itself should be regarded as preliminary because atmospheric scattering effects, discrete dust and condensate clouds, surface frosts, and surface photometric effects have not been completely removed, only minimized. The reference map has been contributed to the Mars Data Consortium at the United States Geological Survey in Flagstaff. Additionally, a map of Martian

BOLOMETRIC ALBEDO MAP OF MARS

Pleskot, L. K. and Miner, E. D.

bolometric normal albedos with corrections for surface photometric and atmospheric scattering effects is under construction (4).

References

(1) Kieffer, H.H. et al. (1977). J. Geophys. Res., 82, p. 4249-4291.

(2) Pleskot, L.K. and E.D. Miner (1981). Icarus, 45, MDAP issue, in press.

(3) Martin, T.Z. et al. (1979). J. Geophys. Res., 84, p. 2830-2842.

(4) Pleskot, L.K. and E.D. Miner (1982). J. Geophys. Res., Colloquium issue, in preparation.

BOLOMETRIC ALBEDO VARIATIONS OF BRIGHT AND DARK MARTIAN AREAS DURING THE VIKING MISSION. L.K. Pleskot and E.D. Miner, Jet Propulsion Laboratory, 4800 Oak Grove Drive, Mail Stop 179-225, Pasadena, CA 91103.

Fig. 1

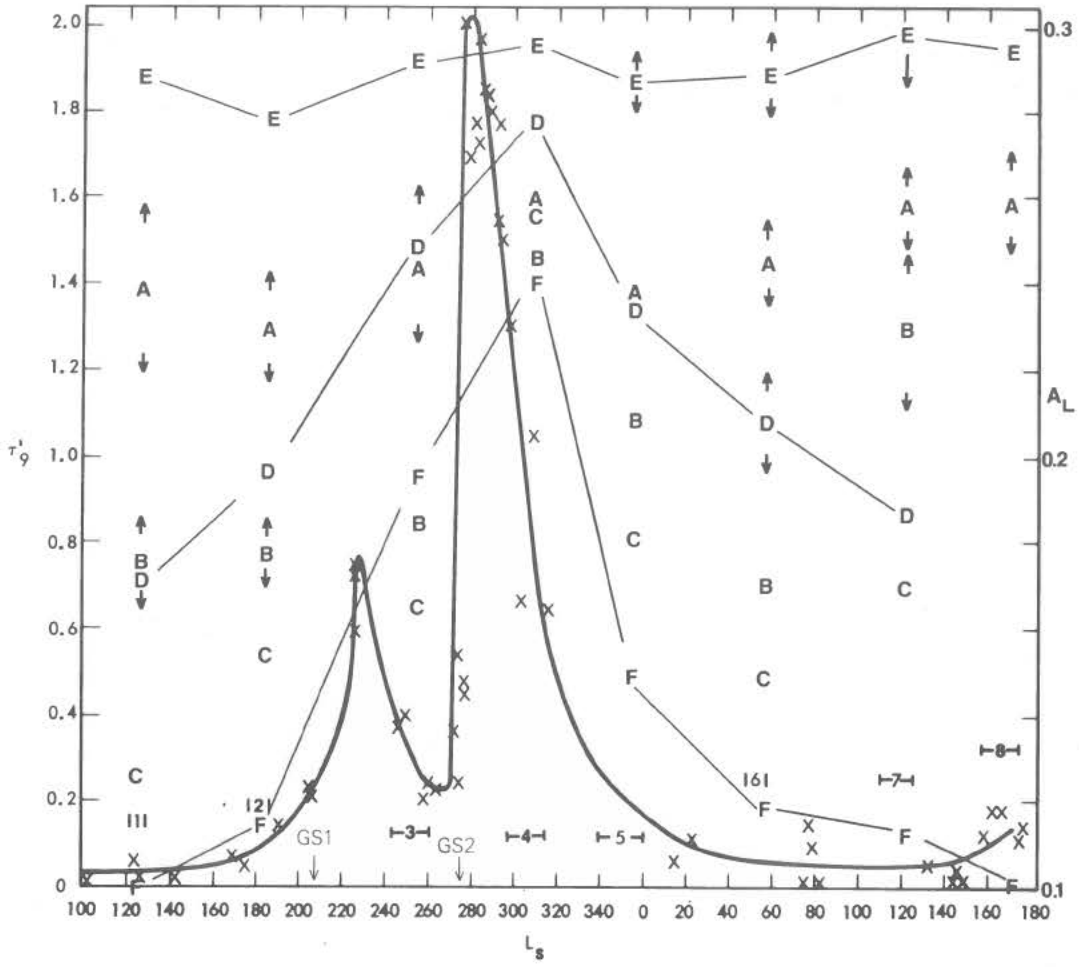

Figure 1 presents a comparison of Martian atmospheric opacity with bolometric Lambert albedos of several bright and dark local Martian areas. τ'_9 is the 9-micron opacity computed from Viking infrared thermal mapper (IRTM) temperatures and adjusted to the surface elevation of Viking Lander 1 by assuming a 10 km dust scale height (1,2). Actual τ'_9 data points are indicated by crosses, and the continuous solid curve is an estimated best fit to the data. The onsets of the first and second global dust storms of 1977 are labeled GS1 and GS2, respectively. Figure 1 spans more than a Martian year in areocentric solar longitude L_s. Bolometric Lambert albedos are derived from IRTM solar band observations. The seven IRTM solar band detectors simultaneously sample a passband of 0.3 to 3.0 μm, corresponding to the

BOLOMETRIC ALBEDO VARIATIONS OF MARTIAN AREAS

Pleskot, L.K. and Miner, E. D.

spectral limits of significant solar illumination, and have a relatively gray spectral response (3). Lambert albedo A_L is the solar band radiance divided by cos i, where i is incidence angle. A_L represents a bidirectional surface albedo relative to a Lambert surface.

Albedo data in figure 1 are taken from the set of eight time-sequential global albedo maps of Pleskot and Miner (2). The time-sequential maps have global longitude coverage from -60^o to $+60^o$ latitude at 1^o by 1^o spatial resolution. Calibration uncertainties are less than 2% of the given albedo values in these maps. Individual time-sequential maps contain data selected under strict geometric, quality, range, and time-of-day constraints for a narrow range of L_s. These constraints are designed to minimize atmospheric or other effects at extreme conditions and albedo uncertainties caused by non-Lambertian surface photometric functions. L_s range of each map are indicated in the figure. The construction process used to produce the set of time-sequential maps ensures that the A_L maps should be representative of true bolometric albedo contrasts (2). Transient phenomena (local dust clouds, condensate clouds, or surface frost), atmospheric scattering effects, and surface photometric effects have not been completely removed from the maps, but such effects have been minimized sufficiently to allow meaningful comparisons between the maps.

The six local areas depicted in figure 1 are lettered A - F and are all near-equatorial in order to maximize L_s coverage. Two bright and four dark regions are included. Each area is 3^o by 3^o, containing nine spatial elements. Error bars indicate the standard deviation of data in each area, and small error bars are not shown. The main contribution to the error bars shown is surface albedo variation across the given 3^o by 3^o area. The names and central locations of these areas are A = Tithonium Chasma (-6^o, 89^oW), B = Juventae Chasma (-5^o, 61^oW), C = Sinus Meridiani (-5^o, 2^oW), D = Cerberus (10^o, 213^oW), E = Medusae Fossae (0^o, 166^oW), and F = Syrtis Major (13^o, 292^oW).

Several important trends are apparent in figure 1. First, bright and dark regions behave differently in response to a dust storm. Dark regions appear to brighten markedly during a storm and then redarken afterwards, while the brighter regions maintain nearly constant brightness. Perhaps, the mobile component of global dust storms has an albedo comparable to that of typical bright regions. Second, dark regions behave differently from each other during dust storms. All dark regions in figure 1 redarken back to original albedos after storm 2, but they do so at different rates. Perhaps, dark areas are generally less homogeneous than bright areas. Also, some dark regions (B and C) rebrighten near $L_s = 100^o$. This phenomenon does not seem to be albedo-dependent but may be longitude-dependent and related to local dust storm sites. Next, an upper limit to solar band opacity τ_s can be computed from observed albedos of brightened dark areas and bright areas during a storm. If the dust's albedo is equal to the albedo of typical bright regions, then $\tau_s = -\ell n[(A - A_B)/(A_D - A_B)]$ where A is apparent dark area albedo, A_B is intrinsic bright area albedo, and A_D is intrinsic dark area albedo. From figure 1, $\tau_s \sim -\ell n[(0.24 - 0.29)/(0.10 - 0.29)] \sim 1.3$. Thus, solar band opaicty is comparable to 9-micron opacity for map 4 and is smaller than anticipated from visual opacity measurements (4).

A final important trend in figure 1 is the decreasing albedo of dark

areas D and F from $L_s = 0^o$ to 160^o. Both areas darken considerably during times of nearly constant or even increasing atmospheric opacity. To the extent that the global τ_9' curve applies to local areas, such behavior is consistent only with a surface cleansing mechanism. Thus, it appears that enough dust was deposited on the surface of Cerberus and Syrtis Major to cause an albedo increase of at least 0.02 following storm 2 of 1977. This deposited dust seems to have been subsequently removed gradually and completely in the case of Syrtis Major. Perhaps, very dark areas such as Syrtis Major can act as local dust sources during globally clear periods on Mars. This suggestion appears to be supported by results of spectral-differencing techniques, as applied to IRTM thermal channel data (5).

References

(1) Martin, T.Z. et al. (1979). J. Geophys. Res., 84, p. 2830-2842.

(2) Pleskot, L.K. and E.D. Miner (1981). Icarus, 45, MDAP issue, in press.

(3) Kieffer, H.H. et al. (1977). J. Geophys. Res., 82, p. 4249-4291.

(4) Pollack, J.B. (1979). J. Geophys. Res., 84, p. 2929-2945.

(5) Christensen, P.R. (1981). Lunar and Planet. Sci., XII, p. 135-137.

VIKING DIFFUSER PLATE MEASUREMENTS: POSSIBLE EVIDENCE FOR DUST IN ORBIT AROUND MARS? L.K. Pleskot and E.D. Miner, Jet Propulsion Laboratory, 4800 Oak Grove Drive, Mail Stop 179-225, Pasadena, CA 91103.

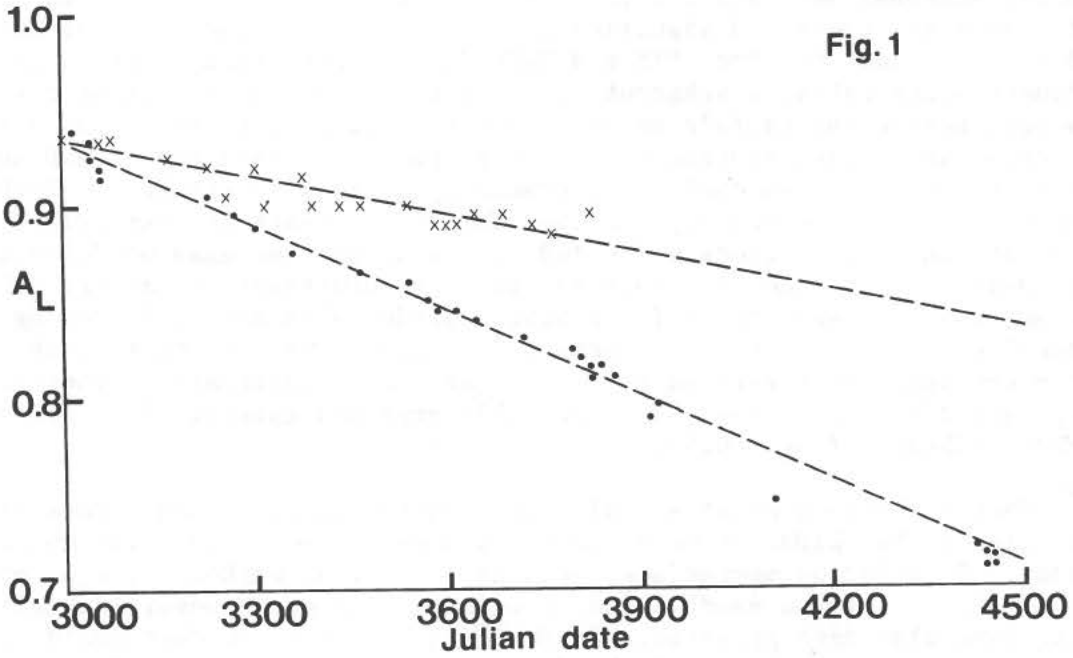

Figure 1 presents a history of Lambert albedos A_L for the Viking Orbiter 1 diffuser plate. The diffuser plate is a small, sandblasted, aluminum square intended as a calibration target for both the Mars atmospheric water detector (MAWD) and infrared thermal mapper (IRTM) instruments. The plate is fixed relative to both instruments at about 45° emission angle for a nominal incidence angle of 45° in a specular configuration. The observations in figure 1 span the entire Viking mission from VO1 revs 55 to 1483. Although Viking Orbiter 2 diffuser observations are basically consistent with those of VO1, no VO2 data are included because they cover only a brief period in the mission. IRTM and MAWD observations in figure 1 are indicated by dots and crosses, respectively.

Bolometric Lambert albedos for the IRTM are derived from solar band observations. The seven IRTM solar band detectors simultaneously sample a passband of 0.3 to 3.0 μm, corresponding to the limits of significant solar illumination, and have relatively gray spectral response (1). Bolometric Lambert albedo is the solar band radiance divided by cos i, where i is incidence angle. A_L represents a bidirectional albedo relative to a diffuse (Lambert) surface. Due to a design error, only three of the seven IRTM solar band detectors could be properly pointed at the diffuser plate. Consequently, IRTM data in figure 1 are the average of observations from

VIKING DIFFUSER PLATE DARKENING

Pleskot, L.K. and Miner, E. D.

detectors D5, D6, and D7. Spectral Lambert albedos from MAWD data are an average of observations from two continuum channels (#2 and #4) in a narrow passband at 1.38 μm (2).

According to both instruments, the VO1 diffuser plate shows substantial apparent darkening throughout the course of the Viking mission. MAWD data contain somewhat more scatter than IRTM observations, but the trend lines in both cases are clear and significant. Overall albedo decreases of about 25% and 10% are indicated for IRTM and MAWD data, respectively. Thus, the diffuser plate exhibits substantial apparent reddening as well as darkening. However, before the plate's apparent decrease in brightness can be attributed to actual darkening, instrumental effects must be considered. MAWD and IRTM detector sensitivities could have gradually decreased with time. MAWD detectors can not be readily examined for such variations, but IRTM detectors have internal calibrations which indicate a slight increase of detector responsivity with time, possibly due to slow outgassing processes. Therefore, the apparent decrease in diffuser plate albedo is an actual darkening (and reddening) of the plate. Furthermore, the darkening appears to have started after the spacecraft arrived at Mars. Laboratory calibrations indicate that preflight diffuser plates were spectrally gray and essentially diffuse with Lambert albedos of $A_L \sim 0.94$.

What mechanisms might explain the observed diffuser plate darkening? Essentially, two kinds of mechanisms are possible — irradiative and depositional. Irradiation mechanisms, such as solar wind darkening, are not likely to be efficient for a sandblasted, aluminum surface. However, depositional mechanisms also have problems. Contamination by Martian dust could provide the proper coloring, but it is hard to account for the required amount of aerosol at orbiter periapsis altitudes. Deposition of infalling satellite dust could provide the correct darkening, but the observed reddening would be difficult to simulate since the satellites are essentially black (3). Contamination by the attitude control system is not possible because the system utilized a pressurized cold gas. Deposition of engine plume contaminants from orbit insertion and trim maneuvers may have occurred, along with subsequent photopolymerization of deposited material. Such a mechanism might be capable of causing the observed darkening and reddening, but quantitative estimates of the effect are rather difficult. Furthermore, the data do not show any marked changes in darkening rate following engine burns. In summary, the VO1 diffuser plate has darkened and reddened considerably throughout the Viking mission, but no adequate spacecraft-related mechanism has been discovered to explain this effect, and Mars-related mechanisms require circumstances not presently postulated for the system.

References

(1) Kieffer, H.H. et al. (1977). J. Geophys. Res., 82, p. 4249-4291.

(2) Farmer, C.B. et al. (1977). J. Geophys. Res., 82, p. 4225-4248.

(3) Pang, K.D. et al. (1978). Science, 199, p. 64-66.

ASTRONOMICAL VARIATIONS, DUST STORM FREQUENCY, AND POLAR LAMINAE.
J. B. Pollack, NASA Ames Research Center, Moffett Field, CA 94035

In this paper, we investigate the ways in which the various astronomical variations can influence the frequency of dust storm activity and hence the amount of dust suspended in the atmosphere and deposited in the polar regions. We also consider the potential impact of dust deposited in the polar regions on the stability of volatiles there.

There are three factors that determine the amount of dust suspended in the Martian atmosphere: the wind speed distribution function, the threshold speed needed to set particles into motion, and the availability of particles with sizes in both the saltation (≈ 100 μm) and suspension (≈ 1 μm) range. We will emphasize the first two factors, although the latter could limit the amount of dust loading under conditions of high dust storm activity. The first factor is not expected to vary significantly with atmospheric pressure until the atmospheric pressure becomes much larger (≈ 100 mb) than its present value, in which case it will shift towards smaller wind speeds. However, the wind speed distribution function can be affected by the amount of sunlight falling on the planet and then will shift towards higher wind speeds near perihelion. Particularly for the current value of the surface pressure, eccentricity variations can therefore impact the frequency of dust storms.

The threshold wind speed for dust movement depends sensitively on the value of the surface pressure. At present, it is only the extreme high speed end of the wind speed distribution function that is capable of producing dust storms. A reduction in the surface pressure by a factor of more than about 3 will result in a complete cessation of dust storms. Conversely, an increase in surface pressure by a factor of 3 will lead to a substantial increase in dust storm frequency. Both types of pressure modulations are predicted to result from obliquity variations through modifications of the partitioning of CO_2 between the atmosphere and regolith. Thus, obliquity variations may be the dominant factor in modulating atmospheric dust loading and hence the dust deposition rate in the polar region, where the laminae were formed.

At present, both the permanent and seasonal polar caps have visible albedos significantly less than unity, as would be expected for a pure ice surface. It is likely that embedded dust particles are responsible for the lower albedo. Consequently, the stability of a permanent CO_2 ice cap can be profoundly affected by the amount of dust suspended in the atmosphere and deposited in the polar regions. The sharp decrease in dust loading at times of lower obliquity will act as a positive feedback mechanism for establishing permanent CO_2 ice deposits at both poles.

THE ANNUAL CYCLE IN ATMOSPHERIC TEMPERATURES AT THE VIKING SITES -- OBSERVATIONS AND MODELING RESULTS; Keith Ronnholm and Conway B. Leovy, Geophysics Program AK-50, University of Washington, Seattle, Wash. 98195

Introduction

Data returned by the Viking Lander meteorology experiment has been analyzed to produce a time series of the daily variations in Martian atmospheric temperature over the first Martian year at both sites. These observations have been compared to time series generated by a radiative-convective equilibrium model and the comparison suggests refinement in the physical properties of the surface materials and of the dust aerosol. Comparisons of the model with radiance data from the Viking Infrared Thermal Monitor (IRTM) (1) has provided a means for inferring large-scale vertical velocities.

Observations

The Viking Lander meteorology experiment measured atmospheric temperatures 1.7 m above the Martian surface. The data were binned into 25 equal time groupings per sol and cubic spline interpolation was used to fill gaps of less than 7 consecutive bins. Data influenced by flow over the lander was excluded from the averages. Daily mean, minimum, and maximum temperatures were determined from the binned data for the first 700 sols, thus documenting more than one Martian annual cycle and extending the work of Ryan and Henry (2). The temperature time series followed the annual cycle in insolation with minimum temperatures of 170 K (Lander 1, 22.3N) and 152 K (Lander 2, 47.7°N). Maximum temperatures recorded were 253 K (Lander 1) and 249 K (Lander 2). The smooth annual cycle was disturbed by the occurance of two global dust storms during which the mean temperature rose slightly and the daily range in temperature decreased. Smaller scale temperature variations of order ±6K having a time scale of 2-7 days were superimposed on the annual cycle and occurred most strongly during autumn and spring at Lander 2. The disturbances associated with these variations have been analyzed in detail by Barnes (3,4) and are attributed to eastward travelling planetary waves.

Model description

A radiative-convective equilibrium model has been developed for application to the Martian atmosphere. The model includes absorption of solar radiation and absorption and emission of thermal radiation by CO_2; scattering, absorption, and emission of solar and infrared radiation by aerosol; convective heat flux from the surface; and conduction into the ground. The delta-Eddington approximation was employed for the aerosol radiation calculation with three aerosol spectral bands in the infrared. Choices of parameter for these bands were obtained from comparisons with a 40 band model based on the data of Toon, Pollack, and Sagan (5). Aerosol optical properties in the visible and optical depths were taken from Pollack et al. (6) and the dust was assumed to be distributed uniformly with atmospheric pressure. The atmosphere was divided into ten layers with maximum resolution near the surface in order to resolve the boundary layer. Convective adjustment was applied to the dry adiabatic lapse rate and the Businger-Dyer empirical model (7) was used to simulate the surface convective heat flux

and near surface temperature profile. The underlying ground surface was characterized by 100 layers of 2 cm thickness, and albedo and uniform thermal inertia as derived by Kieffer (8). After a 20 sol initial stabilization period, the model was run for the full annual cycle producing a time series of temperatures for comparison with the observations. The time series of equivalent radiance temperatures that would be seen by the IRTM 15 μm channel was also generated.

Model results, Lander 1

Model temperatures for VL-1 were higher than those observed; typically +10K for minimum and mean and +20K for the 15 μ band equivalent temperature. However, the daily range in temperature was very well simulated for the entire year including dust storm periods. The temperature discrepancies may be due to a combination of factors, including: rising motion above the site, a higher single scattering albedo for the dust aerosol, non uniform dust distribution in the vertical, variation of surface and/or aerosol optical properties with season, or smaller ratios of infrared to visible optical depths than those assumed. The discrepancy in the simulated 15 μm band radiance clearly points to rising motion and consequent dynamical cooling as one important factor, however.

Model results, Lander 2

Model temperatures at Lander 2 were generally quite close to those observed during spring and autumn but were too cold during mid-winter. The overall agreement suggests that the physical properties of the surface and aerosol at the Lander 2 site were adequately represented by the model. Excellent agreement between the model and observations was obtained during the mid-winter period by including large-scale subsidence with typical velocities of 2-6 cm/s. This subsidence over Lander 2 and the corresponding rising motion over Lander 1 are consistent with a global scale thermally forced Hadley circulation such as that modeled by Haberle (9).

References

(1) Martin, T. Z. and Kieffer, H. H. (1979) J. Geophys. Res., 84, 2843-2852.

(2) Ryan, J. A. and Henry, R. M. (1979) J. Geophys. Res., 84, 2821-2829.

(3) Barnes, J. R. (1980) J. Atmos. Sci., 37, 2002-2015.

(4) Barnes, J. R. (1981) J. Atmos. Sci., 38, 225-234.

(5) Toon, O. B., Pollack, J. B. and Sagan, C. (1977) Icarus, 30, 663.

(6) Pollack, J. B., Colburn, D. S., Flasar, F. M., Kahn, R., Carlston, C. E., and Pidek, D. (1979) J. Geophys. Res., 84, 2929-2945.

(7) Businger, J. A., Wyngaard, J. C., Izumi, Y., and Bradley, E. F. (1971) J. Atmos. Sci., 28, 181-189.

(8) Kieffer, H. H., Martin, T. Z., Peterfreund, A. R., Jakowsky, B. M., Miner, E. D., and Palluconi, F. D. (1977) J. Geophys. Res., 82, 4249-4292.

(9) Haberle, R. M. (1981) Some Effects of Global Dust Storms on the Atmospheric Circulation of Mars. Ph.D. Thesis, Dept. of Amtos. Sci., University of Washington, Seattle 19895.

GEOMORPHIC EVOLUTION OF MARS, Lisa A. Rossbacher, Dept. of Geological and Geophysical Sciences, Princeton University, Princeton, NJ 08540 (Current address: Dept. of Geology, Whittier College, Whittier, CA 90608)

The surface of Mars contains a rich record of the processes that have acted on it during its history; such an extensive record is unique in the Solar System. The landforms on a planetary surface are the result of interactions through time between the surficial materials and the effective energy driving the planet's geomorphic processes. Thus, the distribution of landforms through time can be used to interpret the geomorphic evolution of the planet and roughly constrain the effective geomorphic energy. The analysis presented here synthesizes and extends existing reconstructions of Mars' geomorphic evolution, which include the tectonic evolution (1) and the planet's cratering history (2,3).

The method used in this study is a modification and extension of a classical geomorphic concept. W.M. Davis (4) stated that all landscapes are a function of process + structure + stage. For application to planetary surfaces in general, processes can be subdivided into process and energy, which is equivalent to intensity. The geomorphic evolution of Mars may then be evaluated through

ENERGY + PROCESS + STRUCTURE + TIME ⟶ HISTORY

The geomorphic evolution of Mars can be described by a series of four geomorphic regimes, each of which is characterized by a dominant process or group of processes. Each regime reworked and modified earlier landforms.

The earliest geomorphic regime on Mars was dominated by impact cratering, resulting in a lunar-like topography. The heavily cratered plains are remanent from this period, which ended with the end of late heavy bombardment, about 3.5 b.y. ago (5). The geomorphic regime that followed was dominated by fluvial and aeolian processes which may have been induced by a denser early atmosphere. These processes caused fluvio-aeolian modification of older cratered topography. Existing evidence for this regime includes the small channels in the heavily cratered terrain (6), whose formation probably coincided with outgassing of the early atmosphere (7). Aeolian landforms from this period have almost certainly been reworked by subsequent activity, but some cemented dunes may still persist from this regime. Wind power, and therefore effectiveness, probably peaked with the maximum atmospheric density during this period. This regime also corresponds with the inferred period of internal heating and partial differentiation of the planet; this internal heating and expansion also initiated tensile stresses in the crust (1). This period ended about 2.5 - 3.0 b.y. ago, probably corresponding with the loss of volatiles from the atmosphere and surface into the subsurface.

GEOMORPHIC EVOLUTION OF MARS

Rossbacher, Lisa A.

The next geomorphic regime was characterized by volcanic and tectonic activity, beginning with plains volcanism, forming some of the intercrater plains, and grading into shield volcanism. The volcanic constructs of the Tharsis and Elysium areas are outstanding examples of the latter. Aeolian activity continued throughout this period, varying as a function of the atmospheric density, which in turn fluctuates with the martian obliquity cycle on a million-year time scale (8,9). This period came to an end with the cessation of the Tharsis volcanism, estimated at approximately 200 - 800 m.y. ago (10). The current geomorphic regime on Mars is dominated by aeolian processes which continue to vary in intensity with the obliquity cycle (9); these changing orbital parameters are probably responsible for the layered polar terrain (11).

Mass movement has been active throughout the history of Mars. Because there is no planet-wide base level, this process is effective only on a local scale. Mass-movement activity probably reached a maximum associated with the uplift of the Tharsis plateu, volcanism, and fracturing. Mass movement is probably also, in part, a function of incorporated volatiles. Lobate debris flows may reflect the presence of subsurface water in solid or liquid form (12). The most spectacular examples are seen in the grabens of the Valles Marineris, but small-scale slumps have been observed at the Viking I lander site (13).

The early lunar topography of Mars was the only regime in which the landforms reflected the dominant processes. All subsequent regimes superimposed younger features on pre-existing forms, creating a palimpsest which records the overlapping and varying geomorphic regimes of different ages. The history of geomorphic processes and their intensity (energy) places rough constraints on the past geomorphic energy budgets for Mars.

This research was supported in part by NASA grant NSG-7568.

References Cited

(1) Toksöz M.N. and Hsui A.T. (1978) Icarus 34, p. 537-547.
(2) Chapman C.R. and Jones K.L. (1977) Ann. Rev. Earth Planet. Sci. 5, p. 515-540.
(3) Neukum G. and Hiller K. (1981) J. Geophys. Res. 86, p. 3097-3121.
(4) Davis W.M. (1899) Geog. J. 14, p. 481-504.
(5) Wetherill G.W. (1975) Proc. Lunar Sci. Conf. 6th, p. 1539-1565.
(6) Pieri D. (1976) Icarus 27, p. 25-50.
(7) McElroy M.B., Kong T.Y., and Yung Y.L. (1977) J. Geophys. Res. 82, p. 4379-4388.
(8) Ward W.R. (1973) Science 181, p. 260-262.
(9) Pollack J.B. (1979) Icarus 37, p. 479-553.

GEOMORPHIC EVOLUTION OF MARS

Rossbacher, Lisa A.

(10) Carr M.H. (1974) J. Geophys. Res. 79, p. 3943-3949.
(11) Cutts J.A. (1973) J. Geophys. Res. 78, p. 4231-4249.
(12) Squyres S.W. (1978) Icarus 34, p. 600-613.
(13) Jones K.L., Arvidson R.E., Guiness E.A., Bragg S.L., Wall S.D., Carlston C.E., and Pidek D.G. (1979) Science 204, p. 799-806.

LABORATORY STUDY OF MARTIAN CLOUD MICROPHYSICS

Kenneth Sassen

University of Utah
Salt Lake City, Utah 84112

ABSTRACT

The microphysical and light scattering properties of the cloud particles likely to be encountered, albeit infrequently, in the Martian atmosphere are currently being studied in our Planetary Atmosphere Simulation chamber. This 50 liter, cryogenic vacuum chamber is 1.1m in height and contains a lower equipment bay with viewports to permit laser scattering studies. A magnetically-coupled slide injector is used to collect cloud particles from the chamber for photomicrographic examination.

Martian cloud simulations are being conducted through an appropriately large range of temperatures using water vapor in carbon dioxide and pure carbon dioxide atmospheres (see Figure 1). Dependence on temperature of ice particle habits is indicated from the preliminary results. Backscatter linear depolarization ratios from 0.633μm laser light appear to be independent of temperature for pure carbon dioxide crystals, but water ice values decrease dramatically at temperatures $\lesssim$ 200° K due to the presence of near-spherical vitreous ice particles.

A comprehensive overview of the properties of these clouds will be presented as the more complete data set becomes available.

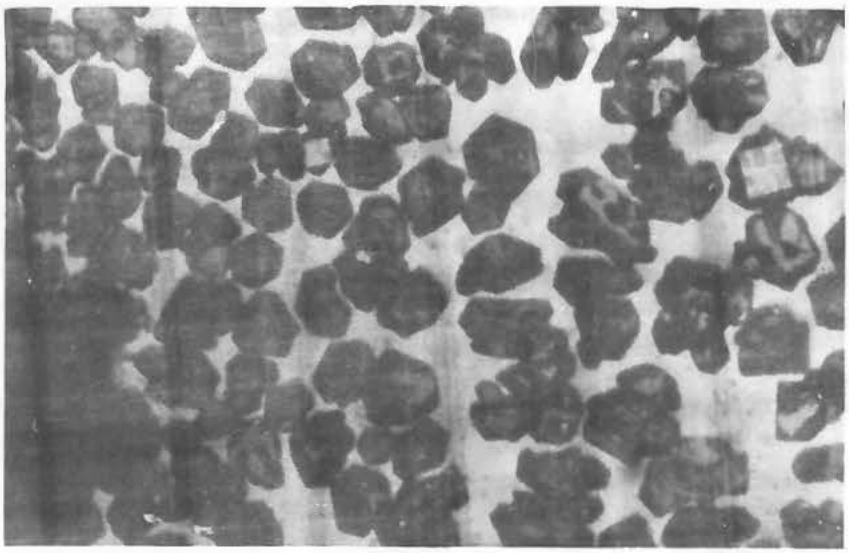

Figure 1. Pure carbon dioxide crystals grown at 145°K and 840 mb. Grid boxes are 135μm.

GEOLOGIC CONSTRAINTS ON THE EVOLUTION OF THE THARSIS REGION. R. S. Saunders, Jet Propulsion Laboratory, California Institute of Technology, Pasadena, California 91109.

Some progress has been made in understanding the tectonic evolution of the Tharsis region by consideration of geologic constraints on models of crustal stress that would arise from the existing gravity and topography. Topographically defined, the Tharsis region is bounded on the east by the Coprates rise which extends southward of Coprates Chasma at 58° West. The region is bounded on the south by Thaumasia, on the west by Olympus Mons and on the north by Alba Patera. The geologic domains within the region have generally southwest, northeast trends. In the southeast, the oldest terrains are defined by the ridged plains of Solis Planum, Sinai Planum and Lunae Planum. The youngest terrains are to the northwest which are occupied by the large shield volcanoes and the most recent lava flows. Gravity anomalies appear to be largely confined to the regions occupied by the most recent surficial units. The general geology and structure of the region has been outlined most recently by Wise et al. (1). We have recently completed detailed quadrangle mapping of ridged plains and graben-like features on Mars and compared them with theoretical stress models derived by Banerdt (this volume). The most important geologic observation to arise from these comparisons is that surface structural features tend to be aligned (parallel or perpendicular) with principal stresses at the surface of the planet. This is not the situation one might predict (see for example Melosh (2)) since in most terrestrial near-surface tectonic situations fracturing occurs at some angle to the principal stress trajectories. Qualitatively this would suggest that the vertical component of the deviatoric stress is non-zero. For the graben this is a situation that implies that fracturing was initiated at some depth within the lithosphere and that the lithosphere itself was not in a hydrostatic condition (Banerdt, personal communication).

Other geologic constraints regarding the origin of Tharsis may be used to address the competing hypotheses of whether the primary origins of the topography associated with Tharsis is by tectonic uplift or by volcanic buildup. The former was proposed early by Phillips et al. (3) based on the existence of elevated older terrain associated with the Claritas Flossae region. The former hypothesis, volcanic buildup, was proposed by Solomon and Head (4). Two geologic constraints would appear at this time to favor the uplift hypothesis. (1) There exists ancient cratered terrain at relatively high elevation within the Tharsis region, that is, in the southern part of Claritas Fossae and in the Thaumasia Fossae region. Thus the volcanic edifice hypothesis would require a two-phase buildup separated by some unknown but perhaps considerable length of time. A second bit of geologic evidence favoring uplift is in the report by Saunders et al. (5) of erosional hogback ridges flanking the uplifted area in the region of the

Tharsis Geologic Constraint

Saunders, R. S.

Coprates rise. The structure and stratigraphic setting suggests that layered materials which are exposed in the nearby Coprates Chasma were tilted somewhat in the uplift and subsequently eroded to produce the cuesta ridges.

A final example of a geologic constraint arises from our recent studies of the ridged plains of Mars. These are the oldest wide-spread units on Mars other than the cratered terrain. They are typified by surficial ridges resembling those on the lunar maria which typically are ten to hundreds of kilometers in length and a few hundred meters to 10 km wide. Regions of the ridged plains that exhibit parallel ridges occur on and nearest to the Tharsis region. They are consistent with present-day compressional stresses rising from the load associated with the central Tharsis region. These ridges may be interpreted to be related to the long-term viscous response of crustal rocks to the Tharsis load. To test this hypothesis, the spacing of the ridges may be considered to be a dominant wavelength of folding. Using a simple relationship developed by Biot (6) we can relate the thickness of the layer to the ratio of the viscosities of the layer and its substrate. The thickness or relative thickness of the layer is estimated by observations of the largest crater that has been completely buried by the plains and a relationship between crater rim height and diameter. It is found that the ratio of ridge spacing to plains thickness is approximately constant over a wide range of ridge spacing and plains widely scattered over Mars. This implies, first of all, that the plains materials have uniform characteristics over Mars and that they have an effective viscosity ratio, plains to substrate, of about 500. This finding tends to confirm the hypothesis that ridge spacing is related to dominant wavelengths of folding and thus tends to confirm a structural and Tharsis-related origin to the ridges. Ridges, of course, if they are viscous phenomena, could form under very low stresses.

The next task is to begin to unravel the stress history of Mars by detailed geologic analysis of the sequence of formation of various structures both ridges and graben, and the sequence, volume, and ages of various volcanic units to further refine the geophysical models.

REFERENCES

(1) Wise, D. U., Golombek, M. P., and McGill, G. E., 1979, Tharsis province of Mars: Geologic sequence, geometry, and a deformation mechanism, Icarus, V. 38, p. 456-472. (2) Melosh, H. J., 1980, Tectonic patterns on a reoriented planet: Mars, Icarus, V. 44, p. 745-751. (3) Phillips, R. J., Saunders, R. S., and Conel, J. E., 1973, Mars, crustal structure inferred from bouguer gravity anomalies: Jour. Geophys. Res., V. 78, p. 4815-4820. (4) Solomon, S. C. and Head, J. W., 1980, Tharsis: An alternative explana-

tion, NASA TM 81776, p. 71-73. Saunders, R. S., et al, 1980, Early volcanic-tectonic province: Coprates region of Mars, NASA TM 81776, p. 74-75. (6) Biot, M. A., 1961, Theory of folding of stratified viscoelastic media and its implications in tectonics and orogenesis: bull. G. S. A., V. 72, p. 1595-1620.

SYRTIS MAJOR REVISITED: A HIGHLAND VOLCANIC PLANUM, NOT A PLANITIA - Gerald G. Schaber and Kenneth L. Tanaka, U.S. Geological Survey, 2255 North Gemini Drive, Flagstaff, AZ 86001; and John K. Harmon, National Astronomy and Ionospheric Center, Arecibo, PR.

By definition [1], a planum on Mars denotes a plateau on high plain (e.g., Lunae Planum, Syria Planum, Hesperia Planum), whereas a planitia is defined as a low plain (e.g., Isidis Planitia, Amazonis Planitia, Utopia Planitia). Immediately following the Mariner 9 mission, the circular plain called Syrtis Major (after the classical low-albedo feature) was labeled a planitia because the elevation data from Mariner 9 indicated that its surface, although not totally at low elevation, rises gradually to the west from the level of Isidis Planitia immediately to the east [2].

Radar elevation-profile data obtained in 1978 at the National Astronomy and Ionospheric Center (Arecibo, P.R.), and included in a recently submitted paper by Simpson et al. [3], reveal that the entire region of Syrtis Major is generally at the same level as or higher than the hilly and cratered and cratered plateau surfaces immediately to the west. East Syrtis Major, a previously unrecognized eastward-facing 0.8° slope between (279° and 285°) was found to characterize its border with Isidis Planitia (Fig. 1). The authors will recommend that the name Syrtis Major Planitia be changed to Syrtis Major Planum so that the change can be reflected on the new 1:15 million-scale global geologic and topographic maps of Mars being prepared under NASA sponsorship.

Gravity [4], topographic, and photogeologic data all clearly support the origin of the generally circular Isidis Planitia as an ancient impact basin. Syrtis Major, on the other hand, is not the site of an impact event as was indicated and reported as a possibility during early 1:5 million-scale geologic mapping from Mariner 9 images [5,6]. Scott and Carr [2] properly mapped the Syrtis Major feature as a major volcanic complex on their 1:25 million-scale geologic map of Mars.

Viking Orbiter images have permitted the mapping of extensive lava flows and the recognition of major volcano-tectonic features within the center of Syrtis Major. Two collapsed calderas 45 and 70 km in diameter have produced late-stage lava flows that radiate out to the north, south, and west, and overlie ridged plains materials (older volcanic flows). The breached collapsed caldera (Cvt-1 in Fig.1) was mapped as a volcanic vent source by Scott and Carr [2]; the circular caldera (Cvt-2 on Fig. 1) has not been previously recognized as a volcanic feature. Older, mostly buried, concentric segments of grabens (see 1, 2, and 3 on Fig. 1) indicate that both calderas lie within a circular, 280-km-diameter, volcano-tectonic collapsed depression that has not been previously recognized. The 1978 Arecibo radar topographic profile across Syrtis Major at lat 10.34° N° shows a slight dip at the location of the suspected depression 292.5° as it crosses the northern edge of this feature at long (Fig. 1). Simpson et al. [3] reported that the regional topographic high, as shown on the radar profile, corresponds to the north flank of the Cvt-1 caldera, and that lava flows appear to have followed the gentle slopes away from the caldera summit (Fig. 1). From the topographic profile, we have calculated regional surface slopes of 0.18° and 0.14°, respectively, immediately east and west of the intersection of the profile with the northern flanks of the caldera. The slopes from the actual caldera summit were not be determined, but should be somewhat higher. Farther east along the profile, the slope increase to 0.25° in the local vicinity of recent fissure volcanism (centered at about lat 12.5° N. and long 282.5°). To the west of caldera

Cvt-1, the profile is almost level until the cratered plateau terrain is encountered at long 301.5° (Fig. 1).

Individual lava flows can be traced as far as 100 km and are as wide as 20 km. The general morphology of the Syrtis Major flows is similar to tht of flows described in the Tharsis region [7]. The flows are not distinguishable in age from the surrounding ridged-plains volcanics by conventional crater-count methods. An average crater count for the entire Syrtis Major region is about 2000 craters > 1 km diameter per 10^6 km^2, an equivalent age to intermediate stages of lava-flow activity at Alba Patera that bury some ring and radial fault systems and are cut by others [8].

The 280-km-diameter circular depression and superposed intracalderas of low to moderate relief within Syrtis Major may represent volcano-tectonic processes typical of intermediate age volcanic centers on Mars that form in two stages of activity according to Scott [9]. In Syrtis Major, the first stages involved the eruption of large volumes of lava, followed by collapse over a circular center of ~300 km in diameter. These early lavas presently appear as the ridged plains unit because, soon after the collapse and shortening (compression) of the surface, ridges formed that obscured any recognizable lava flow fronts. This process also occurred in the lunar maria and the mercurian smooth plains. The second stage of volcanism in Syrtis Major consisted of moderate-sized eruptions that emplaced lavas with mappable flow fronts. The sources of these lavas include the graben formed from the initial collapse of the summit region, and also localized centers that produced both calderas with diameters of tens of kilometers (Cvt-1, Cvt-2) and a smaller cinder cone or composite cone vents (X) illustrated in Fig. 1. U.S. Geological Survey research funded under NASA Contract W13,709.

References

[1] International Astronomical Union (1974) Proc. 15th General Assembly (Sydney 1973) and Extraordinary General Assembly (Poland, 1973), Trans. of the IAU XVB, G. Contopoulos and J. Jappel, eds., D. Reidel Publishing Co., Boston, MA, p. 106.

[2] Scott, D. H. and Carr, M. H. (1978) Geologic map of Mars. U.S. Geol. Survey Misc. Geol. Inv. Series I-1083.

[3] Simpson, R. A., Tyler, G. L., Harmon, J. K., and Peterfreund, A. R. (1981) Radar measurement of small-scale surface texture: Syrtis Major. Submitted to Icarus.

[4] Sjogren, W. L. (1979) Mars gravity: High resolution results from Viking Orbiter II. Science 203, p. 1006-1010.

[5] Meyer, J. D. and Grolier, M. J. (1977) Geological map of the Syrtis Major quadrangle of Mars. U.S. Geol. Survey Misc. Geol. Inv. Map Series I-955.

[6] Schaber, G. G. (1977) Geologic map of the Iapygia quadrangle of Mars. U.S. Geol. Survey Misc. Geol. Inv. Map Series I-1020.

[7] Schaber, G. G., Horstman, K. C., and Dial, A. L., Jr. (1978) Lava flow materials in the Tharsis region of Mars. Proc. Lunar Planet. Sci. Conf. 9th, p. 3433-3458.

[8] Scott, D. H. and Tanaka, K. L. (1981) Mars Tharsis region: Volcano-tectonic events in the stratigraphic record. Proc. Lunar Planet. Sci. Conf. 11th, p. 2403-2421.

[9] Scott, D. H. (1981) Volcanoes and volcano-tectonic structures: Western hemisphere of Mars (abs.), this volume.

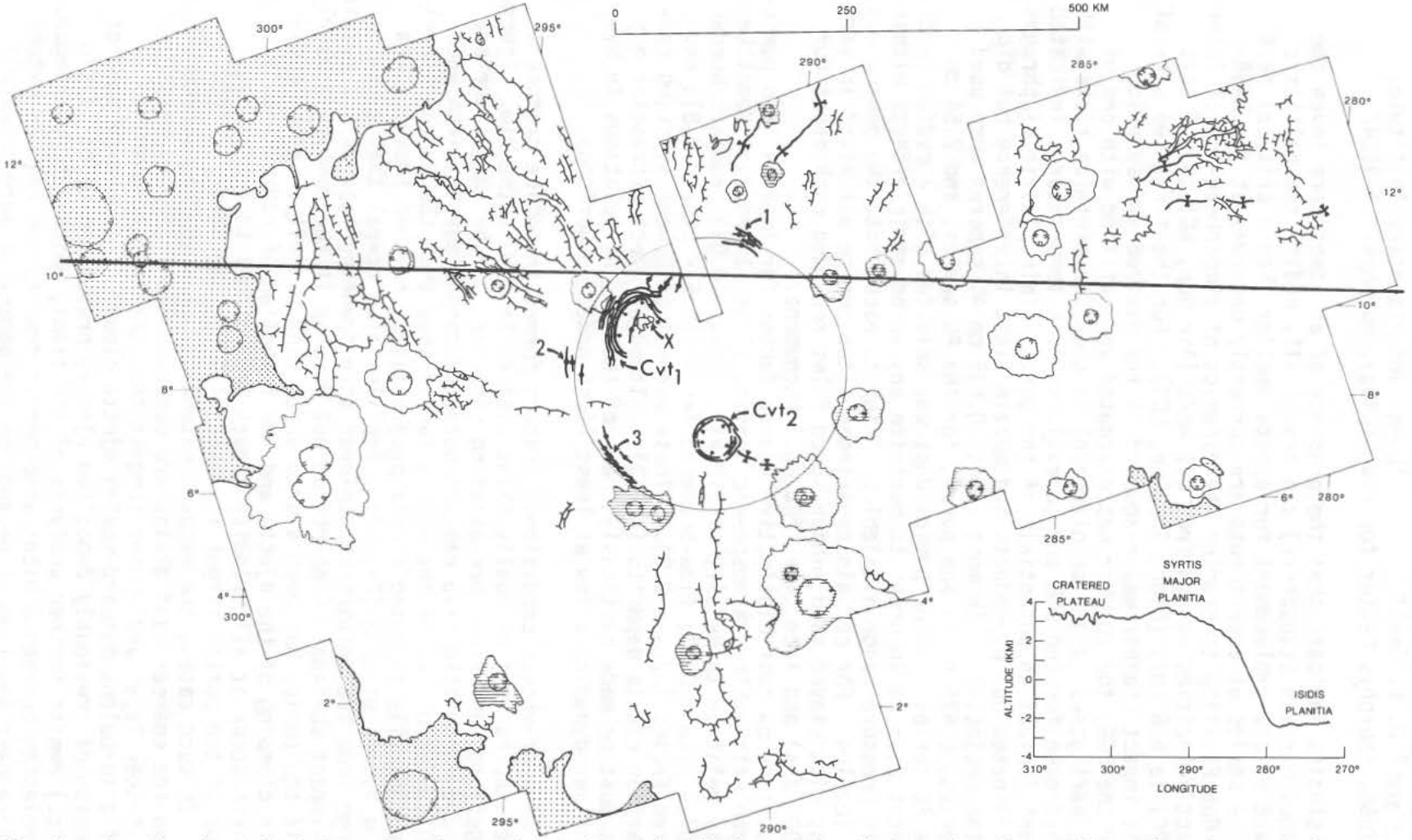

Fig.1- Geologic sketch map of central Syrtis Major Planitia showing distribution of lava flow fronts( ), grabens( ), rilles( ), calderas(Cvt-1,Cvt-2), volcanic cones (X), crater deposits(schematically the horizontal bars), ridged plains(blank) and cratered plateau(dotted). Large circle represents schematically the area of proposed volcanotectonic collapse as indicated by concentric grabens at 1, 2 and 3. Map produced from base mosaic of Viking(late-orbit) frames 375S26-32, 375S08-13 and 377S51-57. Radar topographic profile at lat 10.35°N. Shown as inset from[3]. *(Figure published courtesy of Icarus, in press.)*

EJECTA EMPLACEMENT AND ATMOSPHERIC PRESSURE: LABORATORY EXPERIMENTS

[1] P. H. Schultz and [2] D. E. Gault [1]Lunar and Planetary Institute, Houston, TX 77058, [2]Murphys Center for Planetology, Murphys, CA 95247

Previous studies indicate that the presence of an atmosphere (even the presently tenuous martian atmosphere) can drastically modify the ballistic trajectories and ejecta emplacement for ejecta smaller than a critical particle size (1). A series of experiments are currently underway at the NASA-Ames Vertical Gun Facility to examine the dynamics of atmosphere-impact interactions. Impact velocities ranged from 0.1 km/s (Air Gun, AG) to 2.5 km/s (Powder Gun, PG) to 6.8 km/s (Light Gas Gun, LGG). For the first two sets of velocities, the impact chamber was evacuated to the desired atmospheric pressure. For the LGG, the chamber was evacuated and refilled with one of two different inert gases (argon or nitrogen) in order to minimize risks with any released hydrogen for the LGG and to evaluate peak temperatures indicated by the different ionization potentials of the gases. Thin plastic diaphragms effectively eliminated gun byproducts and muzzle blast interference but did not fragment the projectile. In most cases, 0.635 cm Al spheres were used for the LGG series; 0.635 cm Al and pyrex, for the PG series; and 2.54 cm nylon, for the AG series . Fine pumice dust was selected with a median particle size of about 0.05 cm in order to maximize any aerodynamic effects within the atmospheric pressure range available. Prior to each shot, the pumice was compacted and leveled. For certain experiments, the pumice was mixed in various proportions with sieved sand. High speed films recorded each event for early time (6000 fps) and late time (400 fps) phenomena.

First results show four distinctive ejecta facies for impacts into pumice dust that change with ambient atmospheric density (Figs. 1 and 2): Moonlike facies (density relative to density of STP air: $\rho/\rho_0 < 0.06$); rampart-bordered facies ($0.07 < \rho/\rho_0 < 0.5$); flow-bordered facies ($0.5 < \rho/\rho_0 < 0.8$); and radially scoured facies ($\rho/\rho_0 > 0.8$). These morphologies bear striking resemblance to martian ejecta deposits (1,2,3). Although direct extrapolations to such scales must be made cautiously, many of the scaling relations in hydrodynamics and aerodynamics allow at least first order comparisons.

EJECTA FACIES

$\rho/\rho_0 < 0.07$: At near-vacuum conditions, craters formed in pumice produce a hummocky ejecta facies that gradually thins with distance from the rim. Ejecta cover the target area and erase pre-existing structure on the target surface.

$0.07 < \rho/\rho_0 < 0.5$: A distinctive rampart-bordered morphology develops when ρ/ρ_0 exceeds 0.07. Profiles of the ejecta facies show that the rampart develops on the exponentially thinning ejecta progressively farther from the rim with increasing values of ρ/ρ_0 (Fig. 3). Profiles also reveal that ejecta deposits uprange from the rampart are thinner than downrange ejecta but remain above the pre-impact surface. Ramparts do not develop if the pumice is poorly compacted or if the pumice has been stored under high humidity. Both conditions result in clumping of the ejecta and the formation of radial ejecta ridges. Ramparts occur at all velocity ranges (< 0.1 km/s to 6.8 km/s). They also occur if the pumice target is mixed with coarser material (#20 sieved sand). In such cases, the rampart extends to greater ranges from the crater rim, and the coarser sand grains are concentrated in the rampart. Analysis of a tracer layer and movies suggest that the rampart develops as a result of a turbulent outward-moving ejecta cloud. The precise mode of formation (erosion of previously deposited ejecta, prevention of ballistic deposition, etc.) awaits further analysis of the films, which has just begun. The apparent relation between ambient atmospheric density and rampart extent indicates that rampart development depends on the amount of aerodynamically

EJECTA EMPLACEMENT AND ATMOSPHERIC PRESSURE

Schultz, P. H. and Gault, D. E.

decelerated ejecta entrapped in the cloud. The formation of ramparts at subsonic impact velocities precludes hypotheses related to air shock interactions. *$0.5 < \rho/\rho_o < 0.8$:* As the relative atmospheric density is increased ($\rho/\rho_o > 0.5$), ramparts become less well defined but the specific transitional morphology appears to depend on impact velocity. At velocities lower than 3 km/s, a thin rampart may encircle mounded near-rim ejecta. At higher velocities (6 km/s), the ejecta exhibit multiple tongues of material extending many crater radii from the rim. These flow-like facies have steep-sided borders and termini that are called here "ejecta flows." Such flows were observed to over-run 4cm-high crater-facing scarps. With the exception of the flow lobes, ejecta facies are restricted to within about 1.5 crater radii (1.5 R) of the rim. Typically the facies nearest the rim exhibit a slightly concave profile. Films indicate that the flow lobes develop as a result of deposition behind a turbulent ground-hugging cloud. A thin layer of red tempera on top of the pumice revealed that the lobes are comprised of eroded surface material and suspended ejecta transported downrange as a turbulent mixture.
$\rho/\rho_o > 0.8$: At the highest atmospheric pressures available, the ejecta facies changed in morphology. Even at the lowest velocities the ejecta deposits form a mounded profile extending to about 1.5-2.0 R from the rim. However, high-velocity impacts (6 km/s) produced a pronounced radial scour expressed as a smooth ejecta facies with radial grooves. Near the rim (within 0.5R), a concave-profile annulus commonly develops. Beyond the radially scoured zone, fine-scale pre-impact detail is preserved. Lower velocity impacts produce traces of radial scouring but such craters are nearly a factor of three smaller in size. Further experiments are necessary to understand if the radial patterns are related to the amount of fine-size ejecta entrapped in the ejecta cloud, to the degree of atmospheric heating by the impact, or to a combination.

POSSIBLE IMPLICATIONS

Schultz and Gault (1) discuss scaling relations between laboratory and martian size impact craters. To first approximation, a dimensionless drag parameter permits comparisons of aerodynamic deceleration on individual ejecta (1,4) and indicates that the transition from a lunar-appearing crater to a radially scoured ejecta facies can occur over a factor of ten in either atmospheric density or median particle size. Under the current martian climate, scaling relations suggest that rampart craters might form if the median ejecta size, s, is 15 cm-100 cm; flow craters, if s=10 cm-15 cm; and radial craters, if s<10 cm. Ejecta size may reflect target properties, but theoretical work (5) suggests that high-velocity impacts may increase the proportion of highly shocked (and therefore comminuted) ejecta. The extrapolated ejecta sizes are very approximate and serve only to illustrate that even under the current martian climate and with reasonable ejecta size ranges, a variety of emplacement styles may occur. Our experiments suggest that: (a.) ejecta ramparts and flows are possible without the presence of water; (b.) the inferred sequence of emplacement of multi-lobed craters where outer ejecta lobes appear to have over-ridden the inner ejecta is physically reasonable (6,7); and (c.) the transition from lunar to rampart to multi-lobed to radial ejecta facies is part of a continuum which depends at least in part on ejecta size. These conclusions do not preclude the importance of *in situ* water or water-ice that can change ejection angle (8) and the median ejecta size (9), thereby enhancing conditions for ejecta flow (1,10).

1. Schultz P.H. and Gault D.E. (1979) *J. Geophys. Res.* 84, 7669-7687. 2. Carr M.H., Crumpler L.S., Cutts J.A., Greeley R., Guest J.E. and Masursky H. (1977) *J. Geophys. Res.* 82, 4055-4065. 3. Mouginis-Mark P. (1979) *J. Geophys. Res.* 82, 8011-8022. 4. Tauber M.E., Kirk D.B. and Gault D.E. (1978) *Icarus* 33, 529-536. 5. Schultz P.H., Orphal D., Miller B., Borden W.F. and Larson S.A. (1981) *Proc. Multi-Ring Basin Conf.* (in press.) 6. Schultz P.H. and Singer J. (1980) *Proc. Lunar Planet. Sci. Conf. 11th*, 2243-2259. 7. Mouginis-Mark P. (1980) *Lunar and Planetary Science XI*, 753-755. 8. Gault D.E. and Greeley R. (1978) *Icarus* 34, 386-495. 9. Lange M.A. and Ahrens T.J. (1981) *Lunar and Planetary Science XII*, 592-594. 10. Greeley R., Fink J., Gault D.E., Snyder D.B., Guest J.E. and Schultz P.H. (1980) *Proc. Lunar Planet. Sci. Conf. 11th*, 2075-2097.

EJECTA EMPLACEMENT AND ATMOSPHERIC PRESSURE

Schultz, P. H. and Gault, D. E.

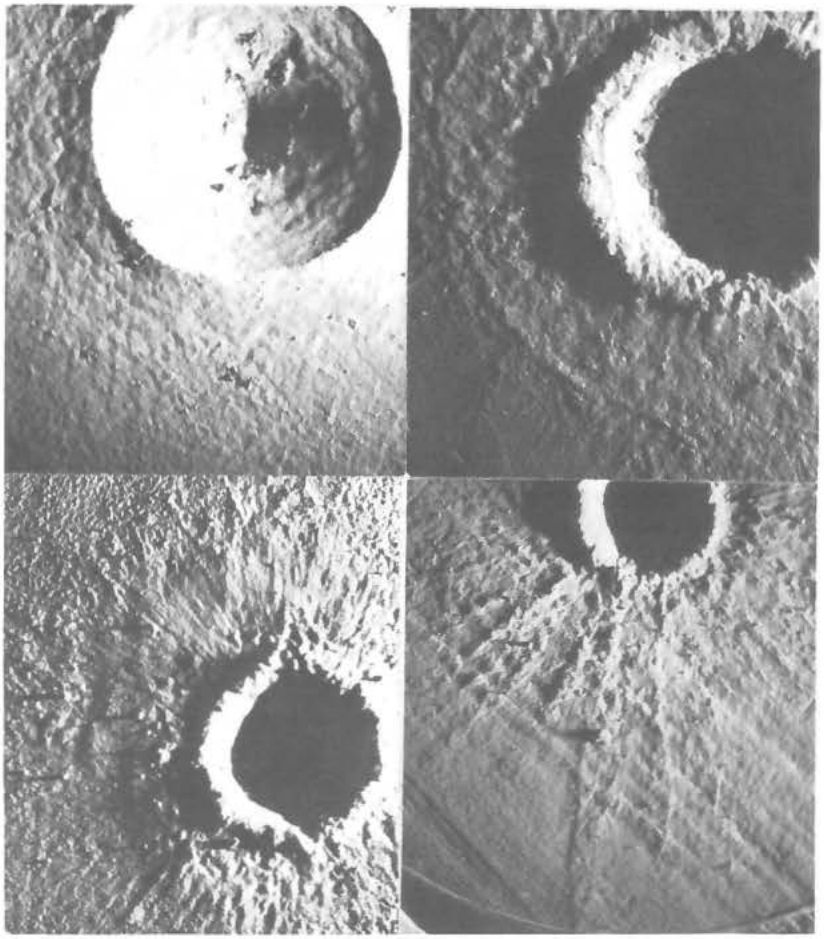

FIGURE 1. Comparison of ejecta facies for different atmospheric pressures (clockwise from upper left): lunar, P=1.5mm (air); rampart, P=190mm (Ar); flow, P= 380mm (Ar); radial, P= 720mm (Ar). Impacts were into compacted pumice with velocity about 6 km/s. Photos not at the same scale.

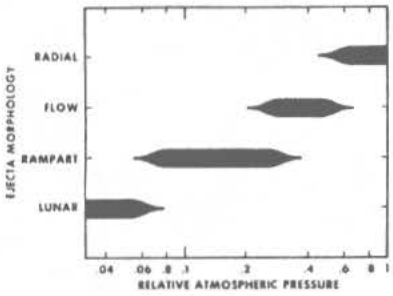

FIGURE 2. Comparison of ejecta facies for different atmospheric pressures (argon) relative to 760mm Hg. Illustration applies only to hypervelocity impacts.

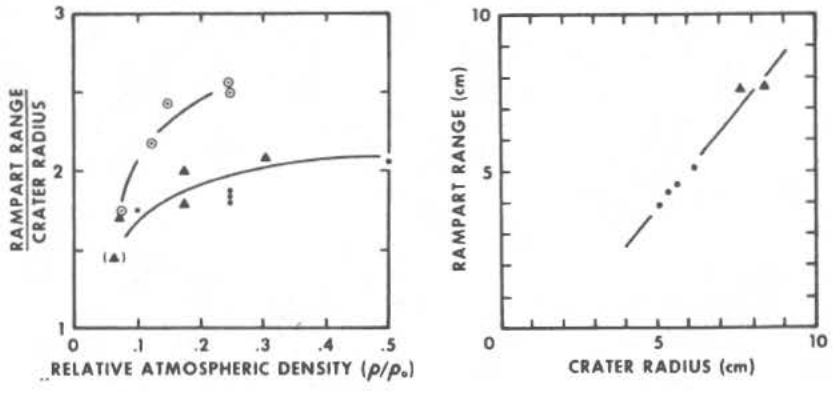

FIGURE 3. Left: Dependence between relative range of rampart from crater rim and relative atmospheric density (adjusted for different gases). Right: Dependence between rampart range (from rim) and crater radius for about the same atmospheric density. Open circles=0.2km/s; dots =2km/s; triangles= 6km/s.

ANCIENT POLAR LOCATIONS ON MARS: EVIDENCE AND IMPLICATIONS

P. H. Schultz and A. B. Lutz-Garihan
Lunar and Planetary Institute, Houston, TX 77058

Broad antipodal areas near the martian equator bear numerous similarities to the present polar deposits. These areas are proposed to be ancient polar deposits left after a major reorientation of the crust with respect to a space-fixed spin axis (1). The equatorial deposits are characterized by locally thick (1-2 km) layered and mantled terrain surrounded by pedestal craters and etched plateaus. Large shifts of the crust resulting in polar wander can be caused by major changes in the moments of inertia, e.g., the development of Tharsis (2,3,4). Paleo-pole migration may contribute to locally disparate erosion rates, large volumes of locally trapped volatiles, and the sequence of certain volcanic centers.

EQUATORIAL LAYERED TERRAINS: Proposed north polar remnants occur in three prominent equatorial regions of mantled and layered terrain between 150°W and 210°W. The largest, thickest, and best preserved region (A) is centered near 155°W and covers about 700,000 km^2. A slightly smaller and more eroded region (B) is centered near 180°W and covers an area of 500,000 km^2. The smallest and most heavily stripped region (C) covers about 40,000 km^2 centered at 210°W. The antipodal regions are centered at 335°W (A', northeast of Schiaparelli), 0°W (B', north of Airy), and 30°W (C', north of Margaritifer Sinus), respectively. The terrain around 180°W is characterized by thick, layered deposits that mantle both the smooth plains to the north and the heavily cratered uplands to the south. The layered deposits around 0° longitude typically are contained within large upland craters, although an extensive mantled region (1,000,000km^2) is centered near 0°.

Characteristic features of the equatorial deposits occur in three broad classes of terrains (Fig. 1): *mantled terrain*, *eroded terrain*, and *proximate terrain*. Broad-scale features characteristic of the equatorial *mantled terrain* include high-standing featureless plains that superpose most other terrains and features. Subdued valleys cross the featureless plains, and some of these valleys form parallel systems that resemble the spiral patterns of valleys in the polar laminated terrain. The most notable aspect of the mantled terrain is the absence of fine-scale features. However, narrow terraces, lineations, fluting, and small (<0.4 km) crescent-shaped pits occur along the boundaries or valley walls of the mantled terrain. The *eroded terrain* includes a wide assortment of features resulting from differential weathering processes: sets of parallel ridges and grooves; rectilinear patterns of ridges; closely spaced knobs; irregular depressions and plateaus; and pedestal craters. The erosional process is highly selective. Exhumed structures are relatively unmodified, thereby indicating a marked difference in cohesion between the stripped mantling material and underlying terrain. Although parallel patterns of ridges and grooves suggest directed wind erosion, pedestal craters typically are symmetrical, i.e. without an aerodynamic shape. *Proximate terrain* includes an assortment of miscellaneous features: large mounds of partly stripped mantled and layered terrains within old craters; "white rock" features; isolated plateaus; pedestal craters; multi-toned crater streaks (5); dune fields; and narrow sinuous ridges.

The association of similar features and processes permits construction of terrain maps as shown in (1). The mantled terrain includes two terrain types: smooth rounded plains and mantled plains. Eroded terrain includes four types: stripped, lineated, knobby, and plateau terrains. These different terrain types exhibit a relatively consistent sequence in both proximity and vertical sequence. The smooth rounded plains occur at the highest elevation. Lineated terrains surround and develop at the expense of the smooth rounded

ANCIENT POLAR LOCATIONS ON MARS

Schultz, P. H. and Lutz-Garihan, A. B.

plains (and in some cases the mantled terrain). Knobby and plateau terrains occur below and adjacent to the lineated terrains. Stripped terrain indicates regions of differential erosion, leaving features such as plateaus and pedestal craters, and occurs throughout the various terrain types.

WHY PALEO-POLES? The equatorial layered terrains bear striking resemblance to the current polar deposits as detailed in (6,7,8,9), including: thick layered deposits; chasma-like valleys; insular remnants of polar "spiraling valleys;" grooved/fluted borders; etched terrain; pedestal craters; narrow ridges; dune fields; crater-fill deposits; and multi-toned crater streaks. Pedestal craters, in particular, are restricted within 40° of the poles (10) yet are clearly associated with the equatorial layered terrains in both hemispheres. In addition, inferred processes currently acting at the pole occur around the proposed equatorial analogs: non-destructive burial and exhumation of relief; rapid erasure of fine-scale features in the mantled deposits; and extreme contrast in erosion rates. The ease with which the polar layered terrains are stripped away may be related to sublimation and removal (ablation) of trapped ices under current atmospheric pressures (11). Such a process could account for the formation of pedestal craters. An impact into polar deposits excavated buried terra material, thereby trapping polar volatiles. As the pole shifted and the regional climate changed, exposed polar ices sublimated, thereby leaving a crater with ejecta facies perched on the trapped polar deposits.

Preliminary results from a different data set provide further support of major polar wander. Highly oblique impacts (<5°) produce a distinctive morphology, as demonstrated in the laboratory and as recorded on the Moon (12): elongate plan; butterfly ejecta pattern; central ridge; and saddle-shaped rim profile. The global distribution of the freshest oblique craters on Mars exhibits a prominent east-west trend of the impact direction (Fig. 2). This can reflect the gradual decay of Phobos/Deimos-type satellites, or a projection effect of near-ecliptic solar orbiting bodies. In contrast, older oblique craters display a prominent N-S trend. Because these craters exhibit a wide range of ages, they are not believed to be part of a single impact swarm. If the current E-W impactors record the orientation of the current martian equator, then the old N-S impactors indicate a significant reorientation.

TIMING, PATH, AND EFFECTS OF POLAR WANDER: Superposed craters and pedestal craters provide a means for estimating the relative age of the proposed paleo-poles. Because of erosional processes, only a few areas can be reliably dated and generally give underestimated ages. Two crater-age indices are used: the number (N) of craters/10^4 km^2 larger than 1 km and the number (N') of craters/10^4 km^2 larger than 10 km. The data indicate that Region A (N $\sim$ 2) is at least as old as Arsia Mons (N $\sim$ 2-20) from ref. (13). Region B (N' $\sim$ 40) and its antipodal deposits B' (N' $\sim$ 30) approximate the age of the Tharsis cratered plains (N' $\sim$ 50, ref. 14). Because Region C is the most heavily eroded, this paleo-pole location and its antipode near Margaritifer Sinus predate most of the major volcanic constructs. The age sequence suggests that the poles shifted eastward (with respect to the present coordinate system) to a stable location near B-B' prior to the emplacement of Lunae Planum (N' $\sim$ 3.5, ref. 15) and the last eruptions at Elysium (N' $\sim$ 1.7, ref. 15). Polar deposits at C' could have been buried by Lunae Planum lavas. The main radial fault systems (and thus the beginning of the Tharsis bulge) slightly postdate Lunae Planum (16). Consequently, the path away from the equator from B-B' to A-A' may reflect the beginning of this major tectonic event. Statistics suggest that the pole was located near A-A' at the time Arsia Mons began construction. The shift from A-A' to the present polar location occurred prior to (or perhaps during) the eruption of Olympus Mons (see Fig. 3).

If the volcanism associated with Arsia Mons is attributed to a large con-

ANCIENT POLAR LOCATIONS ON MARS

Schultz, P. H. and Lutz-Garihan, A. B.

vective plume fixed with respect to the spin axis, then this plume will trace a northeastward path as the paleo-pole shifts northeastward from A-A' to the current polar position. Such a path might account for the sequence of volcanism from Arsia Mons to Ascraeus Mons.

REFERENCES

1. Schultz P.H. and Lutz-Garihan A.B. (1981) *Lunar and Planetary Science XII*, p. 946-948. 2. Goldreich P. and Toomre A. (1969) *J. Geophys. Res.* 74, 2555-2569. 3. Murray B.C. and Malin M.C. (1973) *Science* 197, 997-999. 4. Melosh H. J. *Icarus* (in press). 5. Thomas P. and Veverka J. (1979) *J. Geophys. Res.* 84, 8131-8146. 6. Sharp R.P. (1973) *J. Geophys. Res.* 78, 4073-4083. 7. Soderblom L.A. *et al.* (1973) *J. Geophys. Res.* 78, 4197-4211. 8. Cutts J. A. (1973) *J. Geophys. Res.* 78, 4231-4249. 9. Cutts J. A. *et al.* (1976) *Science* 194, 1329-1337. 10. Mouginis-Mark P. (1979) *J. Geophys. Res.* 84, 8011-8022. 11. Howard A.D. (1978) *Icarus* 34, 581-599. 12. Gault D.E. and Wedekind J.A. (1979) *Proc. Lunar Planet. Sci. Conf. 9th*, 3843-3875. 13. Carr M.H. *et al.* (1977) *J. Geophys. Res.* 82, 3985-4015. 14. Carr M.H. (1975) USGS Inv. Map I-893. 15. Plescia J.B. and Saunders R.S. (1979) *Proc. Lunar Planet. Sci. Conf. 10th*, p. 2841-2859. 16. Wise D.M. *et al.* (1979) *Icarus* 38, 456-472.

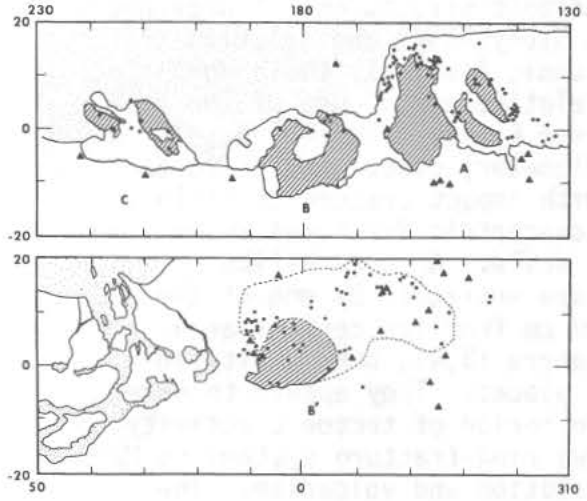

FIGURE 1. Abridged terrain map of paleo-pole regions indicating mantled terrain (striped) and surrounding eroded terrain with pedestal craters (dots) and craters with mounded floor material (triangles).

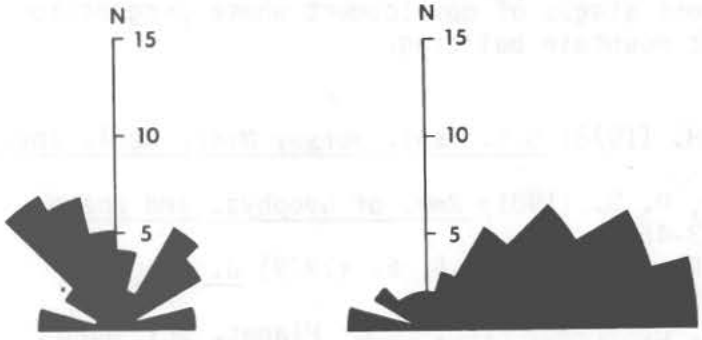

FIGURE 2. Rose diagrams of oblique crater directions for ancient (left) and recent (right) impacts.

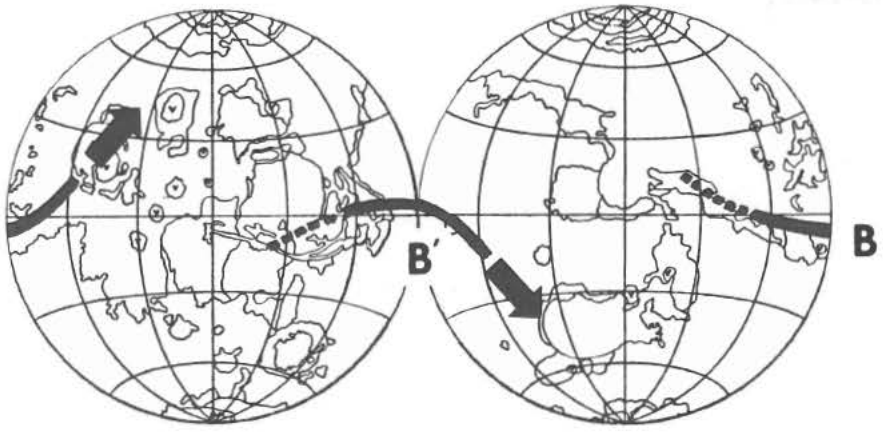

FIGURE 3. Global view showing proposed path of paleo-poles. During relatively rapid polar shifts, deposits do not accumulate to great depths.

VOLCANOES AND VOLCANO-TECTONIC STRUCTURES - WESTERN HEMISPHERE OF MARS; David H. Scott, U.S. Geological Survey, Flagstaff, Arizona 86001.

Observations recorded in this study were made from detailed geologic mapping of Mars' western hemisphere between lat 60° N. to 60° S. and long 0° to 180° W. Medium- to high-resolution Viking images were used over most of the region. Previous work, aside from topical studies of particular areas of interest, consists of geologic quadrangle maps at 1:5 million-scale by authors in the Mars Mariner 9 geologic mapping program, a 1:25 million-scale geologic map (1) also from this program, and a comprehensive review and synthesis of martian volcanoes (2) incorporating data from existing maps. These maps show the areal distribution of the more prominent volcanoes and structures but are limited in many places by the lower quality and resolution of the Mariner pictures. The present study has revealed many volcanoes and volcano-tectonic structures not previously recognized in the western hemisphere. The study shows the relation of these structures to regional and local tectonic features, their morphologic classification, stratigraphic units, and relative ages. One of the most interesting discoveries was made in the Tempe Fossae area (40° N., 70° W.) where two, possibly three, large (250-km diameter) circular structures occur (Fig. 1). They are not associated with impact craters or basins, have no visible relief, and are ringed by concentric fractures resembling those around Alba Patera, but on a smaller scale. A caldera-like depression and a small but prominent dome are encircled by one of the structures; lava flows extend more than 100 km from its central area. These flows, like some erupted from Alba Patera (3,4), bury faults in places but are transected by them in other places. They appear to have been extruded episodically over a sustained period of tectonic activity.

The occurrence of these and other known ring-fracture systems on Mars suggests a continuum between structural evolution and volcanism. The circular structures show different stages of development whose progression appears to culminate in volcanic mountain building.

References

(1) Scott, D. H. and Carr, M. H. (1978) U.S. Geol. Survey Misc. Geol. Inv. Map I-1083.

(2) Greeley, Ronald and Spudis, P. D. (1981) Rev. of Geophys. and Space Phys. 19, no. 1, p. 13-41.

(3) Wise, D. U., Golombek, M. P., and McGill, G. E. (1979) J. Geophys. Res. 84, p. 7934-7939.

(4) Scott, D. H. and Tanaka, K. L. (1980) Proc. Lunar Planet. Sci. Conf. 11th, p. 2403-2421.

Volcanoes - Mars Western Hemisphere

Scott, D. H.

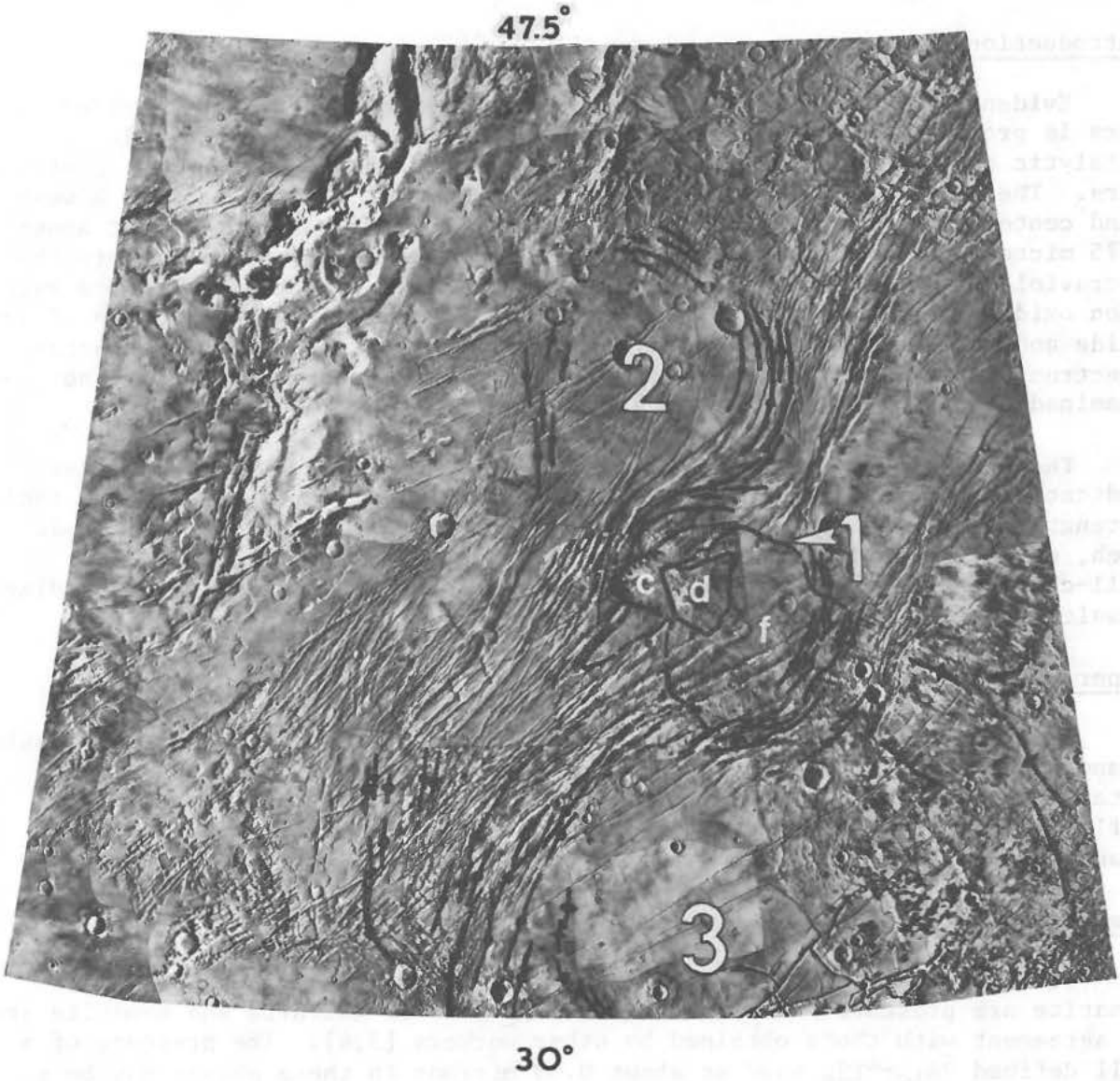

Fig. 1. Circular structures (1,2,3) in Tempe Fossae. Ring fractures (line with ball) and ridges (line with double arrow) accented in places by dark line. Structure 1 includes dome (d), caldera (c), and lava flows within dashed area (f).

DIFFUSE REFLECTANCE SPECTRA OF THE IRON OXIDES AND THEIR APPLICATION TO THE MARTIAN BRIGHT REGION MINERALOGY

David M. Sherman, Virginia Mee Burns and Roger G. Burns
Department of Earth and Planetary Sciences
Massachusetts Institute of Technology
Cambridge, Massachusetts 02139

Introduction

Evidence for the existence of iron oxides and iron oxide hydroxides on Mars is provided by the magnetic properties of the soil, the possible catalytic properties and features in the Earth-based remote sensing spectra of Mars. The reflectance spectra of the Martian bright regions exhibit a weak band centered at 0.87-0.88 microns, a reflectance maximum centered at about 0.75 microns and a steep charge-transfer absorption edge extending into the ultraviolet [1]. These features are also exhibited by the spectra of several iron oxide phases. Several workers have presented reflectance spectra of iron oxide and iron oxide hydroxide phases in an attempt to model the reflectance spectrum of Mars. We present additional spectra of phases which have not been examined before (akaganéite, feroxhyte and ferrihydrite).

The existence of a specific iron oxide phase may provide a sensitive indicator of the chemical environment of the Martian regolith (e.g. pH, ionic strength, oxidation rates and possible photochemical mechanisms) [2] . As such, we feel that it is important to work with very specific and well-characterized phases rather than materials such as limonite and oxidized basalt.

Experimental

Except for the natural hematite sample, all phases were synthesized using standard methods and characterized by x-ray diffraction. Spectra were obtained using a Cary 17 spectrophotometer with an integrating sphere reflectance accessory. Spectra were obtained relative to a sealed MgO standard and the specular component was eliminated.

Results and Discussion

Our spectra of ferrihydrite, feroxyhyte, akaganeite, goethite, and hematite are presented in Figure 1. Our spectra of goethite and hematite are in agreement with those obtained by other workers [3,4]. The presence of a well defined $^6A_{1g}$-^4T2_g band at about 0.63 microns in these phases may be a function of crystallinity. Transmission spectra of goethite and akaganeite are significantly different from the reflectance spectra of these minerals [5]. Reflectance spectra of hematite show the $^6A_1 \rightarrow {}^4T_1$ reflectance minimum to be centered at 0.87 microns with the bright feature (reflectance maximum) centered at about 0.75 microns in agreement with other workers [3,6]. Our laboratory reflectance spectra of goethite show the $^6A_1 \rightarrow {}^4T_1$ band to be centered at 0.92 microns with the bright feature centered at 0.77 microns in agreement with other workers [3,4]. In contrast to the spectra of other iron oxides at small particle sizes, the $^6A_1 \rightarrow {}^4T_2$ band is quite prominent and well defined in goethite spectra; this feature is centered at 0.68 microns.

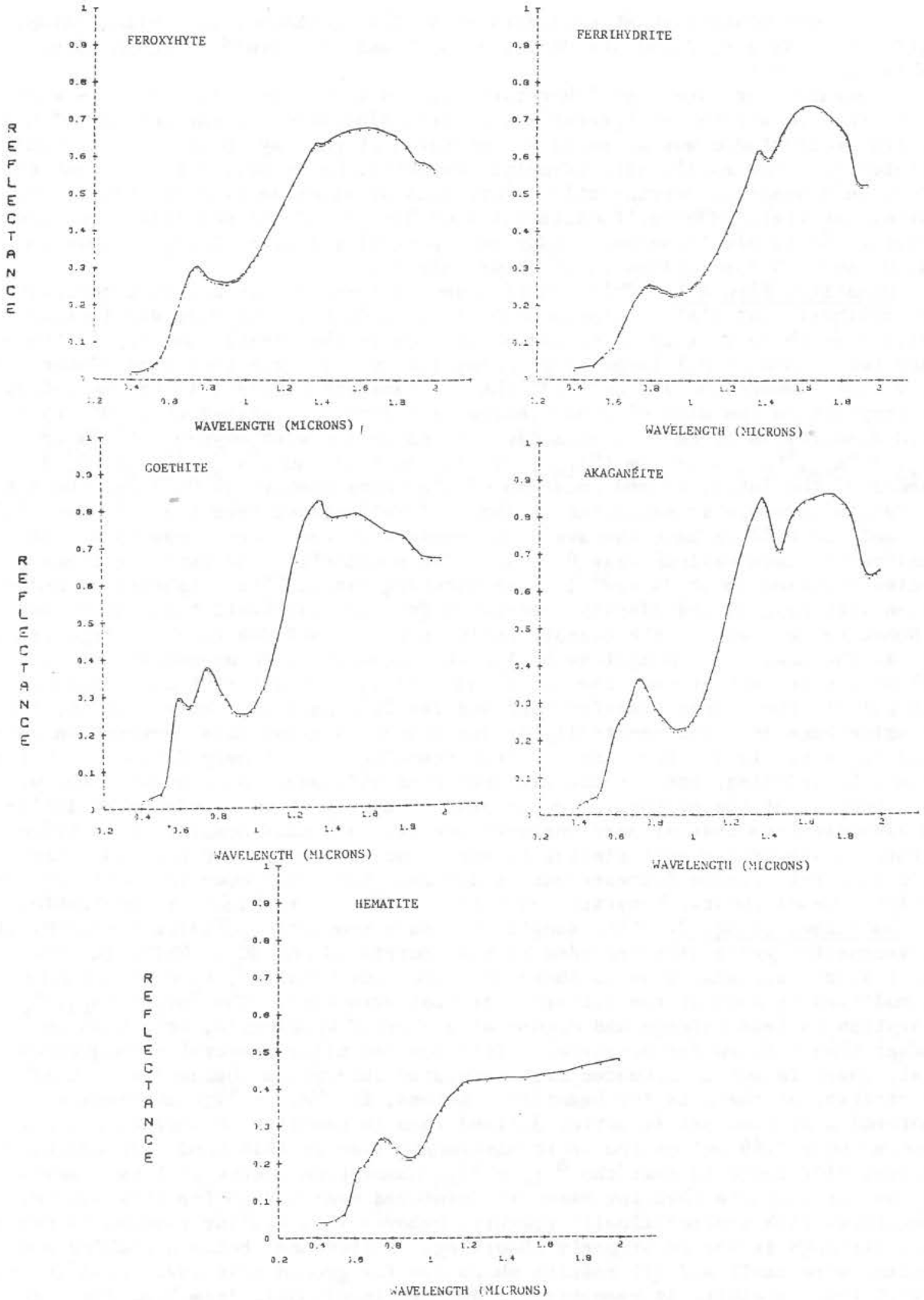
FEROXYHYTE
FERRIHYDRITE
GOETHITE
AKAGANÉITE
HEMATITE
REFLECTANCE
WAVELENGTH (MICRONS)

Figure 1

SOME OBSERVATIONAL CONSTRAINTS ON IRON MINERALOGY IN MARTIAN BRIGHT SOILS. R.B. Singer, Planetary Geosciences, Hawaii Institute of Geophysics, Honolulu, HI 96822.

Presented here are some laboratory studies to be used with previous work (1) to help constrain interpretations of iron mineralogy on the surface of Mars. Spectral reflectance was measured for mixtures of pure synthetic hematite and goethite with montmorillonite (Wyoming bentonite, Wards Sci. Est.) to test the effect on diagnostic ferric-oxide absorptions of dilution by a spectrally more neutral material. Montmorillonite was used because of its possible occurrence on Mars, and to simultaneously study the spectral effect of ferric oxides on clay OH and H_2O absorptions in the near infrared.

Hematite, Figure 1. This hematite sample (α-Fe_2O_3) is a very fine-grained pure synthetic material manufactured by Alfa Products. The very distinctive spectrum is characterized by strong absorption in the visible and high reflectance (weak absorption) longward of about 1.0 μm. The greatest contributors to the visible absorption are O^{2-}-Fe^{3+} charge transfers centered in the near-U.V. Superimposed on the wing of these charge transfers are "spin-forbidden" crystal-field absorptions of Fe^{3+} in octahedral coordination with oxygen: ∿0.53 μm ($^6A_{1g} \rightarrow {}^4A_{1g}, {}^4E_g$), ∿0.62 μm ($^6A_{1g} \rightarrow {}^4T_{2g}$), and ∿0.86 μm ($^6A_{1g} \rightarrow {}^4T_{1g}$) (2,3). Because of the intensity and location of the sharp doublet at 0.53 μm, the net absorption envelope is saturated at about 3% reflectance from the U.V. past 0.5 μm, and the 0.62 μm band appears as a shoulder on the steep slope up to the local reflectance maximum near 0.75 μm. The montmorillonite used for these studies contains about 3% Fe^{3+} (4) substituting for Al^{3+} in octahedral coordination with oxygen, and displays very weak Fe^{3+} crystal field bands analogous to hematite, as well as the overall reflectance dropoff due to the charge transfers in the near U.V. A mixture of 1.0 wt.% hematite with montmorillonite, well shaken but not ground, shows a slight increase in all Fe^{3+} absorptions, particularly the charge transfer edge and the 0.53 μm band. Note that the ferric oxide here is still spectrally dilute enough to allow these absorption features to be resolved. The same 1.0 wt.% hematite, when finely dispersed in the mixture by grinding, has a radically increased influence and dominates the visible spectrum of the mixture. In the near IR the spectrum is virtually indistinguishable from that of pure montmorillonite. 5.0 wt.% hematite in a ground mixture is spectrally very similar to pure hematite out to 1.0 μm, and causes a noticeable reflectance increase out to 2.5 μm. Note that even in small concentrations the diagnostic hematite absorption features are highly recognizable.

Goethite, Figure 2. This sample is a pure synthetic goethite (α-FeOOH) of sub-micrometer grain size provided by R.V. Morris (NASA-JSC). While the spectral features are analogous to those described for hematite, some of the details are modified because of the different crystal structure. The $^6A_{1g} \rightarrow {}^4A_{1g}, {}^4E_g$ absorption is less intense and occurs at a shorter wavelength, near 0.46 μm (rather than 0.53 μm for hematite). This has two major spectral consequences. First, there is not an extended flat saturated absorption throughout most of the visible, as there is for hematite. Second, the $^6A_{1g} \rightarrow {}^4T_{2g}$ absorption (centered near 0.64 μm) is better defined than in hematite because of a local maximum (near 0.69 μm) on the short wavelength side of this band. An additional spectral difference is that the $^6A_{1g} \rightarrow {}^4T_{1g}$ absorption occurs at longer wavelengths for goethite than for hematite, centered near 0.9 μm for this sample. In mixtures with montmorillonite goethite behaves in a similar fashion to hematite, although is not as strongly absorbing. Differences between shaking and grinding were small and all results shown are for ground mixtures. Even at the 1 wt.% level goethite is recognizable and distinguishable from hematite. As with the previous case beyond 1.2 μm the clay spectrum is not altered substantially by goethite contents great enough to have a drastic effect in the visible.

FERRIC IRON MINERALOGY ON MARS

SINGER, R.B.

Discussion. A quick review of observed spectral reflectance for martian bright regions is appropriate at this point. Figure 3 represents an average composite bright region spectrum from telescopic observations (5). There is an intense but smooth reflectance decrease from a peak near 0.75 μm to the near U.V., certainly caused by Fe^{3+} in some form. A shallow, asymmetric band with a minimum near 0.87 μm can be reasonably assigned to the $^6A_{1g} \rightarrow {}^4T_{1g}$ absorption, while the only other indication of a crystal-field band is a slight change in spectrum slope between 0.5 and 0.6 μm, due to the $^6A_{1g} \rightarrow {}^4T_{2g}$ absorption around 0.62 μm (2). There is no evidence for a well defined band at .45-.53 and no saturation of the absorption envelope until the U.V. (Other features in this spectrum, further in the infrared, are largely due to Mars atmospheric CO_2 and are discussed elsewhere [5]). The experimental results presented above demonstrate that the well defined spectral signatures of crystalline ferric oxides are not adequately masked by dilution with a resonable neutral substance to be major constituents of telescopically observed martian bright soils. Only a very limited amount of opaque material, which would tend to further mask the distinct Fe^{3+} absorptions, could be added without lowering the overall reflectance below measured values (∿0.4 peak). A crystalline ferric-oxide content of 18-20 wt.%, the number measured by the Viking XRF experiment (4), would cause an unmistakable diagnostic signature , which has not been observed. A previously published laboratory study of nontronite and nontronite mixtures (1) has shown that based on related spectral evidence the bulk of the ferric iron on Mars cannot exist in a crystalline clay structure either. The observed combination of intense absorption in the visible with poorly defined band structure is apparently indicative of a large degree of disorder of the Fe^{3+} sites. Spectral reflectance measurements of four ferric-iron rich X-ray amorphous soils from Hawaii, of the type discussed by Evans and Adams (6), are shown in Figure 4. These soils differ somewhat in history and chemistry but are all palagonites in the sense that they are hydrated and oxidized alteration products of mafic volcanic glass. Iron-oxide content, nearly all ferric-iron, ranges from about 10 to 15 wt.%. These materials demonstrate Fe^{3+} absorptions of a magnitude and shape similar to telescopic observations of Mars, as do some synthetic Fe-Si gels (7).

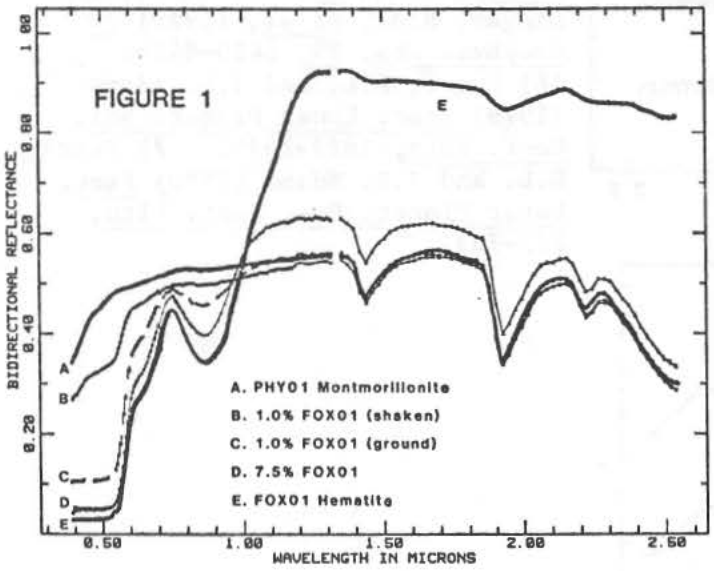

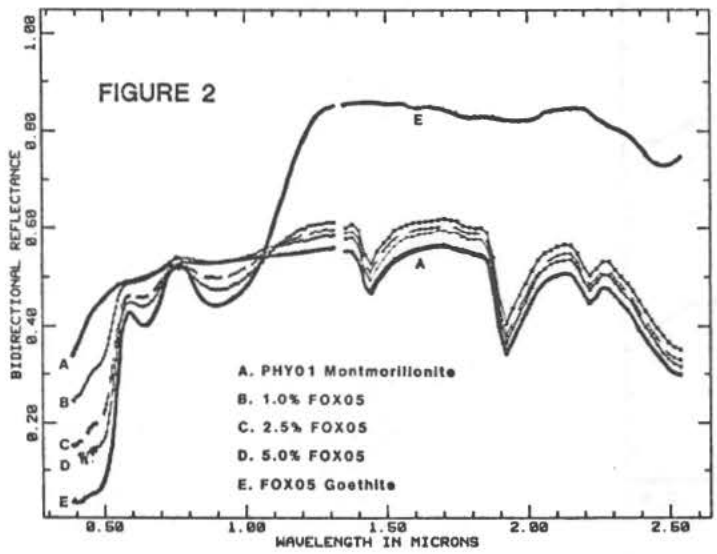

Conclusions. The results presented here demonstrate a basic property of spectral reflectance of mineral mixtures and can be extrapolated to include other crystalline Fe^{3+} bearing phases.

FERRIC IRON MINERALOGY ON MARS

SINGER, R.B.

These results, along with some presented earlier (1,7), indicate that minerals generally considered prevalent on the surface of Mars, crystalline ferric oxides and iron-bearing clays, are not consistent with observed spectral data. Fe^{3+} in well-ordered octahedral crystal sites produces distinctive well-defined absorption bands which cannot be adequately masked to agree with Mars observations. Significant disordering of Fe^{3+} sites, such as found in amorphous materials (gels), is apparently required to produce Mars-like spectral reflectance characteristics.

Acknowledgements. I wish to thank John Adams, Dianne Evans, and Dick Morris for providing some laboratory samples and useful discussions, and Roger Burns for helpful information about Fe^{3+} crystal field spectra. Sumner Matsunaga helped with sample preparation and data collection and reduction. This work was funded by NASA MDAP grant NSG 7590.

References. (1) Singer, R.B. (1981) Lunar Planet. Sci. XII, 996-998; (2) Huguenin, R.L., et al. (1977) Lunar Sci. VIII, 478-480; (3) Burns, R.G. and D.J. Vaughan (1975) in Infrared and Raman Spectroscopy, C. Karr Jr., ed., Academic Press, 39-72; (4) Baird, A.K., et al. (1977) J. Geophys. Res. 82, 4595-4624; (5) Singer, R.B., et al. (1979) J. Geophys. Res. 84, 8415-8426; (6) Evans, D.L. and J.B. Adams (1979) Proc. Lunar Planet. Sci. Conf. 10th, 1829-1834. (7) Evans, D.L. and J.B. Adams (1980) Proc. Lunar Planet. Sci. Conf. 11th, 757-763.

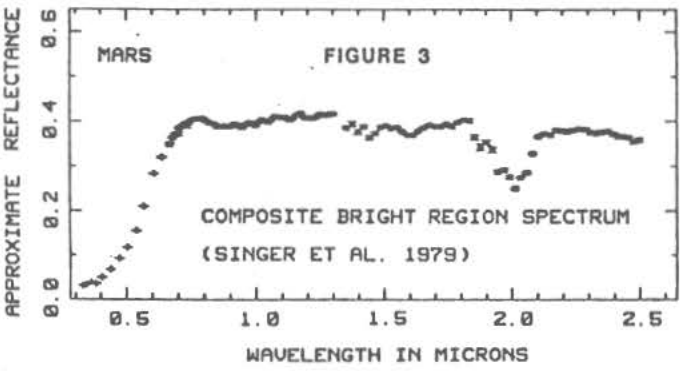

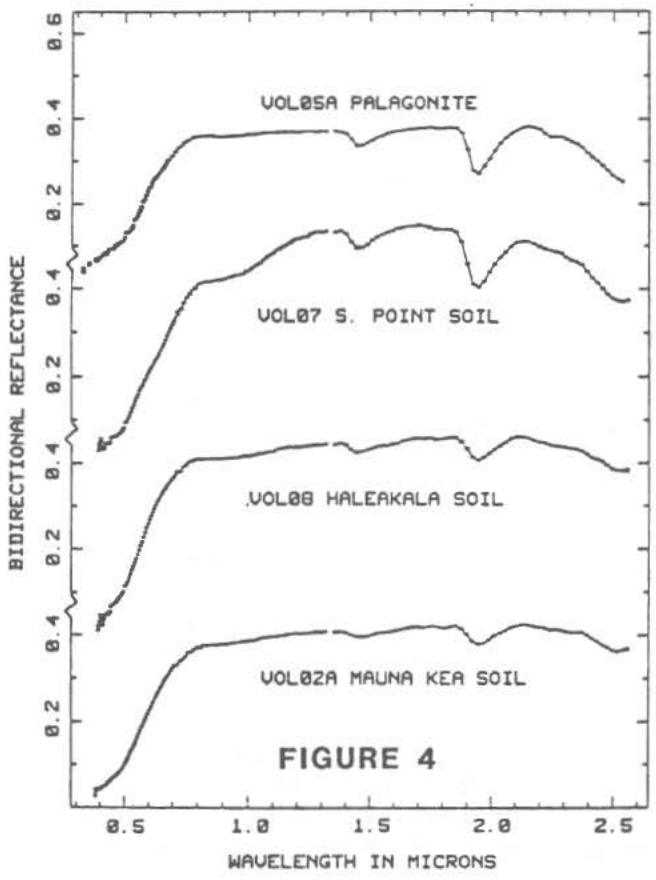

FIGURE 4

THE SOLAR WIND INTERACTION WITH MARS RE-VISITED, James A. Slavin and Robert E. Holzer, Institute of Geophysics and Planetary Physics, University of California, Los Angeles, California 90024

Due to a paucity of observational data, no clear consensus has been reached concerning the general nature of the solar wind interaction with Mars. In particular, the previous analyses are still at odds regarding the existence of a small intrinsic field magnetosphere at Mars as opposed to a Venus-type ionospheric interaction (e.g. 6, 16). Table 1 presents a comprehensive listing of the various magnetic moments that have been inferred for this planet. Parameterized in terms of magnetic moment, the values in excess of $\sim 1 \times 10^{22}$ G-cm^3 correspond to interactions in which the intrinsic field dominates while induced fields and cometary processes involving the neutral atmosphere become increasingly important below this level. Even the more recent examinations of this problem have done little to limit the range of possible interaction processes with moments of 0.2 to 2.5×10^{22} G-cm^3 being reported (16, 6). This study reviews the previous work and contributes to the resolution of this question in three ways. First, an improved determination of effective obstacle altitude and shape is obtained from the Mars 2, 3, and 5 bow shock encounters through the use of a recently published catalag of gasdynamic flow solutions (21). Secondly, building upon the Pioneer Venus findings at a field-free planet (2, 8), it is shown that the Martian ionosphere cannot support a Venus-type ionopause at the obstacle altitudes inferred through our modeling of the bow wave observations even when maximal induced ionospheric magnetic fields and solar maximum EUV levels are assumed. These results allow an effective Mars magnetic dipole moment of $1.4\ (\pm 0.7) \times 10^{22}$ G-cm^3 to be determined which stands off the solar wind over the dayside hemisphere at altitudes ranging from $\sim$ 500 at the subsolar point to $\sim$ 1000 km near the terminator with no direct aid from the ionosphere under average solar wind/magnetospheric conditions. Thirdly, a search of published Mars and Mariner radio occulation measurements produced no evidence for the existence of an ionopause at Mars in agreement with the Viking study of Lindal et al. (13). Rather, the electron density altitude profiles appear qualitatively consistent with the Martian ionosphere terminating in a chemopause associated with the effects of magnetospheric convection as first proposed by Bauer and Hartle (1). However, during intervals of enhanced solar wind dynamic pressure and/or significant dayside magnetic merging it is expected that the solar wind will be able to reach low altitudes, $\lesssim$ 300 km, where the ionosphere, and eventually the neutral atmosphere (23, 9, 2), will participate in deflecting/absorbing the incident flow.

Table 1. Summary of Inferred Martian Magnetic Moments

M_{ms} (10^{22} G-cm^3)	Study	Basis
	Mariner 4	
≤ 8	Van Allen et al. (22)	Lack of interaction signature (particles)
≤ 8	O'Gallagher and Simpson (14)	Lack of interaction signature nature (particles)
≤ 2.4	Smith et al. (18)	Lack of interaction signature (magnetic field)
≤ 8	Lazarus et al. (12)	Lack of interaction signature (plasma)
0.8	Smith (18)	Modeling bow shock position
1.7	Dryer and Heckman (7)	Gasdynamic modeling of bow shock position
≤ 1.7	Spreiter and Rizzi (20)	Gasdynamic modeling of bow shock position
	Mars 2 & 3	
2.4	Dolginov et al. (4)	Modeling in situ magnetic field (dayside)
2.4	Gringauz et al. (10)	Gasdynamic modeling of bow shock position
	Mars 2, 3 & 5	
2.55 ± 0.36	Dolginov (5)	Modeling in situ magnetic field (dayside and nightside) and bow shock/magnetopause position
≤ 0.9	Russell (15)	Modeling bow shock position
≤ 0.2	Russell (16)	Lack of magnetospheric signatures
1.7 - 2.5	Dolginov (6)	Modeling in situ magnetic field (dayside and nightside) and bow shock/magnetopause position
1.2	Smirnov et al. (17)	Modeling in situ magnetic field (dayside and nightside)
0.8	Intriligator and Smith (11)	Pressure balance across solar wind-obstacle interference
1.4 ± 0.7	This study	Gasdynamic modeling of bow shock position

References

1. Bauer, S.J., and R.E. Hartle (1973), J. Geophys. Res., 78, 3169-3171.
2. Brace, L.H., R.F. Theis, W.R. Hoegy, J.H. Wolfe, J.D. Mihalov, C.T. Russell, R.C. Elphic, and A.F. Nagy (1980), J. Geophys. Res., 85, 7663-7678.
3. Cloutier, P.A., M.B. McElroy, and F.C. Michel (1969), J. Geophys. Res., 74, 6215-6228.
4. Dolginov, Sh.Sh., Ye.G. Yeroshenko, and L.N. Zhuzgov (1973), J. Geophys. Res., 78, 4779-4786.
5. Dolginov, Sh.Sh. (1976), Physics of Solar Planetary Environments, ed. D.J. Williams, AGU, p. 872-888.
6. Dolginov, Sh.Sh. (1978), Cosmic Res., 16, 204-213.
7. Dryer, M., and G.R. Heckman (1967), Solar Physics, 2, 112-124.
8. Elphic, R.C., C.T. Russell, J.A. Slavin, and L.H. Brace (1980), J. Geophys. Res., 85, 7679-7696.
9. Gombosi, T.I., T.E. Cravens, A.F. Nagy, R.C. Elphic, and C.T. Russell (1980), J. Geophys. Res., 85, 7747-7753.
10. Gringauz, K.I., V.V. Bezrukikh, T.K. Breus, M.I. Verigin, G.I. Volkov, and A.V. Dyachkov (1974), Cosmic Res., 12, 535-546.
11. Intriligator, D.S., and E.J. Smith (1979), J. Geophys. Res., 84, 8427-8435.
12. Lazarus, A.J., H.S. Bridge, J.M. Davis, and C.W. Snyder (1967), Space Research. VII, 1296-1305.
13. Lindal, G.F., H.B. Hotz, D.N. Sweetnam, Z. Shippony, J.D. Brenkle, G. V. Hartsell, and R.T. Spear (1979), J. Geophys. Res., 8443-8459.
14. O'Gallagher, J.J., and J.A. Simpson (1965), Science, 149, 1233-1239.
15. Russell, C.T. (1977), Geophys. Res. Lett., 4, 387-390.
16. Russell, C.T. (1978), Geophys. Res. Lett., 5, 85-88.
17. Smirnov, V.N., A.N. Omel'chenko, and O.L. Vaisberg (1978), Cosmic Res., 16, 688-692.
18. Smith, E.J., L. Davis, Jr., P.J. Coleman, Jr., and D.E. Jones (1965), Science, 149, 1241-1242.
19. Smith, E.J. (1969), Advanced Space Experiments, eds. O.L. Tiffany and E.M. Zaitzeff, AAS, 103-130.
20. Spreiter, J.R., and A.W. Rizzi (1972), Planet. Space Sci., 20, 205-208.
21. Spreiter, J.R., and S.S. Stahara (1980), J. Geophys. Res., 85, 7715-7738.
22. Van Allen, J.A., L.A. Frank, S.M. Krimigis, and H.K. Hills (1965), Science, 149, 1228-1233.
23. Wallis, M.K. (1973), Planet. Space Sci., 21, 1647-1660.

SIGNIFICANCE OF LARGE OPEN SPACES WITHIN THE NORTH POLAR DUNE FIELDS ON MARS. Roger S. U. Smith, Geology Department, University of Houston, Houston, TX 77004

Large open spaces, much larger than the spacing between dune ridges, occur within the circumpolar dune fields in the northern hemisphere of Mars. Many open spaces are centered about hills and their forms can either be concentric to the hills or elongate but fixed by the hills' positions. These hill-anchored open spaces display even size of dune ridges on their margins; others that exhibit distinctly-larger dune ridges along one margin may not be controlled by topography but represent breakup of dunes within the space and accumulation of the released sand into a single, large transverse ridge downwind. Studies of open spaces within terrestrial dune fields, both on Landsat and aerial imagery, suggest that unanchored open spaces may be common where dune fields have been flooded intermittently, as on the floors of closed desert basins, but concentric, anchored open spaces occur about hills within fields of transverse dunes. Most large open spaces on Earth seem to be of a third sort, interconnected interdune flats separating discrete dune fields or isolated composite forms, but this sort seems rare on Mars.

If large open spaces are devoid of dunes, they must either: a) have formed at or before the time of dune accumulation (eg, hills); b) represent an environment where dunes are destroyed and their constituent sand dispersed (eg, flooded shallow basins on Earth); or c) represent an environment across which sand can move without forming discernable dunes. If open spaces formed after the enclosing dunes, the bulk of the sand that once covered them must either: a) been fixed within the open space; b) escaped by wind action; or c) been added to the mass of dunes downwind. The margins of some open spaces on both Earth and Mars show clearly the last alternative in a conspicuous "rolled-up" margin, taller and broader than adjacent dune ridges ("ramparts" of Breed, Grolier and McCauley (1)). Unlike longitudinal dune systems, the continuous transverse ridges so common on Mars should prevent downwind escape of ordinary sand grains. Except where "rolled-up" margins occur, it seems likely that most open spaces are controlled by features that predate the development of the dune fields in their present form. Some are clearly anchored by raised crater rims to form equant to oval open spaces; others show just a trace of higher ground within them, but centered and of similar shape.

Tsoar, Greeley and Peterfreund (2) attributed some open spaces anchored by crater rims to scour around the craters. On Earth, however, such scour "tails" behind hills seem most common within fields of longitudinal dunes, whereas open spaces in the north polar region of Mars occur within fields of dunes generally acknowledged to be transverse (1,2,3). On Earth, a hill within a field of transverse dunes commonly generates a dune-free "moat" that mimics the hill's shape, so circular hills (eg, crater rims) generate circular open spaces. Oval open spaces may represent elongation in the net direction of the dominant wind in a reversing wind regime, such as the regime proposed by Tsoar et al (2). If so, these features may prove useful in assessing wind dominance over much longer intervals than can be inferred from the orientation of dune forms. Further investigation of terrestrial open spaces is needed to verify or discard this conjecture.

The character of open spaces localized by hills within fields of transverse dunes constrains the origin and migration of these dunes during their

OPEN SPACES IN DUNE FIELDS ON MARS

Smith, R.S.U.

present cycle of development. Open spaces that are concentric about their central hills imply strongly that the surrounding dunes have undergone little net migration since they formed because it is difficult for long, straight, transverse dune ridges to reform downwind of a hill. Because long, unbroken transverse dunes cannot transmit sand downwind, most dunes surrounding such open spaces were probably built from a blanket of sand of fairly uniform thickness, perhaps brought into the area by non-eolian processes. These concentric open spaces probably represent sites where opposing winds balance one another; such balance could explain the remarkable continuity and linearity of some martian transverse dunes, forms considered inherently unstable by Bagnold (4) in unidirectional wind regimes.

REFERENCES CITED

1) Breed, C.S., Grolier, M.J., and McCauley, J.F., (1979) J. Geophys. Res. 84, 8183-8204.
2) Tsoar, Haim, Greeley, Ronald, and Peterfreund, A.R., (1979) J. Geophys. Res. 84, 8167-8182.
3) Cutts, J.A., Blasius, K.R., Briggs, G.A., Carr, M.H., Greeley, Ronald, and Masursky, Harold, (1976) Science 194, 1329-1337.
4) Bagnold, R.A., 1941, The physics of blown sand and desert dunes: London: Methuen, 265p.

FROM THARSIS TO THOLUS: EVOLUTION OF THE MARTIAN LITHOSPHERE AND ITS RESPONSE TO VOLCANIC LOADS

Sean C. Solomon[1], James W. Head[2], and Robert P. Comer[1]
[1]Dept. of Earth and Planetary Sciences, Massachusetts Institute of Technology, Cambridge, MA 02139
[2]Dept. of Geological Sciences, Brown University, Providence, RI 02912

Introduction. The characteristics of the lithosphere on a planet are governed by interior temperatures and their evolution with time. In turn, these lithospheric properties help control the location and magnitude of volcanism, surface loading, and tectonic activity. In this paper we evaluate the relationships, on a variety of scales, between the lithosphere and major geological processes on the surface of Mars. We first consider the response of the Martian lithosphere to such loads as volcanic constructs and basin fill, including both brittle (faulting) and viscoelastic behavior as possible responses. We then extend such concepts to larger scale volcanic provinces, including Elysium and Tharsis. A major theme on Mars has been a spatially variable lithospheric thickness; these variations have been strongly reflected in both the tectonic response to surface loads and the localization of major volcanic provinces.

Lithospheric Thickness Heterogeneity. Superiosostatic loading on a planetary surface leads to lithospheric flexure and, for sufficiently large loads, to bending stresses capable of fracturing the lithosphere. The radial distance of fractures from a given load is a sensitive indicator of the thickness of the elastic lithosphere [1], i.e. the upper third to half of the thermal lithosphere capable of supporting large shear stresses for geologically long times. We have used plate flexure theory and observed lithospheric failure features associated with several Martian features to evaluate the thickness of the elastic lithosphere as a function of time and space [2]. The features suitable for study, in approximate order of decreasing age, are the Isidis basin, Alba Patera, Elysium Mons, Arsia Mons, Pavonis Mons[3], Ascraeus Mons and Olympus Mons [4]. All are known, on the basis of gravity data [5], to be associated with large free-air gravity highs and thus to exert a substantial vertical load on the Martian lithosphere. Except for Olympus Mons, all these features have associated graben and normal faults with generally concentric orientations, though often these faults are also elements of larger-scale regional trends [6].

In the simplest model of lithospheric loading by such features, the lithosphere is regarded as a thin elastic shell overlying an inviscid interior [7], and the flexural deformation and stress are calculated from an assumed load consistent with present topography and gravity. The locations of concentric graben surrounding the loads are then inverted [8] to obtain the thickness T of the elastic lithosphere at the time the graben were formed. The results of this procedure are given in Table 1. It is clear from the table that there is not a progressive increase in T with time for Mars. The largest values are for the oldest and youngest loads in the table. We suggest that a more important control on T than age of the load is proximity to a major volcanic province. Roughly comparable values for T (25 to 50 km), as determined by the local lithospheric response to loading, are obtained for the Alba Patera region, for Elysium and for Tharsis. The Isidis basin, located far from any contemporaneous volcanic center, and Olympus Mons, situated well off the main Tharsis uplift as well as more youthful than the Tharsis shelds,

show in their tectonics the signature of much thicker (100-200 km) elastic lithospheres.

The main disadvantage of these simple models is that they fail to account for the effects of temporal variations in the load and in the lithosphere. These variations include (1) evolution of the load with time, (2) increases in lithosphere thickness with time, (3) stress relaxation in the lithosphere due to viscoelastic, rather than purely elastic, behavior, and (4) viscous relaxation in the asthenosphere. The time scale for variation (4) is almost certainly far shorter than the time scales for the other three, and we therefore treat the asthenosphere as an inviscid liquid. A more general model incorporating an evolving load on a viscoelastic lithosphere of changing thickness is difficult, but we have solved two special cases which illustrate the important effects of competing time dependent processes: a thickening elastic lithosphere with an evolving load, and an evolving load on a viscoelastic lithosphere of fixed thickness [10]. These models, when applied to Martian loading problems, change the detailed estimates but not the relative magnitudes of the lithospheric thicknesses shown in Table 1.

Evolution of Tharsis. The Tharsis province of Mars, by virtue of its large scale and its complex and extended history of volcanic and tectonic activity, is a focal point for discussions of Martian geologic evolution. The traditional explanation of Tharsis [11,12] is that broad updoming of the lithosphere caused by a thermal or chemical anomaly in the mantle led to fracturing and the volcanic emplacement of thin plains units and later of the large shields. Evidence cited in support of the model includes the broad topographic high of the Tharsis region, the large elevation of surface units mapped as relatively old on the basis of density of craters and fractures, and the generally radial trends to most extensional fractures in and near the Tharsis area.

This traditional model for Tharsis encounters several difficulties. At the long wavelengths of the Tharsis topographic and gravity anomalies, the stresses produced by uplift are not consistent with the observed tectonic features [3]. Further, the lateral temperature contrast required to support doming by thermal expansion, if an essentially isostatic process as on Earth, is too large [13]. Finally, the Elysium province of Mars is a smaller scale analog of the Tharsis region [14] that presumably had a similar origin. Because the topographic and gravity highs [5] associated with Elysium persist despite the greater age of Elysium volcanism compared to the latest volcanic units on Tharsis [12], a thermal anomaly beneath Elysium cannot be the sole explanation for the present topography.

We have thus suggested [15] an alternative explanation for the events of the Tharsis (and Elysium) region. In briefest terms, the explanation contains three elements: (1) As demonstrated above, the elastic lithosphere of Mars throughout much of its history has been heterogeneous in thickness (i.e., in temperature). Stress due both to global and local causes was concetrated in zones of thin lithosphere, foremost among which was (perhaps a small fraction of) the Tharsis region, preferentially concentrating fracturing in such areas. (2) Intense fracturing was conducive to local volcanism. The heating associated with volcanism maintained a locally thin elastic lithosphere, thus insuring that further fracturing and volcanism would be concentrated in the same area. (3) Tharsis topography was produced primarily by volcanic construction. The topographic and gravity highs have been supported against complete isostatic compensation by the strength of a broadly thick (if locally thin) lithosphere.

This alternative explanation has a number advantages over the doming hypothesis. The stresses associated with a broad Tharsis load are consistent with the radial extensional tectonic features [3,16]. The crustal thickening required by the hypothesis of a constructional origin for the Tharsis and Elysium provinces is consistent with gravity and topographic data [17]. Neither the magnitude of the Tharsis gravity or topographic anomalies nor the persistence of Elysium topography for a geologically long time poses any difficulty. While the youngest volcanic plains in the Tharsis region may be relatively thin [18], the thickness of earlier volcanic units is not well constrained. The comparatively old, high standing surfaces in the Tharsis area, by this hypothesis, may be the still exposed surfaces of volcanic constructs from an early episode of Tharsis activity, perhaps dating as far back as the end of heavy bombardment. In this scenario for Tharsis, no special or anomalous properties need to be attributed to the mantle beneath major volcanic provinces. Rather the location of prolific volcanism on Mars is governed primarily by the sites of easiest access of magma to the surface, as is the case for mid-ocean ridge volcanism on Earth.

Conclusions. The thickness of the lithosphere on Mars has played an essential role in the tectonic and volcanic evolution of that planet. For volcanic shields and filled basins, the heterogeneous lithospheric thickness has led to a spatially varied response to surface loads. The thinnest lithosphere has been the site of enhanced fracturing and volcanic activity, leading to the development of the major volcanic provinces of Mars by volcanic construction, loading, and tectonic response extending over a large fraction of Martian history.

References. [1] S.C. Solomon and J.W. Head, JGR, 84, 1667, 1979. [2] S.C. Solomon, J.W. Head and R.P. Comer, NASA TM 80339, 60, 1979. [3] R.J. Phillips et al., JGR, in press, 1981. [4] C.H. Thurber and M.N. Toksoz, GRL, 5, 997, 1978. [5] W.L. Sjogren, Science, 203, 1006, 1979. [6] D.H. Scott and M.H. Carr, USGS Map I-1083, 1978. [7] J.F. Brotchie, Mod. Geol., 3, 15, 1971. [8] R.P. Comer, S.C. Solomon and J.W. Head, PLPSC 10th, 2441, 1971. [9] R.P. Comer and S.C. Solomon, LPSXII, 166, 1981. [10] R.P. Comer, S.C. Solomon and J.W. Head, LPSXI, 171, 1980. [11] M.H. Carr, JGR, 79, 3943, 1974. [12] D.U. Wise, M.P. Golombek, and G.E. McGill, Icarus, 38, 456, 1979. [13] N.H. Sleep and R.J. Phillips, GRL, 6, 803, 1979. [14] M.C. Malin, GSA Bull., 88, 908, 1977. [15] S.C. Solomon and J.W. Head, LPSXI, 1063, 1980. [16] D.L. Turcotte et al., JGR, in press, 1981. [17] B.G. Bills and A.J. Ferrari, JGR, 83, 3497, 1978. [18] J.B. Plescia and R.S. Saunders, PLPSC 11th, 2423, 1980.

Table 1. Estimate of the thickness of the elastic lithosphere on Mars assuming static loads and no viscous relaxation in the lithosphere [2].

Feature	Lithospheric thickness T, km	Relative age of load
Isidis Basin	>100	oldest
Alba Patera	25-50	oldest
Elysium Mons	50±10	oldest
Arsia Mons	25-50	intermediate
Pavonis Mons	30±10	intermediate
Ascraeus Mons	40±15	intermidiate
Olympus Mons	>200 [9]	youngest

THE GEOLOGY OF TYRRHENA PATERA: IMPLICATIONS FOR MARTIAN CENTRAL VENT PYROCLASTIC VOLCANISM.

Paul D. Spudis and Ronald Greeley, *Department of Geology, Arizona State University, Tempe, Arizona 85281.*

Introduction. Tyrrhena Patera (-22^{o}, 254^{o}) is one of the older martian central vent volcanoes. It is located in Hesperia Planum, a smooth lava plain region in the martian cratered terrain hemisphere. Tyrrhena Patera falls into a limited category of structure, termed highland patera (1); to date, only four such structures have been identified on Mars (2). Highland paterae are among the oldest of the martian central volcanoes and appear to be confined to geologically older regions of Mars. It is suggested that these structures are the remnants of a style of martian volcanism that occurred early in the volcanic history of the planet and decreased with time.

Geology of Tyrrhena Patera. Tyrrhena Patera, along with the other highland paterae Hadriaca and Amphitrites, is located on an extension of a ring of the Hellas basin (3) which probably controlled the distribution of early volcanism in this region of Mars. Tyrrhena Patera (approximately 250 km in diameter) is an extremely low profile structure; Earth-based radar data indicate total relief of less than 1000 meters (4), making the average slope of the volcano less than 0.2^{o}. The structure may be subdivided into several distinctive photogeologic units (2). The oldest materials associated with the volcano consist of eroded units that are now partly exposed north and west of the volcanic center. These materials display structure concentric to the main edifice, possibly indicating an early stage of caldera collapse. Directly overlying this unit are radially-furrowed materials that comprise the bulk of the volcano. These units appear to consist of easily eroded materials and are interpreted as ash deposits erupted during the main shield-building stage of Tyrrhena Patera. The uppermost unit displays lava channels and wrinkle ridges; this unit is interpreted as lava, erupted in the waning stage of activity. Possibly contemporaneous with the emplacement of the lavas, the entire structure was partly embayed by the surrounding lavas of Hesperia Planum. Thus, the volcano may have been originally of considerably greater size. Subsequent partial collapse of the structure is evident by the presence of normal faults that cut the upper shield lavas. A summary of the events envisioned in the production of Tyrrhena Patera is shown in Figure 1.

Implications for early martian pyroclastic volcanism. Although Tyrrhena Patera is not an unique structure within the martian uplands, volcanoes of similar type are rare. All but one of the highland paterae are associated with Hellas basin ring structure. It is possible that this type of volcano was more prevalent in earlier times, but it is difficult to explain their relative scarcity since some are apparently well preserved. If their interpretation as ash shield volcanoes is correct, martian **central-vent** pyroclastic volcanism has not been widespread. We interpret the production of ash shields as resulting from subsurface interaction of rising magma with widespread ground ice (phreatomagmatic processes). A mechanism has been proposed that would produce an extensive ground ice reservoir as a result of early fluvial drainage and subsequent freezing (5). If this hypothetical ground ice reservoir were present throughout the old cratered terrain as proposed, the extensive volcanism apparent in this region (6) should have produced a variety of landforms resulting from volcano-ice interaction. Numerous other structures on the planet have been proposed as representative of these processes (7, 8).

These observations suggest that martian **central vent** pyroclastic volcanism has not been a volumetrically significant process. This is not to say that pyroclastic volcanism in itself has been rare. Other studies (9, 10, 11) suggest regional deposits of pyroclastics are present in various locations on Mars. In addition, some of the plateau plains, previously proposed as predominantly volcanic (2, 6), appear to be at least partly composed of friable, wind-erodible products that may be ancient ash flows. It appears that most martian pyroclastic deposits do not have recognizable

THE GEOLOGY OF TYRRHENA PATERA

Spudis, P. D. and Greeley, R.

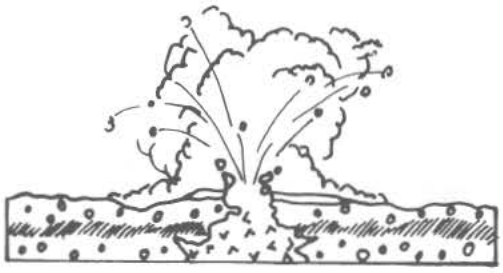

1. ERUPTION THROUGH ICE-SATURATED UNCONSOLIDATED MATERIALS (MEGA-REGOLITH) PRODUCING LARGE VOLUMES OF PYROCLASTIC DEPOSITS

2. PARTIAL COLLAPSE OF STRUCTURE, EVIDENCED BY QUASI-CONCENTRIC TEXTURE IN ETCHED MATERIALS

3. EROSION OF FRIABLE PYROCLASTIC DEPOSITS

4. PARTIAL BURIAL OF STRUCTURE BY HESPERIA PLANUM FLOOD LAVAS

5. ERUPTION OF SMALL VOLUME OF LAVA FROM CENTRAL REGION OF VOLCANO

FIGURE 1. Sequential diagrams showing development of Tyrrhena Patera (from reference 2).

source vents, but their regional extent suggests voluminous fissure-type eruptions rather than the point sources evident in the Tyrrhena-type structures. Further study of the other less well-characterized volcanoes in the martian uplands may reveal that an early pyroclastic phase has been an important part of the eruption histories of these structures.

References

(1) Plescia J. B. and Saunders R. S. (1979) *Proc. Lun. Planet. Sci. Conf.* 10th, 2841–2859.
(2) Greeley R. and Spudis P. D. (1981) *Rev. Geophys. Space Phys. 19*, 13–41.
(3) Peterson J. E. (1978) *Proc. Lun. Planet. Sci. Conf.* 9th, 3411–3432.
(4) Downs G. S., Reichley P. E. and Green R. R. (1975) *Icarus 26*, 273–312.
(5) Carr M. H. (1979) *J. Geophys. Res. 84*, 2995–3007.
(6) Greeley R. and Spudis P. D. (1978) *Geophys. Res. Lett. 5*, 453–455.
(7) Hodges C. A. and Moore H. J. (1979) *J. Geophys. Res. 84*, 8061–8074.
(8) Frey H., Jarosewich M. and Partridge K. (1981) *Lun. Planet. Sci. XII*, 300–302.
(9) Scott D. H. and Tanaka K. L. (1980) *NASA Tech. Memo. 82385*, 255–257.
(10) Ward A. W. (1979) *J. Geophys. Res. 84*, 8147–8166.
(11) Morris E. C. (1981) *J. Geophys. Res.* (in press).

This work is supported by the NASA Planetary Geology Office, Mars Data Analysis Program, through Grant NSG–7548 to Arizona State University.

EOLIAN STRATIGRAPHY OF THE WEST CENTRAL EQUATORIAL REGION OF MARS: VIKING LANDER 1 AND ORBITER COLOR OBSERVATIONS. Edwin L. Strickland, III
Dept. Earth, Planet. Sci. Washington University, St. Louis, Mo. 63130

Soil stratigraphic units recognized at the Viking 1 site correlate with color/albedo units seen in Viking Orbiter color images surrounding the site. Several of these units extend from the Lunae Planum highlands, west of Chryse, east to Schiaparelli basin and Sabaeus Sinus. Their morphology and contact relations vary little over this 8000 km. distance. Eolian mantle and bedrock geologic units are largely covered and obscured by these units. However, topography and (probably) meter-scale roughness have controlled the deposition and erosion of these eolian units. The sediments probably were transported into this region in eolian suspension, building up a succession of thin (less than meters thick) layers over wide regions. Progressive eolian erosion is now stripping these units, removing them in suspension, and exposing their stratigraphic sequence.

Distinct soil stratigraphic units are visible in color-enhanced images of the Viking 1 site. They are identified on the basis of color, texture, surface morphology, and contact relations (1). The uppermost unit is a thin, discontinuous, bright, and relatively "red"* soil. It probably is underlain by another thin and patchy layer: "green-blue" soil. "Blue drift" soils, generally covered by the "red" and "green-blue" soils, cover much of the site. Viking 1 landed straddling the edge of one of these drifts. A unique patch of crust-like "orange-red" soil was exposed at the edge of the drift, where retrorocket exhaust apparently scoured away a few centimeters of "blue drift" soil. The "blue drift" soil, and probably the "orange-red" soil, rest on the lowermost unit: "rocky blue" soil. A sixth soil unit, "dark red" soil, caps the "Big Joe" boulder near the lander, and surrounds several nearby boulder clusters. Its stratigraphic position is not well defined by the lander images, but it probably lies below the "blue drift" soil, and above the "rocky blue" soil. The soil units at the Viking 2 site, nearly halfway around the planet, greatly resemble those at the first site. This suggests that such soil units are widely distributed on Mars.

Study of color-enhanced Viking Orbiter images of regions near the Viking 1 site, and a natural color mosaic of the west-central equatorial region (2), suggests that the soil units observed by VL-1 can be observed from orbit, and extend laterally for thousands of kilometers. Chryse Planitia, at 1 and 4 km./pixel resolution, has a uniformly "red", moderately high albedo surface. These images were taken during the extended mission, when the Viking 1 site's soils were covered by a thin layer of bright "red" dust. This was deposited during the first winter; the bright "red" soil observed earlier may have been the deposit of previous dust storms. Other color/albedo units around the Chryse basin lose contrast and fade-out as they enter the basin. This unit, called here the Xanthe unit (after the classical bright albedo feature of west Chryse) is the uppermost unit in the Orbiter color/albedo stratigraphy.

At the mouth of Kasei Vallis, N. W. of Chryse, dark albedo features show dark "blue" and possibly "blue-green" colors. Similar features to the N. E. and E. form Niliacus Lacus at the southern end of Mare Acidalium. Craters McLaughlain and OXI-Lu have dark "blue" crater streaks that merge with the edge

* Colors referred to are relative to scene averages, as displayed in color-enhanced images.

EOLIAN STRATIGRAPHY: WEST CENTRAL EQUATORIAL REGION

Strickland, E. L., III

of Niliacus Lacus. Further east, in Oxia, isolated dark "blue" crater streaks occur, and to the S. and S. W., they merge to form the classical dark albedo features of Oxia Palus, Sinus Meridiani, Margaritifer Sinus, and Aurorae Sinus. This unit, the Sinus Meridiani unit, is bordered throughout this region by a bright "red" border, against darker, intermediate albedo "red" surfaces.

The bright "red" border widens along the margins of the dark markings near the equator. It forms independent crater streaks, caps mesas in the channels entering S. E. Chryse, and forms irregular patches along the border of Lunae Planum and the S. Chryse highlands. This unit may be called the Eos unit, where it separates Aurorae Sinus and Margaritifer Sinus.

The intermediate albedo "red" unit, the Oxia unit, extends without interruption from the Lunae Planum highlands, across the S. Chryse highlands, the mouths of Simud, Tiu, and Ares Valles, the cratered plains of Oxia, nearly to the rim of the Schiaparelli basin. Here, and to the north, the Oxia unit terminates against the brighter "red" cratered highlands of west Arabia (Moab in the old nomenclature). Along the southern half of this border, it forms dark "red" crater tails against the Arabia unit, as the Eos unit does against Oxia in the S. Chryse highlands, and the Sinus Meridiani unit does against the Eos unit in Oxia Palus. Crater ARA-Sn, at 16°N., 347°W., ideally shows the sequence of these units. An irregular dark "blue" patch of Sinus Meridiani unit in the center is surrounded by a thin bright border of Eos unit and a wider dark border of the darker "red" Oxia unit, against the moderately bright "red" background of the Arabia unit. The Oxia unit is always separated from the Sinus Meridiani unit by the Eos unit, except near the mouth of Kasei Vallis, where contact relations may be obscured by patches of the Xanthe unit, and near the Schiaparelli basin, where complex albedo patterns and a sixth unit obscure contact patterns.

The sixth unit, the Deucalionis unit, forms the bright classical albedo feature of Deucalionis Regio, south of Sinus Meridiani and Sinus Sabaeus. Here, bright patches on Sinus Meridiani unit in crater bottoms, and bright crater streaks abruptly merge to form a nearly continuous bright region. To the south, in Pandorae Fretum, irregular patches and dark lines reappear. At the west end of Pandorae Fretum, the bright Deucalionis unit breaks up, exposing typical materials of the Sinus Meridiani unit. Between Orbiter 1 revolutions 593 and 669, several dark "blue" patches of Sinus Meridiani unit appeared or darkened south of Schiaparelli basin and Sinus Sabaeus. Pandorae Fretum regularly darkens during the martian southern summer. Dark streaks and patches similar to those in this region, but further south, enlarged and darkened during the Mariner 9 mission. These are thought to form by eolian stripping of a thin layer of bright dust from a darker surface. The Deucalionis unit, like the Xanthe unit, probably consists of a thin dust deposit from the annual dust storms.

Unambiguous evidence of the vertical stratigraphic sequence of these units is rarely available in Orbiter imagery at kilometer resolution. To obtain more information on the contact relations of these units, several higher resolution black and white images of selected features were databased. This procedure removes most camera signatures, illumination shading, and projects the images into Mercator projection. These images will be combined with color information from the km. resolution color images to yield synthetic high-resolution color images. A unique 20 m./pixel color image S. of Schiaparelli basin is also being prepared.

EOLIAN STRATIGRAPHY: WEST CENTRAL EQUATORIAL REGION

Strickland, E. L., III

Becquerel crater (8.4°W., 21.3°N.), in the Oxia Palus region, contains dark "blue" soils that form dune masses, and less dark, featureless "blue" patches. The dunes are not well resolved at 75 m./pixel resolution, but appear to have maximum dimensions of about 300 meters. Surrounding the dune fields, and extending downwind (southwest) from them, are areas with higher albedo and weaker "blue" coloring. Some areas may have "blue-green" color. These members of the Sinus Meridiani unit are surrounded by the higher albedo border of the Eos unit. That unit forms several crater tails downwind of small craters on the floor of Becquerel, against the darker Oxia unit. The Sinus Meridiani unit probably consists of small "blue" drifts, ≤75 m., resting on the bright "red" Eos unit. The Oxia unit surrounding these units is then interpreted as the lowest of these three units.

The topography of Becquerel crater, and the smaller craters in this area is quite subdued, and little difference is visible between the areas covered by these three units. Relief may be slightly sharper in the "blue" crater tail region, as suggested by Kieffer, et al. (2). They suggest that the crater tails are areas of turbulent wind scour, where dark "blue" bedrock is exposed. However, this cannot be reconciled with the subdued, mantled character of the southern rim of Becquerel, and fails to explain the consistant relation of dark "blue" splotches in crater floors with "blue" wind tails downwind of them. These dark streaks do not resemble the dark erosional streaks and patches of Pandorae fretum. Finally, their hypothesis does not explain the systematic appearance of one unit as crater tails near its border with only one of its adjacent units. Perhaps previous erosion of mantle deposits downwind of craters produced greater meter-scale roughness, that now impedes erosional stripping of these units.

One additional unit in crater Becquerel is the Bequerel Cratered Plateau. This bright "red" plateau shows concentric banding resembling the layered terrain of the polar regions. It has a sharp, unmantled appearance, and looks severely eroded. Yardang grooves cross most of its surface where it has been imaged at high resolution. Similar materials form layered plateaus in Henry crater (11°N., 336°W.), nearby ARA-Ng, and "White Rock" to the south. These units, with superimposed craters, are clearly much older than color/albedo units that dominate the west central equatorial region of Mars.

(1) Strickland, E. L., III (1979) Proc. Lunar Planet. Sci. Conf. 10th., P. 3055-3077.
(2) Kieffer, H. H., et al. (1981) submitted to Proc. Lunar Planet. Sci. Conf. 12th.

Table. Preliminary stratigraphic columns.

Viking 1 Site		West Central Equatorial Region
"Bright Red" soil	- - - - - - - ? - -	Bright "red" Xanthe and Deucalionis
"Green-blue" soil	- - - - - - - - ? - -	Dark "blue" and possible "blue-green" Sinus Meridiani units
"Blue drift" soil	- - - - - - -	
"Orange-red" soil	- - - - - - - ? - -	Bright "red" Eos unit
? "Dark red" soil	? - - - - - - ? - -	Intermediate "red" Oxia unit
"Rocky blue" soil	- - x x x x	Bright "red" Arabia unit

RECENT WEATHERING OF ROCKS AT THE VIKING LANDING SITES: EVIDENCE FROM ENHANCED IMAGES AND SPECTRAL ESTIMATE RATIOS. Edwin L. Strickland, III
Dept. Earth, Planet. Sci., Washington Univ., St. Louis, Mo. 63130

Color enhanced images of the Viking Landing sites (1) show that many of the rock surfaces have high albedo and a unique "green" color -- relative to the scene average -- not shared by any other material at the landing sites. The closest match of materials at the sites to these "green" rocks is the "green-blue" soil, present in small patches at the Viking 1 site. This unit has intermediate albedo, and a very weak "green-blue" color similar to the rocks'. The surfaces of the "green" rocks were interpreted to be a weathering coating, formed in situ from the underlying rock materials (1). The "green-blue" soil was suggested to be a thin, patchy eolian deposit, coating both "blue drift" soils and the "rocky flats" patch of duricrust. Spectral estimate ratios (2) of materials at the Viking 1 site, now show that there is a clear spectral similarity between the "green" rock surfaces and the "green--blue" soil. A recent enhancement of an image of sample trenches at "rocky flats" showed that no "orange-red" duricrust is present under the "green-blue" surface; only "rocky blue" soil is present. Thus, "green-blue" soil is present only on the surfaces of "blue" soil units. These materials belong to a well defined spectral sequence that includes many of the units at the Viking 1 site. This sequence may represent the results of recently or currently active weathering processes on Mars.

Using a modification of a technique described by Huck, et al. (3), I estimate the spectral radiance of the light entering the Lander's cameras. Useful spectral radiance estimates extend from 0.45 micrometers (blue) to 1.0 micrometers in the near IR. Despite the low -- 6 channel -- spectral resolution and spectral aliasing of the Lander camera data, these spectral estimates quantitatively characterize first order spectral differences between the martian surface materials.

Spectral radiance estimates are obtained for a few tens of pixels covering targets selected from color enhanced images. Relative spectral reflectance estimates are constructed by dividing the radiance estimate for a target by the estimate for a dust free, sunlit gray-patch on one of the Lander's test charts. Figure 1 shows the reflectance estimate obtained for the martian surface scene average in frame 12A168. To study the spectral differences between various surface units, I construct spectral estimate ratios by dividing a target's radiance estimate by the scene average's estimate. Thus, the estimate ratio for a target shows its spectral properties relative to the scene average reflectance estimate in figure 1.

Spectral estimate ratios for "blue", "green", and "yellow" rocks are shown in figure 2. These represent averages of spectra of multiple targets, except for the "yellow" rock. The "blue" rocks' spectrum slopes sharply downwards from the blue end, is concave upwards in the green region near 0.5 micrometers, and is darker than the scene average in the red and IR portions of the spectrum. The dropoff at the IR end suggests the presence of relatively strong absorption at or beyond 1.0 micrometers. This is consistent with the "blue" rocks being relatively unweathered mafic igneous rocks.

The "green" rocks' spectrum shows the appearance of strong absorption at the blue end, and a distinctive "hump" in the curve appears in the green at

RECENT WEATHERING AT THE VIKING LANDING SITES

Strickland, E. L., III

0.50 to 0.525 micrometers. This is responsible for the bright "green" color of these rocks in the color enhanced images. (Note that the real color of the rocks is a moderate olive brown, compared with a scene average of moderate yellowish brown.) The "green" rocks are significantly brighter than the scene average: about 30% in the near IR. The ~1.0 micron absor tion is still present, though not as strong.

The "yellow" rock's spectrum continue the trend. Reflectance at short wavelengths drops off even stronger than the "green" rocks', while the "hump" peaks at longer wavelengths, forming a plateau around .6 micrometer. It remains high through the near IR, with the 1 micron absorption still present, but, again, weaker.

Figure 3 shows again the "yellow" rock's spectral estimate ratio, but now compares it with "orange-red" cobbles, "orange-red" soil (duricrust) and "red" soil. Absorption at short wavelengths continues to increase, but the "hump" flattens out in the "orange-red" units, the overall albedo starts to drop, and the entire spectral ratio slopes up toward the near IR. The ~1.0 micron feature is still weakly present in the "orange-red" cobbles, but is inverted in the "orange-red" soils' spectrum; it is now weaker than in the scene average. Instead, weak absorption appears at about 0.95 micrometers, corresponding to the dip in the reflectance estimate curve for the scene average.

The "red" soils' spectrum is only a poor continuation of this spectral sequence. While it continues the decline in albedo at long wavelengths, nearly paralleling the "orange-red" soils' spectrum, it doesn't bend in the visible, and crosses the "orange-red" soils' curve at the blue end. The match of the "orange-red" soil, and the poor fit to the spectral sequence of the "red" soil, both may be coincidental. Both soils appear (1) to be eolian units transported into this site, and unrelated to the rock materials there.

Figure 4 compares the "green"rocks' spectrum with that of three "green--blue" soils. The vertical scale of the soils has been expanded 3.75 times, and they have been vertically displaced for clarity. BGS-1 lies adjacent to "blue" soils, and appears to include some in its spectrum. The other "green-blue" soils strongly resemble the "green" rocks' spectrum; the center of the "green" hump is at shorter wavelengths, accounting for the weak "green-blue" color of these soils in the enhanced images. This strongly suggests that this soil is a weathering product of "blue" soils (which spectrally resemble "blue" rocks but have less spectral contrast).

In (1), I suggested that the "green-blue" soil is a thin, patchy eolian unit deposited on most other soils at this site. A new alternative is that this soil represents the *in situ* formation of the "green" weathering product on undisturbed soil. In (4, these abstracts) I present a preliminary correlation between the Viking 1 site stratigraphy and a proposed eolian unit stratigraphy for the west central equatorial region of Mars. The "blue drift" soil at the Viking 1 site may correspond to the dark "blue" Sinus Meridiani unit. Undisturbed areas of "dark blue" soil may start to accumulate "green" weathering product on grain surfaces. These areas would lighten with time, and develop a relatively high green/(violet + orange) ratio in Orbiter color images. Preliminary analysis of 3-color images of the "blue" materials at the mouth of Kasei Vallis, in the Oxia Palus region, and near

the Schiaparelli basin suggests significantly higher than average "green" ratios for some intermediate albedo portions of the Sinus Meridiani unit. This, together with incomplete coverage of the Eos unit by Sinus Meridiani materials and a dusting of recent bright storm dust, may explain the unique, patchy color/albedo pattern of the Sinus Meridiani unit.

References: (1) Strickland, E. L., III Proc. Lunar, Planet. Sci. Conf. 10th. (1979), p. 3055-3077. (2) Strickland, E. L.,III. In Reports of Planetary Geology Program, 1978-1979. NASA TM-80339 p. 71-74. (3) Huck, et al., NASA TM-72692. (4) Strickland, E. L. III, Eolian Stratigraphy of the West Central Equatorial Region of Mars: Viking Lander 1 and Orbiter Color Observations. these abstracts.

Fig. 1.

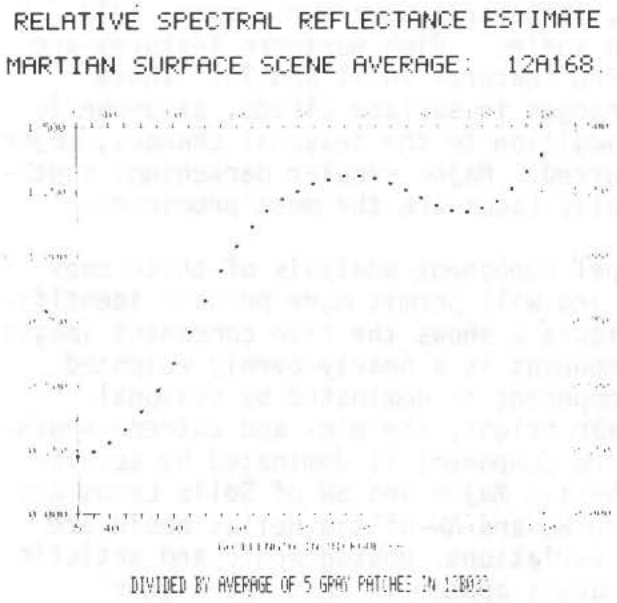

Fig. 2.

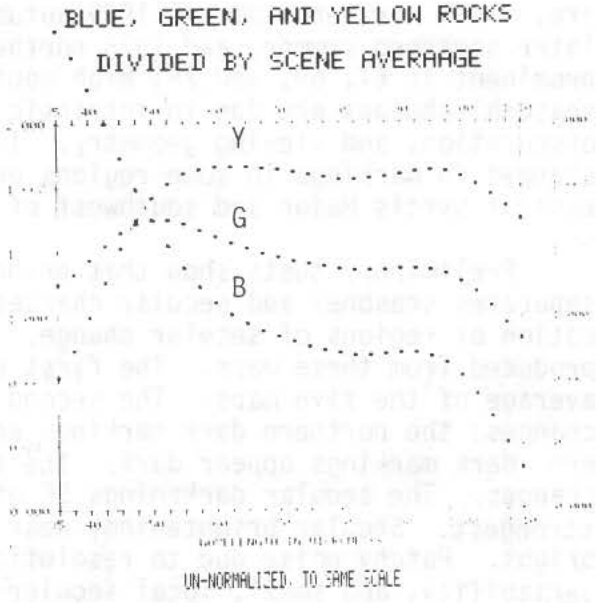

Fig. 3.

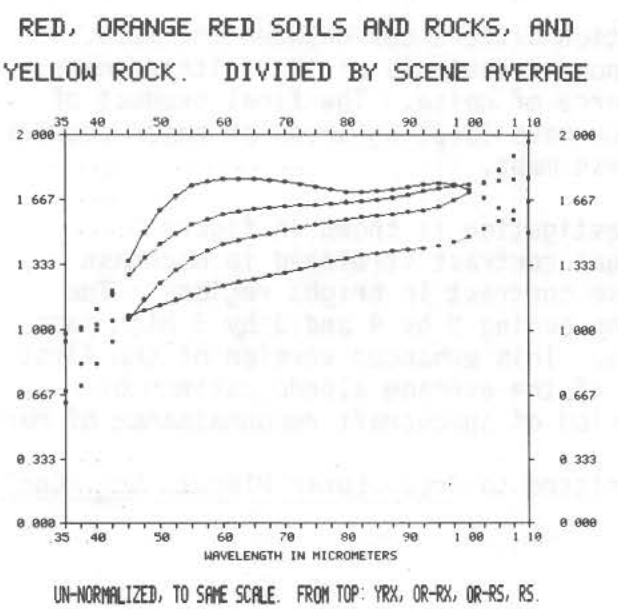

Fig. 4.

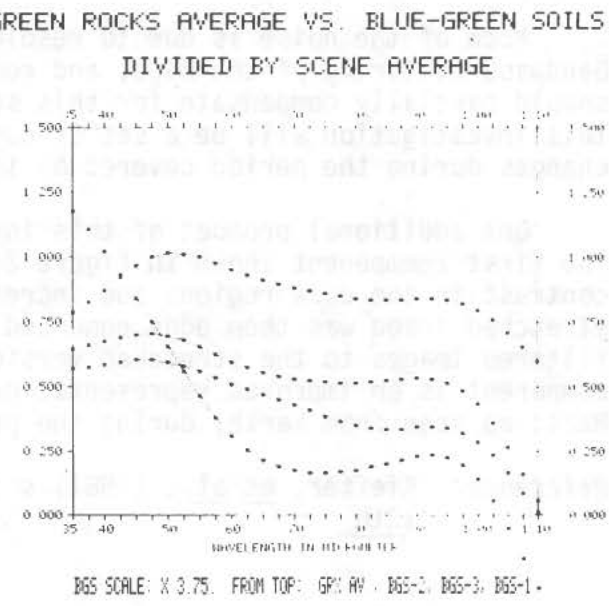

SEASONAL AND SECULAR CHANGES OF MARTIAN ALBEDO PATTERNS: ANALYSIS OF AIRBRUSHED ALBEDO MAPS. Edwin L. Strickland, III, Dept. Earth, Planet. Sci., Washington University, St. Louis, Mo. 63130

Airbrushed albedo maps of Mars were prepared for Lowell Observatory for the years 1967, 1969, 1971, 1973, and 1978. These maps are now available in Mars Consortium format: simple cylindrical projection at 1/4° resolution (1). Despite the inherently qualitative nature of these maps, principal component analysis of these maps has identified patterns of seasonal and secular albedo change during this period. A contrast stretched version of the first component image provides an excellent representation of the seasonally averaged albedo patterns of Mars as seen from Earth.

The original maps are shown in figure 1. The corresponding Mars seasons are: 1967 northern summer, 1969 autumn, 1971 early southern summer, 1973 later southern summer, and 1978 northern spring. High northern features are prominent in 67, 69, and 78; high southern features in 71 and 73. These seasonal changes are due to intrinsic changes in surface albedo, atmospheric obscuration, and viewing geometry. In addition to the seasonal changes, major changes in markings in some regions occurred. Major secular darkenings southeast of Syrtis Major and southwest of Solis Lacus are the most prominent.

Preliminary tests show that principal component analysis of these maps separates seasonal and secular changes, and will permit more precise identification of regions of secular change. Figure 2 shows the five component images produced from these maps. The first component is a nearly evenly weighted average of the five maps. The second component is dominated by seasonal changes: the northern dark markings appear bright; the mid- and extreme-southern dark markings appear dark. The third component is dominated by secular changes. The secular darkenings SE of Syrtis Major and SW of Solis Lacus are strongest. Secular brightenings near 180°W, and NW of the Hellas basin are bright. Patchy noise due to resolution variations, photographic and artistic variability, and small, local secular changes appear in this and higher components. The fourth component shows the mid-southern dark markings, and more patchy noise. The fifth component is dominated by the patchy noise.

Much of the noise is due to resolution differences between the maps. Bandpass filtering of the maps, and component analysis of the filtered maps, should partially compensate for this source of noise. The final product of this investigation will be a set of coded maps locating areas of major secular changes during the period covered by these maps.

One additional product of this investigation is shown in figure 3. The first component shown in figure 2 was contrast stretched to decrease contrast in the dark regions and increase contrast in bright regions. The stretched image was then edge enhanced by adding 9 by 9 and 3 by 3 high pass filtered images to the stretched version. This enhanced version of the first component is an improved representation of the average albedo pattern of Mars, as seen from Earth, during the period of spacecraft reconnaisance of Mars.

Reference: Kieffer, et al., (1981) submitted to Proc. Lunar Planet. Sci. Conf. 12th.

SEASONAL AND SECULAR CHANGES

Strickland, E. L., III

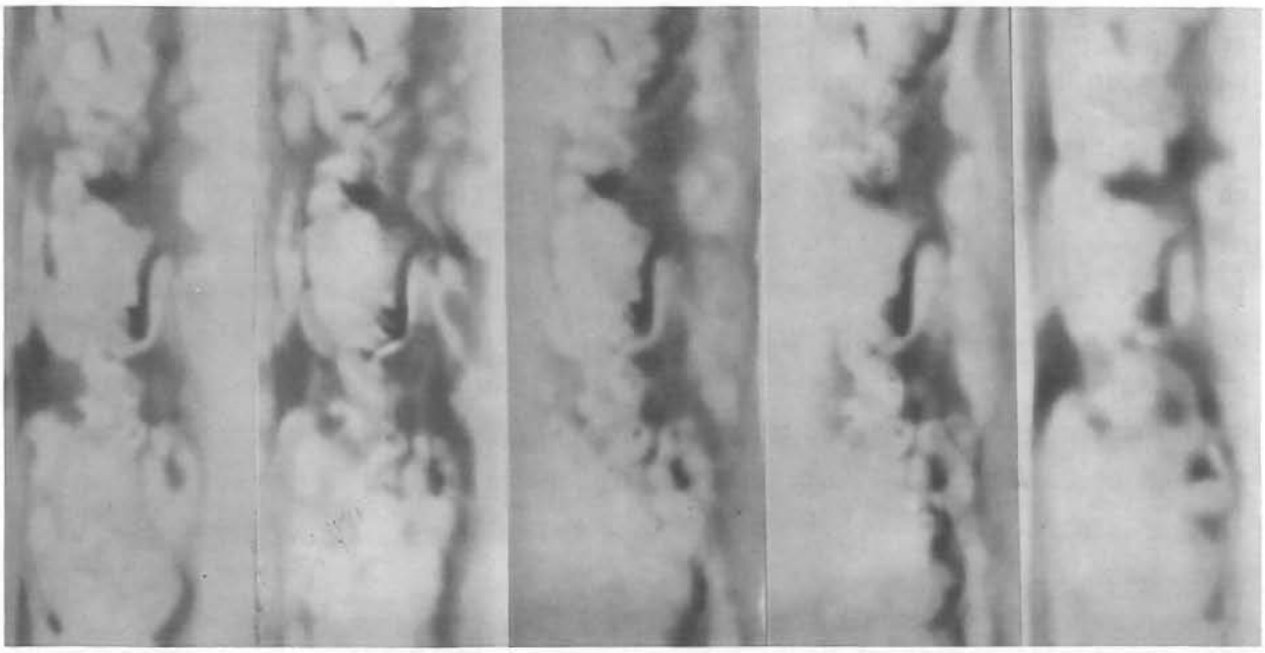

Fig. 1
1967 1969 1971 1973 1978

Fig. 2
Cmp. 1 Cmp. 2 Cmp. 3 Cmp. 4 Cmp. 5

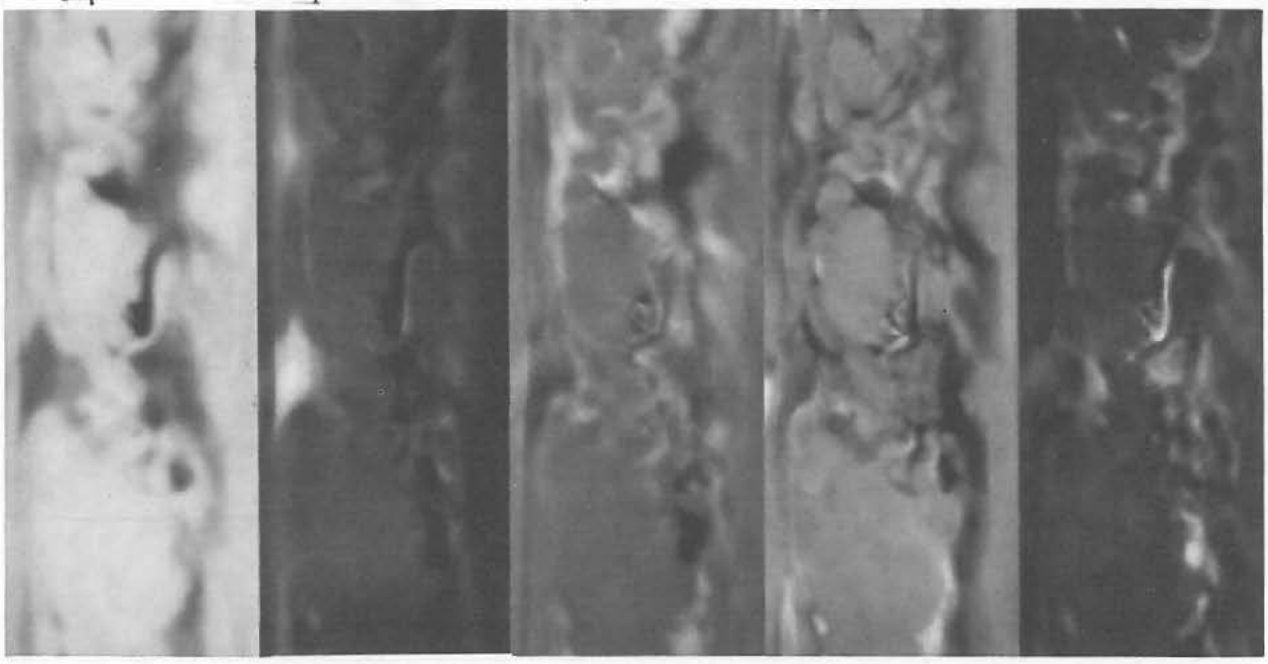

Fig. 3. Enhanced version of first component map.

SKETCH MAP OF THE EOLIAN UNITS OF THE WEST CENTRAL EQUATORIAL REGION OF MARS. Edwin L. Strickland, III, Dept. Earth, Planet. Sci., Washington Univ., St. Louis, Mo. 63130

Six stratigraphic units of eolian sediments have been identified in a natural color Viking Orbiter mosaic of the west central equatorial region of Mars (1). The region stretches 8000 km. from the Lunae Planum highlands east to the western Arabia highlands. The figure shows a preliminary sketch map of these units. Thomas and Veverka (2), report that the dark "blue" crater streaks in the Oxia region lengthened between the Mariner 9 and Viking missions, and during the Viking missions. They attributed these changes to deflation of dark material from dune masses in the craters' floors, and downwind transport and re-deposition of these materials.

References: (1) Strickland, E. L., III, Eolian Stratigraphy of the West Central Equatorial Region of Mars: Viking Lander 1 and Orbiter Color Observations. (these Abstracts). (2) Thomas, P., and Veverka, J., J. Geophys Res. (1979) 84, B14, 8131-8146.

Figure 1.

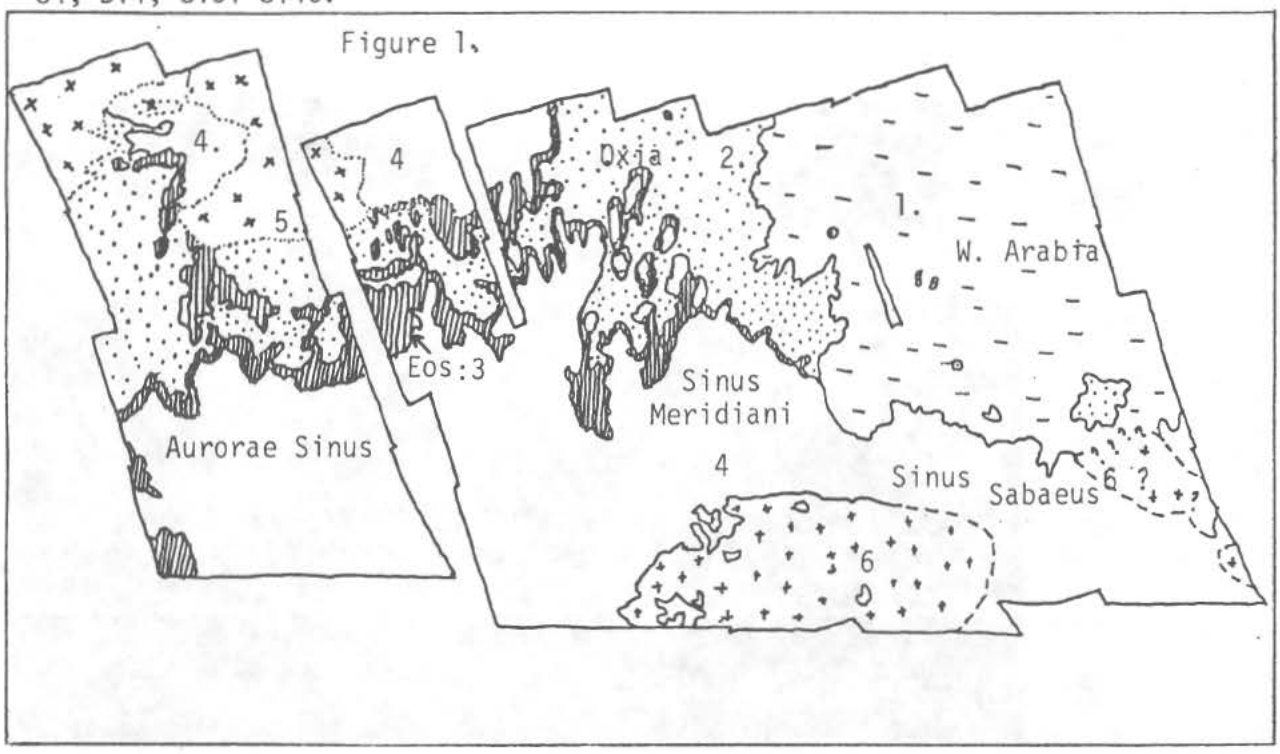

Stratigraphic sequence:

----- Uncertain boundaries

5 Xanthe

6 Deucalionis

4 Sinus Meridiani

3 Eos

2 Oxia

1 Arabia

SPECTRALLY CODED ALBEDO MAPS OF MARS: EARTHBASED SPECTRA THROUGH SIMULATED LANDER'S EYES. Edwin L. Strickland, III, Dept. Earth, Planet. Sci. St. Louis, Mo. 63130, and Dr. Robert B. Singer, Hawaii Institute of Geophysics, Univ. Hawaii at Manoa, Honolulu, Hi. 96822

We have been comparing spectral data derived from Viking Lander images with visible and near infrared earthbased spectrophometry (1) of regions on Mars (2). The Viking Lander data has very high spatial resolution (centimeters) but very poor spectral resolution: six channels from 0.45 micrometers to 1.0 micrometers (blue to near IR). Conversely, the earthbased spectra have low spatial resolution (a few hundred kilometers spot size), but high spectral resolution: 25 channels

Two techniques have been used to date to compare these data. Using earthbased spectra degraded to the Viking Lander camera's bandpasses, we have 1.) made direct channel-by-channel comparisons, and 2.) generated spectral estimate ratios (3) for both sets of data, and compared these. To avoid the difficult problems posed by instrumental calibration differences, different viewing geometries, and martian atmospheric effects, we have compared the variety within each set of data to each other, not absolute spectral reflectances. We tried two assumptions. First, we assumed that the bright "red" soil seen at the Viking 1 site (4,5) was spectrally similar to the spectrally homogenous bright "red" regions seen from Earth. Second, pre-supposing that the average of the different units at the Viking 1 site is similar to the average of the earthbased spectra, we compared spectra relative to the bulk averages of each set of data. The two techniques and two assumptions yielded equivalent results.

The spectral variety of the earthbased spectra resembles that of the soils at the Viking 1 site. Analogs of the "red", "blue", and possibly "green-blue" soils were found. A clear analog of the "orange-red" soils was not found. Dust cloud spectra resemble the "orange-red" soils, but the differences in scattering conditions make meaningful comparison impossible. "Blue" rocks at the Viking site resemble the "blue" soils, but have higher spectral contrast than "blue" soils and the "bluest" earthbased spectra. Analogs of the "green" and "yellow" rocks are not present in the earthbased spectra, with the possible exception of spectrum 69-06 which resembles "green" rocks.

A third technique for comparing the earthbased and lander data is to color code target locations on albedo maps of Mars with color information derived from the earthbased spectra. Red, green, and blue simulated Viking Lander data from selected earthbased spectra were plotted in Mars Consortium format at 1^{o} pixel size. Repeat filtering spread the spots until their size approximated the telescopic field of view on Mars when the spectra were taken. The maps were then color ratioed to generate color-information ratios, and these three ratios were multiplied by selected Mars Consortium albedo maps to yield spectrally coded albedo maps of Mars. This process is identical to that used to generate color enhanced Viking Lander images (4).

Four maps have been produced using enhanced versions of the Lowell Observatory airbrushed albedo maps: 1.) Seven 1969 spectra plotted on the 1969 albedo map. 2.) 17 dust free 1973 spectra on the 1973 albedo map. 3.) 9 dust cloud and partially dust cloud covered 1973 spectra on the 1973 albedo map., and 4.) All 24 dust free spectra on a weighted average of the of the '67, '69, '71, '73, and '78 maps.

SPECTRALLY CODED ALBEDO MAPS OF MARS

Strickland, E. L., III

Other maps, using Pleskot's prelimilary bolometric Lambert albedo map, synthesized from Viking IRTM broadband albedo data may be generated. In addition, maps will be generated using the spectral data convolved to simulate the Viking Lander's 3 infrared channels. Copies of the maps, and discussion of them will be displayed at the Colloquium.

References: (1) McCord, et al., (1977), Icarus 31, 25-39. (2) Singer and Strickland (1981) (abstract) in Lunar and Planetary Sci. XII, Lunar and Planetary Science Institute. (3) Strickland, (1980) in Reports of Planetary Geology Program, 1978-1979. NASA-TM -80339. (4) Strickland, (1979) Proc. Lunar Planet. Sci. Conf. 10th., p. 3055-3077. (5) Strickland, (1981) Eolian Stratigraphy of the West Central Equatorial Region of Mars, (these abstracts). (6)

Figure. Enhanced Red, Green, and Blue components of map 4: 24 dust free 1969 and 1973 spectra coded onto the edge sharpened weighted average of the 5 earthbased albedo maps.

Red

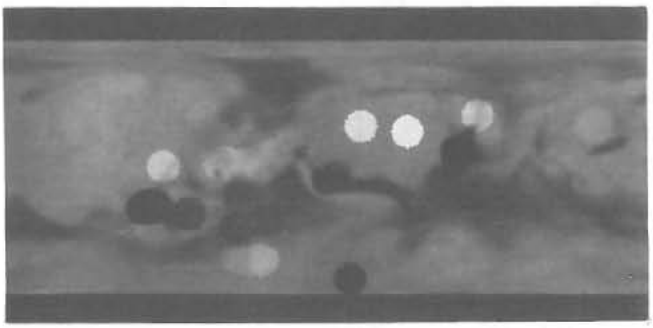

Green

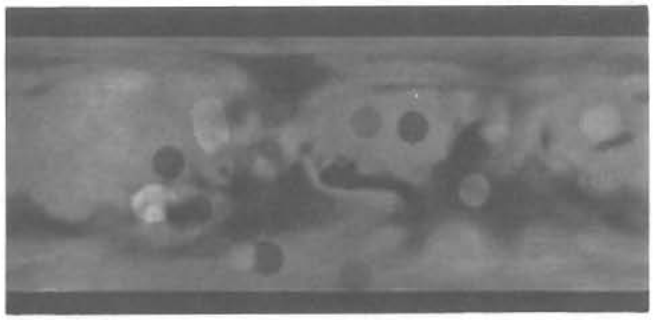

Blue

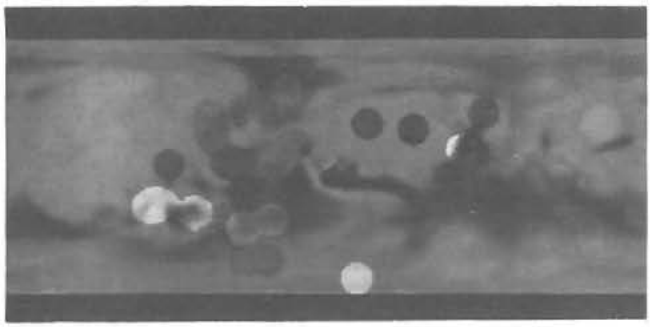

STRUCTURE OF OLYMPUS MONS AUREOLES AND PERIMETER ESCARPMENT;
Kenneth L. Tanaka, U.S. Geological Survey, Flagstaff, AZ 86001

The origin of two unique martian geologic features, the Olympus Mons aureoles and basal perimeter escarpment, has been studied by numerous planetary scientists (1,2,3,4,5,6). Recent work by Morris (7) indicates that the aureole materials, which appear to have sources in their centers, may be pyroclastic; Morris recognized, however, that the aureoles show several features not generally associated with ash flows on Earth (8). For this reason and because major uncertainties remain in interpretation of the perimeter escarpment, an analysis of the structure and morphometry of these aureoles has been undertaken to provide a more comprehensive understanding of these features in light of the overall volcanotectonic history of Olympus Mons.

Preliminary observations of the aureoles show the following major, generally intralobe structural features, some of which have been recognized previously (7) (fig. 1):

i) Closely spaced ridges, 3 km wide and <500 m high, separated by V-shaped troughs; generally concentric with aureole lobes; perimeter ridges commonly raised and sinuous.
ii) Sinuous troughs, steep sided, 3 to 4 km wide, >500 m deep; found in lobe interior areas.
iii) Long, linear grabens and normal faults, varying vertical separation.
iv) Lateral, intralobe flank ridges and faults, long (≥350 km), curvilinear; higher than adjacent interior lobe deposits.
v) Differential emplacement masses (<1000 km^2) bounded by tear faults in aureoles.

Possible mechanisms for the formation of the above features include:

1) Association of primary structures with rapid-flow emplacement of aureole lobes, as indicated by the lateral extent and low gradient of the aureole lobes; features (i) and (iv) are analogous to ridges observed on terrestrial landslides, such as the Blackhawk slide (9).
2) Secondary viscous flow movement, slumping, and sliding, accentuating feature (i) and accounting for features (v) and some of (ii) and (iii).
3) Compaction causing deformation controlled by underlying topography, which may explain some peculiar ridge-and-valley orientations.
4) Collapse due to magma withdrawal, creating features (ii) and (iii) and forming large depressions in aureole centers; concomitant seismic activity may trigger feature (v).
5) Subsidence from crustal loading, continuing the collapse faulting.
6) Wind and other weathering processes, accentuating existing structural forms and sculpturing new forms such as yardangs, prominent on lowest exposed lobe(s).

The Olympus Mons escarpment is as unique a volcanic feature as the aureoles but shows poorer exposures. New topographic data (10) and close examination of Viking imagery reveal new clues to escarpment formation. Although partly buried by slides and lava flows, the following structures can be observed: 1) the head of the scarp is generally 9 to 10 km above the martian datum; the base varies from 2 km on the northwest to 5 km on the southeast; slope gradients of the escarpment face range up to 12°; 2) the escarpment overlies aureole material in places (fig. 2); 3) the northwest face shows layering of loose and consolidated material; the southeast face is built up by 1-km-thick resistant benches (fig. 3); 4) the unit above the scarp resembles fractured plains material (fig. 4), which is

interpreted as fractured basalt in other locations (11); prominent radial and concentric faults showing vertical separation and imbricate thrust faults are found locally in this unit; 5) Reentrants in the scarp on the west side, formed by landslides morphologically similar to those off the three Tharsis Montes; other buried reentrants do not correlate well with youngest aureole lobes.

The aureole and escarpment structures indicate that the aureole lobes are not rock slides off the escarpment and thus the escarpment is not an erosional remnant (8). Structures in and above the escarpment show no alinement with regional trends. Finally, no evidence has been found for structural emergence of the scarp or lowering of the aureoles along the escarpment. The basal escarpment, then, represents the edge (subsequently modified) of a deposit emplaced before late-stage Olympus Mons shield volcanism. A subice mechanism is not favored because of the need for an extremely varied and localized climate and the general lack of expected periglacial and channeling features associated with ice and water, found in other areas of Mars.

Some possible emplacement mechanisms favored here are:

1) The basal pedestal delineated by the escarpment was emplaced as the last major aureole deposit.
2) The basal pedestal consists of lavas from a stage of intermediate composition volcanism.
3) Modification of the above deposits by gravity sliding of plates of consolidated lavas over pyroclastic and other unconsolidated material; slides imbricate along perimeter.

Further structural analysis, topographic refinement, gravity modeling and terrestrial analog studies will aid a comprehensive development of the volcanotectonic history of Olympus Mons and its aureole deposits.

References

[1] Carr M. H. (1973) Jour. Geophy. Res., v. 78, p. 4049-4062.
[2] King J. S. and Riehle J. R (1974) Icarus, v. 23, p. 300-317.
[3] Head J. W., Settle Mark and Wood C. A. (1976) Nature, v. 263, p. 667-668.
[4] Harris S. A. (1977) Jour. Geophy. Res., v. 82, no. 20, p. 3099-3107.
[5] Lopes R. M. C., Guest J. E. and Wilson, C. J. N. (1979) NASA Tech. Mem. 81776, Reports of Planet. Geol. Prog., p. 176-178.
[6] Hodges C. A. and Moore H. J. (1979) Jour. Geophy. Res., v. 84, no. B14, p. 8061-8074.
[7] Mooris E. C. (1980) NASA Tech. Mem. 82385, Reports of Planet. Geol. Prog., p. 252-254.
[8] Morris E. C. (1981) Jour. Geophy. Res., in press.
[9] Shreve R. L. (1968) Geol. Soc. Am., Sp. Paper 108, 47 p.
[10] Wu S. C. (1981) Topography of Olympus Mons (this publ.).
[11] Scott D. H. and Tanaka K. L. (1980) Proc. Lunar Planet. Sci. Conf. 11th, v. 3, p. 2403-2421.

OLYMPUS MONS AUREOLES AND ESCARPMENT

Tanaka, K. L.

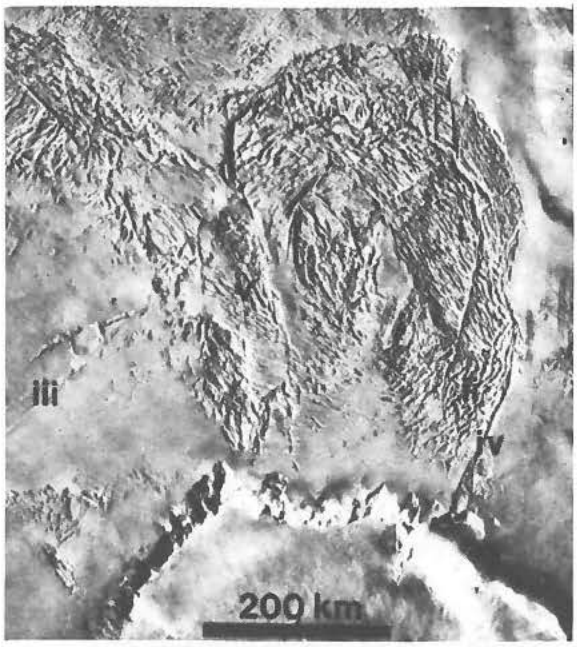

Figure 1. Northern and part of northwestern uppermost Olympus Mons aureole lobes and northern part of the shield and perimeter escarpment. Roman numerals refer to examples of features described in text. Viking image 738A09

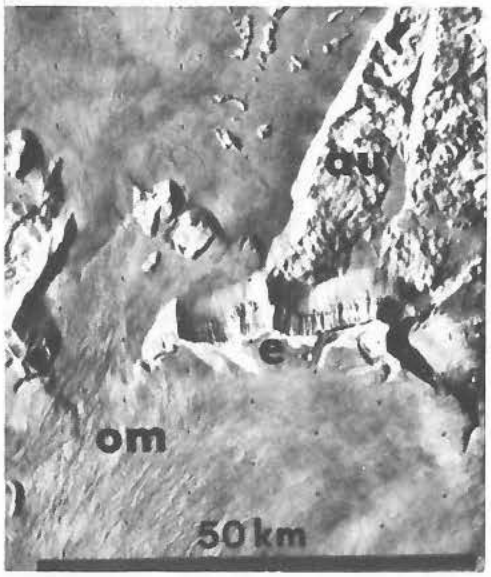

Figure 2. Best exposed contact of excarpment unit (e) overlying aureole material (au) along northern scarp edge. Young lavas from shield (om) cascaded over escarpment. Viking image 48B14

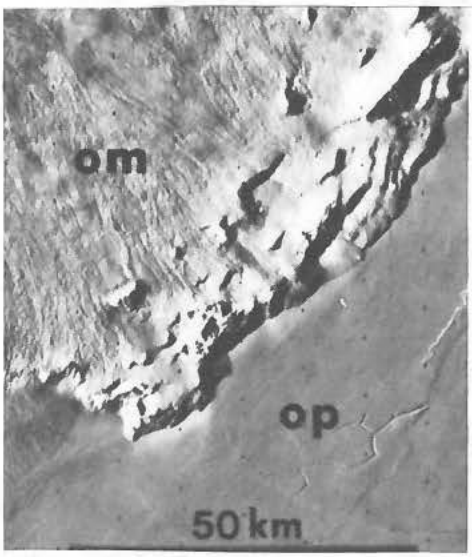

Figure 3. Laterally continuous 1-km-high steps in southeast flank of escarpment. Olympus Mons shield lavas (om) partly bury escarpment and, in turn, are embayed by younger Olympus plains lavas (op). Viking image 45B44

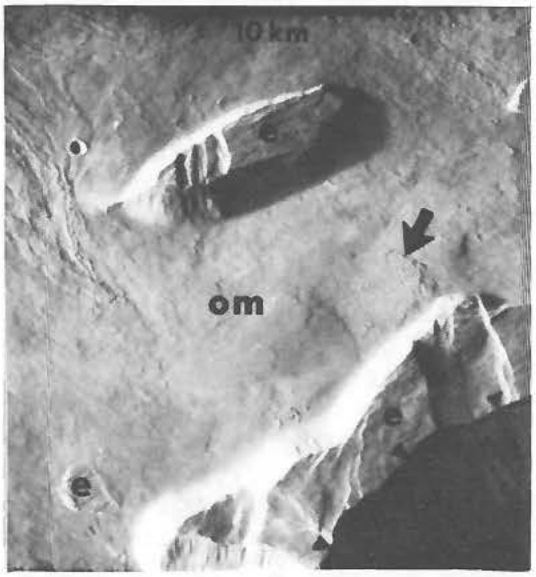

Figure 4. Fault blocks of escarpment unit (e) above the southeast escarpment margin (lined and arrowed). Note embayed lava flow with corda (large arrow) within the shield lavas (om). Viking image 468S66

THE EOLIAN BUDGET ON MARS: CLUES FROM WIND-STREAK STUDIES AND OTHER WIND MARKERS. P. Thomas, J. Veverka, P. Gierasch, J. Magalhaes, S. Lee. Laboratory for Planetary Studies, Cornell University, Ithaca, New York 14853

The occurrence and variability of wind streaks provide important constraints on possible Mars eolian sediment budgets, both on seasonal and long-term timescales. The budget involves two major size components: dust and sand, which respond differently to the meteorological wind cycles on the planet and are subject to different production and loss mechanisms.

SAND MOVEMENT: Information on the transport of sand-sized particles can be obtained from several sources: wind streaks originating from dune deposits, dune forms, the interaction of dune fields with topography, as well as from other indicators of wind direction. A fundamental Mars problem is to understand why dune deposits are so restricted in their distribution, being generally confined to two latitudinal belts (Figure 1a). In Figure 1b we have sketched the major meridional winds on the planet inferred from our study of wind streaks. The two concentrations of dunes (which, although of dissimilar distribution, are of comparable volume) occur in those latitude belts where strong meridional winds of opposite directions occur during the martian year.

The gathering/dispersal of an initial uniformly distributed sand cover into latitudinal concentrations can be modelled, using wind direction data from streak directions (1,2,3) and estimates of wind velocities (4,5). Although the calculation is somewhat uncertain, several interesting results emerge (Figure 2): (a) the present wind regimes can lead to the observed latitudinal concentrations, (b) these concentrations require times longer than 10^6 years to become established, and (c) the present dune distribution does not imply any special or isolated sources of sand-sized materials.

DUST TRANSPORT: The disappearance, reorientation, and formation of dust streaks indicates a wide range of source locales for dust, and a wide but uneven distribution of dust fallout. Although considerable dust probably reaches the north polar region, the streak data suggest there may be little or no net annual accretion of dust on the permanent cap. Retention of subtle albedo markings in the area of the annual cap, streaks that indicate dust transport off the summer cap, and erosional streaks in the permanent cap, all strongly imply that net deposition over several years probably is extremely small (< 10 μm?). Theoretical considerations also suggest much of the dust deposited in the annual cap can be removed. The generally erosional nature of the layered deposits, the transport of dust off the cap, and the evident complex cycling of sand in the same regions, all suggest that the present is not a good measure of the conditions that led to the formation of polar layered deposits in either hemisphere.

TOPOGRAPHIC EFFECTS ON TRANSPORT: Models of the generation of slope winds indicate that threshold velocities are exceeded significantly at night on the flanks of Tharsis volcanoes. These calculations are consistent with streak observations which suggest effective slope winds over the whole Tharsis bulge, Olympus Mons, Alba Patera, Elysium Mons, and other regional slopes. Such slopes

suffer erosion of dust storm fallout more easily than do regionally flat areas. In areas of low or modest regional slope the effects of topography on sediment transport become subordinate to latitudinal effects.

There is evidence that flow from the north polar region avoids the elevated areas of Arabia, Alba Patera, and the volcanic centers in Tharsis, thereby contributing to the shaping of some of the classical albedo markings in the northern hemisphere (e.g., Mare Acidalium).

It is significant that there are no large "dust bowls" on the planet. At the present time, Hellas has a rough, probably erosional floor. There is strong evidence that the amount of eolian cover is very thin in most places within Hellas.

LONG-TERM IMPLICATIONS:

a) At least one of the meridional wind systems (#2) sketched in Figure 1B should reverse every 50,000 years (6,7). The dune fields in low latitude craters are small enough that they can be reoriented on such time-scales.

b) The 50,000 year cycle appears to be too short to reorient the vast dune deposits at high latitudes, and far too short to change the latitude distribution of the dunes in any significant way.

c) The apparently low dust deposition rates at the north pole today, seem to suggest that the polar laminae form on time-scales longer than 10^6 years, or under dust transport conditions which differ strongly from those effective at present.

REFERENCES:

1. Arvidson, R. E. (1974). Icarus 21, 12-27.
2. Thomas, P., and Veverka, J. (1979). Jour. Geophys. Res. 84, 8131-8146.
3. Thomas, P. (1981). Submitted to Icarus.
4. French, R. G., and Gierasch, P. J. (1979). Jour. Geophys. Res. 84, 4634-4642.
5. Haberle, R. M., Leovy, C. G., and Pollack, J. B. (1979). Icarus 39, 141-183.
6. Ward, W. R. (1974). Jour. Geophys. Res. 79, 3375-3386.
7. Arvidson, R. E., Guinness, E., and Lee, S. (1979). Nature 278, 533-535.

ACKNOWLEDGMENT: This research was supported by NASA Grants NSG 7546, NAGW 111, and NSG 7612.

EOLIAN BUDGET ON MARS

Thomas, P. et al.

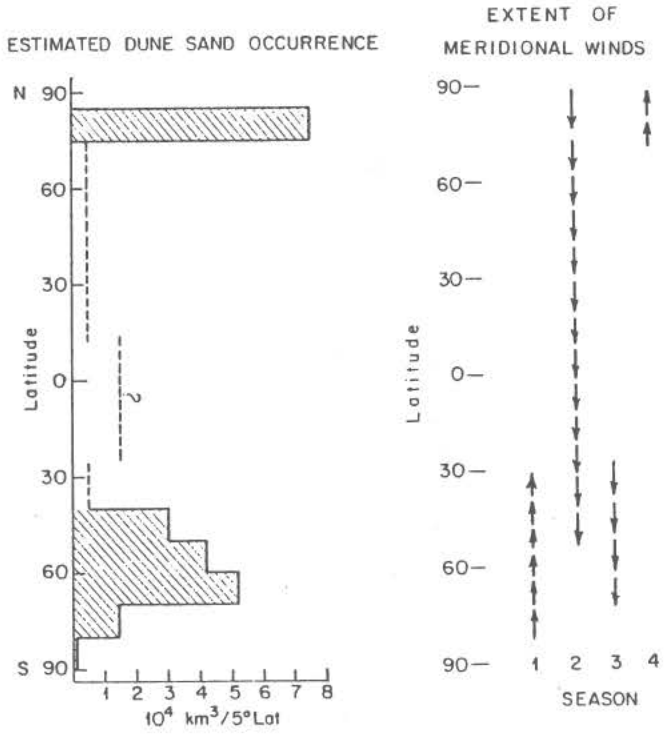

FIGURE 1a. Estimates of the occurrence of dune sands on Mars; while the absolute volumes are uncertain, the narrow concentration near 80°N and wide belt 40-70°S probably have comparable amounts of sand. Estimates of dune volumes in low latitudes are more uncertain.

FIGURE 1b. Schematic map of latitudinal ranges of major meridional winds on Mars deduced from wind streaks and dunes. (1) Southern spring. (2) Northern winter, Southern summer. (3) late Southern summer. (4) Northern summer (?); season is uncertain but well documented.

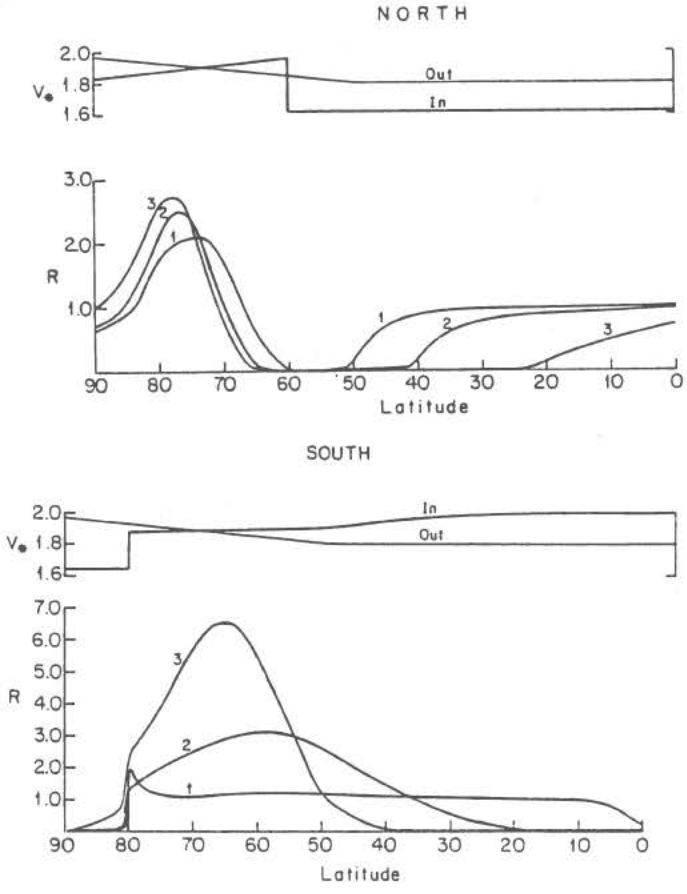

FIGURE 2. Model of latitudinal concentration of dune sand from an initially even distribution 10 meters deep over 1% of the area (1 latitude bins). Assumed shear velocities in a two-system approximation of data in Fig. 1b are indicated at top. Wind strengths and fractions of year over which these winds are effective are based on observations of streak changes and published theories of wind regimes on Mars. Note that the North loses sand to the South in this example. Time step 1 = 500,000 years; 2 = 10^6 years; 3 = 2×10^6 years. R is ratio of sand volume to initial cover. Threshold velocity assumed varies with effective season.

MARS ATMOSPHERIC SURFACE PRESSURE AT VIKING LANDERS 1 AND 2 DURING THE FIRST TWO YEARS, J. E. Tillman, Department of Atmospheric Sciences, AK-40, University of Washington, Seattle Wa., 98195.

Surface pressure observations at the Viking Lander 1 and 2 sites have provided major insight into Martian meteorological processes covering time scales of from minutes to multiple years and which are related to both local and global phenomena. Lander 1 has returned pressure and other meteorological data for more than 2.5 Mars years and is programmed to continue operating until 1994, almost 9 Mars years. Synoptic and local phenomena have been considered at length during various seasons (1,2,3,4) and inferences about global dust storms have been made from these pressure measurements (1,2,5,6,7). During the first year, two major dust storms could be observed in the daily average pressure statistics while only one is evident during the second year. A careful examination of the two storms during the first year, reveals that the first storm is evident in the pressure trace at LS = 207, may have a two sol precursor, but doubles in amplitude within a single sol while the second storm occurrs at LS = 312, increases gradually over 10 sols, but is optically more opaque (8) and has greater daily variations. During the second Viking year, analysis of the daily variation of pressure indicates that there were no dust storms as intense as either storm of the first year and certainly not as intense as the second storm of the first year. This is supported by the absence of a perturbation of Lander 2's winter average pressure during the second year as well as continuity in the synoptic periods for this time interval. The pressure variation during the minimum is essentially identical from the first to the second year, indicating that the amount of CO_2 condensed is not significantly influenced by annual variations in dustiness. Both similarities and differences between the first and second years data are presented.

Tillman, J.E. (1977) Proc. Symposium on Planetary Atmospheres, Royal Society of Canada, Ottawa, p. 145-149.
Tillman, J. E., Henry, R. M. and Hess, S. L. (1979), J. Geophys. Res., 82, p. 2947-2955.
Hess, S. L., Henry, R. M., Leovy, C. B., Ryan, J. A. and Tillman, J. E., (1977), J. Geophys. Res. 82, p. 4559-4574.
Ryan, J. A., Henry, R. M., Hess, S. L., Leovy, C. B., Tillman, J. E., and Walec, C., (1978), Geophys. Res. Letters, 5, p. 715-718.
Hess, S. L., J. A. Ryan, J. E. Tillman, R. M. Henry and C. B. Leovy, (1980), Geophys. Res. Letters, 7, p. 197-200.
Leovy, C. B. (1979), Ann. Rev. Astron. Astrophysics, p. 387-413.
Leovy, C. B. and Zurek, R. W. (1979), J. Geophys. Res., 84, p. 2956-2968.
Pollack, J. B., Colburn, D. S., Flasar, F. M., Kahn, R., Carlston, C. E., and Pidek, D. (1979), J. Geophys. Res. 84, p. 2929-2945.
4, p. 2929-2945.

GLOBAL MAP OF EOLIAN FEATURES ON MARS, A. W. Ward, P. J. Helm, N. Witbeck, and M. Weisman, U.S. Geological Survey, Flagstaff, Arizona 86001

An inventory of eolian features on Mars based on Mariner 9 and Viking Orbiter images, has been completed. Ten types of features were identified and mapped at a scale of 1:5 million. These types are 1) light streaks and frost streaks, 2) dark streaks, 3) barchan dunes, 4) transverse dunes, 5) wavy (crescentic) dunes, 6) eroded dunes, 7) yardangs, 8) deflation pits and hollows, 9) wind grooves, and 10) sand sheets or "splotches". The features were mapped in groups, not as individual landforms. Their geographic position, orientation, and season were recorded.

In the north polar region, light and frost streaks show NW winds. Dark streaks are randomly distributed. Barchan dunes (which occur well away from the pole) show mostly SW and NW winds, but a few record NE and E winds. Transverse dunes (which occur near the residual frost cap) show both E and W winds. Other erosional features are not statistically significant.

From the high northern latitudes to the equator, light streaks show NE, SE, SW, and NW winds (in order of abundance). Dark streaks show mostly NE and NW winds. Yardangs and deflation pits show the same principal winds as do the light streaks.

In the low southern latitudes, light streaks and transverse dunes record mostly NW and NE winds. Dark streaks record NE, SE, and NW winds.

In high southern latitudes, the few light streaks record E and NE winds. The abundant dark streaks record NE and SE winds, and a few show NW winds. Transverse dunes record NE and SW winds.

In the south polar region, light and frost streaks record SW and NW winds, whereas dark streaks record SE winds. Transverse dunes also show SE winds.

The distribution of most depositional features has been predicted [1-5] and recorded [6,7]. The wind patterns recorded conform to global circulation conditions of southern spring and summer more than to those of northern spring and summer [7].

We consider that erosional features indicate long-term wind trends, whereas depositional features record more recent storm winds. However, in most cases, the wind directions indicated by pits, yardangs, and other erosional features correspond to those shown by streaks. The paucity of erosional features alined with different ancient winds could be due to three factors: 1) yardangs and pits are carved in highly friable rocks (e.g. loess, thick duricrust deposits, poorly welded tuffs) [8,9] and have lifetimes of 10^4 - 10^5 years (on the order of axial precession time scales); 2) the directions of ancient winds of periods when Mars' axial

tilt and seasons were reversed are not greatly different from those of the present; 3) pits, yardangs, and grooves are largely controlled by structure, being defined in part by regional or planetary structural/topographic features that are parallel to present-day winds and may have channeled ancient oblique winds.

References:

[1] Sagan, C., Veverka, J., Fox, P., Dubisch, R., French, R., Gierasch, P., Quam, L., Lederberg, J., Levinthal, E., Tucker, R., and Eross, B. (1973) Jour. of Geophys. Res., v. 78, p. 4163-4196.

[2] Conrath, B., Curran, R., Hanel, R., Kunde, V., Maguire, W., Pearl, J., Pirraglia, J., Welker, J., and Burke, T. (1973) Jour. of Geophys. Res., v. 78, p. 4267-4290.

[3] Pollack, J. B., Colburn, D., Kahn, D., Hunter, J., Van Camp, W., Carlston, C. E., and Wolf, M. R. (1977) Jour. of Geophys. Res., v. 82, p. 4479-4496.

[4] French, R. G. and Gierasch, P. G. (1979) Jour. of Geophys. Res., v. 84, p. 4634-4642.

[5] Haberle, R. B., Leovy, C. B., and Pollack, J. B. (1979) Icarus, v. 39, p. 151-183.

[6] Thomas, P., Veverka, J., and Campos-Marquett, R. (1979) Jour. of Geophys. Res., v. 84, p. 4621-4633.

[7] Thomas, P. (1980) Bull. Amer. Astronom. Soc., v. 12, no. 3, p. 723.

[8] Ward, A. W. (1978): Ph.D. thesis, Univ. of Washington, Seattle, 201 p.

[9] Ward, A. W. (1979) Jour. of Geophys. Res., v. 84, p. 8147-8166.

RIDGE-FAULT INTERSECTIONS AND THARSIS TECTONICS. Thomas R. Watters and Ted A. Maxwell, National Air and Space Museum, Smithsonian Institution, Washington, D.C. 20560.

The ridges surrounding the Tharsis region of Mars have been studied by many workers in order to determine their relationship to the tectonic history of the area (1,2,3,4). As part of a global study of the ridges and their intersections with canyon, rilles and other topographic breaks, several cross-cutting relationships in the Tharsis region have been noted that do not strictly result from proposed models for Tharsis tectonics.

We examined all the available 1:2,000,000 controlled photomosaics of the region, as well as individual frames, and located areas where ridges interact with other features. Ridges were classified as either symmetric or asymmetric on the basis of their cross sectional symmetry, and their relationship to an associated feature, or features, were described. Some results are given in Table 1. Associated features studied include erosional escarpments, faults, impact craters, depositional escarpments, fault escarpments, and canyons. Faults were the most common associated feature, occurring in eight of thirteen areas studied in the region. Trends of ridges and faults were measured where possible. To determine the degree to which ridges and faults are related to Tharsis, radials were projected from points of intersection between faults and ridges to the topographic high on Syria Planum. This high corresponds to the center of intersections of projected faults of the Tharsis radial system (1). Where possible, the angle between the projected radial and the strike of the fault, as well as the trend of the ridge, were measured (see Table 1). This data supports a general relationship between ridges and faults through a stress field centered in the Tharsis region. However, the observed angular differences between strikes of faults and perpendiculars of ridges to the radials indicates it is not perfect. In addition, it is clear from Figure 1 that the magnitude of the deviations from orthogonality is not dependent on distance. Of the eight areas where faults and ridges interact, seven show faults clearly cutting ridges. Figure 2 shows an example of these cross-cutting relationships in an area where deviations from Tharsis-related stress

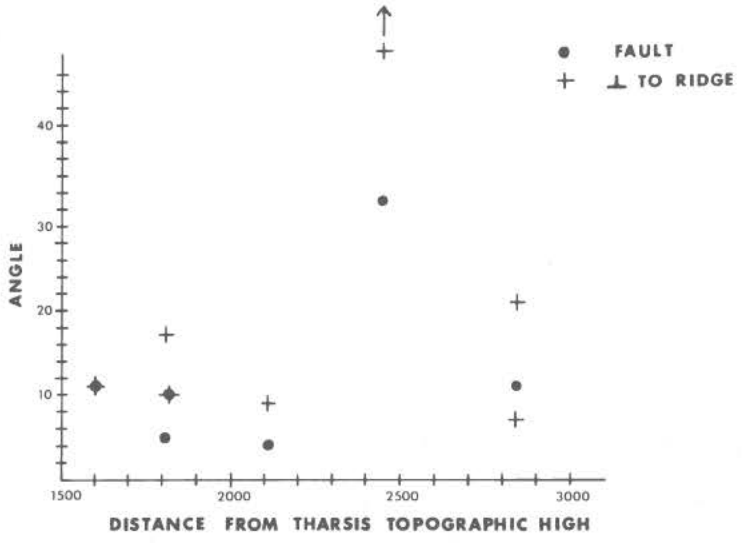

Fig. 1. Distance (km) from Tharsis topographic high vs. angle between strike of fault and perpendicular of ridge to radial.

TABLE 1

Region MC-#	Lat./ Long.	Ridge[1] Symmetry	Associated Features	Description	Δ-Angle[2] Fault-Radial	Δ-Angle[2] Ridge-Radial
Coprates MC-18SW	20°S 71°W	A	Fault	N-S trending ridge cut by E-W striking fault swarm. A portion of the ridge is visible within the graben.	11°	79°
Coprates MC-18SE	28°S 64°W	S	Fault	N13°E trending ridge cuts an eroded fault striking N69°W.	4°	81°
Coprates MC-18SE	19°S 67°W	A	Faults	N-S trending ridge cut by a roughly E-W striking fault swarm.	10°	80°
Lunae Palus MC-10NW	26°N 78°W	A	Faults, Erosional escarpment	Headward erosion of N-S trending ridge resulted in a V-shaped canyon. Uneroded portions of the ridge are cut by N65°E striking fault swarm.	33°	148°
Memmonia MC-16SE	20°S 155°W	S	Faults, Impact crater	Large N-S trending ridge cutting an impact crater and terminated at one end by a N68°E striking fault swarm. Smaller N31°W trending ridge terminated at both ends and cut by the fault swarm.	11°	Large ridge: 97°E Small ridge: 111°E
Thaumasia MC-2S	44°S 89°W	A	Fault	N80°E trending ridge is cut by a N26°W striking fault.	5°	107°

[1]A: Asymmetric, S: Symmetric

[2]Differences in angle between fault or ridge with radial to topographic high; 0° for fault column indicates radial orientation; 90° for ridge indicates true orthogonality.

orientations are greatest. Two patterns of graben are present in the region; a system of dominantly linear trends oriented N65°E, and a possibly younger, curvilinear system of graben with more northerly orientations. The faulting of ridges in this region suggests an extensional stress system occurring after ridge formation. Only two areas have been noted where ridges cross-cut faults; in the plains south of Valles Marineris, and possibly north of Ophir Chasma.

Phillips and Lambeck (2) calculated principal stress trajectories for a self-gravitating elastic model due simply to crustal loading of the Tharsis region and found a high degree of orthogonality between the tensile and compressional stresses. They found the same relationships between the tensional and compressive features in the area. Our observations indicate a somewhat less striking degree of orthogonality between the ridges and faults. If both structures formed by either simple crustal failure or catastrophic failure(5) due to the Tharsis load, then ridge and fault formation should have been coincident. Based on crater ages, Wise et al. (1) supports an approximately coincident formation of the ridges with the radial fault system, although ridges may have slightly predated faults. However, if this were true, ridges cross-cutting faults would be common. Based on our observations we suggest that most of the ridges formed in an event, or events, which predate the development of the Tharsis radial fault system. If this is the case, a simple loading model may not be adequate. The evidence suggests a more complex history involving pulses of tectonic activity, most of which postdate the major ridge forming events in the Tharsis region.

References

1. Wise D.V., Golombek M.P. and McGill G.E. (1979) Icarus, 38, 456-472.
2. Phillips R.J. and Lambeck K. (1980) Rev. Geophys. Space Phys. 18, 27-76.
3. Lucchitta B.K. and Klockenbrink J.L. (1981) Moon and Planets, 24, 415-429.
4. Saunders R.S., Bills T.G. and Johansen L. (1981) Proc. LPSC 12, 924-925.
5. Arvidson R.E., Goettel K.A. and Hohenberg C.M. (1980) Rev. Geophys. Space Phys. 18, 565-603.

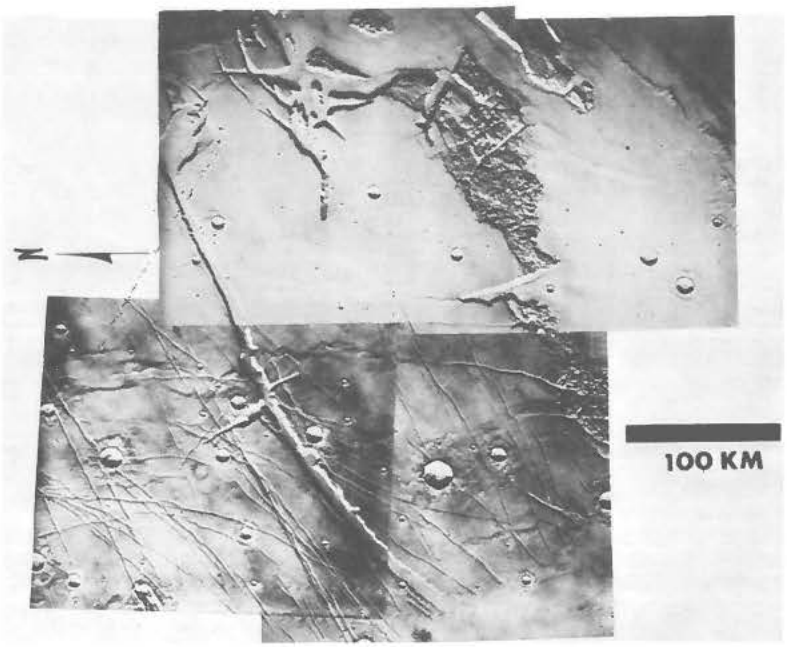

Fig. 2. Area in the Lunae Palus region.

SPATIAL ANALYSIS OF THARSIS AND HEBRIDEAN IGNEOUS CENTERS.

J.L.Whitford-Stark
Geology Department,University of Missouri,Columbia,MO.65211.

Analyses of terrestrial volcanoes have led to the proposal (1,2) that volcano spacing is proportional to lithosphere thickness or is determined by fractures whose spacing is proportional to lithosphere thickness. Furthermore, that as the lithosphere thickens with time, then volcano spacing should increase(1). The present analysis compares the Hebridean Province of Western Europe with the Tharsis Province of Mars.

The Hebridean Province lay close to the boundary of the two plates which separated to form the present North Atlantic and the regional vent distribution was controlled by an anisotropic horizontal stress system(3). Figure 1a shows the distribution of the Hebridean intrusive centers. Excluded are some submarine features(4,5) which have not been sufficiently studied to permit their identification as true Tertiary intrusive centers and flood basalts which did not give rise to massive central vent volcanoes(e.g.,Antrim,Faeroes). Included are granite intrusives which may or may not have been associated with extrusive activity(e.g.,Lundy). Radiometric dating indicates that the major part of the Province formed over a period of approximately 15 m.y.(6). The Tharsis Province also lay close to an area interpreted to have been subjected to horizontal crustal motion(7). The massive extrusive centers(figure 1a) were emplaced over a long time period; up to 3,700 m.y., depending on the chronology that is employed(8).

A network analysis using distance matrices has been performed for both areas. Figure 1a illustrates the networks in which the outer centers of activity have been joined and the inner centers linked by lines representing the shortest distances to nearest neighbors; no lines crossing. Figure 1b illustrates the preferential NNW-SSE alignment of the Hebridean features and the almost random distribution of the Tharsis features. Figure 1c shows the separation distances of the centers normalized to the length of the longest connecting link. Aside from the peak at short separations for the Hebridean Province, both histograms peak at about 1/3 to 2/5 the longest separation distance; approximately 150 km and 800 km for the Hebrides and Tharsis respectively.

Figure 2a is an attempt to illustrate how Tharsis volcanism may have developed. The rationale for this model includes the average age of cessation of activity for each volcano(8), the existence of gravity anomalies(9), and the size of the edifices (10). Major uncertainties arise from the impossibility in determining the time of initiation of activity at each volcano, the inability to recognize totally buried constructs, and errors of dating by crater-counting techniques. In 2a, 1 represents the earliest activity and 4, the latest. In 2b these same subdivisions do show preferential alignments along NE and NW directions. In 2c the data suggest an increase in the spacing of volcanoes to the present. Other data indicate that the size of a volcano

HEBRIDES AND THARSIS

Whitford-Stark,J.L.

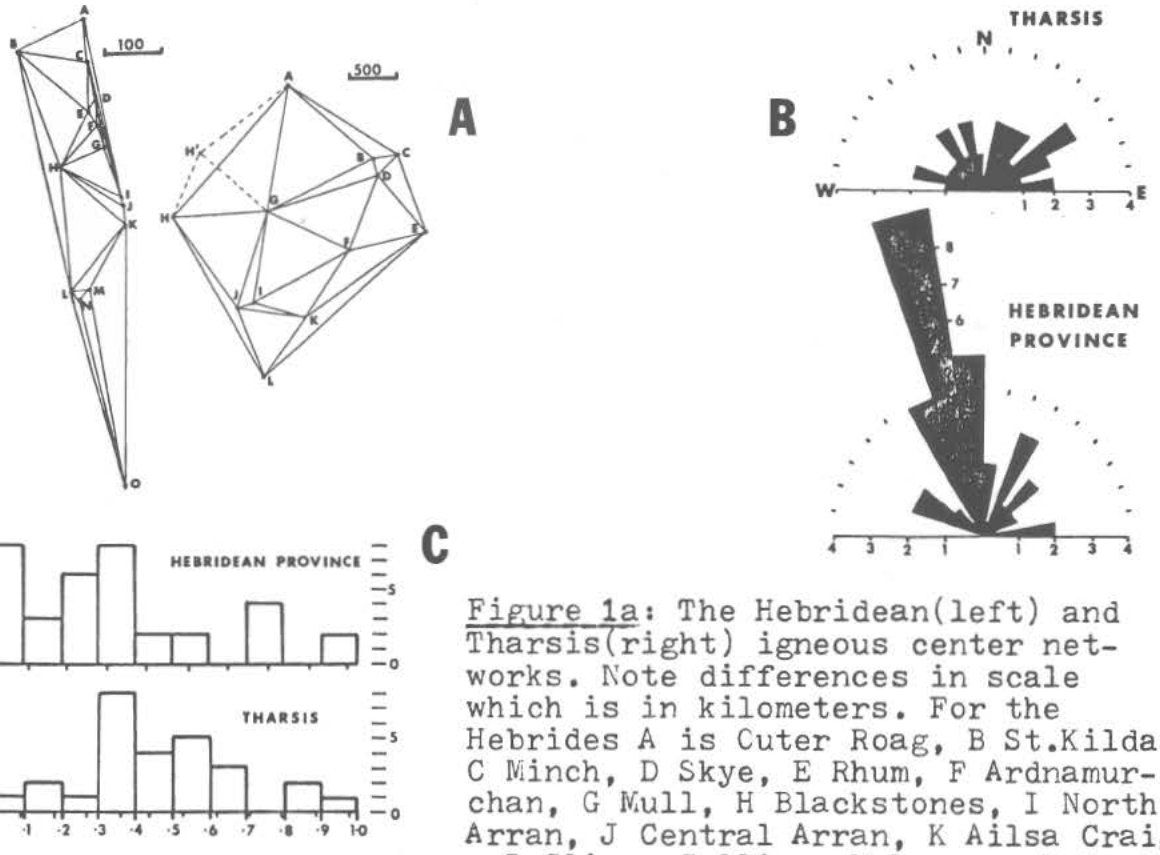

Figure 1a: The Hebridean(left) and Tharsis(right) igneous center networks. Note differences in scale which is in kilometers. For the Hebrides A is Outer Roag, B St.Kilda, C Minch, D Skye, E Rhum, F Ardnamurchan, G Mull, H Blackstones, I North Arran, J Central Arran, K Ailsa Craig, L Slieve Gullion, M Mourne, N Carlingford, O Lundy. For Mars A is Alba Patera, B Uranius Tholus, C Uranius Patera, D Ceraunius Tholus, E Tharsis Tholus, F Ascraeus Mons, G Jovis Tholus, H Olympus Mons, H' a possible early center now infilled - not used in analysis, I Ulysses Patera, J Biblis Patera, K Pavonis Mons, L Arsia Mons. Figure 1b:Rose diagram illustrating orientations of network connections in fig. 1a. The horizontal axis indicates the number of links within each 10 degree sector. Because of the method of construction of figure 1a(see text), some of the orientations are spurius and, because they are not completely connected networks, some possible orientations are omitted. Figure 1c: Histogram Illustrating the separation distances of volcanic centers normalized to the length of the greatest separation distance within each province. True separation distances are indicated by the additional horizontal scale; these being at intervals of 50 km and 200 km for the Hebridean Province and Tharsis respectively. Vertical axis indicates the number of links falling within each 0.1 unit.

appears to be proportional to the average separation distance to its nearest neighbors if an allowance is made for the burial of certain constructs by later lavas.

References: 1) Vogt,P.R.(1974) Earth Planet Sci.Lett. 21, 235-252. 2) Mohr,P.A. and Wood,C.A.(1976) Earth Planet.Sci. Lett. 33, 126-144. 3) Brooks,M.(1973) J.of Geology 81, 81-88. 4) Chalmers, J.A. and Weskon,P.G.(1979) Scott.J.Geol. 15, 333-341.

HEBRIDES AND THARSIS

Whitford-Stark, J.L.

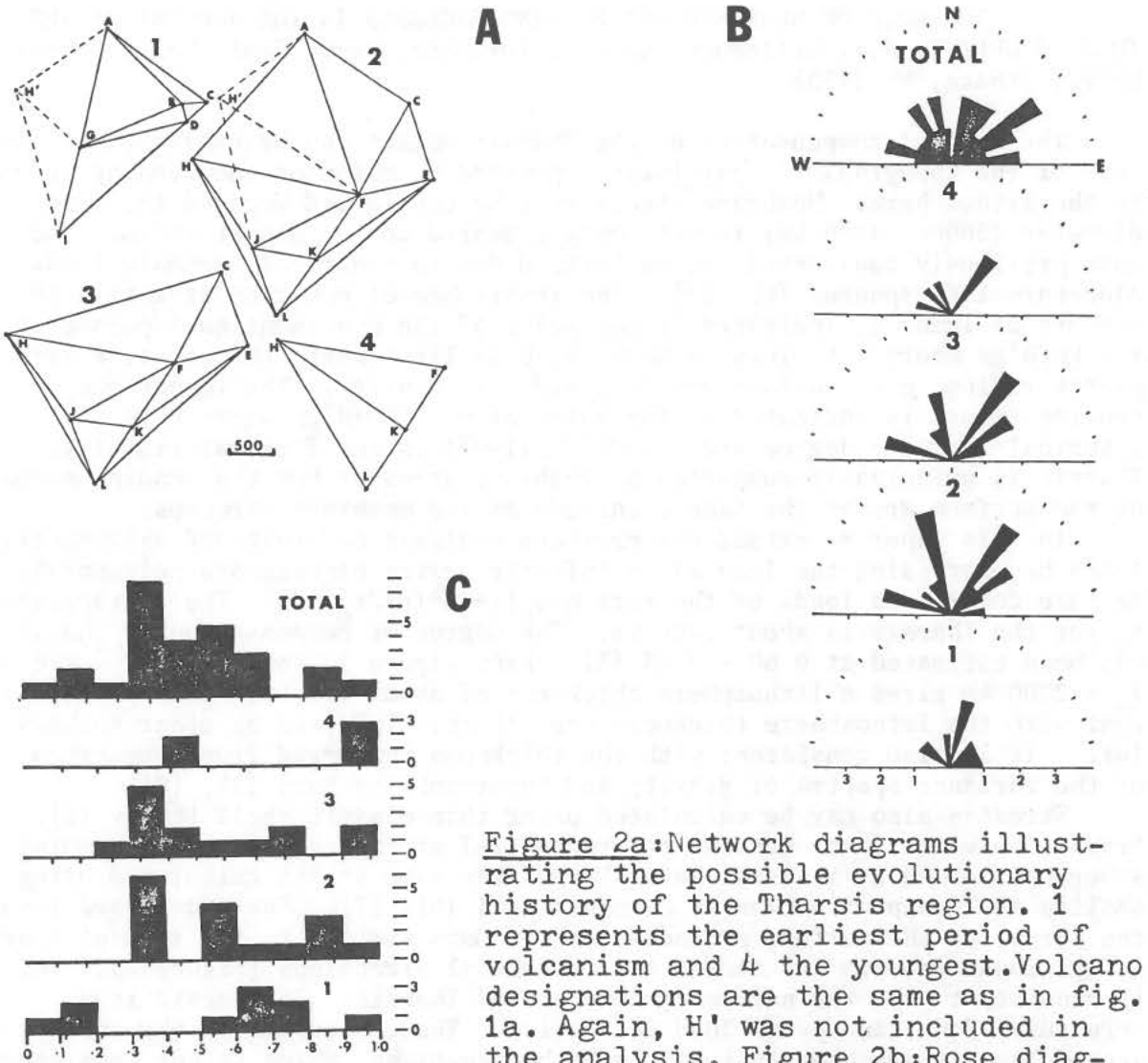

Figure 2a: Network diagrams illustrating the possible evolutionary history of the Tharsis region. 1 represents the earliest period of volcanism and 4 the youngest. Volcano designations are the same as in fig. 1a. Again, H' was not included in the analysis. Figure 2b: Rose diagrams for each of the areas of figure 2a plus the total distribution from 1b. Note that when broken down into subsystems, preferential alignments become more pronounced. Figure 2c: Histogram of link length normalized to the longest link length for each of the networks in fig. 2a. Additional horizontal scale is in units of 200 km. Vertical scale indicates the number of links within each 0.1 division. Note a trend to increasing separation with time, although preferential separations of 800 and 1,200 km are maintained fairly consistently.

References(contd): 5) Donovan,D.T.(1968) In Geology of Shelf Seas(ed.D.T.Donovan) Oliver & Boyd,p. 1-14. 6) Fitch,F.J.et al (1978) Jl.geol.Soc.Lond. 135, 499-512. 7)Wise,D.U. et al(1979) Icarus 38, 456-472. 8) Plescia,J.B. and Saunders,R.S.(1979) Proc.Lunar Planet.Sci.Conf.10th,p.2841-2859. 9) Sjogren,W.L. (1979) Science 203, 1006-1010. 10) Pike,R.J.(1978) Proc.Lunar Planet,Sci.Conf.9th., p.3239-3273.

THE ROLE OF MEMBRANE AND BENDING STRESSES IN THE SUPPORT OF THE THARSIS UPLIFT: R.J. Willemann and D.L. Turcotte, Dept. Geol. Sci., Cornell Univ., Ithaca, NY 14853

The partial compensation of the Tharsis uplift can be explained if the load of the topography is partially supported by membrane and bending stresses in the lithosphere. Membrane stress must be considered because the load diameter (3000 - 4000 km) is not small compared to the planet radius. We have previously considered the deflection due to spherical harmonic loads on planetary lithospheres [1], [2]. The importance of membrane stress in the support of loads is indicated by the value of the nondimensional parameter $\tau = Eb/R^2g\rho$ where E is Young's modulus, b is lithosphere thickness, R is planet radius, g is surface gravity, and ρ is density. The importance of bending stress is indicated by the value of $\sigma = \ell^4 D/R^4 g\rho$ where ℓ is the spherical harmonic degree and $D = Eb^3/12(1-\nu^2)$ is the flexural rigidity. Tharsis is principally supported by membrane stresses but the bending stresses at the surface are of the same magnitude as the membrane stresses.

In this paper we extend our previous analysis to arbitrary axisymmetric loads by expressing the load as an infinite series of Legendre polynomials. We have considered loads of the form $q=q_o[1+\cos(\pi x/x_o)]/2$. The appropriate x_o for the Tharsis is about 2000 km. The degree of compensation of Tharsis has been estimated at 0.60 - 0.65 [3]. From Figure 1, specifying $c \simeq 0.6$ at $x_o = 2000$ km gives a lithosphere thickness of about 180 km. This is consistent with the lithosphere thickness near Tharsis inferred by other authors [4]. It is also consistent with the thickness inferrred from comparison of the variance spectra of gravity and topography of Mars [1], [2].

Stresses also may be calculated using thin elastic shell theory [5]. Around the wider lunar mascons the tangential stress calculated by summing spherical harmonics is tensional, whereas the same stress calculated using a shallow shell approximation is compressional [6], [7]. For a downward load the stress at the surface around a load on Mars similar to the size of Tharsis is tensional in both the radial and tangential directions (Figure 2). This is consistent with the narrow grabens around Tharsis. If Tharsis is a structural dome, an upward load is implied. Then, stresses at the surface around Tharsis are compressional in both directions, which is not consistent with the observed faulting.

[1] Turcotte D.L., Willemann R.J., Haxby W.F. and Noberry J. (1981) J. Geophys. Res., in press.
[2] Willemann R.J. and Turcotte D.L. (1981) Proc. Lunar Planet. Sci. Conf. 12th, submitted for publication.
[3] Bills B.G. and Ferrari A.J. (1978) J. Geophys. Res., 83, 3497-3508.
[4] Thurber C.H. and Toksöz M.N. (1978) Geophys. Res. Lett., 5, 977-980.
[5] Kraus H. (1967) Thin Elastic Shells, John Wiley, New York.
[6] Comer R.P., Solomon S.C. and Head J.W. (1979) Proc. Lunar Planet. Sci. Conf. 10th, p. 2441-2463.
[7] Solomon S.C. and Head J.W. (1980) Rev. Geophys. Space Phys., 18, 107-142.

SUPPORT OF THARSIS

Willemann, R.J. and Turcotte, D.L.

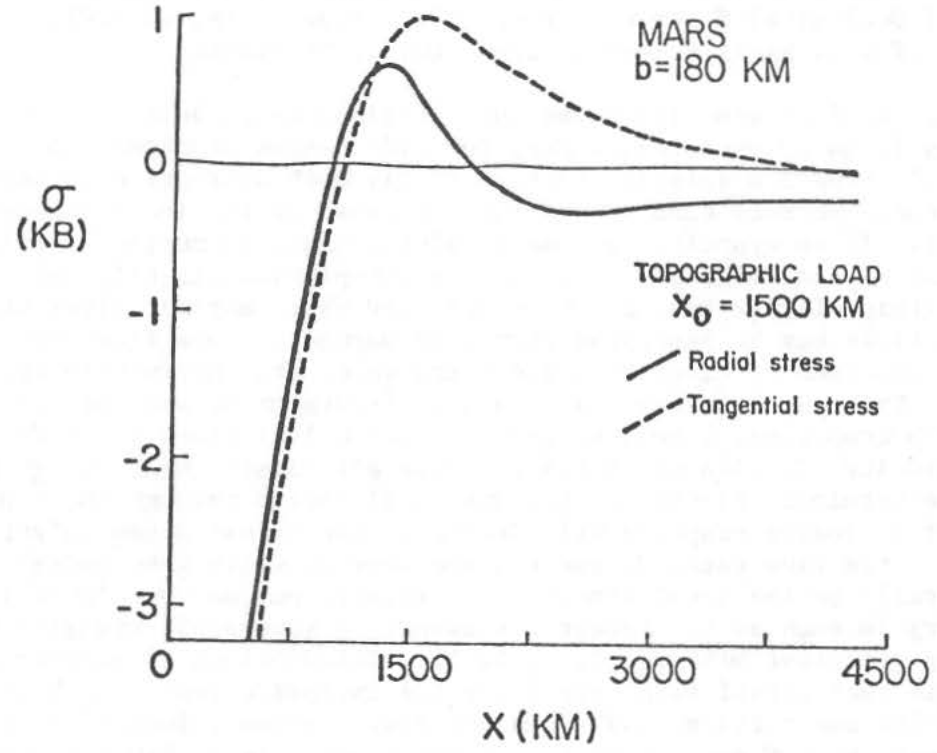

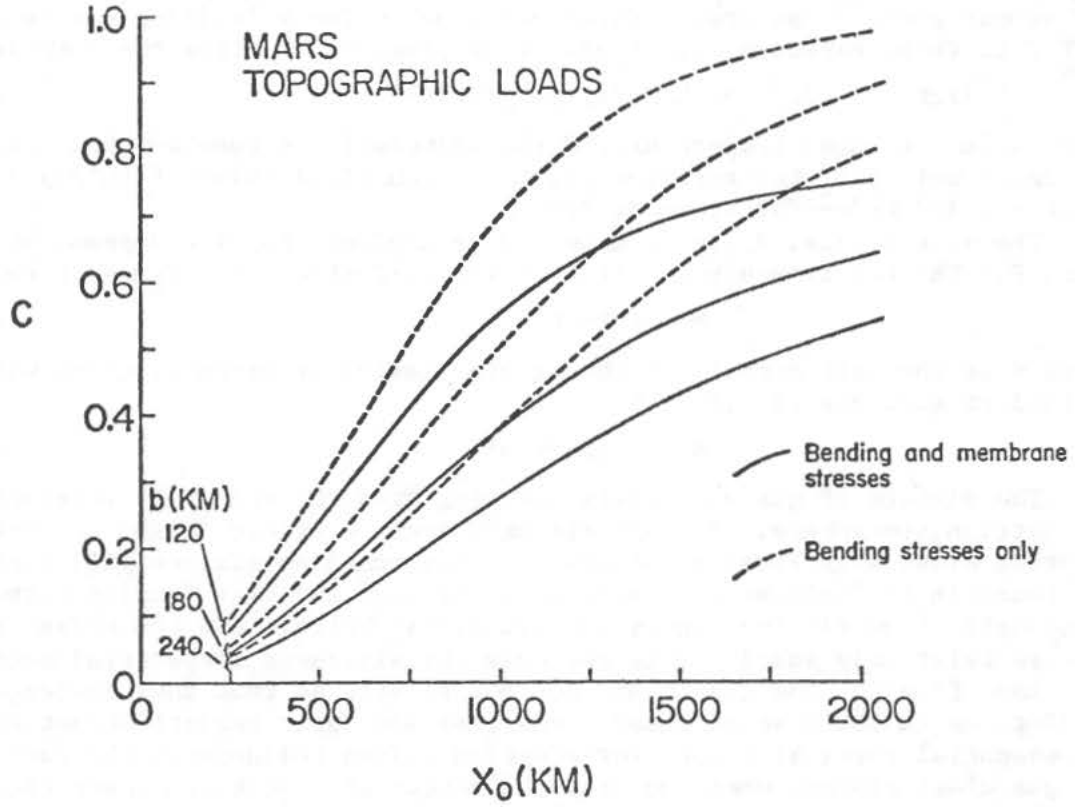

THEORETICAL ANALYSES OF MARTIAN EXPLOSIVE ERUPTION MECHANISMS. L. Wilson Dept. of Environmental Sciences, Univ. of Lancaster, Lancaster LA1 4YQ, U.K. and Dept. of Geological Sciences, Brown Univ., Providence, RI 02912 and J. W. Head, Dept. of Geological Sciences, Brown Univ., Providence.

Disruption of an erupting magma into scoriaceous or pumiceous clasts and released gas is to be expected on Mars for wide ranges of magma composition, magma volatile type and volatile content (1,2); such disruption is potentially much more common on Mars than on the Earth because of the lower atmospheric pressure (1). If an eruptive episode involving magma disruption continues for more than several minutes, a plinian or sub-plinian air-fall deposit may be formed: this will be true for both acid and basic magmas; alternatively, pyroclastic flows may be generated from acid magmas or lava flows may form from the coalescence of clots of basic magma which stay hot within the eruption cloud. This paper presents a numerical treatment of some of the mechanisms of such eruptions, extending some earlier calculations for Mars (2).

The velocity, U, with which the gas (and all clasts small enough to have a negligible terminal velocity in the gas) will emerge through the vent in this type of explosive eruption will depend on the released gas weight fraction, N, the mass flow rate, M, and the pressure at which they emerge, P. P will generally be the local atmospheric pressure but may be higher if the vent geometry is such as to prevent a subsonic to supersonic transition in the emerging gas/clast mixture (1, 3, 4, 5). Calculations of eruption velocities in terrestrial (5,6) and lunar (1) explosive eruptions have been extended to include martian conditions and Fig. 1 gives values of velocity, U_o, as a function of N and M when the released volatile is H_2O for standard vent pressure, P_o, of 3 millibars (300 N/m^2), chosen as representative of the summit areas of several martian volcanoes. The velocities can be converted to those expected, U, at any other pressure, P, from the formula

$$1/2U^2 = 1/2U_o^2 + N(QT/x) \log_e(P_o/P) \quad (1)$$

where T is the magma temperature, Q the universal gas constant and x the molecular weight of the exsolved gas: the numerical value of (QT/x) is about 5×10^5 m^2/s^2 for steam at 1100 K.

The vent radius, R, to be expected in a given eruption depends on N, M, U and P. The relationship is given by the definition of the mass flux:

$$M = U\pi R^2 B \quad (2)$$

where B is the bulk density of the erupted gas/clast mixture, given with sufficient accuracy (1,5,6,) by

$$B = P/[N(QT/x)] \quad (3)$$

The mixture of gas and clasts emerging from the vent will interact with the martian atmosphere. In some circumstances, a stable, high, convecting eruption cloud will form; in others (7), the emerging mixture will form a low fountain (a "collapsed" eruption cloud) over the vent feeding either a pyroclastic flow (if the clasts are relatively brittle and the median grain size is relatively small, as is the case for siliceous terrestrial magmas) or a lava flow (if the clasts are hot and plastic so that they coalesce on landing, as in the case of some terrestrial and lunar basaltic eruptions (1)). The essential physical reason for eruption column collapse is the fact that the gas/clast mixture emerging from the center of a vent is denser than the surrounding atmosphere and may decelerate under gravity to a negligible speed before enough atmospheric gas has been mixed into the center of the cloud by

large-scale turbulence and heated by contact with the magmatic clasts to provide buoyancy. It is known from the study of turbulent jets (8) that the inner edge of the zone of mixing between eruption products and atmospheric gas should propagate at a constant rate into an eruption cloud from the edge of the vent, thus arriving at the center line at some height, Y, equal to a constant, K, times the vent radius, R. The upward velocity on the center line at this height must clearly still be somewhat greater than zero if collapse is to be avoided, requiring

$$Y < U^2/[2\ g(1 - (A/B))] \quad (4)$$

where g is the local gravity and A is the atmospheric density given by

$$A = P/[(QT_a)/y] \quad (5)$$

in which T_a is the atmospheric temperature and y the atmospheric molecular weight. Combining all these relationships, the condition for avoiding column collapse is

$$R < U^2/[2\ K\ g(1 - ZN)] \quad (6)$$

where

$$Z = (y/x)\ (T/T_a) \quad (7)$$

For the Earth's atmosphere, we can take T_a = 290 k, y = 28.8, and for Mars, T_a = 215 K, y = 44; using T = 1100 K and x = 18 for steam we find Z = 6.1 for eruptions on Earth and Z = 12.5 for eruptions on Mars. The combinations of values of N, U and R at which the transition from stable eruption cloud to collapsed cloud occurs have been calculated for terrestrial eruptions (5,7,9) and the insertion of sets of these values into equation (6) using Z = 6.1 gives an average value of K = 33. Using this value of K and the relationship between U, N and M given in Fig. 1 we find the column collapse conditions given in Table 1. These data are used to define the dashed line in Fig. 1 which marks the boundary between stable, convecting eruption clouds (on the left of the figure) and collapsed clouds feeding ignimbrites or lava flows.

It has been shown both theoretically (10, 11, 12, 13) and by observation (11, 12, 13) that the height, H, of a stable eruption cloud is essentially proportional to the fourth root of the heat (and, hence, mass) release rate from the vent. The full relationship involves properties of the atmosphere and is of the form (10):

$$H = [J\ M^{1/4}\ T_a^{3/8}]/[y^2\ P^2\ c^2\ g\ |L|^3\ \{1 + (dT/dh)/L\}^3]^{1/8} \quad (8)$$

where c is the atmospheric specific heat, L is the dry adiabatic lapse rate and dT/dh is the true rate of temperature decrease with height; J represents a number of universal constants which have been collected together. Suitable numerical values would be, for the lower parts of the Earth's atmosphere, T_a = 288 K, y = 28.8, $P_o = 10^5$ N/m^2, c = 1000 J kg^{-1}K^{-1}, L = -9.6 K/km, dT/dh = -4K/km (14) and, for eruptions taking place at the 3 millibar pressure level in the Mars atmosphere, T_a = 200 K, y = 44, P_o = 300 N/m^2, c = 770 J kg^{-1}K^{-1}, L = -5.4 K/km and dT/dh = -2 K/km (15). Insertion of these two sets of values in turn into equation (8) shows that eruption clouds can be expected to rise about 4.9 times higher on Mars than on Earth for the same eruption rate. The average rise height, H, for a mass eruption rate, M, can therefore be written:

$$(H/km) = S\ [M/(kg/s)]^{1/4} \quad (9)$$

where S = 0.21 for the Earth (12) and the above calculation gives S = 1.03 for Mars; thus, for example, an effusion rate of 10^8 kg/s will yield a 21 km

high eruption cloud on the Earth and a 103 km high cloud on Mars. Equation (9) has been used to calculate the eruption cloud heights given at the top of Fig. 1.

It has been noted (16) that, in several cases the total width, measured at right angles to the downwind elongation direction, of an air-fall deposit on Earth is approximately equal to the height of the eruption cloud from which it is deposited. The cloud heights in Fig. 1 therefore imply that martian air-fall deposits may manifest themselves as areas of blanketed terrain with shorter dimensions of at least tens of km and possibly in excess of 100 km.

References. 1) L. Wilson and J. W. Head (1981) J. Geophys. Res. 86, 2871. 2) L. Wilson and J. W. Head (1981) Lunar Pl. Sci. 12, 1194. 3) S. W. Kieffer (1977) J. Geophys. Res. 82, 2895. 4) G. S. Steinberg and A. S. Steinberg (1975) J. Geophys. Res. 80, 1600. 5) L. Wilson et al. (1980) Geophys. J. Roy. Astron. Soc. 63, 117. 6) L. Wilson (1980) J. Volcanol. Geotherm. Res. 8, 297. 7) R. S. J. Sparks and L. Wilson (1976) J. Geol. Soc. Lond. 132, 441. 8) L. Prandtl (1949) The essentials of fluid dynamics, Blackie & Son, London. 9) R. S. J. Sparks et al. (1978) J. Geophys. Res. 83, 1727. 10) B. R. Morton et al. (1956) Proc. Roy. Soc. A. 234, 1. 11) L. Wilson (1976) Geophys. J. Roy. Astron. Soc. 45, 543. 12) L. Wilson et al. (1978) J. Geophys. Res. 83, 1829. 13) M. Settle (1978) J. Volcanol. Geotherm. Res. 3, 309. 14) C. Barth (1974) Ann. Rev. Earth Pl. Sci. 2, 333. 15) S. L. Valley (1965) Handbook of Geophysics and space environments, McGraw-Hill, New York. 16) L. Wilson (1980) pp 31-35 in Thera and the Aegean World II, proc. 2nd Internat. Congress, Ed. C. Doumas, published by "Thera and the Aegean World", London.

Table 1. For several exsolved magma water contents, N, in martian plinian eruptions, values are given for R_c, the critical vent radius below which a convecting eruption cloud will be stable and above which pyroclastic flows (or, in the case of basaltic magmas, lava flows) will be formed, for U_c, the eruption velocity in the vent when the vent radius is equal to R_c and the vent pressure is three millibars, and for M_c, the mass eruption rate corresponding to U_c and R_c.

N (wt% H_2O)	0.1	0.2	0.5	1	2	3.5	5
R_c (m)	20	80	220	490	1140	2900	6400
U_c (m/s)	80	145	230	330	470	635	770
M_c (kg/s)	5.3×10^4	8.8×10^5	4.1×10^6	1.5×10^7	5.7×10^7	2.8×10^8	1.2×10^9

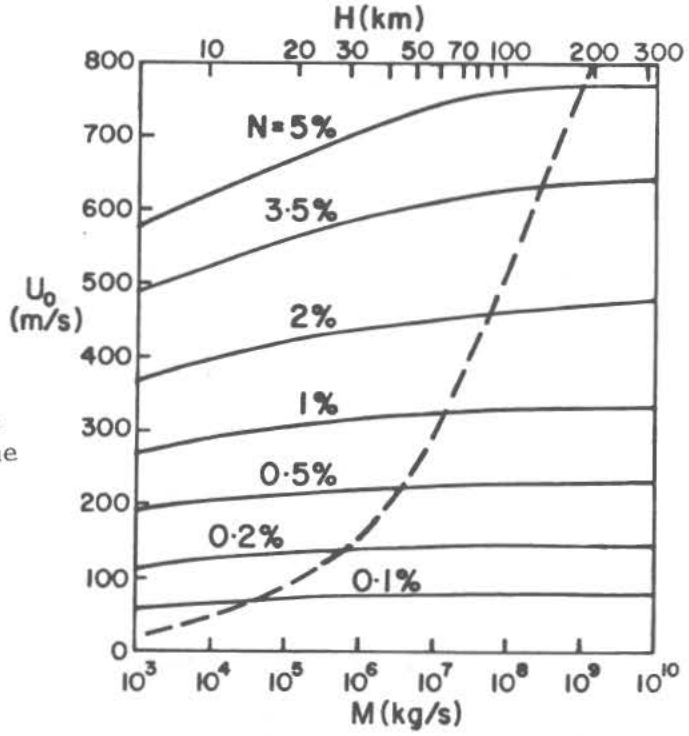

Figure 1. The variation of U_0, the velocity of gas and small clasts emerging through the vent in a martian plinian eruption as a function of M, the mass eruption rate and N, the exsolved magma water content. The scale at the top gives the eruption cloud heights, H, corresponding to the values of M at the bottom. Eruption columns are stable for values of M and N lying to the left of the dashed line but will otherwise collapse to form much lower fountains over the vent feeding pyroclastic flows or lava flows.

EXPLOSIVE VOLCANISM ON HECATES THOLUS, II: ESTIMATES OF ERUPTION CHARACTERISTICS

L.Wilson[+*], P.J.Mouginis-Mark[*] and J.W.Head[*]. [+]Department of Environmental Sciences, Lancaster University, Lancaster, UK. [*] Department of Geological Sciences, Brown University, Providence RI 02912.

Introduction: The Elysium Volcanoes on Mars have been recognized for some time as likely candidates for explosive volcanic eruptions (1, 2). In a companion abstract (3), we described morphological evidence for a very recent large-scale explosive event on Hecates Tholus (32°N, 209°W), using reasoning different from that presented earlier by Reimers and Komar (2). Our interpretations of explosive activity are based on the observations of a paucity of small craters and channel source areas to the west of the caldera, and faint radial striations on the southwest flanks of the volcano (3). In this analysis, we follow the implications of assuming that these two features on Hecates were indeed generated by explosive activity, and that the eruptions took one of two forms: 1) that the mantled region west of the caldera is the product of an air-fall (plinian-style) eruption; and 2) that the radial grooves are related to the formation of pyroclastic flows.

Air-Fall Model: Prominent on the flanks of Hecates Tholus (Fig. 1) are approximately 240 craters less than 2 km in diameter. Although the difficulty in positively identifying volcanic versus impact craters is acknowledged, image resolution (40-50 meters) is sufficient in many instances to identify raised rims on the craters, suggesting an impact origin (4). On the assumption that most craters are indeed impact craters, their areal distribution should reflect the resurfacing history of the volcano. Prominent in a contour map of crater distribution (Fig. 2, ref. 3) is the small number of craters west of the caldera, which almost exactly coincides with the area without channels (Fig. 3, ref. 3). We hypothesize here that this lack of small craters and channels was caused by a thick, relatively recent, volcanic air-fall deposit.

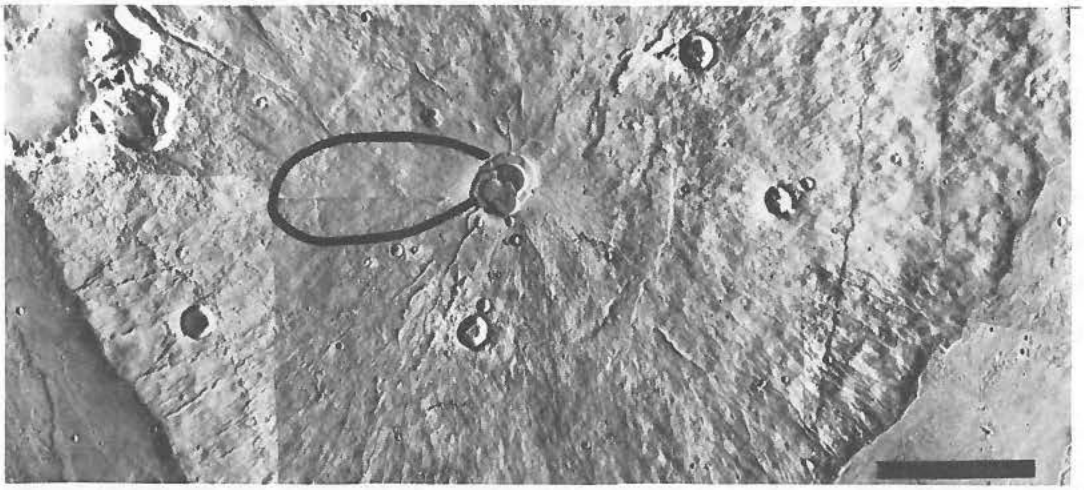

Fig.1: Photomosaic of Hecates Tholus, showing nested summit caldera, and the asymmetry in the small crater and channel distributions. Outlined area is interpreted to be the air-fall deposit, while the radial striae are found on the SW (lower left) flank. Scale bar is 25 km. Viking images 651A15-23.

resulting vent structure diameter is then about 1.5 km for an atmospheric pressure of 3 mb: a size comparable to the dimensions of some of the sub-circular ridge-and-depression features seen inside, and in the vicinity of, the summit caldera.

Pyroclastic Flow Model: If the radial grooves on the southwestern flank of Hecates Tholus are regarded as the products of a single major eruptive episode that initiated pyroclastic flows, an attempt can be made to investigate the eruption conditions provided that some plausible assumptions are made. The distribution of these grooves (Fig. 1; ref. 3) shows that there is a zone without surface scouring that has a diameter of about 30 km, and is centered just to the northwest of the summit caldera. It will be assumed that this diameter is a measure of the width of the fountain structure over the vent which feeds the ignimbrite. Within the fountain, the motions of the gas and pyroclasts are largely upwards in the center and downwards around the periphery (12); large lateral velocities, leading to surface erosion, do not occur within this region. A simple model of such a system (12) shows that, if the fountain radius is R_F, the central, rising jet of erupted material has a radius, R_J, of about $0.7R_F$. If it is assumed that the pressure in this central jet is close to the local atmospheric pressure (which will probably not be true within the vent proper but should be true not far above it) then the vertical velocity, U, and the bulk density, B, of the erupted mixture of gas and clasts can be calculated as a function of the exsolved volatile content, N, of the magma (9). The mass eruption rate, M, is then given by $M=B\ U\pi R_J^2$. In the present case we have R_F = 15 km and so R_J = 10.5 km. Table 1 gives some values of U and B for N in the range 1 to 5 wt% H_2O, and also the implied values of M which range from 1.4-3 x 10^9 kg/s. Such values are well above the limiting mass eruption rates above which pyroclastic flow formation should occur on Mars (9) and so the analysis is internally consistent. As an example of a possible eruption duration, the time required to erupt the 45 km^3 total volume represented by the summit calderas at the above rates would lie between 12 and 25 hours.

Table 1. Values of exsolved magma water content, N, and corresponding values of eruption velocity, U, and bulk density of erupting mixture of gas and clasts, B, for pyroclastic eruptions at the summit of Hecates Tholus with an ambient pressure of 3 millibars. The implied value of mass eruption rate, M, found from the equation in the text is also given.

N (wt% H_2O)	1	2	3.5	5
U (m/s)	325	460	630	770
B (kg/m^3)	0.060	0.030	0.017	0.012
M (kg/s)	3.0 x 10^9	2.1 x 10^9	1.7 x 10^9	1.4 x 10^9

References: 1) Malin M.C. (1977) Geol.Soc.Amer.Bull. 88, 908-919. 2) Reimers C.E. & Komar P.D. (1979) Icarus 39, 88-110. 3) Mouginis-Mark P.J. et al. (1981) this vol. 4) Blasius K.R. (1976) Icarus 29, 345-361. 5) Pike R.J. (1980) PLPSC 11th, 2159-2189. 6) Walker G.P.L. (1980) J.Volcanol.Geotherm.Res. 8, 69. 7) Wilson (1980) pp. 31-35 in: Thera and the Aegean World II, Proc. 2nd.Int.Cong., London. 8) Wilson L. (1976) Geophys.J.Roy.Astron.Soc. 45, 543. 9) Wilson L. & Head J.W. (1981) this vol. 10) Ledbetter M.T. & Sparks R.S.J. (1979) Geology 7, 240. 11) Sparks R.S.J. & Wilson L. (1976) J.Geol.Soc.Lond. 132, 441. 12) Sparks R.S.J. et al. (1978) J.Geophys.Res. 83, 1727.

EXPLOSIVE VOLCANISM II

Wilson, L. et al.

If the average diameter of the craters present within the unblanketed zone near the summit is about 500 meters, data from Pike (5) would suggest that the corresponding average crater depth would be about 100 meters. From the distribution of observed craters, the outer edge of the substantially mantled region (taken to be the 25 crater/250 km^2 contour) may be approximated as a circle of radius 25 km. If it is assumed that the thickness of this mantle deposit at its center is 100 meters (equal to the average depth of the hidden craters), and that the deposit decreases linearly from the center to the edge, the implied volume of the air-fall is $\sim$ 65 km^3. Taking the bulk density of the deposit as 1000 kg/m^3 (a compromise between the likely densities of pumiceous and scoriaceous clasts) the equivalent dense rock (2800 kg/m^3) volume is $\sim$ 23 km^3. This rock volume corresponds to a mass of $\sim$ 6.5 x 10^{13} kg, and compares favorably with the masses of air-fall pumice deposits on Earth, which appear to range up to values of 3 x 10^{13} kg (6), a factor of 2 smaller than on Mars. It is therefore tempting to speculate that the formation of part, or all, of the summit caldera on Hecates was a consequence of collapse following the proposed air-fall eruption: the caldera complex consists of an outer elliptical depression of volume $\sim$ 28 km^3, and a group of at least three inner craters with a total volume of $\sim$ 10 km^3. Thus the observed summit crater volume is greater than that inferred for the air-fall deposit, permitting the possibility of additional material being distributed upon the more distant flanks of the volcano.

An attempt can also be made to estimate the maximum height of the eruption cloud producing the air-fall deposit. It has been shown (7) that for several terrestrial plinian eruptions the width of the deposit measured near the vent (in a direction perpendicular to the downwind dispersal axis) is quite close to the eruption cloud height. It is likely that the same relationship holds for Mars, since the shape of an eruption cloud is controlled mainly by the way atmospheric gas is entrained into the cloud and by the atmospheric scale height (8): the entrainment process will be exactly the same on Mars and the Earth, and the atmospheric scale heights are only about 25% different (9). The height of an eruption cloud on Earth is controlled almost entirely by the mass eruption rate from the vent, and recent calculations have established the appropriate scaling relationships for Mars (9). The length of the shorter axis of the Hecates Tholus mantle deposit (corresponding to the N-S diameter of the 25 crater contour; Fig. 2, ref. 3) is at least 50 km and possibly 75 km. If this is a measure of the eruption cloud height, the mass discharge rate must have been at least 5.5 x 10^6 to 3.0 x 10^7 kg/s (9). The time required to erupt the inferred mass of 6.5 x 10^{13} kg would then be up to 137 or 25 days respectively. This first time interval is much longer than the duration of any single historic terrestrial plinian eruption, but could represent the aggregate of several eruptive episodes. In contrast, the 25 day eruption compares favorably with the 20-27 days estimated for one prehistoric Central American eruption (10).

The diameter of the surface vent structure (more exactly, the diameter of the region occupied by the erupting gas/clast mixture after decompression to local atmospheric pressure) can be calculated from the mass eruption rate, the atmospheric pressure and the exsolved magma content (9). The minimum diameter is found by using the minimum volatile content consistent with the eruption volume remaining stable against collapse to form pyroclastic flows (11) which for an eruption rate of 3 x 10^7 kg/s is 1.5 wt% H_2O (9). The

CALDERAS ON EARTH AND MARS. Charles A. Wood, SN6/NASA Johnson Space Center, Houston, TX 77058

Calderas, formed by partial emptying of near surface magma chambers, are the largest type of roughly circular volcanic depressions on Earth. Arbitrarily, calderas have been defined as having diameters (CD) >1 km, although the key characteristic is that calderas, unlike smaller craters, involve large-scale collapse. Ideally, the morphology of a caldera should provide clues to the mechanism of its formation and the nature of associated magmas, however, there have been too few studies of terrestrial calderas to define explicit morphology/mechanism/composition relationships. The present note synthesizes various qualitative and quantitative data for terrestrial calderas, and uses these results for interpreting martian calderas.

Terrestrial Calderas. Although investigations of caldera forms and origins were widespread during the first third of this century, the publication[1] of Williams' classic memoir "Calderas and their origins" apparently stifled research on the subject, except for the latter discovery of resurgent calderas[2], and Pike's[3] recent compilation and analysis of crater and caldera dimensions. The classification of calderas is based upon their presumed formation mechanisms[4], but since few have been observed to form, this criterion varies according to progress in geologic studies of calderas. Thus, the "Atitlan" type of caldera (only one example known) was originally postulated to have collapsed due to removal of magma to build three stratovolcanoes on its flanks[4]. Recent geologic studies[5], however, document that the caldera is the probable source of ~300 km^3 of pumice, suggesting that it may have actually formed by a Valles-type explosive mechanism.

Table 1 combines geologic characteristics[4] of calderas with average values of their dimensions (derived from data compiled by Pike[3]). Details of the correlation of caldera types defined by process[4] and geometry[3] will be discussed elsewhere: the following observations are derived from the table.

a. Dimensional data are available for ~110 calderas, but statistics are very incomplete, especially for large, but low and inconspicuous calderas (e.g., Valles type), therefore it is likely that the Earth possesses an estimated 150-300 calderas. Note, however, that the vast majority of the Earth's volcanoes are basaltic, apparently caldera-free, submarine mountains on the Pacific Ocean floor.

b. Nearly 90% of the documented calderas are associated with the eruption of silicic materials, and probably all of the undetected calderas are also. Nearly all calderas with D > 10 km are silicic.

c. The majority of silicic calderas form near subduction zones, although the largest (Valles type) also occur in areas of crustal extension. Basaltic calderas are best developed at oceanic hot spots, but smaller ones also occur in other tectonic settings.

d. Valles type calderas are the largest on Earth and produce the majority of silicic igneous rock.

e. Basaltic shields of the Hawaiian type are the largest mountains on Earth, as is well known, but their calderas account for <<1% of their total volume, and are formed by eruptions of only a few km^3 of lava flows, perhaps in association with larger phreatomagmatic eruptions of ash[6].

f. Silicic caldera diameters (CD) are 20-40% of the basal diameters of their associated volcanoes (VD). For basaltic calderas CD = 7-14% of VD, except for the unique volcano Masaya (55%).

Martian Calderas. Twenty volcanic calderas are known on Mars (Table 1), nearly all of which are much larger than terrestrial calderas. Martian caldera-bearing mountains were originally classified into three types[7]: montes, tholi, and paterae, but recently some of the type assignments have been ques-

tioned[8,9], while a fourth type has been recognized[10], and a fifth hypothesized[11]. Photogeologic evidence convincingly demonstrates that the surfaces of the montes consist of basalt-like lava flows[9], but there is considerable uncertainty concerning the composition (silicic/basic) and nature (lava flow/pyroclastic flow/pyroclastic fall) of tholi, paterae and other suggested caldera structures. Although Pike[3] has demonstrated that montes, tholi, and paterae cluster in three groups dimensionally, indicating that these cartographic designations have general genetic significance, there are differences within each group. Thus, Hecates Tholus is much more mons-like than tholus-like[3], and it and Elysium Mons are a distinct subtype of shield structure. Similarly, Tharsis Tholus appears to be the summit region of a larger shield volcano that is buried to an unknown depth by later lavas from a different source. Evidence comes largely from occurrence of two or more large but incomplete caldera rims underlying the central collapse complex. Other tholi and paterae suggested to be mons-type structures[8,9] are not convincing: Calderas of Jovis Tholus and Uranius Patera, for example, are not nested, and lack the concentric fractures and graben characteristic of the larger montes. If Ulysses Patera is a shield volcano[9] its caldera has a circular symmetry and simplicity unlike the Tharsis shield calderas; thus it is reasonable to assume an origin unlike the larger montes.

The most perplexing martian calderas are the highland paterae group of Plescia and Saunders[10]. The radiating channels from the centers of these structures have been interpreted as due to erosion of a pyroclastic material[9], an idea supported by the ages of the volcanoes. The three highland paterae formed between 2-3 b.y. ago[10], during which interval 6 other montes and tholi, which lack radiating channels, also formed, thus implying that paterae are formed of materials different from those of other martian volcanoes. If these paterae are made up of pyroclastic deposits, they may be basaltic, due to eruption through a permafrost layer in the regolith[9]. If this is the explanation, the failure of other volcanoes, formed during the same interval, to have radiating gullies could imply an uneven distribution of permafrost. Speculations can be endless when facts are sparse.

Conclusions. There are more calderas on Earth than on Mars by an order of magnitude; this ratio would increase dramatically if equal time intervals were considered, for martian calderas have ages of $\sim 10^9$ yrs, but terrestrial examples are only 10^5-10^7 yrs. old. The difference in caldera frequency presumably reflects a lack of conditions necessary to form calderas, for volcanic plains cover ~60% of Mars[9] (compare to ~70% for Earth). Most terrestrial calderas result from large eruptions of silicic magma which preferentially forms near subduction zones. Mars appears to lack subduction zones, and exhibits no convincing evidence for silicic volcanism[12]. Thus, most martian calderas appear to have formed in the equivalent of "mid-plate" or "hot spot" tectonic environments, and indeed the majority of martian volcanoes seem to have formed by effusive eruptions of a basalt-like lava, similar to terrestrial hot spot volcanoes like Mauna Loa. In detail, the montes most resemble Galapagos shields[13], rather than the Hawaiian examples, based on the importance of concentric structures (e.g., concentric fissure flow on Arsia Mons; Figure 17 of Ref. 14), and similar patterns of caldera and edifice evolution. Like the Galapagos volcanoes[15], Tharsis calderas grow larger, simpler, and more circular with age[13]. As caldera diameter on Earth appears to nearly equal magma chamber width and depth[16], the systematic change in caldera size for Tharsis shields implies a rising and/or enlarging magma reservoir with long-term volcano evolution.

Most martian volcanoes are surrounded and buried to an unknown depth by later lavas from other sources, as is also true for many terrestrial cones.

CALDERAS ON EARTH AND MARS

Wood, C. A.

Plescia and Saunders[17] convincingly argued that the smaller volcanoes in the Tharsis region are not buried by more than roughly 0.5 - 1 km of later lava, and thus the low relief volcanoes in Tharsis are not deeply buried montes type shields. Intrinsic low relief and un-montes-like calderas imply that these tholi, etc., represent different styles of volcanism (e.g., Masaya-like?); the question is why did they develop as they did and where they are?

Highland paterae, the Aeolis "stratovolcano" of Greeley and Spudis[9], and the two zero relief Amphitrites calderas(?)[10] differ considerably from the montes. Nearly all of these volcanoes occur in the southern, cratered highlands of Mars, and nearly all have radiating channels or gullies, whereas the smooth-flanked montes and tholi type volcanoes are restricted to the northern lowlands where a 2-4 km thickness of megaregolith has apparently been removed. If phreatomagmatic basaltic eruptions built these volcanoes[9,18] it may be that much larger quantities of groundwater/permafrost were available in the megaregolith highlands than on the low northern plains.

References (1) Williams, H. (1941) Univ. Cal. Pub. Bull. Dept. Geol. Sci. 25, 239-346. (2) Smith, R. L. and Bailey, R. A. (1968) G.S.A. Mem. 116, 613-662. (3) Pike, R. J. (1978) Proc. Lunar Planet. Sci. Conf. 9th, 3239-3273. (4) Williams, H. and McBirney, A. (1979) Volcanoes. Freeman, Cooper & Co. San Francisco. (5) Rose, W. I. et al. (1980) Bull. Volc. 43, 131-154. (6) Holcomb, R. (1980) USGS Open File Rept. 81-354. (7) McCauley, J. F. (1972) Icarus 17, 289-327. (8) Solomon, S. and Head, J. W. (1980) Rpts. Planet. Geol. Program 1979-80, 71-73. NASA TM 81776. (9) Greeley, R. and Spudis, P. (1981) Rev. Geophys. Space Phys. 19, 13-41. (10) Plescia, J. B. and Saunders, R. S. (1979) Proc. Lunar Planet. Sci. Conf. 10th, 2841-2859. (11) Scott, D. H. and Tanaka, K. L. (1980) Repts. Planet. Geol. Prog. 1980. NASA TM 82385, 255-257. (12) Francis, P. and Wood, C. A., this volume. (13) Wood, C. A. (1976) EOS 57, 344. (14) Schaber, G. G. et al. (1978) Proc. Lunar Planet. Sci. Conf. 9th, 3433-3458. (15) Nordlie, B. (1973) G.S.A. Bull. 84, 2931-2956. (16) Konyangi, R. Y. et al. (1976) USGS Prof. Paper 800-D, 89-97. (17) Plescia, J. B. and Saunders, R. S. (1980) Proc. Lunar Planet. Sci. Conf. 11th, 2423-2436. (18) Reimers, C. E. and Komar, P. D. (1979) Icarus 39, 88-110.

TABLE 1: CALDERA TYPES AND CHARACTERISTICS

Type	Tectonic Setting	Number	Magma	Collapse Mechanism	Volcano Type	CD	CD/VD	Circularity	Pike[3] Class
Hawaii	hot spot	8	thol	d, l, r	shield	6.5	0.07	0.42	KTH
Galapagos	hot spot	8	thol	d, l, a, c	shield	3.5	0.09	0.59	KTG
Askja	sub, ext	14	alk bst	d, l, s, a	shield	4.1	0.14	0.49	KM
Masaya	sub	1?	cal-alk bst	cs	shield	8.2	0.55	0.28	U
Valles	sub, ext	22	rhy	i, s, c	none	20.7	0.38	0.48	AP
Krakatoa	sub	29	and, dac	i, s	stratovolcano	6.6	0.31	0.56	KCS
Katmai	sub	1?	and, rhy	d	none	3.6	0.23	0.37	KC?
Olympus	?	4	bst?	d, l, c	shield	84	0.17	0.58	MM
Elysium	?	2	bst?	d, l	shield	13	0.05	0.63	MM
Ceraunius	?	9	bst??	?	tholus	47	0.37	0.63	MT
Tyrrhena	?	3+	?	s?	highland patera	55	0.24	?	-
Alba	?	1	bst?	s?	alba	115	0.11	?	-
Amphitrites	?	2+	bst?	s?	?	120	1	?	-
Aeolis	?	1+	?	?	stratovolcano	6	0.32	?	-

NOTES: Volcano types and geologic characteristics for Earth from Williams and McBirney[4]; dimensional value averages from data in Pike[3]. Askja is a new caldera type based upon Pike's[3] recognition of alkalic basalt shields.

Abbreviations: sub = subduction zone; ext = extension; thol = tholeiitic; alk bst = alkalic basalt; rhy = rhyolith; d = drainage; l = lavas; r = rift zones; a = ashes; c = circumferential fissures; i = ignimbrites; s = summit; CS = cauldron subsidence; CD = caldera diameter (km); VD = volcano basal diameter

TOPOGRAPHIC MAP OF OLYMPUS MONS; Sherman S. C. Wu, P. A. Garcia, Raymond Jordan and F. J. Schafer, U.S. Geological Survey, Flagstaff, AZ 86001

The topographic map of Olympus Mons of Mars (Fig. 1) was compiled from 91 stereo pairs of Viking Orbiter photographs. For this compilation, special techniques were used that had been developed to enable systematic mapping of Mars from the Orbiter photographs, despite their extremely narrow field-of-view [1]. A total of 316 control points were produced from a block of 103 photographs by analytical aerotriangulation methods.

Olympus Mons is probably the largest volcano in our Solar System. It covers an area about the size of the state of Arizona. Estimates of its height above the surrounding area [2,3,4,5,6,7,8,9] range from 17 to 23 km. The U.S. Geological Survey 1:25,000,000 map [10] shows a height of 27 km above the Mars topographic datum [11,12]. The newly compiled map (Fig. 1) shows a peak elevation of 26,400 m.

Olympus Mons has the general form of terrestrial basaltic shields constructed almost entirely from lava flows [5]. Figure 2 shows profiles measured along the east, west, south, and north sides of the volcano. Slopes measured from these profiles fall into three groups. Slopes of 2° to 3° prevail at elevations ranging from 2 to 7 km. Slopes are 7.5° to 24° between elevations of 7 and 16 km (due mainly to the presence of several steep scarps within this elevation range, whose relief is as much as 8 km in the north and 5 km in the southeast). Slopes are 2.3° to 6.3° from an elevation of 13 km to the outside rim of the caldera 24 km. Blasius [4,5] has reported an average flank slope of 3.3°. A total volume for Olympus of 2.7×10^6 km^3 has also been reported by Blasius [5]. Calculations based on the new map (Fig. 1) give a total volume of 2.594×10^6 km^3 above an elevation of 5 km. If estimated volumes between elevations of 2 and 5 km are added to this figure, the total volume above the elevation of 2 km is 3.862×10^6 km^3. Table 1 lists segmental volumes at increments of 1 km and cumulative volumes from the top of the volcano.

References

[1] Wu, S. S. C., Elassal, A. A., Jordan, Raymond, and Schafer, F. J. (1981) Planetary and Space Sci. (in press).
[2] Arthur, D. W. G. (1976) Photogram. Record, 8, p. 617-630.
[3] Blasius, K. R. (1973) Jour. of Geophys. Res., 78(20), p. 4411-4423.
[4] Blasius, K. R., Roberts, W. J., Cutts, J. A., Duxbury, T. C., and Glackin, D. L. (1978) Tenth Annual Div. of Planetary Sci./American Assoc. for the Adv. Sci. meeting, Nov. 1978, Pasadena, CA., 4 p.
[5] Blasius, K. R. and Cutts, J. A. (1981) Icarus (in press).
[6] Davies, M. E. (1974), Icarus, 21(3), p. 230-235.
[7] Davies, M. E. and Arthur, D. W. G. (1973) Jour. of Geophys. Res. 78(20), p. 4355-4394.
[8] Hord, C. W., Barth, C. A., and Stewart, A. I. (1972) Icarus, 17(2), p. 443-456.
[9] Wu, S. S. C., Schafer, F. J., Nakata, G. M., and Jordan, Raymond (1973), Jour. of Geophys. Res. 78(20), p. 4405-4410.
[10] U.S. Geological Survey (1976) Topographic Map of Mars, U.S. Geological Survey, I-961.
[11] Wu, S. S. C. (1975) U.S. Geological Survey Interagency Rep. 63, 193 p.
[12] Wu, S. S. C. (1981) International Review, Annales de Geophysique Central National de la Recherche Scientifique, p. 147-160.

TOPOGRAPHIC MAP OF OLYMPUS MONS

WU, Sherman S. C. et al.

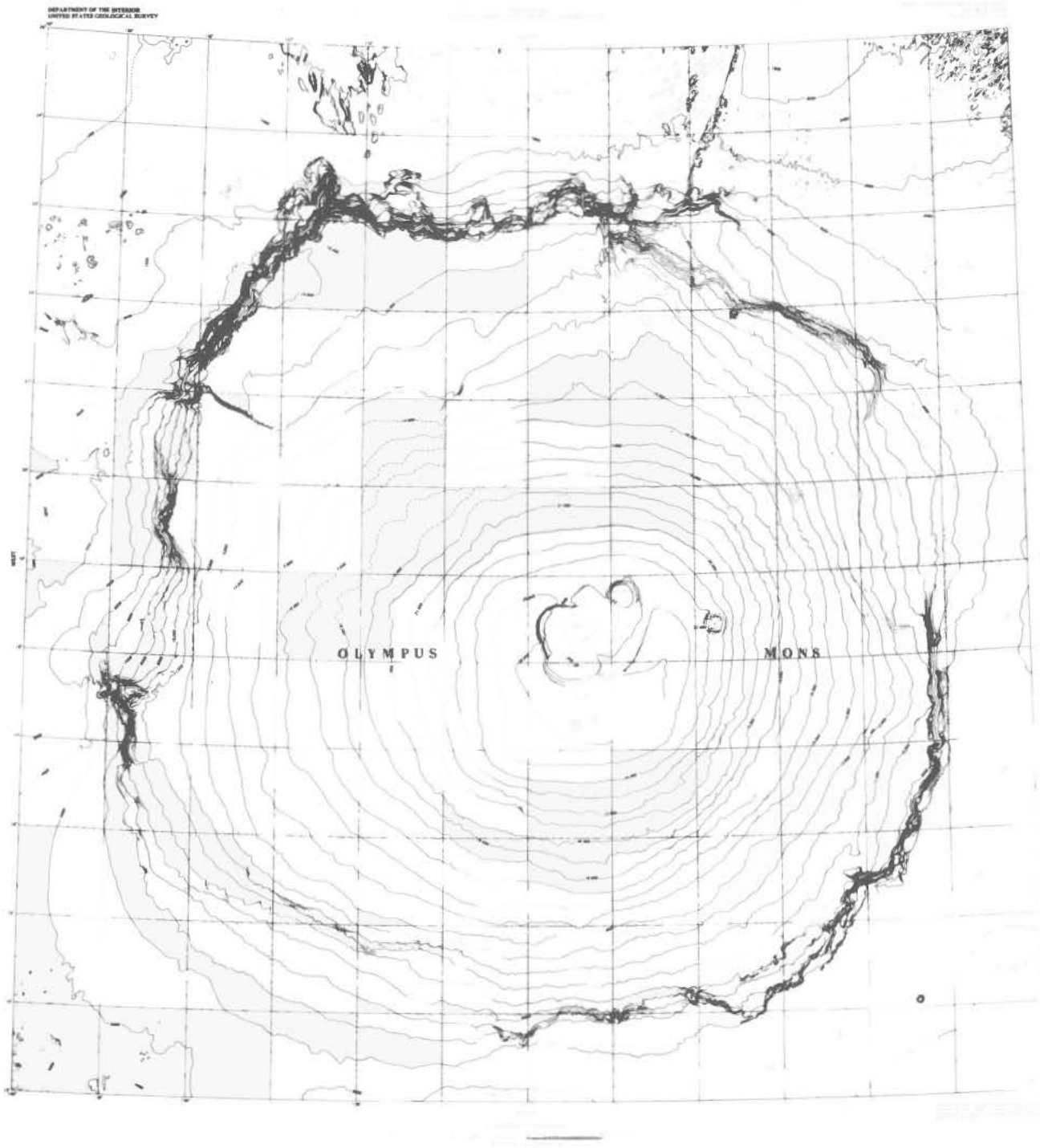

Figure 1. Topographic map of Olympus Mons on Mars. The map was compiled at a scale of 1:1,000,000 with a contour interval of 200 m. Contours and elevations are expressed in meters and are referred to the Mars topographic datum. Dashed contours are approximate. The grid is a transverse Mercator projection with the central meridian at 134°W longitude.

TOPOGRAPHIC MAP OF OLYMPUS MONS

WU, Sherman S. C. et al.

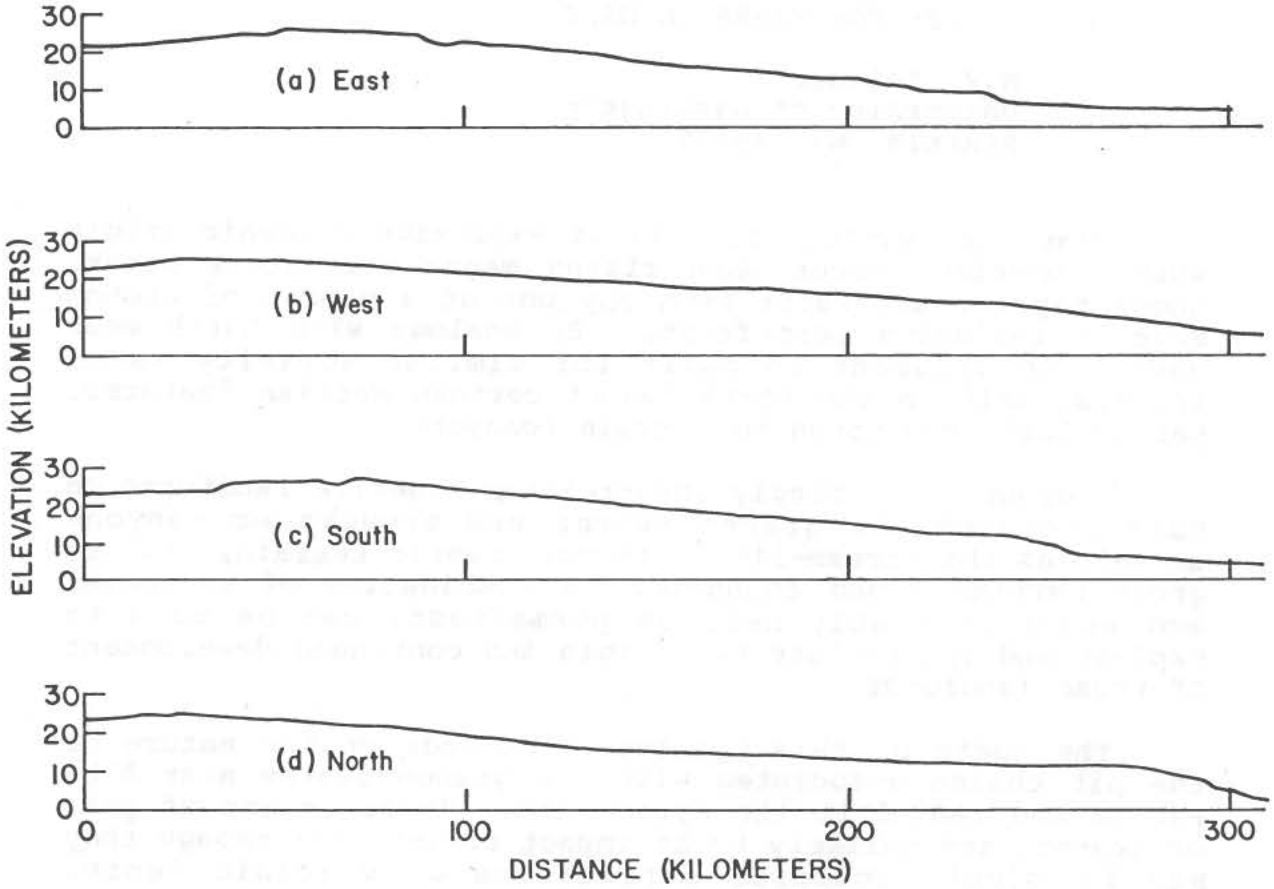

Figure 2. Profiles of Olympus Mons. All are drawn from the approximate center of the summit caldera at lat 18.4°N., long 133.45°W. (a) and (b) are drawn due east and west, respectively. (c) and (d) are drawn due south and north, respectively. Horizontal and vertical scales are 1:2,000,000.

	Elev (km)	Vol. of Segment	($x10^6$ km^3) Accum	Elev (km)	Vol. of Segment	($x10^6$ km^3) Accum	Elev (km)	Vol. of Segment	($x10^6$ km^3) Accum
above	26	0.0004	0.0004	17	0.073	0.336	9	0.223	1.553
	25	0.006	0.007	16	0.088	0.424	8	9.236	1.789
	24	0.013	0.020	15	0.103	0.527	7	0.247	2.036
	23	0.022	0.042	14	0.120	0.647	6	0.262	2.298
	22	0.029	0.071	13	0.140	0.787	5	0.296	2.594
	21	0.035	0.106	12	0.158	0.945	4	0.365	2.959
	20	0.043	0.149	11	0.180	1.125	3	0.436	3.395
	19	0.052	0.201	10	0.205	1.330	2	0.467	3.862
	18	0.061	0.263						

Table 1. Volume determination of Olympus Mons. Volumes were calculated for individual segments bounded by contour lines on the map (Fig. 1) by use of a planimeter. Scale variations due to the distortion of the map projection are corrected mathematically. The third column lists cumulative volumes downward from the top.

A CASE FOR MAARS ON MARS

M.E. Zeitner
University of Washington
Seattle, WA 98195

Maars are rimless craters of explosive volcanic origin which sometimes occur when rising magma encounters water. Magma may contact water from any one of a number of ground sources including permafrost. By analogy with Earth maar models an argument is built for similar activity as an integral unit in the formation of certain Martian features, particularly the troughed terrain (canyons).

A group of seemingly interrelated nagative landforms on Mars includes the graben swarms and troughs or canyons as well as the stream-like valleys, chaotic terrain, and the great Martian flood channels. A combination of volcanism and water (probably held as permafrost) can be used to explain and interrelate the origin and continued development of these landforms.

The basis of this hypothesis depends on the nature of the pit chains associated with the graben swarms near Alba Patera and radial to the Syria Rise. These chains of pits or craters are unlikely to be impact craters (1) though they may be simply collapse depressions or volcanic vents. Alternatively, they may be maars.

The presence of pit chains near Martian canyons led Sharp (2) to the hypothesis that the pits enlarge and coalesce as they erode, thus forming the canyons. In any event, available images show evidence of maar-type formations in the vicinity of the graben swarms and canyons. These formations are small, rimless craters that occur in chains along relatively deep-seated grabens (2). Additionally, Carr and Schaber (3) have noted permafrost features in the general area. Future work to determine the exact character of these craters, whether maars or collapse depressions, would yield greater understanding of the graben-canyon-volcano system as a whole.

References

1. GUEST, J., P. Butterworth, J. Murray, and W. O'Donnell. Planetary Geology. New York: John Wiley & Sons, 1979.

2. SHARP, R.P. (1973) Mars: Troughed terrain. JGR 78, 4063-4072.

3. CARR, M.H. and G.G. Schaber. (1977) Martian permafrost features. JGR 82, 4039-4054.

ASCRAEUS MONS: VOLCANIC SURFACE PROPERTIES DERIVED FROM IRTM DATA

James R. Zimbelman and Ronald Greeley, *Department of Geology, Arizona State University, Tempe, Arizona 85287*

Ascraeus Mons is the northernmost of the three large shield volcanoes which comprise the Tharsis Montes (1). These volcanoes have been observed for over 15 years but relatively little is known about their surface properties and eruptive styles. The Infrared Thermal Mappers (IRTMs) on the Viking orbiters measured the surface temperature on Mars which can be related to the average grain size or texture of the surface. High resolution infrared data and photogeologic mapping characterize the surface properties of Ascraeus Mons which may shed light on its volcanic history.

Figure 1 shows the major geologic features of Ascraeus Mons and the groundtrack of the IRTM data. Viking images clearly show the sharp contact between flows of the shield and the surrounding plains. High resolution images of the summit caldera (401B17-23) show sharp contacts between the relatively uniform caldera floors and the complexly faulted caldera walls, as well as several fresh-appearing channeled lava flows on the summit rim. Farther down the shield (401B01-10) the lava flows are much less distinct. The infrared data are of sufficient resolution to distinguish between the main structural and geologic features of the shield and the caldera.

Figure 2 shows the infrared data, compiled from 840 individual 20 μm brightness temperature measurements; these data are the best resolution infrared data available for Ascraeus Mons. Each of the seven detector spots in the IRTM chevron have a ground resolution of 3.5 km^2 but, due to the large spacecraft velocity at periapsis, each measurement is stretched along the groundtrack to a resolution of ~17 km^2 (roughly equivalent to a rectangle 2 by 8.5 km). Jakosky (2) demonstrated the effect of decreasing gas pressure and atmospheric radiation with increasing elevation on the thermal measurements. These effects were removed to obtain values for the average particle diameters and thermal inertias shown in Figure 2c. The average particle diameter represents the response of an ideal surface, uniformly composed of one particle size, completely filling the resolution cell area; such a surface would have temperatures consistent with the thermal inertias obtained from the nighttime temperature observations (3, 4). A mixture of larger and smaller particles can result in an average particle diameter intermediate between the true sizes. The difference between 11 μm and 20 μm temperatures for the entire region indicates that there is a combination of blocks and finer material both on and off the shield; in this case, the average particle size provides a measure of the relative contribution from larger blocks. The albedo of the surface was taken as 0.25 for all of the data; a $\pm$0.05 albedo change from this value results in a $\mp$0.15 thermal inertia change. It should be noted that improved elevation data could alter the corrected values of Figure 2c; a $\pm$1 km elevation change from the profile in Figure 2b would result in a $\pm$0.12 thermal inertia change.

The IRTM data indicate that the entire shield is surfaced by particles with relatively uniform average size. Mariner 9 studies suggested that elevation effects alone could not account for the low temperatures of the Tharsis area (5). The shield material is coarser (blockier) than the surrounding plains; moderate resolution thermal mapping indicates Ascraeus Mons, as well as the other large shields, are within an immense region of finer average particle size (3, 6). The sharp contact between the shield and the plains, coincident with the average particle size changes and break in slope, emphasizes the distinct nature of these two units. The shield and the plains may have had different histories and/or resurfacing processes active on them. The caldera walls have the largest average particle sizes for the shield (three were detected), indicating the rough surface texture visible in the images continues down to the size of individual blocks or particles. The lowermost caldera floor and the summit areas within ~10 km of the caldera rim have similar, lower average particle sizes than the shield as a whole. The caldera floor appears smoother in the images than the summit area; presumably some fine component has been added to both of these surfaces and it is sufficiently thin

ASCRAEUS MONS: VOLCANIC SURFACE PROPERTIES

Zimbelman, J. R. and Greeley, R.

that the summit flows are not masked. Theoretical considerations for martian eruptions indicate that ash deposits may have resulted from explosive volcanism (7). It is possible that the finer material at the caldera rim is ash but the lack of a systematic trend of fine material toward the summit limits the potential distribution of ash. It is unlikely that extensive ash eruptions occurred unless they were so widely dispersed that the entire shield was covered. This apparent lack of ash is consistent with the lack of photogeologic evidence for explosive activity associated with caldera collapse (8).

A local deviation from the average shield particle diameter occurs at longitude 103°. This corresponds to a terrace on the shield flank, as noted on other shields as well (9). Viking images provide no indication for the distinction of this terrace or for the lack of distinction of other terraces also included in the data. A fresh crater at longitude 102.3° has a blockier surface much like a similar crater in Syrtis Major (4). The symmetric variation in particle size for the plains immediately adjacent to the shield have no associated surface features visible in the images.

In summary, the Ascraeus Mons shield material is clearly distinct in surface properties from the surrounding plains. The shield material displays an uniform average particle size over its entire profile. The caldera walls are considerably blockier than either the caldera floor or the summit area around the caldera rim. These observations make it difficult for the volcano to have experienced large explosive activity or to be the source for the finer average grain size of the surrounding plains.

References

(1) Carr M. H. (1975) U. S. Geol. Surv. Map I–893. (2) Jakosky B. J. (1979) *J. Geophys. Res. 84,* 8252–8262. (3) Kieffer H. H. et al. (1977) *J. Geophys. Res. 82,* 4249–4291. (4) Zimbelman J. R. and Greeley R. (1981) *Lunar and Planet. Sci. XII,* 1230–1232. (5) Kieffer H. H. et al. (1973) *J. Geophys. Res. 78,* 4291–4312. (6) Zimbelman J. R. and Kieffer H. H. (1979) *J. Geophys. Res. 84,* 8239–8251. (7) Wilson L. and Head J. W. (1981) *Lunar and Planet. Sci. XII,* 1194–1196. (8) Mouginis-Mark P. (1981) *Lunar and Planet. Sci. XII,* 726–728. (9) Carr M. H. et al. (1977) *J. Geophys. Res. 82,* 3985–4015. (10) U. S. Geological Survey Topographic Map I–977 (1976).

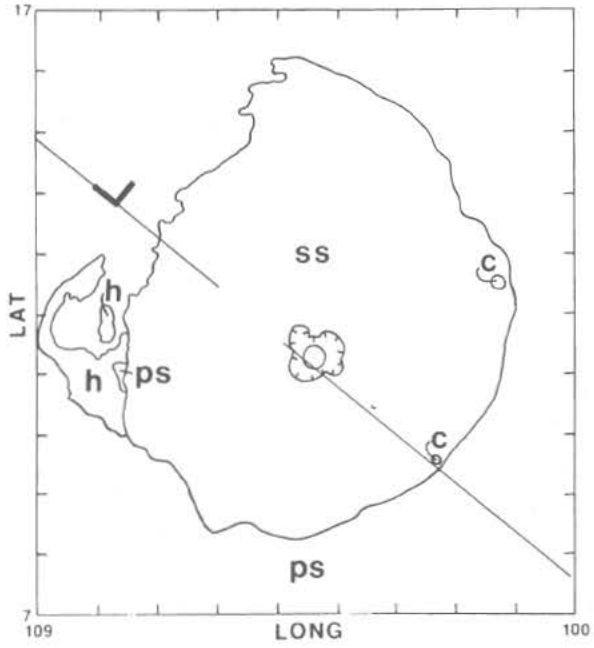

FIGURE 1

Figure 1. Geologic sketch map of Ascraeus Mons, after Carr (1). Units: ss–sparsely cratered shield material, ps–sparsely cratered plains material, h–hilly material, c–fresh crater material. Diagonal line indicates IRTM groundtrack and chevron orientation (gap is result of in-flight calibration).

Figure 2. a) Simplified version of IRTM data. Curve indicates average temperature for a given longitude. Local temperature variations are indicated as vertical lines with a dot at the extreme value. Data are from rev 543 of orbiter 1; midnight corresponds to longitude 102°. b) Elevation profile along groundtrack shown in figure 1. Data are from (10). c) Thermal data after correction for elevation effects. Average particle diameters and their corresponding thermal inertias are from (5). Albedo = 0.25.

ASCRAEUS MONS: VOLCANIC SURFACE PROPERTIES

Zimbelman, J. R. and Greeley, R.

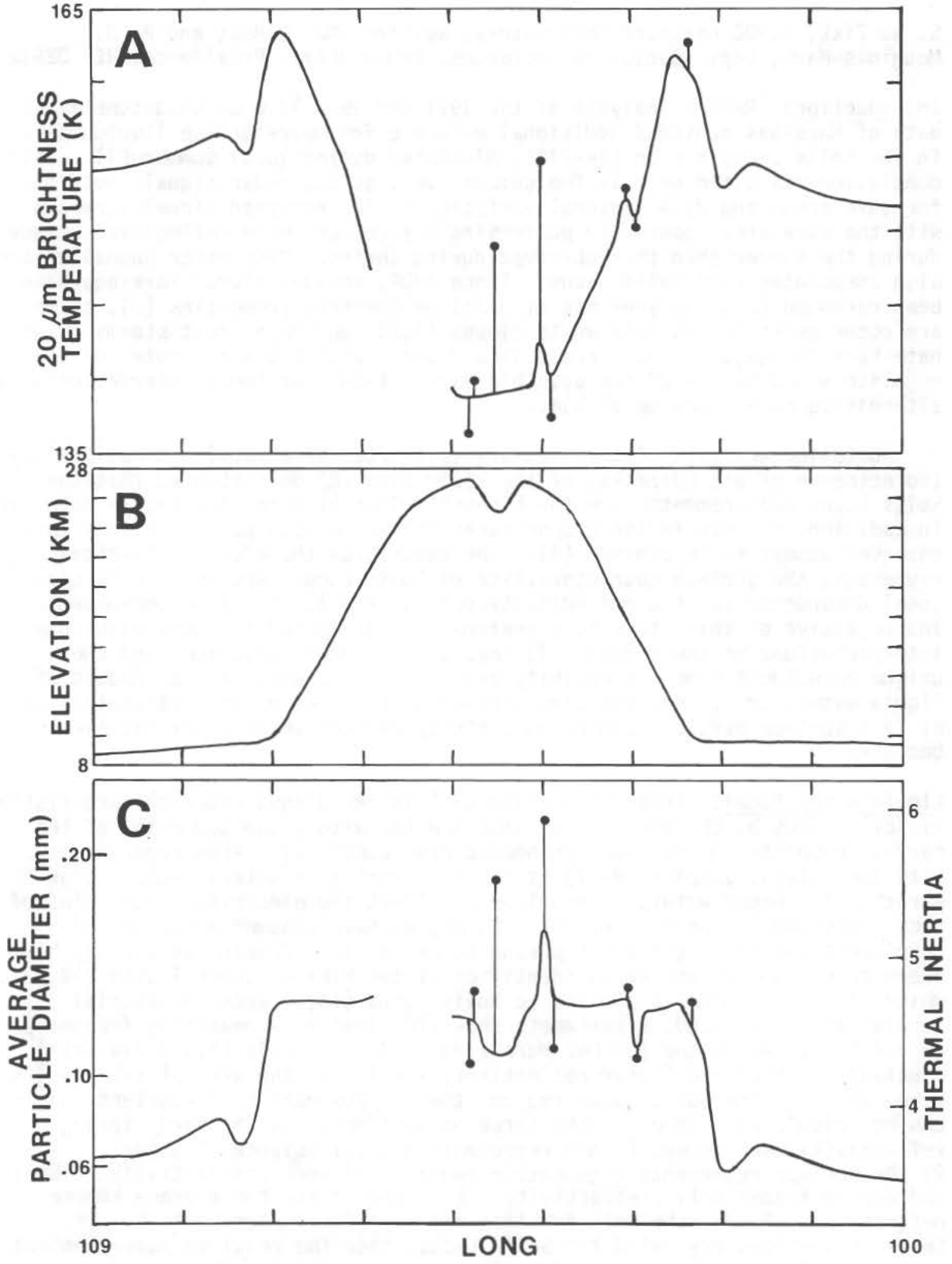

FIGURE 2

ALTERNATIVE MODELS FOR THE SOLIS LACUS RADAR ANOMALY ON MARS.

S. H. Zisk, NEROC Haystack Observatory, Westford MA 01886; and P. J. Mouginis-Mark, Dept. Geological Sciences, Brown Univ., Providence, RI 02912

Introduction: Recent Analysis of the 1971 and 1973 12.6 cm Goldstone radar data of Mars has provided additional evidence for near-surface liquid water in the Solis Lacus region (14-21°S, 84-100°W) during local summer (1). This conclusion was based on: 1) The unique, very strong radar signals returned for this area; and 2) A seasonal variation in the returned signal strength, with the same area apparently possessing a smoother, more reflective surface during the summer than that observed during spring. Many other anomalies are also associated with Solis Lacus: Since 1909, unusual albedo markings have been recorded (2), the area has atypical photometric properties (3), there are occurrences of discrete white clouds (4,5), and major dust storms originate here (5,6,7). In each case, liquid water within the top meter of the regolith would be one of the possible explanations for these observations, but alternative models may be viable.

Detailed analysis of the accuracy (estimates of errors) and reliability (coincidence of groundtracks) of the radar data (8) demonstrated that the Solis Lacus measurements have the highest reliability for the entire data set. In addition, offsets in the groundtracks for which seasonal variations were observed appear to be minimal (8). The radar data therefore realistically represents the surface characteristics of Solis Lacus, and the strong seasonal dependence for the reflectivity values (Fig.1) is a true phenomenon. The objective of this study is therefore to address the two most plausible interpretations of these data: 1) That the seasonal variation (and the unique coincident high reflectivity and C-factor values) is the product of liquid water; or 2) That the time variation is caused by the redistribution of fine surface particles covering a highly reflective layer of massive bedrock.

Liquid water Model: This model would explain the unique radar characteristics of Solis Lacus by the presence of liquid water within the top meter of the martian regolith during southern hemisphere summer (1). From experiments with terrestrial samples (9-11) it is clear that free water, rather than structurally bound water, is required to affect the electrical properties of rocks observed by radar. For Solis Lacus, we have assumed a variety of regolith types ranging from pure sand to dense clay, drawing an analogy between these samples and soils identified at the Viking Lander 1 site (12,13), which is morphologically similar to Solis Lacus (14). When terrestrial samples are dessicated, experiments show (10) that at a measuring frequency of 1.4 GHz (near to the 2.4 GHz Mars radar) all the soils have a dielectric constant of about 3.0 (radar reflectivity $\cong$ 6%). If the terrestrial results were valid for the Solis Lacus region, then approximate water-content values can be calculated. Here we make three assumptions: 1) The early spring reflectivity measurement ($\sim$ 8%) represents a total absence of water; 2) the surface represents a geometric addition of rock (reflectivity = 16%); and dry or frozen soil (reflectivity = 6%); and 3) for the average summer reflectivity of 12%, the soil fraction has a uniform water content. If these assumptions are valid for Solis Lacus, then the required water content during local summer would vary from 8% by volume if the soil were sand, to 12% by volume in clay (10). Other water, soil and rock distributions are

Solis Lacus Radar Anomaly

Zisk, S. H. and Mouginis-Mark, P. J.

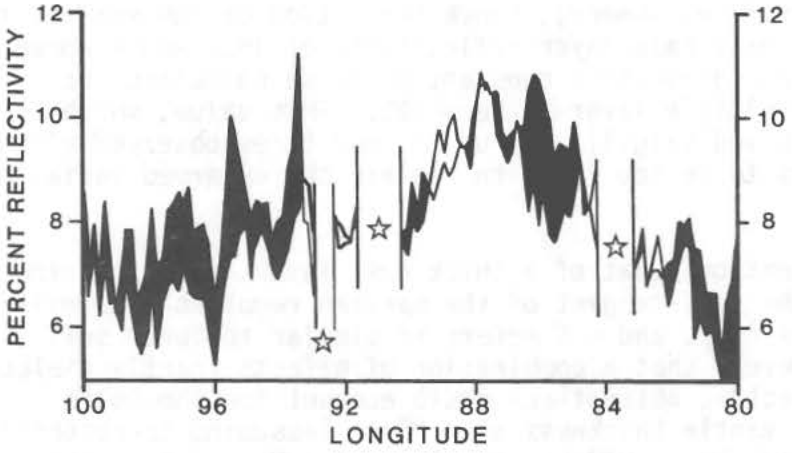

Fig. 1: Differences in radar reflectivity at 15.44°S for Solis Lacus. Black areas denote places where the reflectivity increased between L_S = 258° and L_S = 273°. Stars denote points where data for one or both periods were not obtained.

likely, however, (e.g. damp patches surrounded by dry areas, ref. 1), in which case the local concentration of liquid water may exceed the above values in order to produce the observed change in reflectivity.

It should be emphasized that these water values were predicted from laboratory experiments using fresh water at room temperature (10). It is likely that water on Mars would be highly saline and therefore more likely to exist in liquid form at some seasons (1, 15). The consequences of this water chemistry on the radar characteristics of Solis Lacus are unknown, however, due to the lack of experimental data at low temperatures and pressures. Thus a more exact calculation of the amount of water needed to produce the radar anomaly remains undetermined. In addition, from the analysis of blue brightenings associated with dust storms originating in Solis Lacus (4,5), it appears that there is a net outflow of water vapor from the area, implying that any such water must be replenished on an annual basis.

Soil/Dust Model: Various mechanisms are possible whereby a surface soil layer overlies a highly reflective layer of bedrock in Solis Lacus, and that this layer is deposited and removed on a seasonal basis. From measurements of suspended particles originating from Solis Lacus, it is apparent that neither the composition (16), nor particle size (17) for this locality is different from other areas of Mars. Thus, for a soil/dust model to be viable, the cause of the variable radar reflectivity must only be due to the thickness of the cover, which can thus be calculated from the masking effect required to explain the radar measurements. For a variable-thickness layer (that is, a variation of at least 1/4 wavelength, or ~3 cm in mantle thickness over the 10x80 km area of the radar resolution cell), the mean reflectivity will depend on the dielectric constants of the soil and fixed-surface layer (18). Although no specific data are available for Mars, a comparison between terrestrial (9-11, 19) and lunar samples (18, 20) shows that loss tangents for these two planets vary by about an order of magnitude, we assume that Mars will have an intermediate value between these two extremes.

A possible mantling mechanism on Mars could take one of two forms: 1) A thin, essentially loss-free layer acting as a matching filter; and 2) A thick layer in part masking the underlying reflection by its signal-absorbing qualities. In either case, the soil-free condition corresponds

to the maximum reflectivity (i.e. summer), since the action of the soil is to reduce the reflectivity. For a base layer reflectivity of 16%, and a worse case soil reflectivity of 3% (dielectric constant < 2), we calculate the mean reflectivity for the multiple layer to be ∿ 12%. This value, which is over twice the minimum observed (Fig.1), and up to four times observed elsewhere on Mars (21), appears to be too large to explain the observed variability in the radar data.

The alternative explanation, that of a thick dust layer, would require a layer ∿ 50 cm thick if the loss-tangent of the martian regolith is similar to terrestrial rock powders (19), and ∿ 5 meters if similar to lunar soil (18). It is possible, however, that a combination of effects (partly dielectric matching, partly dielectric absorption) could account for the Solis Lacus radar anomaly with a mantle thickness of ∿ 20 cm (assuming terrestrial loss tangents). Such a thickness would be very large for Mars, since the material must all be removed in a period of ∿ 10 weeks (1), which is an excessive erosion rate when compared to observations from the Viking Landers (22). Because either soil/dust model would require the removel and subsequent deposition (or recreation) of a comparable layer by the next martian year, we believe that a mantle model is the less likely explanation of the observed radar characteristics of Solis Lacus. The liquid water model (1) remains the most plausible, albeit controversial, explanation for this phenomenon.

References: 1) Zisk S.H. & Mouginis-Mark P.J. (1980) Nature 288, 735-738. 2) Dollfus A. (1973) 1st. Int. Colloq. Mars. CalTech. 3) Young A.T. & Collins B. (1971) J. Geophys. Res. 76, 432-437. 4) Smith A. & Smith B. (1972) Icarus 16, 509-521. 5) Huguenin R.L. et al. (1979)NASA-TM 80339, 208-214. 6) Huguenin R.L. et al. (1980) NASA-TM 81776, 215-216. 7) Martin L.J. (1974) Icarus 23, 108-115. 8) Zisk S.H. & Mouginis-Mark P.J. (1981) Lunar Plan. Sci. XII, 1239-1241. 9) Katsube T.J. & Collett L.S. (1973) Proc. Lunar Sci. Conf. 4th, 3111-3131. 10) Wang J.R. & Schumugge T.J. (1980) IEEE Trans. Geosci. Rem. Sen. GE-18, 288-295. 11) Olhoeft G.R. (1981) J. Geophys. Res. 86, 931-936. 12) Moore H.J. et al. (1977) J. Geophys. Res. 82 4497-4523. 13) Moore H.J. et al. (1979) J. Geophys. Res. 84, 8365-8377. 14) Mouginis-Mark P.J. et al. Lunar Plan. Sci. XI, 762-764. 15) Brass G.W. (1980) Icarus 42, 20-28. 16) McCord T.B. et al. (1977) Icarus 31, 25-39. 17) Pang K. & Hord C.W. (1973) Icarus 18, 481-488. 18) Gold T. et al. (1976) Proc. Lunar Sci. Conf. 7th, 2593-2603. 19) Campbell M.J. & Ulrichs J. (1969) J. Geophys. Res. 74, 5867-5881. 20) Olhoeft G.R. et al. (1975) Proc. Lunar Sci. Conf. 6th, 3333-3342. 21) Downs G.S. et al. (1975) Icarus 26, 273-312. 22) Arvidson R.E. et al. (1979) Nature 278, 533-535.

WATER VAPOR DISTRIBUTION IN THE MARTIAN ATMOSPHERE DURING NORTHERN SPRING: DATA FROM THREE MARS' YEARS; Richard W. Zurek, Jet Propulsion Lab/ California Institute of Technology, Pasadena, CA 91109, and Lisa A. Wainio, Cal State University, Los Angeles, CA 90032

Data taken during the Viking Survey Mission by the Mars Atmospheric Water Vapor Detector (MAWD) onboard Viking Orbiter 1 have been used to examine the interannual variability of water vapor in the Martian atmosphere from late northern winter (L_s = 340°) through spring to early northern summer (L_s = 120°). For the L_s range 80° to 120°, data from three consecutive Martian years are now available. Because the Survey Mission data are not continuous in L_s and generally have poor longitudinal coverage as well, period maps (global displays of water vapor in 10° x 10° spatial bins for periods covering 15° of L_s) comparable to those in (1,2) have not been constructed. Instead, the Survey Mission data have been used to define various longitudinal and temporal constraints (typically ±5° in L_s) which are then imposed on the more numerous data from the earlier nominal and extended Viking missions.

The Survey Mission data confirm the major latitudinal trends for this L_s period indicated by analysis of the earlier data (2,3): column water abundances increase with latitude from nearly zero amounts at the edge of the south polar seasonal cap to moderate quantities (10-20 pr μm) in northern midlatitudes. To the north of these latitudes, the water amounts decrease with increasing latitude during much of northern spring, but continue to increase right up to the pole during early summer. The most noteworthy differences between the Survey Mission data and the earlier observations are: 1) smaller water abundances observed during spring ($25° \leq L_s \leq 65$) north of 70° for the third year data, except for 2) a temporary reversal in the third year at $L_s \sim 56°$ of the latitudinal gradient of atmospheric water vapor north of 45°, and 3) appreciably more (increases of 10-15 pr μm) water vapor north of 30° at northern summer solstice of the third Martian year relative to the earlier years observed by Viking. The first of these differences, namely the smaller observed water amounts in the arctic during the third year, may be due to the masking effects of a polar haze. Different rates of release or quantities of water available for release from year to year in the receding north polar seasonal cap may also play a role. Besides providing strong evidence that such differences do occur, the reversal of the latitudinal gradient of water vapor noted above is strongly reminiscent of an apparent release of water from the receding south polar seasonal cap observed during southern spring (4).

1. Farmer C. B., Davies D. W., Holland A. L., LaPorte D. D. and Doms P. E. (1977) J. Geophys. Res. 82, p. 4225-4247.

2. Jakosky B. M. and Farmer C. B. (1981) In preparation.

3. Farmer C. B. and Doms P. E. (1979) J. Geophys. Res. 84, p. 8289-8293.

4. Davies D. W. and Wainio L. A. (1981) Icarus, in press.

HEAVENLY BODY INDEX*

*Pagination refers to first page of the paper in which a heavenly body is cited.

SUBJECT INDEX*

*Pagination refers to first page of the paper in which a subject is cited.

E

F

G

H

I

J

K

L

M

N

O

P

R

S

T

U

V

W

X

Y

AUTHOR INDEX*

*Pagination refers to the first page of the paper in which an author is cited.

I

J

K

L

M

N

P

R

S

T

V

W

Y

Z